UAB
Universitat Autònoma de Barcelona

Nanostructured Metallic Complexes as Antitumoral Selective Agents

Roger Gómez Herrera

ADVERTIMENT. L'accés als continguts d'aquesta tesi queda condicionat a l'acceptació de les condicions d'ús establertes per la següent llicència Creative Commons: https://creativecommons.org/licenses/?lang=ca

ADVERTENCIA. El acceso a los contenidos de esta tesis queda condicionado a la aceptación de las condiciones de uso establecidas por la siguiente licencia Creative Commons: https://creativecommons.org/licenses/?lang=es

WARNING. The access to the contents of this doctoral thesis it is limited to the acceptance of the use conditions set by the following Creative Commons license: https://creativecommons.org/licenses/?lang=en

Universitat Autònoma de Barcelona

Departament de Química

Facultat de Ciències

Nanostructured Metallic Complexes as Antitumoral Selective Agents

Roger Gómez Herrera

Ph.D. Thesis, 2025

Ph.D. in Materials Science

Catalan Institute of Nanoscience and Nanotechnology

Director:

Prof. Daniel Ruiz Molina

Dr. Fernando Novio Vázquez

Tutor:

Dr. Fernando Novio Vázquez

Memòria presentada per aspirar al Grau de Doctor per Roger Gómez Herrera

Roger Gómez Herrera

Vist i Plau,

Prof. Daniel Ruiz Molina

(Director)

Dr. Fernando Novio Vázquez

(Director i Tutor)





Bellaterra, 10 d'octubre de 2025

Fer el pas d'una disciplina a una altre ha estat el repte més gran, però també la meva millor escola; Entendre que adaptar-me no és perdre les arrels, però estendre-les en un sòl diferent.

Agraïments

Acabar una Tesi és entendre que no podrà ser mai perfecte, i si ho penses, llavors segur que no ho és. Per molt esforç que un hi posi, mai serà capaç de posar en lletra i dades tot allò que vol i desitja. La realitat ens torça i obliga a prendre camins que un voldria esperar no veure. Però també ens fa créixer, i aquells senders foscos i desconeguts que hom potser no vam voler recórrer en un principi, s'acaben convertint en els més idonis i adequats per arribar allà on desitgem. Al final del dia, tot és estar ben preparat i acceptar que el camí mai serà fàcil. Com diu el meu director de Tesi *"un mar tranquil no ha fet mai bon mariner".* Encara que a vegades va seguit d'un *"me cogeré a estos datos como naufrago a un palo"* però aquesta última part no fa falta recordar-la gaire...

Però ara arriba el moment que tots desitgeu, quan començo a mencionar persones i us busqueu.

Aquesta Tesi va començar molt abans de la meva inscripció a l'escola de doctorat i no es pot entendre sense una petita estada a l'estranger, la qual tothom que m'envolta ja està cansat de sentir-me repetir vegada rere vegada. Acabat de sortir de la carrera i el màster, no tenia les idees clares, però em va sorgir d'anar a fer una estada a la universitat de Marburg, Alemanya. Allà vaig passar uns mesos que no oblidaré, plens de bons moments però també de dolents. Si mai he estat a punt d'abandonar la Tesi va ser llavors, malgrat encara no haver-la començat. La meva estada em va fer entendre el mal tràngol que alguns doctorands han passat, i que podria jo també passar. Sort de les persones que em van envoltar en aquell període, que em van ajudar a tirar endavant i mantenir l'esperança per a començar el doctorat en quan tornés a casa. Gràcies **Lei**, **Patrick**, **Van Tuan**, **Valeska**, **Anett** i **Chiraf**.

Un cop retornat d'aquesta estada, ja sí, oficialment vaig començar el doctorat. Primer a un entorn del qual n'era especialment familiar, la torre de química de la UAB. Allà em vaig retrobar amb antics companys; **Daniel Torralba**, amb qui entre punya i punya vam, si més no, crear una creixent amistat, i qui a dia d'avui encara em pregunta *"¿Por qué tienes móvil si no usas nunca WhatsApp para avisarme?"*. **Alba López**, amb qui hem compartit la carrera, el màster i per a sorpresa de tots dos també el doctorat, el mateix grup d'investigació i centre... dues vegades. Sempre he admirat la teva capacitat de portar la tesi i m'has ajudat a tranquil·litzar-me en aquells moments nerviosos. Tu no ho sabies, però m'has marcat camí. **Marc Baten**, per mi vas ser aquell mentor no oficial a les meves etapes d'estudiant. Entenies que de la inexperiència no en pot sortir la perfecció, i et prenies el temps que fes falta per ensenyar-nos i fer-nos, encara que només fos una mica, persones més competents. **Marc Gómez**, no puc imaginar el laboratori 457 si no és amb tu, de principi a fi. Tu sempre n'has format part, en totes les etapes que he passat per allà, com a veí del laboratori del davant. **Jaume Otaegui**, tot i que només vam compartir unes horetes a l'UV d'en Jordi, sorprenentment els nostres camins es van tornar a creuar quan vaig anar a l'ICN2. Has sigut, indubtablement, una persona amb gran vocació per formar les noves generacions.

També vaig conèixer cares noves. Com tots aquells estudiants que només m'han acompanyat un temps fugaç; **Josep** a qui espero que el doctorat et vagui tan bé com el talent que has mostrat al laboratori. **Joana**, amb el potencial que mostraves no dubto que hagis aconseguit les teves metes en la indústria. **Oriol** i **Mario**, amb qui només vam compartir unes setmanes, però també espero

que hagueu aconseguit les vostres metes. A tots aquells estudiants que ara empreneu els vostres primers passos fora la universitat, només puc desitjar que no perdeu els vostres somnis i els perseguiu fins que el cor us digui prou. Però aquests no són els únics estudiants que vaig conèixer; **Cristina** i **Pau**, sempre aconseguíeu irradiar una felicitat que pocs mai aconseguiran. **Aleix**. Ens vam inscriure alhora al doctorat, i quan buscava ajuda o tenia dubtes sempre recorria a tu. Sempre t'has mostrat amb una tranquil·litat que m'ha relaxat en aquells moments més tensos. **Amanda**, a qui he vist des del TFG al TFM i al doctorat, sempre he trobat molt encoratjador com has anat superant-te i creixent.

Més endavant, vaig canviar de centre, ara a l'ICN2. En algun moment havia de deixar enrere el meu camp de química orgànica i començar a fer nanopartícules. La transició no va ser fàcil, era un centre desconegut, en un entorn desconegut, amb unes persones desconegudes i treballant en un camp d'investigació completament nou. En aquell moment tampoc érem gaires al grup, o com a mínim en el mateix edifici de l'ICN2.

Per sort, vaig ser guiat per persones a qui a dia d'avui encara admiro pel seu gran coneixement. **Salvi Suárez**, per mi has sigut el meu supervisor de laboratori extraoficial. , Quan més falta ha fet t'has posat a l'altura de la situació, i alhora ens has donat tota la corda que necessitàvem per créixer individual i independentment. Si necessitàvem consell et prenies el teu temps. Sempre m'has tractat amb professionalitat i alhora proximitat. I el més important, no ens has tractat mai amb condescendència ni has minimitzat les nostres propostes. M'has fet sentir com un investigador d'igual importància que qualsevol altre quan estaves tu assegut a la taula de col·laboracions. **Junda Zhang**, amb tu he compartit les mateixes pors i dubtes, els dos veníem d'un entorn de química orgànica i els dos hem tingut por de perdre el nostre arrelament. Amb tu hem discutit mecanismes de síntesi i intercanviat tècniques de purificació. Sempre recordaré quan vaig tenir la gran responsabilitat de fer-te arribar el certificat de matrimoni, i gairebé el llenço a les escombraries. **Ivana Cavaliere**, a dia d'avui potser encara no ho saps, però vas guanyar-te una reputació dintre tot el campus de la UAB com la noia del cross-flow. Precisament, tu me'n vas ensenyar, i espero que estiguis orgullosa que gràcies a aquesta ensenyança he pogut perpetuar el teu llinatge en les futures generacions. **Jose Bolaños**, et vas establir com el referent de bio de l'ICN2. En aquells moment no ens veiem gaire, sempre amunt i avall entre la facultat de medicina i l'ICN2. Ara, compartint despatx he vist el gran treballador que estàs fet.

Però que hi ha de tots aquells que he anat coneixent després?

Com a resultat de la meva feina, un dels primers llocs que vaig visitar van ser els meus companys de grup del CM3. **Àlex Julià**, et vas mostrar des del primer moment com una persona alegre i amb un immens coneixement. Eres de les poques persones que veia a l'hora que anava a treballar, encara que fos quan jo marxava i tu arribaves. Has sigut una persona amb extremada resiliència i has treballat dur per portar la teva spin-off fins on ha arribat a dia d'avui. Espero continuar veient el teu somriure i escoltar els teus comentaris sarcàstics, encara que ara t'has quedat sense poder preguntar-me *"i què, quan acabes la tesi?"* per esgrimir-me. **Noel Muñoz**, has sigut un d'aquells casos que ha passat d'estudiant de TFG-TFM a estudiant de doctorat en el mateix grup. Ets una persona molt treballadora i els teus èxits fins a dia d'avui ho demostren. També has demostrat ser una excel·lent persona, i pel que escolto, també mestre. **Aleix Carrascull**, ets una llegenda del grup, amb un gran coneixement tant de ciència com de tot el

que passa dins i fora del lab. He pogut fer molt bon safareig amb tu, i he passat molt bona companyia al teu costat. Ets d'aquelles persones amb qui no notes mai que et robin el temps.

Va ser per aquelles dates que vas tornar al grup, **Belén Pepió**. També vas ser una d'aquelles sorpreses que et fan veure com petit és el món. Vam compartir classe al màster, i ja allà ens havíem fet bons amics. Tu has sigut una d'aquelles acompanyants de trajecte dels qui et sents afligit quan t'acomiades. Hem compartir moltes nits de sèries i pel·lícules al teu pis, jocs de taula com Amperius III d'Adkin, cuina de panellets, i ens hem fet de confidents mil i una vegades. Et considero una de les millors amigues que podria haver fet en aquest trajecte. Ara que ja no estic al laboratori espero que recordis no ensumar mai cap reactiu desconegut. Amb tu també van arribar amistats com la de l'**Aritz**, qui m'ha ajudat a no veurem sobrepassat en les fases finals de la tesi, i en **Leandro**, qui sempre ha mostrat una expertesa i una saviesa envejable en un doctor.

En el temps que ha seguit, i perdoneu-me si no soc capaç de recordar amb exactitud l'ordre d'arribada, el nostre grup va créixer ràpidament de mida.

Paulino Duel, amb tu vaig trobar un company de química. Et vas mostrar una persona madura, capaç de prendre les decisions difícils davant situacions difícils. Et desitjo el millor allà on estiguis ara.

A la meva oficina van arribar companys nous; **Jennifer Pérez** et vas convertir en la meva MA. Vas treure un somriure al catalanet enfadat de darrere la pantalla de l'ordinador, que lentament em vas anar decorant. Hem compartit grans converses, sessions de gym i frases del Senyor dels Anells diàries. Ens em assessorat mútuament, hem fet safareig, i compartit secrets que pocs més coneixen. Hem anat a fer "zumitos" i creat la nostra tradició de capgirar tots els noms possibles. Em vas treure la tranquil·litat a la meva solitària oficina, però al final del dia, me n'alegro molt. T'odio amb molt d'amor. **Dani Lesta**, vas ser una força per al canvi, em vas donar alegries diàries i una filosofia de vida que et feia entendre que no tot és sempre tant important com et fan creure.

També hi va haver incorporacions al CM3; **Diptiman**, **Luzca** i **Sohini** vau entrar tots tres molt pròxims l'un de l'altre i vau omplir el CM3 d'un dinamisme que francament, no hi havia abans. Poc després vas arribar, **Lorenzo Vallan.** Et respecto pels teus grans coneixements, esperit aventurer en les teves estades a l'estranger i capacitat d'aprenentatge. Tens una curiositat natural que em fa redescobrir l'esperit d'investigador.

Maria Cristina, **Naroa** i **Mario** vau entrar a distink i, malgrat he tingut enveja eterna perquè no havíeu de fer presentacions de grup, he gaudit de la vostra companyia cada cop que veníeu a robar-me el forn.

Poc després va ser el teu torn, **Sara Pugliese**. Al principi potser et feia una mica de por i respecte, però espero que a dia d'avui ja no te'n faci tant. No he tingut mai cap problema en respondre't dubtes i fer-te de pseudopsicoleg. Has tingut un període mogut a l'ICN2, ple d'alts i baixos.Espero que amb la forta amistat que hem anat teixint, els alts cada vegada ho siguin més i els baixos cada vegada una miqueta menys. Ets una persona molt vàlida, intel·ligent i amb empenta. Has lluitat per adaptar-te en un país estrany amb un idioma estrany. Has fet l'esforç per aprendre de tot i tenir una mentalitat oberta. Molta força Sara!

Pol Ubago, no vas ser estudiant meu, però com ja t'he comentat alguna vegada, m'he sentit com l'avi que, a esquena dels teus pares, t'ha consentit científicament parlant. Espero no haver sigut massa dur quan et criticava sarcàsticament. Has de saber que vaig gaudir molt dels croissants que vas portar l'últim dia! Has pres bones decisions a la vida, i anar-te'n a estudiar a Dinamarca n'és una!

També he de fer especial menció a tots aquells estudiants de qui he sigut supervisor. **Núria Viader**, junts vam treballar en un mateix projecte descobrint alhora com avançar. Tu em creies molt intel·ligent, però només anava un pas per davant. **Francesco Pastorello** em vas fer patir algun moment, però una cosa que no puc negar són les memòries que a dia d'avui encara comparteixo de la teva estada. Em feies riure i passar una mica millor el dia a dia.

En els últims mesos de la Tesi també he conegut tota la família de l'IBB. **Marta** i **Eddi**, ens heu fet d'assessors cada vegada que teníem dubtes i em vau acollir al grup des del primer moment. **Pau**, vaig fer el teu doble quan vas marxar a Leiden i al tornar per fi et vaig poder conèixer. Ets una persona optimista, encara que de vegades massa. Gràcies per incloure'm en qualsevol activitat de grup. **David**, només una cosa a dir, de res pel paper. **Miguel**, m'has rebut cada dia a l'IBB amb un somriure, una broma o un comentari sarcàstic. Ets aquell que veu tothom arribar i algun dia, en acabar la tesis, marxar. Suposo que aquest dia m'ha arribat a mi.

També he d'agrair tots aquells amics que m'han acompanyat des del principi al final. Gràcies **Guillem Castilla**, has sigut un gran amic des de la carrera. Eres el meu contacte d'emergència quan necessitava alguna cosa urgent. També he pogut compartir temps amb tu, en natura mentre fèiem llenya o netejàvem la finca, una connexió que comparteixo amb poca gent. Desitjo que el teu canvi de carrera professional sigui tot un èxit, tinc tota la meva fe dipositada en tu! **Cristina Garcia** has sigut una amiga des de la meva infància i m'has seguit tota la meva trajectòria en investigació, saps tots els esforços que m'ha costat, igual com jo sé els teus. Ets una persona determinada amb qui sempre puc treure inspiració. **Adrià Malagón**, et considero la persona més pròxima de la carrera, mantenint el nostre vincle del cafè anual per posar-nos al dia. Espero no tornar a anar a la muntanya amb tu, perquè ja no tinc edat de jugar-me la vida en excursions de pixapi de Barcelona.

Daniel Ruíz, *"y la abuela fuma"*, *"Con estos bueyes tenemos que arar"*, *"Con estas alforjas tenemos que cargar"*, *"Me cago en la UAB"*, *"Eres un francotirador"* i moltes més són les frases que he escoltat de tu. Mai he sentit pressió en les reunions diàries amb tu i m'has assessorat sense pèls a la llengua. M'he sentit sempre al teu equip. M'has tractat com un adult i investigador. Has sigut un director excel·lent.

Claudio Roscini, les teves teories boges van desencadenar el capítol ,és important i que ha donat més feina d'aquesta Tesi. Per això, gràcies (però amb una mica de rancor). Ets una persona que no té problemes en tornar al laboratori quan algú t'ho demana, i això no és freqüent. Espero que mai canviïs i continuïs demostrant dia a dia el líder que estàs fet.

Fernando Novio, no sé com t'ho has fet però sempre ho has aconseguit, Sempre m'has trobat finançament quan ho necessitava. Sense tu, la Tesi hauria estat materialment impossible. Has sigut l'altra cara de la moneda, amb tu podia comptar on en Dani no arribava, i t'ho agraeixo.

Per descomptat, també he d'agrair tota la meva família, que m'han suportat en el dia a dia. Potser no acabàveu d'entendre com funcionava tot, però mai us ha fet falta per comprendre tots aquells moments en que estava nerviós, o parlava a les parets preparant presentacions. Heu sigut vitals per al meu èxit. **Mama**, **Papa,** gràcies de tot cor. **Aina**, **Bernat**, gràcies per fer-me companyia.

Finalment em queda només una persona per agrair.

Núria Basanta Pons, t'estimo. No ens ho esperàvem, però va sorgir. Potser van ser les hores rere hores que ens quedàvem fent ROS o fluorescència. Els experiments en MRI per agents de contrast. Els *in vivo* impossibles. Però poc a poc vam anar parlant més, primer a la feina, després fora. Ens anàvem trobant, i al final va acabar passant. Estic profundament agraït de tenir-te de companya de vida. Va ser total casualitat que treballéssim junts, però les col·laboracions tenen això, mai saps com poden acabar. I en el nostre cas han acabat en parella. La teva companyia ha sigut clau en tot moment, sobretot en els últims mesos de la tesi, de la qual m'has ajudat enormement. No puc esperar perquè arribi el teu torn, i siguis tu el sac de nervis a qui s'hagi d'aguantar.

A tots, la meva família, però sobretot l'última persona que he mencionat, us estimo. Heu format part de la meva vida igual com jo espero haver-ne format part de la vostra.

Roger Gómez Herrera

Abstract

Glioblastoma multiforme (GBM) is the most aggressive primary brain tumour in adults. The current clinical standard treatment, established back in 2005, includes surgical resection followed by radiotherapy and temozolomide chemotherapy. Still, GBM presents a median survival rate of less than two years and less than 6% five-year survival. This situation underscores the need to develop better therapeutic agents. Pt compounds, like cisplatin, remain among the most potent anticancer agents. However, these drugs encounter obstacles in GBM due to blood–brain barrier permeability, systemic toxicities, and resistance.

This Thesis develops on Pt-based drugs that address these barriers by exploring multi-target nanotherapies that improve tumour selectivity and targeting, minimize systemic exposure, while exploiting local therapeutic windows. In these lines we investigate combination therapies, and bioinspired biomaterials as strategies to overcome these limitations. More specifically, this Thesis focuses on four research lines whose novelty varies as described next:

First, Pt(IV) catechol-based coordination nanoparticles (CNP) formed by oxidative polymerization of a Pt(IV) prodrug monomer (**PtBC**). This platform yields melanin-like nanoparticles (NPs), a Trojan-horse approach for brain diseases, with pH and redox-sensitive Pt(IV) release.

Second, squaraine (SQ)-based Pt(II) supramolecular NPs combining photoactivated chemotherapy (PACT) and photodynamic (PDT) prospects of SQs. According with the experimental results, PACT was discarded while interesting PDT effects were found on SQ supramolecular NPs without Pt.

Third, a bi-functional core-shell NP was designed with a superparamagnetic iron-oxide (SPION) core and a zirconium-based CNP shell bearing 9,10-diphenylanthracene moieties. The shell is capable to store singlet oxygen under ultraviolet irradiation and release it on demand via magnetic hyperthermia (MHT) generated by the SPION core. *In vitro* studies on GL261 murine GBM model display a cooperative heat and reactive oxygen species (ROS) cytotoxicity effect. *In vivo* experiments demonstrated the core-shell NP to be highly specific and sensitive to traverse relaxation weighted (T_{2w}) magnetic resonance imaging. Unexpectedly, the platform demonstrated as selective contrast agent for bladder at very low concentrations, far from the GBM target. On this research a second NP platform based the CNP shell itself was developed and displayed excellent cytotoxic effect on GL261 murine GBM model under MHT stimulus.

Fourth, based on the PtBC monomer developed in the first approach, we developed bioinspired catechol-based Pt(IV) free-standing membranes (FSMs) as conformable, wet-adhesive patches for insertion into resection cavities. This FSMs are formed by oxidative co-polymerization between a **PtBC** monomer and an amine co-monomer to yield malleable membranes that release Pt locally. Physicochemical characterisation, controlled-release assays and *in vitro* cytotoxicity against GBM lines demonstrated the FSM's potential as a post-surgical local therapy with plausible ROS synergistic effects.

All in all, this Thesis provides proof-of-concepts for multimodal treatments, exploiting complementary mechanisms (DNA damage, oxidative stress, hyperthermia and sustained local delivery) to increase tumour selectivity and reduce systemic toxicity.

Table of Contents

TABLE OF CONTENTS ..... **I**

LIST OF ABBREVIATIONS ..... **V**

LIST OF MOLECULES ..... **IX**

CHAPTER 1 - GENERAL INTRODUCTION **1**

1.1. GLIOBLASTOMA **3**

1.1.1. Glioblastoma: Nature and Etiology 3
1.1.2. Symptoms and Incidence 4
1.1.3. Therapy Resistant Tumour Development 5
1.1.4. Prognosis and Available Treatments 6
1.1.4.1. Brief Historical Perspective 6
1.1.4.2. Temozolomide: Gold Standard Drug Treatment 7
1.1.4.3. Limitations of Temozolomide 8
1.1.4.4. Alternative Drugs to Temozolomide 8
1.1.5. Platinum-Based Drugs 9
1.1.5.1. Families and Areas of Application 9
1.1.5.2. Mechanisms of Action of Platinum-Based Drugs 11
1.1.5.3. Side Effects and Chemical Alternatives 13
1.1.6. Platinum-Based Drugs in Glioblastoma 16
1.1.6.1. Precedents 16
1.1.6.2. Limitations of Pt-Based Drugs 17
1.1.7. Use of Nanoparticles in Biomedical Applications 18
1.1.7.1. Properties of Nanoparticles 18
1.1.7.2. Representative Nanoformulations for Glioblastoma Treatment 19
1.1.7.3. Specific Platinum-Based Nanoformulations 20

1.2. SCOPE OF THIS THESIS **23**

1.2.1. Bioinspired Polymeric Neuromelanin-like Pt(IV) Nanoparticles 23
1.2.2. Supramolecular Photoactivatable Squaraine Pt(II) Nanoparticles 24
1.2.3. Pt-based Nanoparticles for Singlet Oxygen Storage and in-situ Magnetic-induced Release 26
1.2.4. Bioinspired Catechol-Based Pt(IV) Free-Standing Membranes for Post-Surgery Glioblastoma Treatment 27

1.3. REFERENCES **29**

CHAPTER 2 - THESIS OBJECTIVES **41**

CHAPTER 3 - BIOINSPIRED POLYMERIC NEUROMELANIN-LIKE PT(IV) AND SUPRAMOLECULAR PHOTOACTIVATABLE SQUARAINE PT(II) NANOPARTICLES **43**

3.1. INTRODUCTION **45**

3.1.1. Bioinspired Neuromelanin-like Pt(IV) Polymeric Nanoparticles 45
3.1.1.1. Precedents 45
3.1.1.2. Catechol-Based Nanoparticles 45
3.1.1.3. Oxidative Polymerisation 46
3.1.1.4. Our Proposed Platform 48
3.1.2. Supramolecular Photoactivatable Squaraine Pt(II) Nanoparticles 49

3.1.2.1. Squaraines 50
3.1.2.2. Squaraines in Photoactivated Chemotherapy 51
3.1.2.3. Supramolecular Squaraine Nanoformulations 52
3.1.2.4. Our Proposed Platform 53

3.2. OBJECTIVES 55

3.3. RESULTS AND DISCUSSIONS 57

3.3.1. Bioinspired Polymeric Neuromelanin-like Pt(IV) Nanoparticles 57
3.3.1.1. Synthesis of the Precursor PtBC 57
3.3.1.2. Synthesis of pPtBC NPs 62
3.3.1.3. Synthesis of pNDGA NPs 64
3.3.1.4. Platinum Drug Release 67
3.3.1.5. *In vitro* studies 68
3.3.1.6. *In vivo* Studies 73
3.3.2. Supramolecular Photoactivatable Squaraine Pt(II) Nanoparticles 77
3.3.2.1. Synthesis of SQL 77
3.3.2.2. Synthesis of SQC 80
3.3.2.3. Synthesis and Characterisation of Supramolecular SQL NPs 80
3.3.2.4. Synthesis and Characterisation of Supramolecular SQC NPs 82
3.3.2.5. SQL and SQL NP: An Optical Study Comparison 84
3.3.2.6. SQC and SQC NP: An Optical Comparison 89
3.3.2.7. Colloidal Stability of SQL NP under Physiological Conditions 90
3.3.2.8. Photodynamic Therapy properties of SQL NPs 92
3.3.2.9. *In vitro* studies of SQL NPs 96

3.4. CONCLUSIONS 99

3.4.1. Bioinspired Polymeric Neuromelanin-like Pt(IV) NPs 99
3.4.2. Supramolecular Photoactivatable Squaraine Pt(II) NPs 100

3.5. MATERIALS AND EXPERIMENTAL METHODS 101

3.5.1. Materials 101
3.5.2. Characterisation 101
3.5.3. *In vitro* assays 104
3.5.4. *In vivo* assays 107
3.5.5. Synthesis procedures 109

3.6. REFERENCES 119

3.7. ANNEXES 127

3.7.1. Bioinspired Polymeric Neuromelanin-like Pt(IV) Nanoparticles for Cancer Treatment 127
3.7.2. Supramolecular Photoactivatable Squaraine Pt(II) Nanoparticles 134

CHAPTER 4 - SINGLET OXYGEN STORAGE AND ON-DEMAND MAGNETIC INDUCED RELEASE FOR A MULTI-APPROACH THERAPY 153

4.1. INTRODUCTION 155

4.1.1. Reactive Oxygen Species 155
4.1.2. Photodynamic Therapy in Glioblastoma Treatment 155
4.1.3. Combination of Photodynamic Therapy and Platinum-Based Chemotherapy for Glioblastoma Treatment 155

4.1.4. Light-Independent ROS Generation Mechanisms 157
4.1.4.1. MHT as a Source of Heat in the Generation of ROS 158
4.1.4.2. Precedents of Combination Therapies Between ROS and MHT 158
4.1.5. Our Approach to ROS Generation via MHT 159
4.1.5.1. Role and families of Core-Shell Nanoparticles in Biomedicine 161

4.2. OBJECTIVES 165

4.3. RESULTS AND DISCUSSIONS 167

4.3.1. Core-shell pDPA-CNP@Fe NPs Platform 167
4.3.1.1. Synthesis of DPA-COOH 167
4.3.1.2. Synthesis of the Super Paramagnetic Iron Oxide NP Core 168
4.3.1.3. Synthesis and Characterisation of pDPA-CNP@Fe NPs 173
4.3.1.4. In vitro Characterisation of pDPA-CNP@Fe NPs 178
4.3.2. pDPA-CNP@Fe NP in Magnetic Resonance Imaging 180
4.3.2.1. Magnetic Resonance Imaging by SPIONs 180
4.3.2.2. *In vitro* Magnetic Resonance Imaging Phantoms 181
4.3.2.3. *In vivo* Magnetic Resonance Imaging Evaluation 183
4.3.3. pDPA-CNP@Fe NP as a Platform in Glioblastoma Treatment 189
4.3.3.1. Characterisation of Optical Properties of pDPA-CNP@Fe NPs 189
4.3.3.2. MHT as a Trigger for SO Release in pDPA-CNP@Fe NP 193
4.3.3.3. *In vitro* Cell Viability Assays of pDPA-CNP@Fe NP 196
4.3.4. Synthesis, Characterisation and Evaluation of Control Platform pDPA-CNP 198
4.3.4.1. Synthesis and Characterisation of pDPA-CNP 198
4.3.4.2. *In vitro* Studies of pDPA-CNP 205
4.3.4.3. Origin of the Interaction with AMFs 216
4.3.4.4. Zirconium Oxide Catalysed ROS Generation 223
4.3.4.5. Singlet Oxygen Load and Unload in pDPA-CNP 225

4.4. CONCLUSIONS 229

4.5. MATERIALS AND EXPERIMENTAL METHODS 231

4.5.1. Materials 231
4.5.2. Characterisations 231
4.5.3. *In vitro* assays 235
4.5.4. *In vivo* assays 238
4.5.5. Synthesis procedures 242

4.6. REFERENCES 247

4.7. ANNEXES 259

4.7.1. Conceptual explanations 259
4.7.1.1. Physicochemical Properties of Magnetic Nanoparticles 259
4.7.1.2. Hysteresis-Induced Heating Mechanisms 260
4.7.1.3. Current Challenges and Limitations of MHT 262
4.7.1.4. Examples of MHT in GBM Models 262
4.7.1.5. SO and Endoperoxide Formation 264
4.7.1.6. Endoperoxide Cleavage and SO Release 266
4.7.2. Experimental Data 269

CHAPTER 5 - DEVELOPMENT OF BIOINSPIRED CATECHOL-BASED PT(IV) FREE-STANDING MEMBRANES FOR POST-SURGERY GLIOBLASTOMA TREATMENT 297

5.1. INTRODUCTION 299

5.1.1. Glioblastoma Surgical Resection 299
5.1.2. Glioblastoma Post-Surgical Tumour Treatment 300
5.1.3. Advanced Biomaterials 301
5.1.3.1. Gliadel® Wafers in Initial Tumour Resection Surgery 301
5.1.3.2. Limitations of Gliadel® Wafers 302
5.1.4. Bioinspired Thin Films as Advanced Biomaterials 303
5.1.4.1. Overview of Thin Films as Advanced Biomaterials 303
5.1.4.2. Mussels as a source of inspiration 305
5.1.5. Catechol-Based Free-Standing Membranes 306
5.1.5.1. State of the Art on Catechol-Based FSMs 306
5.1.5.2. Our Approach to FSM Preparation 307
5.1.6. Bioinspired Catechol-Based Pt(IV) FSMs for Post-Surgery Glioblastoma Treatment 308
5.1.6.1. The Rationale for the Selection of FSMs as a Platform 308
5.1.6.2. Advantages of Incorporating a Pt(IV) Prodrug in FSMs 309
5.1.6.3. Design of Pt(IV)-based FSMs 309

5.2. OBJECTIVES 311

5.3. RESULTS AND DISCUSSIONS 313

5.3.1. Synthesis and Characterisation of FSM-PtBC 313
5.3.2. Studies on the Formation of FSM-PtBC 318
5.3.3. Platinum Content and Release Profile 321
5.3.4. Development of Control Membrane FSM-TrisCat 322
5.3.5. *In vitro* Cell Viability Evaluation 323
5.3.6. Post-*in vitro* Cell Viability FSM-PtBC Characterisation 326
5.3.6.1. Optical Analysis 327
5.3.6.2. Scanning Electron Microscopy Imaging 327
5.3.6.3. X-Ray Photoelectron Spectroscopy Analysis 328
5.3.7. Photothermal-Induced Heating of FSM-PtBC 330

5.4. CONCLUSIONS 333

5.5. MATERIALS AND EXPERIMENTAL METHODS 335

5.5.1. Materials 335
5.5.2. Characterisations 335
5.5.3. *In vitro* assays 336
5.5.4. Synthesis procedures 337

5.6. REFERENCES 339

5.7. ANNEXES 349

5.7.1. Conceptual Explanations 349
5.7.1.1. Advanced Biomaterials 349
5.7.1.2. Types of Advanced Biomaterials 350
5.7.1.3. Examples of DOPA-Containing Biomaterials in Biomedical Applications 354
5.7.2. Experimental Data 356

CHAPTER 6 - GENERAL CONCLUSIONS 361

List of Abbreviations

ABDA 9,10-anthracenediyl-bis(methylene)dimalonic acid

ACN Acetonitrile

AMF Alternating magnetic field

BBB Blood-brain barrier

BSA Bovine serum albumin

BTB Blood-tumour barrier

CA Contrast agent

CDDP Cisplatin

CED Convection-enhanced delivery

CNP Coordination nanoparticles

CNS Central nervous system

CT Chemotherapy

DA Dopamine

DCA Dichloroacetate

DCC N,N'-Dicyclohexylcarbodiimide

DCFCDA 2',7'-dichlorofluorescin diacetate

DHN 1,5-dihydroxynaphthalene

DHR123 Dihydrorhodamine 123

DLS Dynamic light scattering

DMF Dimethylformamide

DMSO Dimethyl sulfoxide

DNA Deoxyribonucleic acid

DOPA 3,4-dihydroxyphenylalanine

DSCP Disuccinic cisplatin

EA Elemental analysis

EDX Energy dispersive X-ray spectroscopy

EELS Electron energy loss spectroscopy

EGCG (−)-epigallocatechin-3-gallate

EGFR Epidermal growth factor receptors

ELNES Energy loss near edge structure

EPR Enhanced permeability retention

ETL Echo train length

FA Flip angle

FBS Fetal bovine serum

FC Field cooling

FDA Federal drug administration

FOV Field of view

FQY Fluorescence quantum yield

FSM Free-standing membrane

FTIR Fourier transform infrared

GBM Glioblastoma

GSH Glutathione

GSSG Glutathione disulfide

HAADF High-angle annular dark-field

HDAC Histone deacetylase

HPLC High-performance liquid chromatography

HRMS High resolution mass spectrometry

i.v. Intravenous

IC_{50} Half maximal inhibitory concentrations

ICP Inductively coupled plasma

iMRI Intraoperative magnetic resonance imaging

IMS Immune-enhancing metronomic schedule

IR Infrared

ISC Intersystem crossing

IT Inter-slice thickness

LbL Layer-by-layer

Mfp Mussel foot protein

MGMT O-6-methylguanine-DNA methyltransferase

MHT Magnetic hyperthermia

MilliQ® Ultrapure type 1

MMAE Monomethyl auristatin E

MNP Magnetic nanoparticles

MOF Metal organic framework

MRI Magnetic resonance imaging

MS Mass spectrometry

MSA Murine serum albumin

MSME Multi-slice multi-echo

MST Magnetic saturation

MTD Maximum tolerated dose

MTT 3-(4,5-dimethylthiazol-2-yl)-2,5-diphenyltetrazolium bromide

MTX Matrix size

MWCO Molecular weight cut-off

NDGA Nordihydroguaiaretic acid

NER Nucleotide excision repair

NEX Number of excitations

NHS N-Hydroxysuccinimide

NIR Near-infrared

NMR Nuclear magnetic resonance

NP Nanoparticle

NS Number of slices

NTA Nanoparticle tracking analysis

OES Optical emission spectrometry

p.i. post-implantation

PACT Photoactivated chemotherapy

PB Phosphate buffer

PBS Phosphate buffer saline

PDA Polydopamine

PDI Polydispersity index

PDT Photodynamic therapy

PEG Polyethylene glycol

PET Positron emission tomography

PGA Polyglycolide

PI Phototoxicity index

PI3K Phosphatidylinositol 3-kinase

PLA Polylactic acid

pNDGA Polymeric **NDGA**

pPtBC Polymeric **PtBC**

PS Photosensitiser

PtBC Pt(IV) bis-catechol

PTT Photothermal therapy

r_1 Longitudinal relaxivity

r_2 Transversal relaxivity

RARE Rapid acquisition with relaxation enhancement

RB Rose Bengal

RCE Relative contrast enhancement

RES Reticuloendothelial system

RGD Arginylgycylaspartic acid

RNA Ribonucleic acid

ROI Region of interest

ROS Reactive oxygen species

RT Radiotherapy

SAR Specific absorption rate

SDS Sodium dodecyl sulphate

SE Standard of error mean

SEM Scanning electron microscopy

SO Singlet oxygen

SOSG Singlet oxygen sensor green

SPION Superparamagnetic iron oxide

SQ Squaraine

SQC Pt(II) squaraine complex

SQL Squaraine ligand

ST Slice thickness

STEM Scanning transmission electron microscopy

T_1 Longitudinal relaxation

T_{1w} T_1-weighted

T_2 Traverse relaxation

T_{2w} T_2-weighted

TA Acquisition time

TE Echo time

TE_{eff} Effective echo time

TEM Transmission electron microscopy

TF Thin film

TGA Thermogravimetric analysis

THF Tetrahydrofuran

TME Tumour microenvironment

TMZ Temozolomide

TR Repetition time

UV Ultraviolet

VTR Variable repetition time

XPS X-ray photoelectron spectroscopy

XRD X-ray diffraction

ZFC Zero-field cooling

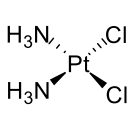
ε Molar extinction coefficient

Φ_Δ Quantum yield

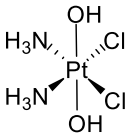
NT Non-toxic

List of Molecules

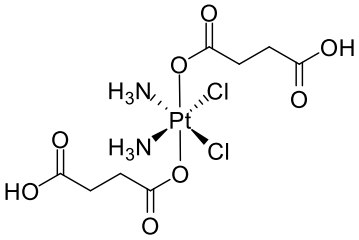
Chapter's 3 Molecules



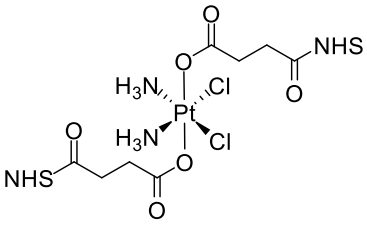
CDDP



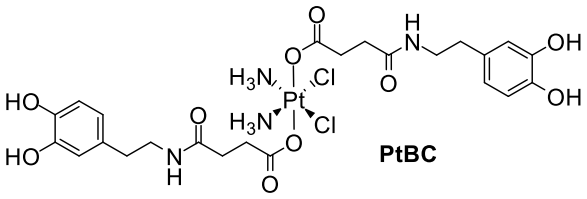
1



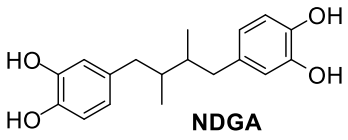
DSCP



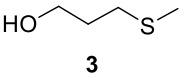
2



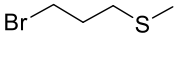
PtBC



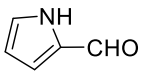
NDGA



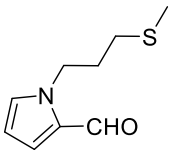
3



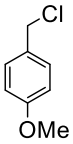
4



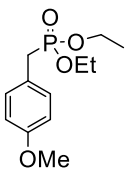
5



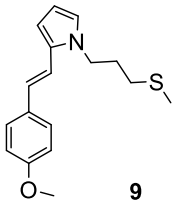
6



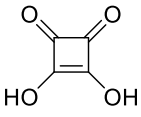
7



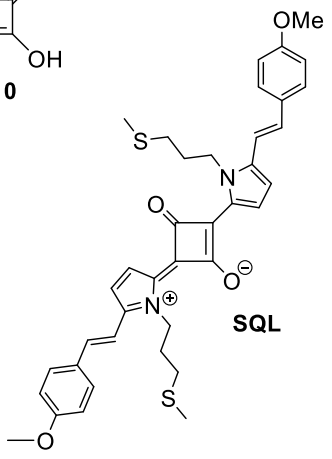
8



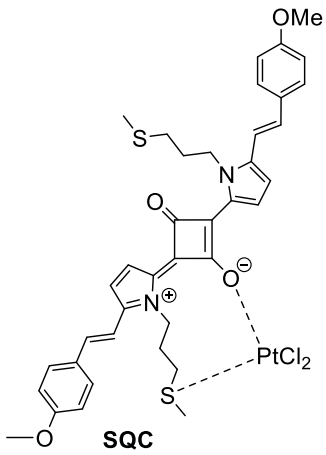
9



10

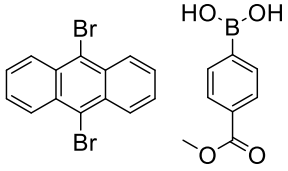


SQL



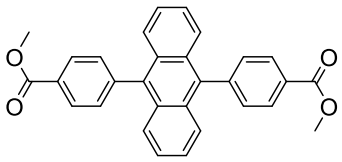
SQC

Chapter's 4 Molecules

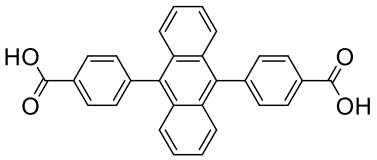


11

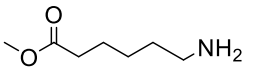
12



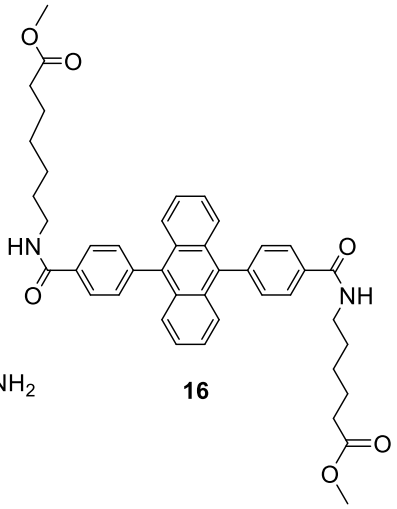
13



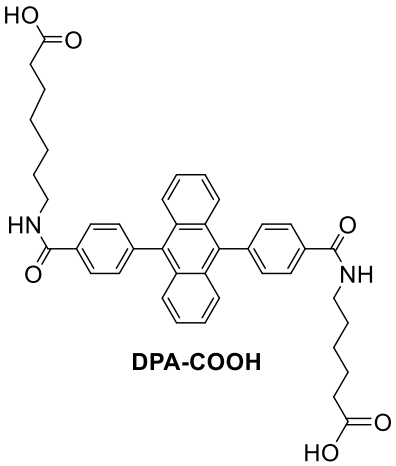
14



15



16



DPA-COOH

Chapter 1

General Introduction

In this Chapter, we delve into glioblastoma (GBM), presenting as the most aggressive and lethal form of primary brain tumour in adults. This Chapter provides an in-depth evaluation of the biological, clinical, and therapeutic approaches to GBM treatment. A particular focus has been put into explaining the current limitations of the standard of care treatments, the exploration of alternative chemotherapeutic strategies, and how they provide insufficient results for its treatment.

For this reason, Pt-based compounds are evaluated as a potential therapeutic alternative, analysing their mechanisms of action, resistance delivery challenges, and systemic toxicities.

1.1. Glioblastoma

Gliomas are brain tumours thought to derive from neurological stem or progenitor cells,[1] and the most common type of primary brain tumour, accounting for 80% of all malignant ones. Malignant gliomas are responsible for 2.5% deaths in the whole aggregate of cancer deaths, and are the third most important cause of death, from cancer, in persons 15 to 34 years of age.[2,3] These tumours can then be sub-classified according to their originating cell (supportive glial cells), including: astrocytoma, oligodendroglioma, mixed gliomas, and ependymoma.[4] The World Health Organisation (WHO) then classifies each of these tumours based on histopathological impression, specifically by the presence of nuclear pleomorphism, increased mitotic activity and cellularity, endothelial cell proliferation, and necrosis, each adding one grade to the tumour up to grade IV.[5]

1.1.1. Glioblastoma: Nature and Etiology

GBM is the most common and life-threatening glioma brain tumour in adults.[6] GBM originates from star-shaped glial cells, falling therefore within the astrocytoma sub-classification.[7] GBM is characterised histologically by considerable cellularity and mitotic activity, vascular proliferation, and necrosis, thus being classified as a grade IV astrocytoma or just grade IV.[8,9] Moreover, GBM is the most common adult glioma, accounting for 54% of all gliomas or 82% of all malignant gliomas (Figure **1.1**).[3] GBM cells are pleomorphic, meaning these tumours vary in shape and size, causing GBM to give rise to the term "glioblastoma multiforme" in the past.[8]

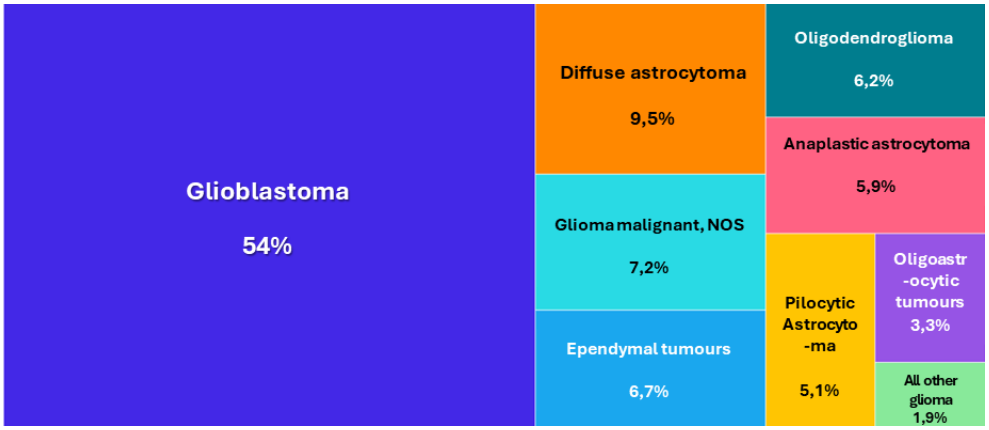


Figure **1.1**. Distribution of primary brain and central nervous system (CNS) gliomas.[3]

Other than age, risk factors of GBM are poorly defined.[10] Development of GBM is related to the dysregulation of the G1/S checkpoint in the cell cycle, the separation point between the growing and the deoxyribonucleic acid (DNA) replication phases. GBM has also been related to the occurrence of many genetic disturbances in glioma cells, which include the loss of genetic material, amplification of multiple genes, as well as mutations in some of them, all of which are a result of somatic mutations.[11,12] So, GBM may occur in the course of genetic diseases like tuberous sclerosis,[13] Turcot syndrome,[14] and neurofibromatosis Type I.[15] Moreover, head injuries because of brain contusions may predispose the onset of GBM.[16] Between women, a higher risk of its occurrence has been observed in postmenopausal women. Research has found suggestive

evidence that ovarian steroid hormones, and specifically estrogens, may play a role in the development of gliomas, suggesting that estrogens may exert a protective effect.[17] Concerning external factors, as it happens with the broad family of gliomas, exposure to high doses of ionising radiation is the only confirmed risk factor for GBM development.[18–20] It has been predicted that the overall risk of developing GBM following radiotherapy (RT) can be as much as 2.5%.[21] Regardless, no evidence shows a risk of developing GBM because of routine exposure to diagnostic radiation.[22]

Finally, worth mentioning, GBM occurs almost exclusively in the brain; however, it can also appear in the brain stem, spinal cord, and cerebellum. 61% of all primary gliomas occur in the four lobes of the brain: frontal (25%), temporal (20%), parietal (13%), and occipital (3%).[23] More than half of patients suffering from GBM present short clinical histories, between 3 and 6 months.[24] On some occasions, symptoms may develop rapidly, which may be mistaken for those of a stroke.[8]

1.1.2. Symptoms and Incidence

Symptoms of GBM can result from two different sources:

***Direct effect due to tissue degeneration*.** These arise from the destruction of brain tissue because of necrosis. Such destruction leads to symptoms such as focal neural deficit and cognitive impairments. Symptoms will depend on the region of the brain affected. For example, tumours located in the temporal lobe area will present hearing and visual problems as well as transient aphasia and sensorimotor deficits from epilepsy, while tumours in the frontal lobe may lead to personality changes. Tumours that present large and significant masses may lead to imbalance and incontinence.[8,25,26]

Secondary effects due to increased intracranial pressure. An Increase in intracranial pressure is a direct consequence of tumour growth and increased edema surrounding the tumour, leading to headaches.[25] Headaches are a hallmark of GBM and are usually of growing intensity without any defining pain pattern. They present the most common in diagnosis and are often in a context of large tumours or significant edema.[27] Other symptoms of increased intracranial pressure are dizziness, fatigue, nausea, vomiting, and neurocognitive slowing.[28]

Incidence of recorded GBM cases in Europe and North America is 2-3 per 100,000 adults each year, and is the highest among malignant primary brain tumours.[29] The ratio of GBM incidence is 30% higher in men than in women.[30] Age-adjusted GBM rates also show to be highest in developed industrial countries.[31] Ethnicity also seems to play an important role, Caucasians are more frequently affected than people of African or Asian descent.[32]

Age is a cornerstone in epidemiology; GBM is primarily diagnosed at an older age, with a median age of 64 years.[33] The incidence rate increases with age, peaking at 75–84 years of age, dropping afterwards.[33] Whereas GBM remains uncommon in children, the incidence rate in the paediatric population (0–18 years old) is 0.85 per 100,000 people.[33,34] Younger population presents an even greater gap between genders, with a threefold increase in GBM incidence in males compared to females.[6]

1.1.3. Therapy Resistant Tumour Development

GBM has demonstrated to be extremely resistant to most treatments because of its heterogeneous nature,[35] a term used to describe tumours composed of a sum of cells that harbour distinct interpatient, intertumoral, functional, and molecular signatures with different sensitivities to anticancer therapies.[36] Heterogenicity can be a result of genetic, transcriptomic, epigenetic, and/or phenotypic changes.[37]

Such a heterogeneous nature is related to a large pool of cancer cells present in GBM with enough genetic variability to adapt and develop resistance before facing extinction. The main drug resistance mechanisms that cancer cells can develop are shown in Figure **1.2**.

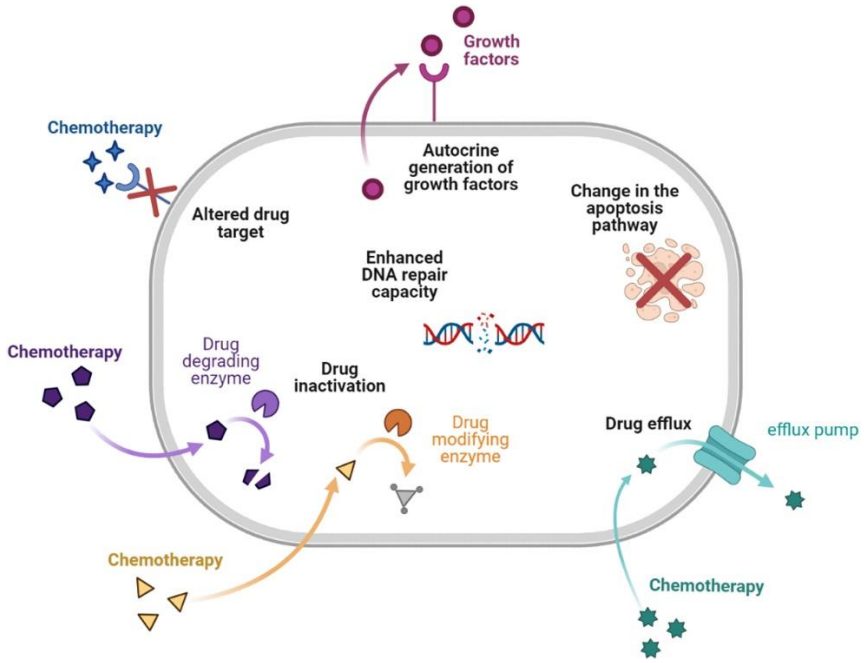


Figure **1.2**. Representation of the possible drug resistance development by cancer cells. Adapted from "Antibiotic Resistance Mechanisms" by BioRender.com (2022). Retrieved from https://app.biorender.com/biorender-templates.

- ***Drug inactivation***: *in vivo* inactivation of drugs involves mechanisms in which the drug may interact with different proteins that can modify, partially degrade or generate complexes with the drug.[38,39]
- ***Alteration of the drug's target:*** Given by mutation of proteins responsible for DNA packaging, making it inaccessible to drugs.[40]
- ***Drug's eflux***: Reduction of drug's concentration due to an improvement in the capacity to transport the drug outside of the cell. The proteins that give rise to this phenomenon are usually from the ATP-binding cassette transporters (ABC) family.[40]
- ***Apoptosis inhibition***: Cellular apoptosis can be induced through two different mechanisms. Both mechanisms, however, end up unifying and activating the same enzymes and proteins. A mutation that disables those common enzymes and proteins causes an inhibition of the apoptosis mechanism.[40]

- ***Repair of damaged DNA***: In response to damaged DNA, the DNA damage response mechanism is activated, meaning that drugs such as platinum antineoplastic drugs are removed from the DNA chains.[40]
- ***Increase of glutathione:*** Increase of the glutathione (GSH) levels inhibits drugs by attaching or reacting with drugs and participating in the extrusion of those, thus avoiding damage to proteins and DNA or participating in processes of DNA repair.[41]

1.1.4. Prognosis and Available Treatments

As a result of the complex nature of GBM, it is a tumour associated with a poor prognosis. The five-year survival rate for GBM patients is 5.1%, and the median survival is less than 2 years upon diagnosis.[42] Several variables affect the prognosis of patients with GBM: age, tumour location, whether the patient receives RT or chemotherapy (CT), preoperative performance and tumour characteristics.[43–46]

Another important factor resulting directly from treatment is tumour surgical resection. Tumour resections higher than 89% provide diagnostic and symptomatic benefits. However, only a resection higher than 98% has been associated with a significant improvement in survival rate, associated with a 1-2 month survival rate increase.[47] GBM is clinically known as prone to diffuse-infiltrative growth, with an aggressive behaviour that leads to high and recurring drug resistance development.[36] Such characteristics make complete surgical resection and drug-based treatments often inefficient.

The current standard clinical protocol for the treatment of GBM was established back in 2005 and involves maximal safe surgical resection of the tumour mass without compromising neurological functions, followed by a combination of daily concomitant CT with temozolomide (TMZ), RT, and adjuvant TMZ.[48] Nonetheless, this protocol represents the culmination on the evolution of previous work and studies.

1.1.4.1. Brief Historical Perspective

In the past, the standard treatment consisted of surgical resection to a feasible extent of tumour mass, followed only by RT. In 1978, however, Walker *et al.* performed a cooperative clinical trial on a battery of nitrosoureas as adjuvant RT agents that showed statistical superiority in survival rates when compared to conventional care, prompting the prescription of the nitrosourea carmustine in some countries.[49] From this point, several group-cooperative trials have investigated the inclusion of various chemotherapeutic regimes to RT.[50,51] Nonetheless, no phase 3 trials of nitrosourea-based adjuvant RT have been able to demonstrate any significant survival benefits when compared with RT alone.[52] Despite this, adjuvant carmustine became commonly prescribed in combination with RT.[53]

It was in the 1980s that Aston *et al.* developed the first antitumour imidazotetrazine, bicyclic ring-systems with multiple nitrogen atoms.[54] Mitozolomide, the lead compound, entered clinical trials in 1983, finishing phase I in 1985, and despite good activity in mice, in clinical trials it showed only limited activity and promoted unpredictable long-lasting haematological effects (blood clots and internal haemorrhages development).[55] As an alternative, a drug from the same

family of compounds, TMZ, an N-methyl derivative, was put forward to be tested, although presenting a different toxicological profile (Figure **1.3**).[56]

Since then, TMZ administration periods and successful clinical trials were undertaken, finally getting approved by the Federal drug administration (FDA) in 1999. Since 2005, TMZ has become the world standard in GBM treatment, consisting of concomitant RT followed by six cycles of adjuvant TMZ.[53,57,58]

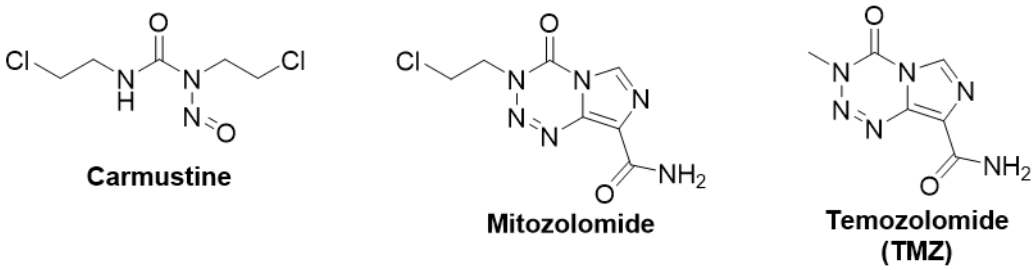


Figure **1.3**. Structural formula of carmustine, mitozolomide and TMZ.

1.1.4.2. Temozolomide: Gold Standard Drug Treatment

TMZ exhibits stomach pH acidity stability and lipophilic nature, which allow it to be used in oral administration with an excellent bio-distribution, including penetration into the CNS across the blood-brain barrier (BBB).[58,59]

However, it is also labile above pH 7, with a plasma half-life of 1.8 hours at pH 7.4.[60] In these conditions, TMZ undergoes spontaneous hydrolysis that, in the presence of water, cascades into the formation of a DNA methylating agent diazomethane, presenting high affinity for the middle guanine residue of GGG DNA sequences (Figure **1.4**).[61,62]

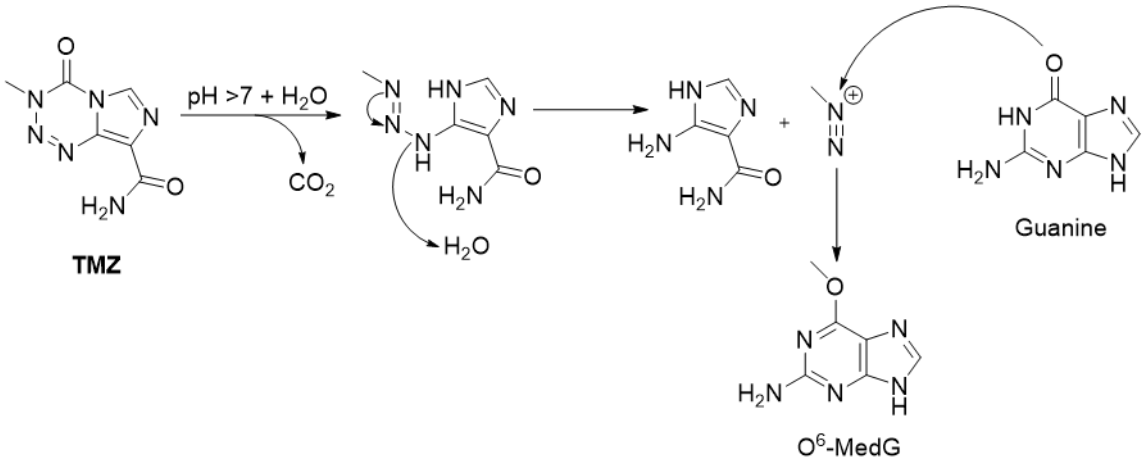


Figure **1.4**. Schematic representation of the mechanism of TMZ, which involves hydrolysis, activation, and alkylation to guanine.

In summary, although methylation at N7 positions of guanine and N3 positions of adenine are more common, methylation at the O^6 position is believed to initiate a sequence of DNA repair mismatching that leads to cell death via apoptosis.[62]

1.1.4.3. Limitations of Temozolomide

Overall, TMZ has demonstrated an increase in patient survival rate and suppressed tumour growth in early stages of the disease. However, the therapeutic outcome of TMZ remains limited by intrinsic and acquired resistance mechanisms, alongside genetic mutations, non-coding ribonucleic acids (RNAs), autophagy, and the tumour microenvironment (TME).[63] TMZ, which is not soluble under physiologic conditions, gets easily inactivated via hydrolysis in cells, and causes severe side effects as a result of off-target DNA damage.[64] Development of TMZ treatment resistance is a common occurrence that can be either inherited or acquired, resulting in treatment failure.[65] Indeed, several GBM cell lines, such as U87, U251, U373, or T98G, have been shown to be capable of developing TMZ resistance.[66–68] An increased expression of the methylated O-6-methylguanine-DNA methyltransferase (MGMT) has been associated to the resistance development towards TMZ.[69] MGMT is a suicide DNA repair enzyme, which demethylates the O^6 position of guanine, and as such avoids the TMZ effect.[70]

Furthermore, the combination of the standard of care RT with TMZ does not improve GBM treatment in a significant way.[71] And even after aggressive therapy, the average survival of patients remains below 2 years.[72] Additionally, the administration of intense TMZ doses used in the clinical protocols provokes relevant side effects, common in the nitrosoureas family, like bone marrow, liver, kidney, lung damage, and an increased chance of developing leukaemia.[73] While at the same time, exhibiting TMZ-specific side effects leading to bone marrow dysregulation like anemia and thrombocytopenia.[74]

1.1.4.4. Alternative Drugs to Temozolomide

Given the poor bioavailability and limitations in therapeutic effectivity of TMZ, having second-line treatment options is crucial to face GBM treatment. Alternative chemotherapeutic choices include principally those detailed below.

Nitrosoureas such as lomustine, carmustine and fotemustine (Figure **1.5**).[75,76] As mentioned, nitrosoureas were the first adjuvant chemotherapeutic agent ever administered for GBM treatment.[49] Nitrosoureas are alkylating agents, generating the alkylation at DNA strands, which results in DNA damage and cellular death. Specifically, chemical decomposition of nitrosoureas in aqueous solutions yields the formation of two reactive species: a chloroethyldiazohydroxide and an isocyanate derivative. The first one decomposes into chloroethyl carbonium ion, forming adducts that cross-link with DNA, while the isocyanate inhibits DNA repair and depletes GSH.[77]

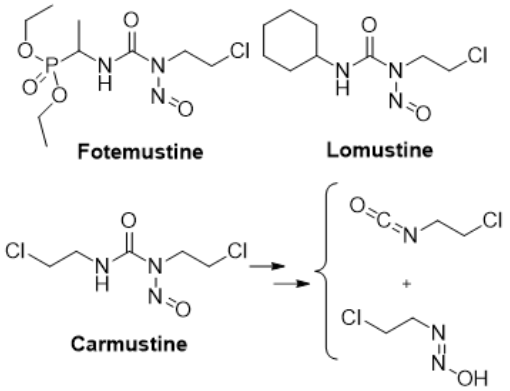


Figure **1.5.** Chemical structure of fotemustine, lomustine and carmustine, and demonstration of degradation of carmustine products, nitrosoureas, undergo in aqueous media.

Antiangiogenic agents are chemical or biological agents that minimise or halt tumour angiogenic behaviour. An example of an antiangiogenic agent used as an alternative to TMZ treatment is Bevacizumab, which consists of human monoclonal antibodies that inhibit vascular endothelial growth factor.[78]

Targeted therapies in GBM have also taken considerable efforts, concentrating on growth factors or proteins such as epidermal growth factor receptors (EGFR),[78] inhibiting protein kinase C,[79] or inhibiting phosphatidylinositol 3-kinase (PI3K) and mammalian target of rapamycin (mTOR) signalling pathways PIK3 and mTOR.[80]

Immunotherapeutic approaches are also being exploited, alone or in combination with standard/novel therapies. Immunotherapy modulates the immune system to attack cancer cells in multiple targets and directions.[81] The immunotherapeutic approaches taken have essentially focused on immune checkpoint inhibitors such as anti-programmed cell death protein (anti-PD-1) and anti-T lymphocyte-associated protein-4 (anti-CTLA-4) or dendritic cell-based vaccine therapies.[70]

All in all, even though over the years different alternatives have been reported, none of them has been consolidated over TMZ. In any case, DNA-damaging agents continue to be of paramount importance in cancer therapy.

1.1.5. Platinum-Based Drugs

Alkylating agents, in cancer treatment, are agents that add alkyl groups to the bases of DNA, which can eventually lead to DNA breaks and cross-links, interfering with DNA replication and transcription, all resulting in cell death.[82] Alkylating agents can be classified as monofunctional (reacting with one DNA strand) or bifunctional (reacting with two DNA strands to create cross-links).[11,19,67,83] Although Pt compounds are very often considered alkylating agents, their resemblance comes from the electrophilic behaviour leading to reaction with nucleophilic residues of DNA molecules.[84] So, a possible reconsideration of Pt-based compounds, renowned for their potent anticancer properties, represents a novel cornerstone.

1.1.5.1. Families and Areas of Application

Pt compounds constitute a group of anticancer agents widely used clinically that are based on DNA-damaging mechanisms. The first Pt anticancer drug introduced in the clinic was cisplatin (CDDP), becoming one of the most important chemotherapeutic agents available for the treatment of a wide variety of solid tumours.[85] CDDP cytotoxicity was discovered by Barnett Rosenberg *et al.* serendipitously in 1965 while researching the effect of electrical fields on bacterial cell division. During his research, Barnett observed that certain Pt compounds, specifically CDDP, inhibited cell division.[86] Later studies elaborated on its efficacy as an anticancer agent in animal models, eventually led to clinical trials, and produced a follow-up paper demonstrating CDDP's antitumour activity in 1969.[87] In 1978, the FDA approved CDDP for use in testicular and ovarian cancer, and one year later, the UK, along with several other EU countries.[88,89] For the following four decades, the main focus was on the synthesis and biological evaluation of CDDP analogues, with much of the early effort aimed at making CDDP-based therapy safer.[90] Classical Pt(II) complexes are square planar, with two monodentate/one

bidentate ligands referred to as "non-leaving group ligands", and two monodentate/ one bidentate "leaving group".[91] The most important drugs discovered during this four-decade period belong to such type of Pt complexes (Figure **1.6**), and consist of:

- ***Carboplatin***, which was discovered and approved in 1989, retains similar efficacy but with less nephrotoxicity, becoming a standard for ovarian cancer.[92] Carboplatin differs from CDDP by replacing the two chloride ions in CDDP with a cyclobutanedicarboxylate group. Near its maximum tolerated dose (MTD) of 400 $mg \cdot m^{-2}$, carboplatin causes less nephrotoxicity, neurotoxicity, and ototoxicity, and is far less emetogenic than CDDP when it reaches its own MTD of around 100 $mg \cdot m^{-2}$.[93]
- ***Nedaplatin***, which followed approval in Japan in 1995, is an analogue aimed at reducing nephrotoxicity.[94] Nedaplatin shares the same amine carrier ligands as CDDP but features a different leaving group, consisting of a five-membered ring where glycolate binds to the Pt ion as a bidentate ligand. It has a short elimination half-life (1.1–4.4 hours) and a pharmacokinetic profile similar to carboplatin derivatives.[94] However, nedaplatin has not undergone advanced clinical phase III or IV trials and is not widely used in clinical practice.
- ***Satraplatin*** is an orally active drug for prostate cancer that passed clinical phase I trials in 1993, but due to mixed results in further clinical studies, it did not receive FDA approval.[95] Satraplatin is a Pt(IV) complex with octahedral geometry consisting of two dicarboxilate moieties at the axial position and one amine from the equatorial position substituted by a cyclohexylamine.[96] The MTD of satraplatin is observed to be 140 $mg \cdot m^{-2}$.[97]
- ***Lobaplatin*** passed phase I clinical trials in 1993 and was developed with a focus on the reduction of nephrotoxicity. It has been used in treating breast, lung, and oesophageal cancers.[98] Lobaplatin has a seven-membered ring structure (1,2-bis(aminoethyl)cyclobutene), which forms the bidentate stable ligand, and lactic acid as the leaving group. Lobaplatin has enantiomeric isomers, and the synthesis of such a drug gives a racemic mixture; however, most of the preclinical and clinical trials have used racemic preparations.[99–102] Observed MTD of lobaplatin reached 85 $mg \cdot m^{-2}$; however, at no point was hydration required to prevent nephrotoxicity.[97]
- ***Oxaliplatin*** was later approved in 1996 in Europe, with special efficacy in colorectal cancer and better activity against certain CDDP-resistant cancers.[103] Oxaliplatin is a diaminocyclohexane-containing Pt. Oxaliplatin can exist as three isomeric conformations that interact differently with DNA, but the trans-I(R,R) isomer of oxaliplatin is the one that shows the most effective against CDDP-sensitive and CDDP-resistant cancer cell lines.[103,104]
- ***Heptaplatin*** passed phase II clinical trials in the treatment of gastric adenocarcinoma in 1999.[105] Heptaplatin has shown MTD's of 600 mg·m-2 and half maximal inhibitory concentrations (IC_{50}) 11.2-fold higher than CDDP, with the increased benefit of high toxicity towards CDDP-resistant cell lines.[106,107]

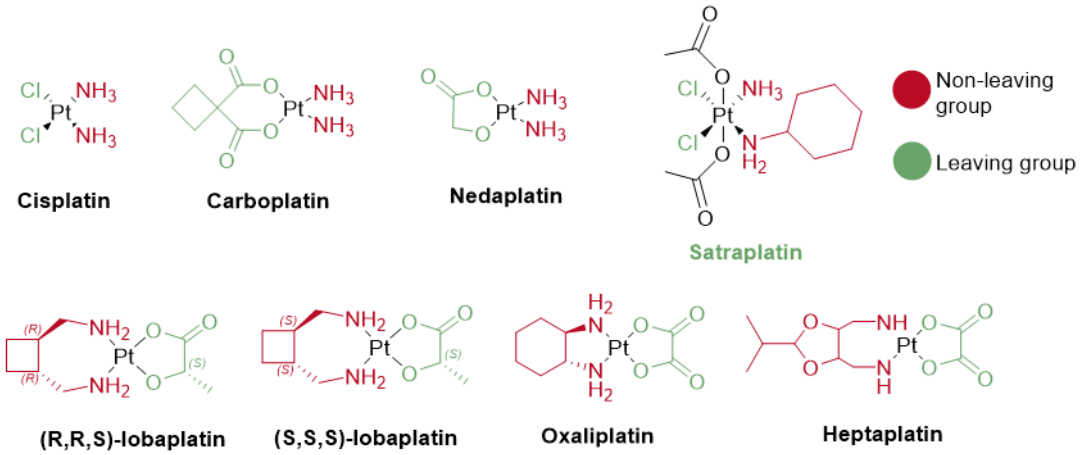


Figure **1.6**. Chemical structure of CDDP, carboplatin, nedaplatin, satraplatin, (R,R,S)-loboplatin, (S,S,S)-lobaplatin, oxaliplatin, and heptaplatin.

1.1.5.2. Mechanisms of Action of Platinum-Based Drugs

Overall, the generalised mechanism of action can be separated into four key steps shared among all the families of classical alkylating-like Pt drugs (Figure **1.7**):[108]

Cellular uptake. Two main pathways explain CDDP uptake by cells: passive diffusion through the plasma membrane and active transport mediated by membrane proteins.[109] The combination of small size and planar geometry of CDDP has long been attributed as supportive of passive diffusion. Further support for a passive diffusion explanation has been the findings that CDDP uptake does not saturate with increasing concentration and is proportional to the administered concentration.[110–112] On the other hand, some findings have suggested that the predominant mechanism of uptake is active transport. Such a hypothesis relies on the reports of CDDP uptake being linked to the expression levels of copper transporter 1 (CTR1).[113–115] For other Pt-based drugs like oxaliplatin, transport efficiency has also been linked to active transport in the form of expression levels of organic cation transporters.[116] Furthermore, transporter protein membrane inhibition with reactive aldehydes has shown inhibition of CDDP uptake, establishing a clear relation between the two.[117] Overall, a combination of both passive and active transport explains best the data accumulated on this topic; however, the relative importance of each mechanism still remains to be determined.[108]

Aquation/activation. Ligand substitution of CDDP is a required step for the Pt complex activation and subsequent binding to DNA, forming lesions that are characteristic of its activity. Such substitution is strongly facilitated by the square-planar geometry of CDDP. CDDP undergoes a ligand substitution prior to DNA binding in which a chloride ligand is replaced by a water molecule.[118,119] The square planar geometry of CDDP allows for free binding ligands to approach from the axial position of the Pt complex and, through a displacement reaction, remove the chlorine ligand.[120] The aquation of CDDP generates a much more reactive species that rapidly reverts to the original CDDP in high chlorine concentrations, like in the bloodstream (~100 mM). At lower concentrations, such as in the cytoplasm (~ 20 mM), the reaction equilibria favour the formation of the aquation product *cis*-$[Pt(NH_3)_2Cl(H_2O)]^+$.[118] The now positively charged Pt complex can be attracted to the negatively charged nuclear DNA.

DNA binding. Once CDDP has been aquated, it can then enter the cell nucleus, and the water-coordinated molecule can be substituted by heterocyclic purine DNA bases. However, it has been observed that interaction with proteins and RNA has also been proposed to play a role.[121–123] The most nucleophilic sites in DNA purine residues are the N7 atoms of such molecules of guanines and adenines, making them preferably platinated. With data showing a first monofunctional Pt-DNA adduct from CDDP.[124] Afterwards, the remaining chloride ligand is then substituted for a second purine base, forming a cross-link on the DNA. Cross-links in DNA can be described as happening on the same strand or on different DNA strands, giving rise to the intrastrand and interstrand DNA cross-links.[124] Chemoselectivity makes some combinations more likely to happen than others. The 1,2-d(GpG) intrastrand cross-link is the most prevalent lesion, at a 65% of total crosslinking fate, 1,2-(ApG) intrastrand at 25% and 1,3-d(GpTpG) intrastrand at 10 % along with small amounts of GpG intrastrand cross-links (Figure **1.8**).[125–127] Just as happens with CDDP, similar cross-links are formed by carboplatin and oxaliplatin with a variation in relative proportions.[128,129] The resulting DNA adducts distort the DNA structure by bending and unwinding the double helix upon interaction with Pt complexes.[130]

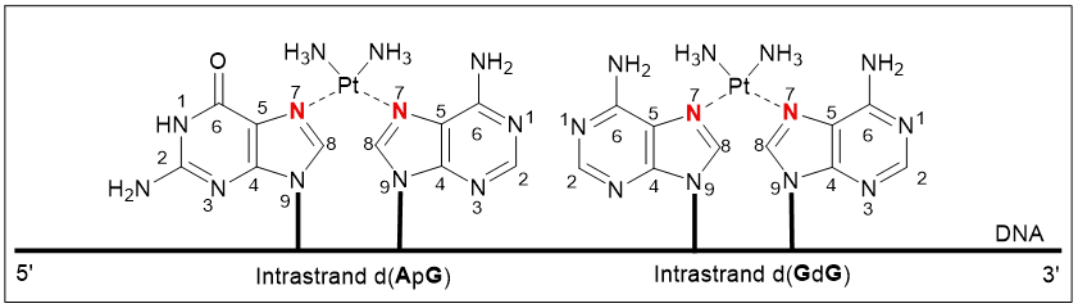


Figure **1.8**. Guanine and adenosine d(ApG) and d(GdG) binding with CDDP.

Cellular processing of DNA lesions that lead to cell death. When cellular DNA gets damaged by interaction with Pt, it halts the G2/M transition of the cell cycle and attempts to repair the platinated DNA.[131] CDDP lesion removal is most usually performed by the nucleotide excision repair (NER) machinery.[132] However, the repair mechanism needs to be able to reach the damaged DNA. Simultaneously, proteins that are not related to the repair mechanism can also bind to the platinated lesion, and they can effectively shield the lesion from the NER. The most classical protein class to interact in this shielding are comprised by the high-mobility group proteins.[133] In the end, if the cell is unable to repair the Pt-DNA damage, the expression of pro-apoptotic proteins increases, promoting release of cytochrome C.[131] These proteases effectively degrade the cell in a process of programmed cell death known as apoptosis.[134]

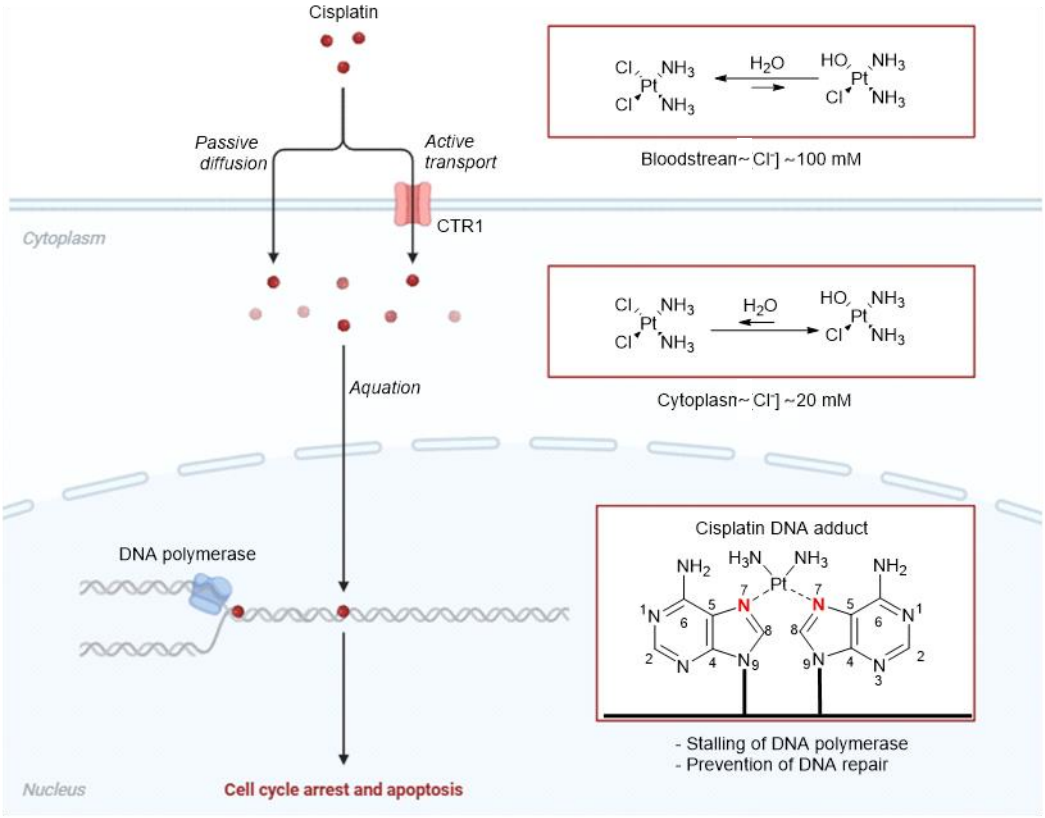


Figure **1.7**. Illustration of the internalisation from CDDP inside a cell through passive diffusion and copper transporter 1 (CTR1), aquation reaction, and DNA binding and interaction.

1.1.5.3. Side Effects and Chemical Alternatives

Despite benefits for rapid first-line treatment with Pt-based drugs, the administration of such Pt(II) drugs is often associated with severe systemic toxicity that result from long-term treatment.[135] For instance, Chovance *et al.* showed that patients who underwent long-term treatment for metastatic germ-cell tumour were susceptible to toxic side effects as a result of the treatment received.[136,137] Survivors of such treatments experienced secondary malignancies, cardiovascular, neuro, renal, and pulmonary toxicity, hypogonadism, infertility and a decline in quality of life.[138,139] His findings also showed a concerning traceable level of CDDP detectable in plasma and urine after decades of the treatment.[138] Overall, 20 to 40% of long-term patients will sustain some form of CDDP-induced peripheral neuropathy, with one third of those susceptible to permanent paraesthesia.[140–143] In terms of ototoxicity, 20 to 75% patients will experience serious/permanent/bilateral sensorineural hearing loss, and 20 to 40% will experience permanent tinnitus, with Fristina *et al.* finding a direct correlation between dose administered and hearing loss.[144,145] In terms of cardiovascular toxicity, patients experiencing late toxicity from CDDP suffered from hypercholesterolemia in 80% of the cases, hypertension in 40% and Raynaud phenomenon in 25%.[146] As for pulmonary toxicity, more than 80% of patients reported lower expiratory volumes.[147] And renal toxicity developing proximal epithelium in the kidneys has been well defined with CDDP treatment in patients for periods longer than 10 years.[148]

To overcome these limitations, two main (though not exclusive) chemical approaches can be followed: development of Pt(IV) prodrugs, and/or the design of Pt-based complexes with

stimuli-responsive properties, such as, the presence redox environment, pH variation, light irradiation, enzyme overexpression, or temperature changes.[149] Both approaches are described next.

Platinum(IV) prodrugs. The anticancer activity of Pt(IV) complexes has been known since the very discovery of CDDP, as reported by Barnett Rosenberg et al. in the 1960s.[86] Pt(IV) prodrugs are octahedral complexes usually prepared by oxidative addition of the square planar Pt(II) complexes, resulting in an equatorial plane retaining the original Pt(II) coordination sphere, and two new axial positions completing the complex.[150] This configuration of Pt(IV) is known as oxoplatin, and allows this compounds to be quite inert to ligand substitutions as the axial positions are blocked, while allowing for tweaking of properties like lipophilicity, bioactivity, redox stability, fluorescence, as well peptides such as arginylgycylaspartic acid's (RGD)[151,152] and chlorotoxin[153] as well as small molecules, such as, biotin,[154] folic acid,[155] while at the same time, glycose and derivates[156,157] conjugated with Pt(IV) to increase targeting ability. Beyond the chemical stability introduced by the axial ligands, Pt(IV) complexes are still susceptible to a two-electron reduction that removes such positions, regenerating the original Pt(II) drug (Figure **1.9**).[158]

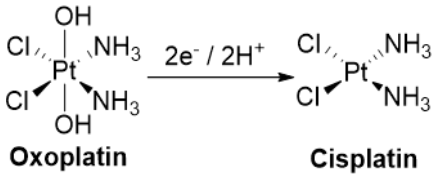


Figure **1.9**. Example of 2 electron reduction from Pt(IV) complex oxoplatin to the Pt(II) reduced form CDDP.

It is believed that Pt(IV) complexes act as prodrugs that are activated intracellularly *in vivo* by reduction processes that transform them to the original Pt(II) complex.[159] Moreover, the reduction seems to be highly selective to intracellular activation, reducing off-target toxicity. Such selectivity to intracellular activation has been attributed to the high ascorbic acid and GSH concentration gradients. Ascorbic acid is present at lower concentrations in blood plasma (50-150 μM) and higher in neutrophilic cells cytoplasm (1 mM). Similarly, intramolecular GSH is shown to range from 1 to 10 mM concentration in normal cells and can also be 2–3 orders of magnitude lower in extracellular media. However, in cancer cells, this concentration can increase up to fourfold.[101,160–162] So, Pt(IV) may remain in the higher oxidation state in the bloodstream, keeping a lower reactivity, and avoiding unwanted side reactions.

"Multi-action" Pt(IV) drugs. The incorporation of axial positions has also benefited the rise in "dual-action" or "multi-action" Pt(IV) prodrugs, which incorporate bioactive ligands that exert biological activity to enhance the activity of the Pt complexes/or overcome drug resistance.[163] These drugs are designed to hit multiple therapeutic targets simultaneously. The clinical approach to overcome cell resistance is to use a combination of drugs that have different toxicology profiles, pharmacokinetics and accumulation. "Multi-action" or "dual-action" Pt(IV) complexes carry several biological activities at once to achieve different functions while using only one drug.[164] Examples of "dual-action" Pt(IV) prodrugs include ethacraplatin,[165] mitaplatin,[166] chalcoplatin,[167] monochalcoplatin,[168] NERI-Pt(IV),[169] Pt(IV) derivatives with inhibitors of cyclooxygenase,[170,171] or histone deacetylase (HDAC) [172,173] (Figure **1.10**).

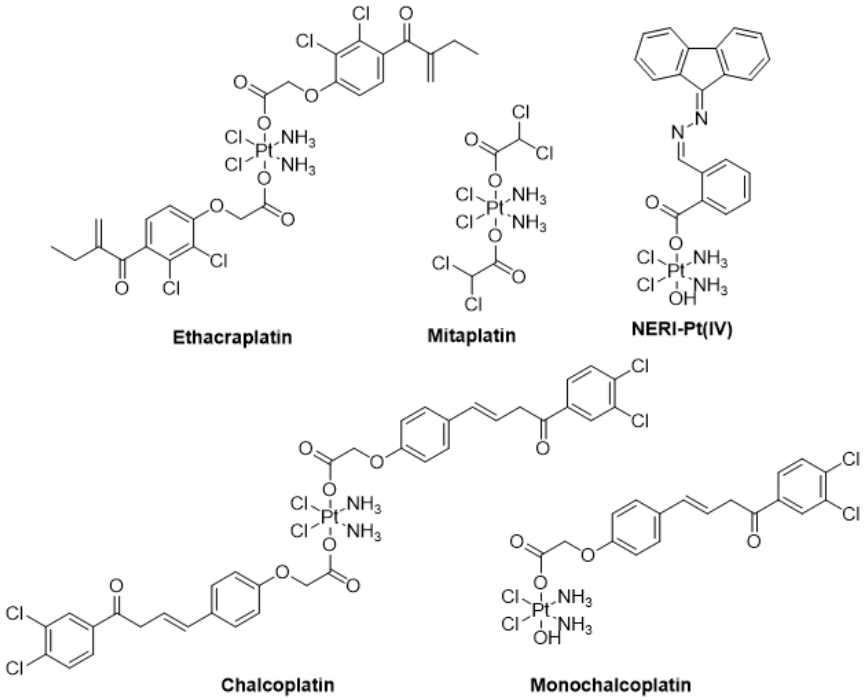


Figure **1.10**. Chemical structure of ethacraplatin, mitaplatin, chalcoplatin, monochalcoplatin, and NERI-Pt(IV).

On the other hand, examples of "multi-action" Pt(IV) drugs have been reported by Gibson and Gandin *et al.* by developing CDDP derivatives via conjugation of two moieties of the HDAC inhibitor 4-phenylbutyric acid at the axial position.[174] Gibson and Gandin *et al.* also reported on triple-action Pt(IV) prodrugs of CDDP with axial ligands that included inhibitors of cyclooxygenase inhibitor, HDAC, or pyruvate dehydrogenase kinase inhibitor,[175] as well as also reporting on quadruple-action Pt(IV) prodrugs that simultaneously release four bioactive agents including CDDP, dichloroacetate, and [Pt(1*S*,2*S*-diaminocyclohexane)(5,6-dimethyl-1,10-phenantrholine)]$^{2+}$.[176] Other groups like Gou *et al.* reported on Pt(IV) prodrugs that conjugated a cancer cell-targeting biotin and a nonsteroidal anti-inflammatory drug, indomethacin (Figure **1.11**).[177] Dhar *et al.* presented a simpler yet effective method to sensitise resistant prostate cancer cells by conjugation of Pt(IV) prodrug with a fatty acid to achieve fatty acid oxidation inhibition and cytotoxicity.[178]

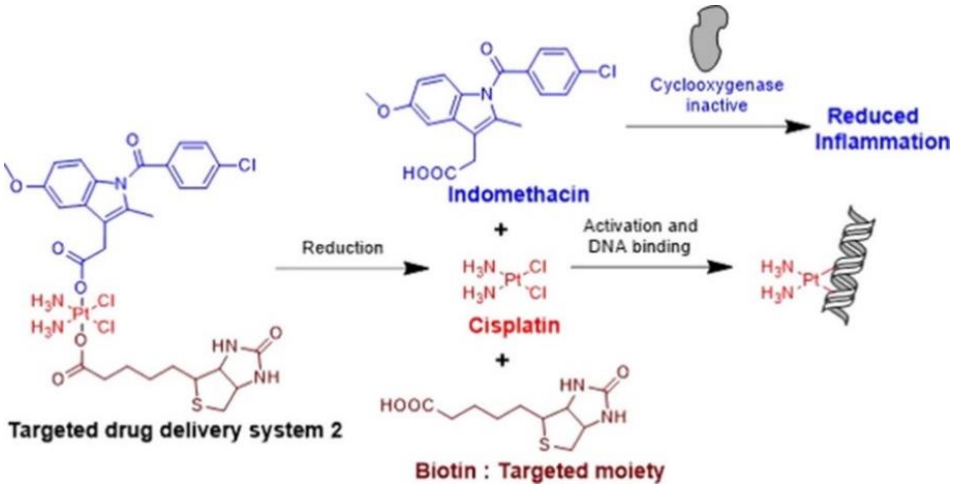


Figure **1.11.** Multi-targeted approach to cancer treatment by Gou *et al.*, focusing on a dual target approach coupled with a biotin targeting moiety that undergoes Pt(IV) reduction activation.[177]

1.1.6. Platinum-Based Drugs in Glioblastoma

1.1.6.1. Precedents

Pt like drugs in GBM are considered a fourth-line chemotherapeutic agent and are only administered once all standard therapeutic protocols have failed. Therefore, most preclinical and clinical settings use carboplatin/CDDP as a "rescue" therapy for high-grade glioma, with patients non-responding to RT, nitrosoureas, or TMZ.[179] In these specific conditions, Pt-based drugs are facing unfavourable scenarios with highly resistant tumours. These settings, overall, have been observed to have limited or non-significant improvement in outcome in the overall survival of patients with brain tumours.[180] For instance, a phase II clinical trial conducted by Brandes *et al*. demonstrated that a TMZ administration regimen preceded by a single dose of CDDP administration showed better results than standard TMZ regimens with low myelotoxicity in recurrent GBM.[181] Moreover, Pt(II) complexes are non-specific chemotherapeutic drugs that, despite their evident efficacy, also induce intense systemic toxicities.[182–184]

However, several studies have also demonstrated the enhanced efficacy of CDDP as an adjuvant in combination with TMZ and RT.[185,186] Anti-angiogenic effects of CDDP have also been observed, as apparent in the works of Mishima *et al.,* with CDDP displaying pleiotropic activities that directly or indirectly affected angiogenic processes.[187] Hess *et al.* demonstrated that a new non-onventional Pt-acridine hybrid agent at *in vitro* conditions using SNB19 and U87 GBM cell line presented excellent results and toxicity profiles superior to CDDP.[188] Combination approaches for GBM treatment have been reported using Pt-based drugs in combination with bee venom,[189] β-elemene (extracted from curcuma wenyuji),[190] topoisomerase II,[191] microRNAs,[192] protein kinases C,[193] bioconjugates combining EGFR targeting,[194] tumour necrosis factor,[195] HDAC inhibitor,[196] and PI3K inhibitors.[197] In addition, nuclear therapy combining CDDP with a combination of p(65)+Be neutrons irradiation was attempted in U87 GBM cells, resulting in an increase in cytotoxicity effects.[198] The works of Nagane, *et al.* showed that administration of a combination of a tyrosine kinase inhibitor and an apoptosis-inducing chemotherapeutic Pt agent provided a basis for combined treatments for historically intractable malignant gliomas.[199] Combination therapies with standard nitrosoureas for GBM treatment have also been studied, Park *et al.* have reported 1-(4-amino-2-methyl-5-pyrimidinyl)methyl-3-(2-chloroethyl)-3-nitrosourea (ACNU) and CDDP have reported to offset drug resistance development,[200] and Buckner et al. conducted a phase III trial with combination therapy of carmustine and CDDP against carmustine alone, displaying more toxicity towards GBM in combination settings.[201]

If we take a closer look at specifically for Pt(IV) prodrugs in GBM, we find prominent examples like the development by Sharpe *et al.*, who developed a Pt(IV) prodrug conjugated to a methyl-tetrahydropyridine (MP-) to target GBM mitochondria and achieve a potent chemotherapeutic intracranial effect in *in vivo* models, as well as potentiating TMZ and TMZ-chemoradiation therapies.[202,203] Sabo *et al.* reported the synthesis of novel cyclohexyl ethylenediamine-N,N'-diacetate containing Pt(IV) complexes. Toxicity profiles demonstrated increased cytotoxicity compared to CDDP and the ligands themselves in the U251 GBM cells panel.[204,205] Bottone *et al.* reported on a new Pt(IV) prodrug with (2-propynyl)octanoic acid (POA) conjugated in the axial positions (Pt(IV)Ac-POA). POA acts as a deacetylase inhibitor, exploiting a "multi-action" Pt(IV) drug tested in rat C6 glioma cells, showing improvement over regular TMZ

RT and inducing chemo-sensitisation.[196] Ranninger *et al.* back in 1999 already reported on a Pt(IV)-bis(monoglutarate) complex that, when evaluated against glioma cells, showed a higher cytotoxic effect than CDDP, inducing apoptosis through a p53-dependent pathway.[206]

At this point, the question arises: *why, if the preclinical studies are favourable, has no product made it through clinical phases?* To answer this question, it is first necessary to review the possible inherent limitations of using these species.

1.1.6.2. Limitations of Pt-Based Drugs

Limitations associated with the Blood-Brain Barrier. The BBB is a highly selective physiological barrier that contributes to scarce drug arrival to the brain. In general, less than 5% of drug plasma concentration can be found in the brain after intravenous (i.v.) administration of Pt-based drugs to non-human primates.[185] With the high specificity of the BBB, which only allows for small lipophilic compounds and endogenous molecules to go through specific transporters, Pt-based complexes experience little to no passive diffusion, resulting in poor activity.[90] Malignant brain tumours can compromise the BBB integrity, which results in the formation of the blood-tumour barrier (BTB), a barrier with very high heterogeneity and characterised by poorly regular permeability.[207] However, even in these situations, only modest Pt uptake was observed.[208] To surpass this limitation, different methods have been explored, such as increasing BBB permeability,[209,210] introduction of biodegradable implants directly to the tumour site,[211,212] the use of a catheter to directly administer drugs into the brain through convection-enhanced delivery (CED) or intranasal (IN) administration.[213] All in all, new approaches that ensure efficient chemotherapeutically significant drug administration still present a major challenge nowadays.

Narrow window of application. Treatment with CDDP has been observed to be an efficient approach for brain tumour treatment; however, it is only effective in a narrow therapeutic window in early stages of the disease.[214] Such findings defy the current standard of CDDP as a late-stage 'rescue' therapy.[179]

Extensive off-target toxicity. Due to the extensive off-target toxicities, nephrotoxicity and neurotoxicity often arise from Pt-based therapy.[215–217] Off-target toxicity is not an isolated issue of Pt-based therapies, since most of the small and all the big molecules from most available treatments fail to even reach the brain within therapeutic levels.[218] Strategies developed to overcome such limitations consider the use of adjuvants, like CDDP delivery within biodegradable polymer implants into the tumour bed of patients[219] or direct injection under CED.[220] However, this can also contribute to severe side effects.[221,222]

Among the different approaches followed over the last years, the use of nanoparticles (NPs) allows for the introduction of systems that are capable of overcoming some of the classical limitations.

1.1.7. Use of Nanoparticles in Biomedical Applications

1.1.7.1. Properties of Nanoparticles

In addition to confer chemical and colloidal stability, NPs exhibit specific properties, such as small size, high surface-to-volume ratio or other physicochemical parameters, which make them unique to improve drug efficiency.

Size. It is an important feature in pharmacokinetics, biodistribution, and cellular interactions, directly impacting drug delivery efficacy and potential toxicity.[223] Concerning the circulation through the bloodstream, the size is also critical. While smaller NPs can accumulate more easily in the leaky blood vessels of tumours than bigger ones, they can also extravasate into normal tissue. On the other hand, larger NPs cannot extravasate as easily and thus their distribution into the bloodstream is highly variable.[224] Shape of the nanocarriers is also important in the impact of fluid dynamics, and thus, influences uptake.[225]

Surface Charge. The charge of nanocarriers also affects stability and distribution in the bloodstream. Positively charged NPs have been shown to be more successful in target tumour vessels while presenting biocompatibility, but also more prone to renal clearance; while a neutral charge after extravasation allows for quicker diffusion of the NPs to the tumour tissue.[226] On top, the surface of the nanocarriers can also be modified with ligands that may prolong blood circulation and promote specific types of endocytosis and cellular uptake.[227] Drugs with poor water solubility may be eliminated from the bloodstream before reaching the tumour site, but the use of hydrophilic NPs to encapsulate these drugs can provide an improvement of their solubility, and thus improve the bioavailability, allowing a more effective delivery.[223]

Targeting. Nanocarriers can be modified to utilise passive and active targeting mechanisms to reach the tumour tissue. The enhanced permeability retention (EPR) effect allows NPs to passively accumulate in the leaky blood vasculature exhibited by tumours without the need to perform any surface modification to the NPs.[223,228,229] The EPR effect is a unique characteristic of solid tumours as a result of their anatomical characteristics (i.e., defective vascular architecture, vascular growth factors, impaired lymphatic recovery, large gaps between endothelial cells in blood and abundant vascular mediators). Tumour vasculature is often highly irregular, exhibiting structural abnormalities such as a defective endothelial lining, the presence of fenestrations, and leaky blood vessels. These abnormalities facilitate the extravasation of macromolecules and NPs from the bloodstream into tumour tissues. In addition to these vascular abnormalities, the dysfunctional lymphatic system commonly observed in tumours significantly impairs the clearance of accumulated substances. As a result, macromolecules and NPs exhibit prolonged retention within the TME compared to normal tissues.[230,231] On the other hand, active targeting utilises, as we have seen, the attachment of ligands to the surface of the nanocarriers.[232] These ligands have high specificity to receptors and other cancer-specific targets that are overexpressed on the surface of tumour cells.[232]

Controlled release. Internal and external stimuli can trigger the release of drugs by producing a change in the nanocarriers' physicochemical structure. Changes in pH, redox, oxygen concentration, and ionic strength in target tissue are examples of internal stimuli. [223] External stimuli, on the other hand, can include temperature, light, ultrasound, magnetic forces, and

electric fields.[223] At the same time, the efficacy as an antitumour drug is also enhanced by additional side mechanisms that enhance cellular internalisation, activation of immune cells, and generation of reactive oxygen species (ROS)[233], on top of the longer half-life and improved cellular uptake and biodistribution.[234]

BBB crossing. NPs' size, surface properties, and functionalization with targeting ligands enable precise drug delivery via BBB crossing. NPs can cross the BBB mainly via passive diffusion, carrier-mediated transport, and receptor-mediated transcytosis.[235] Key factors influencing BBB crossing include NP size, surface charge, and functionalization with ligands that target specific BBB transporters.[235–237]

1.1.7.2. Representative Nanoformulations for Glioblastoma Treatment

***Preclinical examples*.** Most of the examples of nanoformulations for GBM treatment take the approach of encapsulation of an active drug, usually TMZ, using some sort of liposome. For example, Wang *et al.* reported a hybrid-targeting lipid core NP with an engineered cell membrane coating that evades immune clearance and enables precise tumour targeting and release of TMZ.[238] Moving away from liposome-based NPs, we can observe albumin-based NPs coated with polymer bearing synaptic acid and encapsulating TMZ to orthotopic C6-bearing BALB/c mice reported by Kumari *et al.,* showing an increased median survival time while decreasing systemic toxicities.[239] Other approaches have focused on encapsulation of inhibitors like EGFR inhibitors, like Zhao *et al.,* by reporting on a cilengitide-loaded NPs in C6-bearing Sprague-Dawley rats with disrupted BBB by transient focused-ultrasound.[240] Another approach uses magnetic targeting, achieving a median survival of up to three times that of detected for free cilengitide administration. [241] Examples with topoisomerase inhibitors can also be found, like the work reported by Louis *et al.,* showing a nanoliposomal formulation encapsulating irinotecan with male athymic rat models using three different administration routes (i.v., CED, and IN).[242] Nitrosoureas have also been the target of encapsulation for drug delivery.[243] Such an approach allows increased solubility in comparison to the free drug, prolonging its survival.[244] In general, the best therapeutic success for these systems was achieved by combining nitrosoureas with other drugs, as Chang *et al.* report, with a carmustine and O6-benzylguanine loaded NPs with chitosan surface-modified poly (lactide-co-glycolides) NPs.[245]

Finally, there are several alternative nanosystems based on inorganic NPs that show potential to be used in GBM treatment. Metallic NPs are the most used approach for GBM among inorganic NPs, since they present the capability to show high internalisation ability, with the potential to be used as RT probes. Some examples can be found using metal oxides,[246] gold,[247] and silver (Figure **1.12**).[248] Nonetheless, few studies have been able to validate BBB crossing for *in vivo* GBM treatment.[249]

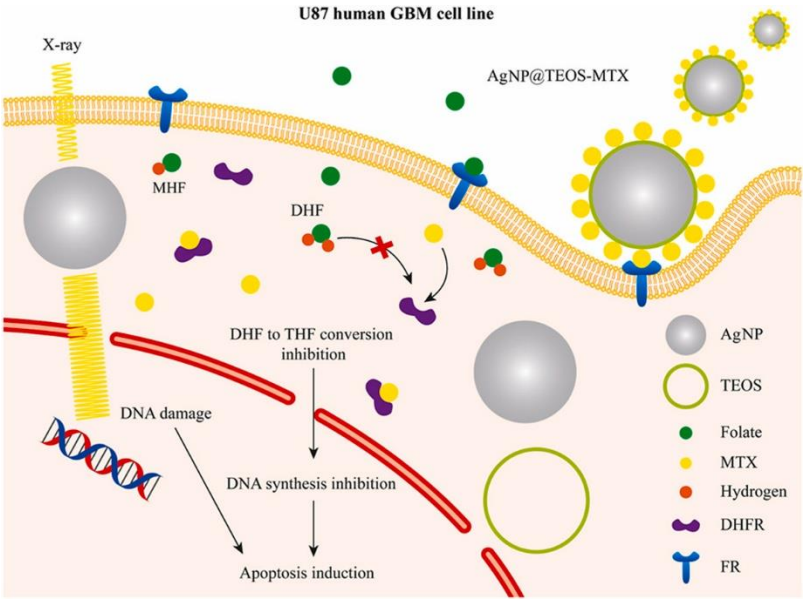


Figure **1.12**. Example of a RT probe for amplifying X-ray radiation of silver NPs as reported by Soroushnasab *et al.*[248]

Clinical representative examples. Progress from preclinical models to clinical trials is less than 8%. As a result, in this new approach to GBM treatment, many fewer examples are available. The most remarkable examples to mention are: i) the aminosilane-coated superparamagnetic iron oxide NP (SPION), termed NanoTherm®, capable of generating heat upon application of an external alternating magnetic field (AMF), inducing thermal ablation of tumour tissue.[250] In phase 2 trials, the use of such NPs doubles the median overall survival of patients with recurrent GBM.[251,252] As a result, NanoTherm® has received approval since 2010 by the European Medicines Agency (EMA); ii) FDA-approved liposomal system Onyvide®, which consists of a PEGylated irinotecan liposomal formulation, aimed to treat metastatic pancreatic cancer, and already investigated in four clinical trials (NCT03119064, NCT00734682, NCT02022644, and NCT03086616), either alone or in combination with TMZ, and administered via i.v. or CED;[253] and iii) Doxorubicin formulation PEGylated liposomal nanostructured Caleyx® and Doxil®, were tested following a Stupp regimen[53] in a phase II clinical trial (NCT00944801); however, results have so far showed non-reliable due to small sample size selection (n=63).[254]

1.1.7.3. Specific Platinum-Based Nanoformulations

Following the great effectiveness of Pt-based drugs for cancer treatment, it is not unexpected to observe Pt-based nanoformulations for GBM treatment being studied. These nanoformulations combine most of the advantages we have been explaining until now, from both Pt and NPs, as explained next:

Cisplatin-Based Nanoformulations. The use of CDDP-based nanoformulations for brain tumour treatment can be pinpointed to at least 12 years ago, and has since then shown encapsulation of CDDP into polymeric NPs,[255–257] polymeric micelles,[258,259] polymeric conjugates,[260] dendrimers,[261,262] liposomes,[263] nanocapsules,[264,265] metallic NPs,[265,266] and silica NPs.[267]

Starting with metal-based NPs, we can observe the work of Coluccia *et al.* as an example of CDDP as a conjugate to gold-based NP for RT, showing a synergistic effect with radiation and magnetic resonance-focused ultrasound. Viability assays with GBM cell lines *in vitro* (U87, U251, T98G,

U138) demonstrated cell growth inhibition compared to free CDDP, with marked synergy with RT.[268] Another example that uses a different metal-based NP is reported by Makharza *et al.,* who described a nanocarrier combining γ-Fe_2O_3 NPs with nanographene oxide for selective loading of CDDP. While graphene allows for high loading, the magnetic properties of the NPs provided magnetic guidance for targeted delivery. As a result, sustained *in vitro* drug release with therapeutic potential against U87 GBM cells was achieved with negligible toxicity.[269]

When we move to lipid NPs, we can observe that commercial agent Lipoplatin™, based on liposomal CDDP, had already reached phase II/III clinical studies for non-small-cell lung cancer,[270] HER2/neu negative metastatic breast tumour,[271] and advanced gastric tumour.[272] Nonetheless, *in vivo* experiments using CED administration showed marked neurotoxicity, resulting in death within a few days, while i.v. administration was well tolerated.[273] From this formulation, a remarkable increase in NPs surface functionalization was observed. Shei *et al.* in this field reported on liposomes with sustained release of CDDP, able to reach relevant intracellular concentration in U87 GBM cell line, thanks to antibody-liposome conjugation against endothelial growth factor and its receptor Type II, which accounts for resistance and rapid progression of brain tumours.[274]

While liposomes have been one of the most developed nanoformulations, polymeric NPs have also been in the spotlight of research for CDDP delivery in GBM treatment. For example, Dhami *et al. studied* a Pt-bearing poly(lactide-co-glycolide) NP coated with protamine. Such NPs showed the capability to cross the BBB in *in vitro* models of bovine brain microvessels endothelial cell assays.[275] A deeper study in pharmacokinetics was carried by Yu *et al.* who demonstrated that CDDP-loaded polymeric NPs showed a longer blood circulation times, with a 46-fold increase in blood Pt concentration in mice rodents than those receiving equivalent dosing of CDDP, with a tumour accumulation as high as 9.4-fold.[276] In GBM, Asharfzadeh *et al.* reported work using PEGylated liposomal CDDP-loaded NPs, which showed cellular uptake in brain tumour increased by 1.7-fold.[277] Keeping the polymeric chemistry, but moving to the field of micelles, the works of Lajous *et al.* showed poly(ethylene oxide)-triblock polymers combined with Gd^{3+} /CDDP to obtain micelles that acted as contrast agents (CAs) while increasing therapeutic effect compared to free CDDP, with a 50-fold increase in human GBM cell line accumulation.[278] In the encapsulation approach to CDDP, Duan *et al.* who reported on a nanogel encapsulation of CDDP via coordination in β-cyclodextrin-conjugated hyaluronic acid that provides GSH responsiveness, providing effective responsiveness against 4T1 cells.[279]

If we move to the last examples, liposomes have also been brought forward in Pt-based nanoformulations. An example of this is the works from Fernandez *et al.* who reported on CDDP complexes encapsulated in lipid particles to target cancer stem cells, demonstrating cytotoxicity against U87 GBM cell models specially when compared to oxaliplatin.[280]

Oxaliplatin-Based Nanoformulations. Oxaliplatin has demonstrated to induce antitumour effects more effectively than CDDP and carboplatin at concentrations lower than those to induce apoptosis, prompting research in the GBM area. Unfortunately, *in vivo* preclinical studies showed unsatisfactory since i.v. administration did not increase the median survival time of F98 glioma-bearing rats.[208] Most common hypothesis links to unsatisfactory BBB crossing, even when compromised by the tumour.[281] To overcome such limitations examples in the literature show targeting peptide functionalization of a polyethylene glycol (PEG)-glutamic acid micelle

functionalized with cyclic Arg-Gly-Asp in order to cross the BBB, target GBM cells and penetrate GBM via the cyclic RGD-mediated transvacuolar transport.[282] To cross the BBB, CED administered liposomal formulation Lipoxal™ successfully improved tumour accumulation and survival time in the same F98 glioma-bearing rats in combination with RT.[283]

***Carboplatin-Based Nanoformulations*.** On a molecular level, carboplatin presents lower nephrotoxicity and ototoxicity than CDDP and oxaliplatin. However lower cellular uptake presented by oxaliplatin leads to less activity.[284] Nonetheless, among the gold standard Pt complexes for cancer treatment, carboplatin exhibits the lowest toxicity while providing the best survival benefits.[285] Carboplatin on its own has already proven a good candidate among the approved Pt drugs for the treatment of human brain tumour. This is possible thanks to the radiosensitizer properties of the Pt-DNA adducts it is capable of forming.[285] Moreover, the benefits of carboplatin in nanoformulations have been studied and reported. For example, covalent coupling of carboplatin to N-(2-Hydroxypropyl)methacrylamide and the tetrapeptide Gly-Phe-Leu-Gly as to incorporate a proteolytic cleavage for intracellular drug delivery, revealed high therapeutic effect in preclinical models that were accepted in a phase I clinical trial.[286–288] We can also find reports from Karanam *et al.* showing the encapsulation of carboplatin within poly (Ɛ-caprolactone) NPs to minimise hemolysis and increase the cytotoxicity effect against U87 human GBM cell line, displaying a remarkable increase against the free drug.[289] As well as the work from Yang *et al.*, displaying a polyaminoacid formulation combining oxaliplatin and aspirin as a prodrug to induce an enhanced immunoresponse while providing chemotherapeutic effect on CT26 cancer *in vivo* cell models.[290]

It has been observed that carboplatin-loaded poly(butyl cyanoacrylate) NPs conjugated to growth factor monoclonal antibodies target GBM with a 40% increased cytotoxicity compared to the free form carboplatin when the nanoformulation follows IN administration. IN administration allowed this drug to present better absorption than free carboplatin without severe damage to the integrity of the nasal mucosa in Wistar rats. Thereafter, suggesting that these nanosystems are suitable to improve the nasal absorption of carboplatin, thereby improving drug-brain delivery.[291]

Nanoformulations based on Pt(IV) oxoplatin. The benefits introduced with Pt(IV) formulations over the standard Pt(II) drugs in GBM treatment, and the advantages of NPs compared to traditional RT, pushed research of Pt(IV)-based drugs in NPs.

Dhar *et al.* reported lipophilic polymeric NPs that showed targeting properties to deliver a Pt(IV)-prodrug into mitochondria. The NP-mediated controlled release of the Pt cargo and subsequent reduction to CDDP allowed for mitochondrial DNA cross-linking, and as such, leading to apoptosis.[255] Wang *et al.* showed polymeric NPs able to encapsulate an oxaliplatin prodrug with a cationic DNA intercalator. These NPs, when administered through CED, were able to inhibit the growth and progression of TMZ-resistant cells and TMZ-resistant human GBM tumours in mice without noticeable toxicity.[292] Also, Arduino *et al*. reported on a PEG-stabilised solid lipid NP containing different Pt(IV) prodrugs derived from kiteplatin. This work shows how such systems are capable of crossing the BBB *in vitro* with improved cellular uptake and higher cellular uptake when compared to the free counterparts.[293]

1.2. Scope of this Thesis

As described so far, GBM treatment has seen little clinical progress for the last 20 years. Even though Pt-based nanodrugs have displayed great potential, they have benefited from little or no attention beyond rescue therapies. This lack of acknowledgement has usually been due to challenges that the formulations must face (i.e., BBB crossing, tumour targeting, administration, renal clearance, *etc.*). Nonetheless, Pt-based NPs have displayed the capabilities to offset these limitations, though, as these platforms are still at early stages of development, further development is warranted.

Herein, we hypothesise that combination therapies aimed to simultaneously face multiple apoptosis/cell death pathways represent an interesting approach, considerably diminishing the capability of cancer cells to mutate and adapt.[294–296] More precisely, we propose three new experimental combinations, whose interest is described next:

1.2.1. Bioinspired Polymeric Neuromelanin-like Pt(IV) Nanoparticles

The use of bio-inspired approaches represents a step forward in cancer treatment.[297] This approach is well represented by polydopamine (PDA) on its nanostructured formulation, mimicking neuromelanin particles found in dopaminergic neurons of the substantia nigra.[298] In addition to their "Trojan-horse" use for brain diseases, they add interesting additional properties thanks to their rich redox chemistry.[299] In this context, our group recently reported a bis-catechol functionalized Pt(IV) (**PtBC**) prodrug complex, used as a building block to obtain Fe-based coordination nanoparticles (CNPs) thanks to the affinity of catechol units to chelate iron metal ions (Figure **1.13**). [297] In fact, *in vivo* intranasal administration of Pt-Fe CNPs in orthotopic preclinical GL261 GBM tumour-bearing mice showed enhanced Pt tumour accumulation and prolonged survival of the tested cohort, in some cases even to complete cure.[297]

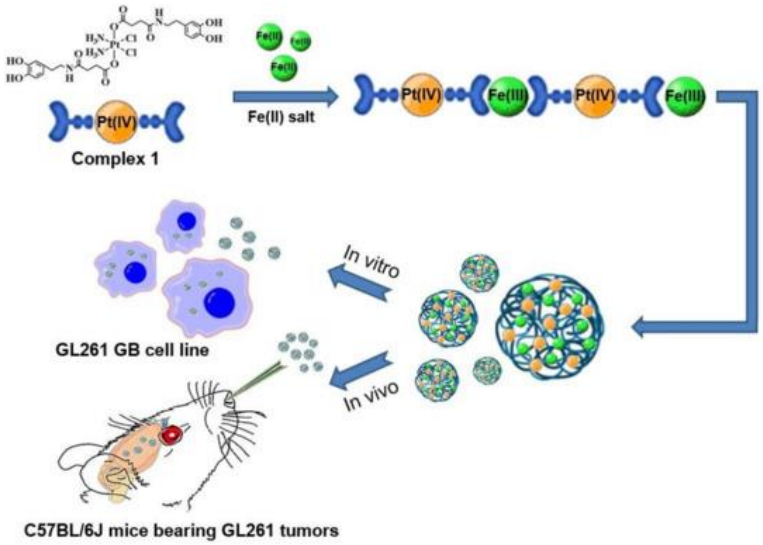


Figure **1.13**. Graphical abstract from Mao *et al.* depicting the use of **PtBC** as a neuromelanin-inspired particle in coordination polymerisation for GBM treatment in GL261 GBM tumour-bearing mice.

These successful initial findings encouraged us to investigate alternative possibilities to optimise the chemotherapeutic effect of this novel family of NPs. One potential approach involves the polymerisation of **PtBC** prodrugs through a bioinspired melanin-like oxidation process by reaction of the Pt complexes with sodium periodate.[300,301] The objective is to synthesise more robust NPs that offer increased Pt payloads and controlled Pt release, aiming to increase the therapeutic efficiency. A schematic representation for the synthesis of these novel polymeric **PtBC** NPs (**pPtBC NPs**) is shown in Figure **1.14**. Using such formulations, we aim to exploit biocompatible formulations with controlled release of active therapeutic Pt drugs through a combination of pH and redox-sensitive properties. Thanks to the redox-active character of polyphenol moieties, these systems are well-known to generate ROS aimed to have synergistic effects with Pt therapies (Figure **1.14**).

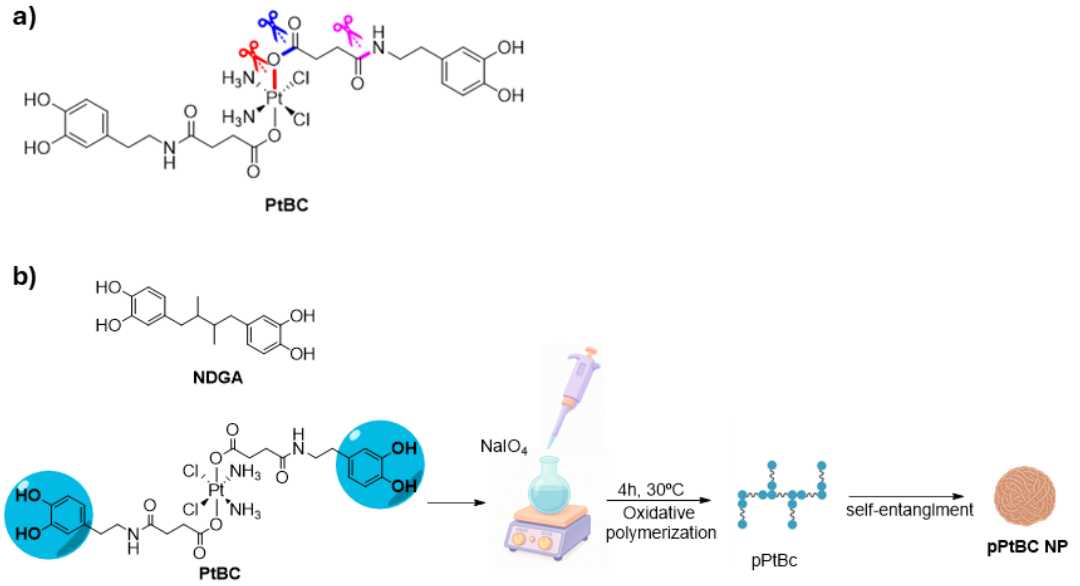


Figure **1.14**. **a)** Redox, pH and/or enzymatically sensitive bonds marked in red, purple and blue for **PtBC**. **b)** Schematic protocol for the synthesis of **pPtBC NPs**, by reaction of **PtBC** with sodium periodate. For comparison purposes, related NPs were obtained with the same methodology but with nordihydroguaiaretic acid (**NDGA**) as ligand, exhibiting a related topology to that of **PtBC**, but lacking the Pt(IV) ion. Depicting a published method as a result of the work on this Thesis. [302]

As a result of the versatile oxidative polymerisation of PtBC, and given the contextual know-how within our research group in catechol polymerisation related therapeutical approaches, an alternative platform to GBM treatment was studied in the following sections of this Thesis.

1.2.2. Supramolecular Photoactivatable Squaraine Pt(II) Nanoparticles

Platforms based on CNPs have represented a new paradigm for light-triggered therapies aimed at controlling the activation of therapeutic reagents.[303] So far, only a few examples in NP-based photoactivated chemotherapy (PACT) have been described. Furthermore, examples usually rely on life-threatening ultraviolet (UV) radiation for activation. An example of this case is the report of CNPs containing a photocleavable *o*-nitrobenzyl[304] unit or photoswitchable[305] diarylethene ligand in Ru-based CNPs.

Nonetheless, other reports have been described for light-induced ROS generation via photodynamic therapy (PDT). For example, phthalocyanine-based coordination polymers that generate ROS in MCF-7 cell cultures and cholesterol derivatives[306], incorporating the photosensitiser (PS) Ce6 in NPs while showing a significant accumulation into tumours through the EPR effect [307], or the combination of both, PDT and PACT.[308]

Beyond these examples, our group recently pioneered green light photoactive Ru-based NPs with high colloidal and chemical stability in physiological solutions (Figure **1.15**). *In vitro* studies with A431 and A549 cancer cell lines revealed an 11-fold increased uptake for the NPs compared to the monomeric complex [Ru(biqbpy)(N-methylimidazole)$_2$]$(PF_6)_2$. After irradiation, the CNPs yielded up to a two-fold increase in cytotoxicity compared to the same CNPs kept in the dark, indicating a selective effect by light irradiation.[309]

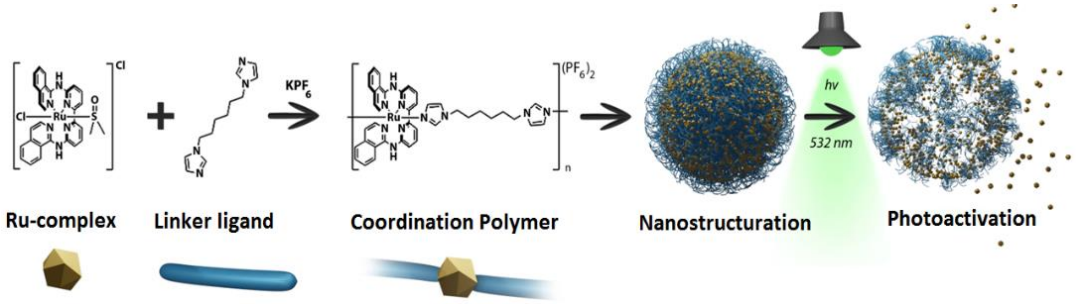


Figure **1.15**. Synthesis of Ru-based PACT-CNP and posterior drug release upon visible light irradiation as reported by Zhang *et al.* [309]

Nonetheless, previous works generally utilise harmful UV light or low penetrating radiation outside the therapeutic window of application, especially Pt-based drugs and platforms.[310] Moreover, the low phototoxicity index (PI) that was experienced by most of the reported examples in the bibliography limits the clinical application of these platforms.

To improve over the previously reported examples, we aim to introduce a versatile supramolecular-based NP based on squaraines (SQ). With this novel family of NPs, we aim to introduce a versatile nanoplatform that combines PACT with PDT, while achieving near-infrared (NIR) photoactivation due to the SQ binding ligand to Pt (Figure **1.16**). SQ-based NPs detailed in this Thesis (with and without Pt for comparison purposes) have been synthesised via supramolecular assembly in a simple one-step process. The resulting NPs have been irradiated in different regions of the spectra to study their absorption and emission properties to assess their photoreactivity. At the same time, ROS generation and Pt release have been studied in different conditions.

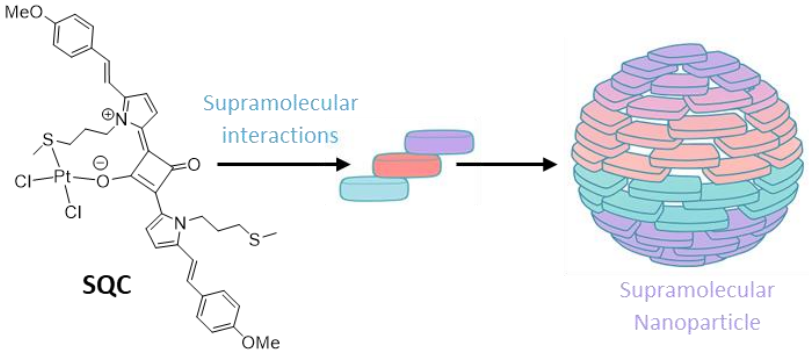


Figure **1.16**. Formation of a supramolecular aggregate using a photosensitive Pt(II) SQ complex (**SQC**).

1.2.3. Pt-based Nanoparticles for Singlet Oxygen Storage and in-situ Magnetic-induced Release

Alternatives to light-induced PDT, or PACT, by other external stimuli are also well known.[311] Therefore, within the context of this Thesis, heat was chosen to simultaneously trigger ROS and Pt(IV) release.

Singlet oxygen (SO) is a crucial ROS in PDT. However, the hypoxic TME limits the production of cytotoxic SO, decreasing the effectiveness of PDT. To overcome this challenge, researchers have explored the development of SO carriers that can capture and release SO in physiological conditions. Among these developments, anthracene-based endoperoxides have shown the ability to generate SO in a controlled manner under thermal- or photo-stimuli. [312]

Taking these previous works as a reference, [312] herein we propose the synthesis of a core-shell NP composed of a SPION core coated by a 9,10-dyphenylantrhacene (DPA) and Zr(IV) coordination polymer. Since DPA can evolve into the endoperoxide form as an SO reservoir, the aim consists of generating SO-loaded-like NPs (PDT-CNPs SO) that release SO in a controlled manner with temperature. With this aim, DPA has been functionalized with alkyl chain-based spacers ending with carboxylic acids that react with Zr(IV) metal ions (Figure **1.17**). The coordination polymer-coated NPs have been synthesised by reaction of the functionalized monomers with a Zr(IV) salt in the presence of the SPIONs. The resulting NPs were completely characterised, and their stimulus-induced behaviour was studied in detail.

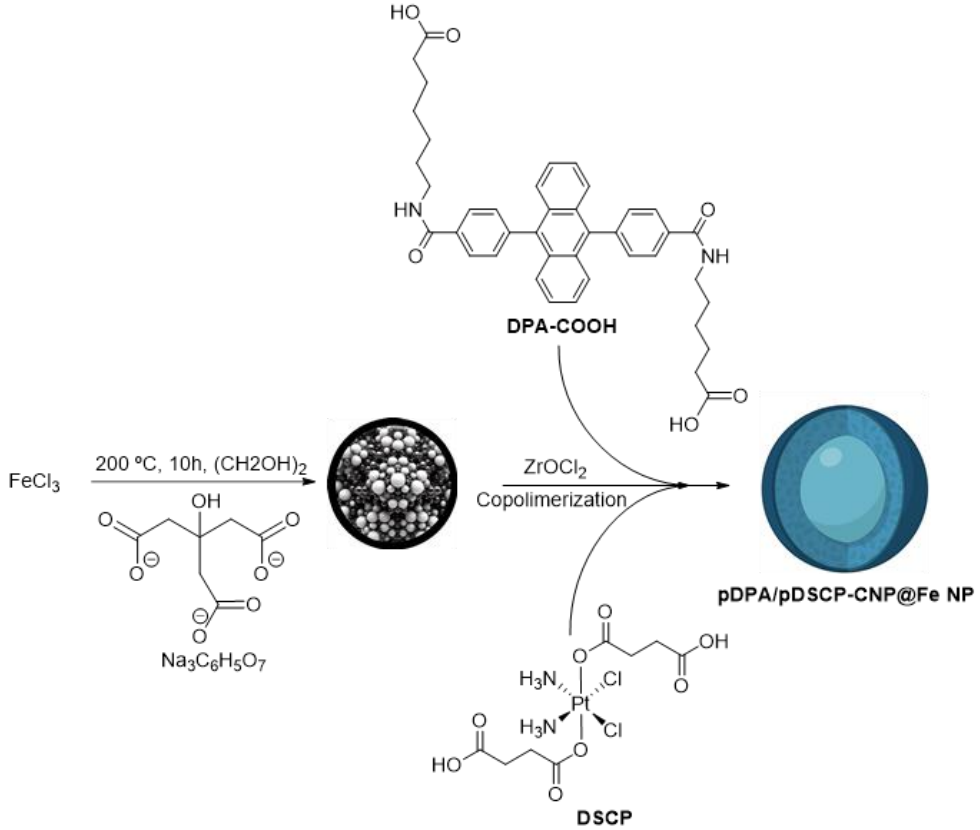


Figure **1.17**. Schematic illustration of the preparation of Pt(IV)-Zr(IV) coordination polymer-based core-shell NP.

1.2.4. Bioinspired Catechol-Based Pt(IV) Free-Standing Membranes for Post-Surgery Glioblastoma Treatment

The development of a platform for local drug delivery in post-surgery tumour cavities using free-standing membranes (FSMs) containing bioinspired neuromelanin-like Pt(IV) compounds was finally evaluated. The behaviour of these catechol-based FSMs is well known within our research group, and has been developed for multiple purposes, ranging from bactericidal to adhesive applications, but never used with this aim.[313–315]

Therefore, the formulation of this platform represents a promising opportunity to combine the capabilities from the *"Bioinspired Neuromelanin-like Pt(IV) Polymeric Nanoparticles "* platform, developed in Chapter 3, with a thin film (TF) formed through catechol polymerisation. Synthesis of this platform follows well-established and robust methods within our research group based on oxidative polymerisation processes using branched amines as polymerising agent (Figure **1.18**).[313] Furthermore, protocols for cell viability assays considering the complex nature of the resulting FSM were developed and adapted to evaluate the feasibility of these systems in GBM treatment. Physico-chemical characterisation of this platform will also give a good understanding of the basic guidelines behind the membrane behaviour.

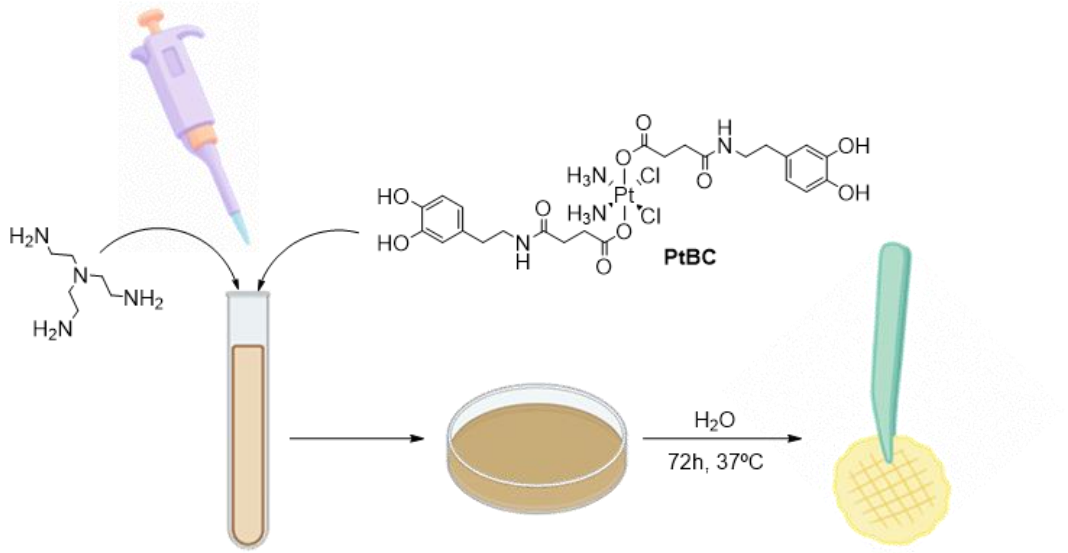


Figure **1.18**. Schematic representation of the synthesis of a **PtBC** FSM (**FSM-PtBC**).

1.3. References

1. Ostrom QT, Bauchet L, Davis FG, et al. The epidemiology of glioma in adults: A state of the science review. *Neuro Oncol*. **2014**;16(7). doi:10.1093/neuonc/nou087
2. European cancer information system. ECIS. Estimates of cancer incidence and mortality in 2020. Joint research centre. **2020**. https://ecis.jrc.ec.europa.eu/
3. Ostrom QT, Gittleman H, Liao P, et al. CBTRUS statistical report: Primary brain and central nervous system tumors diagnosed in the United States in 2007–2011. *Neuro Oncol*. **2014**;16. doi:10.1093/neuonc/nou223
4. Figarella-Branger D, Appay R, Metais A, et al. The 2021 WHO classification of tumours of the central nervous system. *Ann Pathol*. **2022**;42(5):367-382. doi:10.1016/j.annpat.2021.11.005
5. Komori T, Muragaki Y, Chernov MF. Pathology and Genetics of Gliomas. *Prog Neurol Surg*. **2018**;31. doi:10.1159/000466835
6. Urbanska K, Sokolowska J, Szmidt M, Sysa P. Glioblastoma multiforme - An overview. *Wspolcz Onkol*. **2014**;18(5). doi:10.5114/wo.2014.40559
7. Brandao M, Simon T, Critchley G, Giamas G. Astrocytes, the rising stars of the glioblastoma microenvironment. *Glia*. **2019**;67(5). doi:10.1002/glia.23520
8. Omuro A, DeAngelis LM. Glioblastoma and other malignant gliomas: A clinical review. *JAMA*. **2013**;310(17). doi:10.1001/jama.2013.280319
9. Delgado-López PD, Corrales-García EM. Survival in glioblastoma: a review on the impact of treatment modalities. *Clin Transl Oncol*. **2016**;18(11). doi:10.1007/s12094-016-1497-x
10. Mesfin FB, Al-Dhahir MA. Gliomas. *StatPearls*. *Pub*. **2020**;(August). https://www.ncbi.nlm.nih.gov/books/NBK441874/
11. Lam PYP, Ditomaso E, Ng HK, Pang JCS, Roussel MF, Hjelm NM. Expression of p19(INK4d), CDK4, CDK6 in glioblastoma multiforme. *Br J Neurosurg*. **2000**;14(1). doi:10.1080/02688690042870
12. Xu G, Li JY. CDK4, CDK6, cyclin D1, p16(INK4a) and EGFR expression in glioblastoma with a primitive neuronal component. *J Neurooncol*. **2018**;136(3). doi:10.1007/s11060-017-2674-7
13. Vignoli A, Lesma E, Alfano RM, et al. Glioblastoma multiforme in a child with tuberous sclerosis complex. *Am J Med Genet A*. **2015**;167(10). doi:10.1002/ajmg.a.37158
14. Dipro S, Al-Otaibi F, Alzahrani A, Ulhaq A, Al Shail E. Turcot Syndrome: A Synchronous Clinical Presentation of Glioblastoma Multiforme and Adenocarcinoma of the Colon. *Case Rep Oncol Med*. **2012**. doi:10.1155/2012/720273
15. Broekman MLD, Risselada R, Engelen-Lee J, Spliet WGM, Verweij BH. Glioblastoma Multiforme in the Posterior Cranial Fossa in a Patient with Neurofibromatosis Type I. *Case Rep Med*. **2009**. doi:10.1155/2009/757898
16. Zhen L, Yufeng C, Zhenyu S, Lei X. Multiple extracranial metastases from secondary glioblastoma multiforme: a case report and review of the literature. *J Neurooncol*. **2010**;97(3). doi:10.1007/s11060-009-0044-9
17. Kabat GC, Etgen AM, Rohan TE. Do steroid hormones play a role in the etiology of glioma? *CEBP*. **2010**;19(10). doi:10.1158/1055-9965.EPI-10-0658
18. Schüz J, Pirie K, Reeves GK, Floud S, Beral V. Cellular Telephone Use and the Risk of Brain Tumors: Update of the UK Million Women Study. *J Natl Cancer Inst*. **2022**;114(5). doi:10.1093/jnci/djac042
19. Johnson KJ, Schwartzbaum J, Kruchko C, et al. Brain tumor epidemiology in the era of precision medicine: The 2017 Brain Tumor Epidemiology Consortium meeting report. *Clin Neuropathol*. **2017**;36(6). doi:10.5414/NP301066
20. Reynoso-Noverón N, Mohar-Betancourt A, Ortiz-Rafael J. Epidemiology of brain tumors. Principles of Neuro-Oncology: Brain & Skull Base. *Springer.* **2020**. doi:10.1007/978-3-030-54879-7_2
21. Enchev Y, Ferdinandov D, Kounin G, Encheva E, Bussarsky V. Radiation-induced gliomas following radiotherapy for craniopharyngiomas: A case report and review of the literature. *Clin Neurol Neurosurg*. **2009**;111(7). doi:10.1016/j.clineuro.2009.03.009
22. Wingren C, James P, Borrebaeck CAK. Strategy for surveying the proteome using affinity proteomics and mass spectrometry. J *Proteomics*. **2009**;9(6). doi:10.1002/pmic.200800802
23. Blissitt PA. Clinical practice guideline series update. *J Neurosci Nurs*. **2014**;46(6). doi:10.1097/JNN.0000000000000088
24. Hanif F, Muzaffar K, Perveen K, Malhi SM, Simjee SU. Glioblastoma multiforme: A review of its epidemiology and pathogenesis through clinical presentation and treatment. *APJCP*. **2017**;18(1). doi:10.22034/APJCP.2017.18.1.3
25. Kumar Praveen J, Clark Michael L. Kumar and Clark's Clinical Medicine - 10th Edition. *Elsevier*. **2020**;10.
26. Chaichana KL, Parker SL, Olivi A, Quiñones-Hinojosa A. Long-term seizure outcomes in adult patients undergoing primary resection of malignant brain astrocytomas: Clinical article. *J Neurosurg*. **2009**;111(2). doi:10.3171/2009.2.JNS081132
27. Mrowczynski OD, Yang AL, Liao J, Rizk E. The Potential of Glioblastoma Patient Symptoms to Diagnose and Predict Survival. *Cureus*. **2021**. doi:10.7759/cureus.16675
28. Roth P, Wick W, Weller M. Steroids in neurooncology: Actions, indications, side-effects. *Curr Opin Neurol*. **2010**;23(6). doi:10.1097/WCO.0b013e32833e5a5d

29. Brenner DR, Gillis J, Demers AA, et al. Projected estimates of cancer in Canada in 2024. *CMAJ*. **2024**;196(18):E615-E623. doi:10.1503/cmaj.240095

30. Bray F, Ferlay J, Laversanne M, et al. Cancer Incidence in Five Continents: Inclusion criteria, highlights from Volume X and the global status of cancer registration. *Int J Cancer*. **2015**;137(9). doi:10.1002/ijc.29670

31. World Health Organization. World cancer report: cancer research for cancer prevention. *Cancer control*. **2020**;199(February).

32. Lin D, Wang M, Chen Y, et al. Trends in Intracranial Glioma Incidence and Mortality in the United States, 1975-2018. *Front Oncol*. **2021**;11. doi:10.3389/fonc.2021.748061

33. Ostrom QT, Price M, Neff C, et al. CBTRUS Statistical Report: Primary Brain and Other Central Nervous System Tumors Diagnosed in the United States in 2016-2020. *Neuro Oncol*. **2023**;25. doi:10.1093/neuonc/noad149

34. Grochans S, Cybulska AM, Simińska D, et al. Epidemiology of Glioblastoma Multiforme–Literature Review. *Cancers*. **2022**;14(10). doi:10.3390/cancers14102412

35. Oliver L, Lalier L, Salaud C, Heymann D, Cartron PF, Vallette FM. Drug resistance in glioblastoma: are persisters the key to therapy? *CDR*. **2020**;3(3). doi:10.20517/cdr.2020.29

36. Dymova MA, Kuligina E V., Richter VA. Molecular mechanisms of drug resistance in glioblastoma. *Int J Mol Sci*. **2021**;22(12). doi:10.3390/ijms22126385

37. Dagogo-Jack I, Shaw AT. Tumour heterogeneity and resistance to cancer therapies. *Nat Rev Clin Oncol*. **2018**;15(2). doi:10.1038/nrclinonc.2017.166

38. Bernhard C, Reita D, Martin S, Entz-Werle N, Dontenwill M. Glioblastoma Metabolism: Insights and Therapeutic Strategies. *Int J Mol Sci*. **2023**;24(11). doi:10.3390/ijms24119137

39. Michael M, Doherty MM. Tumoral drug metabolism: Overview and its implications for cancer therapy. *J Clin Oncol.* **2005**;23(1). doi:10.1200/JCO.2005.02.120

40. Housman G, Byler S, Heerboth S, et al. Drug resistance in cancer: An overview. *Cancers.* **2014**;6(3). doi:10.3390/cancers6031769

41. Valenti GE, Tasso B, Traverso N, Domenicotti C, Marengo B. Glutathione in cancer progression and chemoresistance: an update. *Redox exp med*. **2023**;2023(1). doi:10.1530/REM-22-0023

42. Ostrom QT, Cote DJ, Ascha M, Kruchko C, Barnholtz-Sloan JS. Adult glioma incidence and survival by race or ethnicity in the United States from 2000 to 2014. *JAMA Oncol*. **2018**;4(9). doi:10.1001/jamaoncol.2018.1789

43. Revilla-Pacheco F, Rodríguez-Salgado P, Barrera-Ramírez M, et al. Extent of resection and survival in patients with glioblastoma multiforme. *Medicine*. **2021**;100(25). doi:10.1097/md.0000000000026432

44. Grasso G. Extent of resection and survival in glioblastoma multiforme. *JAMA Oncol*. **2016**;2(11):1508-1509. doi:10.1001/jamaoncol.2016.3806

45. Wang T, Niu X, Gao T, et al. Prognostic Factors for Survival Outcome of High-Grade Multicentric Glioma. *World Neurosurg*. **2018**;112. doi:10.1016/j.wneu.2018.01.035

46. Burger PC, Green SB. Patient age, histologic features, and length of survival in patients with glioblastoma multiforme. *Cancer*. **1987**;59(9). doi:10.1002/1097-0142(19870501)59:9<1617::AID-CNCR2820590916>3.0.CO;2-X

47. Lacroix M, Abi-Said D, Fourney DR, et al. A multivariate analysis of 416 patients with glioblastoma multiforme: Prognosis, extent of resection, and survival. *J Neurosurg*. **2001**;95(2). doi:10.3171/jns.2001.95.2.0190

48. Komotar RJ, Otten ML, Moise G, Connolly ES. Radiotherapy plus concomitant and adjuvant temozolomide for glioblastoma—A critical review. *Clin Med Oncol*. **2008**;2. doi:10.4137/cmo.s390

49. Walker MD, Alexander E, Hunt WE, et al. Evaluation of BCNU and/or radiotherapy in the treatment of anaplastic gliomas. A cooperative clinical trial. *J Neurosurg*. **1978**;49(3). doi:10.3171/jns.1978.49.3.0333

50. Chang CH, Horton J, Schoenfeld D, et al. Comparison of postoperative radiotherapy and combined postoperative radiotherapy and chemotherapy in the multidisciplinary management of malignant gliomas. A joint radiation therapy oncology group and eastern cooperative oncology group study. *Cancer*. **1983**;52(6). doi:10.1002/1097-0142(19830915)52:6<997::AID-CNCR2820520612>3.0.CO;2-2

51. Shapiro WR, Green SB, Burger PC, et al. Randomized trial of three chemotherapy regimens and two radiotherapy regimens in postoperative treatment of malignant glioma. *J Neurosurg*. **1989**;71(1). doi:10.3171/jns.1989.71.1.0001

52. Stupp R, Hegi ME, van den Bent MJ, et al. Changing Paradigms—An Update on the Multidisciplinary Management of Malignant Glioma. *Oncologist*. **2006**;11(2). doi:10.1634/theoncologist.11-2-165

53. Stupp R, Mason WP, van den Bent MJ, et al. Radiotherapy plus Concomitant and Adjuvant Temozolomide for Glioblastoma. *N Engl J Med*. **2005**;352(10). doi:10.1056/nejmoa043330

54. Stevens MFG, Hickman JA, Stone R, et al. Antitumor Imidazotetrazines. 1. Synthesis and Chemistry of 8-carbamoyl-3-(2-chloroethyl)imidazo[5,l-d]-l,2,3,5-tetrazin-4(3H)-one, A Novel Broad-spectrum Antitumor Agent. *J Med Chem*. **1984**;27(2). doi:10.1021/jm00368a016

55. Hickman JA, Stevens MFG, Gibson NW, et al. Experimental Antitumor Activity against Murine Tumor Model Systems of 8-Carbamoyl-3-(2-chloroethyl)imidazo[5,1-d]-1,2,3,5-tetrazin-4(3H)-one (Mitozolomide), a Novel Broad-Spectrum Agent. *Cancer Res*. **1985**;45(7).

56. Newlands ES, Stevens MFG, Wedge SR, Wheelhouse RT, Brock C. Temozolomide: A review of its discovery, chemical properties, pre-clinical development and clinical trials. *Cancer Treat Rev*. **1997**;23(1). doi:10.1016/S0305-7372(97)90019-0

57. Brandes AA, Tosoni A, Cavallo G, et al. Temozolomide 3 weeks on and 1 week off as first-line therapy for recurrent glioblastoma: Phase II study from GICNO. *Br J Cancer*. **2006**;95(9). doi:10.1038/sj.bjc.6603376

58. Newlands ES, Blackledge GRP, Slack JA, et al. Phase I trial of temozolomide (CCRG 81045: M&U 39831: NSC 362856). *Br J Cancer*. **1992**;65(2). doi:10.1038/bjc.1992.57

59. Reid JM, Stevens DC, Rubin J, Ames MM. Pharmacokinetics of 3-methyl-(triazen-1-yl)imidazole-4-carboximide following administration of temozolomide to patients with advanced cancer. *Clin Cancer Res*. **1997**;3(12 I).

60. Tsang LLH, Farmer PB, Gescher A, Slack JA. Characterisation of urinary metabolites of temozolomide in humans and mice and evaluation of their cytotoxicity. *Cancer Chemother Pharmacol*. **1990**;26(6). doi:10.1007/BF02994094

61. Ostermann S, Csajkag C, Buclin T, et al. Plasma and cerebrospinal fluid population pharmacokinetics of temozolomide in malignant glioma patients. *Clin Cancer Res*. **2004**;10(11). doi:10.1158/1078-0432.CCR-03-0807

62. Mrugala MM, Chamberlain MC, Hutchinson F. Mechanisms of disease: Temozolomide and glioblastoma - Look to the future. *Nat Clin Pract Oncol*. **2008**;5(8). doi:10.1038/ncponc1155

63. Li H, Wu Y, Chen Y, et al. Overcoming temozolomide resistance in glioma: recent advances and mechanistic insights. *Acta Neuropathol Commun*. **2025**;13(1):126. doi:10.1186/s40478-025-02046-4

64. Fang C, Wang K, Stephen ZR, et al. Temozolomide nanoparticles for targeted glioblastoma therapy. *ACS Appl Mater Interfaces*. **2015**;7(12). doi:10.1021/am5092165

65. Zhang J, F.G. Stevens M, D. Bradshaw T. Temozolomide: Mechanisms of Action, Repair and Resistance. *Curr Mol Pharmacol*. **2011**;5(1). doi:10.2174/1874467211205010102

66. Pu J, Yuan K, Tao J, et al. Glioblastoma multiforme: an updated overview of temozolomide resistance mechanisms and strategies to overcome resistance. *Discov Oncol Springer.* **2025**;16(1). doi:10.1007/s12672-025-02567-3

67. Jiang G, Jiang AJ, Xin Y, Li LT, Cheng Q, Zheng JN. Progression of O6-methylguanine-DNA methyltransferase and temozolomide resistance in cancer research. *Mol Biol Rep*. **2014**;41(10). doi:10.1007/s11033-014-3549-z

68. Montaldi AP, Godoy PRDV, Sakamoto-Hojo ET. APE1/REF-1 down-regulation enhances the cytotoxic effects of temozolomide in a resistant glioblastoma cell line. *MRGTEM*. **2015**;793. doi:10.1016/j.mrgentox.2015.06.001

69. Pepponi R, Marra G, Fuggetta MP, et al. The effect of O6-alkylguanine-DNA alkyltransferase and mismatch repair activities on the sensitivity of human melanoma cells to temozolomide, 1,3-bis(2-chloroethyl)1-nitrosourea, and cisplatin. *J Pharmacol Exp Ther.* **2003**;304(2). doi:10.1124/jpet.102.043950

70. Medikonda R, Dunn G, Rahman M, Fecci P, Lim M. A review of glioblastoma immunotherapy. *J Neurooncol*. **2021**;151(1). doi:10.1007/s11060-020-03448-1

71. Yalamarty SSK, Filipczak N, Li X, et al. Mechanisms of Resistance and Current Treatment Options for Glioblastoma Multiforme (GBM). *Cancers*. **2023**;15(7). doi:10.3390/cancers15072116

72. Alphandéry E. Glioblastoma treatments: An account of recent industrial developments. *Front Pharmacol*. **2018**;9(SEP). doi:10.3389/fphar.2018.00879

73. Aliyu A, Shaari MR, Sayuti NSA, et al. N-ethyl-n-nitrosourea induced leukaemia in a mouse model through upregulation of vascular endothelial growth factor and evading apoptosis. *Cancers*. **2020**;12(3). doi:10.3390/cancers12030678

74. Huang B, Yu Z, Liang R. Effect of long-term adjuvant temozolomide chemotherapy on primary glioblastoma patient survival. *BMC Neurol*. **2021**;21(1). doi:10.1186/s12883-021-02461-9

75. Cantidio FS, Gil GOB, Queiroz IN, Regalin M. Glioblastoma — treatment and obstacles. *Pract Oncol Radiother* **2022**;27(4). doi:10.5603/RPOR.a2022.0076

76. Nam JY, De Groot JF. Treatment of glioblastoma. *J Oncol Pract*. **2017**;13(10):629-638. doi:10.1200/JOP.2017.025536

77. Brandes AA, Bartolotti M, Tosoni A, Franceschi E. Nitrosoureas in the Management of Malignant Gliomas. *Curr Neurol Neurosci Rep*. **2016**;16(2). doi:10.1007/s11910-015-0611-8

78. Diaz RJ, Ali S, Qadir MG, De La Fuente MI, Ivan ME, Komotar RJ. The role of bevacizumab in the treatment of glioblastoma. *J Neurooncol*. **2017**;133(3). doi:10.1007/s11060-017-2477-x

79. Kreisl TN, Kotliarova S, Butman JA, et al. A phase I/II trial of enzastaurin in patients with recurrent high-grade gliomas. *Neuro Oncol*. **2010**;12(2). doi:10.1093/neuonc/nop042

80. Heffron TP, Ndubaku CO, Salphati L, et al. Discovery of Clinical Development Candidate GDC-0084, a Brain Penetrant Inhibitor of PI3K and mTOR. *ACS Med Chem Lett*. **2016**;7(4). doi:10.1021/acsmedchemlett.6b00005

81. Bergman PJ. Cancer Immunotherapies. *Vet Clin North Am Small Anim Pract*. **2019**;49(5). doi:10.1016/j.cvsm.2019.04.010

82. Baraldi PG, Cacciari B, Guiotto A, Romagnoli R, Zaid AN, Spalluto G. Heterocyclic Analogs of DNA Minor Groove Alkylating Agents. *Curr Pharm Des*. **2022**;4(3). doi:10.2174/1381612804032210071252 43

83. Ralhan R, Kaur J. Alkylating agents and cancer therapy. *Expert Opin Ther Pat*. **2007**;17(9). doi:10.1517/13543776.17.9.1061

84. Rottenberg S, Disler C, Perego P. The rediscovery of platinum-based cancer therapy. *Nat Rev Cancer*. **2021**;21(1). doi:10.1038/s41568-020-00308-y

85. Lu E, Gareev I, Yuan C, et al. The Mechanisms of Current Platinum Anticancer Drug Resistance in the Glioma. *Curr Pharm Des*. **2022**;28(23). doi:10.2174/1381612828666220607105746

86. Rosenberg B, Van Camp L, Krigas T. Inhibition of cell division in Escherichia coli by electrolysis products from a platinum electrode [17]. *Nature*. **1965**;205(4972). doi:10.1038/205698a0

87. Rosenberg B, VanCamp L, Trosko JE, Mansour VH. Platinum compounds: A new class of potent antitumour agents [24]. *Nature*. **1969**;222(5191). doi:10.1038/222385a0

88. Rosenberg B. CISPLATIN: ITS HISTORY AND POSSIBLE MECHANISMS OF ACTION. *Cisplatin*. **1980**. doi:10.1016/b978-0-12-565050-2.50006-1

89. Schaeppi U, Heyman IA, Fleischman RW, et al. cis-Dichlorodiammineplatinum(II) (NSC-119 875): Preclinical toxicologic evaluation of intravenous injection in dogs, monkeys and mice. *Toxicol Appl Pharmacol*. **1973**;25(2). doi:10.1016/S0041-008X(73)80009-2

90. Alfonso-Triguero P, Lorenzo J, Candiota AP, Arús C, Ruiz-Molina D, Novio F. Platinum-Based Nanoformulations for Glioblastoma Treatment: The Resurgence of Platinum Drugs? *Nanomaterials*. **2023**;13(10). doi:10.3390/nano13101619

91. Browning RJ, Reardon PJT, Parhizkar M, et al. Drug Delivery Strategies for Platinum-Based Chemotherapy. *ACS Nano*. **2017**;11(9). doi:10.1021/acsnano.7b04092

92. Peckham MJ, Horwich A, Brada M, Drury A, Hendry WF. Cis-diammine-1, 1-cyclobutane dicarboxylate platinum II (carboplatin) in the treatment of testicular germ-cell tumours: a preliminary report. *Cancer Treat Rev*. **1985**;12(SUPPL. A). doi:10.1016/0305-7372(85)90025-8

93. van der Vijgh WJF. Clinical Pharmacokinetics of Carboplatin. *Clin Pharmacokinet*. **1991**;21(4). doi:10.2165/00003088-199121040-00002

94. Sasaki Y, Tamura T, Eguchi K, et al. Pharmacokinetics of (glycolato-0,0')-diammine platinum (II), a new platinum derivative, in comparison with cisplatin and carboplatin. *Cancer Chemother Pharmacol*. **1989**;23(4). doi:10.1007/BF00451649

95. Murrer BA, Abel G, McKeage MJ, et al. Preclinical Antitumor Evaluation of Bis-acetato-ammine-dichloro-cyclohexylamine Platinum(IV): An Orally Active Platinum Drug. *Cancer Res*. **1993**;53(11).

96. Bhargava A, Vaishampayan UN. Satraplatin: Leading the new generation of oral platinum agents. *Expert Opin Investig Drugs*. **2009**;18(11). doi:10.1517/13543780903362437

97. McKeage MJ, Mistry P, Ward J, et al. A phase I and pharmacology study of an oral platinum complex, JM216: dose-dependent pharmacokinetics with single-dose administration. *Cancer Chemother Pharmacol*. **1995**;36(6). doi:10.1007/BF00685793

98. Gietema JA, De Vries EGE, Sleijfer DT, et al. A phase I study of 1, 2-diamminomethyl-cyclobutane-platinum (II)-lactate (D-19466; lobaplatin) administered daily for 5 days. *Br J Cancer*. **1993**;67(2). doi:10.1038/bjc.1993.73

99. Mellish KJ, Barnard CFJ, Murrer BA, Kelland LR. DNA-binding properties of novel cis- and trans platinum-based anticancer agents in 2 human ovarian carcinoma cell lines. *Int J Cancer*. **1995**;62(6). doi:10.1002/ijc.2910620612

100. Choy H. Satraplatin: An orally available platinum analog for the treatment of cancer. *Expert Rev Anticancer Ther*. **2006**;6(7). doi:10.1586/14737140.6.7.973

101. McKeage MJ. Lobaplatin: A new antitumour platinum drug. *Expert Opin Investig Drugs*. **2001**;10(1). doi:10.1517/13543784.10.1.119

102. O'Neill CF, Koberle B, Masters JRW, Kelland LR. Gene-specific repair of Pt/DNA lesions and induction of apoptosis by the oral platinum drug JM216 in three human ovarian carcinoma cell lines sensitive and resistant to cisplatin. *Br J Cancer*. **1999**;81(8). doi:10.1038/sj.bjc.6694381

103. Kidani Y, Inagaki K, Iigo M, Hoshi A, Kuretani K. Antitumor Activity of 1,2-Diaminocyclohexane-Platinum Complexes against Sarcoma-180 Ascites Form. *J Med Chem*. **1978**;21(12). doi:10.1021/jm00210a029

104. Raymond E, Faivre S, Chaney S, Woynarowski J, Cvitkovic E. Cellular and molecular pharmacology of oxaliplatin. *Mol Cancer Ther*. **2002**;1(3).

105. Kim NK, Im SA, Kim DW, et al. Phase II clinical trial of SKI-2053R, a new platinum analog, in the treatment of patients with advanced gastric adenocarcinoma. *Cancer*. **1999**;86(7). doi:10.1002/(SICI)1097-0142(19991001)86:7<1109::AID-CNCR3>3.0.CO;2-G

106. Grizzi F, Chiriva-Internati M. Cancer: Looking for simplicity and finding complexity. *Cancer Cell Int*. **2006**;6. doi:10.1186/1475-2867-6-4

107. Ueda H, Sugiyama K, Tashiro S, Yokota M. Mechanism of the protective effect of sodium malate on cisplatin- induced toxicity in mice. *Biol Pharm Bull*. **1998**;21(2). doi:10.1248/bpb.21.121

108. Johnstone TC, Suntharalingam K, Lippard SJ. The Next Generation of Platinum Drugs: Targeted Pt(II) Agents, Nanoparticle Delivery, and Pt(IV) Prodrugs. *Chem Rev*. **2016**;116(5). doi:10.1021/acs.chemrev.5b00597

109. Romani AMP. Cisplatin in cancer treatment. *Biochem Pharmacol*. **2022**;206. doi:10.1016/j.bcp.2022.115323

110. Zhang C, Xu C, Gao X, Yao Q. Platinum-based drugs for cancer therapy and anti-tumor strategies. *Theranostics*. **2022**;12(5). doi:10.7150/thno.69424

111. Binks SP, Dobrota M. Kinetics and mechanism of uptake of platinum-based pharmaceuticals by the rat small intestine. *Biochem Pharmacol*. **1990**;40(6). doi:10.1016/0006-2952(90)90400-F

112. Martinho N, Marquês JMT, Todoriko I, Prieto M, de Almeida RFM, Silva LC. Effect of Cisplatin and Its Cationic Analogues in the Phase Behavior and Permeability of Model Lipid Bilayers. *Mol Pharm*. **2023**;20(2). doi:10.1021/acs.molpharmaceut.2c00321

113. Howell SB, Safaei R, Larson CA, Sailor MJ. Copper transporters and the cellular pharmacology of the platinum-containing cancer drugs. *Mol Pharmacol*. **2010**;77(6). doi:10.1124/mol.109.063172

114. Arnesano F, Nardella MI, Natile G. Platinum drugs, copper transporters and copper chelators. *Coord Chem Rev*. **2018**;374. doi:10.1016/j.ccr.2018.07.003

115. Howell SB, Abada P. Regulation of cisplatin cytotoxicity by Cu influx transporters. *Met Based Drugs*. **2010**. doi:10.1155/2010/317581

116. Zhang S, Lovejoy KS, Shima JE, et al. Organic cation transporters are determinants of oxaliplatin cytotoxicity. *Cancer Res*. **2006**;66(17). doi:10.1158/0008-5472.CAN-06-0769

117. Dornish JM, Pettersen EO. Requirement of a reactive aldehyde moiety for aldehyde-mediated protection against cis-dichlorodiammineplatinum-inducedcell inactivation. *Biochem Pharmacol*. **1990**;39(2). doi:10.1016/0006-2952(90)90030-O

118. Reishus JW, MartinJr DS. cis-Dichlorodiammineplatinum(II). Acid Hydrolysis and Isotopic Exchange of the Chloride Ligands. *J Am Chem Soc*. **1961**;83(11). doi:10.1021/ja01472a009

119. Cis-Dichlorodiammineplatinum(II). *Cancer Res* Springer; **2011**:869-869. doi:10.1007/978-3-642-16483-5_1188

120. Ligand Substitution Reactions. *J Organomet Chem*. **2007**. doi:10.1007/978-3-540-46129-6_7

121. Casini A, Reedijk J. Interactions of anticancer Pt compounds with proteins: An overlooked topic in medicinal inorganic chemistry? *Chem Sci*. **2012**;3(11). doi:10.1039/c2sc20627g

122. Mezencev R. Interactions of Cisplatin with non-DNA Targets and their Influence on Anticancer Activity and Drug Toxicity: The Complex World of the Platinum Complex. *Curr Cancer Drug Targets*. **2015**;14(9). doi:10.2174/1568009614666141128105146

123. Osborn MF, White JD, Haley MM, DeRose VJ. Platinum-RNA modifications following drug treatment in S. cerevisiae Identified by click chemistry and enzymatic mapping. *ACS Chem Biol*. **2014**;9(10). doi:10.1021/cb500395z

124. Bancroft DP, Lepre CA, Lippard SJ. 195Pt NMR Kinetic and Mechanistic Studies of cis- and trans-Diamminedichloroplatinum(II) Bindin to DNA. *J Am Chem Soc*. **1990**;112(19). doi:10.1021/ja00175a020

125. Fichtinger-Schepman AMJ, Lohman PHM, van der Veer JL, den Hartog JHJ, Reedijk J. Adducts of the Antitumor Drug cis-Diamminedichloroplatinum(II) with DNA: Formation, Identification, and Quantitation. *Biochemistry*. **1985**;24(3). doi:10.1021/bi00324a025

126. Kartalou M, Essigmann JM. Recognition of cisplatin adducts by cellular proteins. *Mutat Res Fundam Mol Mech Mutagenesis.* **2001**;478(1-2). doi:10.1016/S0027-5107(01)00142-7

127. Messori L, Merlino A. Cisplatin binding to proteins: Molecular structure of the ribonuclease A adduct. *Inorg Chem*. **2014**;53(8). doi:10.1021/ic500360f

128. Blommaert FA, van Dijk-Knijnenburg HCM, Dijt FJ, et al. Formation of DNA Adducts by the Anticancer Drug Carboplatin: Different Nucleotide Sequence Preferences in Vitro and in Cells. *Biochemistry*. **1995**;34(26). doi:10.1021/bi00026a031

129. Woynarowski JM, Chapman WG, Napier C, Herzig MCS, Juniewicz P. Sequence- and region-specificity of oxaliplatin adducts in naked and cellular DNA. *Mol Pharmacol*. **1998**;54(5). doi:10.1124/mol.54.5.770

130. Scovell WM, Collart F. Unwinding of supercoiled DNA by cis- and trans-diamminedichloroplatinum(II): Influence of the torsional strain on DNA unwinding. *Nucleic Acids Res*. **1985**;13(8). doi:10.1093/nar/13.8.2881

131. Wang D, Lippard SJ. Cellular processing of platinum anticancer drugs. *Nat Rev Drug Discov*. **2005**;4(4). doi:10.1038/nrd1691

132. Kar A, Agarwal S, Singh A, Bajaj A, Dasgupta U. Insights into molecular mechanisms of chemotherapy resistance in cancer. *Transl Oncol*. **2024**;42. doi:10.1016/j.tranon.2024.101901

133. Voong CK, Goodrich JA, Kugel JF. Interactions of hmgb proteins with the genome and the impact on disease. *Biomolecules*. **2021**;11(10). doi:10.3390/biom11101451

134. Todd RC, Lippard SJ. Inhibition of transcription by platinum antitumor compounds. *Metallomics*. **2009**;1(4). doi:10.1039/b907567d

135. Chovanec M, Abu Zaid M, Hanna N, El-Kouri N, Einhorn LH, Albany C. Long-term toxicity of cisplatin in germ-cell tumor survivors. *Ann Oncol*. **2017**;28(11). doi:10.1093/annonc/mdx360

136. Haugnes HS, Bosl GJ, Boer H, et al. Long-term and late effects of germ cell testicular cancer treatment and implications for follow-up. *J Clin Oncol*. **2012**;30(30). doi:10.1200/JCO.2012.43.4431

137. Fung C, Dinh PC, Fossa SD, Travis LB. Testicular cancer survivorship. *JNCCN*. **2019**;17(12). doi:10.6004/jnccn.2019.7369

138. Fung C, Fossa SD, Williams A, Travis LB. Long-term Morbidity of Testicular Cancer Treatment. *Urol Clin North Am*. **2015**;42(3). doi:10.1016/j.ucl.2015.05.002

139. van Leeuwen M, Kieffer JM, Efficace F, et al. International evaluation of the psychometrics of health-related quality of life questionnaires for use among long-term survivors of testicular and prostate cancer. *HQLO*. **2017**;15(1). doi:10.1186/s12955-017-0670-4

140. Glendenning JL, Barbachano Y, Norman AR, Dearnaley DP, Horwich A, Huddart RA. Long-term neurologic and peripheral vascular toxicity after chemotherapy treatment of testicular cancer. *Cancer*. **2010**;116(10). doi:10.1002/cncr.24981

141. El Ouardi N, Woopen H, Huehnchen P, et al. 393 Long-term neurological side effects in long-term survivors with ovarian cancer. *BMJ*; **2020**:A163.3-A163. doi:10.1136/ijgc-2020-igcs.340

142. Sprauten M, Darrah TH, Peterson DR, et al. Impact of long-term serum platinum concentrations on neuro- and ototoxicity in cisplatin-treated survivors of testicular cancer. *J Clin Oncol*. **2012**;30(3). doi:10.1200/JCO.2011.37.4025

143. Brydøy M, Oldenburg J, Klepp O, et al. Observational study of prevalence of long-term Raynaud-like phenomena and neurological side effects in testicular cancer survivors. *J Natl Cancer Inst*. **2009**;101(24). doi:10.1093/jnci/djp413

144. Travis LB, Fossa SD, Sesso HD, et al. Chemotherapy-induced peripheral neurotoxicity and ototoxicity: New paradigms for translational genomics. *J Natl Cancer Inst*. **2014**;106(5). doi:10.1093/jnci/dju044

145. Frisina RD, Wheeler HE, Fossa SD, et al. Comprehensive audiometric analysis of hearing impairment and tinnitus after cisplatin-based chemotherapy in survivors of adult-onset cancer. *JCO*. **2016**;34(23). doi:10.1200/JCO.2016.66.8822

146. Feldman DR, Schaffer WL, Steingart RM. Late cardiovascular toxicity following chemotherapy for germ cell tumors. *JNCCN*. **2012**;10(4). doi:10.6004/jnccn.2012.0051

147. Haugnes HS, Aass N, Fosså SD, et al. Pulmonary function in long-term survivors of testicular cancer. *J Clin Oncol.* **2009**;27(17). doi:10.1200/JCO.2008.18.5181

148. Fosså SD, Aass N, Winderen M, Börmer OP, Olsen DR. Long-term renal function after treatment for malignant germ-cell tumours. *Ann Oncol*. **2002**;13(2). doi:10.1093/annonc/mdf048

149. Wang X, Wang X, Jin S, Muhammad N, Guo Z. Stimuli-Responsive Therapeutic Metallodrugs. *Chem Rev*. **2019**;119(2). doi:10.1021/acs.chemrev.8b00209

150. Gibson D. Platinum(IV) anticancer agents; are we en route to the holy grail or to a dead end? *J Inorg Biochem*. **2021**;217. doi:10.1016/j.jinorgbio.2020.111353

151. Massaguer A, González-Cantó A, Escribano E, et al. Integrin-targeted delivery into cancer cells of a Pt(iv) pro-drug through conjugation to RGD-containing peptides. *Dalton Trans*. **2015**;44(1). doi:10.1039/c4dt02710h

152. Gandioso A, Shaili E, Massaguer A, et al. An integrin-targeted photoactivatable Pt(iv) complex as a selective anticancer pro-drug: Synthesis and photoactivation studies. *Chem Commun*. **2015**;51(44). doi:10.1039/c5cc03180j

153. Shrestha A, Lahooti B, Mikelis CM, Mattheolabakis G. Chlorotoxin and Lung Cancer: A Targeting Perspective for Drug Delivery. *Pharmaceutics*. **2022**;14(12). doi:10.3390/pharmaceutics14122613

154. Hua W, Zhao J, Hu W, Gou S. Combination of 7-hydroxycoumarin in a platinum(IV) complex derived from cisplatin enhanced cytotoxicity with multiple mechanisms of action. *J Inorg Biochem*. **2018**;186. doi:10.1016/j.jinorgbio.2018.05.015

155. Halwai K, Khanna S, Gupta G, Wahab S, Khalid M, Kesharwani P. Folate-conjugated carbon nanotubes as a promising therapeutic approach for targeted cancer therapy. *J Drug Target*. **2025**;33(1):1-16. doi:10.1080/1061186X.2024.2393423

156. Patra M, Johnstone TC, Suntharalingam K, Lippard SJ. A Potent Glucose-Platinum Conjugate Exploits Glucose Transporters and Preferentially Accumulates in Cancer Cells. *Angew Chem Int Ed*. **2016**;55(7). doi:10.1002/anie.201510551

157. Ma J, Yang X, Hao W, Huang Z, Wang X, Wang PG. Mono-functionalized glycosylated platinum(IV) complexes possessed both pH and redox dual-responsive properties: Exhibited enhanced safety and preferentially accumulated in cancer cells in vitro and in vivo. *Eur J Med Chem*. **2017**;128. doi:10.1016/j.ejmech.2017.01.032

158. Wexselblatt E, Gibson D. What do we know about the reduction of Pt(IV) pro-drugs? *J Inorg Biochem*. **2012**;Vol 117. doi:10.1016/j.jinorgbio.2012.06.013

159. Hall MD, Mellor HR, Callaghan R, Hambley TW. Basis for design and development of platinum(IV) anticancer complexes. *J Med Chem*. **2007**;50(15). doi:10.1021/jm070280u

160. Jeong EM, Yoon JH, Lim J, et al. Real-Time Monitoring of Glutathione in Living Cells Reveals that High Glutathione Levels Are Required to Maintain Stem Cell Function. *Stem Cell Rep*. **2018**;10(2). doi:10.1016/j.stemcr.2017.12.007

161. Washko P, Rotrosen D, Levine M. Ascorbic acid transport and accumulation in human neutrophils. *J Biol Chem*. **1989**;264(32). doi:10.1016/s0021-9258(19)47256-6

162. Michelet F, Gueguen R, Leroy P, Wellman M, Nicolas A, Siest G. Blood and plasma glutathione measured in healthy subjects by HPLC: Relation to sex, aging, biological variables, and life habits. *Clin Chem*. **1995**;41(10). doi:10.1093/clinchem/41.10.1509

163. Wang Z, Deng Z, Zhu G. Emerging platinum(iv) prodrugs to combat cisplatin resistance: From isolated cancer cells to tumor microenvironment. *Dalton Trans*. **2019**;48(8). doi:10.1039/c8dt03923b

164. Babak M V., Zhi Y, Czarny B, et al. Dual-Targeting Dual-Action Platinum(IV) Platform for Enhanced Anticancer Activity and Reduced Nephrotoxicity. *Angew Chem Int Ed*. **2019**;58(24). doi:10.1002/anie.201903112

165. Wee HA, Khalaila I, Allardyce CS, Juillerat-Jeanneret L, Dyson PJ. Rational design of platinum(IV) compounds to overcome glutathione-S- transferase mediated drug resistance. *J Am Chem Soc*. **2005**;127(5). doi:10.1021/ja0432618

166. Dhar S, Lippard SJ. Mitaplatin, a potent fusion of cisplatin and the orphan drug dichloroacetate. *Proc Natl Acad Sci U S A*. **2009**;106(52). doi:10.1073/pnas.0912276106

167. Ma L, Ma R, Wang Y, et al. Chalcoplatin, a dual-targeting and p53 activator-containing anticancer platinum(iv) prodrug with unique mode of action. *Chem Commun* **2015**;51(29). doi:10.1039/c4cc10409a

168. Ma L, Wang N, Ma R, et al. Monochalcoplatin: An Actively Transported, Quickly Reducible, and Highly Potent PtIV Anticancer Prodrug. *Angew Chem Int Ed*. **2018**;57(29). doi:10.1002/anie.201804314

169. Tian R, Ma H, Zhu S, et al. Multiplexed NIR-II Probes for Lymph Node-Invaded Cancer Detection and Imaging-Guided Surgery. *Adv Mater*. **2020**;32(11). doi:10.1002/adma.201907365

170. Neumann W, Crews BC, Sárosi MB, et al. Conjugation of cisplatin analogues and cyclooxygenase inhibitors to overcome cisplatin resistance. *Chem Med Chem*. **2015**;10(1). doi:10.1002/cmdc.201402353

171. Cheng Q, Shi H, Wang H, Min Y, Wang J, Liu Y. The ligation of aspirin to cisplatin demonstrates significant synergistic effects on tumor cells. *Chem Commun* **2014**;50(56). doi:10.1039/c4cc00419a

172. Kim J, Jo C, Lim WG, et al. Programmed Nanoparticle-Loaded Nanoparticles for Deep-Penetrating 3D Cancer Therapy. *Adv Mater*. **2018**;30(29). doi:10.1002/adma.201707557

173. Facchetti G, Petrella F, Spaggiari L, Rimoldi I. Malignant Pleural Mesothelioma: State of the art and advanced cell therapy. *Eur J Med Chem*. **2017**;142. doi:10.1016/j.ejmech.2017.07.063

174. Raveendran R, Braude JP, Wexselblatt E, et al. Pt(iv) derivatives of cisplatin and oxaliplatin with phenylbutyrate axial ligands are potent cytotoxic agents that act by several mechanisms of action. *Chem Sci*. **2016**;7(3). doi:10.1039/c5sc04205d

175. Petruzzella E, Sirota R, Solazzo I, Gandin V, Gibson D. Triple action Pt(iv) derivatives of cisplatin: A new class of potent anticancer agents that overcome resistance. *Chem Sci*. **2018**;9(18). doi:10.1039/c8sc00428e

176. Petruzzella E, Braude JP, Aldrich-Wright JR, Gandin V, Gibson D. A Quadruple-Action Platinum(IV) Prodrug with Anticancer Activity Against KRAS Mutated Cancer Cell Lines. *Angew Chem Int Ed*. **2017**;56(38). doi:10.1002/anie.201706739

177. Hu W, Fang L, Hua W, Gou S. Biotin-Pt (IV)-indomethacin hybrid: A targeting anticancer prodrug providing enhanced cancer cellular uptake and reversing cisplatin resistance. *J Inorg Biochem*. **2017**;175. doi:10.1016/j.jinorgbio.2017.07.002

178. Guin S, Ashokan A, Pollack A, Dhar S. Lipid Metabolism Modulatory Cisplatin Prodrug Sensitizes Resistant Prostate Cancer toward Androgen Deprivation Therapy. *ACS Pharmacol Transl Sci*. **2024**;7(9):2820-2826. doi:10.1021/acsptsci.4c00301

179. Roci E, Cakani B, Brace G, et al. Platinum-based chemotherapy in recurrent high-grade glioma patients: retrospective study. *Med Arch*. **2014**;68(2). doi:10.5455/medarh.2014.68.140-143

180. Newton HB, Page MA, Junck L, Greenberg HS. Intra-arterial cisplatin for the treatment of malignant gliomas. *J Neurooncol*. **1989**;7(1). doi:10.1007/BF00149377

181. Brandes AA, Basso U, Reni M, et al. First-line chemotherapy with cisplatin plus fractionated temozolomide in recurrent glioblastoma multiforme: A phase II study of the Gruppo Italiano Cooperativo di Neuro-Oncologia. *J Clin Oncol*. **2004**;22(9). doi:10.1200/JCO.2004.11.019

182. Qi L, Luo Q, Zhang Y, Jia F, Zhao Y, Wang F. Advances in Toxicological Research of the Anticancer Drug Cisplatin. *Chem Res Toxicol*. **2019**;32(8). doi:10.1021/acs.chemrestox.9b00204

183. Alassadi S, Pisani MJ, Wheate NJ. A chemical perspective on the clinical use of platinum-based anticancer drugs. *Dalton Trans*. **2022**;51(29). doi:10.1039/d2dt01875f

184. Wlodarczyk MT, Dragulska SA, Camacho-Vanegas O, et al. Platinum(II) Complex-Nuclear Localization Sequence Peptide Hybrid for Overcoming Platinum Resistance in Cancer Therapy. *ACS Biomater Sci Eng*. **2018**;4(2). doi:10.1021/acsbiomaterials.7b00921

185. Jacobs S, McCully CL, Murphy RF, Bacher J, Balis FM, Fox E. Extracellular fluid concentrations of cisplatin, carboplatin, and oxaliplatin in brain, muscle, and blood measured using microdialysis in nonhuman primates. *Cancer Chemother Pharmacol*. **2010**;65(5). doi:10.1007/s00280-009-1085-7

186. Zheng Y, Hunting DJ, Ayotte P, Sanche L. Role of secondary low-energy electrons in the concomitant chemoradiation therapy of cancer. *Phys Rev Lett*. **2008**;100(19). doi:10.1103/PhysRevLett.100.198101

187. Mishima K, Mazar AP, Gown A, et al. A peptide derived from the non-receptor-binding region of urokinase plasminogen activator inhibits glioblastoma growth and angiogenesis in vivo in combination with cisplatin. *Proc Natl Acad Sci U S A*. **2000;**97(15). doi:10.1073/pnas.150239497

188. Hess SM, Anderson JG, Bierbach U. A non-crosslinking platinum-acridine hybrid agent shows enhanced cytotoxicity compared to clinical BCNU and cisplatin in glioblastoma cells. *Bioorg Med Chem Lett*. **2005**;15(2). doi:10.1016/j.bmcl.2004.10.049

189. Kunzelmann K, Ousingsawat J, Benedetto R, Cabrita I, Schreiber R. Contribution of anoctamins to cell survival and cell death. *Cancers*. **2019**;11(3). doi:10.3390/cancers11030382

190. Gajski G, Čimbora-Zovko T, Rak S, Osmak M, Garaj-Vrhovac V. Antitumour action on human glioblastoma A1235 cells through cooperation of bee venom and cisplatin. *Cytotechnology*. **2016**;68(4). doi:10.1007/s10616-015-9879-4

191. Macieja A, Kopa P, Galita G, Pastwa E, Majsterek I, Poplawski T. Comparison of the effect of three different topoisomerase II inhibitors combined with cisplatin in human glioblastoma cells sensitized with double strand break repair inhibitors. *Mol Biol Rep*. **2019**;46(4). doi:10.1007/s11033-019-04605-0

192. Li J, Song J, Guo F. miR-186 reverses cisplatin resistance and inhibits the formation of the glioblastoma-initiating cell phenotype by degrading Yin Yang 1 in glioblastoma. *Int J Mol Med*. **2019**;43(1). doi:10.3892/ijmm.2018.3940

193. Hodeify R, Megyesi J, Tarcsafalvi A, Safirstein RL, Price PM. Protection of cisplatin cytotoxicity by an inactive cyclin-dependent kinase. *Am J Physiol Renal Physiol*. **2010**;299(1). doi:10.1152/ajprenal.00151.2010

194. Barth RF, Wu G, Hans Meisen W, et al. Design, synthesis, and evaluation of cisplatin-containing EGFR targeting bioconjugates as potential therapeutic agents for brain tumors. *Onco Targets Ther*. **2016**;9. doi:10.2147/OTT.S99242

195. Fakiruddin KS, Lim MN, Nordin N, Rosli R, Abdullah S. Chemo-sensitization of CD133+ cancer stem cell enhances the effect of mesenchymal stem cell expressing TRAIL in non-small cell lung cancer cell lines. *Biology*. **2021**;10(11). doi:10.3390/biology10111103

196. Ferrari B, Urselli F, Gilodi M, et al. New Platinum-Based Prodrug Pt(IV)Ac-POA: Antitumour Effects in Rat C6 Glioblastoma Cells. *Neurotox Res*. **2020**;37(1). doi:10.1007/s12640-019-00076-0

197. Gwak HS, Shingu T, Chumbalkar V, et al. Combined action of the dinuclear platinum compound BBR3610 with the PI3-K inhibitor PX-866 in glioblastoma. *Int J Cancer*. **2011**;128(4). doi:10.1002/ijc.25394

198. Runge R, Reissig F, Herzog N, Oehme L, Brogsitter C, Kotzerke J. Combining Cisplatin with Different Radiation Qualities—Interpretation of Cytotoxic Effects In Vitro by Isobolographic Analysis. *Pharm J*. **2023**;16(12). doi:10.3390/ph16121720

199. Nagane M, Narita Y, Mishima K, et al. Human glioblastoma xenografts overexpressing a tumor-specific mutant epidermal growth factor receptor sensitized to cisplatin by the AG1478 tyrosine kinase inhibitor. *J Neurosurg*. **2001**;95(3). doi:10.3171/jns.2001.95.3.0472

200. Park CK, Park SH, Lee SH, et al. Methylation status of the MGMT gene promoter fails to predict the clinical outcome of glioblastoma patients treated with ACNU plus cisplatin: Original Article. *Neuropathology*. **2009**;29(4). doi:10.1111/j.1440-1789.2008.00998.x

201. Buckner JC, Ballman K V., Michalak JC, et al. Phase III trial of carmustine and cisplatin compared with carmustine alone and standard radiation therapy or accelerated radiation therapy in patients with glioblastoma multiforme: North Central Cancer Treatment Group 93-72-52 and Southwest Oncology Group 9503 trials. *J Clin Oncol*. **2006**;24(24). doi:10.1200/JCO.2005.04.6979

202. Raghavan S, Baskin DS, Sharpe MA. MP-Pt(IV): A MAOB-sensitive mitochondrial-specific prodrug for treating glioblastoma. *Mol Cancer Ther*. **2020**;19(12). doi:10.1158/1535-7163.MCT-20-0420

203. Sharpe M, Baskin D. CADD-18. MP-Pt(IV): A MAOB SENSITIVE MITOCHONDRIAL SMART BOMB FOR TREATING GLIOMA. *Neuro Oncol*. **2018**;20(suppl_6). doi:10.1093/neuonc/noy148.1163

204. Lazić JM, Vučićević L, Grgurić-Šipka S, et al. Synthesis and in vitro anticancer activity of octahedral platinum(IV) complexes with cyclohexyl-functionalized ethylenediamine-N,N'-diacetate- type ligands. *ChemMedChem*. **2010**;5(6). doi:10.1002/cmdc.201000058

205. Mihajlović LE, Savić A, Poljarević J, et al. Novel methylene modified cyclohexyl ethylenediamine-N,N'-diacetate ligands and their platinum(IV) complexes. Influence on biological activity. *J Inorg Biochem*. **2012**;109. doi:10.1016/j.jinorgbio.2012.01.012

206. González VM, Amo-Ochoa P, Pérez JM, et al. Synthesis, characterization, and DNA modification induced by a novel Pt-Berenil compound with cytotoxic activity. *J Inorg Biochem*. **1996**;63(1). doi:10.1016/0162-0134(95)00175-1

207. Arvanitis CD, Ferraro GB, Jain RK. The blood–brain barrier and blood–tumour barrier in brain tumours and metastases. *Nat Rev Cancer*. **2020**;20(1). doi:10.1038/s41568-019-0205-x

208. Charest G, Sanche L, Fortin D, Mathieu D, Paquette B. Optimization of the route of platinum drugs administration to optimize the concomitant treatment with radiotherapy for glioblastoma implanted in the Fischer rat brain. *J Neurooncol*. **2013**;115(3). doi:10.1007/s11060-013-1238-8

209. Kovacs ZI, Burks SR, Frank JA. Focused ultrasound with microbubbles induces sterile inflammatory response proportional to the blood brain barrier opening: Attention to experimental conditions. *Theranostics*. **2018**;8(8). doi:10.7150/thno.24181

210. Sharabi S, Bresler Y, Ravid O, et al. Transient blood–brain barrier disruption is induced by low pulsed electrical fields in vitro: an analysis of permeability and trans-endothelial electric resistivity. *Drug Deliv*. **2019**;26(1). doi:10.1080/10717544.2019.1571123

211. Graham-Gurysh E, Moore KM, Satterlee AB, et al. Sustained Delivery of Doxorubicin via Acetalated Dextran Scaffold Prevents Glioblastoma Recurrence after Surgical Resection. *Mol Pharm*. **2018**;15(3). doi:10.1021/acs.molpharmaceut.7b01114

212. Tabet A, Jensen MP, Parkins CC, Patil PG, Watts C, Scherman OA. Designing Next-Generation Local Drug Delivery Vehicles for Glioblastoma Adjuvant Chemotherapy: Lessons from the Clinic. *Adv Healthc Mater*. **2019**;8(3). doi:10.1002/adhm.201801391

213. Shi M, Sanche L. Convection-Enhanced Delivery in Malignant Gliomas: A Review of Toxicity and Efficacy. *J Oncol*. **2019**. doi:10.1155/2019/9342796

214. Enríquez Pérez J, Fritzell S, Kopecky J, Visse E, Darabi A, Siesjö P. The effect of locally delivered cisplatin is dependent on an intact immune function in an experimental glioma model. *Sci Rep*. **2019**;9(1). doi:10.1038/s41598-019-42001-7

215. Eiseman JL, Beumer JH, Rigatti LH, et al. Plasma pharmacokinetics and tissue and brain distribution of cisplatin in musk shrews. *Cancer Chemother Pharmacol*. **2015**;75(1). doi:10.1007/s00280-014-2623-5

216. McWhinney SR, Goldberg RM, McLeod HL. Platinum neurotoxicity pharmacogenetics. *Mol Cancer Ther*. **2009**;8(1). doi:10.1158/1535-7163.MCT-08-0840

217. Chattaraj A, Syed MP, Low CA, Owonikoko TK. Cisplatin-Induced Ototoxicity: A Concise Review of the Burden, Prevention, and Interception Strategies. *JCO Oncol Pract*. **2023**;19(5). doi:10.1200/op.22.00710

218. Pardridge WM. The blood-brain barrier: Bottleneck in brain drug development. *NeuroRx*. **2005**;2(1). doi:10.1602/neurorx.2.1.3

219. Sheleg S V., Korotkevich EA, Zhavrid EA, et al. Local chemotherapy with cisplatin-depot for glioblastoma multiforme. *J Neurooncol*. **2002**;60(1). doi:10.1023/A:1020288015457

220. White E, Bienemann A, Taylor H, Hopkins K, Cameron A, Gill S. A phase I trial of carboplatin administered by convection-enhanced delivery to patients with recurrent/progressive glioblastoma multiforme. *Contemp Clin Trials*. **2012**;33(2). doi:10.1016/j.cct.2011.10.010

221. Massimino M, Spreafico F, Riva D, et al. A lower-dose, lower-toxicity cisplatin-etoposide regimen for childhood progressive low-grade glioma. *J Neurooncol*. **2010**;100(1). doi:10.1007/s11060-010-0136-6

222. Ferrari B, Roda E, Priori EC, et al. A New Platinum-Based Prodrug Candidate for Chemotherapy and Its Synergistic Effect With Hadrontherapy: Novel Strategy to Treat Glioblastoma. *Front Neurosci*. **2021**;15. doi:10.3389/fnins.2021.589906

223. Wicki A, Witzigmann D, Balasubramanian V, Huwyler J. Nanomedicine in cancer therapy: Challenges, opportunities, and clinical applications. *J Control Release*. **2015**;200. doi:10.1016/j.jconrel.2014.12.030

224. Tee JK, Yip LX, Tan ES, et al. Nanoparticles' interactions with vasculature in diseases. *Chem Soc Rev*. **2019**;48(21). doi:10.1039/c9cs00309f

225. Truong NP, Whittaker MR, Mak CW, Davis TP. The importance of nanoparticle shape in cancer drug delivery. *Expert Opin Drug Deliv*. **2015**;12(1). doi:10.1517/17425247.2014.950564

226. Stylianopoulos T, Poh MZ, Insin N, et al. Diffusion of particles in the extracellular matrix: The effect of repulsive electrostatic interactions. *Biophys J*. **2010**;99(5). doi:10.1016/j.bpj.2010.06.016

227. Tran S, DeGiovanni P, Piel B, Rai P. Cancer nanomedicine: a review of recent success in drug delivery. *Clin Transl Med*. **2017**;6(1). doi:10.1186/s40169-017-0175-0

228. Albanese A, Tang PS, Chan WCW. The effect of nanoparticle size, shape, and surface chemistry on biological systems. *Annu Rev Biomed Eng*. **2012**;14. doi:10.1146/annurev-bioeng-071811-150124

229. Bregoli L, Movia D, Gavigan-Imedio JD, Lysaght J, Reynolds J, Prina-Mello A. Nanomedicine applied to translational oncology: A future perspective on cancer treatment. *Nanomedicine*. **2016**;12(1). doi:10.1016/j.nano.2015.08.006

230. Wu J. The enhanced permeability and retention (Epr) effect: The significance of the concept and methods to enhance its application. *J Pers Med*. **2021**;11(8). doi:10.3390/jpm11080771

231. Fang J, Islam W, Maeda H. Exploiting the dynamics of the EPR effect and strategies to improve the therapeutic effects of nanomedicines by using EPR effect enhancers. *Adv Drug Deliv Rev*. **2020**;157. doi:10.1016/j.addr.2020.06.005

232. Afzal O, Altamimi ASA, Nadeem MS, et al. Nanoparticles in Drug Delivery: From History to Therapeutic Applications. *Nanomaterials*. **2022**;12(24). doi:10.3390/nano12244494

233. Alphandéry E. Nano-therapies for glioblastoma treatment. *Cancers*. **2020**;12(1). doi:10.3390/cancers12010242

234. Michael JS, Lee BS, Zhang M, Yu JS. Nanotechnology for treatment of glioblastoma multiforme. *J Transl Int Med*. **2018**;6(3). doi:10.2478/jtim-2018-0025

235. Zha S, Liu H, Li H, Li H, Wong KL, All AH. Functionalized Nanomaterials Capable of Crossing the Blood-Brain Barrier. *ACS Nano*. **2024**;18(3). doi:10.1021/acsnano.3c10674

236. Hersh AM, Alomari S, Tyler BM. Crossing the Blood-Brain Barrier: Advances in Nanoparticle Technology for Drug Delivery in Neuro-Oncology. *Int J Mol Sci*. **2022**;23(8). doi:10.3390/ijms23084153

237. Senanayake D, Yapa P, Dabare S, Munaweera I. Precision targeting of the CNS: recent progress in brain-directed nanodrug delivery. *RSC Adv*. **2025**;15(32):25910-25928. doi:10.1039/D5RA03578C

238. Garcia-Peiro JI, Ortega-Liebana MC, Adam C, et al. Dendritic Platinum Nanoparticles Shielded by Pt-S PEGylation as Intracellular Reactors for Bioorthogonal Uncaging Chemistry. *Angew Chem Int Ed*. **2025**;64(14). doi:10.1002/anie.202424037

239. Kumari S, Ahsan SM, Kumar JM, Kondapi AK, Rao NM. Overcoming blood brain barrier with a dual purpose Temozolomide loaded Lactoferrin nanoparticles for combating glioma (SERP-17-12433). *Sci Rep*. **2017**;7(1). doi:10.1038/s41598-017-06888-4

240. Zhao YZ, Lin Q, Wong HL, et al. Glioma-targeted therapy using Cilengitide nanoparticles combined with UTMD enhanced delivery. *J Control Release*. **2016**;224. doi:10.1016/j.jconrel.2016.01.015

241. Xu HL, Yang JJ, ZhuGe DL, et al. Glioma-Targeted Delivery of a Theranostic Liposome Integrated with Quantum Dots, Superparamagnetic Iron Oxide, and Cilengitide for Dual-Imaging Guiding Cancer Surgery. *Adv Healthc Mater*. **2018**;7(9). doi:10.1002/adhm.201701130

242. Louis N, Liu S, He X, et al. New therapeutic approaches for brainstem tumors: a comparison of delivery routes using nanoliposomal irinotecan in an animal model. *J Neurooncol*. **2018**;136(3). doi:10.1007/s11060-017-2681-8

243. Ruiz-Molina D, Mao X, Alfonso-Triguero P, et al. Advances in Preclinical/Clinical Glioblastoma Treatment: Can Nanoparticles Be of Help? *Cancers*. **2022**;14(19). doi:10.3390/cancers14194960

244. Fisusi FA, Siew A, Chooi KW, et al. Lomustine Nanoparticles Enable Both Bone Marrow Sparing and High Brain Drug Levels - A Strategy for Brain Cancer Treatments. *Pharm Res*. **2016**;33(5). doi:10.1007/s11095-016-1872-x

245. Liu C, Yao S, Li X, Wang F, Jiang Y. iRGD-mediated core-shell nanoparticles loading carmustine and O6-benzylguanine for glioma therapy. *J Drug Target*. **2017**;25(3). doi:10.1080/1061186X.2016.1238091

246. Nozhat Z, Wahab A, Mushtaq A, Iqbal MZ, Kong X. Metformin loaded Mn3O4@SiO2 core–shell nanoparticles for glioblastoma multiforme targeted therapy. *Colloids Surf B*. **2025**;254:114789. doi:https://doi.org/10.1016/j.colsurfb.2025.114789

247. Alle M, G B reddy, Kim TH, Park SH, Lee SH, Kim JC. Doxorubicin-carboxymethyl xanthan gum capped gold nanoparticles: Microwave synthesis, characterization, and anti-cancer activity. *Carbohydr Polym*. **2020**;229. doi:10.1016/j.carbpol.2019.115511

248. Soroushnasab H, Gharbavi M, Eskandari M, Rezaeejam H, Ghorbani R, Johari B. Methotrexate-conjugated silver nanoparticles enhance chemoradiotherapy effects on U87 human glioblastoma multiforme cells: As a radiosensitizer agent to improve X-irradiation efficacy. *J Drug Deliv Sci Technol*. **2025**;107:106791. doi:https://doi.org/10.1016/j.jddst.2025.106791

249. Pinel S, Thomas N, Boura C, Barberi-Heyob M. Approaches to physical stimulation of metallic nanoparticles for glioblastoma treatment. *Adv Drug Deliv Rev*. **2019**;138. doi:10.1016/j.addr.2018.10.013

250. Bobo D, Robinson KJ, Islam J, Thurecht KJ, Corrie SR. Nanoparticle-Based Medicines: A Review of FDA-Approved Materials and Clinical Trials to Date. *Pharm Res*. **2016**;33(10). doi:10.1007/s11095-016-1958-5

251. Zhao M, van Straten D, Broekman MLD, Préat V, Schiffelers RM. Nanocarrier-based drug combination therapy for glioblastoma. *Theranostics*. **2020**;10(3). doi:10.7150/thno.38147

252. Maier-Hauff K, Ulrich F, Nestler D, et al. Efficacy and safety of intratumoral thermotherapy using magnetic iron-oxide nanoparticles combined with external beam radiotherapy on patients with recurrent glioblastoma multiforme. *J Neurooncol*. **2011**;103(2). doi:10.1007/s11060-010-0389-0

253. Beier CP, Schmid C, Gorlia T, et al. RNOP-09: Pegylated liposomal doxorubicine and prolonged temozolomide in addition to radiotherapy in newly diagnosed glioblastoma - A phase II study. *BMC Cancer*. **2009**;9. doi:10.1186/1471-2407-9-308

254. Ananda S, Nowak AK, Cher L, et al. Phase 2 trial of temozolomide and pegylated liposomal doxorubicin in the treatment of patients with glioblastoma multiforme following concurrent radiotherapy and chemotherapy. *J Clin Neurosci*. **2011**;18(11). doi:10.1016/j.jocn.2011.02.026

255. Feldhaeusser B, Platt SR, Marrache S, et al. Evaluation of nanoparticle delivered cisplatin in beagles. *Nanoscale*. **2015**;7(33). doi:10.1039/c5nr03447g

256. Battogtokh G, Akala EO. Development of Multifunctional Targeted Dual-Loaded Polymeric Nanoparticles for Triple-Negative Breast Cancer Treatment. *Pharmaceutics*. **2025**;17(4). doi:10.3390/pharmaceutics17040425

257. Kim JH, Kim YS, Park K, et al. Antitumor efficacy of cisplatin-loaded glycol chitosan nanoparticles in tumor-bearing mice. *J Control Release*. **2008**;127(1). doi:10.1016/j.jconrel.2007.12.014

258. Di Y, Zhang H, Luo Z, et al. Synergistic chemotherapy/photothermal therapy for cancer treatment using a co-delivery system of cisplatin and novel conjugated polymers. *Polym Chem*. **2024**;15(28):2883-2898. doi:10.1039/D4PY00502C

259. Ak G, Akartas I, Özel B, et al. Preparation, characterization and in vitro evaluation of cisplatin-bound triblock polymeric micelle solution for ovarian cancer treatment. *Drug Dev Ind Pharm*. **2021**;47(8). doi:10.1080/03639045.2021.1989451

260. Dragulska SA, Acosta Santiago M, Swierczek S, et al. Synthesis and Characterization of Poly(Lactic-Co-Glycolic Acid)–Paclitaxel (PLGA-PTX) Nanoparticles Evaluated in Ovarian Cancer Models. *Pharmaceutics*. **2025**;17(6). doi:10.3390/pharmaceutics17060689

261. Mekonnen TW, Darge HF, Tsai HC, et al. Combination of ovalbumin-coated iron oxide nanoparticles and poly(amidoamine) dendrimer-cisplatin nanocomplex for enhanced anticancer efficacy. *Colloids Surf B*. **2022**;213. doi:10.1016/j.colsurfb.2022.112391

262. Khodabakhshi MJ, Panahi HA, Konoz E, Feizbakhsh A, Kimiagar S. Synthesis of pH and thermo-sensitive dendrimers based on MoS2 and magnetic nanoparticles for cisplatin drug delivery system by the near-infrared laser. *Polym Adv Technol*. **2021**;32(4). doi:10.1002/pat.5199

263. Ghanbarikondori P, Aliakbari RBS, Saberian E, et al. Enhancing Cisplatin Delivery via Liposomal Nanoparticles for Oral Cancer Treatment. *IJCB*. **2025**;40(2):211-217. doi:10.1007/s12291-024-01239-3

264. Alotaibi B, El-Masry TA, Elekhnawy E, et al. Aqueous core epigallocatechin gallate PLGA nanocapsules: characterization, antibacterial activity against uropathogens, and in vivo reno-protective effect in cisplatin induced nephrotoxicity. *Drug Deliv*. **2022**;29(1). doi:10.1080/10717544.2022.2083725

265. Joshy KS, Augustine R, Hasan A, et al. Cisplatin encapsulated nanoparticles from polymer blends for anti-cancer drug delivery. *New J Chem*. **2022**;46(12). doi:10.1039/d1nj04311k

266. Stavropoulou AP, Theodosiou M, Sakellis E, et al. Bimetallic gold-platinum nanoparticles as a drug delivery system coated with a new drug to target glioblastoma. *Colloids Surf B*. **2022**;214. doi:10.1016/j.colsurfb.2022.112463

267. Li H, Wang Y, Zhou S, Liu J, Jin Y. Apatinib-loaded silicate nanoparticles coated with macrophage membranes and PD-1 antibody for enhanced chemo-immunotherapy in ovarian cancer via VEGFR2 and PD-1 dual inhibition. *Colloids Surf B*. **2025**;254:114790. doi:https://doi.org/10.1016/j.colsurfb.2025.114790

268. Coluccia D, Figueiredo CA, Wu MYJ, et al. Enhancing glioblastoma treatment using cisplatin-gold-nanoparticle conjugates and targeted delivery with magnetic resonance-guided focused ultrasound. *Nanomedicine*. **2018**;14(4). doi:10.1016/j.nano.2018.01.021

269. Makharza SA, Cirillo G, Vittorio O, et al. Magnetic graphene oxide nanocarrier for targeted delivery of cisplatin: A perspective for glioblastoma treatment. *Pharm J*. **2019**;12(2). doi:10.3390/ph12020076

270. Kosmas C, Angel J, Athanasiou A, et al. 9088 Phase III study of Lipoplatin plus Gemcitabine versus Cisplatin plus Gemcitabine in advanced NSCLC; interim analysis. *Eur J Cancer, Suppl*. **2009**;7(2). doi:10.1016/s1359-6349(09)71801-4

271. Farhat F, Kattan J, Ibrahim K, et al. 457 Preliminary results of a phase II study of lipoplatin (liposomal cisplatin)–vinorelbine combination as first line treatment in HER2/neu negative metastatic breast cancer (MBC). *Eur J Cancer, Suppl*. **2010**;8(3). doi:10.1016/s1359-6349(10)70478-x

272. Koukourakis MI, Giatromanolaki A, Pitiakoudis M, et al. Concurrent liposomal cisplatin (Lipoplatin), 5-fluorouracil and radiotherapy for the treatment of locally advanced gastric cancer: A phase I/II study. *Int J Radiat Oncol Biol Phys*. **2010**;78(1). doi:10.1016/j.ijrobp.2009.07.1733

273. Huo T, Barth RF, Yang W, et al. Preparation, Biodistribution and Neurotoxicity of Liposomal Cisplatin following Convection Enhanced Delivery in Normal and F98 Glioma Bearing Rats. *PLoS One*. **2012**;7(11). doi:10.1371/journal.pone.0048752

274. Shein SA, Kuznetsov II, Abakumova TO, et al. VEGF- and VEGFR2-Targeted Liposomes for Cisplatin Delivery to Glioma Cells. *Mol Pharm*. **2016**;13(11). doi:10.1021/acs.molpharmaceut.6b00519

275. Dhami NK, Pandey RS, Jain UK, Chandra R, Madan J. Non-aggregated protamine-coated poly(lactide-co-glycolide) nanoparticles of cisplatin crossed blood-brain barrier, enhanced drug delivery and improved therapeutic index in glioblastoma cells: In vitro studies. *J Microencapsul*. **2014**;31(7). doi:10.3109/02652048.2014.913725

276. Yu H, Tang Z, Zhang D, et al. Pharmacokinetics, biodistribution and in vivo efficacy of cisplatin loaded poly(l-glutamic acid)-g-methoxy poly(ethylene glycol) complex nanoparticles for tumor therapy. *J Control Release*. **2015**;205. doi:10.1016/j.jconrel.2014.12.022

277. Ashrafzadeh MS, Akbarzadeh A, Heydarinasab A, Ardjmand M. In vivo glioblastoma therapy using targeted liposomal cisplatin. *Int J Nanomedicine*. **2020**;15. doi:10.2147/IJN.S255902

278. Lajous H, Riva R, Lelièvre B, et al. Hybrid Gd3+/cisplatin cross-linked polymer nanoparticles enhance platinum accumulation and formation of DNA adducts in glioblastoma cell lines. *Biomater Sci*. **2018**;6(9). doi:10.1039/c8bm00346g

279. Duan QY, Zhu YX, Jia HR, et al. Platinum-Coordinated Dual-Responsive Nanogels for Universal Drug Delivery and Combination Cancer Therapy. *Small*. **2022**;18(46). doi:10.1002/smll.202203260

280. Fernandez de Larrinoa P, Kichler A, Dontenwill M, et al. N-Heterocyclic carbene platinum complexes encapsulated in lipid particles: a novel strategy to target cancer cells and cancer stem cells in glioblastoma. *RSC Med Chem*. **2025**. doi:10.1039/d5md00460h

281. Fortin D, Desjardins A, Benko A, Niyonsega T, Boudrias M. Enhanced chemotherapy delivery by intraarterial infusion and blood-brain barrier disruption in malignant brain tumors: The Sherbrooke experience. *Cancer*. **2005**;103(12). doi:10.1002/cncr.21112

282. Miura Y, Takenaka T, Toh K, et al. Cyclic RGD-linked polymeric micelles for targeted delivery of platinum anticancer drugs to glioblastoma through the blood-brain tumor barrier. *ACS Nano*. **2013**;7(10). doi:10.1021/nn402662d

283. Shi M, Fortin D, Paquette B, Sanche L. Convection-enhancement delivery of liposomal formulation of oxaliplatin shows less toxicity than oxaliplatin yet maintains a similar median survival time in F98 glioma-bearing rat model. *Invest New Drugs*. **2016**;34(3). doi:10.1007/s10637-016-0340-0

284. Ho GY, Woodward N, Coward JIG. Cisplatin versus carboplatin: Comparative review of therapeutic management in solid malignancies. *Crit Rev Oncol Hematol*. **2016**;102. doi:10.1016/j.critrevonc.2016.03.014

285. Zheng Y, Sanche L. Mechanisms of Nanoscale Radiation Enhancement by Metal Nanoparticles: Role of Low Energy Electrons. *Int J Mol Sci*. **2023**;24(5). doi:10.3390/ijms24054697

286. Gianasi E, Buckley RG, Latigo J, Wasil M, Duncan R. HPMA copolymers platinates containing dicarboxylato ligands. Preparation, characterisation and in vitro and in vivo evaluation. *J Drug Target*. **2002**;10(7). doi:10.1080/1061186021000072456

287. Gianasi E, Wasil M, Evagorou EG, Keddle A, Wilson G, Duncan R. HPMA copolymer platinates as novel antitumour agents: In vitro properties, pharmacokinetics and antitumour activity in vivo. *Eur J Cancer*. **1999**;35(6). doi:10.1016/S0959-8049(99)00030-1

288. Rademaker-Lakhai JM, Terret C, Howell SB, et al. A phase I and pharmacological study of the platinum polymer AP5280 given as an intravenous infusion once every 3 weeks in patients with solid tumors. *Clin Cancer Res*. **2004**;10(10). doi:10.1158/1078-0432.CCR-03-0315

289. Karanam V, Marslin G, Krishnamoorthy B, et al. Poly (ε-caprolactone) nanoparticles of carboplatin: Preparation, characterization and in vitro cytotoxicity evaluation in U-87 MG cell lines. *Colloids Surf B*. **2015**;130. doi:10.1016/j.colsurfb.2015.04.005

290. Yang J, Su T, Wang Q, Shi R, Ding J, Chen X. Glucose Metabolism-Targeted Poly(amino acid) Nanoformulation of Oxaliplatin(IV)-Aspirin Prodrug for Enhanced Chemo-Immunotherapy. *Adv Mater*. **2025**;37(12). doi:10.1002/adma.202419033

291. Hassanzadeganroudsari M, Soltani M, Heydarinasab A, Apostolopoulos V, Akbarzadehkhiyavi A, Nurgali K. Targeted nano-drug delivery system for glioblastoma therapy: In vitro and in vivo study. *J Drug Deliv Sci Technol*. **2020**;60. doi:10.1016/j.jddst.2020.102039

292. Wang Y, Jiang Y, Wei D, et al. Nanoparticle-mediated convection-enhanced delivery of a DNA intercalator to gliomas circumvents temozolomide resistance. *Nat Biomed Eng*. **2021**;5(9). doi:10.1038/s41551-021-00728-7

293. Arduino I, Depalo N, Re F, et al. PEGylated solid lipid nanoparticles for brain delivery of lipophilic kiteplatin Pt(IV) prodrugs: An in vitro study. *Int J Pharm*. **2020**;583. doi:10.1016/j.ijpharm.2020.119351

294. Mokhtari RB, Homayouni TS, Baluch N, et al. Combination therapy in combating cancer. *Oncotarget*. **2017**;8(23). doi:10.18632/oncotarget.16723

295. Wang T, Narayanaswamy R, Ren H, Torchilin VP. Combination therapy targeting both cancer stem-like cells and bulk tumor cells for improved efficacy of breast cancer treatment. *Cancer Biol Ther*. **2016**;17(6). doi:10.1080/15384047.2016.1190488

296. Yuan S, Wang F, Chen G, et al. Effective elimination of cancer stem cells by a novel drug combination strategy. *Stem Cells*. **2013**;31(1). doi:10.1002/stem.1273

297. Mao X, Wu S, Calero-Pérez P, et al. Synthesis and Validation of a Bioinspired Catechol-Functionalized Pt(IV) Prodrug for Preclinical Intranasal Glioblastoma Treatment. *Cancers*. **2022**;14(2). doi:10.3390/cancers14020410

298. Liu L, Ye Q, Lu M, et al. A new approach to reduce toxicities and to improve bioavailabilities of platinum-containing anti-cancer nanodrugs. *Sci Rep*. **2015**;5. doi:10.1038/srep10881

299. Zhang S, Wang R, Wang G. Impact of Dopamine Oxidation on Dopaminergic Neurodegeneration. *ACS Chem Neurosci*. **2019**;10(2). doi:10.1021/acschemneuro.8b00454

300. Labet M, Thielemans W. Synthesis of polycaprolactone: A review. *Chem Soc Rev*. **2009**;38(12):3484-3504. doi:10.1039/b820162p

301. Wei Q, Zhang F, Li J, Li B, Zhao C. Oxidant-induced dopamine polymerization for multifunctional coatings. *Polym Chem*. **2010**;1(9):1430-1433. doi:10.1039/c0py00215a

302. Gómez-Herrera R, Alfonso-Triguero P, Mao X, et al. Bioinspired neuromelanin-like Pt(iv) polymeric nanoparticles for cancer treatment. *Nanotechnol Rev*. **2024**;13(1). doi:10.1515/ntrev-2024-0118

303. Bastiancich C, Da Silva A, Estève MA. Photothermal Therapy for the Treatment of Glioblastoma: Potential and Preclinical Challenges. *Front Oncol*. **2021**;10. doi:10.3389/fonc.2020.610356

304. Zhang Y, Guo Y, Wu S, Liang H, Xu H. Photodegradable Coordination Polymer Particles for Light-Controlled Cargo Release. *ACS Omega*. **2017**;2(6). doi:10.1021/acsomega.7b00440

305. Hu XG, Li X, Yang SI. Novel photochromic infinite coordination polymer particles derived from a diarylethene photoswitch. *Chem Commun* **2015**;51(53). doi:10.1039/c5cc02447a

306. Huang Z, Huang L, Huang Y, et al. Phthalocyanine-based coordination polymer nanoparticles for enhanced photodynamic therapy. *Nanoscale*. **2017**;9(41). doi:10.1039/c7nr05402e

307. Yang Y, Zhu W, Feng L, et al. G-Quadruplex-Based Nanoscale Coordination Polymers to Modulate Tumor Hypoxia and Achieve Nuclear-Targeted Drug Delivery for Enhanced Photodynamic Therapy. *Nano Lett*. **2018**;18(11). doi:10.1021/acs.nanolett.8b02732

308. Liu J, Yang G, Zhu W, et al. Light-controlled drug release from singlet-oxygen sensitive nanoscale coordination polymers enabling cancer combination therapy. *Biomaterials*. **2017**;146. doi:10.1016/j.biomaterials.2017.09.007

309. Zhang J, Ramu V, Zhou XQ, et al. Photoactivable ruthenium-based coordination polymer nanoparticles for light-induced chemotherapy. *Nanomaterials*. **2021**;11(11). doi:10.3390/nano11113089

310. Dai Z, Wang Z. Photoactivatable Platinum-Based Anticancer Drugs: Mode of Photoactivation and Mechanism of Action. *Molecules*. **2020**;25(21). doi:10.3390/molecules25215167

311. Ding D, Feng Y, Qin R, et al. Mn 3+ -rich oxide/persistent luminescence nanoparticles achieve light-free generation of singlet oxygen and hydroxyl radicals for responsive imaging and tumor treatment. *Theranostics*. **2021**;11(15). doi:10.7150/thno.62437

312. He Y, Tang J. Anthracene-Based Endoperoxides as Self-Sensitized Singlet Oxygen Carriers for Hypoxic-Tumor Photodynamic Therapy. *Adv Healthc Mater*. **2025**;14(2). doi:10.1002/adhm.202403009

313. Bolaños-Cardet J. *Mussel-Inspired Adv Mater for Biomedical Applications*. **2025**.

314. Bolaños-Cardet J, Ruiz-Molina D, Yuste VJ, Suárez-García S. Bioinspired phenol-based coatings for medical fabrics against antimicrobial resistance. *Chem Eng J*. **2024**;481. doi:10.1016/j.cej.2024.148674

315. López-Moral A, Bolaños-Cardet J, Alibés R, et al. A bioinspired and environmentally sustainable polyphenol-based water adhesive. *J Colloid Interface Sci*. **2025**;680:987-996. doi:10.1016/j.jcis.2024.11.042

Chapter 2

Thesis Objectives

Given what has been previously introduced, the primary aim of this Thesis will be to develop new therapeutic platforms for GBM treatment. Emphasis will be placed on combination therapy strategies that involve the release of chemotherapeutic Pt and the generation of ROS, as well as the selective activation of these agents under specific stimuli.

Thereafter, the following targets were proposed:

3. Development of bioinspired **pPtBC NP**, a CNP capable of achieving a pH and redox-sensitive Pt(IV) release coupled with passive ROS generation.

For this purpose, the following will be necessary:

- Synthesis and characterisation of molecular **PtBC**.
- Synthesis and characterisation of nanostructured **pPtBC NP**.
- Characterisation of ROS and Pt release profiles of **pPtBC NP**.
- *In vitro* characterisation of **pPtBC NP**.
- Preclinical *in vivo* evaluation in GBM settings of **pPtBC**.

Building on established chemistry and our research group's expertise in alternative supramolecular structures and oxidative polymerisation of catechol-based moieties, the development of **FSM-PtBC** will be investigated as a post-surgery FSM for in situ release of Pt and ROS, provided sufficient time is available.

4. Development of supramolecular nanostructured **SQC NP**, a platform capable of combining PACT and PDT to achieve spatiotemporal release of Pt(II) and ROS cytotoxic species on demand under irradiation.

For this purpose, the following will be necessary:

- Synthesis and characterisation of molecular **SQC**.
- Synthesis and characterisation of nanostructured **SQC NP**.
- Photochemical, ROS and PT release characterisation of **SQC NP**.
- *In vitro* characterisation of **pPtBC NP**.
- Preclinical *in vivo* evaluation in GBM settings of **pPtBC**.

5. Development of core-shell **pDPA/pDSCP-CNP@Fe**, a platform capable of absorbing SO under irradiation and releasing it, together with a Pt(II) cytotoxic cargo, under thermal stimulus provided by magnetic hyperthermia (MHT). Furthermore, the platform will also be studied in MRI for possible theragnostic applications.

For this purpose, the following will be necessary:

- Synthesis and characterisation of molecular **DPA-COOH**, **Fe-Clustered NP** and **DSCP**.
- Synthesis and characterisation of nanostructured **pDPA/pDSCP-CNP@Fe**.
- Photochemical and magnetic characterisation of **pDPA/pDSCP-CNP@Fe.**
- *In vitro* characterisation of **pDPA/pDSCP-CNP@Fe**.
- *In vitro* and *in vivo* evaluation of **pDPA/pDSCP-CNP@Fe** as an MRI CA.
- Preclinical *in vivo* evaluation in GBM settings of **pDPA/pDSCP-CNP@Fe**.

Chapter 3

Bioinspired Polymeric Neuromelanin-like Pt(IV) and Supramolecular Photoactivatable Squaraine Pt(II) Nanoparticles

This work reports on two platforms for cancer treatment based on Pt coordination complexes.

The first platform studied consists of bioinspired neuromelanin-like Pt(IV) polymeric NPs with dual-responsive drug release under acidic or reductive intracellular conditions, aimed to achieve a selective cytotoxicity within the TME (Figure **3.1**). This platform displays a high drug loading capacity, chemical stability, and biocompatibility. *In vitro* settings demonstrated efficient cellular uptake and Pt-DNA binding efficiency, particularly in glioma (GL261) cells, alongside cytotoxicity comparable to that of **CDDP** across various cancer lines, including resistant strains. *In vivo* studies, conducted via IN administration, displayed favourable tolerability and Pt accumulation in the brain and tumour tissue. However, therapeutic efficacy in GL261 tumour-bearing mice was lacking, with no significant tumour shrinkage or survival benefit observed under a metronomic dosing schedule.

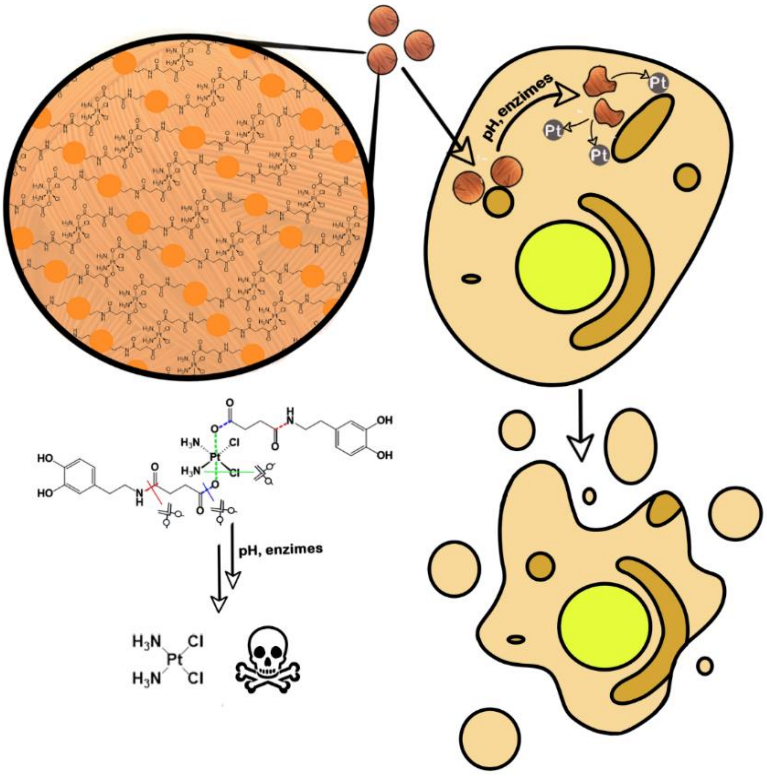


Figure **3.1**. Graphical abstract showing the Pt(IV) complex bonds susceptible to cleavage due to pH or enzymatic action, a concept of the CNP developed and the degradation and subsequent release of cytotoxic cargo under pH or enzymatic action, leading to cell death.

The results of this work have been presented in:

- "*Nanotechnology Reviews, Vol. 13 (Issue 1), pp. 20240118.*[1]"
- Nanobiomed 2023 congress and 5th SPLC-CRS Young Scientist Meeting, under the title "Intranasal Administration of Pt(IV) Nanoparticles for Glioblastoma Treatment"

The second platform aims to explore the photochemical reactivity of SQ dyes to enable PACT, with success in characterising and developing a photo-responsive platform with proven capabilities to release Pt under NIR (785 nm) irradiation. Nonetheless, the physicochemical flexibility of supramolecular aggregation of SQs enabled the development of a non-Pt-loaded platform based on supramolecular interactions that displayed the generation of ROS upon 470 nm irradiation via Type I mechanisms, only in the nanoparticulate form, and significant phototoxicity dependent on irradiation against A549 lung carcinoma cells.

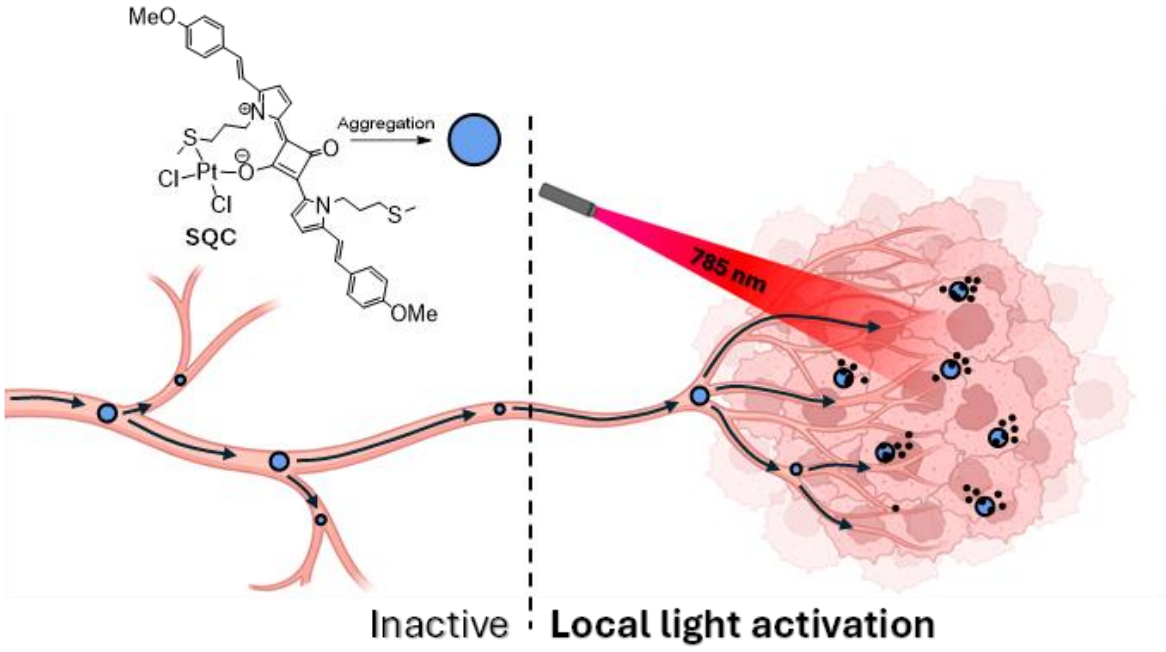


Figure **3.2**. Graphical abstract showing the structure of the starting SQ Pt(II) complex, and the light dependant activation and release of the cytotoxic cargo.

The results of this work have been presented in:

- "*Supramolecular Photoactivatable Squaraine Pt(II) Nanoparticles for Cancer Treatment",* submitted for publication.

3.1. Introduction

3.1.1. Bioinspired Neuromelanin-like Pt(IV) Polymeric Nanoparticles

3.1.1.1. Precedents

Pioneering work of our group reported successful neuromelanin-like CNP for controlled dopamine (DA) release and IN replacement in Parkinson's disease.[2] More recently, and following this approach, we reported on a polymeric network using Pt(IV) prodrugs as building blocks coordinated with iron ions, with remarkable *in vitro* and *in vivo* GBM activity. A representative scheme of the synthesised **PtBC** building block and the corresponding polymerisation process yielding the NPs is shown in Figure **3.3**.[3]

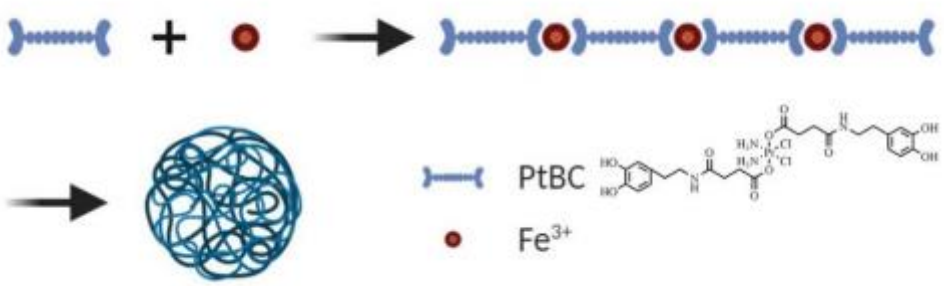


Figure **3.3**. Schematic representation of the synthetic approach followed for the synthesis of Pt(IV)-based CNPs.[3]

Aiming to explore the potential of this novel family of NPs, herein we propose the synthesis of novel NPs by replacing the formation of coordination bonds with the oxidative coupling of the catechol units.

3.1.1.2. Catechol-Based Nanoparticles

These functional groups have gained significant attention due to their polymerisation capabilities and the wide range of natural compounds in which they can be found, demonstrating exceptional chemical versatility.[4] Catechols are comprised of an aromatic phenyl backbone with two hydroxyl groups.[5] Catechol-based polymers have increasingly been taking a more critical role in medicinal chemistry over the last few decades. For instance, curcumin, baicalein, luteolin, (–)-epigallocatechin-3-gallate (EGCG), and quercetin represent catechol polyphenols with a variety of biomedical applications (Figure **3.4**).[6–8]

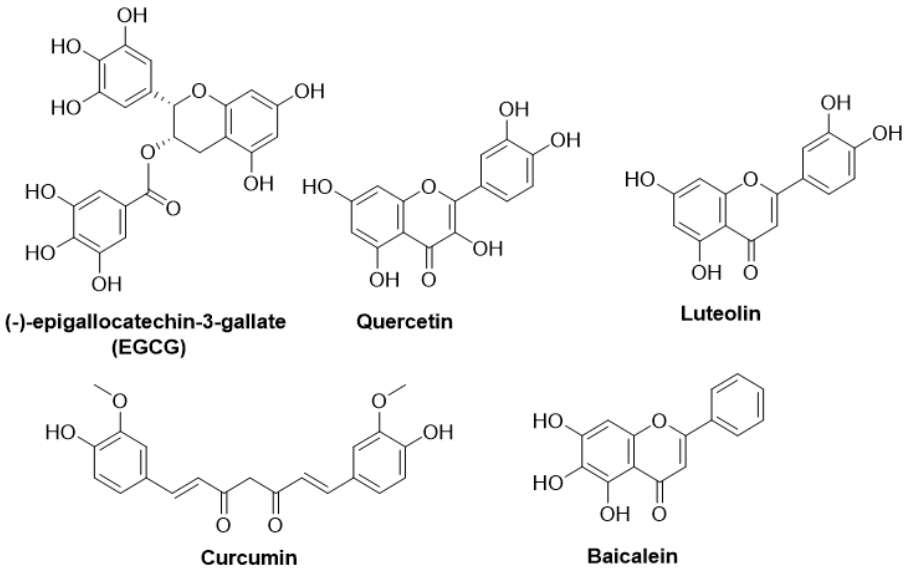


Figure **3.4**. Structural formula of EGCG, Quercetin, Luteolin, Curcumin and Baicalein.

Catechols benefit from unique structural properties that enable them to perform metal-chelating, fibril-disassembly, and enzyme-binding functions.[9–12] More importantly, chemical properties endow them with a unique duality between pro-oxidant and antioxidant activity. For instance, EGCG induced oxidative stress in oral cancer and premalignant cells, while in normal human gingival fibroblasts, EGCG acted as an antioxidant.[13] This capacity enables catechols to switch between oxidative pro-apoptotic and reductive protective activities, depending on the environment they are found in cancer cells.[13] Importantly, catechols play an important role in ROS mediation and regulation in cells.[13] This allows catechols, such as curcumin, baicalein, luteolin, and EGCG, to show promise in cancer treatment by directly inhibiting cancer cell growth, promoting apoptosis, and enhancing the effectiveness of existing therapies, including CT and RT.[14–18]

Beyond direct action, catechols are also being explored as components of advanced drug delivery systems, such as pH-responsive polymers for targeted drug release and bio-inspired prodrugs for specific cancer types like GBM. [3,5,19,20]

DA, a specific class of catecholamine, has been observed to play a multifaceted role in GBM development, encompassing tumour growth regulation, immune modulation, drug efficacy enhancement, and angiogenesis modulation. Thereafter, the use of DA, as a class of catechol, has been a significant source of inspiration for the design of platforms developed in our research group in the field of GBM treatment.

3.1.1.3. Oxidative Polymerisation

Formally, oxidative polymerisation consists of the abstraction of two hydrogen atoms from monomers, yielding further polymerisation as a result of condensation, and thus can be classified as polycondensation. The applicable monomers are mostly aromatic compounds. However, the reaction mechanism in such reactions is usually unclear, and the coupling selectivity is generally not easy to control.[21] Examples of oxidative polymerisation can be found plentifully, including phenols (mono or multi-substituted),[22,23] naphthols,[24] anilines,[25,26] thiophenols,[27,28] pyrroles,[29,30] and thiophenes.[31,32]

DA and related catechols also exhibit such capabilities. However, we still lack a profound knowledge of the polymerisation mechanisms and structural certainty of the product resulting from DA oxidative polymerisation. In any case, polymerisation must first be triggered by catechol oxidation to its quinone derivative through multiple approaches, among them, chemical oxidation using sodium periodate.[33,34] The pH can also significantly influence this process, with alkaline conditions accelerating oxidation by lowering the redox potential of catechols.[35] From this point, multiple synthetic pathways may take place along the polymerisation (Figure **3.5**):

- **PDA formation**. DA also presents an intrinsic set of characteristics that make polymerisation especially complex. Formation of PDA includes the formation of the quinone intermediate that, through a combination of cyclisation and further oxidations, yields a melamine-like adduct that aggregates into oligomers through a combination of covalent and non-covalent interactions. That eventually self-entangle together to end up forming a PDA structure through non-specific interactions.[36–38]
- **Aryloxy radical coupling**. The quinone groups can also react via reverse dismutation with an unoxidized catechol, yielding two highly reactive semiquinone radicals. The formed radicals can couple to form di-DOPA crosslinks.[39]
- **Formation of quinone-amine adducts**. Quinones can react with amines via a Michael-type addition or Schiff base reactions, which can lead to quinone-amine adducts. Aromatic amines typically favour Michael-type addition, while aliphatic amines undergo Schiff base reactions.[40]

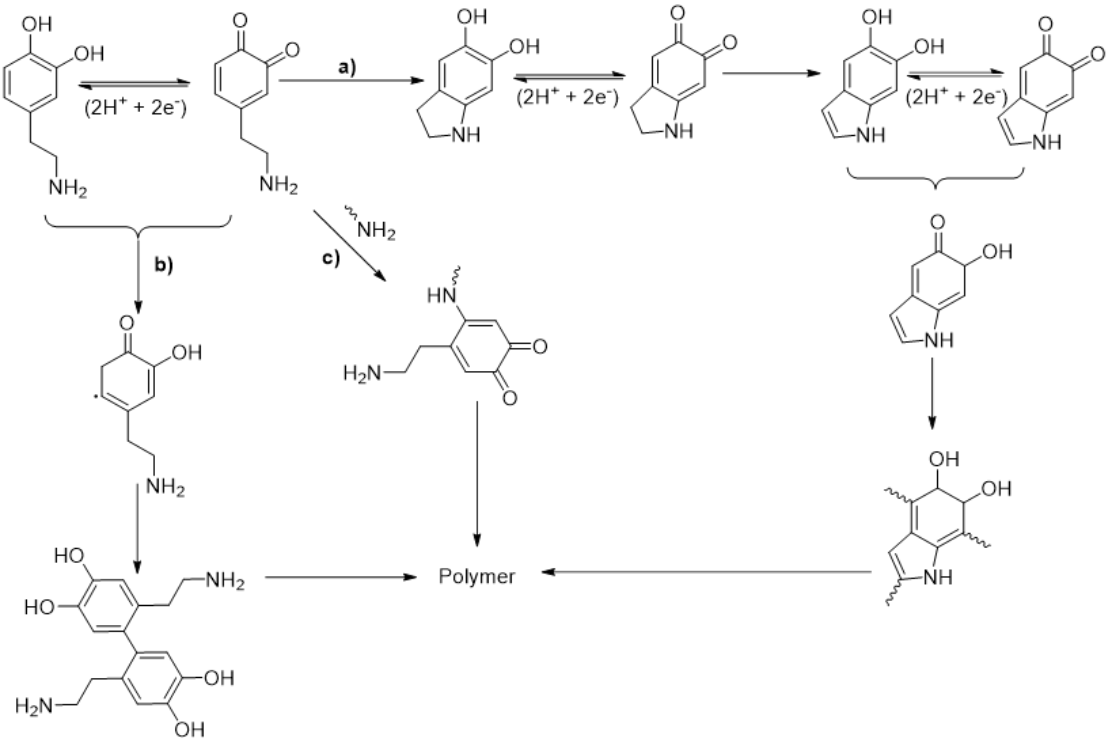


Figure **3.5**. Reaction mechanism of PDA formation via **a)** DA oxidation, **b)** Aryloxy radical coupling reaction, and **c)** Quinone reaction with amines.[41]

3.1.1.4. Our Proposed Platform

Aimed to increase the Pt(IV) encapsulation yield, we aim to modify the chemical and colloidal stability as well as the biodistribution of this family of bioinspired NPs. More precisely, **pPtBC** was proposed as a building block to undergo oxidative polymerisation following the reaction mechanisms described in the previous section. For comparison purposes, **NDGA** and the polymeric material (i.e., **pNDGA**) will also be obtained, as it presents as a polyphenol with well-described antitumoral capabilities and a similar morphology but lacking the Pt(IV) core (Figure **3.6**).[42]

PtBC presents multiple breaking points via either redox or hydrolysis in slightly acidic pHs, such as that of the TME, that allow for controlled drug release in GBM settings. This combination, and the nature of Pt(IV) complexes, allow for selective tumour targeting and activation. At the same time, a polymeric network obtained from oxidative polymerisation of **PtBC, pPtBC**, allows for relative chemical stability and high drug loading coefficients in the form of a CNP.[5] Furthermore, the role of catechols in ROS-mediated apoptotic death is well known and exploited in cancer therapy.[14-18] Thereafter, the catechol moieties from **PtBC** allow envisioning a multifunctional therapeutic approach to GBM treatment via chemotherapeutic and ROS-mediated cell death. Furthermore, the role of catechols in ROS-mediated apoptotic death is well known and exploited in cancer therapy.[14-18] Thereafter, the catechol moieties from **PtBC** allow envisioning a multifunctional therapeutic approach to GBM treatment via chemotherapeutic and ROS-mediated cell death.

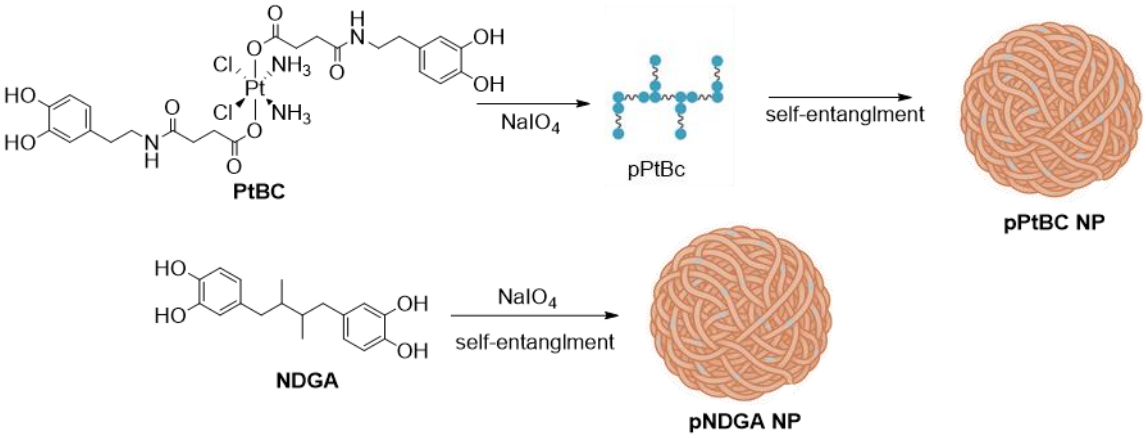


Figure **3.6**. Simplified Pt(IV) loaded CNPs obtention from starting monomer **PtBC** under oxidative reaction conditions.

3.1.2. Supramolecular Photoactivatable Squaraine Pt(II) Nanoparticles

The second platform studied uses PACT, an emerging therapeutic modality, to trigger the release of cytotoxic cargo under irradiation at a specific wavelength, providing spatiotemporal precision and minimising systemic toxicity.[43,44] Some examples of PACT in cancer treatment can be found reported by Luo et al. with a Paclitaxel-PS bonded dimer that, upon laser irradiation, exposes the release of the Paclitaxel drug.[45] Another example includes ruthenium-based complex PF6, reported by Chen *et al.,* presenting potent light-activated cytotoxicity in U87MG GBM cells while sparing healthy neurons.[46] Examples using NPs can be found reported by Cho et al. with PS cholesterol e6 chemotherapeutic prodrug covalently linked to monomethyl auristatin E (MMAE) prodrug NP, which enhances apoptosis after visible light irradiation generates ROS, activating the MMAE prodrug.[47] Or more prominently, with Pt NPs, we have the reports from Hao *et al.,* who introduced thioketal bonds to connect camptothecin drug with a PS to form a prodrug incorporated into Pt NPs for enhanced chemo-PDT of colon cancer.[48] Much less work has been done with SQ Pt(II) NPs, despite its interest in the molecular form of SQ.[49]

In addition to PACT, SQs are highly desired in PDT settings. This is because SQ dyes are known for their extremely intense absorption bands, high molar absorption coefficients, excellent photoconductivity, narrow absorption peaks in the NIR range, outstanding photostability, and high intersystem crossing (ISC) quantum yields for ROS generation.[50-52] Furthermore, SQ dyes can be considered as a stimuli-responsive PS, activated only when irradiated with light of a specific wavelength.[53]

PDT involves the generation of ROS upon excitation of a PS.[54,55] Converting, as a result, oxygen into ROS.[56] The outcome of such transformations induces cytotoxic effects in targeted cells. The production of ROS can be produced through two main reaction pathways (Type I and Type II).[57] Type I mechanism involves the generation of radical species through either hydrogen abstraction or redox processes between a sensitiser in an excited triplet state, generated by the ISC mechanism, with biomolecules in the environment that trigger the generation of superoxide anions or hydroxyl radicals.[58] In the Type II mechanism, the most usual one, the sensitiser in the triplet excited state directly generates SO ($^1O_2$) from ground-state molecular oxygen ($^3O_2$) through an energy transfer process [59] ROS and free radicals generated are then the leading cause of oxidative stress and various oxidising substrates, which results in cell death (Figure **3.7**).[60,61]

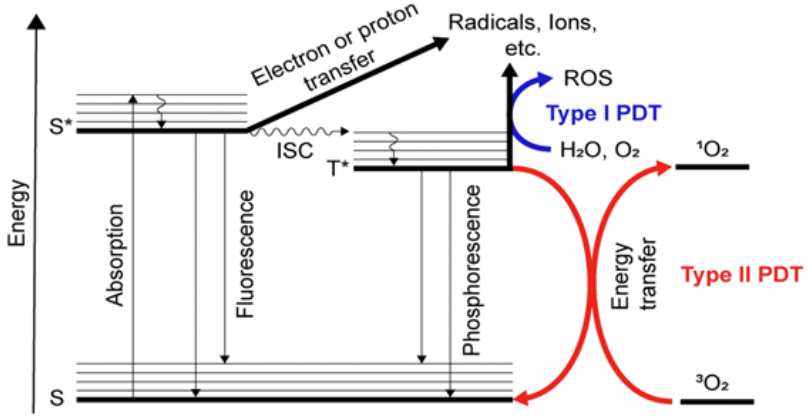


Figure **3.7**. Schematic diagram of the available energy transfer processes of a PS upon excitation and the ISC.[58]

Overall, SQs present as one of the few NIR dyes that are easy to synthesise and still present strong and sharp absorption bands that can help to induce photochemical reactions.[56] Interestingly, one important property of PACT is its ability to overcome one of the limitations of PDT, the hypoxic TME.[56] While PDT Type II, the most often approach to PDT, requires the presence of molecular oxygen to promote cell death, PACT is an approach that involves the use of a prodrug activated by light irradiation.[62]

3.1.2.1. Squaraines

SQs are a family of chromophores which share many structural and photophysical properties with cyanines. Structurally, SQs are a class of organic dyes with an electron-deficient four-membered oxocyclobutenolate core ring central to the structure. Such a ring has been stabilised by the presence of two resonance-stabilised electron-donor-rich functional groups at diametrically opposite sides of the core. This arrangement leads to a highly electron delocalized structure. The nature of the electron-rich functional groups are usually anilines or heterocycles such as trimethylindolenine, benzothiazoles, and benzoselenazoles (Figure **3.8**).[63] The planar structures, and zwitterionic properties of SQs confer strong absorption and emission characteristics in the NIR region.[64] The absorption and fluorescence properties of the SQ dyes usually show absorption band maxima in the range of 628–704 nm and fluorescence band maxima in the range of 656–724 nm.[65]

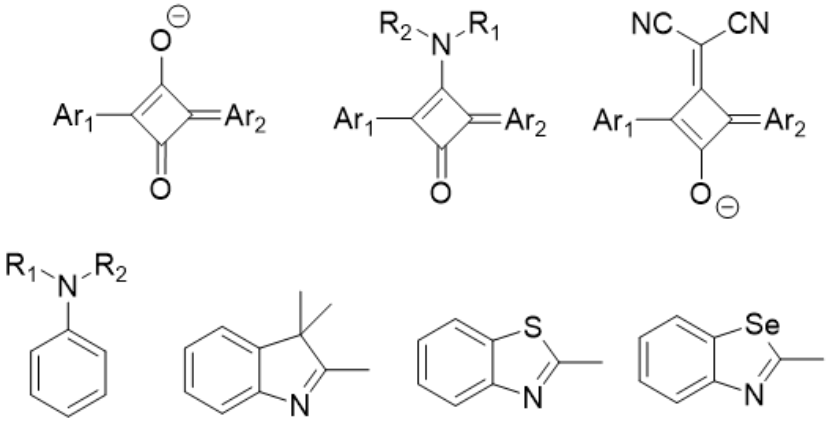


Figure **3.8**. Electron-poor oxocyclobutenolates (top row) and electron-rich functional groups used in SQ synthesis (bottom row), showing a generic aniline, trimethylindolenine, benzothiazole, and benzoselenazole from left to right.

NIR dyes absorb light within the 700–1500 nm range, which includes the first and second therapeutic windows. These windows are optimal for *in vivo* imaging and therapeutic applications since light scattering, absorption, and autofluorescence from biomolecules are minimised, enabling deeper penetration of NIR light into the tissue.[64] However, there are relatively few classes of NIR dyes that are both easy to synthesise and readily available. These include cyanine dyes, phthalocyanines, porphyrins, and boron-dipyrromethane, and finally, SQ dyes.[66-69]

SQ dyes have been broadly studied since the late 60's to the beginning of the 90's, and from the very beginning, both their physical and chemical properties have been of great interest for these compounds.[70-72] But it is most to our interest the applications in PDT and self-assembly of aggregates.[73,74]

3.1.2.2. Squaraines in Photoactivated Chemotherapy

Different approximations and designs of specific SQs in PACT can be found in the bibliography. Kevin *et al.* presented the first work on this topic in the scientific literature. Kevin displayed the development of photoactivatable hemi-SQ-Type Pt(II) asymmetric complexes that used UV and visible light to photoactivate and produce photodegradation compounds, capable of showing remarkable cytotoxicity to HeLa, A2780, and the **CDDP**-resistant A2780/cis cell lines.[74] Recent work involving PACT systems based on SQs, use the unique capability of the cyclobutadiene moiety of SQs to undergo a photoactivated conversion to their corresponding bisketene.[49] Even though this process is thermally reversible in non-nucleophilic solvents, in the presence of a nucleophilic solvent such as water, the bisketen unit undergoes an irreversible addition reaction, preventing reversible ring closure (Figure **3.9**).[76,77]

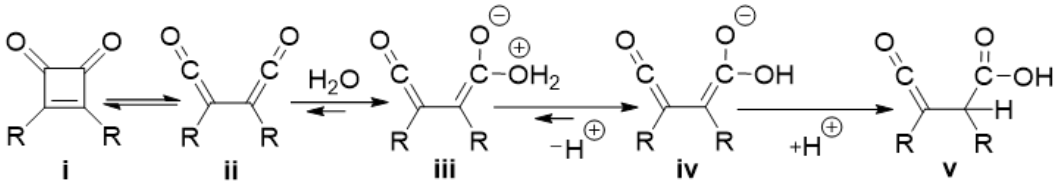


Figure **3.9**. SQ ring opening and reversible bisketene formation followed by irreversible water addition.[76,77]

This irreversible behaviour, which can lead to SQ degradation, has been exploited in the design of Pt(II) photocages using SQs for Pt(II) stabilisation and subsequent release under irradiation to achieve PACT settings (Figure **3.10**).[49]

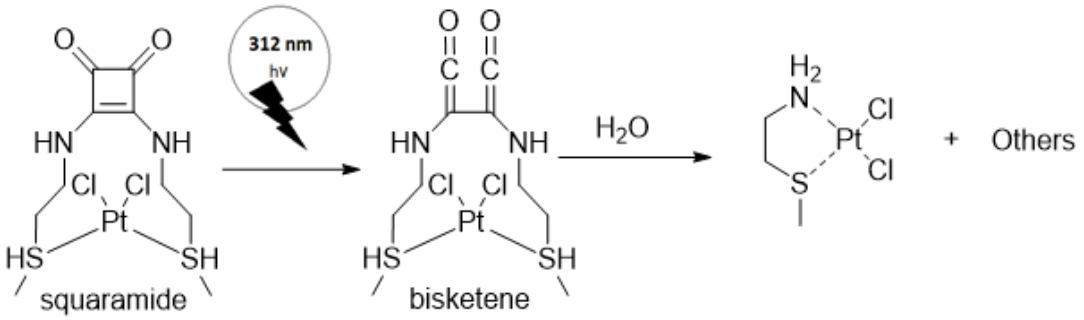


Figure **3.10**. Representation of the process reported by Kevin *et al.*[49] in which a SQ undergoes ring opening under selective light irradiation to undergo the release of cytotoxic Pt(II) photoproducts.

However, as reported, this novel approach has some limitations that need to be addressed: the need for ionising radiation for the activation of the photocage and poor biological media solubility.[49] Another issue that needs to be addressed, and is shared with other PDT drugs, is the problems arising from systemic drug administration and how to increase selective targeting. As an example, FDA-approved Photofrin®, the first SQ-based PDT systemic drug approved, is well known for causing intense inflammatory and necrotic reactions at the treated site and prolonged widespread photosensitivity for up to several weeks post PDT because of accumulation in undesired tissues.[78,79]

3.1.2.3. Supramolecular Squaraine Nanoformulations

3.1.2.3.1. Origin of the supramolecular nanoparticles

Supramolecular chemistry offers a way to create highly ordered structures using noncovalent interactions. Soft supramolecular NPs are self-assembled structures made from small building blocks, stabilised by noncovalent interactions, selective host–guest interactions, or a combination of these. In these assemblies, the binding and unbinding processes occur without breaking or altering the original components.[80]

In this context, SQs are, in general, highly planar conjugated aromatic molecules with electron-conjugated systems that can form π-stacking interactions between dye molecules.[81] Thus, the formation of supramolecular aggregates is a common consequence of π-stacking interactions that has been reported multiple times with SQ systems that present extended π-systems. On top of this, SQs' poor water solubility enhances aqueous aggregation formation, which in turn forces SQ molecules close enough to undergo the aforementioned π-stacking, forming supramolecular aggregates or NPs.[82-84] This is because solvent effects can vary the affinity and interaction between the individual components and the formed self-assembled systems.[82-84]

The formation of aggregates is an interesting feature of self-assembled structures with crucial changes in their spectral and other functional properties.[85] The absorption spectra of SQ aggregates are highly dependent on the type of aggregation that occurs. The formed aggregates can be either parallel-oriented (H-aggregates) or in a head-to-tail arrangement (J-aggregates).[86-88] The former are characterised by a blueshift absorption band while the latter show a redshift absorption band. In this context, SQs represent a family of chromophores with a high tendency to form aggregates even in solution.[89]

3.1.2.3.2. Applications

Supramolecular-based materials based on SQs also have a wide array of applications in material science and biomedical applications, although a bit narrower than free molecular SQs. Such materials can range from molecular aggregates of two or more SQ molecules, to NP encapsulation or the obtention of entirely aggregation-based NPs.[90] Examples of such applications of the SQ aggregates are listed below:

- **Aggregation/disaggregation-based metal optical detection.** Ajayaghosh *et al.* reported on Ca^{2+} and Mg^{2+} aggregation-based systems, upon coordination and disaggregation of supramolecular aggregates to quench or generate fluorescence.[91] Later works showed similar properties for specific metal sensing (Figure **3.11**). [92-94]

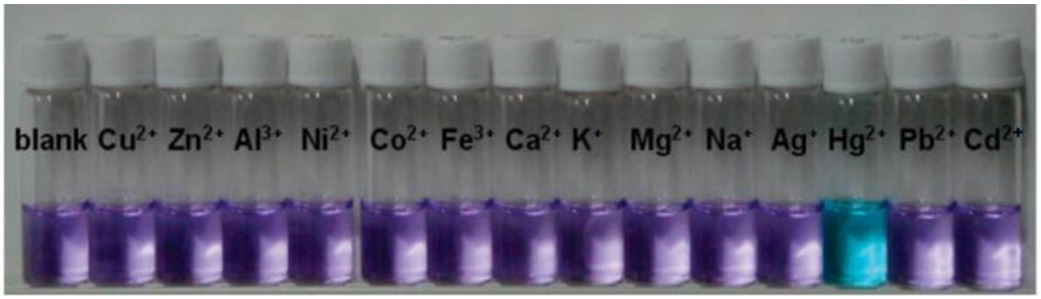


Figure **3.11**. Colour changes upon addition of different metal ions in the presence of a fluorescent sensitive SQ to Hg^{2+} as reported by Cheng *et al.* [95]

- ***Biosensors***. For instance, the development of fluorescent sensors of GSH developed by Pang *et al.,* who exploited the disaggregation of SQs as a fluorescence signal trigger.[96] Or Delcamp *et al.,* who reported fluorescence-triggered bovine serum albumin (BSA) aggregation with molecular SQs.[97]
- **Photovoltaic cell applications**. Such applications can range from dye-sensitised solar cells,[98] organic solar cells,[99] and perovskite solar cells.[100]

More relevant for this Thesis is their use in photo-triggered bio-applications:

- **Photothermal therapy.** Dereje *et al.* reported on molecular SQ-loaded mesoporous silica NPs for antimicrobial infection photothermal therapy (PTT).[101] Other examples follow j-aggregates formation in amphiphilic nano-carriers made from a PEG polymer as reported by Xie *et al.*[102] or Sun *et al.*[103] Other more recent examples come from Wang *et al.*, who report on a powerful NIR-II SQ-based H-aggregate dimers that display ultrahigh photothermal conversion efficiency encapsulated in a lipidic nanocapsule for effective photoacoustic imaging-guided PTT.[104]
- **Photodynamic therapy**. Examples with supramolecular based SQ compounds range from the reports of SQs as PSs in poly lactic-co-glycolic acid loaded NPs for antimicrobial PDT as reported by Degnet *et al.*,[51] supramolecular zinc oxide SQ layered nanohybrids reported by Bagchi *et al.,*[105] to nanovesicles based on quaternary ammonia compounds loaded with SQ dyes shown by Nicolò *et al.,*[106] to combination therapies with PTT, like reports from Weiguo *et al.*, who reported on supramolecular H-aggregates of SQ to achieve nanoprecipitates based on the molecular dye for effective ROS generation,[72] or mitochondrial-targeted nanophotosensitises NIR-activatable and photodegradable SQ self-assembling NP as reported by Huang *et al.*[107]
- **Photoactivated chemotherapy.** When it comes to PACT-based therapies using SQ aggregates, however, no examples can be found in the literature, and the most similar approach can only be found in molecular SQs, as has already been mentioned before by the works from Kevin et al.[49], demonstrating a gap in the field that is open for exploration.

3.1.2.4. Our Proposed Platform

Our research builds on the promising PACT potential of SQs, which offers advantages over PDT, particularly in overcoming the oxygen dependency of PDT within hypoxic tumour environments. Unlike previous examples of molecular SQs in PACT that rely on ionising energy for activation, we have intended to optimise the synthetic versatility of SQs to shift their activation energies into the NIR/IR region (Figure **3.12**).[49]

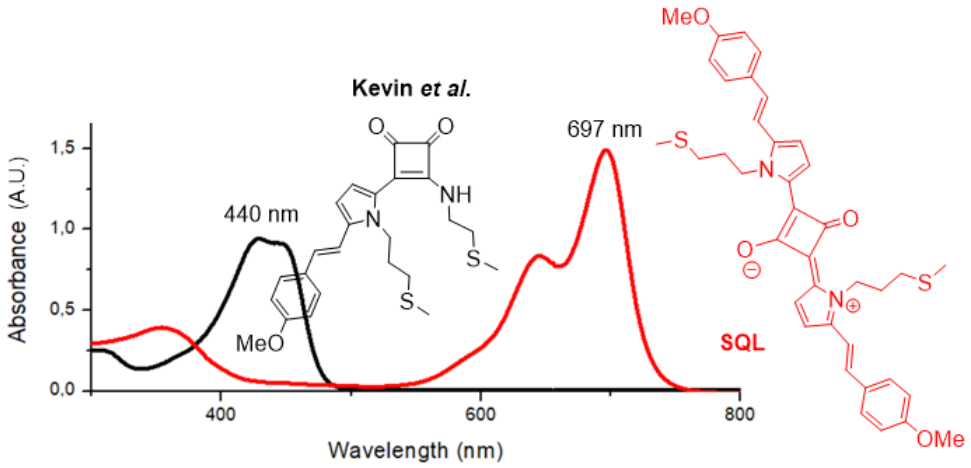


Figure **3.12**. Comparative UV-vis spectra between the reported SQ by Kevin *et al.* used in PACT[49] (**black**) and our proposed SQ molecule **SQL** (**red**).

This adjustment aligns with the first therapeutic/biologic windows of application (i.e., 650 nm to 950 nm), for deeper tissue penetration and reduced off-target effects during light activation. [200] Additionally, we propose to nanostructurate the Pt-SQ complexes considering the supramolecular interactions between SQ dye molecules. Nanostructuration offers several benefits, including improved tumour accumulation and targeting via the EPR effect, as well as addressing natural limitations of SQs, such as poor water solubility and low bioavailability.

As such, we aim to synthesise a suitable SQ ligand (**SQL**) that fulfils our NIR photosensitivity. We will then prepare a Pt(II) complex version of such molecule (**SQC**) that will then undergo supramolecular aggregation to obtain a photoactive NP based on supramolecular interactions (**SQC NP**) (Figure **3.13**). At the same time, a blank comparison NP without Pt (**SQL NP**) based on the original **SQL** will also be prepared.

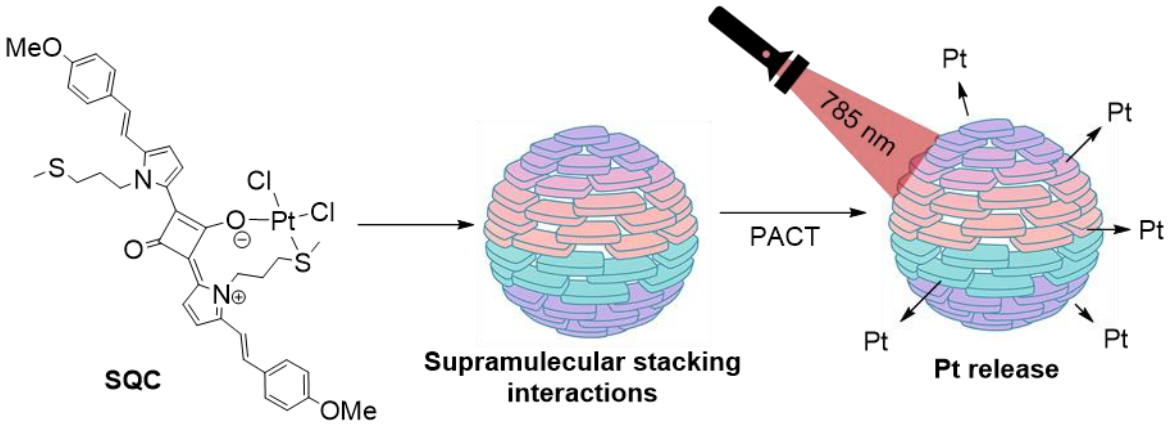


Figure **3.13**. Graphical summary showing the two key steps of this approach, nanoparticulation of the SQ Pt(II) complex and Pt release under irradiation at 785 nm.

In addition, given the examples reported in the literature emphasising the role of SQ in PDT, SQC NP will also be studied for such a purpose. In addition, the **SQL NP** comparative platform will also be studied for this same PDT approach. Therefore, if successful, achieving a multiapproach therapeutic platform with spatial selectivity to irradiation.

3.2. Objectives

On the front of **Bioinspired Neuromelanin-like Pt(IV) Polymeric Nanoparticles,** the objectives will be:

1. To design and synthesise novel functional nanostructured polymers containing a **CDDP** prodrug as a building block. Such a system should exhibit chemical and colloidal stability under physiological conditions.
2. To study drug loading and release profiles of such systems under physiological-like conditions and tumour-like environments.
3. To study the *in vitro* and *in vivo* behaviour of such NPs and validate the therapeutic effect when compared to **CDDP**.
4. To validate the *in vivo* NPs as therapeutic agents for GBM therapy using IN administration as a novel and alternative administration route.

To achieve such objectives, the following steps will need to be carried out:

- Synthesis of a **PtBC** suitable for oxidative polymerisation.
- Oxidative polymerisation of PtBC for the synthesis of pPtBC NPs and their physico-chemical characterisation (Figure **3.14**).
- Synthesis of CNP analogues without Pt(IV) (**NDGA**) as control and comparative platforms.
- Assessment of drug release in simulated physiological conditions.
- Cellular uptake and DNA-Pt binding characterisation.
- *In vitro* cytotoxicity determination against a set of GBM, fibroblast, **CDDP**-resistant and HeLa cells, and determination of ROS generation.
- *In vivo* tolerability and biodistribution via IN administration determination.
- *In vivo* anticancer efficacy in GBM tumour-bearing C57BL/6J mice.

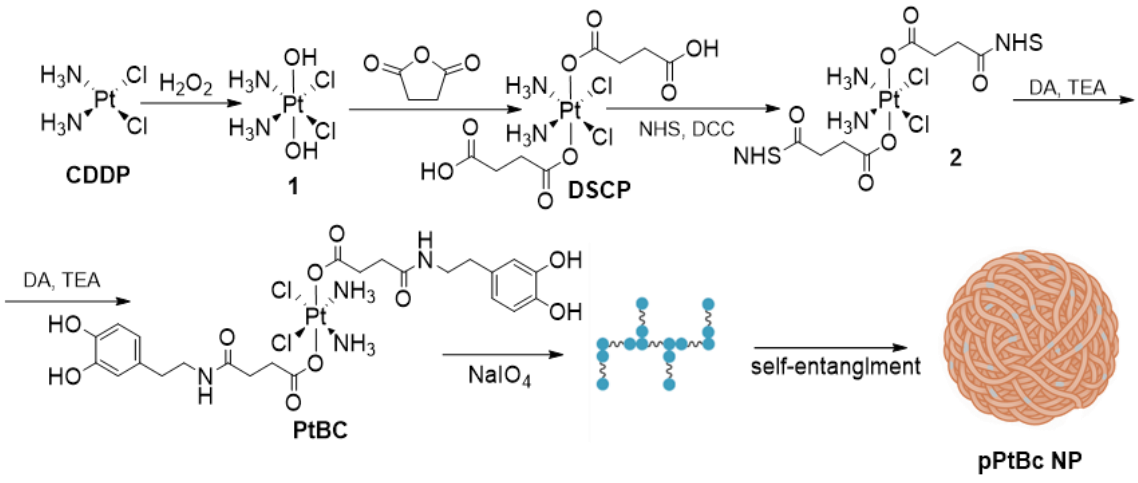


Figure **3.14**. Synthetic steps for the preparation of the target **PtBC** monomer, followed by oxidative polymerisation and obtention of the target coordination **pPtBC NP**.

The objectives for **Supramolecular Photoactivatable Squaraine Pt(II) Complex NPs** will be:

1. To design and synthesise supramolecular photoactivatable **SQC NPs** with good chemical and colloidal stability in physiological conditions.
2. To study drug loading and release profiles of such systems under physiological-like conditions and tumour-like environments with light.
3. To study the *in vitro* and *in vivo* behaviour of such NPs and validate the therapeutic effect.
4. To validate the *in vivo* NPs as therapeutic agents for GBM therapy using IN administration as a novel and alternative administration route.

To achieve such objectives, the following steps will need to be carried out:

- Synthesis of target molecular **SQL** and **SQC** from suitable starting reagents and characterisation of the obtained products (Figure **3.15**).
- Synthesis and characterisation of **SQC NP** from **SQC**, as well as **SQL NP** from the starting molecular **SQL**, because of its value as a blank comparison and potential in photoactive ROS generation (Figure **3.15**).
- Characterisation and evaluation of Pt cytotoxic cargo loading as well as release under specific irradiation stimulus at biologically safe wavelengths for **SQC NP**.
- Validation and determination of photoactivation behaviour from **SQL** and **SQC** and supramolecular aggregates **SQC NP** and **SQL NP**.
- Determination and characterisation of total cellular uptake and total Pt binding from **SQC NP**.
- *In vitro* cytotoxicity determination against a set of GBM, fibroblast, **CDDP**-resistant and HeLa cells.
- *In vivo* tolerability and biodistribution studies via IN administration.
- *In vivo* anticancer efficacy in GBM tumour-bearing C57BL/6J mice.

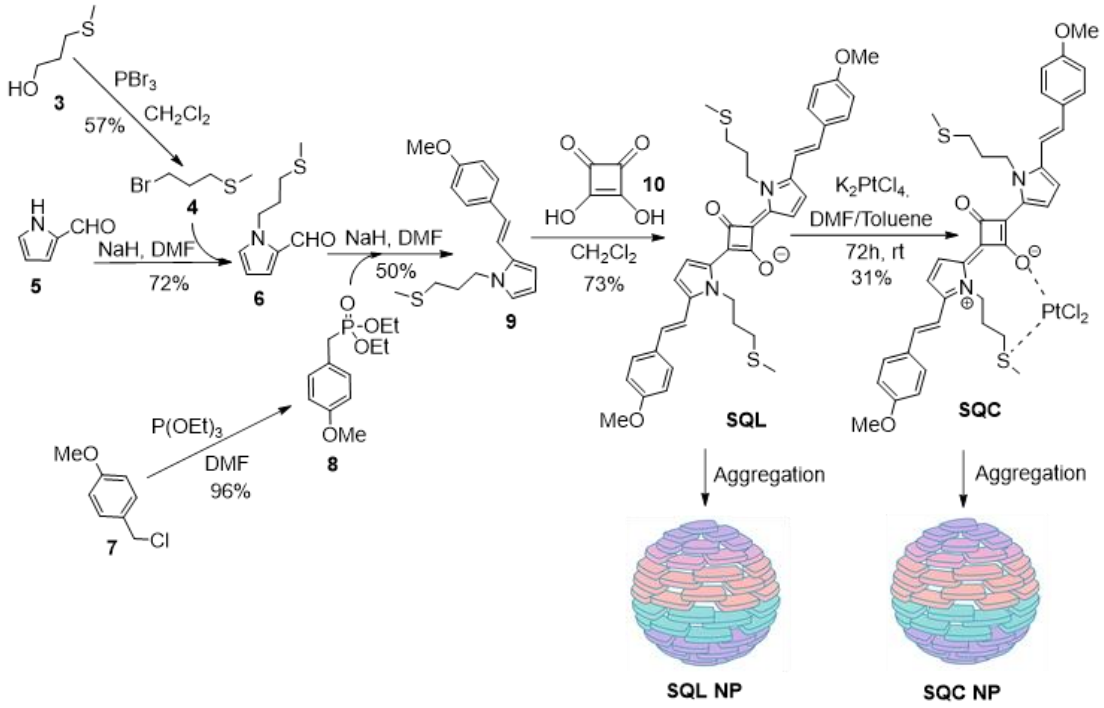


Figure **3.15**. Synthetic steps for the preparation of the target Pt(II) SQ complex and supramolecular aggregates from the Pt(II) SQ complex and the SQ ligand.

3.3. Results and Discussions

3.3.1. Bioinspired Polymeric Neuromelanin-like Pt(IV) Nanoparticles

Part of the work in this Chapter has been done in collaboration with Prof. Julia Lorenzo and former student from the Nanosfun group, Dr. Xiaoman Mao, especially for the studies of cellular uptake, tolerability and biodistribution *in vivo* experiments, and Dr. Paula Alfonso, for the work on *in vitro* cytotoxicity studies.

3.3.1.1. Synthesis of the Precursor PtBC

PtBC is a Pt(IV) complex with octahedral molecular functionality, with two catechol-containing moieties coordinating on the axial positions of the Pt complex. Similar pyrogallol-based compounds have also been studied.[109] Taking advantage of the expertise of our research group in synthesising Pt(IV) oxo-complexes,[3,110] we proposed the synthetic route detailed in Figure **3.16** for the obtention of **PtBC**:

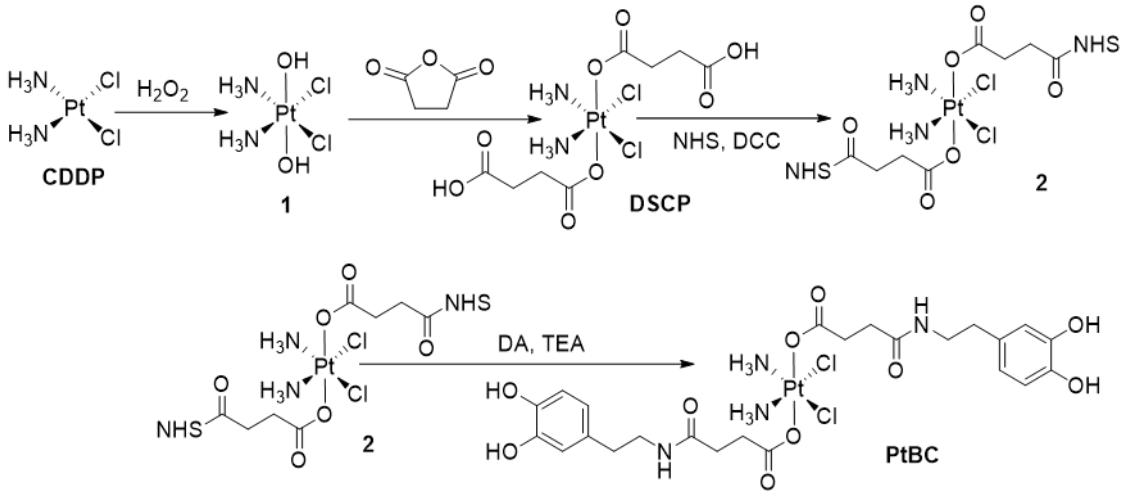


Figure **3.16**. A synthetic route was taken to yield **PtBC** from a commercially available starting material.

The synthesis of the **PtBC** has been developed to use as a starting material the already commercially available anticancer Pt agent, **CDDP**. The synthesis of the **PtBC** has been developed to use as starting material the already commercially available anticancer Pt agent, **CDDP**. The synthetic route consists of a four-step synthesis. First step consists of an oxidation of the commercially available **CDDP** to c,c,t-$Pt(NH_3)_3Cl_2(OH)_2$ (oxoplatin, **1**). The following step will consist of a ring-opening nucleophilic attack on succinic anhydride, obtaining disuccinic cisplatin (**DSCP**). Activation of this last compound using N,N'-Dicyclohexylcarbodiimide/ N-Hydroxysuccinimide (DCC/NHS) will then be carried out, obtaining intermediate **2**. Finally, the Pt monomer complex **PtBC** will be obtained using a nucleophilic substitution with catecholamine DA. Thus, successfully obtaining the final product **PtBC** with an overall yield of 19**%.**

3.3.1.1.1. Synthesis of Oxoplatin

Oxoplatin **1** was obtained via an oxidation reaction of **CDDP** with hydrogen peroxide, which yields product **1** as yellow crystals with a yield of 74% (Figure **3.17**).

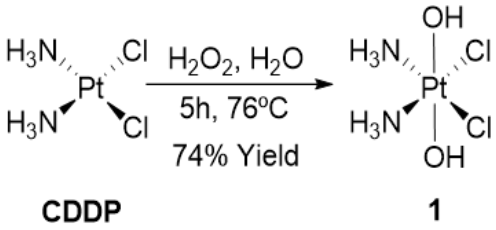


Figure **3.17**. Synthesis of oxoplatin **1** from **CDDP**.

Oxoplatin Fourier transform infrared (FTIR) spectrum shows two distinctive signals at 3515 cm^{-1} and 557 cm^{-1}, corresponding to the O-H and Pt-O bond stretching vibrations, respectively. These signals arise from the presence of the new hydroxyl groups found in oxoplatin (Figure **3.18**).[111] Original spectrum can be found in Annexe **3.1**.

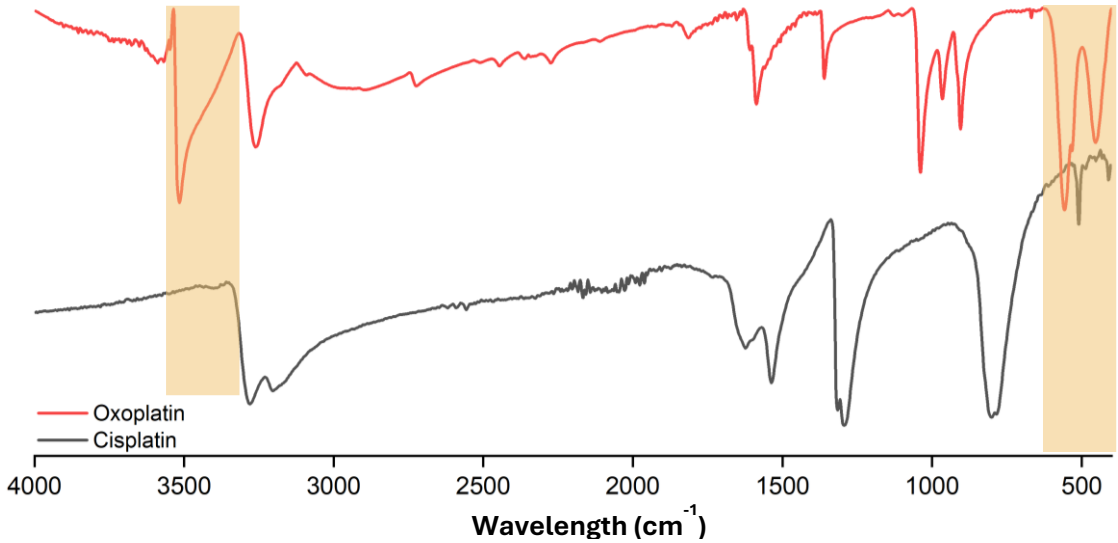


Figure **3.18**. FTIR comparison between Oxoplatin **1** (red) and **CDDP** (black).

3.3.1.1.2. Synthesis of Disuccinic Cisplatin

DSCP was prepared via a nucleophilic attack on one of the carbonyls of succinic anhydride from the hydroxyl group of oxoplatin (**1**), which acts as the nucleophile (Figure **3.19**). This results in the ring opening of the anhydride and the obtention of the targeted molecule **DSCP** as a yellow powder with a yield of 76%.

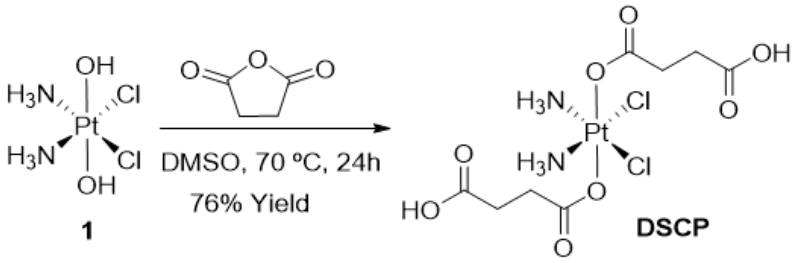


Figure **3.19**. Synthesis of **DSCP** from **1**.

A combination of nuclear magnetic resonance (NMR) and FTIR can prove the successful obtention of the targeted product. On one hand, **DSCP**'s FTIR showed that the previous sharp signal from oxoplatin at 3516 cm^{-1} was replaced by a broader signal at around 2900-3400 cm^{-1} from the O-H bond of the carboxylic acid. On top, a new band at 1630–1730 cm^{-1} from the C=O bond appeared (Figure **3.20**). Original spectrum can be found in Annexe **3.3**.

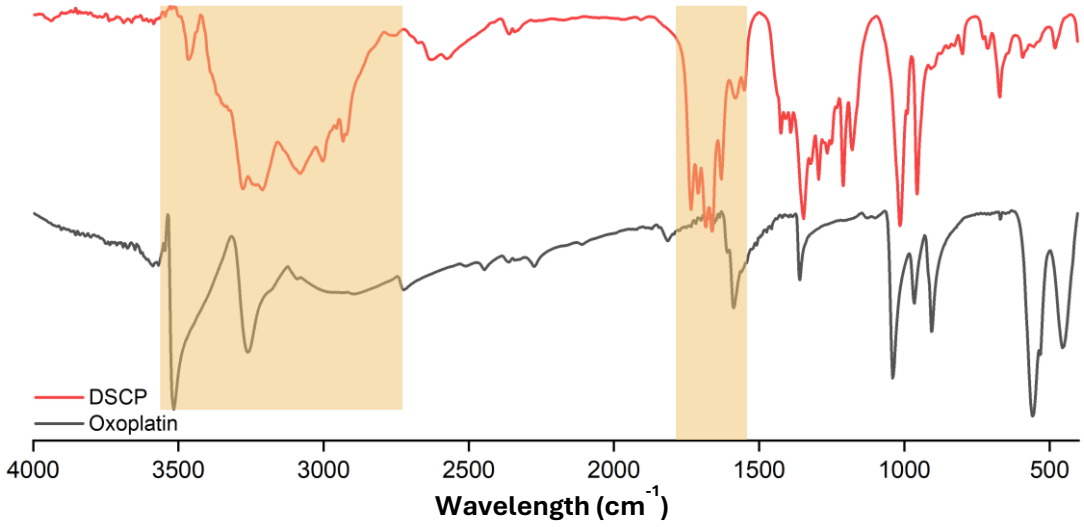


Figure **3.20**. FTIR comparison between **DSCP** (red) and **1** (black).

On the other hand, **DSCP**'s ^{1}H-NMR will present signals at the aliphatic region at 2.37 ppm and overlapped with the dimethyl sulfoxide (DMSO) residual solvent signal at 2.50 ppm. These signals correspond to the protons belonging to the succinic acid ligands coordinating with Pt. These signals, despite being aliphatic, are in relatively high field due to the proximity to electron-withdrawing groups. At the same time, these protons present multiplicities of triplets as is expected from the coupling of these signals between the two different protons available. Signals at 12.07 ppm are expected to belong to the acidic protons of DSCP and broad signals at 6.48 ppm to belong to the amine ligands (Figure **3.21**).

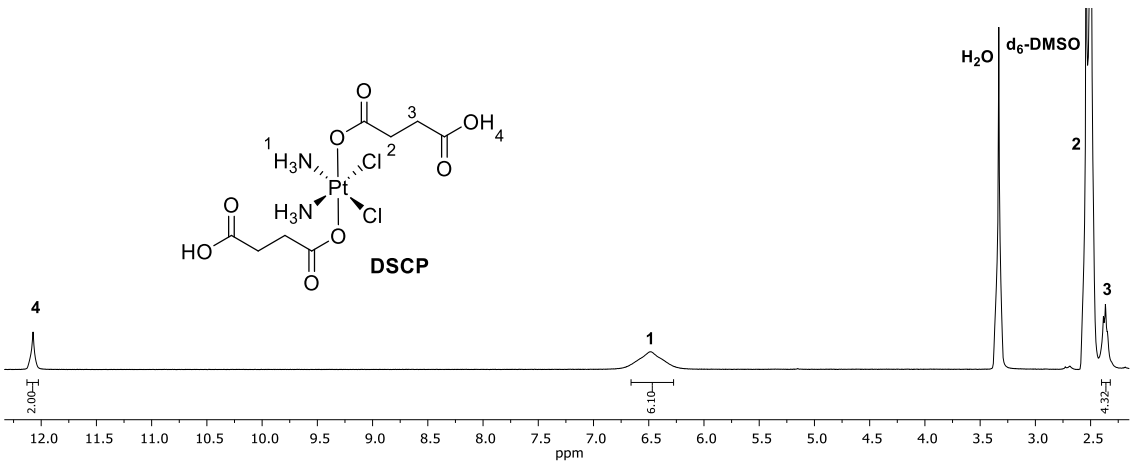


Figure **3.21**. ^{1}H-NMR of **DSCP**.

3.3.1.1.3. Synthesis of Succinic Acid-NHS Activate

Direct synthesis from **DSCP** to obtain the target **PtBC** prodrug is improvable to happen. This is because it would entail using a primary amine to perform a substitution reaction on a carboxylic acid to displace a hydroxyl group. The most probable product from such a reaction would be nothing else than a protonated amine and a deprotonated carboxylate. As a result, an activation step is required. This step will consist of furbishing the **DSCP** with a functional group that can readily act as a leaving agent, such as NHS.

NHS is introduced after DCC activation via a regular displacement, obtention the targeted NHS ester **2** as a pale-yellow powder with a 62% yield (Figure **3.22**).

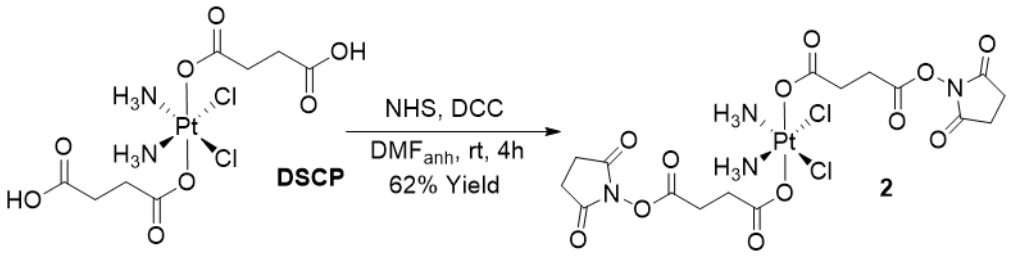


Figure **3.22**. Synthesis of **2** from **DSCP**.

A dead giveaway of a successful synthesis of the NHS ester **2** can be found in the ^{1}H-NMR spectrum (Figure **3.23**). For the target molecule a new set of signals arising from the newly introduced NHS will be observable 2.85 ppm as a multiplate that merges with the previous aliphatic proton signals.

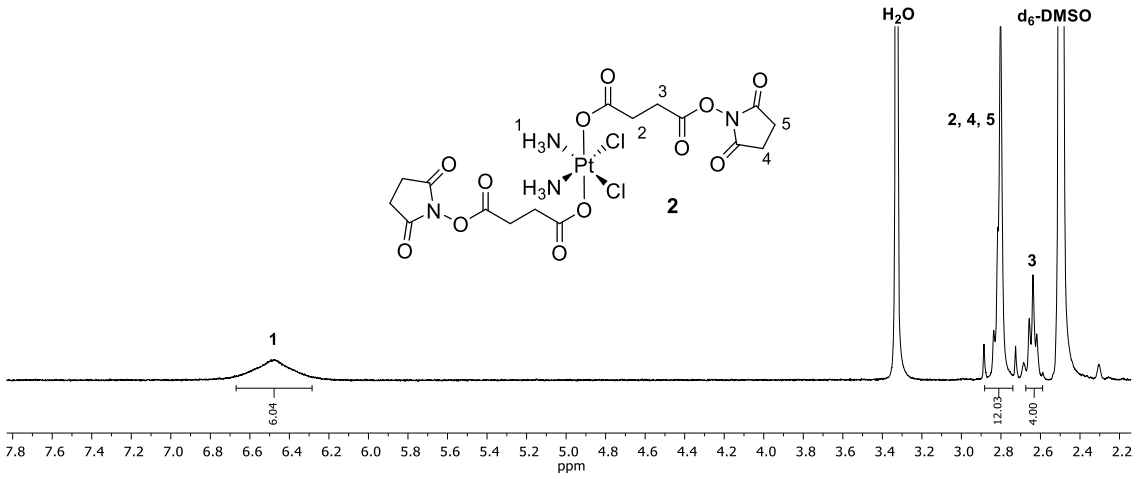


Figure **3.23**. ^{1}H-NMR of succinic acid-NHS activate **2**

3.3.1.1.4. Synthesis of PtBC

The obtention of the final monomeric prodrug **PtBC**, consists in the introduction of a DA moiety, and displacing the NHS group introduced previously with **2**. DA contains a primary amine that is commercially available as a chloride salt, making the use of some triethyl amine base (3 eq) necessary in order to obtain a more reactive DA form. This process will produce the **PtBC** as an intense yellow powder with a 57% yield (Figure **3.24**).

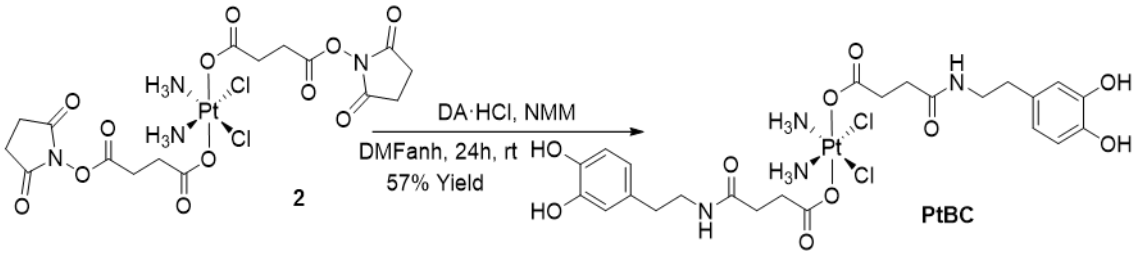


Figure **3.24**. Synthesis of **PtBC** from **2**.

The introduction of the DA moiety will allow us to spot new signals at the ^{1}H-NMR spectrum (Figure **3.25**). New, aromatic, signals corresponding to the catechol ring of DA will appear at 6.70, 6.67 and 6.55 ppm, and integrating for 6 protons, the totality of the DA ring. As well as two new signals at the aliphatic region corresponding to the new two aliphatic carbons of DA at 2.66 ppm and at 3.34 ppm, although the last one overlapped with the solvent residual peak of methanol. Further ^{13}C-NMR and 2D NMR (COSY, HSQC and HSMBC) confirm the expected molecular composition (Annexe **3.7** to **3.9**).

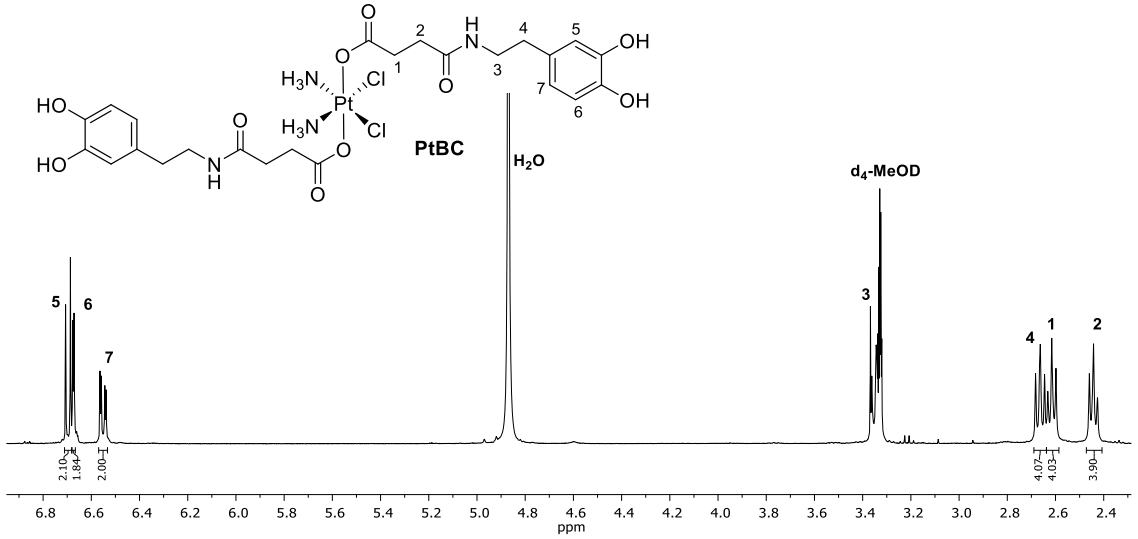


Figure **3.25**. ^{1}H-NMR of **PtBC**.

Most definitely, however, is the high-resolution mass spectrometry (HRMS) (Annexe **3.12**). This shows an M+Na^{+} of 827.1166 amu with a calculated value of 827.1180 amu, and an M+H^{+} of 805.1353 amu with a calculated value of 805.1361 amu. Thus, confirming the obtention of the **PtBC** molecule.

Overall, the total synthesis of the **PtBC** has been conducted in a linear synthetic route that consisted of only four steps and gave an overall yield of 19% with relative ease and only two steps requiring to work in inert atmosphere.

3.3.1.2. Synthesis of pPtBC NPs

Many different conditions can trigger catechol polymerisation, but the use of chemical polymerisation is among the most employed.[112] The **pPtBC NPs** were obtained directly by the oxidation of terminal catechol moieties from the **PtBC** prodrug using sodium periodate ($NaIO_4$) (Figure **3.26**).

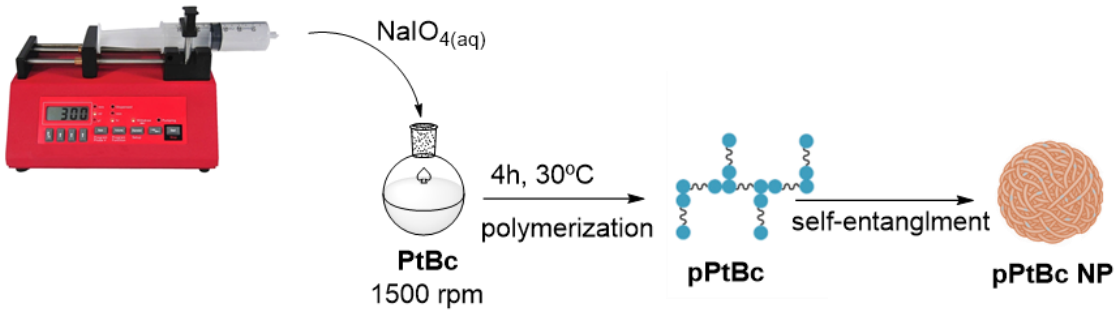


Figure **3.26**. Schematic representation of the procedure followed for the nanoparticulation of **PtBC** based on oxidative polymerisation.

This methodology is well known for catechol polymerisation, and reports on the literature can be found following the same guidelines.[34,113] The reaction was carried out in a slow and controlled manner. The addition of NaIO4 in aqueous solution was carried out over extended periods of time. Addition was made on a flask containing our prodrug while vigorously stirred and dissolved in a 1:1 ethanol:water volume ratio. After 3 hours of reaction and under gentle heating at 30 °C, the **pPtBC NPs** were obtained as a brown precipitate.

3.3.1.2.1. Chemical Characterisation of pPtBC NPs

FTIR characterisation showed that peaks in the 1200-1400 cm^{-1} region, characteristic of catechol, shifted noticeably from the **PtBC** starting product. Noticeably, the O-H stretching significantly decreased in size, while peaks at 1197, 1283 and 1327 cm^{-1} disappeared, and a broadened peak at 1279 cm^{-1} from oxidation products of DA appeared (Figure **3.27**). Original spectrum can be found in Annexe **3.13**.

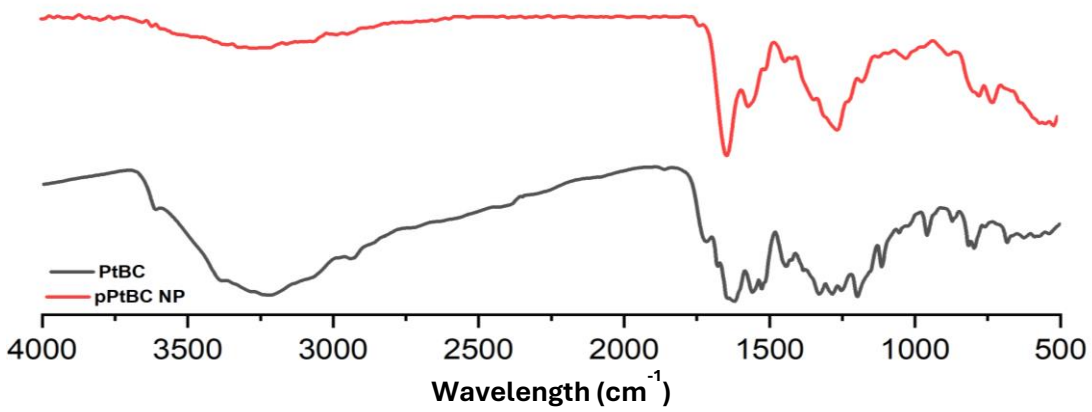


Figure **3.27**. FTIR comparison between **pPtBC NP** (red) and **PtBC** (black).

Inductively coupled plasma-optical emission spectrometry (ICP-OES) was performed to determine the Pt load in the NPs. Compared to the theoretical value, the Pt mass is lower than expected, from 24% to 17%. A possible explanation for the decrease in Pt content w/w could be attributed to a NP weight increase due to the incorporation of sodium and other ions present in the media into the NP. The hydrodynamic size and ζ-potential of **pPtBC NP** were measured using dynamic light scattering (DLS) (Figure **3.28**). Particles showed sizes of 234.6 ± 0.5 nm with a low polydispersity index (PDI) of 0.087 ± 0.022 and a ζ-potential of -37.1 ± 0.95 mV.

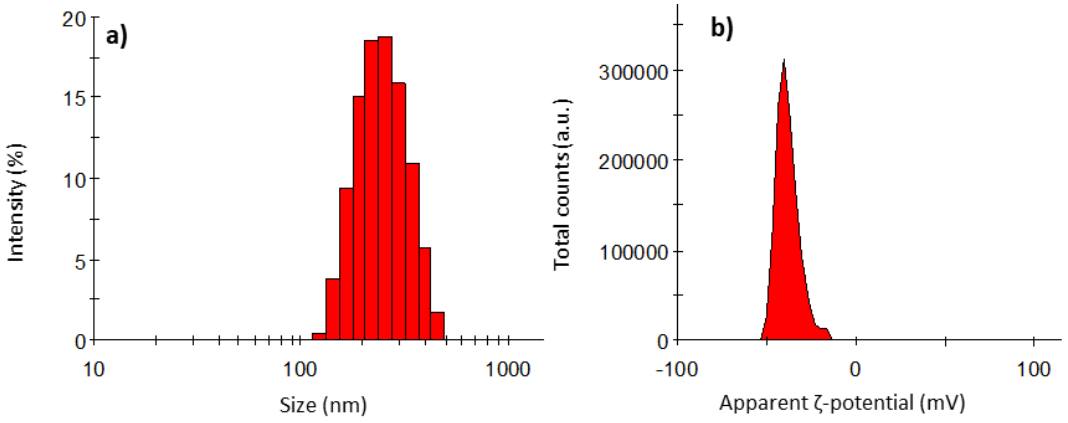


Figure **3.28**. **a)** Representative size distribution, and **b)** Representative ζ-potential of **pPtBC NPs** by DLS.

As we stated, size can considerably influence the NPs' interaction with cells, and the biodistribution *in vivo*. Particles smaller than 20 nm are easily excretable, while NPs larger than 200 nm are captured by macrophages and accumulate in the spleen. Furthermore, blood circulation time and the EPR effect are more effective in sizes between 30 and 200 nm.[114-117] As observed, **pPtBC NPs** fall on the edge of these values, which could lead to longer blood circulation time, bioavailability and improved accumulation in tumours, increasing the potential for GBM treatment. Even more, if we aim to work in intra-brain applications, it has been observed that NP sizes bigger than 100 to 120 nm present serious problems in crossing the BBB.[118] In this scenario, the proposal of using IN administration as a path to reach the brain seems an adequate option. IN administration avoids the restrictive nature of the BBB and allows for bigger NP permeability to reach the brain, while presenting as a non-invasive administration route.[119] On top of this, our very low PDI will ensure a homogeneous behaviour of our NPs. This leads to lower aggregation and better biodistribution and homogeneity.[120]

Nonetheless, the size and size cutoff of the different administration routes are not the only challenge NPs in administration face. Surface charge of NPs influences interaction of NPs and proteins in the bloodstream as well as acts as a point of contact with any membrane that NPs interact with, affecting pharmacokinetics and biodistribution. Positively charged NPs may improve cellular uptake due to their interactions with the cell membrane. Nonetheless, cationic NPs have been observed to be rapidly removed from circulation due to an increased protein absorption that results in nonspecific uptake by macrophages.[121] Low surface charge allows better biodistribution, and extreme charges induce phagocytosis by macrophages.[122] Since **pPtBC NPs** are negatively charged, they will most probably not benefit from better uptake as seen, but also will not risk rapid reticuloendothelial system (RES) clearance.

3.3.1.2.2. Morphological Characterisation of pPtBC NPs

The **pPtBC NPs** morphology was studied using scanning electron microscopy (SEM) imaging (Figure **3.29**). Our NPs presented very spherical shapes and homogeneity across all samples. Size, as characterised by SEM, gave sizes of 157 ± 0.5 nm. A discrepancy in size can be observed between the SEM histogram and DLS, although discrepancies between techniques can be pointed towards i) the measurement of a hydrodynamic size by DLS, and ii) an equal weight distribution in the SEM histogram between all samples rather than DLS.

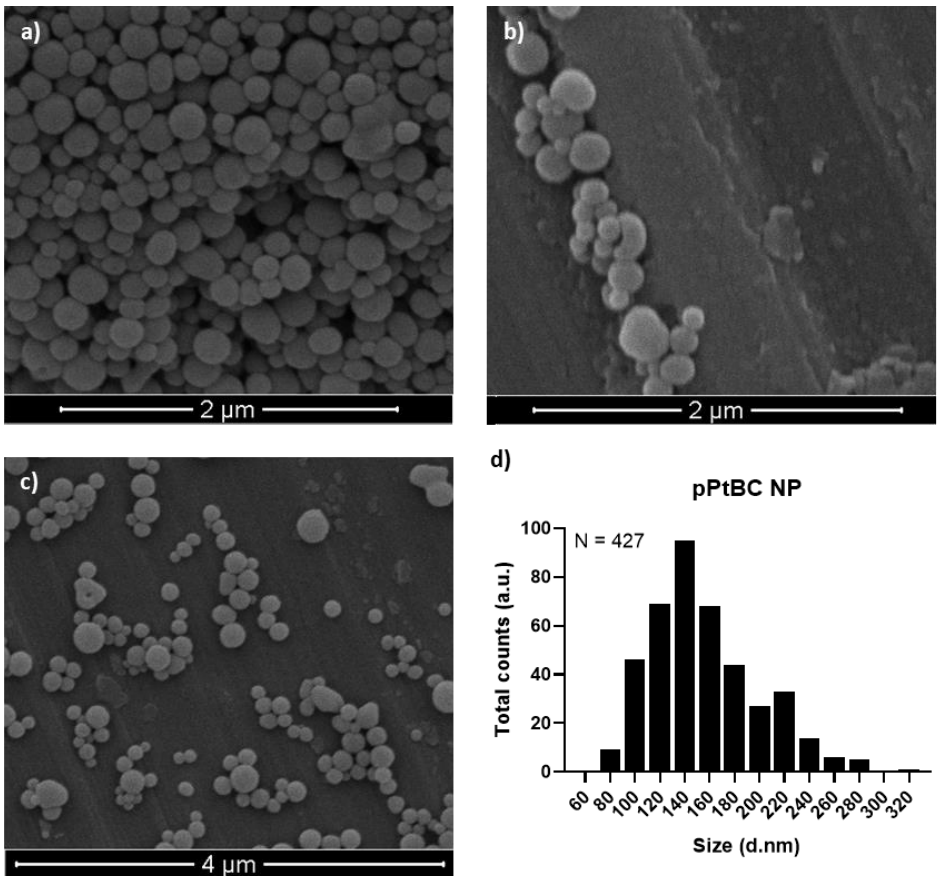


Figure **3.29**. **a-c)** Representative SEM image of **pPtBC NPs** under a 5 nm Pt thin film coating for imaging. **d) pPtBC NPs** size distribution by image size counting.

3.3.1.3. Synthesis of pNDGA NPs

Catechol-containing molecules like flavonoids are well known for their anticancer, antibacterial and antiviral activity. Catechols can achieve such results thanks to their redox-modulating capabilities.[123,124] Thereafter, for comparative purposes, NPs using **NDGA** as an analogous bis-catechol ligand that does not contain a Pt(IV) core were synthesised and characterised.

Using the same methodology as described previously, the **pNDGA NPs** were obtained through oxidative polymerisation of **NDGA** (Figure **3.30**). **NDGA** shares a similar morphology to that of **PtBC** since both molecules are elongated, present a sterically voluminous centre and have catechol moieties at the terminal ends.

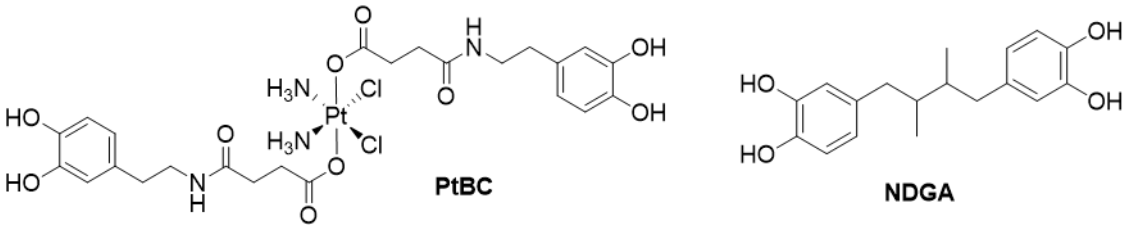


Figure **3.30**. Molecular structure of **PtBC** and **NDGA**.

The structural similarity between **NDGA** and **PtBC** also allows for the polymerisation of **NDGA** following the same principles of oxidative polymerisation applied to **PtBC** (Figure **3.31**).

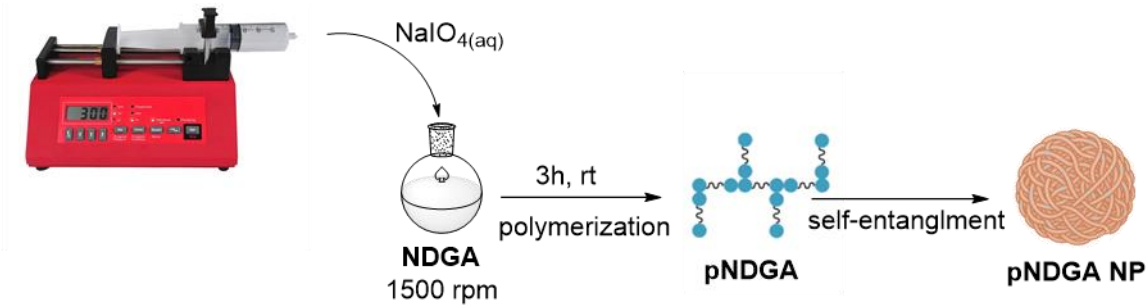


Figure **3.31**. Schematic representation of the procedure followed for the nanoparticulation of **NDGA** based on oxidative polymerisation.

In short, the reaction of **pNDGA NPs** consisted of addition of $NaIO_4$ dropwise to a flask containing the **NDGA** reactant dissolved in a 1:1 ethanol:water volume ratio. The reaction is then kept at room temperature for 4 hours, isolated by centrifugation and washed several times in ethanol and water, obtaining the NPs as a brown precipitate resuspended in water for storage.

3.3.1.3.1. Chemical Characterisation of pNDGA NPs

FTIR characterisation showed, again, peaks at the 1200-1400 cm^{-1} catechol region that shifted noticeably from the starting product **NDGA** (Figure **3.32**). Peaks at 1393, 1354, 1325, and 1292 cm^{-1} disappeared, while a broadened peak at 1279 cm^{-1} and at 1725 cm^{-1} from oxidation products of DA appeared. Original spectrum can be found in Annexe **3.15**.

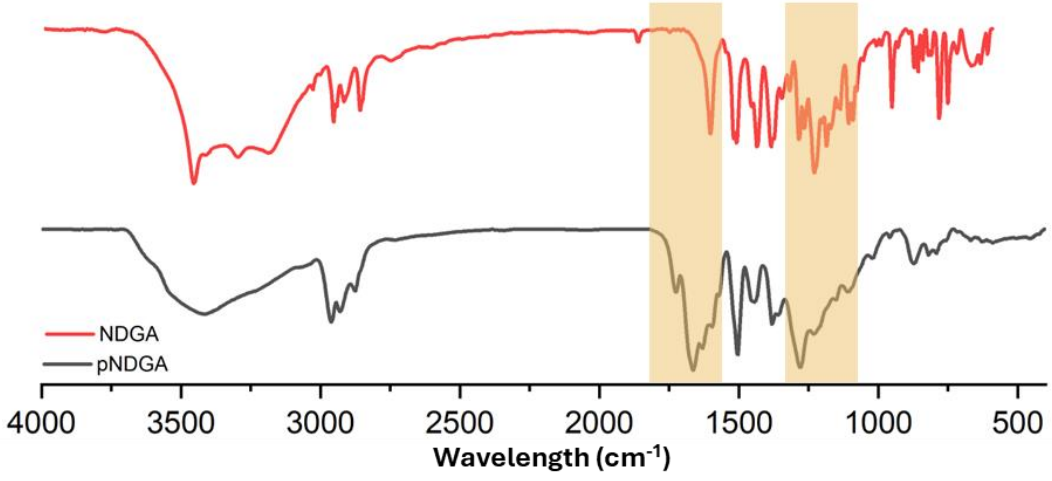


Figure **3.32**. FTIR comparison between **NDGA** (red) and **pNDGA** (black).

The hydrodynamic size and ζ-potential of **pNDGA NPs** were measured using DLS (Figure **3.33**). The particles presented sizes of 214.2 ± 0.8 nm with a very low PDI of 0.07 ± 0.02 and a ζ-potential of -28.7 ± 0.5 mV. Overall, **pNDGA NPs** are quite homogeneous in terms of size and PDI. However, they present a slightly higher surface charge than **pPtBC NPs**.

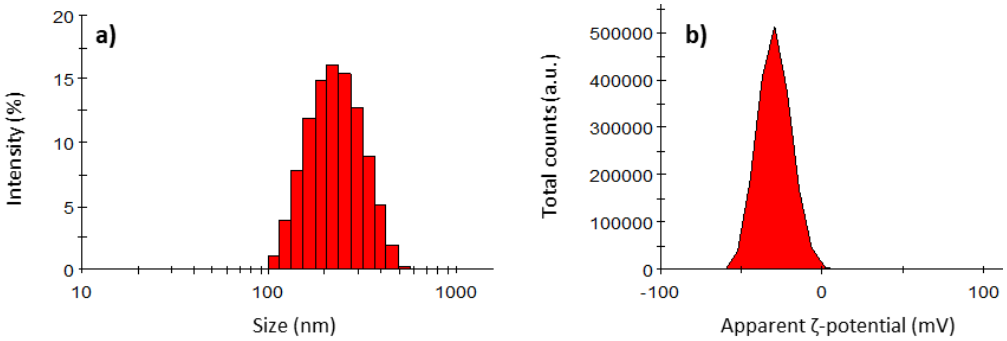


Figure **3.33. a)** Representative size distribution, and **b)** Representative ζ-potential of **pNDGA NPs** by DLS.

3.3.1.3.2. Morphological Characterisation pNDGA NPs

The **pNDGA NPs** morphology was also studied using SEM imaging (Figure **3.34**). **pNDGA NPs** presented very spherical and homogeneous shapes, and a size analysed with SEM that gave sizes of 260 ± 0.5 nm, which fell in accordance with the DLS results. In this, we observe a closer correlation than that of **pPtBC NP** towards the results of DLS, it is also to no surprise as the PDI values of **pNDGA NP** presents smaller, thus more homogeneous in size. **pNDGA** and **pPtBC NPs** present similar sizes, PDI, morphology and close surface charge; therefore, we can assume similar supramolecular interactions, leading to **pNDGA NP** as a potential candidate to work as a homologous system to **pPtBC NPs** for comparison purposes.

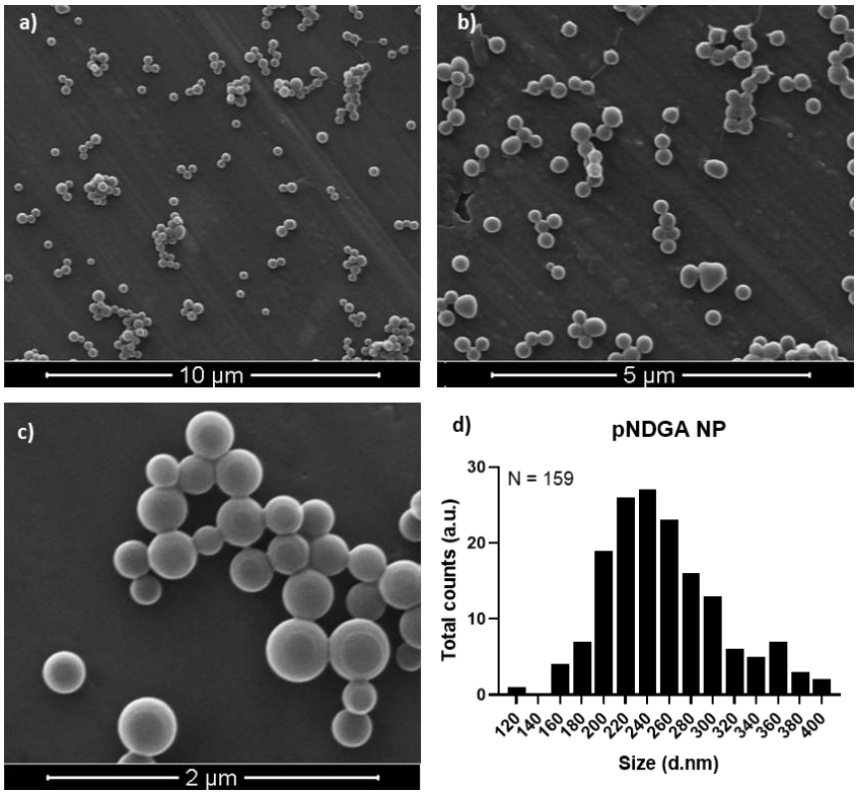


Figure **3.34. a-c)** Representative SEM image of **pNDGA NPs** under a 5 nm Pt thin film coating for imaging. **d) pNDGA NPs** size distribution by image size counting.

3.3.1.4. Platinum Drug Release

A fundamental step to take before attempting any cytotoxicity studies is to assess if our NPs are capable to release the Pt cargo. The obtained **pPtBC NPs** targeted in this project are supposed to be pH, redox, and enzymatic-sensitive due to the presence of the amide, carboxylic, and oxo coordination bonds from the complex ligands. Such bonds may be cleaved under weakly acidic media like the extracellular tumour environment or endo/lysosomal compartments.[125,126] Another opportunity for release that was also targeted, was the redox environment from cells with our Pt(IV) metal core of the complex capabilities to undergo reduction to Pt(II) intracellularly.[127,128]

Thereafter, a dialysis method was used to obtain the release profiles for our NPs (Figure **3.35**). In order to better replicate *in vitro* physiological media pH 7.4 was chosen, as well as pH 5.4 to mimic acidic tumoral tissues and lysosomal conditions.[129-131] In a phosphate buffer (PB) solution, **pPtBC NPs** were allowed to evolve in a dialysis bag for a period of 48 hours in their respective pH ranges. Released Pt was quantified by ICP-mass spectrometry (MS).

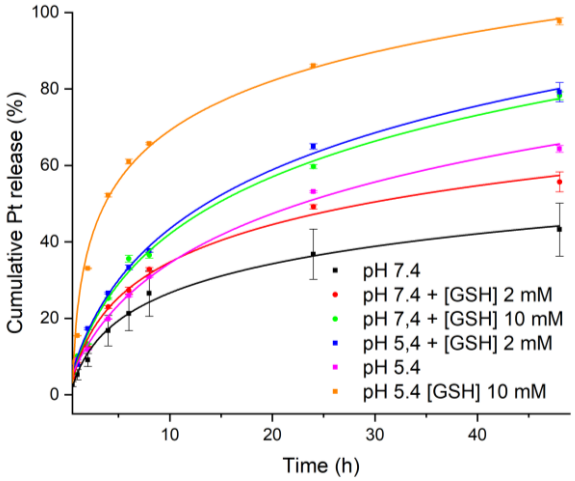


Figure **3.35**. Cumulative Pt release from **pPtBC NPs** at pH 5.4 and 7.4 and in the presence of GSH (2 and 10 mM).

In both pH, a typical release profile can be observed. As expected, the decrease in pH induced a faster Pt release due to the increased hydrolysis of the different coordination and chemical bonds. After 48 hours, at pH 7.4 a 43.20 ± 6.92% Pt release was calculated, whereas the release at pH 5.4 was of 64.34 ± 0.9%.

These results demonstrate a pH-sensitive NP that can release the payload in a controlled manner with different profiles depending on the environment's pH. Pt release from the NP can result from i) hydrolysis of the coordination bonds between Pt and succinyl-bearing carboxylic acid, and ii) the dissociation of catechol-amides (amide bonds prove weak to hydrolysis and promote the cleavage and release of Pt) (Figure **3.36**).

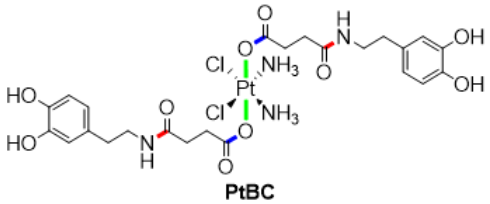


Figure **3.36**. Representation of PtBC with pH and redox-sensitive bonds marked as red (amide), blue (carboxylic) and green (coordination).

Another important consideration is the reductive power or redox homeostasis of cells. As already mentioned in the introduction, intracellular presence of reduced GSH and glutathione disulfide (GSSG) are responsible for maintaining the reductive environment inside cells. Intracellular concentration of GSH is known to range from 1 to 10 mM in normal cells and can also be 2-3 orders of magnitude lower in extracellular media. However, in cancer cells, this concentration can increase up to fourfold.[132] In the brain, the concentration of GSH is around 1-2 mM.[133] Sensitivity to these molecules can then mean the possibility of targeted therapies.[134,135] Catechol moieties present responsiveness to GSH-GSSG systems and have also been studied.[136] These reports need to be added to the possibility of the Pt(IV) complex to undergo reduction, collapsing the two catechol moieties bonded to itself on the axial positions and promoting the Pt release.[137,138]

Therefore, to test the influence of the presence of this reductive environment, the release profile was repeated at 2 mM and 10 mM of GSH concentrations with the same previous conditions and method (Figure **3.35**). As observed, the release of Pt was also promoted by GSH. At pH 7.4, mM Pt release at 2 mM concentration GSH was of 55.70 ± 2.63% and at 10 mM concentration, GSH release reached 78.23 ± 1.05% after 48 hours. As for pH 5.4, Pt release at 2 mM concentration GSH was 79.16 ± 2.53% and at 10 mM concentration GSH, release reached totality at 97.70 ± 0.92% after 48 hours.

All in all, we have proven that **pPtBC NPs** are sensitive to pH and GSH at the same time. In both cases, promoting an activation and release of the Pt cargo. Thus, we can ascertain that our NPs are providing selectivity towards tumour tissues. These results give us hope for a more controlled activation of our cytotoxic cargo and an increase in effectiveness as well as a reduction of side effects when compared to other non-selective drugs.

3.3.1.5. *In vitro* studies

3.3.1.5.1. Cellular Uptake and DNA-Bound Pt

Therapeutic efficacy of an anticancer agent depends significantly on the capacity to accumulate within the target (i.e., the intracellular concentration). Accumulation can be directly connected to various factors such as the kinetics of uptake pathways, metabolism, and/or cellular efflux.[139] It has been reported that increasing the surface lipophilicity of NPs enhances their affinity to cell membranes, including those of the BBB, whereas hydrophilic NPs follow the opposite trend.[140] Precisely because of the polymeric and highly lipophilic nature of **pPtBC NPs**, such composition could hold potential to facilitate the NPs transport. Thereby, augmenting their cellular interactions and uptake within the targeted tumour cells.

Thereafter, it is not only important to study the Pt release capability but also the cellular uptake of our NPs. To evaluate the intracellular internalisation, monomeric **PtBC** ligands and **pPtBC NPs** (0.1 mM referred to Pt) were co-incubated with human cervical cancer cell line HeLa, the non-malignant human fibroblast cell line 1Br3G, and murine glioma cell line GL261 for 6 hours and afterwards digested and analysed using ICP-MS. HeLa cells were chosen as the standard representative for cancer cells. 1Br3G as fibroblasts were selected as they could serve as a comparison of behaviour with healthy cells. Finally, GL261 were chosen as a glioma-related cell

line from a mouse that will give the most information in relation to the applicability with any *in vivo* studies that we might perform (Figure **3.37**).

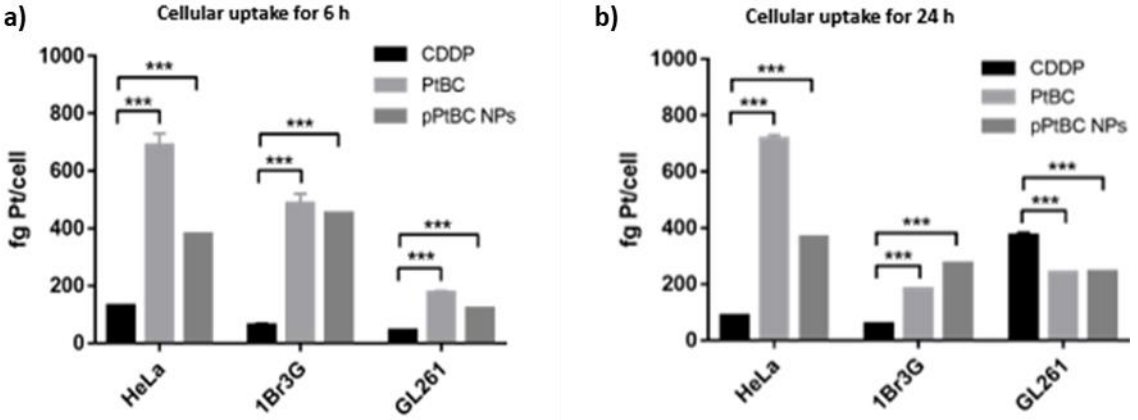


Figure **3.37**. Cellular uptake of **CDDP**, **PtBC** and **pPtBC NPs** in HeLa, 1Br3G and GL261 cell line for **a)** 6 hours and **b)** 24 hours. All drugs were incubated at a concentration of 100 µM referred to Pt. Each value represented as mean ± standard of error mean (SE), n=3. * stands for $p < 0.05$, ** for $p < 0.001$, *** for $p < 0.0001$.

Cellular uptake achieved, from higher to lower concentrations, presented **PtBC** > **pPtBC NPs** > **CDDP**. It is supposed that small molecules, such as **CDDP** and **PtBC,** typically enter cells through passive diffusion. However, cellular internalisation of **CDDP** may be dominated by active transport carriers present on the cell membrane, especially copper and organic cation transporters.[141,142] The carrier-mediated endocytosis requires energy consumption, unlike passive diffusion, which might explain, when combined with the increased lipophilicity of **PtBC,** the lower cellular uptake of **CDDP** compared to **PtBC.** On the contrary, NPs commonly rely on endocytosis pathways for internalisation as they are too big to benefit from passive diffusion, which is also energy dependent. Such behaviour could explain the lower internalisation of **pPtBC NPs** when compared to **PtBC**. However, many parameters govern NPs internalisation, such as size, shape, surface charge, functionalisation, and hydrophobicity, among the most important.[143,144]

After a 24-hour exposure, the cellular uptake of all these species remained relatively stable in HeLa cells, pointing towards rapid internalisation and reaching equilibrium already after 6 hours. Nonetheless, in the other two cell lines, intracellular concentrations continued to fluctuate even at 24-hour intervals. In 1Br3G, **CDDP** concentration remained comparable to that at 6 hours, while **PtBC** and **pPtBC NPs** concentration decreased considerably, though still significantly higher than **CDDP**. Interestingly, the trend in GL261 cells inverted. The cellular uptake of **CDDP** increased 8.5 times in comparison to the intracellular concentration at 6 hours, surpassing the levels of **PtBC** or **pPtBC NPs**.

Additionally, DNA-bound Pt studies were also carried out by incubation of **CDDP**, **PtBC**, and **pPtBC NPs** (100 µM) with HeLa, 1Br3G, and GL261 cells for 24 hours. Then, nuclear DNA was extracted, purified, and quantified using UV-vis absorbance. At the same time, the amount of Pt bound to the DNA was quantified using ICP-MS (Figure **3.38**).

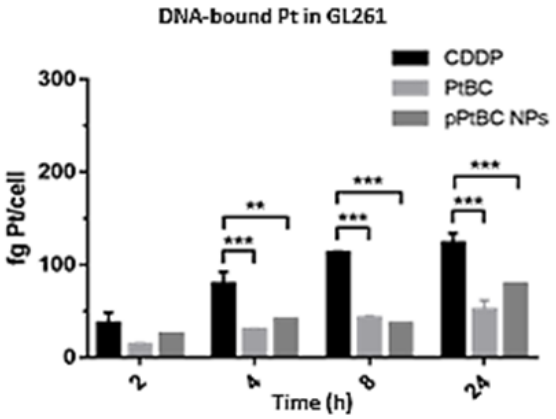


Figure **3.38.** DNA-bound Pt after exposure to **CDDP**, **PtBC**, and **pPtBC NPs** for 24 hours at a concentration of 100 μM referred to Pt. Each value represented as mean ± SE, n=3. * stands for $p < 0.05$, ** for $p < 0.001$, *** for $p < 0.0001$.

DNA-bound Pt concentration from **CDDP** was notably higher than that of **PtBC** and **pPtBC NPs**, indicating that **CDDP** entering cells can effectively access the nucleus to bind to DNA. **PtBC** and **pPtBC NPs** presenting the same binding rates could suggest that the main limitation to DNA binding comes from prodrug activation and molecular affinity, and not from supramolecular limitations as a result of drug cargo not being released. **CDDP**, a smaller molecule, already in a Pt(II) binding capable state, unsurprisingly displays the best affinity for DNA. **CDDP** presents as a small complex, capable of easily penetrating the nucleus and holding liable ligands for aquation and DNA binding. Therefore, while NP release is not a limiting factor to DNA interaction, intracellular reduction from Pt(IV) to bioavailable Pt(II) from **PtBC** appears to be, resulting in lower binding rates.

3.3.1.5.2. Cytotoxicity

After studying the Pt release and the DNA binding affinity from our **PtBC** and **pPtBC** we proceeded to trying to correlate these results with the cytotoxic studies. Thus, *in vitro* cytotoxicity of **PtBC** and **pPtBC NPs** was evaluated and compared against the clinical standard **CDDP**. For the study, HeLa, 1Br3G, GL261, the ovarian cancer A2780, and the **CDDP**-resistant counterpart A2780/cis cell lines were chosen.

Previous studies have shown that nanocarriers can bypass the drug efflux of resistant cells, leading to modulating or overcoming cancer cell resistance.[145,146] As such, inclusion of a **CDDP** resistant cell line as well as the non-resistant counterpart may help us evaluate the effect of resistance against our nanoformulation.

The study was conducted using the well-established PrestoBlue™ method, collecting data at both 24- and 72-hour intervals. The IC_{50} were calculated using GraphPad Prism (version 8.0) and can be found summarised in Table **3.1**. The results showed that at 24 hours, **PtBC** and **pPtBC NPs** offered comparable cytotoxicity for HeLa and 1Br3G, while in the case of GL261 and A2780, the IC_{50} value for **PtBC** is almost half of that found for **pPtBC NPs**. IC_{50} values were slightly higher than those found for **CDDP**, except for the A2780 cell line, where **PtBC** outperformed **CDDP**. After 72 hours of exposure, the cytotoxicity difference between **PtBC**, **pPtBC NPs** and **CDDP** diminished, approaching comparable IC_{50} values for HeLa (even smaller for **pPtBC NPs**), GL261, and A2780. In the case of 1Br3G and A2780/cis, both **PtBC** and **pPtBC NPs** also exhibit similar values but double those found for **CDDP**.

Table 3.1. IC_{50} of **CDDP**, **PtBC** and **pPtBC NPs** against a panel of cell lines.

		Cell lines				
	Compounds	**HeLa**	**1Br3G**	**GL261**	**A2780**	**A2780/cis**
24 h	**CDDP**	15.98 ± 1.04	45.07 ± 4.60	5.61 ± 0.28	13.95 ± 1.24	23.68 ± 1.74
	PtBC	29.94 ± 1.04	56.09 ± 1.18	17.40 ± 1.08	10.98 ± 0.56	18.39 ± 1.85
	pPtBC NPs	22.09 ± 1.09	56.30 ± 1.32	33.56 ± 1.36	18.44 ± 2.19	31.40 ± 2.28
72 h	**CDDP**	2.34 ± 0.30	4.63 ± 0.42	2.16 ± 0.26	1.57 ± 0.08	5.22 ± 1.21
	PtBC	1.85 ± 0.36	10.80 ± 0.60	4.17 ± 0.12	2.59 ± 0.33	9.12 ± 0.69
	pPtBC NPs	0.65 ± 0.14	8.01 ± 0.72	4.64 ± 0.05	3.10 ± 0.32	10.50 ± 0.84

If we consider that the polymeric NPs need a certain time to release the Pt and be reduced to the active Pt(II) in the intracellular environment, higher IC_{50} values would be expected at shorter times, while equilibrating over longer periods of time because of NP internalisation, Pt release and subsequent reduction. This tendency was expected to be observed, especially in comparison to **PtBC**. However, in this study, it was not. Nevertheless, Pt release studies help explain this behaviour. The fast Pt release achieved (Figure **3.37**) makes it so that at a 24-hour interval most of the cytotoxic cargo of **pPtBC NPs** has already been released. Therefore, Pt concentration in the media will be comparable to that of the **PtBC** cell samples, indicating the slow and sustained activation of the prodrug.

Overall, **PtBC** and **pPtBC NPs** still behave like **CDDP,** as expected from a Pt-based cytotoxic species, and showed less cytotoxicity towards 1Br3G and A2780/cis. Fluctuations within cytotoxicity among different cell lines for our NPs are expected, as pathways for NPs uptake and detoxification are greatly influenced by cell type.[146]

More importantly, despite **PtBC** and **pPtBC NPs** displaying lower Pt-DNA binding affinity (Figure **3.38**), they still exhibited comparable anticancer activities over 24-hour periods when compared to the higher DNA-binding affinity **CDDP**. These results suggest that their cytotoxicity is not limited only to Pt-DNA adduct formation. An increasing number of reports have demonstrated that Pt agents can also bind to other cellular macromolecules, such as RNA and proteins, and may even be capable of inducing immunogenic effects.[147,148] With some reports even displaying Pt complexes with high cytotoxicity, like CDDP, yet displaying no DNA binding at all in ovarian cancer.[149]

The *in vitro* cytotoxicity of **NDGA** and **pNDGA NPs** was also tested for comparison purposes against the same panel of cancer cells (Table **3.2**). As can be seen, **NDGA** showed very low cytotoxicity in all cell lines except for A2780 or A2780/cis. Surprisingly, in these cases, IC_{50} values were comparable and even smaller than **CDDP**. Worth mentioning, **pNDGA NPs** were non-toxic in any given concentration range with a cell viability close to 100% in all cell lines, either for 24 or 72 hours.

Table 3.2. IC_{50} of **NDGA** and **pNDGA NPs** against a panel of cell lines, NT standing as non-toxic.

		Cell lines				
	Compounds	**HeLa**	**1Br3G**	**GL261**	**A2780**	**A2780/cis**
24 h	**NDGA**	164.15 ± 0.02	NT	109.45 ± 1.95	8.94 ± 0.69	15.67 ± 2.14
	pNDGA NPs	NT	NT	NT	NT	NT
72 h	**NDGA**	55.65 ± 6.21	14.20	81.73 ± 2.40	7.82 ± 0.39	12.96 ± 1.48
	pNDGA NPs	NT	NT	NT	NT	NT

NDGA cytotoxicity cannot be attributed to any neoplastic effect, as **NDGA** has no Pt to act as an alkylating-like drug. Specific mechanisms of the pro-apoptotic **NDGA** properties are still partially unknown. However, recent breakthroughs point to **NDGA** promoting mitochondrial stress by inducing oxygen consumption alterations that lead to ROS production.[150]

3.3.1.5.3. Determination of Reactive Oxygen Species Production

As we have explained in the introduction, during the oxidation process of catechol moieties, reactive oxygen species can be generated. This process can potentially result in excessive oxidative stress that could harm cells. Such phenomena lead to toxicity and inflammation that cause cellular damage. Additionally, ROS can cause premature ageing, chronic inflammatory conditions and even neoplastic transformations.[151] Thereafter, the contribution of ROS to the cytotoxicity of **pPtBC NP** and **PtBC** was evaluated.

Using fluorescent probe for ROS detection 2',7'-dichlorofluorescin diacetate (DCFCDA) in HeLa, 1Br3G and GL261, cells were exposed to different oxidising agents including **NDGA**, **pNDGA NPs**, **PtBC** and **pPtBC NPs**. H_2O_2 was used as a reference to compare the ROS production with the different species (Figure **3.39**). After 24 hours of exposure, strong DCFCDA fluorescence was only observed in all the cell cultures treated with **NDGA** and the H_2O_2 positive control. Interestingly, neither **PtBC** nor the polymeric **pPtBC**/**pNDGA NPs** triggered the formation of ROS in any of the tested cell lines in a statistically significant manner (Figure **3.48**), excluding as a result any contribution from ROS generation to the cytotoxicity of **PtBC** and **pPtBC NP**. Additionally, as observed, **CDDP** itself did not induce ROS generation.

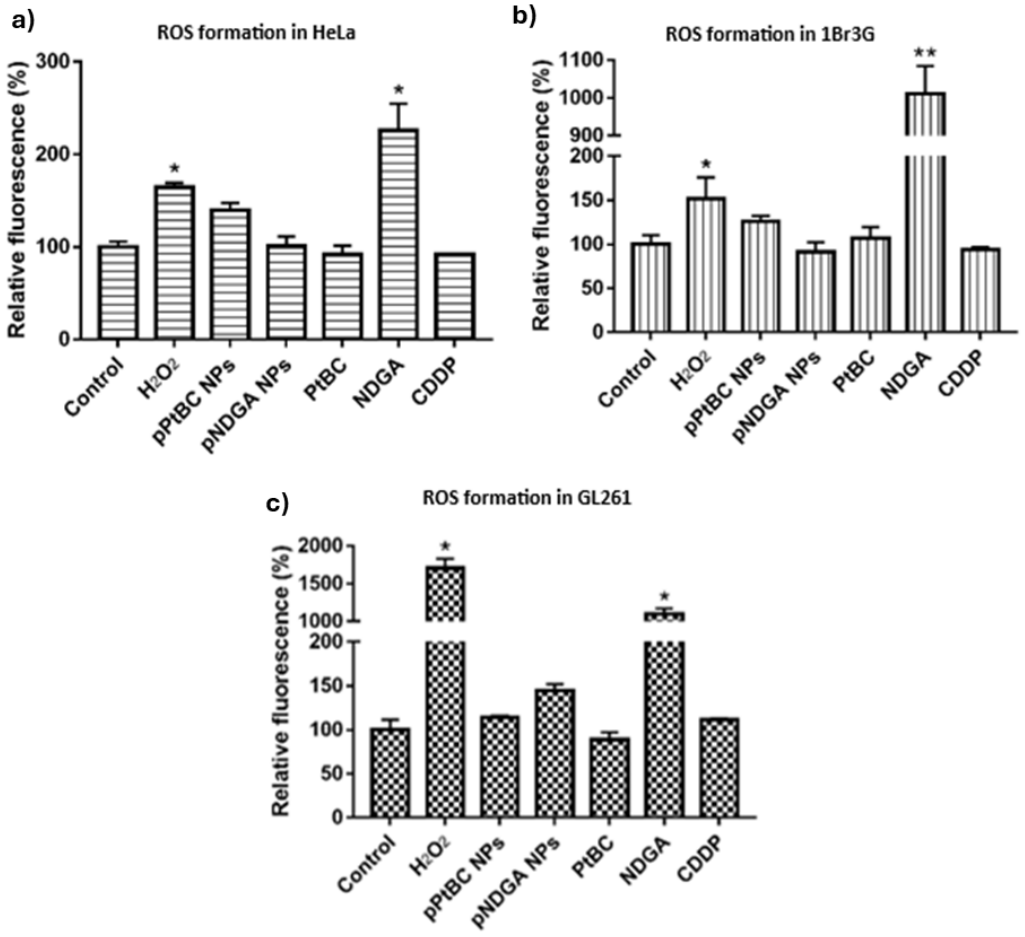


Figure **3.39**. ROS generation triggered by different compounds and **pPtBC NPs** in **a)** HeLa, **b)** 1Br3G and **c)** GL261 cell lines. The concentration of H_2O_2 was 0.1 mM, **pNDGA NPs** at 0.2 mM, other agents at their corresponding IC_{50}s**.** Each value represented as mean ± SE, n=3. * stands for $p < 0.05$, ** for $p < 0.001$, *** for $p < 0.0001$.

3.3.1.6. *In vivo* Studies

As briefly mentioned in the characterisation of **pPtBC NPs**, IN administration has been proposed due to the laxer limitations this path presents in intra-brain delivery. This administration route could be an effective mode to administer drugs and prodrugs to reach the brain through olfactory nerves placed in the nasal cavity. Furthermore, the precedent for this work from Dr. Xiaoman Mao, also did IN administration of the **PtBC**-Fe coordinate. Thereafter, the same administration was followed, as it provides a framework for better delivery, while allowing for comparative and close correlation to previous works.

Currently, there is a lack of studies and reports that detail the biodistribution of Pt nanostructured agents through this pathway. While some studies demonstrate that nanocarriers can enhance drug transport from the nasal cavity to the brain via olfactory and trigeminal pathways, challenges remain in optimising particle size, surface chemistry, and biocompatibility to ensure efficient delivery and safety.[152-154] However, there is a gap in detailed data on the biodistribution, long-term toxicity, mechanism of brain entry, and the therapeutic efficacy of Pt nanomaterials via IN administration.

Nonetheless, the promising prospects of such administration could hold significant value for future treatment. Reports have displayed increased Pt absorption to the brain via IN administration when compared to i.v. administration.[155]

3.3.1.6.1. Safety and Tolerability

Safety and tolerability of **PtBC** and **pPtBC NPs** were assessed in a dose-escalation experiment using wild-type C57BL/6J mice. Increasing doses (0.9, 1.2, and 1.5 mg Pt·kg^{-1}) were administered over three consecutive weeks.[156] Body weight, water/food consumption, and mouse behaviour were evaluated three times a week over 4 weeks, overlaying with the normal body weight progression of C57BL/6J mice (control). No evident systemic toxicity was found as all treatment groups' body weight remained stable until the end of the study (Figure **3.40.a**). Moreover, no adverse effects related to the treatment, such as weight loss, food consumption, mortality or any other clinical signs, were observed for all mice during the study relative to the control group.

3.3.1.6.2. Biodistribution

The accumulation in tumours assay was carried out using GL261 GBM orthotopic tumour-bearing C57BL/6J mice with an average size of 24.96 ± 2.7 mm^3 and body weight of 22.7 ± 0.2 g, using the highest dose from the tolerability assessment, at 1.5 mg Pt·kg^{-1} of mice (Figure **3.40.b**).

After IN administration, Pt was predominantly found to accumulate preferably in GBM tumour, kidneys, lungs, and brain in that order. The spleen, liver and heart showed minimal accumulation. As such, Pt retention in the tumour reached the highest level at 3.51 ± 0.36% initial dose·g^{-1}, whereas the brain lungs and kidney it measured 2.53 ± 0.98%, 2.6 ± 0.69, and 3.0 ± 0.43% initial dose·g^{-1}, respectively. Nonetheless, no statistically significant differences were observed in Pt retention between the tumour and the other organs. However, considering the tumour and brain collectively, Pt accumulation in the CNS was remarkably higher than in other organs.

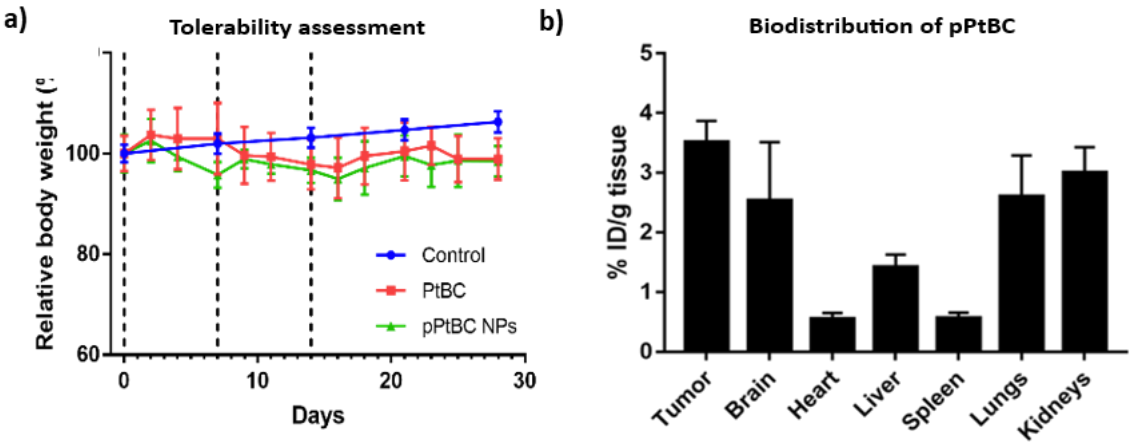


Figure **3.40**. **a)** Mice tolerability assessment of mice for **PtBC** and **pPtBC NPs** over 4 weeks. Both drugs were administered in incremental doses of 0.9, 1.2 to 1.5 mg Pt·kg^{-1} body weight via IN weekly, n=3. The control group, comprising n=360, had data sourced from Jackson Laboratory (https://www.jax.org/jax-mice-and-services/strain-data-sheet-pages/body-weight-chart-000664). **b)** Biodistribution of **pPtBC NPs** in mice GL261 tumour-bearing 1 hour after administration. Mice were IN administered with **pPtBC NPs** at a dose of 1.5 mg Pt·kg^{-1} and sacrificed 1 hour post administration. Dash lines stand for administration days. Each value represented as mean ± SE, n=3.

3.3.1.6.3. Anticancer Efficacy

The *in vivo* efficacy of **pPtBC NPs** was tested in GL261 GBM tumour-bearing C57BL/6J mice. Preclinical models for GBM treatment have displayed immunotherapy as a viable approach to boost the anticancer efficiency of therapeutic drugs.[157] Studies have proven that TMZ administered using the "Immune-Enhancing Metronomic Schedule (IMS)" produced significantly better survival rate than non-IMS protocols.[158] As such, it was found that a 6-day administration schedule that matches the mice's immune cycle length produced better results in comparison to previously described schedules.[158]

As Pt agents have been readily reported to trigger immunogenic effects,[159,160] therapy of **pPtBC NPs** was given the IMS schedule starting on day 6 post-implantation (p.i.) with a 6-day interval.

In this *in vivo* study, a total of 6 mice were randomly divided into two groups: control and **PtBC NPs** administered. Mice from the **PtBC NPs** group were intranasally administered 1.5 mg Pt·kg^{-1} body weight, in accordance with the highest doses in the tolerability assessment. The mice from the control group were untreated. Treatment of mice started on day 6 p.i. with a tumour volume of 1.84 ± 1.08 mm^3 without significant differences in tumour volumes between both groups. Usage of **PtBC NPs** as a therapeutic drug proved to be inefficient in comparison with the control group, with no significant tumour shrinkage in comparison to control group (Figure **3.41**).

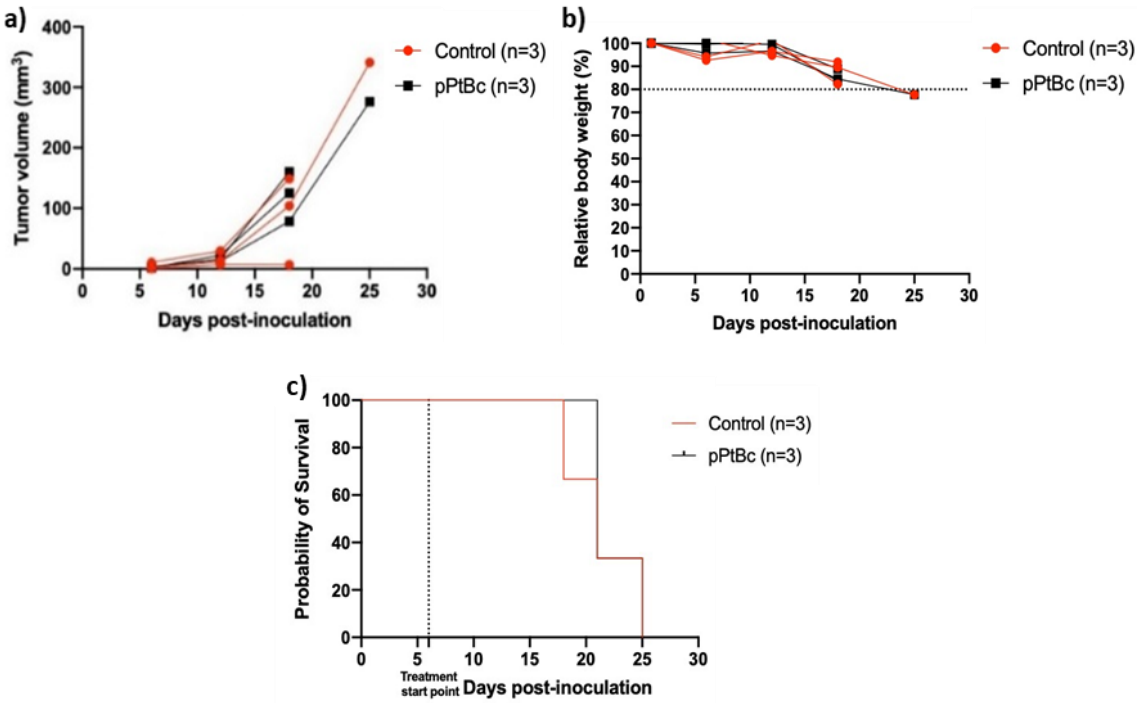


Figure **3.41**. **a)** Tumour volume evolution of mice from the untreated control and treated with **PtBC NPs** (1.5 mg Pt·kg^{-1}). **b)** Evolution of body weights of mice in IMS schedule from control and **PtBC NPs** (1.5 mg Pt·kg^{-1}). Horizontal dash line indicates the euthanize point corresponding to the 20% body weight reduction considered for the welfare of the treated mice. **c)** Kaplan-Meier survival curves of control and **PtBC NPs** Each value represented as mean ± SE, n=3.

Median Survival of control and **PtBC NPs**-treated groups were 21 days for both, further proving the previous point. The body weights of both groups were tracked during the therapy and recorded twice a week. Displaying body weight of both groups followed the same tendency and dropped under 80% at the same rate. Due to welfare and ethical considerations, all animals who present a body weight reduction of more than 20% had to be euthanised.

In vivo results suggest that our NPs are ineffective in the treatment of GBM when IN administered. Control and treated mice showed the same behaviour on all parameters analysed concluding in the same median survival of 21 days.

Moreover, many questions arise about the final composition of the NPs that reach the tumour. We have no answers as to what the fate of the carriers are, when are they degraded, in what state do they reach the tumour, or even if the NPs are capable to cross the nasal cavity at all. Only data we have are the biodistribution results that display the bioaccumulation of Pt.

Current *in vitro* models, that attempt to study nasal absorption and drug transport, give information on the transport across the cells or paracellularly at the olfactory bulb, but concurrent factors such as mucus, mucins, clearance, anatomical and physiological factors involved in keeping the nose functional are not taken in consideration. Even more, the cellular models contain receiving lumen that does not fully reflect the required transport from the mucosa to the receiving nerves.[161] Our research group has attempted in the past modelling of *in vitro* IN administration to test its uses but encountered the same limitations as mentioned, giving rise to uncertain results. Precisely because of this, an important leap, research-wise, between *in vitro* and *in vivo* results arises in the research community, making results in IN administration unpredictable.

In summary, **pPtBC NPs** have proven great *in vitro* cytotoxicity, comparable to that of standard **CDDP**. However, they may lack potency to achieve significant *in vivo* therapeutic effectivity and more studies are necessary to increase the knowledge on the fate of this type of NPs after IN administration.

3.3.2. Supramolecular Photoactivatable Squaraine Pt(II) Nanoparticles

3.3.2.1. Synthesis of SQL

The synthesis of **SQL** is based on modifications of well-established protocols at Prof. Joan Pau Bayon's research group and was carried out in his lab under his supervision (Figure **3.42**). Since then, part of this synthesis, until intermediate **9**, has been published by his group, and further details can be found in their publication.[49]

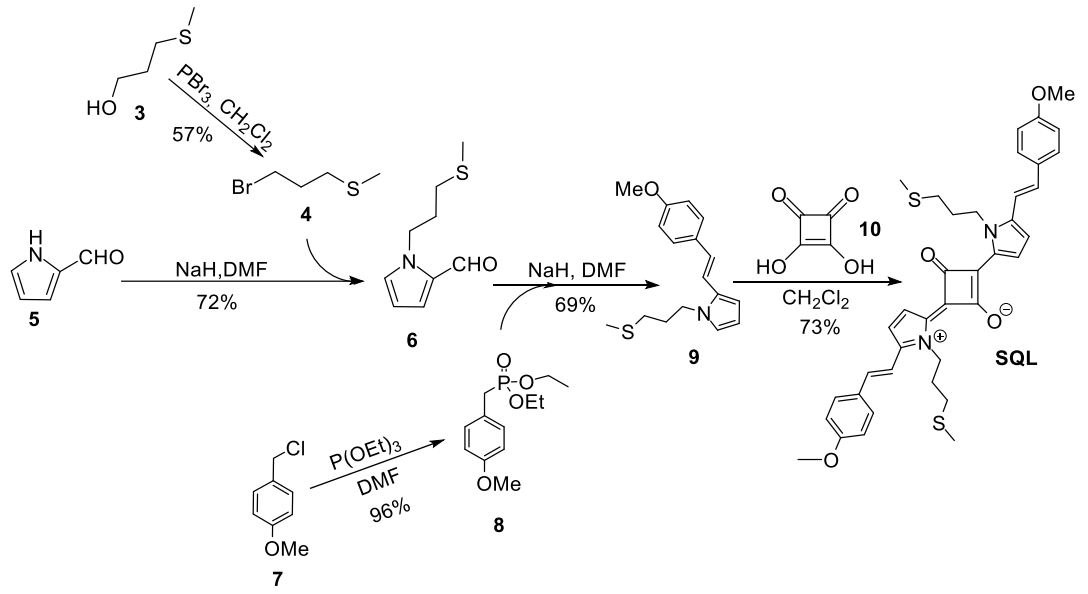


Figure **3.42**. Synthetic route taken to yield **SQL** from commercially available starting material.

A convergent synthesis was planned for **SQL** using as starting material **3**, **5** and **7,** which are commercially available. The first step of the synthesis consists of the preparation of pyrrole **6**. This step involves a nucleophilic substitution on the brominated primary carbon from **4**. Sodium hydride will be used as a base to deprotonate the most acidic proton in our starting material pyrrole **5**, allowing it to act as a nucleophile, and achieving a 72% yield. Bromine **4** used in this step has been prepared via alcohol bromination of thioalcohol **3** using PBr_3 as a brominating agent, with a yield of 57%. Phosphonate **8** was prepared by phosphonation of benzyl chloride **7** using triethyl phosphite, yielding a 96% conversion. Following this, a Horner-Wadsworth-Emmons reaction was performed between the previous phosphonate **8** and pyrrole **6**. In this reaction, sodium hydride was used to obtain the stabilised phosphonate carbanions from **8**. The product of this reaction, pyrrole **9**, was obtained with a 50% yield.

The last, and previously not reported, step was carried out as a one-pot synthesis using sodium hydride as a base to generate a suitable nucleophile from pyrrole **9**. As such, a Michael-like addition between deprotonated pyrrole **9** and squaric acid **10** will then follow, yielding the final **SQL** (Figure **3.43**). This synthesis was carried out in ethanol under heating and non-anhydrous conditions, yielding the 1,3-SQ isomer condensation product stereoselectively. Initial chromatographic purifications of the product were substituted by crystallisation in CH_2Cl_2/hexane to obtain a pure product with a 73% yield.

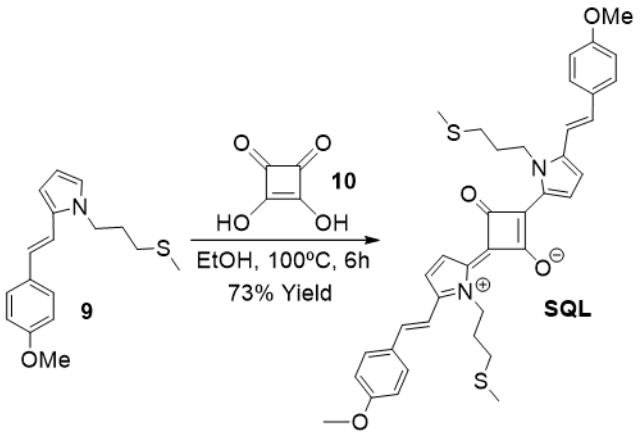


Figure **3.43**. Synthesis of **SQL** from **9**.

Formation of **SQL** was corroborated by ^{1}H-NMR spectroscopy, showing a clear shift in intensity to those signals most affected by the change in electron density in the conjugation system (Figure **3.44**). The alpha protons from the N-pyrrole position suffer the biggest shift to a higher field, from 4.11 to 4.93 ppm. This is a result of suddenly being exposed to very electron-withdrawing nitrogen that lost its non-conjugating electron pair. The same happens with the protons conjugated in the beta position from the pyrrole ring, from 6.87 and 6.68 to 7.83 and 6.93 ppm. Overall, but to a lower degree, such shift can be observed in most of the signals directly conjugated in this delocalised ring as a direct consequence of the exposure to the electron-poor SQ core.

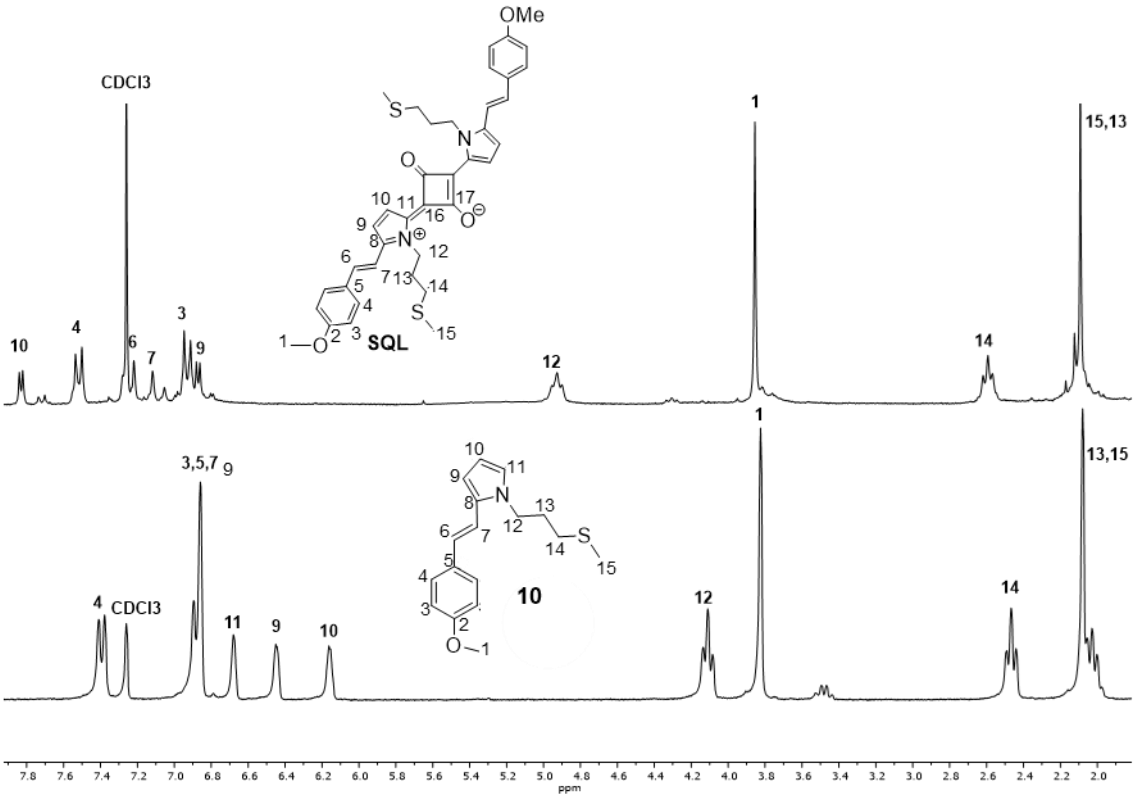


Figure **3.44**. ^{1}H-NMR data comparison between **SQL** and **10**.

Apart from ^{1}H-NMR spectral data, HRMS proved the obtention of **SQL** (Annexe **3.26**). This shows a M+Na^{+} of 653.2486 amu with a calculated value of 653.2502 amu, and a M+H^{+} 675.2321 amu with a calculated value of 675.2322 amu.

The stereoselectivity of the 1,3-SQ vs the 1,2-SQ can be understood by checking the reaction mechanism. Usually, most of the products described for this type of reactions correspond to the 1,3-regioisomer. However, depending on the reaction conditions, the formation of the 1,2-isomer can be driven.[162] For this purpose, the reaction conditions chosen were specifically targeting the use of nucleophilic and protonated solvents, as this allowed specific targeting of the 1,3-regioisomer. The reaction mechanism governing regioselectivity can be seen in Figure **3.45**, using squaric acid (**10**) as a case example.

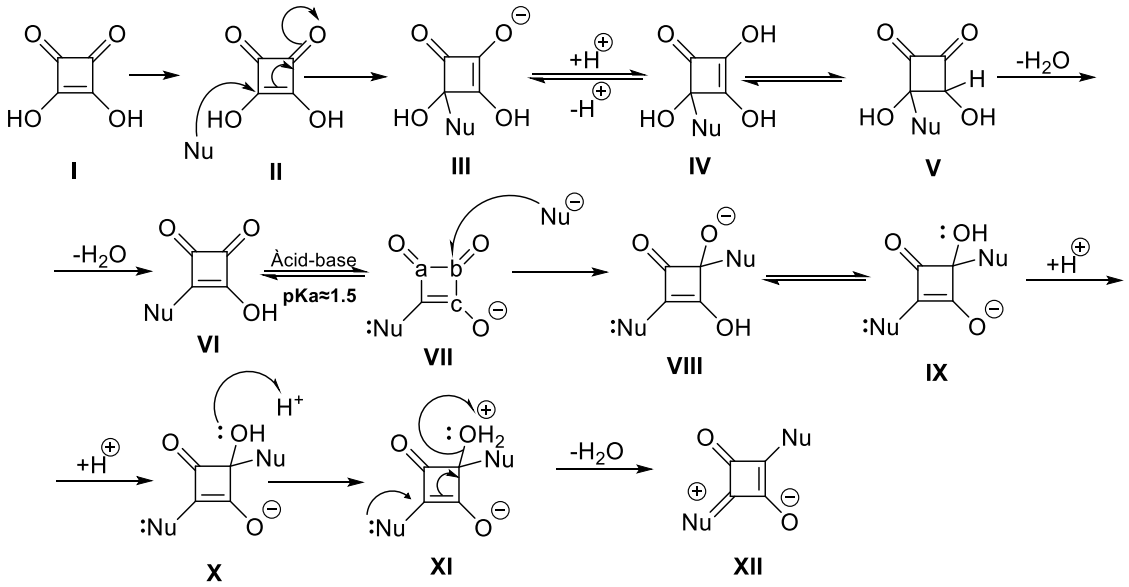


Figure **3.45**. Mechanistic pathway for the formation of 1,3-SQ from squaric acid (**10**) as the starting material.

The reaction mechanism of our system can be explained by a conjugated addition to the double bond of the squaric acid **I**-**II**. This step follows a similar profile to a Michael addition-elimination mechanism. The first step consists of the addition of a nucleophile (**Nu**) to the double bond of the squaric acid. The newly formed product **III** is then susceptible to undergo protonation (**IV**). This leads to an electronic reorganisation, resulting in a keto-enol tautomery (**IV**-**V**). A water elimination step follows and yields a hemisquaric acid capable of taking another nucleophile (**VI**). However, this type of hemisquaraines present very acidic pKa's around 1.5 that lead to deprotonation with ease. As a result, the fast proton exchange happens first (**VII**). This reaction causes a shift in electronic density that leads to an electron enrichment on conjugated positions **a** and **c**, thus making position **b** the most susceptible for the next nucleophilic attack. This attack leads to the formation of **VIII.** This intermediate undergoes proton exchange, yielding **IX**, which, after protonation, leads to **X**. Subsequent protonation (**XI**) and electron reorganisation yield water elimination, obtaining the final product **XII**.

3.3.2.2. Synthesis of SQC

The **SQC** was obtained via coprecipitation of the formed product. A dimethylformamide (DMF) solution, tetrachlorplatinate (II) and a solution of toluene containing **SQL** were mixed and maintained 72 hours under vigorous stirring. The resulting product was presented as insoluble in a DMF-toluene mixture and precipitated as a metallic green solid that, after successive water, ethanol, tetrahydrofuran (THF) and hexane washings, was isolated in a 30% yield (Figure **3.46**).

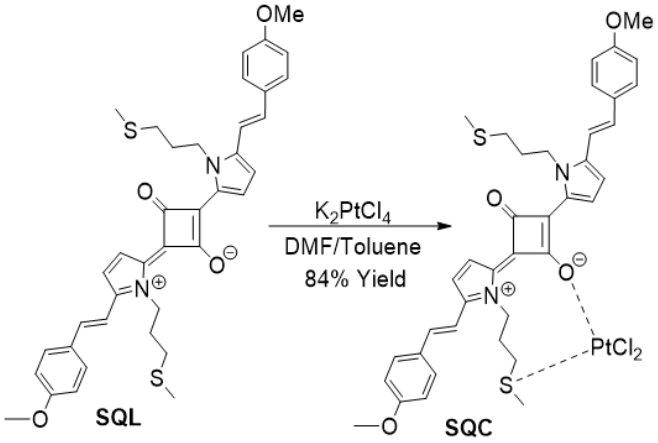


Figure **3.46**. Synthesis of **SQC** from **SQL** via coprecipitation reaction.

Taking into account the plausible modes of coordination, the 1,3-SQ stereoisomer gives rise to the possibility of a double incorporation of Pt(II) into the structure by coordination with the two juxtaposed and exposed carbonyl groups. Energy dispersive X-ray spectroscopy (EDX) and HRMS have been used to determine the mode of coordination. Thus, EDX shows a 1:1 sulphur to Pt relationship that matches with a one-to-one Pt incorporation (Annexe **3.48**). Additionally, the HRMS shows an $[M+Na^+]$ of 941.1352 amu with a calculated value of 940.1347 amu for a single Pt(II) incorporation, compatible with a $C_{38}H_{40}Cl_2N_2NaO_4PtS_2$ formula matching the expected molecular weight (Annexe **3.31**).

3.3.2.3. Synthesis and Characterisation of Supramolecular SQL NPs

In a typical experiment, **SQL** was dissolved in THF and rapidly added to a flask containing ultrapure type 1 water (MilliQ®) under vigorous stirring at 1500 rpm. The solution is maintained under stirring for 10 minutes, and the product was washed with copious amounts of MilliQ® water and isolated by centrifugation (Figure **3.47**).

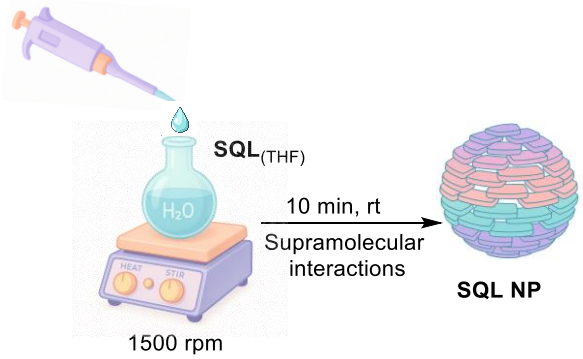


Figure **3.47**. Schematic representation of the procedure followed for the **n**anoparticulation of **SQL NPs** based on supramolecular interactions.

A clear colour change from green (THF) to blue (water) in the solution indicates a variation in the photophysical properties related to the aggregation process (Figure **3.48**).

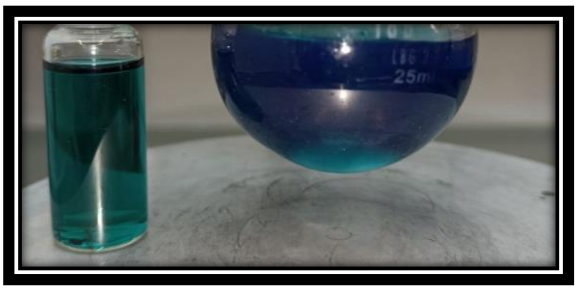


Figure **3.48**. Representative colour shift from **SQL** (green, left) to **SQL NP** (blue, right).

The first characterisation technique used to determine the presence of **SQL NPs** was DLS and nanoparticle tracking analysis (NTA). The measurements performed directly by DLS on the water dispersion revealed the presence of nanosized particles with hydrodynamic sizes of 170.3 ± 7.0 nm and a very low PDI of 0.056 ± 0.005 (Figure **3.49.a**). NTA analysis gave a mean size of 81.2 ± 0.8 nm, also with a very low PDI of 0.074 ± 0.002 (Annexe **3.35**). This discrepancy in values between DLS and NTA can be attributed to DLS measuring the change in time of light scattering intensity, and is biased towards larger particles (sensitive to aggregates). However, NTA tracks individual particle positional changes via Brownian motion, providing a number-weighted distribution underestimating the true size of certain particles.

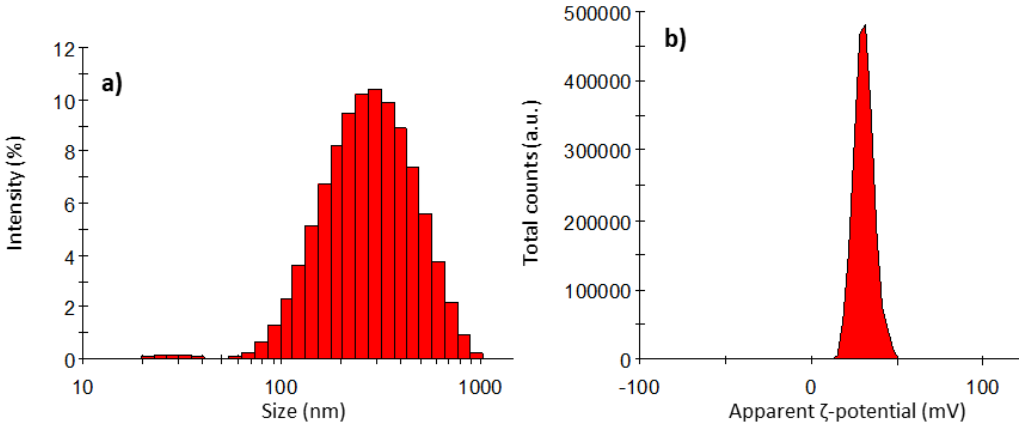


Figure **3.49**. **a)** Representative size distribution, and **b)** Representative ζ-potential of **SQL NPs** by DLS.

Just as we explained previously, size can considerably influence the in vivo biodistribution of NPs, with suitable particle sizes between 30-200 nm to maximise the EPR effect in tumours[114-117] and cross physiological barriers,[118], while particles larger than 200 nm are captured within the spleen. In this context, our results indicate optimal values with low PDI for the synthesised **SQL NPs**, leading to lower aggregation and homogeneous biodistribution.[120]

Surface charge of **SQL NPs** showed a ζ-potential of -21.4 ± 0.38 mV (Figure **3.49.b**). With this value, **SQL NPs** hold a relatively good colloidal dispersion. ζ-potential values above ± 20 mV are generally considered stable, and values above ± 40 mV indicate good to excellent stability. Higher absolute value signifies a stronger repulsive force between particles, which prevents aggregation and sedimentation. Moreover, ζ-potential can impact the targeting and cellular uptake of NPs, and *in vivo* circulation, adhesion, biodistribution, toxicity and clearance.[122]

The NPs' morphology was analysed by SEM imaging (Figure **3.50**). The **SQL NPs** present very spherical shapes and morphology across all samples studied. The calculated mean size gives a value of 154.6 ± 54.6 nm, in agreement with the results from DLS.

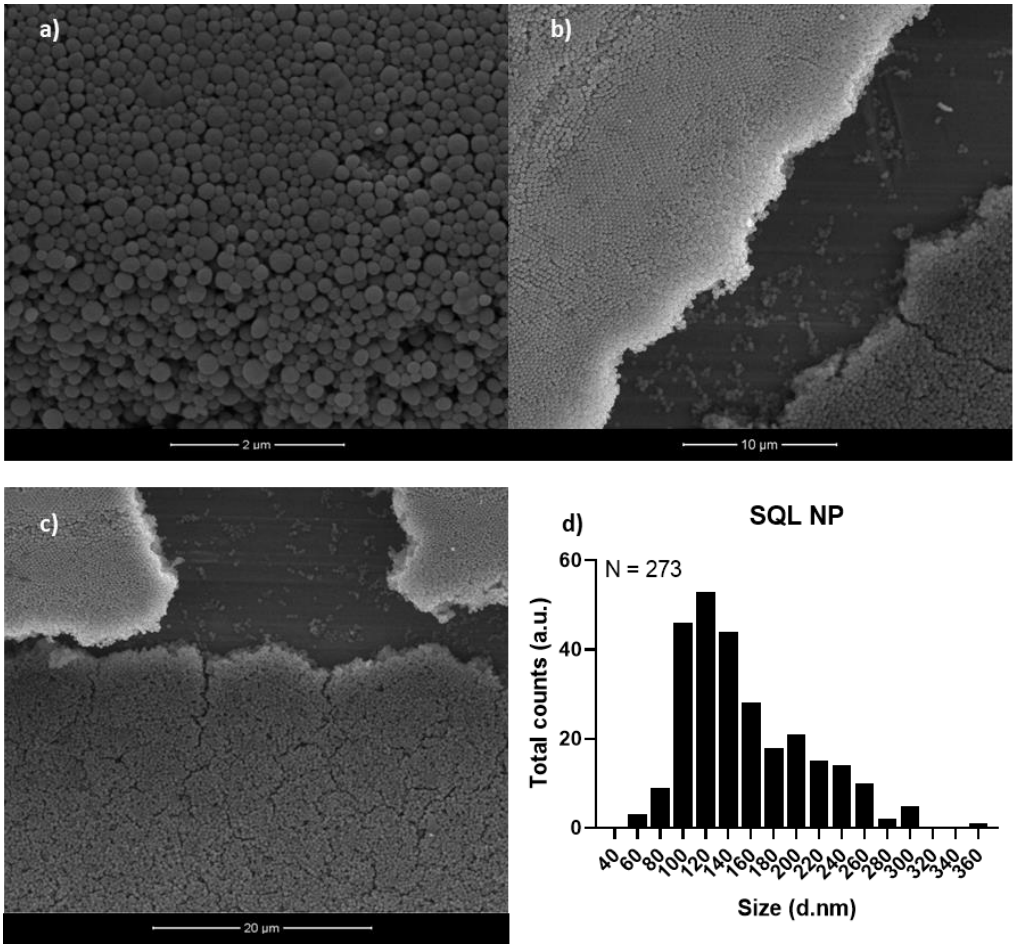


Figure **3.50**. **a-c)** Representative SEM image of **SQL NP** under a 5 nm Pt thin film coating for imaging. **d) SQL NP** size distribution by SEM image size counting.

3.3.2.4. Synthesis and Characterisation of Supramolecular SQC NPs

The synthesis of **SQC NPs** followed a similar procedure to that used for **SQL NPs**. For this, **SQC** was dissolved in DMSO and rapidly added to a flask containing MilliQ® water under vigorous stirring. The reaction was kept under stirring for 10 minutes, and finally the product was washed with water and isolated by centrifugation (Figure **3.51**).

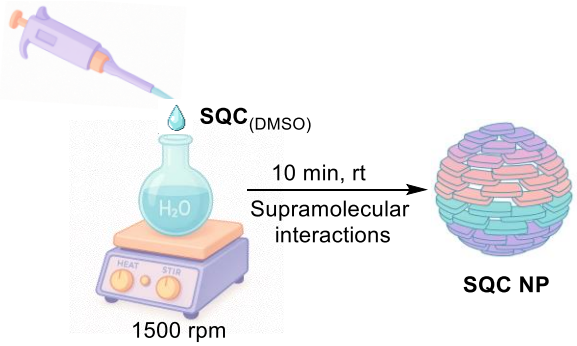


Figure **3.51.** Schematic representation of the procedure followed for the nanoparticulation of **SQC** based on exploiting supramolecular interactions.

The hydrodynamic size of **SQC NP** measured by DLS (Figure **3.52.a**) and NTA (Annexe **3.51**) showed particle showed sizes of 256.4 ± 1.95 nm with a considerably big PDI of 0.265 ± 0.027, and 155.5 ± 0.8 nm with also a relatively big PDI of 0.102 ± 0.004, respectively. Although a discrepancy between NTA and DLS is observed again, just as happened before in **SQL NPs**, this time a large PDI is also observed. Thereafter, indicating a very wide dispersity of the NP population. Surface charge potential of **SQC NP** presents a positive ζ-potential of 30.6 ± 0.351 mV (Figure **3.52.b**). This remarkable change in surface ζ-potential from negative (**SQL NPs**) to positive (**SQC NPs**) can be envisioned as a result of the Pt(II) atom locking on the most electron-rich functional groups of the SQ. The Lewis acid capabilities of Pt(II) lead to locking of the most electron-rich functional groups, preventing them from freely interacting with the NPs surface while providing the positive cationic charge on the system.

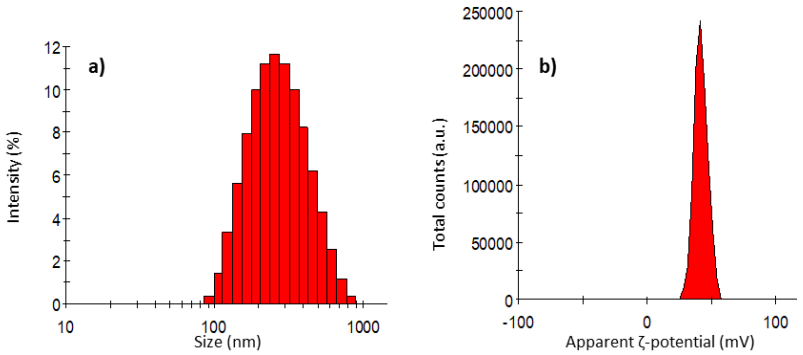


Figure **3.52**. **a)** Representative size distribution analysis, and **b)** Representative ζ-potential of **SQC NPs** by DLS.

The significance of the high PDI can be spotted in SEM images (Figure **3.53**), where **SQC NPs** have shown roughly spherical morphology, with sizes of 48.5 ± 12.3 nm.

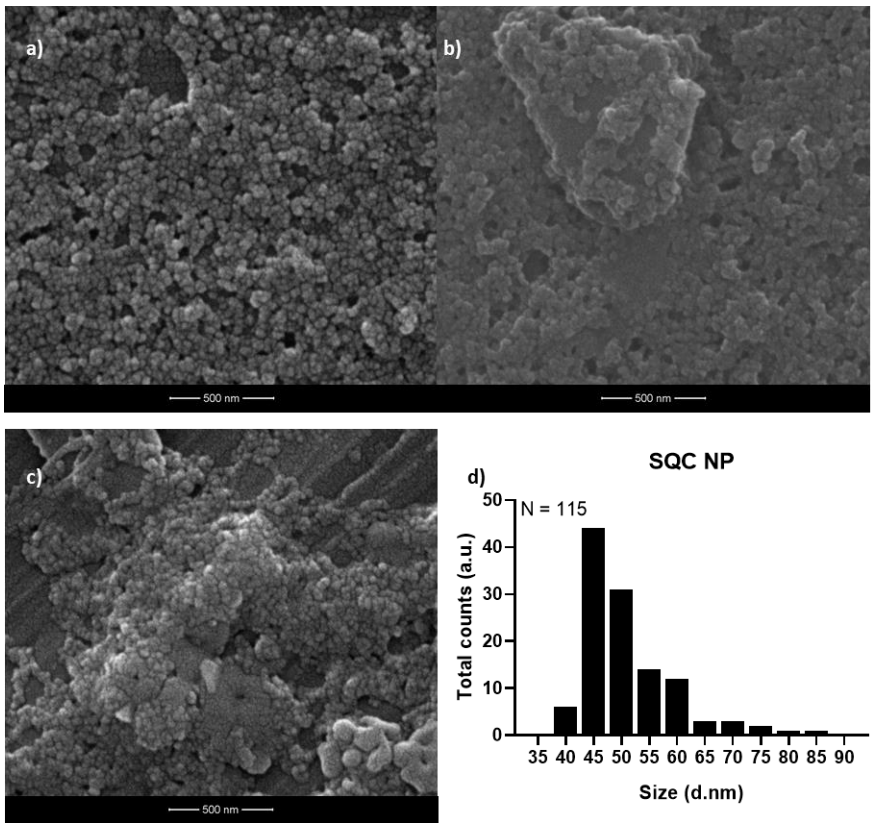


Figure **3.53**. **a-c)** Representative SEM image of **SQC NP** under a 5 nm Pt thin film coating for imaging. **d) SCQ NP** size distribution by SEM image size counting.

The incorporation of a metal atom in the structure of **SQC** undermines the very planar and aromatic structure of the original **SQL**. The metal also electronically impoverishes the system and thus hinders the π-π stacking capabilities of these compounds. Overall, we are diminishing the planarity and electron density of these systems for proper stacking interactions, hindering these interactions. Therefore, less homogeneity is achieved overall in the NP formation, so larger PDI's are obtained. Thereof, a dissonance between the estimated DLS sizes and SEM imaging is spotted.

Additionally, the Pt content of the resulting NPs was determined by ICP-OES. Pt loading was observed to be lower than the expected theoretical value, from 21.2% to 8.6% (w/w). One possible explanation for this Pt decreased content could be related to the discoordination of Pt from the ligand induced by water during the assembly. Water, present during the nanoparticulation reaction, may displace the SQ from the Pt coordination sphere through aquation reactions.[163]

3.3.2.5. SQL and SQL NP: An Optical Study Comparison

3.3.2.5.1. Absorption

As commented in the introduction, the absorption spectra of SQ aggregates are highly dependent on the type of aggregation that occurs (Figure **3.54**). The formed aggregates can be either parallel-oriented (H-aggregates) or in a head-to-tail arrangement (J-aggregates).[86-88] A blueshifted absorption band characterises the former, while the latter shows a redshifted absorption band.

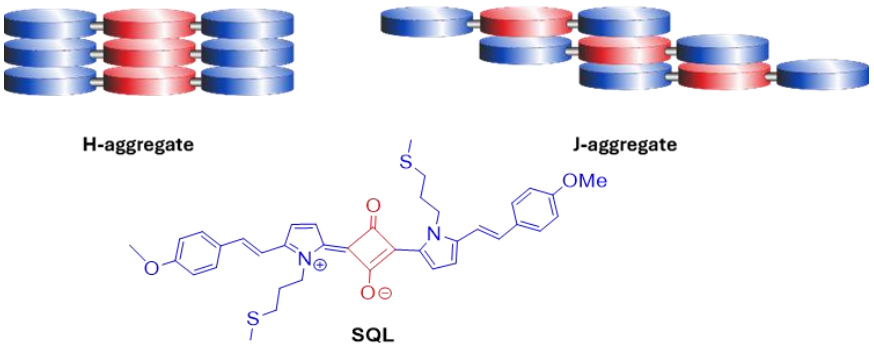


Figure **3.54**. Simplified representation of H- and J-aggregations for **SQL**.

H-aggregates are characterised by the head-to-head packing of the transition dipoles, which results in the blue-shifted absorption and poor luminescence properties. On the contrary, J-aggregates are related to the head-to-tail transition dipole arrangement, and the principal characteristic is that they exhibit a sharp and intense, red-shifted absorption band and normally increasing fluorescent properties.[164] SQs can form both types of aggregates depending on their structure and the environmental conditions.[83] However, the numerous possible organisation patterns in reported cases make the precise control of properties of the synthesised material difficult. Therefore, it is important to understand the relationship between optical properties and molecular dye aggregation to optimise their performance for different applications, including medical applications.

As observed in Figure **3.55**, the UV-vis absorption spectrum of **SQL** shows a clear and sharp absorption band centred at 699 nm and a second one of lower intensity as hypsochromic vibronic shoulder band at 649 nm. These spectra are usual for SQs with very strong molar absorptivity.[64] **SQL** shows maximum of absorptions at λ_{max}, (nm) presenting molar extinction coefficient (ε, $M^{-1}{\cdot}cm^{-1}$): 649 ($5.5{\times}10^4$) and 699 ($1.2{\times}10^5$). On the other hand, the absorption spectrum of the **SQL NP** broadens, and the molar absorptivity decreases by about an order of magnitude with λ_{max}, nm presenting ε ($M^{-1}{\cdot}cm^{-1}$): 659 ($2.9{\times}10^4$), 724 ($2.4{\times}10^4$). At the same time, the absorption also displays a slight bathochromic shift. The shift in the absorption spectrum can be directly linked to the aggregation type of our SQs. In this case, a broadening in both directions is indicative that both J and H aggregation are occurring.

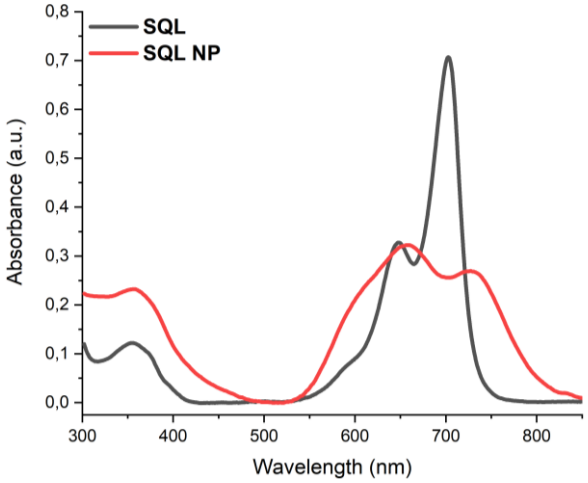


Figure **3.55**. UV-vis spectrum of **SQL** in THF (black) and **SQL NP** in water (red).

Since the aggregation is based on supramolecular assembly, these interactions must be reversible. In fact, when **SQL NPs** present stronger solvent-based interactions than supramolecular interactions between monomers, NP monomers get solvated and experience disaggregation. **SQL NPs** show an absorption spectrum in water clearly differentiated from that of the original SQ free molecule **SQL**. To evaluate the reversibility of the supramolecular assembly, **SQL NPs** were suspended in a solvent capable of performing solvation interactions stronger than the stacking ones from the NPs (i.e., THF). Thereafter, the absorption spectrum of the original **SQL** must be recovered, as observed in Figure **3.56**.

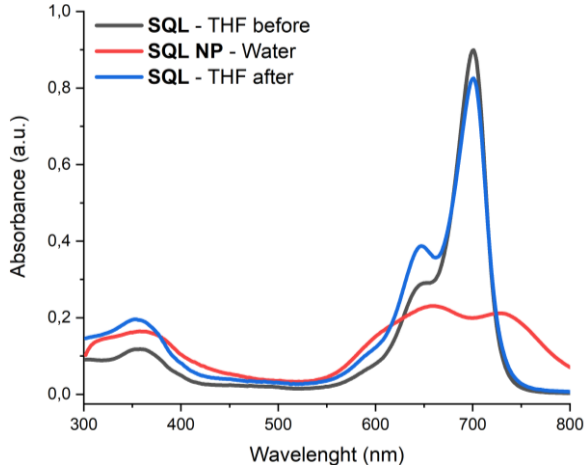


Figure **3.56**. UV-vis spectrum of **SQL** behaviour in THF and water.

Therefore, we can confirm that our platform is based on reversible supramolecular interactions. Aggregation-based solvent dependency was also studied, adding increased amounts of water to a THF solution containing **SQL** monomeric form. In Figure **3.57,** the evolution of UV-vis spectra can be observed when the % of water is increased, where the formation of H- and J-aggregates is perfectly visible depending on the water content.

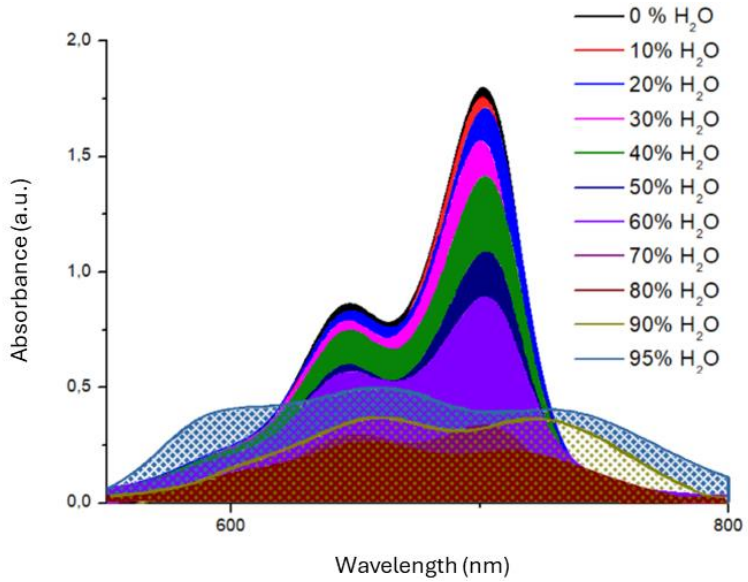


Figure **3.57**. UV-vis spectrum of **SQL** in THF and incremental presence of water.

Broadening of the **SQL** monomer as a result of aggregation formation of **SQL NP** can be observed at low water percentages. At high water concentration (70-80%), the absorption starts to widen its base, red-shifting (formation of J-aggregates) and blue-shifting (formation of H-aggregates).

Formation of H- and J-aggregates is dominated by activation and stabilisation energies that favour or disfavour kinetic or thermodynamic products. To understand whether we have one product or the other, we can help our system reach equilibrium and favour the formation of the most thermodynamically stable compound with assisted external heating. Thus, when an aqueous solution containing **SQL NPs** was heated at 70 °C for up to 24 hours, it was observed that the initial, red-shifted aggregate species started to convert to blue-shifted aggregates (Figure **3.58**). This caused the formation of an increased population of H-aggregation. It is supposed that the dynamic conversion (J → H) results from intramolecular reorganisation of individual molecules within the aggregate. At the initial stages, both H- and J-aggregates seem to be formed, although type J-aggregate seems to compose most of the backbone of the structure (higher redshift than blueshift). H-aggregates are the less energetically favourable aggregate because of the smaller overlap of conjugated backbones (smaller π-π interaction) and are more sensitive to the steric hindrance at the centre of the chromophore (in comparison with J-aggregate).[85] This indicates that, during fast aggregation processes, the formation of both thermodynamic (H-aggregation) and kinetic (J-aggregation) supramolecular stacking occurs, both coexisting at room temperature. However, when the system is allowed enough energy to reach equilibrium, conversion to the more stable thermodynamic product of aggregation (H-aggregate) starts occurring. This observed thermotropic behaviour has also been reported for other SQs in solid state.[81,165]

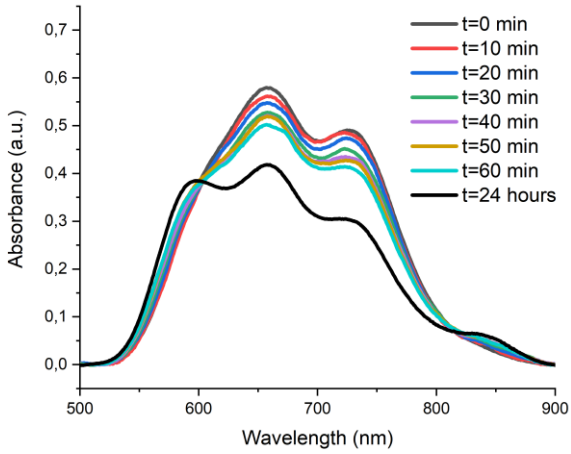


Figure **3.58**. UV-vis spectrum of **SQL** in water under constant heating source at 70 °C for a total of 24 hours.

3.3.2.5.2. Emission

Fluorescence emission of SQ compounds generally presents a large Stokes shift, low fluorescence intensity and higher photosensitisation rates.[166,167] A large Stokes shift can be of interest for any labelling and tracking of drug administration. High spatial resolution due to the Stokes shift allows for better resolution of fluorescent probes. Thereafter, fluorescence emission of **SQL** was recorded and compared to its absorption (Figure **3.59**). Fluorescence of the monomer in THF showed the typical spectrum profile of SQs, with a maximum emission at λ_{max}~ 718 nm, under excitation at 675 nm, nonetheless presenting a low fluorescence quantum yield (FQY) at FQY = 0.04 (4%) and a small Stokes shift (16 nm).

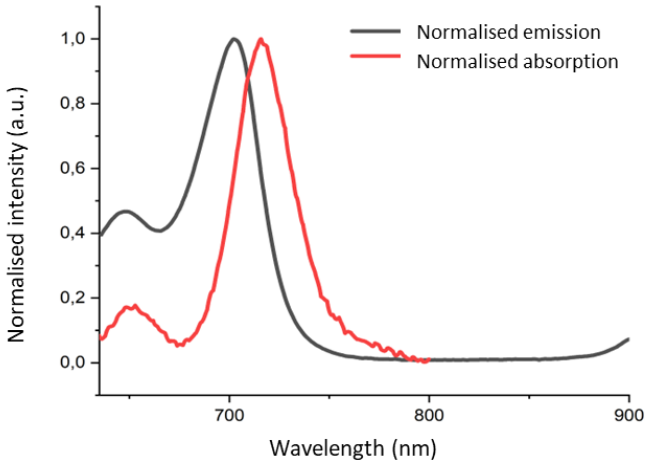


Figure **3.59**. Normalised UV–vis absorption and fluorescence emission (under 675 nm excitation) of **SQL** in THF.

When **SQL** is nanostructured in aqueous solution, the fluorescence is completely quenched (Annexe **3.46**). This effect is most probably due to NP induced scattering and self-absorption of emitted light. It is known that SQ aggregation forms non-fluorescent aggregates that affect their quantum yields, fluorescence lifetimes, and photostabilities, limiting their use for sensing in aqueous media or for biological sensing applications.[168] Self-absorption and loss of fluorescence from the nanostructured platform **SQL NP** means, in part, that less energy loss processes occur in the system, giving better chances for other processes, such as the needed ISC for ROS generation.

3.3.2.5.3. Light-Induced Photo-Reactivity

The photochemical properties under NIR irradiation of **SQL** and **SQL NP** were studied because of their benefits for biomedical applications in terms of skin penetration and harmlessness.[108] For this purpose, samples of **SQL** in THF and SQL NP in water were irradiated at 785 nm with an intensity of 250 mW (Figure **3.60**). In these settings, while the monomer does not suffer from photodegradation in acetonitrile (ACN), the nanostructured ligand showed a notable degradation in water. Reported examples of photodegradation of SQ attributed this phenomenon to the related process of SQ ring opening, resulting in a loss of system conjugation.[49] The resulting photodegradation products do not present precipitation under visual inspection.

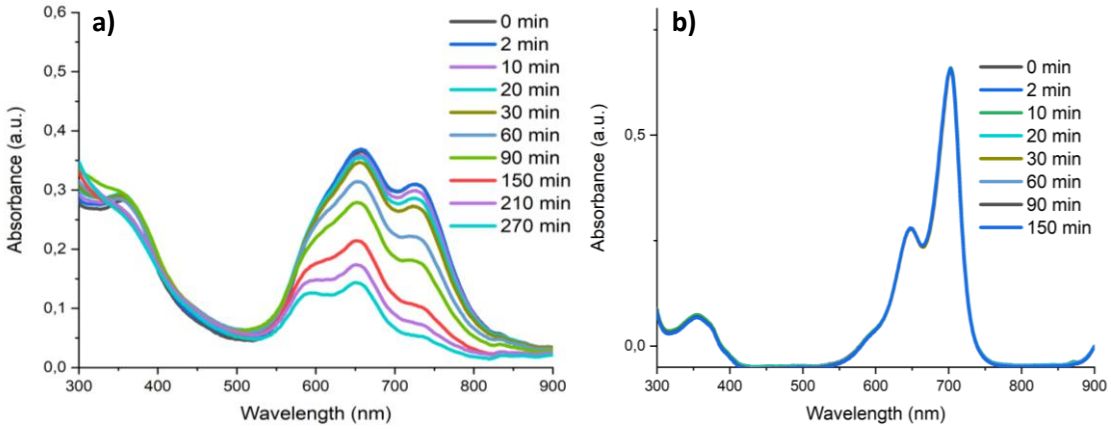


Figure **3.60**. UV-vis spectra obtained at different times for **a) SQL NP** in water and **b) SQL** in ACN under irradiation at 785 nm with a laser at 250 mW at a concentration of 0.15 µM **SQL**.

Interestingly, if the same experiment is repeated in the absence of oxygen and saturated with nitrogen, photodegradation of **SQL NP** was slowed greatly, and only observed some at large periods of time, which could likely be attributed to the inherent air leaking from the sealed cuvettes experienced over time (Figure **3.61**). The participation of oxygen in the degradation process has been reported previously in the literature, indicating that this effect could be due to the formation of a charge-transfer encounter complex between the SQ and the molecular oxygen, eventually evolving in the formation of different chemical species.[169]

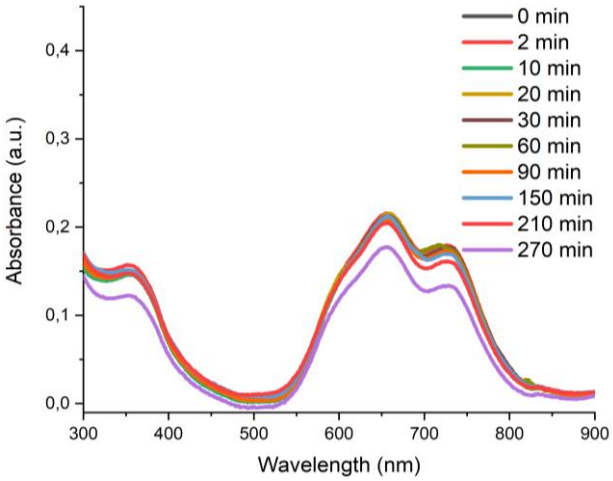


Figure **3.61**. UV-vis spectra of **SQL NP** in nitrogen-saturated water in a sealed cuvette.

3.3.2.6. SQC and SQC NP: An Optical Comparison

3.3.2.6.1. Absorption

The SQ-Pt complex **SQC** presents the typical two sharp absorption bands[64] in DMSO at 655 nm and 710 nm, with λ_{max}, (nm) presenting ε ($M^{-1}{\cdot}cm^{-1}$): 655 (1.9×10^4), 710 (2.3×10^4). Overall, **SQC** presents a slight bathochromic shift to longer wavelengths, while the nanoparticulate system SQC NP presents a more broadened and lower molar absorption coefficient at their maximums (Figure **3.62**). The NP's absorption spectrum shows clear broadening in both lower and higher wavelengths, and a clear new overlap between the previous peaks. The new ε decreases in **SQC NPs** with λ_{max}, (nm) presenting ε ($M^{-1}{\cdot}cm^{-1}$): 659 (1.5×10^4).

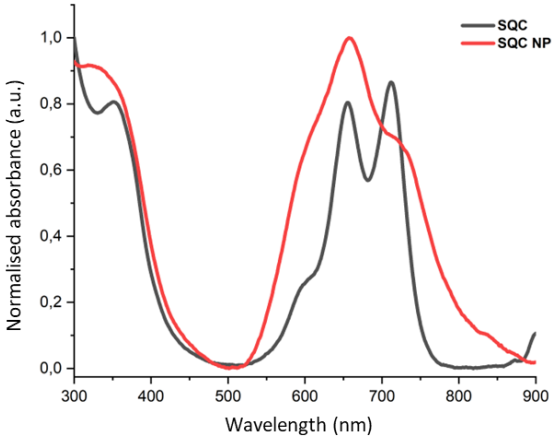


Figure **3.62**. Normalised UV-vis spectrum of SQC and nanoparticulate system SQC **NP**.

3.3.2.6.2. Light-Induced Photo-Reactivity

A first study was carried out to assess the capability to undergo photoactivation to release Pt when irradiating at 785 nm at 250 mW. Irradiation of both SQC NP in water and Pt monomer SQC in DMSO, at 785 nm (250 mW), was carried out (Figure **3.63**). As observed, in the case of the **SQC**, no photoactivation occurs as no overlap from **SQC** absorption with the emission source occurs. Interestingly, for **SQC NP** a clear decrease of absorption over time is observed when irradiated. This behaviour related to its degradation is relatively fast, with a 50% degradation after 30 minutes of irradiation.

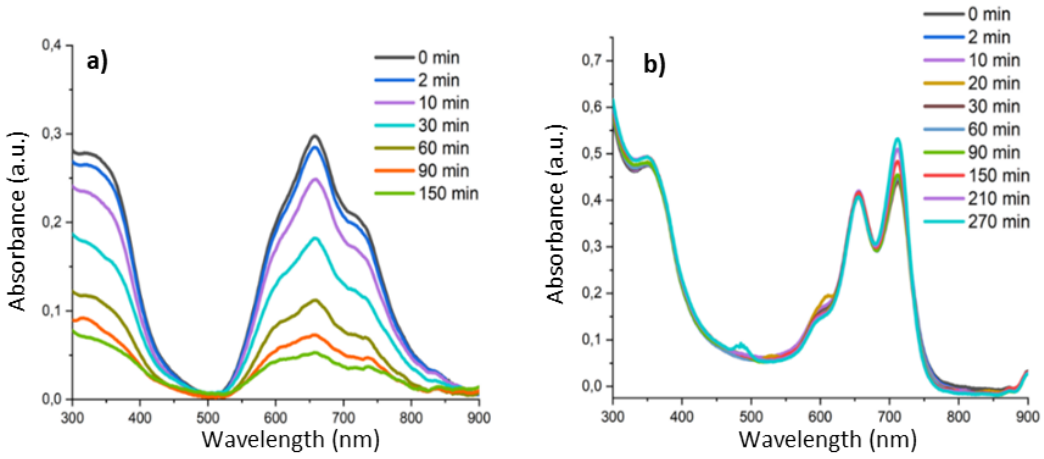


Figure **3.63**. UV-vis spectra over time of **a) SQC NP** and **b) SQC**, under irradiation at 785 nm with a laser at 250 mW. Concentration of 0.15 μM **SQC**.

To determine the Pt release from **SQC NP** induced by NIR irradiation, a dialysis method was used (Figure **3.64**). In such setting, a dialysis bag with our sample NPs was irradiated at 785 nm (250 mW). The photodegradation process was allowed to progress for 24 hours, and aliquots were taken at different time points. Pt concentration in every aliquot was determined using ICP-MS (Annexe **3.50**).

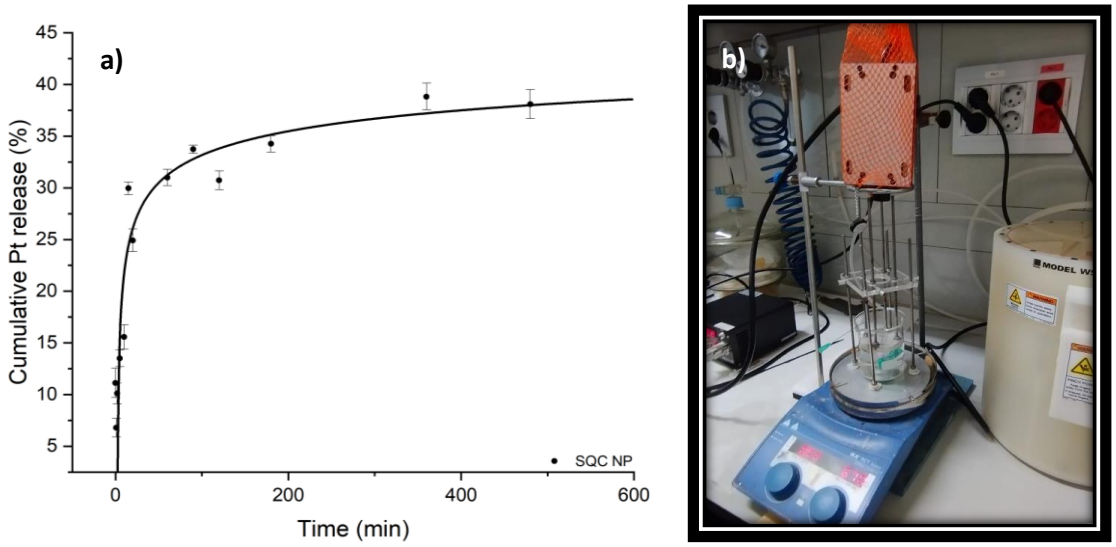


Figure **3.64**. Pt release experiment with **a)** Cumulative Pt release (%) over time, and **b)** set up used for the study of Pt release with a collimated laser providing irradiation (785 nm) from the top, directly to the sample.

The results from such experiment displayed a clear release profile from **SQC NPs**. During the first 3 hours, a burst release with a 34% cumulative release was observed. Afterwards, a plateau was reached with a slow and sustained release reaching the total cumulative release of 40% at 24 hours. Overall, the Pt release can be considered relatively low. Moreover, a precipitate was formed during irradiation. ICP-MS analysis of such precipitate revealed the presence of the remaining 60% of Pt (Annexe **3.50**). On one hand, we are observing photodegradation and the release of Pt cargo. On the other hand, a structural change that causes agglomeration/crystallisation may happen while removing the sample from the solution. As such, less Pt would be available for release, explaining this result.

All in all, the overall low synthetic yield for **SQC NPs** synthesis and the limited Pt release made it unfeasible to conduct enough experiments to accumulate statistically relevant data for such project. This limitation became even more evident when trying to conduct *in vitro* studies in an adequate and limited timeframe. Therefore, from now on, we decided to focus our efforts on the PDT properties of **SQL NPs** under physiological conditions.

3.3.2.7. Colloidal Stability of SQL NP under Physiological Conditions

Colloidal stability of NPs in physiological media is crucial for their biomedical applications. The presence of proteins, salts, and varying pH can cause NPs to aggregate, impairing their function and leading to rapid clearance. Good colloidal stability in physiological conditions allows NPs to remain in suspension in the bloodstream and ensure longer circulation time, desirable for an effective therapeutic action.

Therefore, colloidal stability of **SQL NPs** was tested in water, in phosphate buffer saline (PBS) and in aqueous solution with PBS and BSA at physiological concentration (30-40 mg·mL^{-1}), and at physiological pH of 7.4. The addition of BSA has been extensively used for dispersing inorganic and polymeric NPs,[170,171] by adsorbing onto their surfaces, preventing aggregation and improving stability through steric and electrostatic repulsion. Generally, BSA is expected to form a protein corona that reduces non-specific interactions in biological environments and improves biocompatibility.

SQL NP in water have previously been observed as presenting sizes by DLS of 170.3 ± 7.0 nm and a very low PDI of 0.056 ± 0.005 (Figure **3.49**). However, in PBS we observe a clear aggregation immediately, increasing PDI to 0.383 ± 0.039 and size to 1213 ± 99 nm and over 72 hours increasing even further to a PDI of 0.217 ± 0.047 and size to 2335 ± 68 nm, as provided by DLS (Figure **3.65 b,d**). When the NPs are dispersed in PBS-BSA solution (Figure **3.65 a,c**), a notable colloidal stabilisation is noted. **SQL NP** start with a PDI of 0.070 ± 0.018 and size of 142.3 ± 2.9 nm, and over a three-day period maintains a very good PDI of 0.079 ± 0.016 and size of 139.3 ± 3.0 nm. These findings indicate a non-statistically significant but trend towards a decrease in size, while keeping constant PDI over 72 hours, as provided by DLS analysis (Figure **3.65.c**).

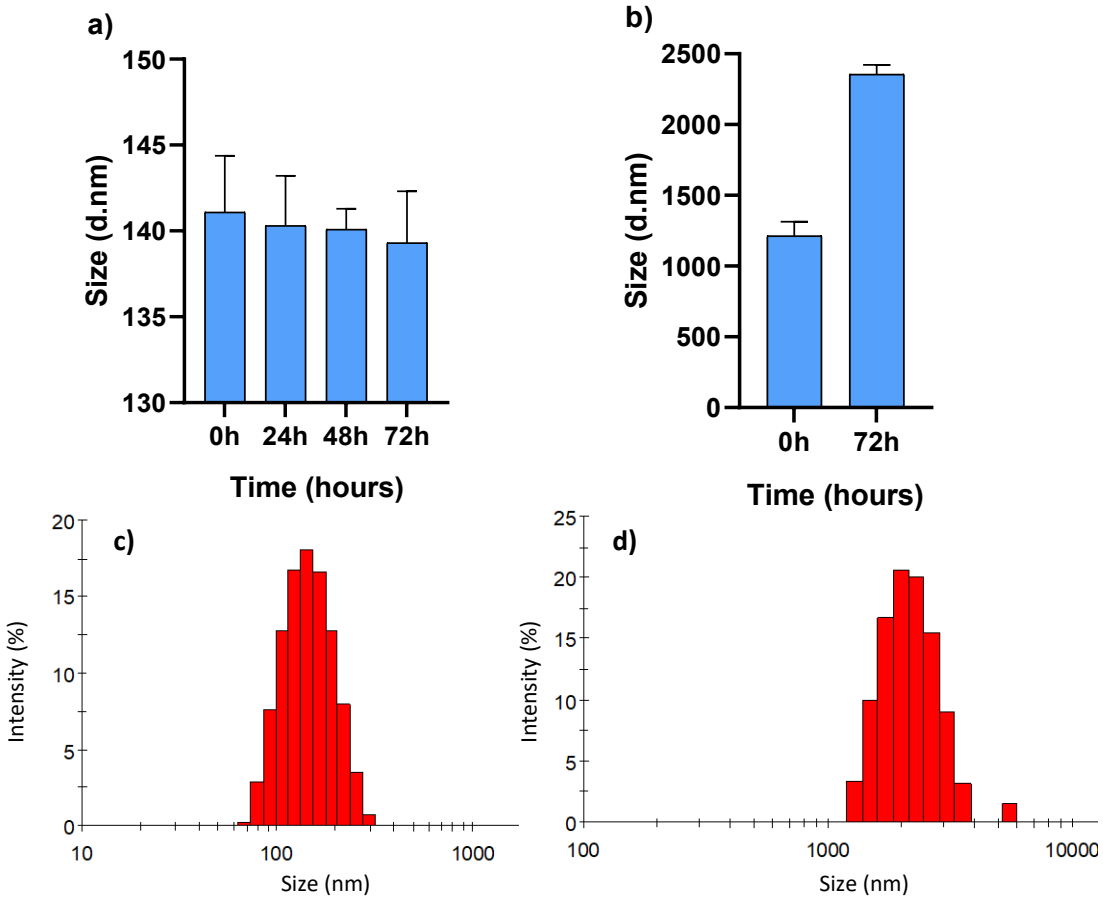


Figure **3.65**. Size distribution plot as given by DLS analysis of **a) SQL NP** in PBS-BSA 20 mg·mL^{-1}, at physiological concentration at pH 7.4, over 72 hours. **b) SQL NP** in PBS physiological concentration at pH 7.4. **c)** Size intensity distribution of **SQL NP** as given by DLS in PBS-BSA 20 mg·mL^{-1}, at physiological concentration at pH 7.4, after 72 hours. **d)** Size intensity distribution of **SQL NP** as given by DLS in PBS physiological concentration at pH 7.4 after 72 hours.

Such results prove that BSA can stabilise colloidally the NPs based on the formation of a protein corona on their surface, preventing aggregation of **SQL NPs**. These findings take special relevance when accounting for the observed behaviour on saline conditions, causing ions and salts to interact with **SQL NPs** and cause aggregation and precipitation, whereas in the presence of BSA, this does not occur.

Reports in the literature have shown the ability of SQs to bind non-covalently to serum albumins, resulting in an increase in the transport and distribution of these molecules *in vivo*.[172] In PDT, the interaction of PSs with BSA and human serum albumin (HSA) has been investigated as a potential delivery system,[173,174] targeting moiety[175] or as a potential increase of photodynamic activity.[176,177]

3.3.2.8. Photodynamic Therapy properties of SQL NPs

These studies were performed in collaboration with the expertise of Dr. Gema Duran from Universidad de Castilla la Mancha.

3.3.2.8.1. Total ROS Generation Quantification

The determination of total ROS generation quantum yields (Φ_Δ) followed an antioxidant trap methodology, using 1,5-dihydroxynaphthalene (DHN). This probe has demonstrated a high ability to capture SO[178] and free radicals, leading to the formation of juglone (Figure **3.66**),[169] so the absorption increases proportionally to trapped ROS. Afterwards, a direct correlation can be made between the absorption increase and the ROS generation rate or Φ_Δ.

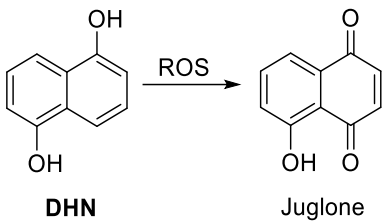


Figure **3.66**. Reaction between ROS and DHN.

This type of essay requires the use of a well-established PS capable of generating ROS. In our study, Rose Bengal (RB) was chosen. This control is used to compare ROS generation rates and use the known RB Φ_Δ to quantify the **SQL NP**'s Φ_Δ. The results of the Φ_Δ can be obtained from Equation **3.1**:

$$\boldsymbol{\Phi_\Delta^x = \Phi_\Delta^{ref} \cdot \frac{k_x}{k_{ref}} \cdot \frac{l_a^{ref}}{l_a^x}} \quad \text{(Equation 3.1)}$$

Where $\boldsymbol{\Phi_\Delta}$ stands for SO Φ_Δ, $\boldsymbol{\Phi_\Delta^x}$ for the case study molecule and $\boldsymbol{\Phi_\Delta^{ref}}$ for the reference molecule, in the solvent the reaction is being carried. $\boldsymbol{k_x}$ and $\boldsymbol{k_{ref}}$ stand for the first-order rate constants (10^{-3} s^{-1}) consumption of DHN. Finally, $\boldsymbol{l_a^{ref}}$ and $\boldsymbol{l_a^x}$ refer to the absorption at the irradiation wavelength of the SO trap in the presence of the reference and the objective sample, respectively.

During these experiments, it was found that optimal conditions for ROS generation required photoexcitation under blue light irradiation at 470 nm at 51.4 mW·cm^{-2}. Under such conditions, it was found that total ROS generation $\boldsymbol{\Phi_{\Delta}^{x}}$ of **SQL NP** was 0.133 (13.3%) (Annexe **3.42**). Control experiments in the dark and absence of irradiation showed that no oxidation was happening in the sample (Annexe **3.36**). ROS generation from the monomer resulted impossible to measure with this essay as the probe is only functional in water-based solvents, and monomer **SQL** is not soluble in such settings.

Overall, although moderately low when compared to other free molecular SQs like the reported 74% Φ_{Δ} from Sriwastav *et. al.*[179], our platform generates ROS and stays inactive in the dark, which is a challenge some probes have faced in the past.[180] Furthermore, most of the SQ probes are lipophilic or only partially soluble in water or related aqueous buffers.[181] As such, there is a need for real water-soluble or water-dispersible compounds, which our platform shows to overcome with **SQL NP**.

After confirming the ability of **SQL NP** to generate ROS, and to get a better idea of the source of the ROS generated, we decided to start the study of specific Type I or Type II photoactivation mechanisms, starting with SO generation.

3.3.2.8.2. Quantification of Singlet Oxygen Generation

The SO Φ_{Δ} determination followed the same principles as the previous experiment, although now, the probe selected was SO specific (i.e., only reacts to SO). For this role, SO trap, 9,10-anthracenediyl-bis(methylene)dimalonic acid (ABDA) was chosen.[182] In this case, however, instead of measuring signal increase via UV-vis, we will follow signal decrease, also via UV-vis at 400 nm. The transformation that ABDA undergoes when reacting with SO is indicated below (Figure **3.67**).

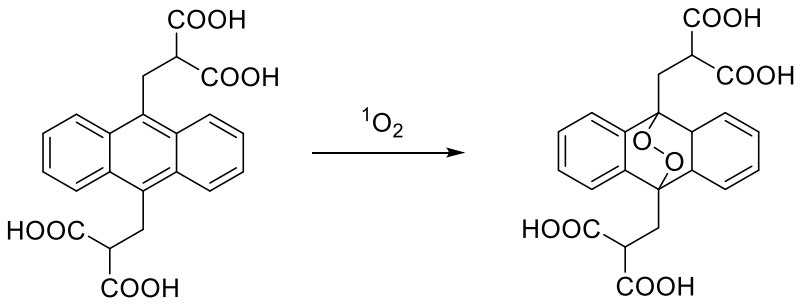


Figure **3.67**. Reaction between SO and **ABDA**.

In this experiment, the cuvette containing the PS (**SQL** or **SQL NP**) and ABDA solution was measured before and after irradiation in water or ACN to measure the SO production of the **SQL** and **SQL NPs**. The cuvette was exposed to blue light (470 nm, 51.4 mW·cm^{-2}) for different periods of time, and the UV-vis spectra were then immediately recorded (Figure **3.68**). As a negative control, ABDA was monitored in a solution with no PS. Finally, neither the monomers in water nor the aggregates in ACN were capable of generating any trace of SO in the dark or under blue light. To explore other irradiation ranges, the samples were irradiated with orange light (617 nm, 47.7 mW·cm^{-2}) and red light (655 nm, 80.6 mW·cm^{-2}) for both monomer and aggregates. In no case, however, was the generation of SO observed.

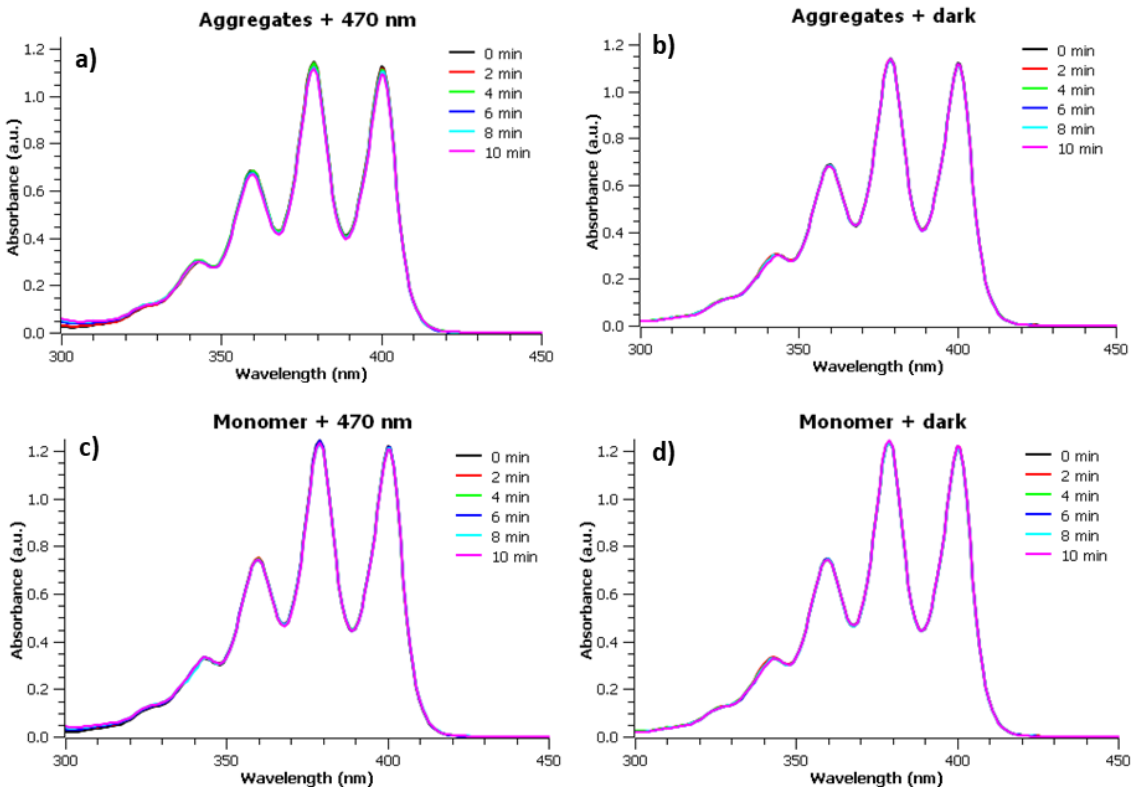


Figure **3.68.** Evolution of the UV-vis spectra of **ABDA a)** With **SQL NP** in water upon blue light irradiation (470 nm, 51.4 mW·cm^{-2}), **b)** With **SQL NP** in water in dark conditions, **c)** With **SQL** in ACN upon blue light irradiation (470 nm, 51.4 mW·cm^{-2}), and **d)** With **SQL** in ACN in dark conditions.

3.3.2.8.3. Quantification of Superoxide Anion Radical Generation.

To explore the Type I photo-mechanisms, we studied the generation of superoxide anion radicals ($O_2^{\bullet-}$) using a superoxide anion radical sensitive probe, more precisely dihydrorhodamine 123 (DHR123).[183] The transformation that DHR123 undergoes when reacting with superoxide ions is indicated below (Figure **3.69**).

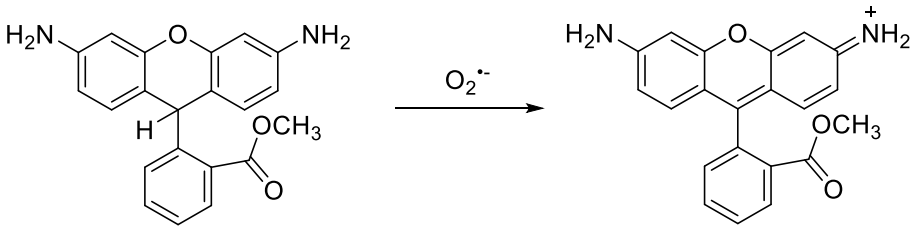


Figure **3.69**. Reaction between singlet superoxide anion radical and **DHR123**.

Once again, the cuvette containing the PS (**SQL** or **SQL NP**) and DHR123 solution was measured before and after irradiation, in water or ACN, to measure the SO production of the monomer and **SQL NPs**. The cuvettes were exposed to blue light (470 nm, 51.4 mW·cm^{-2}) for different periods of time, and the UV-vis spectra were then immediately recorded. As a negative control, **DHR123** was monitored in a solution with no PS. In this experiment, however, SO quenching is necessary, and sodium azide was added. Our reference RB was also replaced by $[Ru(bpy)3]^{2+}$ as a reference complex for the generation of the superoxide anion radical.

Opposite to the previous ones, the generation of superoxide is clear and evident in the case of **SQL NP** under blue light in water. In ACN, where the SQ is in monomeric form, the PS does not generate any superoxide radical. More notably, the same experiment was conducted in the presence of the superoxide inhibitor ascorbic acid, and no generation occurred in such conditions. However, in the same experiment in the presence of the SO inhibitor, sodium azide, the generation of superoxide remained unaltered. Notably, no superoxide generation is observed in any setting for monomeric **SQL** (Figure **3.70**). The same experiments were also conducted in the dark, and no superoxide was detected. Such information confirms that our superoxide formation comes only after nanostructuration from **SQL NP**, and that such generation is also specific of the interaction between PS and light. The same reactions were performed under irradiation with orange light (617 nm, 47.7 mW·cm^{-2}) and red light (655 nm, 80.6 mW·cm^{-2}), with no detection of superoxide formation for both, monomer and aggregates.

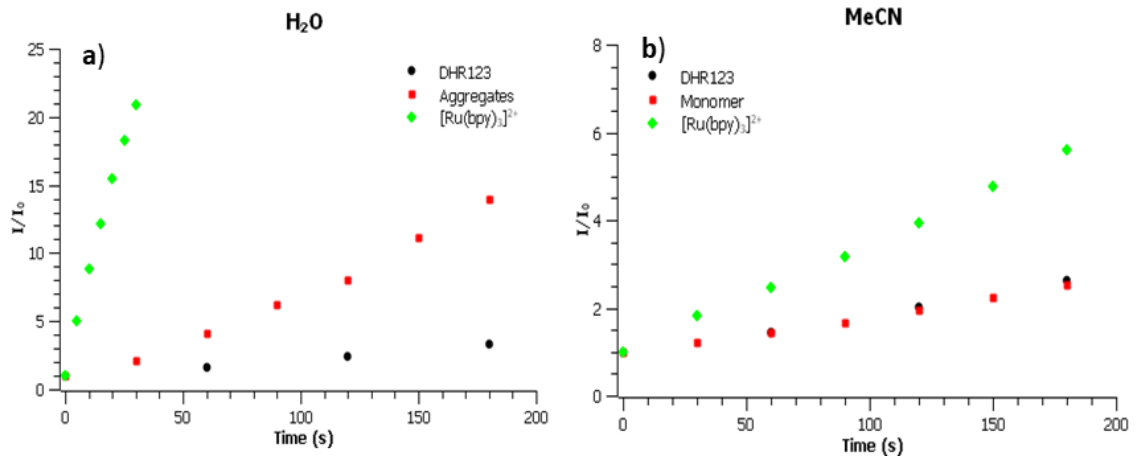


Figure **3.70**. Comparative plots of I/I_0 as a function of time for the experiment of photooxidation of **DHR123** under blue light irradiation (470 nm, 51.4 mW·cm-2) in **a) SQL NP** in water and **b) SQL** in ACN.

A total ROS generation Φ_Δ of 0.133 falls considerably short when compared to newly reported SQs studied in PDT. SQ dyes have been reported as suitable for second-generation PDT and present ΦΔ that reach all the way up to 0.93.[184-186] One major difference, however, is the fact that all of them are being used as discrete molecules. As mentioned, aggregation of SQs quenches fluorescence as well as Φ_Δ.[187,188] As a result, there are few reports of Φ_Δ for SQ NPs based on supramolecular aggregation. Although most of the reported cases for SQ-based sensitisers having PDT activity have been proposed to act via the Type II mechanism of photoactivation, some research studies have shown that some π-extended SQ systems are able to initiate radical chain reactions that lead to Type I photodynamic processes.[169] This information supports our experimental finding of **SQL NP** promoting the generation of Type I ROS.

What seems more interesting, however, is the fact that ROS generation is supramolecular dependent, as the monomeric unit is unable to produce any at all. Instead, the supramolecular association and supramolecular J- and H-aggregation are enabling our platform to undergo excited state ISC and generate those superoxide species. Such results go against the quenching of aggregates on ROS generation, and our results manifest that H- and J-aggregation can enhance ISC and facilitate Type I photoactivation.

During the development of this Chapter, newer research on SQ supramolecular-based systems that generate Type I ROS reached publication.[73] Interestingly, such publications give footing to what we have been observing. In the work of Qiao *et. al., they report an SQ-based aggregation NP that shows increased Type I ROS generation and could only hint at an effect on aggregation,* inducing an increase.[73] Our work falls in accordance with such findings, while at the same time further improving on the topic. While our ROS generation Φ_Δ falls short of that of Qiao's publication, we present a turn-on effect on Type I ROS generation upon aggregation, which conclusively proves the aggregation-induced Type I ROS generation.

3.3.2.9. *In vitro* studies of SQL NPs

3.3.2.9.1. Cytotoxicity

Cytotoxicity of **SQL NP** was studied in the human lung adenocarcinoma A549 cell line, chosen because it presents as one of the more hypoxia-resistant variant cell lines. **SQL NPs** at 5 mg·mL^{-1} were dispersed with cell culture media at concentrations ranging from 0.2 to 250 μg·mL^{-1}. Cells were treated in dark conditions or irradiated. The irradiation protocol consisted of the pre-incubation of cells with the NPs for 4 hours to enable their intracellular accumulation, followed by 1 hour of blue light irradiation (λ: 460 nm, 24.1 J·cm^{-2}). The effect on cell viability was determined by a 3-(4,5-dimethylthiazol-2-yl)-2,5-diphenyltetrazolium bromide (MTT) assay after 48 hours. The IC_{50} of the NPs was established based on the dose-response curves generated with Gen5 software (BioTek) (Figure **3.71**).

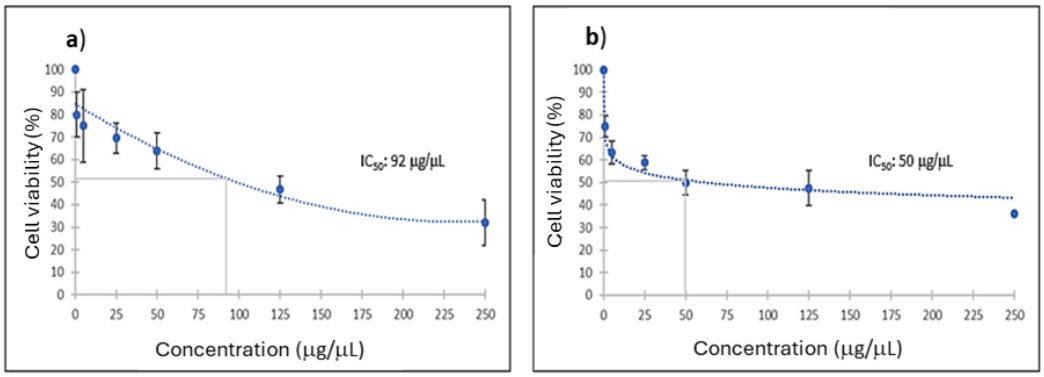


Figure **3.71**. Effect of **SQL NP** on cell viability after 48 hours in **a)** the dark or **b)** with blue light photoactivation. Data represents the mean ± SE, n=3.

At a 48-hour timeframe, **SQL NP** showed an IC_{50} value of 92 μg·μL^{-1} (0.14 μM). More importantly, after irradiation, the IC_{50} reduces to 50 μg·μL^{-1} (0.08 μM). Such results show a remarkable difference in the IC_{50} values for the **SQL NP** with and without irradiation, showing very low IC_{50} activity in the dark, and a cell-dependent PI value of 1.84. Remarkably, these values are in consonance with previously reported values for other π-extended SQs and empowers our idea of a water-stable supramolecular SQ platform for PDT applications.[169]

3.3.2.9.2. Cellular Uptake

As mentioned previously, **SQL NP** presents no fluorescence spectrum because of the self-aggregation of monomeric SQ, resulting in an effective quenching of fluorescence emission. On the other hand, free molecular **SQL** does. The idea behind this essay thus focuses on finding whether fluorescence is being emitted from our sample, meaning disaggregation of **SQL NP**, giving an idea of NP stability in intracellular environments.

As such, A549 cells were seeded in a six-well plate, allowed to grow and adhere for 24 hours and treated with a concentration of 0.1 mg·mL^{-1} of SQL NP at a 6-hour time frame. The media was then removed and stored for analysis, while the cells were lysed in PBS-1% sodium dodecyl sulphate (SDS) or THF, collected and stored for analysis. **SQL NP** presence is then determined via fluorescence spectroscopy with excitation wavelength at 678 nm and emission wavelength of 718 nm (Figure **3.72**). 1% SDS + THF lysed cells were added as a control to corroborate that THF lysing provided adequate cell membrane rupture and intracellular cargo release.

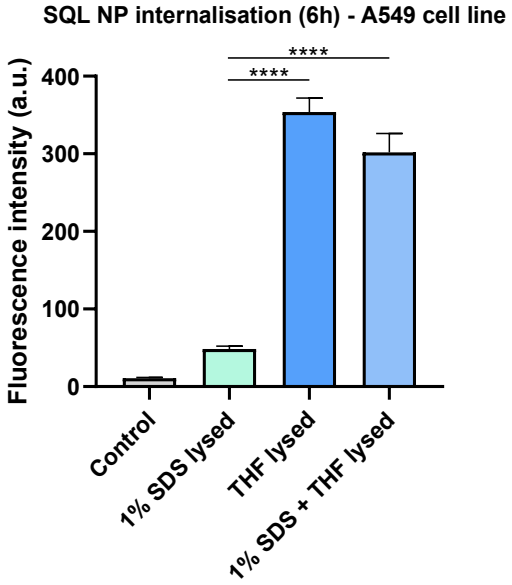


Figure **3.72**. **SQL NP** internalisation (0.1mg·mL^{-1}) in A549 cell line after 6 hours. Data displays fluorescence intensity as measured at excitation wavelength of 678 nm and emission wavelength of 718 nm. Data represents the mean ± SE, n=3. Statistical differences were calculated using one-way ANOVA, followed by Turkeys multiple comparison test, where (*) denotes $P < 0.05$, (**) denotes $P < 0.01$, (***) denotes $P < 0.001$, and (****) denotes $P < 0.0001$.

The results from a 6-hour time frame internalisation assay display that control cells do not present fluorescence. Cells lysed with 1% SDS present some fluorescence, while cells lysed with THF present a 7-fold increase in fluorescence with respect to the 1% SDS lysed cells.

1% SDS lysed sample presents fluorescence emission, which means that a small part of NPs is disaggregated. This disaggregation leads to formation of fluorescent monomer **SQL**, yielding the fluorescence observed. Nonetheless, mechanisms might exist that degrade, extravasate or remove the **SQL** monomer. As such, we can only analyse data as a snap picture at the 6-hour time frame.

In this time frame we can, however, analyse the % of **SQL NPs** that have undergone disaggregation.

The results from cells lysed with 1% SDS indicate that, inside cells, **SQL NP** undergoes partial degradation over time, generating fluorescence as a result of the release of molecular **SQL**, which is itself fluorescent. However, leftover **SQL NPs** that are not disaggregated could be present. As such THF lysing was employed. Cells lysed with THF disaggregate to totality the **SQL NP**, generating the maximum of fluorescence corresponding to the total amount of **SQL** molecules. Thus, the difference of such fluorescence with that observed in 1% SDS experiment gives us the % of disaggregation. The result of such comparison gives a 13.7% ± 1.9 disaggregation of **SQL NP** to **SQL** inside cells in the first 6 hours (Figure **3.73**).

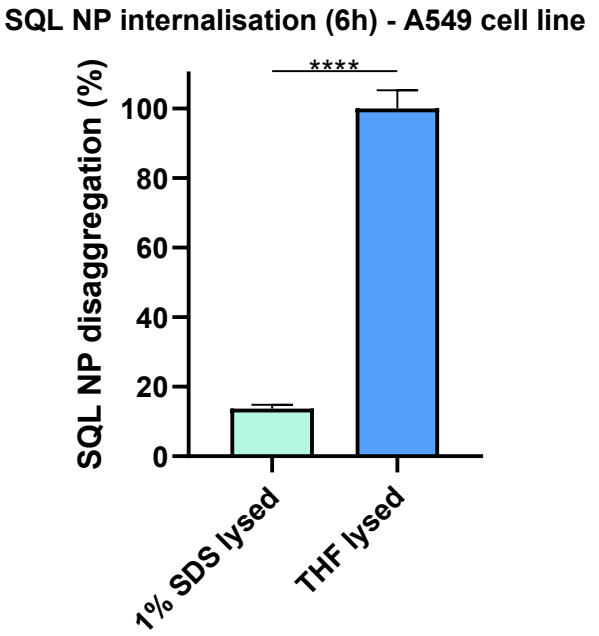


Figure **3.73**. Normalised fluorescence intensity of **SQL NP** internalisation (0.1 mg·mL^{-1}) in A549 cell line after 6 hours. Data represents the mean ± SE, n=3. Statistical differences were calculated using one-way ANOVA, followed by Turkeys multiple comparison test, where (*) denotes P < 0.05, (**) denotes P < 0.01, (***) denotes P < 0.001, and (****) denotes P < 0.0001.

Such results show that SQL NPs are not impervious to intracellular environments; however, it does show considerable biostability and resilience to degradation, with one tenth of the total population present in the disaggregate state. The increase in fluorescence after internalisation can be used as a good indicator of nanoparticulate stability over time. An internalisation time of 6 hours with little degradation as observed via fluorescence spectroscopy indicates that during the incubation and treatment of *in vitro* cytotoxicity assays, NPs remained quite stable and, consequently, susceptible to ROS generation. On top of this, fluorescence increase can also be used as a tracker to **SQL NP** stability post administration in theragnostic settings.

3.4. Conclusions

3.4.1. Bioinspired Polymeric Neuromelanin-like Pt(IV) NPs

Despite the low ROS generation and unsatisfactory *in vivo* therapeutic efficiency, we conclude that **pPtBC NPs**, a bioinspired CNP, exhibited significant pH and GSH-dependent Pt(IV) release sensitivity, with promising *in vitro* cytotoxicity profiles comparable to the gold standard **CDDP**.

A summary of the landmarks of this work is:

- Successfully establishing a synthetic route for the obtention of a Pt(IV) monomer, PtBC, using CDDP as a starting material, via a four-step synthetic route. The final **PtBC** drug was synthesised in an overall 20% yield and characterised via FTIR, NMR and HRMS, confirming the obtention of a reproducible synthetic methodology.
- Successfully synthesising the nanostructured platform **pPtBC NPs** via oxidative polymerisation, presenting spherical morphologies, average size of 234.6 ± 0.5 nm with a very low PDI of 0.087 ± 0.022 and a ζ-potential of -37.1 ± 0.95 mV, and a Pt cargo of 17% (w/w).
- An analogous nanostructured platform, **pNDGA NPs** without Pt cargo, was obtained for comparison purposes using the same synthetic methodology. The resulting NPs present spherical morphologies and sizes of 214.2 ± 0.8 nm with a very low PDI of 0.07 ± 0.02 and a ζ-potential of -28.7±0.5 mV.
- **pPtBC NPs** displayed dual responsiveness to pH and reducing agent GSH, clearly showing increased Pt release under acidic and reductive environments that mimicked the TME.
- Overall, **PtBC** and **pPtBC** displayed lower DNA-Pt adduct formation than **CDDP** but bigger uptake kinetics. However, both **PtBC** and **pPtBC** showed comparable or superior cytotoxicity in comparison to **CDDP** in various cancer cell lines over 72-hour time periods. Indicating a controlled and continuous onset of action.
- Studies with **pNDGA** supported the conclusions that observed cytotoxicity arise from Pt-mediated mechanisms, rather than ROS generation as a result of catechol moiety oxidation.
- *In vivo* studies have shown excellent tolerability of **pPtBC NPs** via IN administration. No adverse effects related to the treatment, such as weight loss, food consumption, mortality or any other clinical signs were observed for all mice during the study relative to the control group.
- Biodistribution studies displayed Pt accumulation in the brain and GBM tumour tissues. If considering the tumour and brain collectively, Pt accumulation in the CNS was higher than in other organs.
- It was observed that the therapeutic efficacy of **pPtBC** *in vivo* failed to show tumour regression or improved survival compared to untreated controls under an IMS schedule.

Given these preliminary results, future work must address the limitations faced in IN administration to increase the effectiveness of this administration route.

As a result of this line of research, all information gathered in this part of the Chapter has been published in a high-impact journal and is open to access for any future researcher to consult.[1]

3.4.2. Supramolecular Photoactivatable Squaraine Pt(II) NPs

As a result of the work performed, we conclude that although SQC NP demonstrated good light-dependent activation in PACT, the platform showed significant limitations in preparation and applicability. However, SQL NPs exhibited promising PDT features via Type I photoactivation with robust turn-on effects, efficient internalisation, and substantial cytotoxicity only under irradiation.

A summary of the landmarks of this work is:

- Development of a successful synthetic route for the obtention of **SQL**, yielding the desired 1,3-SQ regioisomer, and **SQC** via a convergent synthetic route. The structural identity was confirmed through NMR, IR and HRMS analysis. A combination of EDX and HRMS find agreement in a 1 to 1 Pt to SQ stoichiometry.
- Supramolecular assembly via π-π stacking and hydrophobic interactions yielded spherical, homogeneous SQL NPs (81.2 ± 0.8 nm, PDI 0.056 ± 0.005, ζ-potential -21.4 ± 0.38 mV), while similar aggregation produced SQC NPs that were heterogeneous and uneven (155.5 ± 0.8 nm, PDI 0.265 ± 0.027, ζ-potential 30.6 ± 0.351 mV, Pt cargo 8.6% w/w).
- **SQL NP** platform displayed aggregation-induced spectral broadening and demonstrated reversible supramolecular assembly behaviour. Under thermotropic studies, H- and J-aggregate interconversion was demonstrated upon heating, indicating the dynamic nature of the self-assembly process that governs SQ aggregation.
- Both **SQL** and **SQC**, as well as their respective NP forms, exhibited strong absorbance in the biological window of application, and maintained photochemical stability in dark conditions.
- The nanostructured form of **SQL** and **SQC** displayed photoresponsiveness to NIR irradiation (785 nm). However, their monomeric forms did not. **SQC NP** displayed a clear light-dependent Pt release profile under irradiation. **SQL NP** underwent photodegradation in an oxygen-dependent manner, as observed via UV-vis spectroscopy. **SQC NPs** also underwent photodegradation, as confirmed via SEM imaging and UV-vis spectroscopy.
- **SQL NP** generated superoxide radicals via Type I PDT, with ROS production dependent on NP assembly. These NPs selectively activated ROS upon blue light irradiation (inactive in the dark), achieving a total ROS quantum yield (ΦΔ) of 0.133.
- *In vitro* cytotoxicity assays against human lung adenocarcinoma A549 cell line demonstrated a PI of 1.84 for **SQL NPs**, while remaining stable in physiological-like conditions when combined with BSA, confirming biocompatibility and colloidal integrity.
- Uptake of **SQL NPs**, followed via fluorescence spectroscopy, showed the ability of the NPs to be uptaken in short periods. The ability to degrade and release a fluorescent probe over time proved the dynamic nature of the NPs, as well as allowing for the follow-up of the uptake of such NPs.

3.5. Materials and Experimental Methods

3.5.1. Materials

Solvents and starting materials were purchased from Merck (Germany) and used as received without further purification. Deuterated solvents were purchased from Eurisotop (Germany). PBS tablets were purchased from Thermo Scientific (USA). DCFCDA was purchased from Merck (Germany).

3.5.2. Characterisation

Nuclear magnetic resonance (NMR) spectra were registered at *Servei de Ressonància Magnètica Nuclear at the Universitat Autònoma de Barcelona*. ^{1}H-NMR were registered at Bruker DPX (250 MHz), Bruker DPX360 (360 MHz) and Bruker ARX400 (400 MHz). Chemical shifts (δ) of protons are described in ppm using the residual deuterated solvent signals as internal reference (chloroform-d_1; 7.26 ppm, DMSO-d_6; 2.5 ppm). ^{13}C-NMR were registered at Bruker ARX400 (100 MHz), chemical shifts (δ) of carbons are described in ppm using the residual deuterated solvent signals as internal reference (chloroform-d_1; 77.16 ppm, DMSO-d_6; 39.52 ppm). 2D COSY, HSQC and HMBC spectra were recorded at Bruker DPX360 (360 MHz) and Bruker ARX400 (400 MHz). Chemical shifts (δ) of protons and carbons are described in ppm using the residual deuterated solvent signals as internal reference (chloroform-d_1; ^{1}H 7.56 ppm or ^{13}C 77.16 ppm, DMSO-d_6; ^{1}H 2.5 ppm or ^{13}C 39.52 ppm). All spectra have been registered at room temperature.

Abbreviations used to describe signal multiplicities have been: s (singlet), d (doublet), q (quadruplet), qt (quintuplet), bs (broad singlet), m (multiplet) and J to indicate coupling constants (Hz).

Infrared Spectrometry (IR) was performed using an MKII Golden gate spectrometer equipped with golden gate singlet reflection diamond ATR (attenuated total reference) at the *Servei d'Anàlisi Química at the Universitat Autònoma de Barcelona*. Each spectrum was acquired between 400 and 4000 cm^{-1} at a spectral resolution of 2 cm^{-1}. Peaks were described in cm^{-1} and intensity described as strong (s), medium (m), and weak (w).

Electron absorption spectrometry (UV-vis) was performed using a Cary 4000 and Cary 600 spectrophotometers (Agilent, USA), in the 200−800 nm wavelength range, using a matched pair (one for the solvent blank and one for the sample) of quartz cuvettes of 1 cm optical path length, and solvents quality high-performance liquid chromatography (HPLC) in water, CH_2Cl_2, DMSO, or THF.

Fluorescence spectra were measured on a HORIBA PTI QuantaMaster 8000 Spectrofluorometer (Horiba, Japan) at a wavelength range of 300-900 nm in a 1 cm optical path long quarts cuvettes in water, CH_2Cl_2, DMSO, or THF.

Fluorescence Quantum Yield (FQY) was measured on a Hamamatsu C9920-02G fluorimeter using an integration sphere in a 1 cm optical path long quarts cuvettes in water, CH_2Cl_2, DMSO, or THF.

Electrospray ionisation mass spectrometry (ESI-MS) has been performed at *Servei d'Anàlisi Química at Universitat Autònoma de Barcelona* using a 1200 RR, Agilent Technologies – mass spectrometer triple-quadrupole – time of flight (QTOF) microTOF-Q (Bruker Daltoniks, USA).

Inductively coupled plasma-mass spectrometry (ICP-MS) was performed at *Parque Científico Tecnológico* of the *Universidad de Burgos,* using an Agilent 8900 ICP-MS/MS with automatic sampler and octupole detector. Measurements were recorded using ^{194}Pt, ^{195}Pt, and ^{196}Pt as Pt tracers.

Dynamic light scattering (DLS) for hydrodynamic size distribution and surface charge potential of NPs (0.5 $mg \cdot mL^{-1}$) were measured using a ZetasizerNano 3600 instrument (Malvern Instruments, UK), with a size range limit from 0.6 nm to 6 nm.

Nanoparticle Tracking Analysis (NTA) was performed at *Institut de Ciència de Materials de Barcelona* at the *Soft Materials Service,* using a Nanosight NS300 (Malvern Instruments, UK).

Scanning Electron Microscopy (SEM) images were obtained using a SEM (FEI Quanta 650 FEG) at an acceleration voltage of 5–20 KV, high-vacuum mode, and an electron gun distance to the sample of 5 mm. SEM samples were prepared by drop-casting the corresponding dispersions of NPs on aluminium tape followed by solvent evaporation under room temperature conditions. Before analysis, the samples were metalised with a thin layer of Pt (thickness of 5 nm) using a sputter coater (Emitech K550).

ImageJ (Copyright (C) 1989, 1991 Free Software Foundation, Inc.) analytical software was used for SEM imaging NPs size analysis using the integrated particle analysis software from binary file images taken from 8-bit format files from SEM imaging.

Pt drug release from pPtBC NPs was evaluated using the dialysis method. Concentrated **pPtBC NPs** (1 $mg \cdot mL^{-1}$) were reconstituted in 1 mL of MilliQ® water and placed in dialysis bags (MWCO=6,000–8,000 Da). The bags were then immersed in sealed beakers containing 40 mL of PBS with pH values set at 7.4 and 5.5. The beakers were then kept at 37 °C with gentle stirring throughout the study. At predetermined time points, a 500 µL aliquot was withdrawn from the dialysate and immediately replaced with an equal volume of fresh buffer. The quantity of released Pt was determined using ICP-MS.

Pt drug release from SQC NPs was evaluated using the dialysis method. Concentrated **SQC NPs** (1 $mg \cdot mL^{-1}$) were reconstituted in 1 mL of MilliQ® water and placed in dialysis bags (MWCO=6,000–8,000 Da). The bags were then immersed in sealed beakers containing 100 mL of PBS with pH values set at 7.4 The beakers were then kept at 37 °C with gentle stirring throughout the study and under direct irradiation with a light source at 785 nm at 250 mW. At predetermined time points a 1 mL aliquot was withdrawn from the dialysate and immediately replaced with an equal volume of fresh buffer. The quantity of released Pt was determined using ICP-MS.

Estimation of ROS formation of pPtBC NPs, pNDGA NPs, PtBC, NDGA, and CDDP. HeLa, 1Br3G, and GL261 cell lines were seeded in black 96-well plates (Corning, USA) at a density of 20,000 cells per well to ensure full confluence. Following a 24-hour incubation, the spent medium was removed, and the cells were rinsed with serum-free medium. Subsequently, pre-warmed PBS containing the fluorescent probe DCFDCA at a final working concentration of 10 mM was added, and the cells were incubated for 30 minutes. Once the probe was internalised, the buffer containing the probe was replaced with either medium alone or media-containing compounds (H_2O_2, **pPtBC NPs**, **pNDGA NPs**, **PtBC**, **NDGA**, and **CDDP**) at the IC_{50} for 24 hours. A positive control with 0.1 mM H_2O_2 was included for comparison. After 24 hours, the fluorescence of each well was measured at 530 nm with excitation at 485 nm using a Victor3 microplate reader (Perkin Elmer, USA). This experiment was independently repeated in triplicate, and the results were normalised based on the negative control, which was loaded with the DCFDCA dye but lacked drug treatment.

Study of photoinduced SO generation of SQL NPs and determination of ROS generation Φ_Δ

DHN probe: In a quartz cell, 0.2 mL of DHN solution, 5 µL of **SQL NP** and 1.795 mL of H_2O were mixed. The final solutions were studied by recording UV-vis absorption spectrum at room temperature under blue light irradiation (λexc=470 nm, "Medusa" photoreactor) for 120 seconds irradiation intervals during a total exposure period of 20 minutes. Absorption UV-vis spectra were recorded after every irradiation interval. The consumption of DHN probe was measured by monitoring its absorbance intensity increase at 426 nm with irradiation time. SO generation Φ_Δ was calculated from equation **1** using RB as reference. In this case, the ϕ_Δ of the references in H_2O is 0.76 for RB.

$$\mathbf{\Phi_\Delta^x} = \mathbf{\Phi_\Delta^{ref}} \cdot \frac{\boldsymbol{k_x}}{\boldsymbol{k_{ref}}} \cdot \frac{\boldsymbol{l_a^{ref}}}{\boldsymbol{l_a^x}} \qquad \text{(Equation } \mathbf{3.1}\text{)}$$

Where ***x*** and ***ref*** subindex correspond to the complex and the reference, $\mathbf{\Phi_\Delta}$ is the SO generation Φ_Δ for RB, ***k*** is the slope of the plots of the normalised absorbance of DHN at 426 nm *vs.* the irradiation time, **F** is the correction factor of absorption, which is given by $\mathbf{F}=1\text{-}10^{-O.D.}$ (where O.D. is the optical density at 470 nm of solutions of complexes and references at the same concentration).

ABDA probe: In a typical experiment, SO generation was studied using the ABDA (Sigma Aldrich, USA) assay. ABDA was selected as SO scavenger due to its fast reaction with this molecule and high selectivity. Fresh stock air-equilibrated solutions of the organic molecule were prepared at $3.00 \cdot 10^{-4}$ M in water (20% DMSO) and ACN. Two solutions of ABDA at $6.00 \cdot 10^{-4}$ M were also prepared in water (50% DMSO) and ACN (50% DMSO). In a quartz cell, 300 µL of PS solution and 500 µL of ABDA solution were mixed with 2.2 mL of water or ACN to obtain a final solution (3 mL) of ABDA (1.00×10^{-4} M) and PS (30 µM) in water (10% DMSO) or ACN (8% DMSO). Then, the cuvette was exposed to blue light (470 nm, 51.4 $mW \cdot cm^{-2}$) for 10 minutes and the UV-vis spectra were recorded at 0, 2, 4, 6, 8, and 10 minutes. The consumption of ABDA was measured by monitoring its absorbance intensity decrease at 400 nm over the irradiation period. As a control an ABDA solution without PS was monitored upon blue light irradiation in both solvents.

Photoinduced superoxide anion radical generation. DHR123 (TargetMol, USA) is used as superoxide anion radical indicator. The organic molecule **SQL** and $[Ru(bpy)_3]^{2+}$, used as reference, were prepared as 30 µM in water (3% DMSO) or ACN, DHR123 was prepared at 30 µM in water

or ACN adding at 3% DMSO. In a quartz cubete, 1 mL of PS solution and 1 mL of DHR123 solution were mixed with 1 mL of water or ACN to obtain a final solution (3 mL) of DHR123 (10 µM) and PS (10 µM) in water (1.1% DMSO) or ACN (0.1% DMSO). Then, the cuvette was exposed to blue light (470 nm, 51.4 $mW \cdot cm^{-2}$) for 180 minutes and the fluorescence spectra were recorded at 0, 30, 60, 90, 120, 150 and 180 minutes. As control, DHR123 solution without PS was monitored upon blue light irradiation in both solvents. For superoxide anion radical quenching experiment as quencher control, ascorbic acid (TCI, Japan) was added to the above solution at 1 mM before light irradiation. For SO quenching experiment, sodium azide (Thermo Scientific, USA) was added to the above solution at 1 mM before light irradiation.

3.5.3. *In vitro* assays

Cell line culture. Human cervical cancer HeLa, non-malignant human fibroblast 1Br3G, murine GBM GL261, human ovarian cancer A2780, CDDP-resistant counterpart A2780/cis, and human lung adenocarcinoma A549 cell lines were obtained from the American Type Culture Collection (ATCC, USA). Specifically, HeLa was cultured in minimum essential medium (MEM Alpha) enriched with 1% GlutaMAX™-, 1Br3G and GL261 in Dulbecco's modified eagle medium enriched with 4.5 $g \cdot L^{-1}$ D-glucose (DMEM (1X) + GlutaMAX™-), A2780 in Roswell park memorial institute medium 1640 (RPMI 1640), A2780/cis in RPMI 1640 enriched with 1 µM of **CDDP**, and A549 in DMEM enriched with 1% L-glutamine. All culture media were enriched with 10% heat-inactivated fetal bovine serum (FBS), and 1% penicillin-streptomycin. The cells were grown as adherent monolayer in a 75 cm^2 cell-culture flask (Nunclon™ Delta Surface, Merck, Germany) and maintained in an incubator (HERAcell, 150i, Thermo Scientific, USA) at 37 °C in 5% CO_2 with a relative humidity of 95%. Cell culture media, FBS, antibiotics, PBS, trypsin, Trypan Blue were procured from Gibco® (Thermo Scientific, USA).

To subculture or collect cells, cells must be in the logarithmic phase growth, which is achieved at around 75% confluence. Once this confluence was reached, the culture medium was removed from the flask. Then, 5 mL of sterile PBS was added to the flask to wash the cells and remove any residual medium. After removing the PBS and repeating the same process once more, 3 mL of trypsin was added, the flask was then returned to the incubator for 3 minutes. If, upon observing the cells under the microscope, ≥ 90% of the cells were detached, 6 mL of fresh medium was added to neutralize the trypsin and facilitate cell collection. The cell suspension was then transferred to a 15 mL Falcon™ tube (Cultek, Spain) and centrifuged (Digicen 21, Ortoalresa, Spain) at 1200 rpm for 5 minutes to collect the cells. The supernatant was discarded, and the cell pellet was resuspended in fresh medium to the desired dilution factor. Then, 1 mL of this resuspension was added to a flask containing 13 mL of fresh medium. To seed the required amount, a cell count was performed, and the necessary number of cells were seeded into the corresponding plate for each experiment.

Cell counting. Cell counting was performed using a Neubauer hemocytometer and Trypan Blue for cell viability assessment. Trypan Blue is a dye that differentiates living cells from dead ones, as dead cells cannot extrude Trypan Blue due to a lack of necessary energy-dependant mechanisms. An aliquot of 10 µL of the cell suspension to be studied was mixed with 10 µL of Trypan Blue. Next, 10 µL of the mixture were placed into the Neubauer hemocytometer, and the number of living cells was counted using an optical microscope.

Cytotoxicity assays of pPtBC. HeLa, 1Br3G, GL261, A2780, and A2780/cis cell lines in the exponential growth phase were seeded into a 96-well plate (Sudelab, Spain) under optimal conditions. Each cell type was seeded at specific densities: HeLa at 2,000 cells/well, 1Br3G at 3,000 cells/well, GL261 at 4,000 cells/well, and both A2780 and A2780/cis at 3,000 cells/well. Specifically, CDDP-containing cell culture media were replaced with fresh RPMI medium without the drug 4 hours before seeding. After 24-hours of incubation, fresh media containing compounds (**pPtBC NPs**, **PtBC**, and **CDDP**) at various concentrations (0, 0.1, 1, 5, 10, 25, 50, 100, 200 µM referred to Pt concentration) were added, and the plates were incubated for either 24 or 72 hours. Subsequently, 10 µL of PrestoBlue™ (0.15 $mg \cdot mL^{-1}$, Thermo Scientific, USA) were added to each treated well, as well as to three wells containing only medium. The plates were then further incubated at 37 °C for 4 hours before measuring the fluorescence at 572 nm with excitation at 531 nm using the Victor3 microplate reader (Perkin Elmer, USA). All experiments were conducted in triplicate, and the data analysed. The calculated IC_{50}s were obtained using GraphPad Prism (version 8.0).

Photocytotoxicity assays of SQL NPs. A549 cell line in the exponential growth phase were seeded into a 96-well plate (Sudelab, Spain) at a density of 3,000 cells/well and allowed to attach for 24 hours. A NPs suspension at 5 $mg \cdot mL^{-1}$ was diluted with cell culture medium at concentrations ranging from 0.2 to 250 $\mu g \cdot mL^{-1}$ for cell treatments. Cells were treated in dark conditions or following a photoactivation protocol, which consisted of the pre-incubation with the NPs for 4 hours to enable their intracellular accumulation, followed by 1 hour of blue light irradiation (λ: 460 nm) with an LED system (LuxLight) that provided a total light dose of 24.1 $J \cdot cm^{-2}$. After 48 hours, the treatments were removed, cells were washed with PBS, and the effect of the complexes on cell viability were determined by MTT assay. Cells were incubated for 2 hours with 100 µL of culture medium supplemented with 10 µL of MTT (Merck, USA) at 0.5 $mg \cdot mL^{-1}$. After discarding the medium, DMSO was added to each well to dissolve the purple formazan crystals. The absorbance of the wells was determined on a Multiscan Plate Reader (Synergy 4, Biotek, USA) at a wavelength of 570 nm. The effect of each treatment was analyzed in triplicate in three independent experiments. The IC_{50} of the NP required was established based on the dose-response curves generated with the Gen5 software (BioTek, USA).

Cellular internalisation studies

CDDP, **PtBC,** and **pPtBC NPs** internalisation: HeLa, 1Br3G, and GL261 cell lines were seeded in six-well plates (Sudelab, Spain) at a density of 300,000 cells/well, in a final volume of 1.5 mL of cell culture media. Following a 24-hour incubation, the old media was replaced with 1 mL of fresh media with **CDDP**, **PtBC**, and **pPtBC NPs** at a concentration of 0.1 mM referred to as Pt. The treated cells were allowed to internalise the compounds for 6 and 24 hours in the incubator. Another cellular internalisation assay was conducted with a reduced concentration of Pt (10 µM) and extended time points of 2, 4, 8, and 24 hours. The media were promptly removed, and the cells were washed twice with cold PBS to eliminate excess compounds. Subsequently, 0.5 mL of trypsin was added to each well for 3 minutes, and a twofold volume of fresh media was added to neutralize the trypsin. After taking an aliquot from each well for cell counting, the remaining cell suspensions were collected into 1.5 mL Eppendorf® tubes (Corning, USA) and centrifuged at 12,000 rpm for 4 minutes. The supernatants were discarded, and the cell pellets were stored at

−80 °C for further quantification by ICP-MS. All experiments were conducted in triplicate, and the data analysed using GraphPad Prism (version 8.0).

SQL NPs internalisation: A549 cell line were seeded in six-well plates (Sudelab, Spain) at a density of 150,000 cells/well, in a total volume of 1 mL of cell culture media. After a 24-hour incubation period, the old media was replaced with 1 mL of new media with SQL NPs at a concentration of 100 $\mu g \cdot mL^{-1}$. The treated cells were allowed to internalize the NPs for 6 hours at the incubator. The media was promptly removed, and the cells were washed twice with cold PBS to eliminate excess NPs. Subsequently, 1 mL of PBS was added, and each well was scraped. Cells were then collected into 1.5 mL Eppendorf® tubes (Corning, USA) and centrifuged at 1,200 rpm for 5 minutes. The supernatants were discarded, and 1 mL of PBS with 1% of SDS or 1 mL of THF were added to lyse the cells. Then, all samples were sonicated for 15 minutes and centrifuged at 12,000 rpm for 5 minutes. The supernatants were collected and measured using fluorescence spectroscopy with excitation wavelength at 678 nm and emission wavelength of 718 nm. All experiments were conducted in triplicate, and the data analysed using GraphPad Prism (version 8.0).

DNA-bound Pt studies. HeLa, 1Br3G, and GL261 cell lines in exponential growth phase were seeded onto cell culture dishes under optimal conditions for each cell line, reaching 50–60% confluence within 24 hours before treatment. Subsequently, **CDDP**, **PtBC**, and **pPtBC NPs** were added at a concentration of 0.1 mM referred to Pt, and the cells were allowed to incubate for an additional 24 hours. Following this incubation period, media containing drugs were removed, and the cells were washed, trypsinised, collected by centrifugation, and rinsed twice with cold PBS to eliminate excess drugs. The resulting cell pellets were resuspended in lysis buffer (pH 8.0, 150 mM Tris-HCl, 100 mM NaCl, and 0.5% (w/v) SDS). The pellets in the buffer were incubated on ice for 15 minutes and then centrifuged at 15,000 rpm for 15 minutes. To each supernatant, 0.1x of the original volume was added of RNase A at 0.2 $mg \cdot mL^{-1}$, and incubated for 1 hour at 37 °C. Subsequently, proteinase K was added at 0.1 $mg \cdot mL^{-1}$ and incubated for 3 hours at 56 °C. Phenol/chloroform/isoamyl alcohol (25:24:1 v/v/v, Thermo Scientific, USA) was added and mixed gently. After a centrifugation of 3 minutes at 15,000 rpm, aqueous phases containing DNA were transferred into sterile tubes. DNA was precipitated with 3 M sodium acetate and absolute ethanol at −20 °C overnight (0.1:1). Then, the DNA samples were centrifuged for 15 minutes at 15,000 rpm, and finally, DNA samples were dried and resuspended in 0.1 mL of elution buffer (pH 8.0, 10 mM Tris-HCl, 1 mM ethylenediaminetetraacetic acid (EDTA)). The concentration of isolated DNA was quantified by measuring the absorbance at 260 nm using a NanoDropTM 1,000 spectrophotometer (Thermo Scientific, USA). The remaining samples were frozen for ICP-MS analysis.

Cell pellets digestion treatments for ICP-MS measurements. Cell pellets were resuspended in approximately 100 mL of concentrated ultrapure HNO_3 (69%, Ultratrace®, ppb-trace analysis grade, Scharlab, Spain) and left to digest overnight. The samples were heated to 90°C until the suspensions became clear. Subsequently, the samples were diluted with 0.5% (v/v) ultrapure HNO_3 to appropriate volumes for later measurements.

3.5.4. *In vivo* assays

Animal studies. Animal experiments and care were conducted in collaboration with duly accredited personnel. Healthy female C57BL/6J mice aged 8-12 weeks, with body weights 22 ± 2 g, were used for *in vivo* studies. The mice were procured from Charles River Laboratories (Charles River Laboratories International, USA) and were accommodated in the Universitat Autònoma de Barcelona's animal facility (Servei d'Estabulari, www.uab.cat/ca/servei-estabulari; accessed on 24 March 2022). Ethical approval for all animal study protocols was obtained from the local ethics committee (Comissió d'Ètica en l'Experimentació Animal i Humana, https://www.uab.cat/etica-recerca; accessed on 24 March 2022), following regional and state legislation (protocol CEEAH-4859). All animals were maintained in consistent housing and controlled conditions: 12-hours light/12-hours dark cycles (light from 8 am to 8 pm), temperature 22 ± 2 °C, relative humidity 55 ± 10%, water and standard food access *ad libitum*, and enriched environment.

Preclinical model generation and treatment administration for GBM anticancer efficacy. The C57BL/6J immunocompetent mice were exposed to enriched environment for 3 weeks before tumour induced, since it was reported that it could significantly reduce glioma growth and improve mice survival by increasing immunological parameters in the brain of mice.[297] Tumours were induced by stereotactic intracranial injection of 10^5 murine GBM GL261 cell line, obtained from the American Type Culture Collection (ATCC, USA), in caudate nucleus. For this, analgesia (meloxicam at 4.0 $mg \cdot kg^{-1}$, Meloxidyl, Ceva, USA) and anaesthesia, a mixture of ketamine (Ketamidor at 125 $mg \cdot kg^{-1}$, Richer pharma, Austria) and xylazine (Xilagesic at 15 $mg \cdot kg^{-1}$, Calier, Barcelona), were administrated subcutaneously and intraperitoneally, respectively. Once mice no longer responded to the toe pinch reflex, they were immobilised in a stereotaxic holder (Kopf Instruments, USA) in a prone position. Then, the incision area was shaved and sterilised, and a 1 cm incision was made to expose the skull. A 1 mm hole was drilled 0.1 mm posterior to Bregma and 2.32 mm to the right of the midline using a microdrill (Fine Science Tools, Germany). Then, a 26G Hamilton syringe (Hamilton Company, USA) positioned on a digital push-pull microinjector (Harverd Apparatus, USA) was used for the injection of 4 µL of 10^5 GL261 cells in medium at a depth of 3.35 mm from the skull surface, at a rate of 2 $\mu L \cdot min^{-1}$. After the injection, the Hamilton syringe remained in place for 2 minutes to minimize cell reflux, then was slowly and carefully withdrawn. Finally, the incision was closed with 6.0 silk suture (Braun, Germany) and disinfected with povidone-iodine (Betadine, Vemedia Pharma, Spain). Mice were actively monitored until fully recovered and were re-administered intraperitoneal analgesia after 24 hours.

To facilitate IN administration, the animals were anaesthetized with isoflurane for a minute and positioned in a supine orientation. Each nostril received a 2 µL dosage of the **pPtBC NPs** formulation, spaced with a 1–2 minutes interval between administrations. The well-being of treated animals was observed, and those exhibiting signs of distress were humanely euthanised in adherence to ethical considerations.

***Magnetic resonance imaging (*MRI).** Mice were subjected to non-invasive brain MRI scans to measure the volumes, localisation, and evolution of the tumour. All MRI studies were performed at the co-managed NMR facility of the Universitat Autònoma de Barcelona and Centro de Inverstigación Biomédica en Red – Bioingeniería, Biomateriales y Nanomedicina (CIBER-BBN, Spain), Unit 25 of NANBIOSIS, http://www.nanbiosis.es. The 7T Bruker Biospec 70/30 USR

spectrometer (Bruker BioSpin GmbH, Germany) equipped with a mini-imaging gradient set (400 $mT \cdot m^{-1}$) was used for MR acquisitions.

Mice were placed in a dedicated imaging bed equipped with an integrated heating system to maintain body temperature and allowed for the administration of anaesthesia (1.5-2% isoflurane in O_2 at 1 $L \cdot min^{-1}$. Respiratory rate was monitored using a pressure probe and maintained between 60–80 breaths per minute. GL261 tumour-bearing mice underwent high-resolution traverse relaxation weighted (T_{2w}) MRI using a rapid acquisition with relaxation enhancement (RARE) sequence for brain tumour visualisation. The imaging parameters were as follows: repetition time (TR)/effective echo time (TE_{eff})=4200/36 ms; echo train length (ETL)=8; field of view (FOV)=19.2 × 19.2 mm; matrix size (MTX)=256 × 256 (75 × 75 µm/pixel); number of slices (NS)=10; slice thickness (ST)=0.5 mm; inter-ST (IT)=0.1 mm; number of averages (NA)=4; and acquisition time (TA)=6 minutes 43 seconds. MRI data were acquired and processed on a Linux workstation using ParaVision 5.1 software (Bruker BioSpin GmbH, Germany).

Tumour volumes were calculated from the MRI scans by delineated regions of interest (ROIs) in each slice using ParaVision 5.1 software to measure tumour area. Subsequently, mice tumour volumes were computed using the following Equation 3.2:

$$TV(mm^3) = \left[(AS_1\ x\ ST)\ +\ \left(\sum_2^{10} AS\ x\ (ST\ +\ IT)\right)\right] x0.075^2 \quad \text{Equation } \mathbf{3.2}$$

where TV is the tumour volume, AS indicates the number of pixels within the ROI defined by tumour boundaries in each MRI slice, ST is the slice thickness (0.5 mm), IT is the inter-ST (0.1 mm), and 0.075^2 signifies the individual pixel surface area in mm^2.

Tolerability assays. Healthy female C57BL/6 mice, aged 8-12 weeks and weighing 20-24 g, were randomly assigned to three groups: control, **PtBC**, and **pPtBC NPs**, with three mice in each group. The drugs were IN administered using a micropipette, while the mice were lightly anaesthetized and positioned horizontally for the procedure. The dosage started at 0.9 mg $Pt \cdot kg^{-1}$ body weight and gradually increased incrementally to 1.5 mg $Pt \cdot kg^{-1}$ over 3 weeks, with doses administered weekly. Initial body weights were recorded, and subsequent monitoring occurred three times a week. Throughout the 4-week study, veterinary personnel closely monitored mice for mortality, food and water consumption, and suffering clinical signs. To assess tolerability in treated mice, we used statistical comparisons among groups utilizing a one-way analysis of variance followed by Bonferroni's multiple comparison test for three or more groups. A statistically significant p value was considered when less than 0.05.

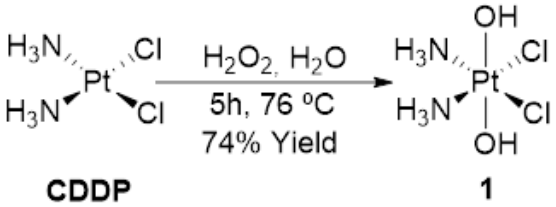
Biodistribution study. For the study, Pt CNPs were administered through IN delivery at a dosage of 1.5 mg $Pt \cdot kg^{-1}$ body weight in GL261 GBM tumour-bearing mice. After 1 hour, the mice were euthanised, and organs such as the brain, tumour, heart, lungs, spleen, liver, and kidneys were removed and weighed. These collected tissues underwent homogenisation in tissue protein extraction reagent (T-PER™, Thermo Scientific, USA) buffer using an ultrasound probe (Branson SFX Ultrasonic disintegrator, Emerson, USA) with 30% amplitude and cycles of 10 seconds on and 15 seconds off. Next, the samples underwent centrifugation at 10,000 rpm for 10 minutes. A portion of each supernatant was extracted for total protein quantification, while the remaining fraction was subjected to digestion following the previously outlined procedure. This prepared the samples for ICP-MS measurement, enabling the determination of Pt concentration.

Tissue digestion treatment for ICP-MS measurements. Tissues were combined with T-PER™ buffer (Thermo Scientific, USA) at a ratio of 10 mL·g^{-1}, then cut into small pieces and subjected to sonication using an ultrasonication microtip (Branson Digital Sonifier 450, Emerson, USA) over repetitive cycles of 10 seconds active and 15 seconds inactive with an amplitude of 40%. The tissue suspensions were then added with aqua regia (all ppb-trace analysis grade) and heated up to 300 °C, with 30% H_2O_2 added in the later digestion process until the suspensions became clear. The clear solutions were then transferred and diluted with 0.5% (v/v) ultrapure HNO_3 to appropriate volumes for the determination of metal contents using ICP-MS.

Statistical analysis. Data were analyzed using GraphPad Prism (version 8.0) and values are represented as the mean ± SE of three independent experiments. Statistical differences were calculated using one-way ANOVA, followed by Turkeys multiple comparison test. The significance threshold for all tests was set at $p < 0.05$, and values falling between 0.05 and 0.1 were regarded as a "trend toward significance".

3.5.5. Synthesis procedures

Synthesis of c,c,t-Pt(NH3)$_3$Cl$_2$(OH)$_2$ (1)



Scheme **3.1**. Synthesis of c,c,t-Pt(NH3)3Cl2(OH)2 (**1**) from **CDDP**.

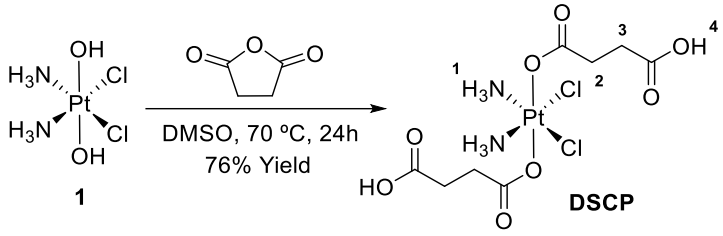
To a suspension of **CDDP** (1.3 g, 4.3 mmol) in 35.8 ml MilliQ® water, hydrogen peroxide 30% (35.8 mL) was added. The resulting pale-yellow suspension was heated to 76 °C for 5 hours under reflux and in the absence of light. Afterwards, the mixture was allowed to cool down to room temperature overnight under continuous stirring. The obtained suspension was then left in the fridge for 3 hours.

The precipitated yellow crystals were then isolated by filtration and washed with ice-cold water, ethanol and ether, affording the final product **1** as a granular crystalline yellow solid (1.063 g, 3.1 mmol, 74% yield)

Spectroscopic information of **1**:

IR *v*: 3783 (m), 3694 (w), 3661 (w), 3579 (w), 3515 (s), 3258 (s), 2989 (s), 2722 (s), 2508 (w), 2445 (m), 2445 (m), 2274 (s), 2107 (s), 1813 (s), 1585 (s), 1488 (m), 1356 (s), 1037 (s), 964 (s), 904 (s), 557 (s), 452 cm^{-1} (s).

Synthesis of dissuccinic cisplatin (DSCP)



Scheme **3.2**. Synthesis of **DSCP** from c,c,t-Pt(NH3)3Cl2(OH)2 (**1**).

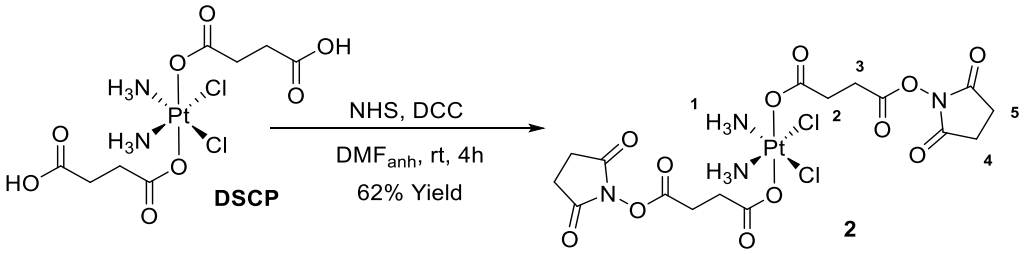
Oxoplatin **1** (561.2 mg, 1.68 mmol) and succinic anhydride (674 mg, 6.74 mmol) were suspended in anhydrous DMSO (2 mL). The resulting suspension was then heated to 76 °C in the dark for 24 hours. The resulting clear yellow solution was lyophilised to remove the solvent. The viscous residue was then sonicated with ethyl acetate to yield a light-yellow solid in suspension.

The precipitate was then filtered and washed with ice-cold acetone, yielding the final **DSCP** product as a light-yellow powder (686 mg, 1.283 mmol, 76% Yield).

Spectroscopic information of **DSCP**:

^{1}H-NMR (360 MHz, DMSO-d_6) δ 12.07 (s, 2H^4), 6.48 (bs, 3H^1), 2.41 – 2.28 (m, 4H^3).; **IR** (KBr) *v*: 3467 (m), 3278 (s), 3081 (s), 3933 (w), 2631 (m), 1734 (s), 1709 (m), 1684 (s), 1661 (s), 1630 (s), 1581 (m), 1551 (w), 1425 (m), 1390 (m), 1346 (s), 1294 (s), 1265 (w), 1210 (s), 1180 (s), 1014 (s), 956 (s), 799 (w), 713 (w), 671 (s), 592 (m), 481 (s) cm^{-1}

Synthesis of diaminobis((4-((2,5-dioxopyrrolidin-1-yl)oxy)-4-oxobutanoyl)oxy)Pt(IV) chloride (2)



Scheme **3.3**. Synthesis of diaminobis((4-((2,5-dioxopyrrolidin-1-yl)oxy)-4-oxobutanoyl)oxy)Pt(IV) chloride (**2**) from of **DSCP**.

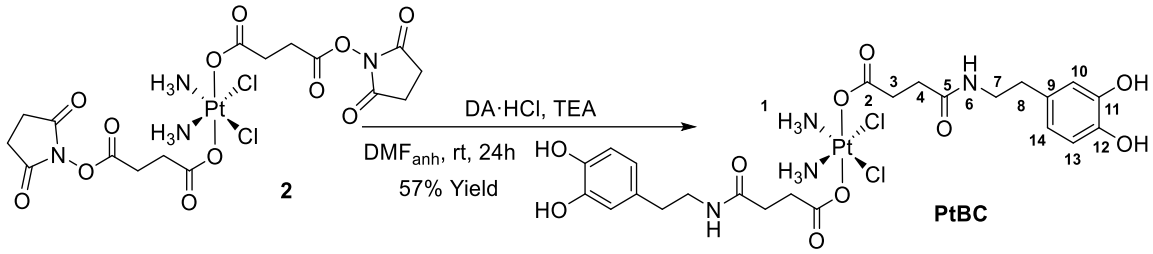
DSCP (0.5 g, 0.93 mmol), DCC (0.58 g, 2.8 mmol), and NHS (0.43 g, 3.75 mmol) were dissolved in anhydrous DMF (4 mL) under argon in the dark. The resulting solution was then stirred overnight. The resulting slurry mixture was stored in the freezer for 4 hours.

The resultant white precipitate, dicyclohexylurea, was removed by filtration. Subsequent to this, a large amount of ethyl acetate was poured into the filtrate and sonicated to obtain an off-white precipitate, which was washed with cold ether and dried to yield the activated ester succinic acid-NHS **2** (0.407 mg, 0.58 mmol, 62%).

Spectroscopic information of **2**:

^{1}H-NMR (360 MHz, DMSO-d6) δ 6.47 (s, 6H^1), 2.85-2.76 (m, 12H^{2,4,5}), 2.64 (t, $J_{3,2}$ = 6.8 Hz, 4H^3).

Synthesis of diaminobis((4-((3,4-dihydroxyphenethyl)amino)-4-oxobutanoyl)oxy)Pt(IV) chloride (PtBC)



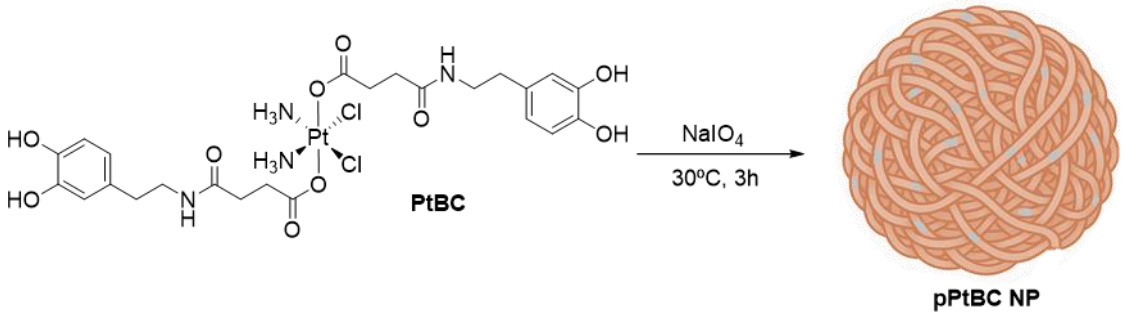
Scheme **3.4**. Synthesis of **PtBC** from diaminobis((4-((2,5-dioxopyrrolidin-1-yl)oxy)-4-oxobutanoyl)oxy)platinum(IV) chloride (**2**).

The activated ester succinic acid-NHS (130 mg, 0.19 mmol) and DA hydrochloride (84 mg, 0.37 mmol) were dissolved in anhydrous DMF (0.6 mL). Triethylamine (TEA, 260 µL, 1.2 mmol) was then added to the solution. As a result, the milky suspension changed to a clear yellow solution. The resulting solution was then left stirring for 24 hours. The reaction was stopped and transferred to a flask filled with toluene. The solvent mixture was then removed under reduced pressure to yield a brownish residue. The crude reaction product was then purified by reverse-phase open-column chromatography with a gradient from 5:95 to 40:60 methanol:water (v/v). Lyophilisation of the collected fractions yielded the final **PtBC** prodrug as a clear yellow powder (85 mg, 0.106 mmol, 57% yield).

Spectroscopic information of **PtBC**:

^{1}H-NMR (400 MHz, Methanol-d4) δ 6.70 (d, $J_{10,14}$ = 8.0 Hz, 1H^{10}), 6.67 (d, $J_{13,14}$ = 2.1 Hz, 1H^{13}), 6.55 (dd, $J_{14,10}$ = 8.1, $J_{14,13}$ = 2.1 Hz, 1H^{14}),3.37-3.35 (m) 2.67 (t, $J_{8,7}$ = 6.5 2H^{8}), 2.62 (t, $J_{3,2}$ = 6.7 Hz, 2H^{3}), 2.44 (t, $J_{2,3}$ = 6.7 Hz, 2H^{2}). **^{13}C-NMR** (101 MHz, MeOD) δ 181.04 (s, C^{2}), 173.85(s, C^{6}), 144.78 (s, C^{11}), 143.30 (s, C^{9}), 130.82 (s, C^{12}), 119.70 (s, C^{14}), 115.54 (s, C^{10}), 114.98 (s, C^{13}), 41.06 (s, C^{7}), 34.46 (s, C^{8}), 31.33 (s, C^{3}), 31.05 (s, C^{2}); **IR *v***: 3609 (w), 3219 (s), 2939 (w), 1716 (w), 1678 (w), 1620 (s), 1558 (s) 1527 (s), 1442 (m), 1328 (s), 1283 (s), 1198 (s), 1115 (s), 958 (s), 872 (m), 796 (s), 683 (m) cm^{-1}; **HRMS (ESI+) *m/z***: [M+H]$^{+}$ Calcd for $C_{24}H_{34}Cl_2N_4O_{10}Pt$ 805,1361; found 805,1353 and [M+Na]$^{+}$ Calcd for $C_{24}H_{34}Cl_2N_4O_{10}Pt$ 827,1180; found 827,1166.

Synthesis of polymeric Pt(IV) bis-catechol NPs (pPtBC NP)



Scheme **3.5**. Synthesis of **pPtBC NP** from **PtBC**.

PtBC (10.0 mg, 0.013 mmol) was dissolved in 6 mL of a 1:1 mixture ethanol:MilliQ® water. Sodium periodate (5.3 mg, 0.024 mmol) was dissolved in 0.4 mL of MilliQ® water. The sodium periodate solution was then added dropwise to the **PtBC** solution, while heated to 30 °C.

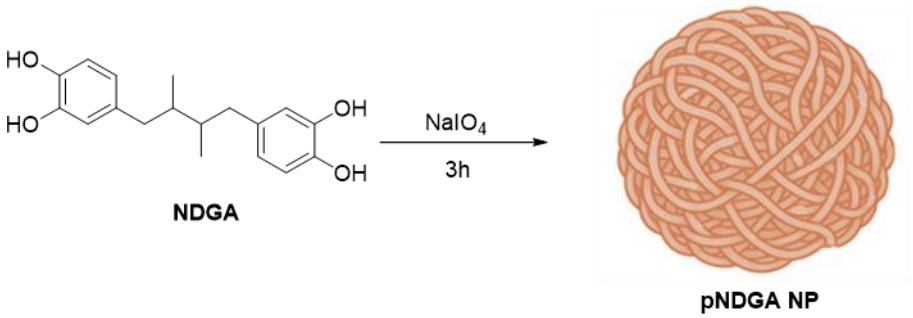
Addition was carried out with a syringe pump and over a period of 1 hour under vigorous stirring. The reaction was then allowed to evolve for 3 hours, heated at 30 °C, and kept in the dark.

The product was then isolated by centrifugation and washed multiple times with ethanol and water, and resuspended in water for storing, yielding **pPtBC NPs** as a brown turbid suspension in a 3.0 mg yield.

Spectroscopic information of **pPtBC NPs**:

IR (KBr) ν: 3256 (s), 1638 (s), 1564 (s), 1438 (w), 1338 (w), 1258 (s), 1173 (w), 1022 (m), 876 (w), 771 (m), 725 (s), 541 (w), 514 (s) cm-1; **Z-Ave (H_2O)** 214.2 ± 0.8 nm; **PDI (H_2O)** 0.07 ± 0.02; **ζ-pot** -37.1 ± 0.95 mV. **ICP-MS Pt** (%(w/w)) calcd. 24% found 17%

Synthesis of polymeric nordihydroguaiaretic acid NPs (pNDGA NPs)



Scheme **3.6**. Synthesis of **pNDGA NPs** from **NDGA**.

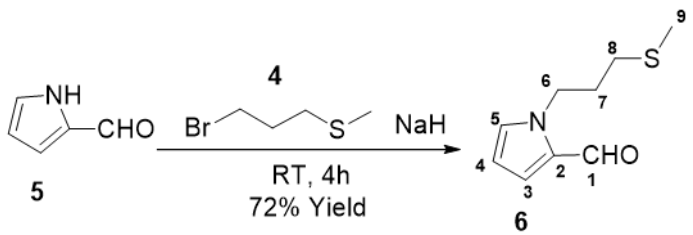
NDGA (20.0 mg, 0.066 mmol) was dissolved in 28 mL of a 1:1 mixture ethanol: MilliQ® water. Sodium periodate (28.2 mg, 0.132 mmol) was dissolved in 4 mL of MilliQ® water. The sodium periodate solution was then added dropwise to the **NDGA** solution. Addition was carried out with a syringe pump, and over a period of 1 hour under vigorous stirring. The reaction was then allowed to evolve for 3 hours in the dark.

The product was then isolated by centrifugation and washed multiple times with ethanol and water, and resuspended in water for storing, yielding 4.5 mg of the **pNDGA NPs** as a brown turbid suspension.

Spectroscopic information of **pNDGA NPs**:

IR (KBr) ν: 3414 (s), 2960 (s), 2929 (s), 2876 (w), 1725 (m), 1663 (s), 1631 (w), 1504 (s), 1443 (s), 1380 (s), 1279 (s), 1230 (w), 1108 (w), 871 (m), 819 (w) cm-1; **Z-Ave (H_2O)** 234.6 ± 0.5 nm; **PDI (H_2O)** 0.087 ± 0.022; ζ-pot -28.7±0.5 mV.

Synthesis of 1-(3-(methylthio)propyl)-1H-pyrrole-2-carbaldehyde (6)



Scheme **3.7**. Synthesis of 1-(3-(methylthio)propyl)-1H-pyrrole-2-carbaldehyde (**6**) from 1H-pyrrole-2-carbaldehyde (**5**).

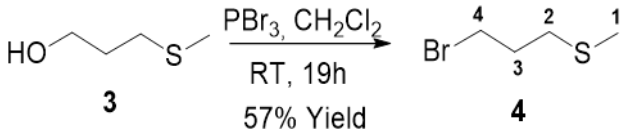
A solution of **4** (1.80 g, 18.4 mmol), in 10.0 mL of anhydrous DMF, was added dropwise to a solution of NaH (60% suspension in mineral oil, 0.74 g, 18.4 mmol) in 15 mL of anhydrous DMF under a nitrogen atmosphere. Afterwards, the solution was left stirring for 30 minutes. **5** (1.75 g, 10.5 mmol) was then added dropwise, leaving the resulting suspension stirring for 4 hours at room temperature. Following up, the reaction was stopped by adding 60 mL of water. Extractions were performed with 30 mL of diethyl ether, and the organic phase washedwith 15 mL of water. The total of organic phases was dried with sodium sulphate anhydrous, filtered and evaporated under reduced pressure conditions, obtaining a dark yellow oil.

The product was then purified by column chromatography (silica gel, hexane/Et_2O, 9:1), obtaining the final product **6** (1.37 g, 7.5 mmol, 72% yield) as a yellow oil.

Spectroscopic information of **6**:

^{1}H-NMR (360 MHz, Chloroform-*d*) δ 9.53 (s, 1H^1), 6.99 (m, 1H^3), 6.94 (m, 1H^5), 6.22 (m, 1H^4), 4.42 (t, $J_{6,7}$ = 6.8 Hz, 2H^6), 2.43 (t, $J_{8,7}$ = 7.0 Hz, 2H^8), 2.10 – 2.02 (m, 5H^{9,7}).

Synthesis of (3-bromopropyl)(methyl)sulfane (*4*)



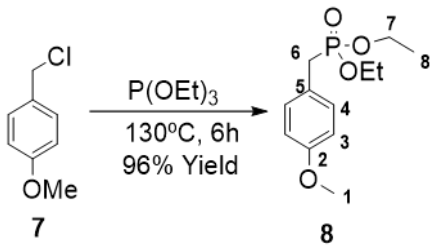
Scheme **3.8**. Synthesis of (3-bromopropyl)(methyl)sulfane (**4**) from 3-(methylthio)propan-1-ol (**3**).

A solution of phosphorous tribromide (2.50 g, 2.44 mL, 23.7 mmol) in 15 mL of anhydrous dichloromethane was prepared and cooled down with an ice bath. Afterwards, a solution of **3** (2.77 g, 0.97 mL, 10.3 mmol) in 10 mL of anhydrous dichloromethane was added dropwise to the reaction mixture under nitrogen atmosphere. The ice bath was withdrawn, and the reaction mixture was left to react overnight at room temperature for a total of 19 hours. The reaction was then stopped by adding 5 mL of water dropwise while cooling the reaction with an ice bath. The organic phase was washed over with 25 mL of $NaHCO_3$ and 25 ml of brine. The organic phase is dried over with sodium sulphate anhydrous, filtered and evaporated under reduced pressure conditions, obtening the final product **4** (2.26 g, 13.4 mmol, 57% yield).

Spectroscopic information of **4**:

^{1}H-NMR (360 MHz, Chloroform-*d*) δ 3.53 (t, $J_{4,3}$ = 6.5 Hz, 2H^4), 2.65 (t, $J_{2,3}$ = 7.0 Hz, 2H^2), 2.20 – 2.08 (m, 5H^{3,1}).

Synthesis of diethyl (4-methoxybenzyl)phosphonate (8)



Scheme **3.9**. Synthesis of (4-methoxybenzyl)phosphonate (**8**) to 1-(chloromethyl)-4-methoxybenzene (**7**).

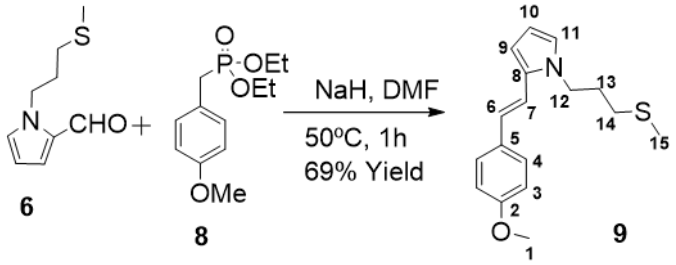
A mixture of **7** (1.45 mL, 10.84 mmol) and triethyl phosphate (3.56 mL, 32.53 mmol) was heated to 130 °C and followed by NMR for a total of 6 hours. Excess of triethyl phosphate was eliminated by evaporation under reduced pressure, affording **8** as a green oil.

The product was then purified by column chromatography (silica gel, hexane/ethyl acetate, 1:1, v/v), giving the pure final product **8** as a yellow oil (2.68 g, 10.00 mmol, 96% yield)

Spectroscopic information of **8**:

^{1}H-NMR (360 MHz, Chloroform-*d*) δ 7.24 (dd, *J* = 8.8, 2.5 Hz, 2H^4), 6.89 (m, 2H^3), 4.11 (dqt *J* = 7.1, 1 Hz, 4H^7), 3.8 (s, 2H^1), 3.11 (d, *J* = 2.5 Hz 2H^6), 1.36-1.27 (dt, *J* = 7.1, 1.0 Hz, 6H^8).

Synthesis of (E)-2-(4-methoxystyryl)-1-(3-(methylthio)propyl)-1H-pyrrole (9)



Scheme **3.10**. Synthesis of (E)-2-(4-methoxystyryl)-1-(3-(methylthio)propyl)-1H-pyrrole (**9**) from 1-(3-(methylthio)propyl)-1H-pyrrole-2-carbaldehyde (**6**).

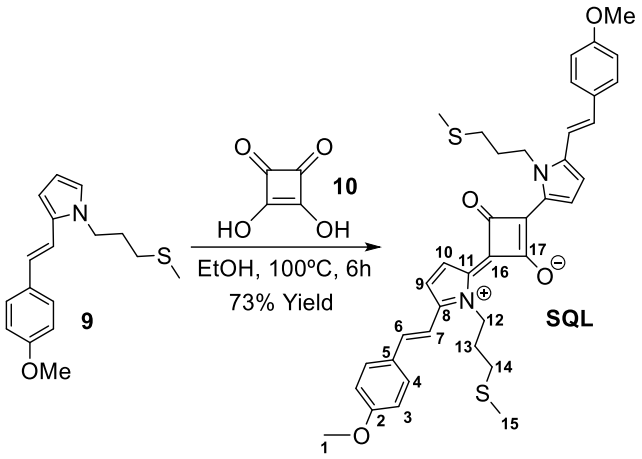
A solution of **6** (1.83 g, 7.1 mmol) in 7 mL of DMF anhydrous was added dropwise to a suspension of NaH (60% suspension in mineral oil, 0.65 g, 16.3 mmol) in 20 mL of DMF while cooling with an ice bath. The resulting solution was then left to stir for 30 minutes under nitrogen atmosphere. Afterwards, a solution of **8** (1,30 g, 7.1 mmol) in 10 mL of DMF was added dropwise while cooling with an ice bath under nitrogen atmosphere. The resulting mixture was then heated slowly from 30 to 50 °C and finally left heating for 1 hour. The resulting solution was then cooled to 0 °C, and 70 mL of water was added. Afterwards, extractions were made with 35 mL of ether three times. The combined organic phases were then dried with sodium sulphate anhydride and filtered.

The final product **9** was then obtained after purification by column chromatography (silica gel, hexane/ethyl acetate 9:1, v/v), affording the pure final product (1.41 g, 4.9 mmol, 69% yield) as a thick yellowish oil.

Spectroscopic information of **9**:

^{1}H-NMR (250 MHz, Chloroform-*d*) δ 7.39 (d, $J_{4,3}$ = 8.1 Hz, 2H^4), 6.94 – 6.82 (m, 5H^{3,6,7}), 6.68 (bs, 1H^{11}), 6.45 (bs, 1H^9), 6.16 (bs, 1H^{10}), 4.11 (t, $J_{12,13}$ = 6.8 Hz, 2H^{12}), 3.82 (bs, 3H^1), 2.46 (t, $J_{14,13}$ = 6.9 Hz, 2H^{14}), 2.15 – 1.95 (m, 5H^{13,15}).

Synthesis of (E)-2-(5-((E)-4-methoxystyryl)-1-(3-(methylthio)propyl)-1H-pyrrol-2-yl)-4-(5-((E)-4-methoxystyryl)-1-(3-(methylthio)propyl)-2H-pyrrol-1-ium-2-ylidene)-3-oxocyclobut-1-en-1-olate (SQL)



Scheme **3.11**. Synthesis of **SQL** from (E)-2-(4-methoxystyryl)-1-(3-(methylthio)propyl)-1H-pyrrole (**9**).

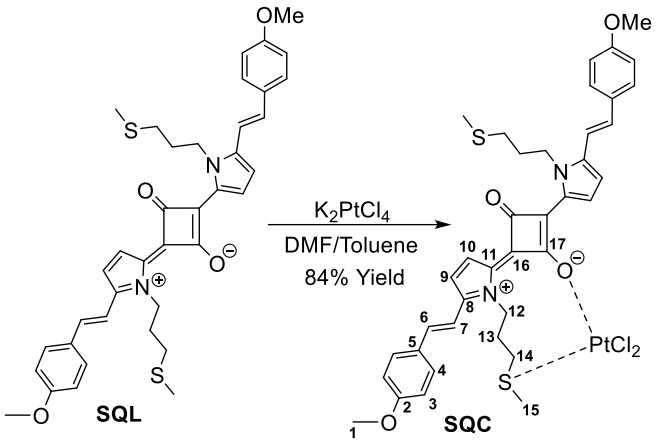
A solution of **10** (17.5 mg, 0.15 mmol) and **9** (88.0 mg, 0.31 mmol) were dissolved in 4 mL of ethanol and left stirring for 16 hours at reflux temperature. Afterwards, the solvent was removed partially under reduced pressure, and the thick paste of the crude product was poured into petroleum ether.

The precipitate obtained was collected by filtration and redissolved in the least amount of dichloromethane possible. **SQL** was precipitated with the slow addition of hexane while cooling in an ice bath. The final product **SQL** was then obtained by filtration, affording the pure final product **SQL** (73.3 mg, 0.11 mmol, 73% yield) as a dark blue crystal.

Spectroscopic information of **SQL**:

^{1}H-NMR (250 MHz, Chloroform-*d*) δ 7.83 (d, $J_{10,9}$ = 4.6 Hz, 2H^{10}), 7.52 (d, $J_{4,2}$ = 8.5 Hz, 4H^4), 7.09 (d, $J_{6,7}$ = 16.0 Hz, 2H^7), 6.93 (d, $J_{2,4}$ = 8.6 Hz, 4H^3), 6.87 (d, $J_{9,10}$ = 4.7 Hz, 2H^9), 4.93 (t, $J_{12,13}$ = 7.0 Hz, 4H^{12}), 3.85 (s, 6H^1), 2.59 (t, $J_{14,13}$ = 6.5 Hz, 4H^{14}), 2.24 – 1.97 (m, 10H^{15,13}). **^{13}C-NMR** (101 MHz, $CDCl_3$) δ 179.94, 159.02, 143.68, 134.38, 128.93, 128.65, 124.54, 121.63, 114.05, 112.11, 109.36, 55.94, 45.31, 31.04, 31.01, 15.62 ppm. **IR *ν*** (cm^{-1}): 2910.54 (w), 2832.95 (w), 1697.70 (s), 1595.91 (s), 1503.55 (w), 1484.29 (w), 1463.11 (w), 1434.62 (w), 1366.31 (s), 1296.74 (m), 1272.51 (w), 1242.35 (s), 1170.81 (s), 1094.44 (s), 1049.44 (W), 1022.42 (s), 943.35 (m), 855.95 (w), 812.53 (m), 666.67 (m), 546.94 (m) **HRMS (ESI+) *m/z***: $[M+H]^+$ Calcd for $C_{38}H_{40}S_2N_2O_4$ 653.2502 ; found 653.2486 and $[M+Na]^+$ Calcd for $C_{38}H_{40}S_2N_2O_4$ 675.2322; found 675.2321.

Synthesis of (E)-3-chloro-4-(5-(4-methoxystyryl)-1-(3-(methylthio)propyl)-1H-pyrrol-2-yl)cyclobut-3-ene-1,2-dione (14) with potassium tetrachloroplatinate (II) (SQC)



Scheme **3.12**. Synthesis of **SQC** from **SQL**.

A solution of **SQL** (35.52 mg, 0.054 mmol) and potassium tetrachloroplatinate (II) (22.59 mg, 0.054 mmol) in 1.6 mL of DMF and 1.6 mL of toluene under anhydrous conditions was left stirring for 72 hours.

The precipitated dark green powder was then isolated by filtration and washed progressively by water, ethanol, THF and hexane. Affording complex **SQC** (41.8 mg, 0.046 mmol, 83.6% yield) as a shiny dark green powder.

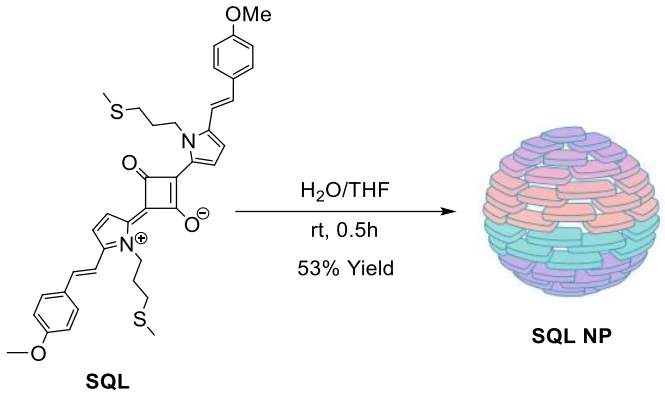
Spectroscopic information of **SQC**:

^{1}H-NMR (360 MHz, DMSO-d_6) δ 7.71 (d, $J_{4,3}$ = 8.4 Hz, 4H^{4}), 7.65 (bs, 2H^{10}), 7.56 (d, $J_{7,6}$ = 15.5 Hz, 2H^{6}), 7.28 (d, $J_{7,6}$ = 15.4 Hz, 2H^{7}), 7.16 (bs, 2H^{9}), 7.02 (d, $J_{4,3}$ = 8.0 Hz, 4H^{3}), 4.89 (bs, 3H^{12}), 3.82 (s, 6H^{1}), 1.98 (m, 10H^{15,13}) **^{13}C RMN** (101 MHz, CDCl3) δ 160.62, 146.46, 135.33, 129.11, 128.67, 114.51, 114.16, 113.40, 112.81, 77.21, 55.41, 44.95, 31.11, 29.69, 15.57 **IR *ν*** (cm^{-1}):3448.17 (w), 2911.89 (w), 2832.69 (w), 1595.47 (s), 1502.45 (m), 1459.44 (w), 1428.39 (m), 1295.75 (m), 1243.40 (s), 1167.51 (s), 1096.97 (s), 1022.87 (m), 944.88 (m), 803.99 (m), 627.09 (w), 505.53 (w). **HRMS (ESI+) *m/z***: [M+Na]$^{+}$ Calcd for $C_{38}H_{40}N_2O_4S_2Pt$ 941.1337; found 941.1352.

Synthesis of squaraine ligand NPs (SQL NP)

SQL (15 mg, 0.022 mmol) was dissolved in 4.5 mL of THF. The resulting **SQL** solution was then rapidly added to a round-bottom flask filled with 220 mL of MilliQ® water under constant magnetic stirring at 1500 rpm. The resulting suspension was left stirring for 30 minutes at room temperature.

Afterwards, the **SQL NPs** formed were isolated by centrifugation and washed with water multiple times. The resulting suspension was then dried under vacuum to yield a fine dark blue powder (8 mg, 0.012 mmol, 53% yield) and stored in the dark.



Scheme **3.13**. **SQL NP** from **SQL**.

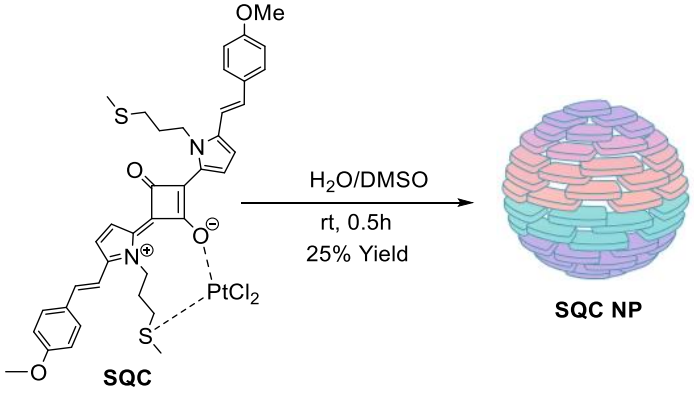
Spectroscopic information of ***SQL NP***:

IR *ν* (cm^{-1}): 2913.41 (w), 2834.05 (w), 1598.01 (s), 1505.02 (s), 1484.92 (w), 1463.17 (w), 1435.74 (w), 1384.46 (m), 1362.33 (m), 1295.02 (m), 1270.58 (w), 1246.35 (s), 1172.31 (s), 1095.08 (s), 1028.91 (s), 947,04 (s), 851.54 (w), 816.33 (s), 797.44 (w), 775.95 (w), 667.90 (w), 638.76 (w), 620.23 (w), 522.91 (w), 438.17 (w), 410.72 (w). **Z-Ave (H_2O)** 170.3 ± 7.1 nm **PDI (H_2O)** 0.06 ± 0.01 **ζ-pot** -21.4 ± 0.379 mV.

Synthesis of squaraine-Pt complex NPs (SQC NP)

SQC (1.0 mg, 0.012 mmol) was dissolved in 326 µL of DMSO. The resulting SQC solution was then rapidly added to a round-bottom flask filled with 14.6 mL of MilliQ® water under constant magnetic stirring at 1500 rpm. The resulting suspension was left stirring for 10 minutes.

Afterwards, the **SQL NP** formed were isolated by centrifugation and washed with water, THF and ethanol multiple times. The resulting suspension was then dried under vacuum to yield a fine dark blue powder **SQC NP** (0.25 mg, 2.5 µmol, 25% yield).



Scheme **3.14**. Synthesis of **SQC NP** from **SQC**.

Spectroscopic information of **SQC NP**:

IR *ν* (cm^{-1}): 2904.31 (s), 2832.88 (s), 1698.09 (s), 1598.91 (s), 1509.35 (w), 1461.44 (w), 1439.61 (w), 1418.86 (m), 1388.60 (m), 1359.43 (m), 1246.00 (s), 1172.14 (s), 1024.94 (s), 959.55 (w), 814.40 (s), 731.04 (w), 523.92 (m). **Z-Ave (H_2O)** 256.4 ± 2.0 nm **PDI (H_2O)** 0.27 ± 0.03 **ζ-pot** 30.6 ± 0.35 mV. **ICP-MS Pt** (%(w/w)) calcd. 21.2% found 8.6%.

3.6. References

1. Gómez-Herrera R, Alfonso-Triguero P, Mao X, et al. Bioinspired neuromelanin-like Pt(iv) polymeric nanoparticles for cancer treatment. *Nanotechnol Rev. 2024*;13(1). doi:10.1515/ntrev-2024-0118
2. García-Pardo J, Novio F, Nador F, et al. Bioinspired theranostic coordination polymer nanoparticles for intranasal dopamine replacement in parkinson's disease. *ACS Nano*. **2021**;15(5). doi:10.1021/acsnano.1c00453
3. Mao X, Wu S, Calero-Pérez P, et al. Synthesis and Validation of a Bioinspired Catechol-Functionalized Pt(IV) Prodrug for Preclinical Intranasal Glioblastoma Treatment. *Cancers*. **2022**;14(2). doi:10.3390/cancers14020410
4. Zhang H, Zhao T, Newland B, Liu W, Wang W, Wang W. Catechol functionalized hyperbranched polymers as biomedical materials. *Prog Polym Sci*. **2018**;78. doi:10.1016/j.progpolymsci.2017.09.002
5. Mao X, Calero-Pérez P, Montpeyó D, et al. Intranasal Administration of Catechol-Based Pt(IV) Coordination Polymer Nanoparticles for Glioblastoma Therapy. *Nanomaterials*. **2022**;12(7). doi:10.3390/nano12071221
6. Arias-Mainer C, Romero-Gavilán F, Cerqueira A, et al. Quercetin-doped sol–gel coatings on titanium implants: a promising approach for enhanced immune response and cell adhesion. *J Mater Chem B*. **2025**;13(24):7048-7061. doi:10.1039/D4TB02821J
7. Wu C, Ning X, Liu Q, Zhou X, Guo H. Sustained Release of Curcumin from Cur-LPs Loaded Adaptive Injectable Self-Healing Hydrogels. *Polymers*. **2024**;16(24):3451. doi:10.3390/polym16243451
8. Yan C, Zhang N, Guan P, et al. Drug-based magnetic imprinted nanoparticles: Enhanced lysozyme amyloid fibrils cleansing and anti-amyloid fibrils toxicity. *Int J Biol Macromol*. **2020**;153. doi:10.1016/j.ijbiomac.2020.03.061
9. Albrecht M. Catecholate-Based Helicates. *Eur J Inorg Chem*. **2020**;2020(23). doi:10.1002/ejic.202000255
10. Zhang W, Wang R, Sun ZM, et al. Catechol-functionalized hydrogels: Biomimetic design, adhesion mechanism, and biomedical applications. *Chem Soc Rev*. **2020**;49(2). doi:10.1039/c9cs00285e
11. Radu ER, Voicu SI, Thakur VK. Polymeric Membranes for Biomedical Applications. *Polymers*. **2023**;15(3). doi:10.3390/polym15030619
12. Zohoorian-Abootorabi T, Meratan AA, Jafarkhani S, Muronetz V, Haertlé T, Saboury AA. Modulation of cytotoxic amyloid fibrillation and mitochondrial damage of α-synuclein by catechols mediated conformational changes. *Sci Rep*. **2023**;13(1). doi:10.1038/s41598-023-32075-9
13. Tao L, Park JY, Lambert JD. Differential prooxidative effects of the green tea polyphenol, (-)-epigallocatechin-3-gallate, in normal and oral cancer cells are related to differences in sirtuin 3 signaling. *Mol Nutr Food Res*. **2015**;59(2). doi:10.1002/mnfr.201400485
14. Amaroli A, Panfoli I, Bozzo M, Ferrando S, Candiani S, Ravera S. The Bright Side of Curcumin: A Narrative Review of Its Therapeutic Potential in Cancer Management. *Cancers*. **2024**;16(14):2580. doi:10.3390/cancers16142580
15. Morshed AKMH, Paul S, Hossain A, et al. Baicalein as Promising Anticancer Agent: A Comprehensive Analysis on Molecular Mechanisms and Therapeutic Perspectives. *Cancers*. **2023**;15(7). doi:10.3390/cancers15072128
16. Çetinkaya M, Baran Y. Therapeutic Potential of Luteolin on Cancer. *Vaccines*. **2023**;11(3). doi:10.3390/vaccines11030554
17. Wang G, Wang Y, Yao L, et al. Pharmacological Activity of Quercetin: An Updated Review. *Evid. Based Complement. Altern. Med*. **2022**;2022. doi:10.1155/2022/3997190
18. Mokra D, Adamcakova J, Mokry J. Green Tea Polyphenol (-)-Epigallocatechin-3-Gallate (EGCG): A Time for a New Player in the Treatment of Respiratory Diseases? *Antioxidants*. **2022**;11(8). doi:10.3390/antiox11081566
19. Su J, Chen F, Cryns VL, Messersmith PB. Catechol polymers for pH-responsive, targeted drug delivery to cancer cells. *J Am Chem Soc*. **2011**;133(31). doi:10.1021/ja203077x
20. Chu S, Shi X, Tian Y, Gao F. pH-Responsive Polymer Nanomaterials for Tumor Therapy. *Front Oncol*. **2022**;12. doi:10.3389/fonc.2022.855019
21. Higashimura H, Kobayashi S. Oxidative Polymerization. In: *Encycl. Polym. Sci. Technol.*. **2016**. doi:10.1002/0471440264.pst226.pub2
22. Kresta J, Tkáč A, Păikryl R, Malík L. Polyphenylene Oxides - the Oxidative Coupling Polymerization of 2,6 Dimethylphenol With CuCl2 — Amine Complex. *J. ELASTOM. PLAST*. **1973**;5(1). doi:10.1177/009524437300500103
23. Erdtman H. Lignins: Occurrence, formation, structure and reactions, K. V. Sarkanen and C. H. Ludwig, Eds., John Wiley & Sons, Inc., New York, 1971. 916 pp. $35.00. *J Polym Sci B*. **1972**;10(3). doi:10.1002/pol.1972.110100315
24. Temma T, Habaue S. Highly selective oxidative cross-coupling polymerization with copper(I)-bisoxazoline catalysts. *J Polym Sci A Polym Chem*. **2005**;43(24). doi:10.1002/pola.21086
25. Saouti F, Belaaouad S, Cherqaoui A, Naimi Y. Polyaniline thin film prepared by electrochemical polymerization method. *Biointerface Res Appl Chem*. **2022**;12(4). doi:10.33263/BRIAC124.55235533
26. Reis R, Duke M, Merenda A, et al. Customizing the surface charge of thin-film composite membranes by surface plasma thin film polymerization. *J Memb Sci*. **2017**;537. doi:10.1016/j.memsci.2017.05.013
27. Tsuchiya K, Ogino K. Catalytic oxidative polymerization of thiophene derivatives. *Polym J*. **2013**;45(3). doi:10.1038/pj.2012.146

28. Zhang K, Dong X, Zeng B, Xiong K, Lang X. Red light photocatalysis of conjugated microporous polymers based on fused thiophenes for selective oxidation of amines. *J Colloid Interface Sci*. **2023**;651. doi:10.1016/j.jcis.2023.08.003
29. Li X, Cao M, Li S, et al. In-Situ Oxidative Polymerization of Pyrrole Composited with Cellulose Nanocrystal by Reactive Ink-Jet Printing on Fiber Substrates. *Polymers*. **2022**;14(19). doi:10.3390/polym14194231
30. Seike M, Uda M, Suzuki T, et al. Synthesis of Polypyrrole and Its Derivatives as a Liquid Marble Stabilizer via a Solvent-Free Chemical Oxidative Polymerization Protocol. *ACS Omega*. **2022**;7(15). doi:10.1021/acsomega.2c00327
31. Goyal M, Agarwal SN, Singh K, Bhatnagar N. Synthesis and characterization of poly [(3,4-ethylenedioxy) thiophene]:polystyrene sulfonate (PEDOT:PSS) for energy storage device application. *J Appl Polym Sci*. **2023**;140(19). doi:10.1002/app.53830
32. Charyton MK, Reiker T, Kotwica K, Góra M, Zacharias H, Boscher ND. Unsubstituted thiophene-diketopyrrolopyrrole conjugated polymer thin films via oxidative chemical vapor deposition - electronic behavior. *Mater Adv*. **2023**;4(12). doi:10.1039/d3ma00197k
33. Varala R, Dubasi N, Seema V, Kotra V. Sodium Periodate (NaIO 4) in Organic Synthesis. *SynOpen*. **2023**;7(4). doi:10.1055/a-2183-3678
34. Szukowska M, Popenda Ł, Coy E, et al. Replacing amine by azide: dopamine azide polymerization triggered by sodium periodate. *Polym Chem*. **2022**;13(22). doi:10.1039/d2py00293k
35. Wardman P. Reduction Potentials of One Electron Couples Involving Free Radicals in Aqueous Solution. *J Phys Chem Ref Data*. **1989**;18(4). doi:10.1063/1.555843
36. Lee H, Dellatore SM, Miller WM, Messersmith PB. Mussel-inspired surface chemistry for multifunctional coatings. *Science*. **2007**;318(5849). doi:10.1126/science.1147241
37. Dreyer DR, Miller DJ, Freeman BD, Paul DR, Bielawski CW. Elucidating the structure of poly(dopamine). *Langmuir*. **2012**;28(15). doi:10.1021/la204831b
38. Hong S, Na YS, Choi S, Song IT, Kim WY, Lee H. Non-covalent self-assembly and covalent polymerization co-contribute to polydopamine formation. *Adv Funct Mater*. **2012**;22(22). doi:10.1002/adfm.201201156
39. Burzio LA, Waite JH. Cross-linking in adhesive quinoproteins: Studies with model decapeptides. *Biochemistry*. **2000**;39(36). doi:10.1021/bi0002434
40. Miserez A, Rubin D, Waite JH. Cross-linking chemistry of squid beak. *J. Biol. Chem.*. **2010**;285(49). doi:10.1074/jbc.M110.161174
41. Yang J, Cohen Stuart MA, Kamperman M. Jack of all trades: Versatile catechol crosslinking mechanisms. *Chem Soc Rev*. **2014**;43(24). doi:10.1039/c4cs00185k
42. Lü JM, Nurko J, Weakley SM, et al. Molecular mechanisms and clinical applications of nordihydroguaiaretic acid (NDGA) and its derivatives: An update. *Med. Sci. Monit.*. **2010**;16(5).
43. Nkune NW, Abrahamse H. The Combination of Active-Targeted Photodynamic Therapy and Photoactivated Chemotherapy for Enhanced Cancer Treatment. *J Biophotonics*. **2025**;18(6). doi:10.1002/jbio.70005
44. Goetzfried SK, Hakkennes MLA, Busemann A, Bonnet S. Toward the Treatment of Glioblastoma Tumors Using Photoactivated Chemotherapy: In Vitro Evaluation of Efficacy and Safety. *ACS Pharmacol Transl Sci*. **2025**;8(2):484-498. doi:10.1021/acsptsci.4c00600
45. Smith ER, Wang JQ, Yang DH, Xu XX. Paclitaxel resistance related to nuclear envelope structural sturdiness. *Drug Resist. Updates.*. **2022**;65. doi:10.1016/j.drup.2022.100881
46. Chen Q, Cuello-Garibo JA, Bretin L, et al. Photosubstitution in a trisheteroleptic ruthenium complex inhibits conjunctival melanoma growth in a zebrafish orthotopic xenograft model. *Chem Sci*. **2022**;13(23). doi:10.1039/d2sc01646j
47. Cho IK, Shim MK, Um W, Kim JH, Kim K. Light-Activated Monomethyl Auristatin E Prodrug Nanoparticles for Combinational Photo-Chemotherapy of Pancreatic Cancer. *Molecules*. **2022**;27(8):2529. doi:10.3390/molecules27082529
48. Hao Y, Chen Y, He X, et al. Polymeric Nanoparticles with ROS-Responsive Prodrug and Platinum Nanozyme for Enhanced Chemophotodynamic Therapy of Colon Cancer. *Adv. Sci.*. **2020**;7(20). doi:10.1002/advs.202001853
49. Morales K, Rodríguez-Calado S, Hernando J, et al. Synthesis and In Vitro Studies of Photoactivatable Semisquarainetype Pt(II) Complexes. *Inorg Chem*. **2022**;61(20). doi:10.1021/ACS.INORGCHEM.1C03957
50. Lu F, Ouyang C, Yu J, et al. Smart Type I Squaraine Nano-Photosensitizer Combined with MnO2 for Tumor-Targeted and Ferroptosis-Induced Immunogenic Photodynamic Therapy. *ACS Appl Mater Interfaces*. **2025**;17(21):30637-30652. doi:10.1021/acsami.5c03956
51. Rojas-Buzo S, Pontremoli C, De Toni S, et al. Hafnium-Based Metal-Organic Framework Nanosystems Entrapping Squaraines for Efficient NIR-Responsive Photodynamic Therapy. *ACS Appl Mater Interfaces*. **2025**;17(1):524-536. doi:10.1021/acsami.4c17018
52. Dereje DM, Pontremoli C, García A, et al. Poly Lactic-co-Glycolic Acid (PLGA) Loaded with a Squaraine Dye as Photosensitizer for Antimicrobial Photodynamic Therapy. *Polymers*. **2024**;16(14). doi:10.3390/polym16141962
53. Ziarani GM, Moradi R, Lashgari N, Kruger HG. Squaraine Dyes. In: *Metal-Free Synthetic Organic Dyes*. Elsevier; **2018**:193-196. doi:10.1016/b978-0-12-815647-6.00015-7

54. Moan J, Peng Q. An outline of the history of PDT. In: *Photodynamic Therapy*. **2007**. doi:10.1039/9781847551658-00001

55. Sharman WM, Allen CM, Van Lier JE. Photodynamic therapeutics: Basic principles and clinical applications. *Drug Discov Today*. **1999**;4(11). doi:10.1016/S1359-6446(99)01412-9

56. Yang H, Cao X, Yang F, et al. A programmable metasurface with dynamic polarization, scattering and focusing control. *Sci Rep*. **2016**;6. doi:10.1038/srep35692

57. Greer A. Christopher Foote's discovery of the role of singlet oxygen [1O2 (1Δg)] in photosensitized oxidation reactions. *Acc Chem Res*. **2006**;39(11). doi:10.1021/ar050191g

58. Ochsner M. Photophysical and photobiological processes in the photodynamic therapy of tumours. *J Photochem Photobiol B*. **1997**;39(1). doi:10.1016/S1011-1344(96)07428-3

59. Garcia-Diaz M, Huang YY, Hamblin MR. Use of fluorescent probes for ROS to tease apart Type I and Type II photochemical pathways in photodynamic therapy. *Methods*. **2016**;109. doi:10.1016/j.ymeth.2016.06.025

60. Schmidt R. Photosensitized Generation of Singlet Oxygen. *Photochem Photobiol*. **2006**;82(5). doi:10.1562/2006-03-03-ir-833

61. Baptista MS, Cadet J, Di Mascio P, et al. Type I and Type II Photosensitized Oxidation Reactions: Guidelines and Mechanistic Pathways. *Photochem Photobiol*. **2017**;93(4). doi:10.1111/php.12716

62. Bonnet S. Why develop photoactivated chemotherapy? *Dalton Transactions*. 2018;47(31). doi:10.1039/c8dt01585f

63. Barbero N, Butnarasu C, Visentin S, Barolo C. Squaraine Dyes: Interaction with Bovine Serum Albumin to Investigate Supramolecular Adducts with Aggregation-Induced Emission (AIE) Properties. *Chem Asian J*. **2019**;14(6). doi:10.1002/asia.201900055

64. Ilina K, MacCuaig WM, Laramie M, Jeouty JN, McNally LR, Henary M. Squaraine Dyes: Molecular Design for Different Applications and Remaining Challenges. *Bioconjug Chem*. **2020**;31(2). doi:10.1021/acs.bioconjchem.9b00482

65. Owens EA, Henary M, El Fakhri G, Choi HS. Tissue-Specific Near-Infrared Fluorescence Imaging. *Acc Chem Res*. **2016**;49(9). doi:10.1021/acs.accounts.6b00239

66. Li P, Liu Y, Liu W, et al. IR-783 inhibits breast cancer cell proliferation and migration by inducing mitochondrial fission. *Int J Oncol*. **2019**;55(2). doi:10.3892/ijo.2019.4821

67. Duan L, Wang L, Zhang C, et al. Role of near-infrared heptamethine cyanine dye IR-783 in diagnosis of cervical cancer and its mechanism. *Int J Clin Exp Pathol*. **2019**;12(6).

68. Abrahamse H, Houreld NN. Genetic aberrations associated with photodynamic therapy in colorectal cancer cells. *Int J Mol Sci*. **2019**;20(13). doi:10.3390/ijms20133254

69. Chen J, Mizumura M, Shinokubo H, Osuka A. Functionalization of boron dipyrrin (BODIPY) dyes through iridium and rhodium catalysis: A complementary approach to α-and β-Substituted BODIPYs. *Chemistry – Eur. J.* **2009**;15(24). doi:10.1002/chem.200802541

70. Law KY. Squaraine Chemistry. Design, Synthesis, and Xerographic Properties of a Highly Sensitive Unsymmetrical Fluorinated Squaraine. *Chem. Mater*. **1992**;4(3). doi:10.1021/cm00021a020

71. Liang K, Law KY, Whitten DG. Synthesis, characterization, photophysics, and photosensitization studies of squaraine-bipyridinium diads. *Journal of Physical Chemistry B*. **1997**;101(4). doi:10.1021/jp962996z

72. Treibs A, Jacob K. Cyclotrimethine Dyes Derived from Squaric Acid. *Angew. Chem. Int. Ed.*. **1965**;4(8). doi:10.1002/anie.196506941

73. Qiao W, Ma T, Xie G, et al. Supramolecular H-Aggregates of Squaraines with Enhanced Type I Photosensitization for Combined Photodynamic and Photothermal Therapy. *ACS Nano*. **2024**;18(37):25671-25684. doi:10.1021/acsnano.4c07764

74. Pamuk Algi M, Sarıgöl R. Squaraine-containing polymeric nanoparticles enable photodynamic and photothermal therapy of cancer cells. *Dyes Pigm.* **2024**;226:112138. doi:https://doi.org/10.1016/j.dyepig.2024.112138

75. Fu N, Allen AD, Kobayashi S, et al. Amino substituted bisketenes: Generation, structure, and reactivity. *J. Org. Chem.*. **2007**;72(6). doi:10.1021/jo062090h

76. Nguyen MT, Raspoet G. The hydration mechanism of ketene: 15 years later. *Can J Chem*. **1999**;77(5-6). doi:10.1139/v99-090

77. Allen AD, Colomvakos JD, Diederich F, et al. Generation of 1,2-bisketenes from cyclobutene-1,2-diones by flash photolysis and ring closure kinetics. *J Am Chem Soc*. **1997**;119(50). doi:10.1021/ja9722685

78. Dougherty TJ, Cooper MT, Mang TS. Cutaneous phototoxic occurrences in patients receiving Photofrin®. *Lasers Surg Med*. **1990**;10(5). doi:10.1002/lsm.1900100514

79. Moriwaki S, Misawa J, Yoshinari Y, Yamada I, Takigawa M, Tokura Y. Analysis of photosensitivity in Japanese cancer-bearing patients receiving photodynamic therapy with porfimer sodium (Photofrin TM) . *Photodermatol Photoimmunol Photomed*. **2001**;17(5). doi:10.1111/j.1600-0781.2001.170507.x

80. Stoffelen C, Huskens J. Soft Supramolecular Nanoparticles by Noncovalent and Host-Guest Interactions. *Small*. **2016**;12(1). doi:10.1002/smll.201501348

81. Kaczmarek-Kędziera A, Ośmiałowski B, Żuchowski PS, Kędziera D. Supramolecular Approach to Tuning the Photophysical Properties of Quadrupolar Squaraines. *Front Chem*. **2022**;9. doi:10.3389/fchem.2021.800541

82. Gunturu KC, Schulzke C. Correction: A computational probe granting insight into intra and inter-stacking interactions in squaraine dye derivatives. *Phys. Chem. Chem. Phys.*. **2021**;23(32). doi:10.1039/d1cp90156g

83. Shen C, Bialas D, Hecht M, Stepanenko V, Sugiyasu K, Würthner F. Polymorphism in Squaraine Dye Aggregates by Self-Assembly Pathway Differentiation: Panchromatic Tubular Dye Nanorods versus J-Aggregate Nanosheets. *Angew. Chem.*. **2021**;133(21). doi:10.1002/ange.202102183

84. Kleine-Kleffmann L, Stepanenko V, Shoyama K, Wehner M, Würthner F. Controlling the Supramolecular Polymerization of Squaraine Dyes by a Molecular Chaperone Analogue. *J Am Chem Soc*. **2023**;145(16). doi:10.1021/jacs.3c01002

85. De Miguel G, Ziółek M, Zitnan M, et al. Photophysics of H- and J-aggregates of indole-based squaraines in solid state. *Journal of Physical Chemistry C*. **2012**;116(17). doi:10.1021/jp210281z

86. Beckers EHA, Meskers SCJ, Schenning APHJ, et al. Influence of intermolecular orientation on the photoinduced charge transfer kinetics in self-assembled aggregates of donor-acceptor arrays. *J Am Chem Soc*. **2006**;128(2). doi:10.1021/ja0568042

87. Spano FC. The spectral signatures of frenkel polarons in H- And J-aggregates. *Acc Chem Res*. **2010**;43(3). doi:10.1021/ar900233v

88. Kaufmann C, Bialas D, Stolte M, Würthner F. Discrete Ï€-Stacks of Perylene Bisimide Dyes within Folda-Dimers: Insight into Long- and Short-Range Exciton Coupling. *J Am Chem Soc*. **2018**;140(31). doi:10.1021/jacs.8b05490

89. Rösch AT, Zhu Q, Robben J, et al. Helicity Control in the Aggregation of Achiral Squaraine Dyes in Solution and Thin Films. *Chem. Eur. J.*. **2021**;27(1). doi:10.1002/chem.202002695

90. Xia G, Wang H. Squaraine dyes: The hierarchical synthesis and its application in optical detection. *J. Photochem. Photobiol. C: Photochem. Rev.*. **2017**;31. doi:10.1016/j.jphotochemrev.2017.03.001

91. Ajayaghosh A, Arunkumar E, Daub J. A Highly Specific Ca2+-Ion Sensor: Signaling by Exciton Interaction in a Rigid-Flexible-Rigid Bichromophoric “H” Foldamer. *Angew. Chem.*. **2002**;114(10). doi:10.1002/1521-3757(20020517)114:10<1844::aid-ange1844>3.0.co;2-g

92. Chen C, Wang R, Guo L, Fu N, Dong H, Yuan Y. A squaraine-based colorimetric and “turn on” fluorescent sensor for selective detection of Hg2+ in an aqueous medium. *Org Lett*. **2011**;13(5). doi:10.1021/ol200024g

93. Zhao CX, Liu JN, Li BQ, et al. Multiscale Construction of Bifunctional Electrocatalysts for Long-Lifespan Rechargeable Zinc–Air Batteries. *Adv Funct Mater*. **2020**;30(36). doi:10.1002/adfm.202003619

94. Li B, Li W, Xu Y, Li J, Tu J, Sun S. A simple approach for the discrimination of surfactants based on the control of squaraine aggregation. *Chem. Commun.*. **2015**;51(78). doi:10.1039/c5cc06086a

95. Chen C, Wang R, Guo L, Fu N, Dong H, Yuan Y. A Squaraine-Based Colorimetric and “Turn on” Fluorescent Sensor for Selective Detection of Hg 2+ in an Aqueous Medium. *Org Lett*. **2011**;13(5):1162-1165. doi:10.1021/ol200024g

96. Xu Y, Li B, Han P, Sun S, Pang Y. Near-infrared fluorescent detection of glutathione via reaction-promoted assembly of squaraine-analyte adducts. *Analyst*. **2013**;138(4). doi:10.1039/c2an36475a

97. Fukuda T, Yokomizo S, Casa S, et al. Fast and Durable Intraoperative Near-infrared Imaging of Ovarian Cancer Using Ultrabright Squaraine Fluorophores. *Angew. Chem. – Int. Ed.* **2022**;61(17). doi:10.1002/anie.202117330

98. Singh AK, Kavungathodi MFM, Mozer AJ, Krishnamoorthy K, Nithyanandhan J. Solvent-Dependent Functional Aggregates of Unsymmetrical Squaraine Dyes on TiO2Surface for Dye-Sensitized Solar Cells. *Langmuir*. **2022**;38(48). doi:10.1021/acs.langmuir.2c02469

99. Vuk D, Radovanović-Perić F, Mandić V, et al. Synthesis and Nanoarchitectonics of Novel Squaraine Derivatives for Organic Photovoltaic Devices. *Nanomet*. **2022**;12(7). doi:10.3390/nano12071206

100. Kim JY, Lee JW, Jung HS, Shin H, Park NG. High-Efficiency Perovskite Solar Cells. *Chem Rev*. **2020**;120(15). doi:10.1021/acs.chemrev.0c00107

101. Gu Z, Tian X, Guang S, Wei G, Mao Y, Xu H. POSS engineering of squaraine nanoparticle with high photothermal conversion efficiency for photothermal therapy. *Spectrochim Acta A Mol Biomol Spectrosc*. 2024;306. doi:10.1016/j.saa.**2023**.123576

102. Xie X, Dong Y, Zhang Y, et al. Readily constructed squaraine J-aggregates with an 86.0 % photothermal conversion efficiency for photothermal therapy. *Bioact Mater*. **2025**;43:460-470. doi:https://doi.org/10.1016/j.bioactmat.2024.09.031

103. Sun P, Wu Q, Sun X, et al. J-Aggregate squaraine nanoparticles with bright NIR-II fluorescence for imaging guided photothermal therapy. *Chem. Commun*. **2018**;54(95). doi:10.1039/c8cc08096h

104. Wang Y, Xia G, Wang J, et al. A synergetic strategy of NIR-II squaraine dyes with ultrahigh photothermal conversion efficiency for photothermal therapy. *Sci China Chem*. **2024**;67(2). doi:10.1007/s11426-023-1830-0

105. Bagchi D, Halder A, Debnath S, Saha P, Kumar Pal S. Exploration of interfacial dynamics in squaraine based nanohybrids for potential photodynamic action. *J Photochem Photobiol A Chem*. **2019**;380. doi:10.1016/j.jphotochem.2019.05.005

106. Bordignon N, Köber M, Chinigò G, et al. Quatsomes Loaded with Squaraine Dye as an Effective Photosensitizer for Photodynamic Therapy. *Pharmaceutics*. **2023**;15(3). doi:10.3390/pharmaceutics15030902

107. Huang C, Ren X, Chen Q, et al. A novel NIR-activatable and photodegradable mitochondria-targeted nano-photosensitizer for superior photodynamic therapy. *Sens Actuators B Chem*. **2025**;424:136896. doi:https://doi.org/10.1016/j.snb.2024.136896

108. Alabugin A. Near-IR Photochemistry for Biology: Exploiting the Optical Window of Tissue. *Photochem Photobiol*. **2019**;95(3):722-732. doi:10.1111/php.13068

109. Dai Y, Guo J, Wang TY, et al. Self-Assembled Nanoparticles from Phenolic Derivatives for Cancer Therapy. *Adv Healthc Mater*. **2017**;6(16). doi:10.1002/adhm.201700467

110. Adarsh NN, Frias C, Ponnoth Lohidakshan TM, et al. Pt(IV)-based nanoscale coordination polymers: Antitumor activity, cellular uptake and interactions with nuclear DNA. *Chem. Eng. J.* **2018**;340. doi:10.1016/j.cej.2018.01.058

111. Johnstone TC, Lippard SJ. Reinterpretation of the vibrational spectroscopy of the medicinal bioinorganic synthon c,c,t-[Pt(NH3)2Cl2(OH) 2] Topical issue in honor of Ivano Bertini. Guest editors: Lucia Banci and Claudio Luchinat. *J. Biol. Inorg. Chem.*. **2014**;19(4-5). doi:10.1007/s00775-014-1109-6

112. Ryu JH, Messersmith PB, Lee H. Polydopamine Surface Chemistry: A Decade of Discovery. *ACS Appl Mater Interfaces*. **2018**;10(9). doi:10.1021/acsami.7b19865

113. Pinnataip R, Lee BP. Oxidation Chemistry of Catechol Utilized in Designing Stimuli-Responsive Adhesives and Antipathogenic Biomaterials. *ACS Omega*. **2021**;6(8). doi:10.1021/acsomega.1c00006

114. Hickey JW, Santos JL, Williford JM, Mao HQ. Control of polymeric nanoparticle size to improve therapeutic delivery. *J. Control. Release.*. **2015**;219. doi:10.1016/j.jconrel.2015.10.006

115. Moghimi SM, Hunter AC, Murray JC. Long-circulating and target-specific nanoparticles: Theory to practice. *Pharmacol Rev*. **2001**;53(2). doi:10.1016/s0031-6997(24)01494-7

116. Jain RK, Stylianopoulos T. Delivering nanomedicine to solid tumors. *Nat Rev Clin Oncol*. **2010**;7(11). doi:10.1038/nrclinonc.2010.139

117. Jhaveri AM, Torchilin VP. Multifunctional polymeric micelles for delivery of drugs and siRNA. *Front Pharmacol*. **2014**;5 APR. doi:10.3389/fphar.2014.00077

118. Meng Q, Meng H, Pan Y, et al. Influence of nanoparticle size on blood-brain barrier penetration and the accumulation of anti-seizure medicines in the brain. *J Mater Chem B*. **2022**;10(2). doi:10.1039/d1tb02015c

119. Mistry A, Stolnik S, Illum L. Nanoparticles for direct nose-to-brain delivery of drugs. *Int J Pharm*. **2009**;379(1-2). doi:10.1016/j.ijpharm.2009.06.019

120. Parmar K, Patel J, Pathak Y. Factors affecting the clearance and biodistribution of polymeric nanoparticles. In: *Pharmacokinetics and Pharmacodynamics of Nanoparticulate Drug Delivery Systems*. Springer International Publishing; **2022**:261-272. doi:10.1007/978-3-030-83395-4_14

121. Arvizo RR, Miranda OR, Thompson MA, et al. Effect of nanoparticle surface charge at the plasma membrane and beyond. *Nano Lett*. **2010**;10(7). doi:10.1021/nl101140t

122. Masserini M. Nanoparticles for Brain Drug Delivery. *ISRN Biochem*. 2013;2013. doi:10.1155/2013/238428

123. Çetinkaya S, Taban Akça K, Süntar I. Flavonoids and anticancer activity: Structure–activity relationship. In: *Stud. Nat. Prod. Chem.*. Vol 74. Elsevier B.V.; **2022**:81-115. doi:10.1016/B978-0-323-91099-6.00017-7

124. Rady I, Mohamed H, Rady M, Siddiqui IA, Mukhtar H. Cancer preventive and therapeutic effects of EGCG, the major polyphenol in green tea. *Egypt. J. Basic Appl. Sci*. **2018**;5(1). doi:10.1016/j.ejbas.2017.12.001

125. Peppicelli S, Bianchini F, Calorini L. Extracellular acidity, a "reappreciated" trait of tumor environment driving malignancy: Perspectives in diagnosis and therapy. *Cancer Metastasis Rev.* **2014**;33(2-3). doi:10.1007/s10555-014-9506-4

126. Mindell JA. Lysosomal acidification mechanisms. *Annu Rev Physiol*. **2012**;74. doi:10.1146/annurev-physiol-012110-142317

127. Ong JX, Lim CSQ, Le H Van, Ang WH. A Ratiometric Fluorescent Probe for Cisplatin: Investigating the Intracellular Reduction of Platinum(IV) Prodrug Complexes. *Angew. Chem. – Int. Ed.* **2019**;58(1). doi:10.1002/anie.201810361

128. Schafer FQ, Buettner GR. Redox environment of the cell as viewed through the redox state of the glutathione disulfide/glutathione couple. *Free Radic Biol Med*. **2001**;30(11). doi:10.1016/S0891-5849(01)00480-4

129. Feng Q, Bennett Z, Grichuk A, et al. Severely polarized extracellular acidity around tumour cells. *Nat Biomed Eng*. **2024**;8(6). doi:10.1038/s41551-024-01178-7

130. Yao J, Czaplinska D, Ialchina R, et al. Cancer cell acid adaptation gene expression response is correlated to tumor-specific tissue expression profiles and patient survival. *Cancers*. **2020**;12(8). doi:10.3390/cancers12082183

131. Silva AS, Yunes JA, Gillies RJ, Gatenby RA. The potential role of systemic buffers in reducing intratumoral extracellular pH and acid-mediated invasion. *Cancer Res*. **2009**;69(6). doi:10.1158/0008-5472.CAN-08-2394

132. Jeong EM, Yoon JH, Lim J, et al. Real-Time Monitoring of Glutathione in Living Cells Reveals that High Glutathione Levels Are Required to Maintain Stem Cell Function. *Stem Cell Reports*. **2018**;10(2). doi:10.1016/j.stemcr.2017.12.007

133. Shukla D, Mandal PK, Tripathi M, Vishwakarma G, Mishra R, Sandal K. Quantitation of in vivo brain glutathione conformers in cingulate cortex among age-matched control, MCI, and AD patients using MEGA-PRESS. *Hum Brain Mapp*. **2020**;41(1). doi:10.1002/hbm.24799

134. Cai X, Dong C, Dong H, et al. Effective gene delivery using stimulus-responsive cationer designed with redox-sensitive disulfide and acid-labile imine linkers. *Biomacromol.* **2012**;13(4). doi:10.1021/bm2017355

135. Zhang J, Ren X, Tian X, et al. GSH and enzyme responsive nanospheres based on self-assembly of green tea polyphenols and BSA used for target cancer chemotherapy. *Colloids Surf B Biointerfaces*. **2019**;173. doi:10.1016/j.colsurfb.2018.10.037

136. Hao YN, Zheng AQ, Guo TT, et al. Glutathione triggered degradation of polydopamine to facilitate controlled drug release for synergic combinational cancer treatment. *J Mater Chem B*. **2019**;7(43). doi:10.1039/c9tb01400d

137. Gabano E, Ravera M, Osella D. Pros and cons of bifunctional platinum(iv) antitumor prodrugs: Two are (not always) better than one. *Dalton Trans*. **2014**;43(26). doi:10.1039/c4dt00911h

138. Schmidt C, Babu T, Kostrhunova H, et al. Are Pt(IV) Prodrugs That Release Combretastatin A4 True Multi-action Prodrugs? *J Med Chem*. **2021**;64(15). doi:10.1021/acs.jmedchem.1c00706

139. Donahue ND, Acar H, Wilhelm S. Concepts of nanoparticle cellular uptake, intracellular trafficking, and kinetics in nanomedicine. *Adv Drug Deliv Rev*. **2019**;143. doi:10.1016/j.addr.2019.04.008

140. Kreuter J. Drug delivery to the central nervous system by polymeric nanoparticles: What do we know? *Adv Drug Deliv Rev*. **2014**;71. doi:10.1016/j.addr.2013.08.008

141. Howell SB, Safaei R, Larson CA, Sailor MJ. Copper transporters and the cellular pharmacology of the platinum-containing cancer drugs. *Mol Pharmacol*. **2010**;77(6). doi:10.1124/mol.109.063172

142. Yonezawa A, Masuda S, Yokoo S, Katsura T, Inui KI. Cisplatin and oxaliplatin, but not carboplatin and nedaplatin, are substrates for human organic cation transporters (SLC22A1-3 and multidrug and toxin extrusion family). *J. Pharmacol. Exp. Ther.* **2006**;319(2). doi:10.1124/jpet.106.110346

143. Augustine R, Hasan A, Primavera R, Wilson RJ, Thakor AS, Kevadiya BD. Cellular uptake and retention of nanoparticles: Insights on particle properties and interaction with cellular components. *Mater Today Commun*. 2020;25. doi:10.1016/j.mtcomm.2020.101692

144. Li B, Lane LA. Probing the biological obstacles of nanomedicine with gold nanoparticles. *Wiley Interdiscip Rev Nanomed Nanobiotechnol*. **2019**;11(3). doi:10.1002/wnan.1542

145. Mao X, Si J, Huang Q, et al. Self-Assembling Doxorubicin Prodrug Forming Nanoparticles and Effectively Reversing Drug Resistance In Vitro and In Vivo. *Adv Healthc Mater*. **2016**;5(19). doi:10.1002/adhm.201600345

146. Mahmoudi M, Laurent S, Shokrgozar MA, Hosseinkhani M. Toxicity evaluations of superparamagnetic iron oxide nanoparticles: Cell "vision" versus physicochemical properties of nanoparticles. *ACS Nano*. **2011**;5(9). doi:10.1021/nn2021088

147. Tesniere A, Schlemmer F, Boige V, et al. Immunogenic death of colon cancer cells treated with oxaliplatin. *Oncogene*. **2010**;29(4). doi:10.1038/onc.2009.356

148. Chapman EG, DeRose VJ. Enzymatic processing of platinated RNAs. *J Am Chem Soc*. **2010**;132(6). doi:10.1021/ja908419j

149. Bose RN, Maurmann L, Mishur RJ, et al. Non-DNA-binding platinum anticancer agents: Cytotoxic activities of platinum-phosphato complexes towards human ovarian cancer cells (Proceedings of the National Academy of Sciences of the United States of America (2008) 105, 47, (18314-18319) DOI: 10.1073/pnas.0803094105). *Proc Natl Acad Sci U S A*. **2009**;106(4). doi:10.1073/pnas.0811947106

150. Vázquez-Cervantes GI, Villaseñor-Aguayo K, Hernández-Damián J, et al. Antitumor effects of nordihydroguaiaretic acid (NDGA) in bladder T24 cancer cells are related to increase in ROS production and mitochondrial leak respiration. *Nat Prod Commun*. **2018**;13(11). doi:10.1177/1934578x1801301128

151. Forooshani PK, Meng H, Lee BP. Catechol Redox Reaction: Reactive Oxygen Species Generation, Regulation, and Biomedical Applications. In: *ACS Symposium Series*. Vol 1252. **2017**. doi:10.1021/bk-2017-1252.ch010

152. Zhang X, Wang M, Liu Z, et al. Transnasal-brain delivery of nanomedicines for neurodegenerative diseases. *Front. Drug Deliv.* **2023**;3. doi:10.3389/fddev.2023.1247162

153. Wu H, Li C, Yuan H, Zhao J, Li S. Brain Delivery Strategies for Biomacromolecular Drugs: Intranasal Administration. *Int J Nanomedicine*. **2025**;20. doi:10.2147/IJN.S520768

154. Dighe S, Jog S, Momin M, Sawarkar S, Omri A. Intranasal Drug Delivery by Nanotechnology: Advances in and Challenges for Alzheimer's Disease Management. *Pharmaceutics*. **2024**;16(1). doi:10.3390/pharmaceutics16010058

155. Hassanzadeganroudsari M, Soltani M, Heydarinasab A, Apostolopoulos V, Akbarzadehkhiyavi A, Nurgali K. Targeted nano-drug delivery system for glioblastoma therapy: In vitro and in vivo study. *J Drug Deliv Sci Technol*. **2020**;60. doi:10.1016/j.jddst.2020.102039

156. Shader RI. Safety Versus Tolerability. *Clin Ther*. **2018**;40(5). doi:10.1016/j.clinthera.2018.04.003

157. McGranahan T, Therkelsen KE, Ahmad S, Nagpal S. Current State of Immunotherapy for Treatment of Glioblastoma. *Curr Treat Options Oncol*. **2019**;20(3). doi:10.1007/s11864-019-0619-4

158. Wu S, Calero-Pérez P, Villamañan L, et al. Anti-tumour immune response in GL261 glioblastoma generated by Temozolomide Immune-Enhancing Metronomic Schedule monitored with MRSI-based nosological images. *NMR Biomed*. **2020**;33(4). doi:10.1002/nbm.4229

159. Hato S V., Khong A, De Vries IJM, Lesterhuis WJ. Molecular pathways: The immunogenic effects of platinum-based chemotherapeutics. *Clin. Cancer Res*. **2014**;20(11). doi:10.1158/1078-0432.CCR-13-3141

160. Roberts NB, Wadajkar AS, Winkles JA, Davila E, Kim AJ, Woodworth GF. Repurposing platinum-based chemotherapies for multi-modal treatment of glioblastoma. *Oncoimmunology*. **2016**;5(9). doi:10.1080/2162402X.2016.1208876

161. Erdő F, Bors LA, Farkas D, Bajza Á, Gizurarson S. Evaluation of intranasal delivery route of drug administration for brain targeting. *Brain Res Bull*. **2018**;143. doi:10.1016/j.brainresbull.2018.10.009

162. Law KY, Bailey FC. Squaraine Chemistry. Synthesis, Characterization, and Optical Properties of a Class of Novel Unsymmetrical Squaraines: [4-(Dimethylamino)phenyl](4′-methoxyphenyl)squaraine and Its Derivatives. *J. Org. Chem.* **1992**;57(12). doi:10.1021/jo00038a010

163. Ahmad S. Kinetic aspects of platinum anticancer agents. *Polyhedron*. **2017**;138. doi:10.1016/j.poly.2017.09.016

164. Priyanka, Bila G, Mavileti SK, et al. A biocompatible NIR squaraine dye and dye-antibody conjugates for versatile long-term in vivo fluorescence bioimaging. *Mater Adv*. **2024**;5(9):3940-3949. doi:10.1039/d4ma00212a

165. Qaddoura MA, Belfield KD, Tongwa P, Desanto JE, Timofeeva T V., Heiney PA. Thermotropic behaviour, self-assembly and photophysical properties of a series of squaraines. *Supramol Chem*. **2011**;23(11). doi:10.1080/10610278.2011.622391

166. Paternò GM, Moretti L, Barker AJ, et al. Near-infrared emitting single squaraine dye aggregates with large Stokes shifts. *J Mater Chem C Mater*. **2017**;5(31). doi:10.1039/c7tc01375b

167. Xu Y, Li Z, Malkovskiy A, Sun S, Pang Y. Aggregation control of squaraines and their use as near-infrared fluorescent sensors for protein. *J. Phys. Chem. B.* **2010**;114(25). doi:10.1021/jp1029536

168. Lima E, Reis L V. "Lights, squaraines, action!" - the role of squaraine dyes in photodynamic therapy. *Future Med Chem*. **2022**;14(19). doi:10.4155/fmc-2022-0112

169. Rapozzi V, Beverina L, Salice P, Pagani GA, Camerin M, Xodo LE. Photooxidation and phototoxicity of π-extended squaraines. *J Med Chem*. **2010**;53(5). doi:10.1021/jm901727j

170. Aggarwal P, Hall JB, McLeland CB, Dobrovolskaia MA, McNeil SE. Nanoparticle interaction with plasma proteins as it relates to particle biodistribution, biocompatibility and therapeutic efficacy. *Adv Drug Deliv Rev*. **2009**;61(6). doi:10.1016/j.addr.2009.03.009

171. Moore TL, Rodriguez-Lorenzo L, Hirsch V, et al. Nanoparticle colloidal stability in cell culture media and impact on cellular interactions. *Chem Soc Rev*. **2015**;44(17). doi:10.1039/c4cs00487f

172. Jisha VS, Arun KT, Hariharan M, Ramaiah D. Site-selective interactions: Squaraine dye-serum albumin complexes with enhanced fluorescence and triplet yields. *J. Phys. Chem. B.***2010**;114(17). doi:10.1021/jp100369x

173. M.Garcia A, de Alwis Weerasekera H, Pitre SP, et al. Photodynamic performance of zinc phthalocyanine in HeLa cells: A comparison between DPCC liposomes and BSA as delivery systems. *J Photochem Photobiol B*. **2016**;163. doi:10.1016/j.jphotobiol.2016.09.002

174. Chen J, Zhang D, Liu B, et al. Photoinduced Precise Synthesis of Diatomic Ir1Pd1-In2O3 for CO2 Hydrogenation to Methanol via Angstrom-Scale-Distance Dependent Synergistic Catalysis. *Angew. Chem. – Int. Ed*. **2024**;63(13). doi:10.1002/anie.202401168

175. Kumbham S, Ghosh A, Ghosh B, Biswas S. Human serum albumin-poly(Lactide)-conjugated self-assembly NPs for targeted docetaxel delivery and improved therapeutic efficacy in oral cancer. *Int J Biol Macromol*. **2022**;222. doi:10.1016/j.ijbiomac.2022.09.250

176. Shi YZ, Xiong S, Zhang Y, et al. Sculpting nanoparticle dynamics for single-bacteria-level screening and direct binding-efficiency measurement. *Nat Commun*. **2018**;9(1). doi:10.1038/s41467-018-03156-5

177. Silva EPO, Ribeiro NM, Cardoso MAG, Pacheco-Soares C, Beltrame M. Photodynamic therapy using silicon phthalocyanine conjugated with bovine serum albumin as a drug delivery system. *Laser Phys*. **2021**;31(7). doi:10.1088/1555-6611/abfe58

178. Kwon N, Kim H, Li X, Yoon J. Supramolecular agents for combination of photodynamic therapy and other treatments. *Chem Sci*. **2021**;12(21). doi:10.1039/d1sc01125a

179. Sriwastav S, Sarkar AR, Datta A, Jana NR, Malik S. Northiosquaraine-Based Nanoparticles for Red-Light-Induced Photodynamic Therapy via Singlet Oxygen Generation. *ACS Appl Nano Mater*. **2024**;7(18):21674-21682. doi:10.1021/acsanm.4c03580

180. Dereje DM, García A, Pontremoli C, et al. Squaraine-loaded mesoporous silica nanoparticles for antimicrobial Photodynamic Therapy against bacterial infection. *Microporous and Mesoporous Mater*. **2024**;372. doi:10.1016/j.micromeso.2024.113096

181. Avirah RR, Jayaram DT, Adarsh N, Ramaiah D. Squaraine dyes in PDT: From basic design to in vivo demonstration. *Org Biomol Chem*. **2012**;10(5). doi:10.1039/c1ob06588b

182. Entradas T, Waldron S, Volk M. The detection sensitivity of commonly used singlet oxygen probes in aqueous environments. *J Photochem Photobiol B*. **2020**;204. doi:10.1016/j.jphotobiol.2020.111787

183. Nam JS, Kang MG, Kang J, et al. Endoplasmic Reticulum-Localized Iridium(III) Complexes as Efficient Photodynamic Therapy Agents via Protein Modifications. *J Am Chem Soc*. 2016;138(34). doi:10.1021/jacs.6b05302

184. Mayerhöffer U, Fimmel B, Würthner F. Bright Near-Infrared Fluorophores Based on Squaraines by Unexpected Halogen Effects. *Angew. Chem. – In. Ed.* **2021**;60(35):18918-18919. doi:10.1002/anie.202108494

185. Mayerhöffer U, Gsänger M, Stolte M, Fimmel B, Würthner F. Synthesis and molecular properties of acceptor-substituted squaraine dyes. *Chem. Eur. J.* **2013**;19(1). doi:10.1002/chem.201202783

186. Cong Z, Li Y, Xia G, et al. Highly efficient crystal red fluorescent 1,2-squaraine dyes with excellent biocompatibility and bioimaging. *Dyes and Pigm*. **2019**;162. doi:10.1016/j.dyepig.2018.10.064

187. Hu J, Zhao B, Wen R, et al. Squaraine Dye-Sensitized Upconversion with Enhanced Stability and Minimized Aggregation-Caused Quenching. *Nano Lett*. **2023**;23(11). doi:10.1021/acs.nanolett.3c01184

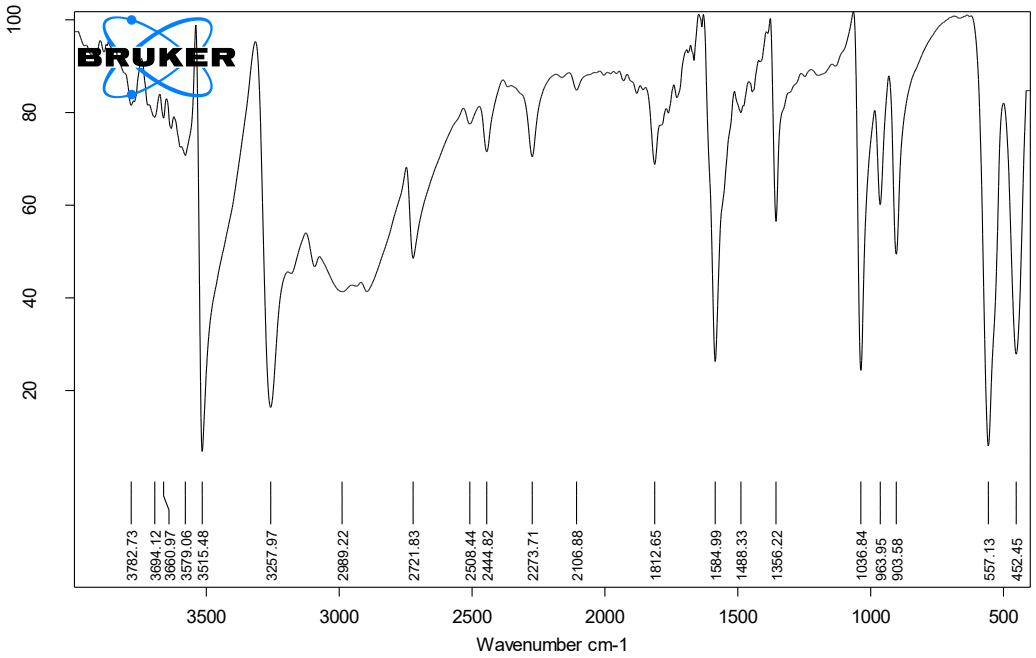
188. Mavileti SK, Kato T, Pandey SS. Clarifying the role of carboxyl functionality in squaraines towards aggregation and self-assembly through photophysical characterization and BSA interactions. *J Mol Struct*. **2024**;1309:138226. doi:10.1016/j.molstruc.2024.138226

189. Garofalo S, D'Alessandro G, Chece G, et al. Enriched environment reduces glioma growth through immune and non-immune mechanisms in mice. *Nat Commun*. **2015**;6. doi:10.1038/ncomms7623

3.7. Annexes

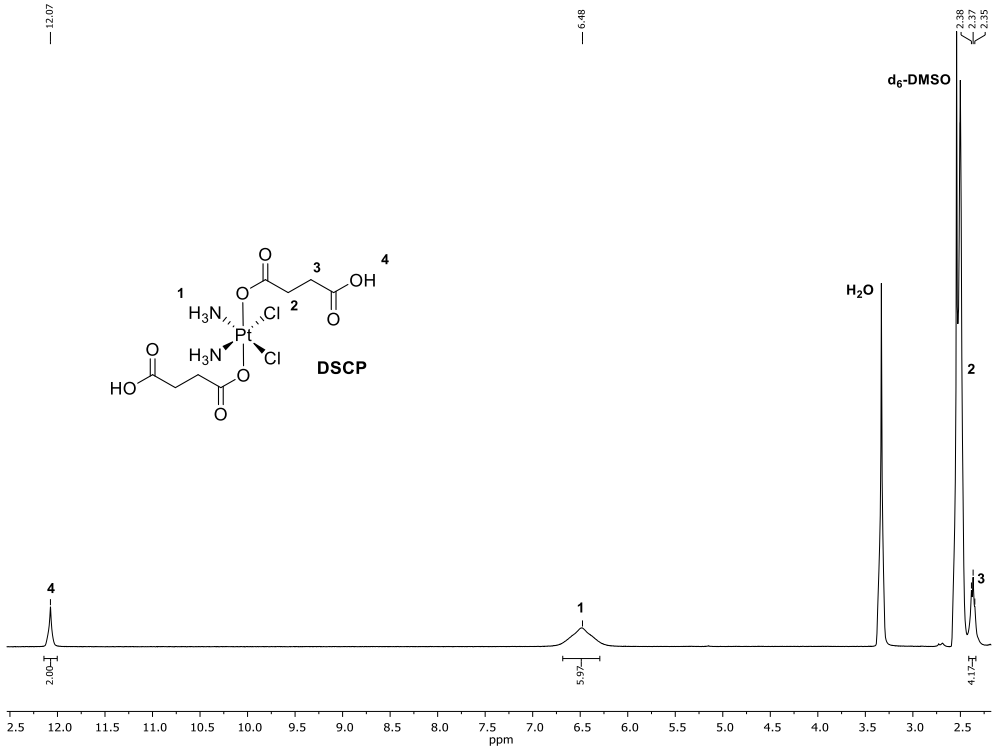
3.7.1. Bioinspired Polymeric Neuromelanin-like Pt(IV) Nanoparticles for Cancer Treatment

Characterisation of c,c,t-Pt(NH_3)$_3$$Cl_2$($OH$)$_2$ (1)

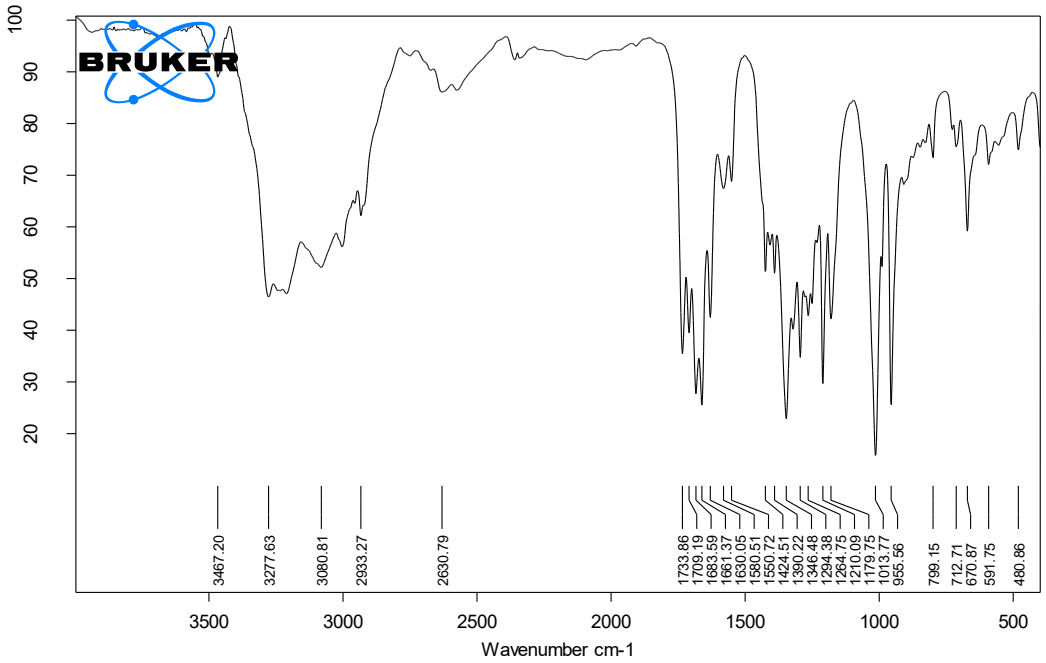


Annexe **3.1**. FTIR of **1**.

Characterisation of Dissuccinic Cisplatin (DSCP)

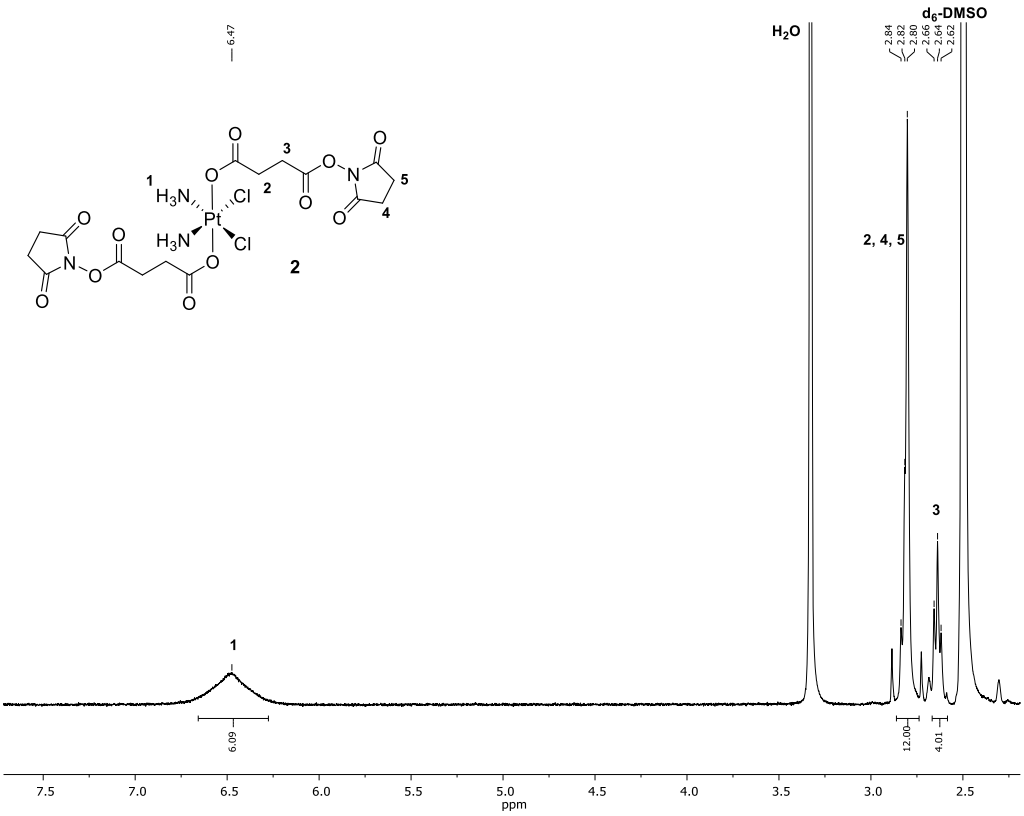


Annexe **3.2**. ^{1}H-NMR of **DSCP**.



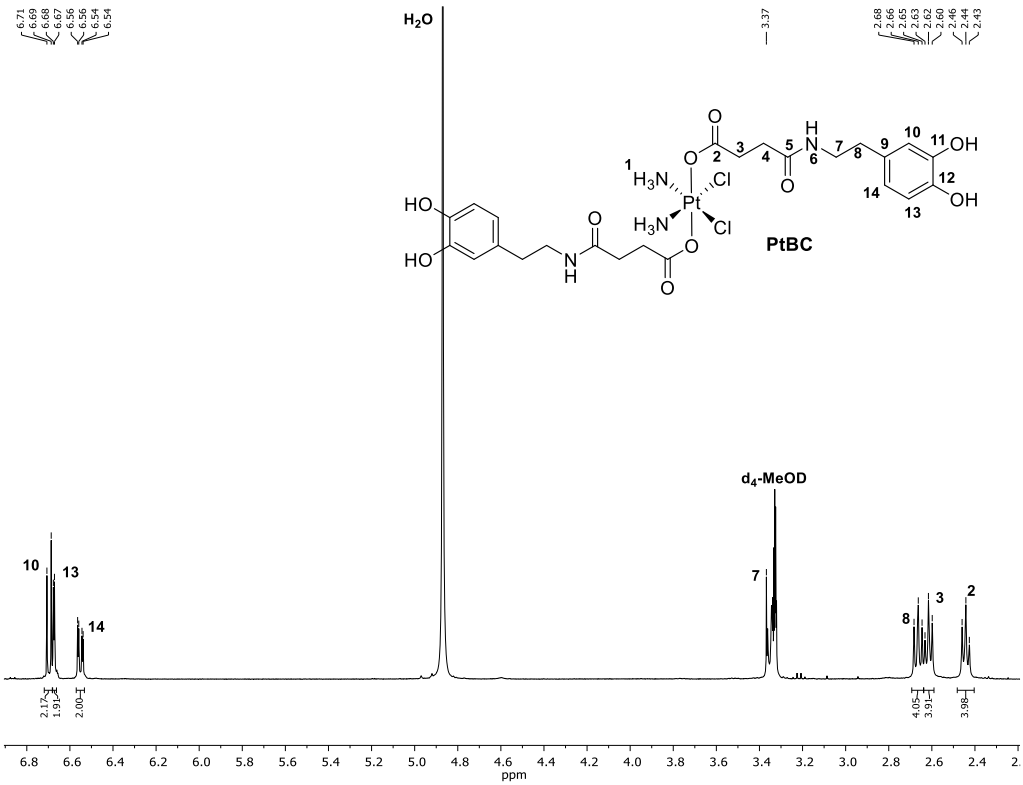
Annexe **3.3**. FTIR of **DSCP**.

Characterization of diaminobis((4-((2,5-dioxopyrrolidin-1-yl)oxy)-4-oxobutanoyl)oxy)Pt(IV) chloride (2)

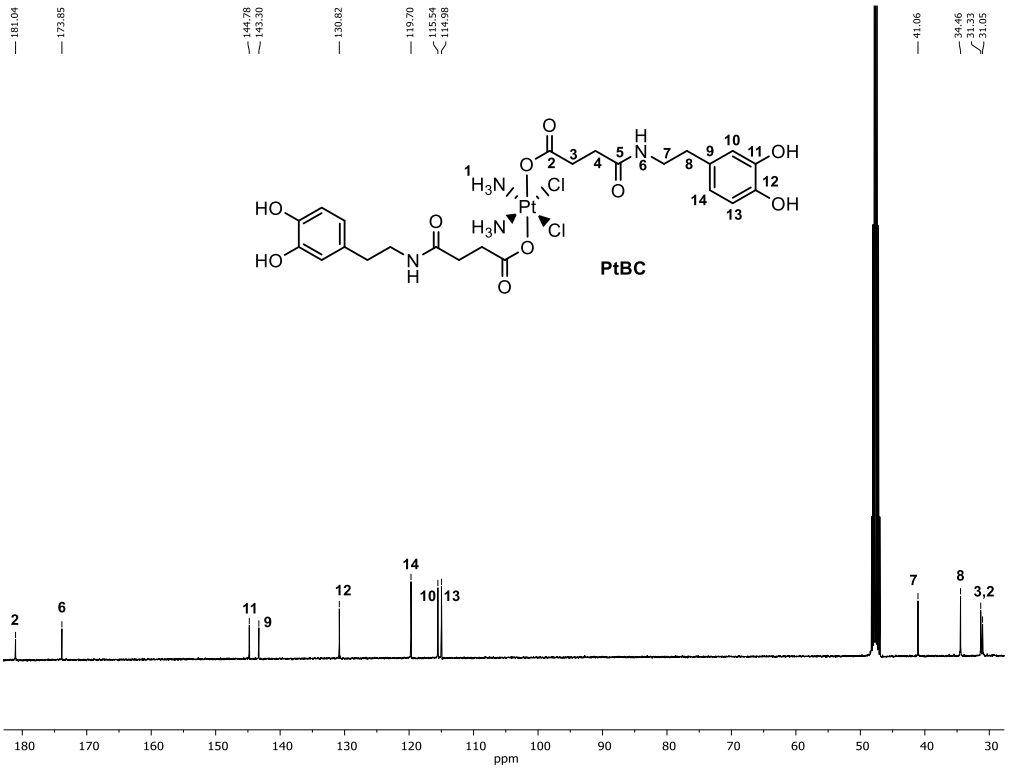


Annexe **3.4**. ^{1}H-NMR of **2**.

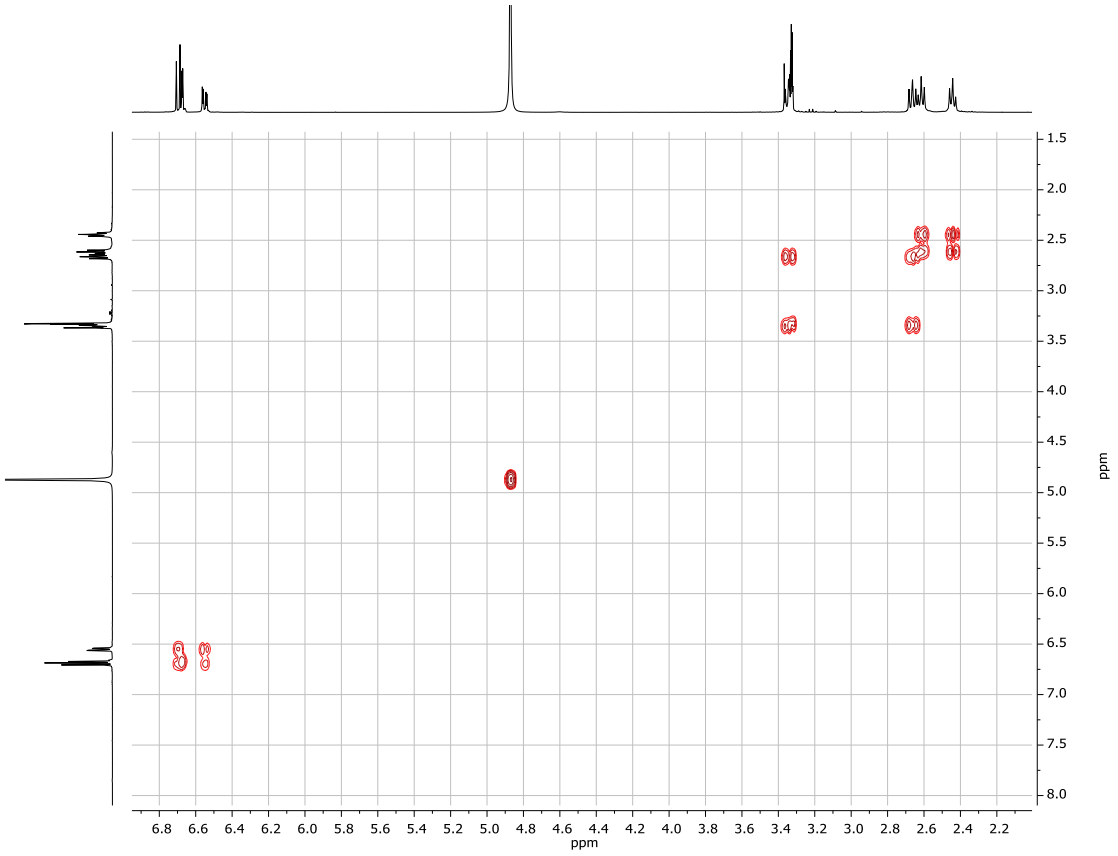
Characterization of diaminobis((4-((3,4-dihydroxyphenethyl)amino)-4-oxobutanoyl)oxy)Pt (IV) chloride (PtBC)



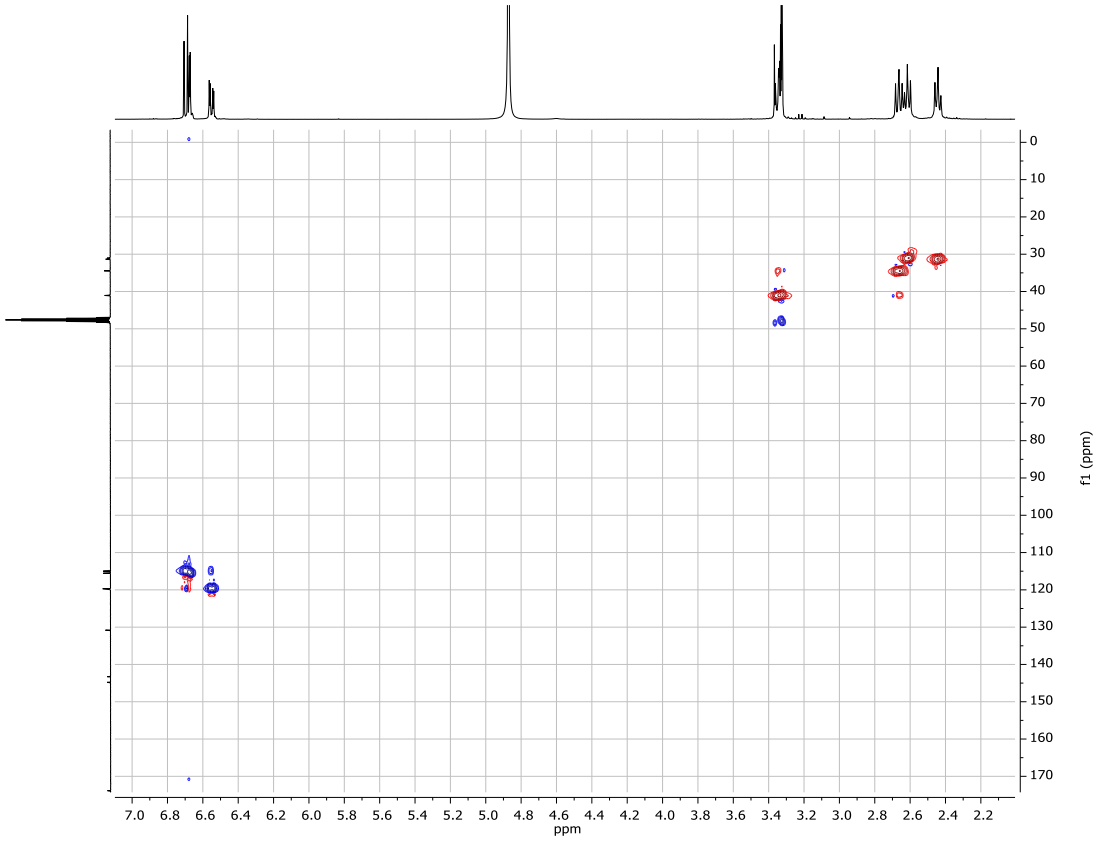
Annexe **3.5**. ^{1}H-NMR of **PtBC**.



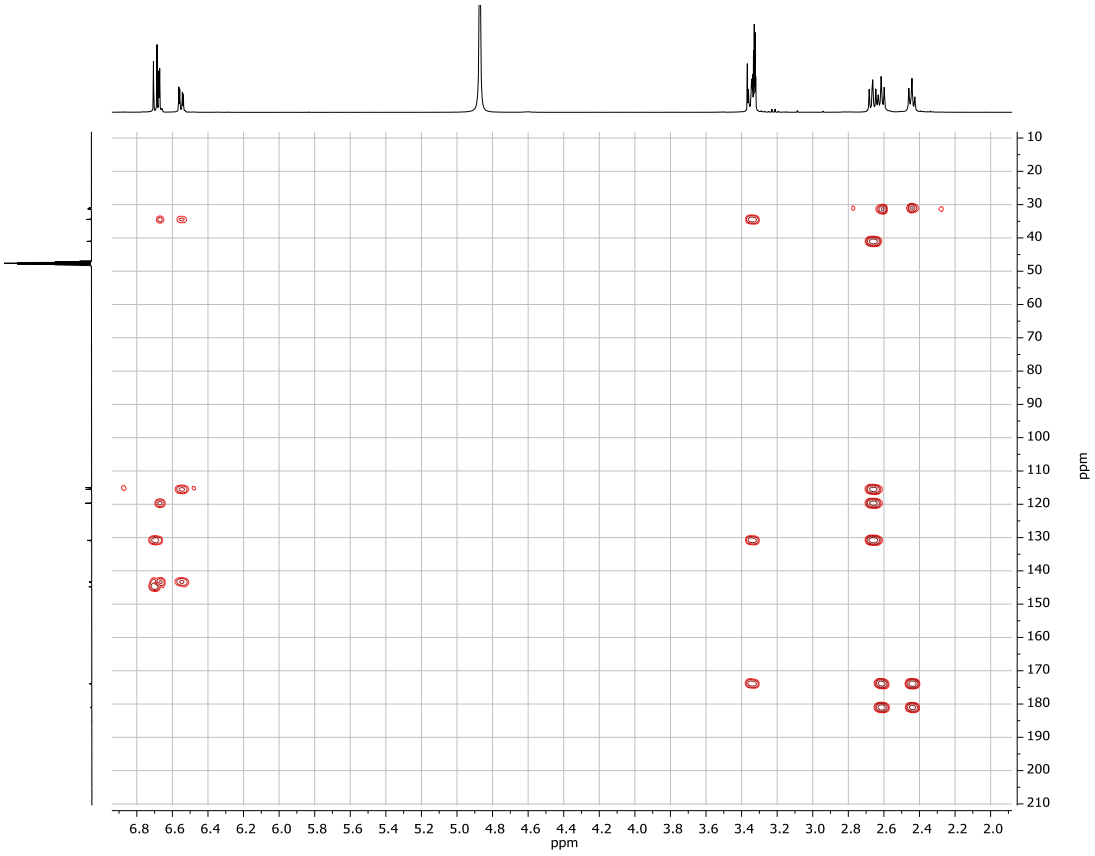
Annexe **3.6**. ^{13}C-NMR of **PtBC**.



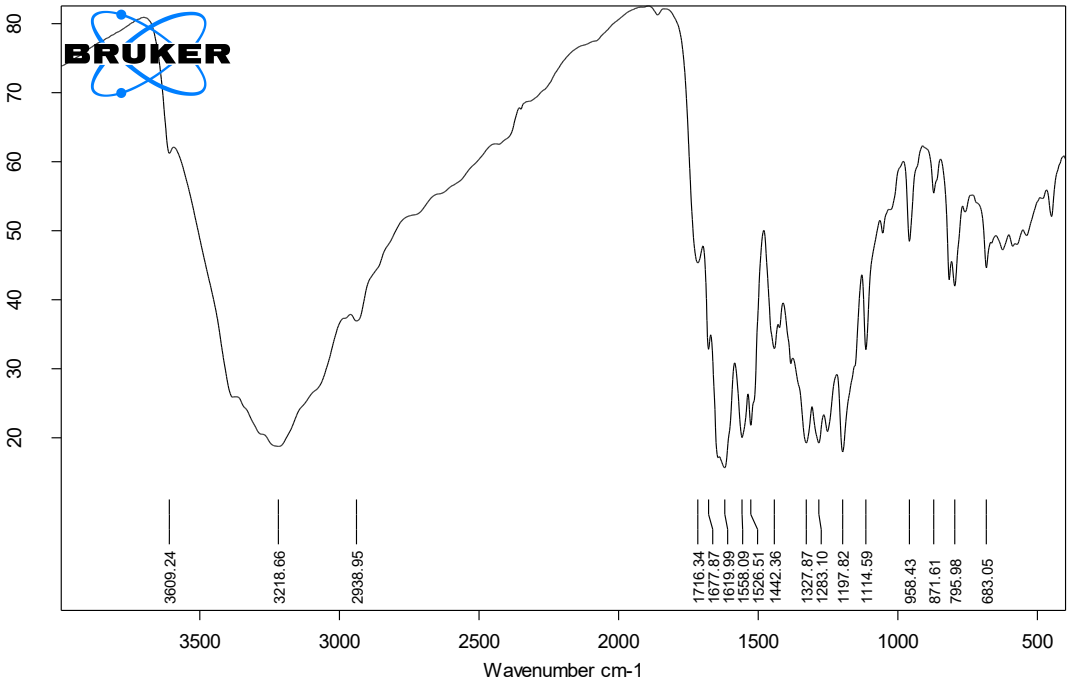
Annexe **3.7**. COSY NMR of complex **PtBC**.



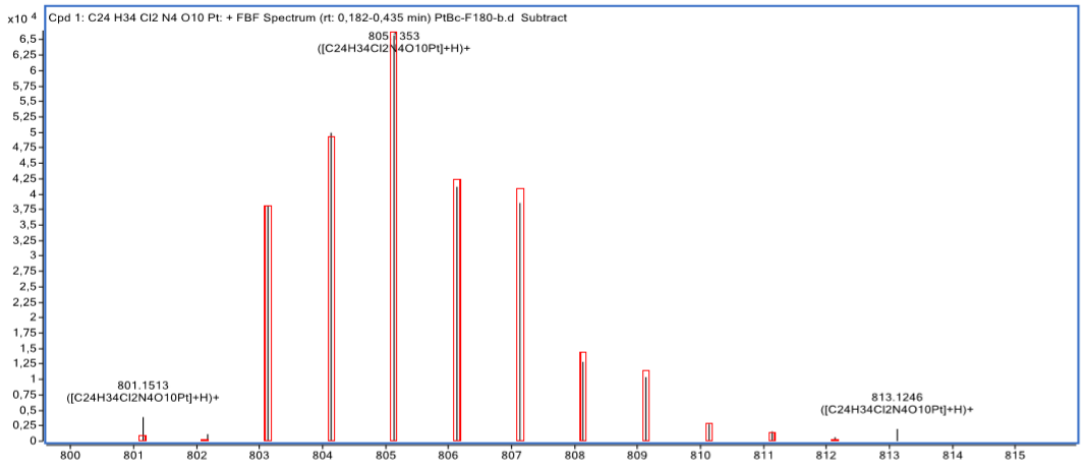
Annexe **3.8.** HSQC NMR of complex **PtBC**.



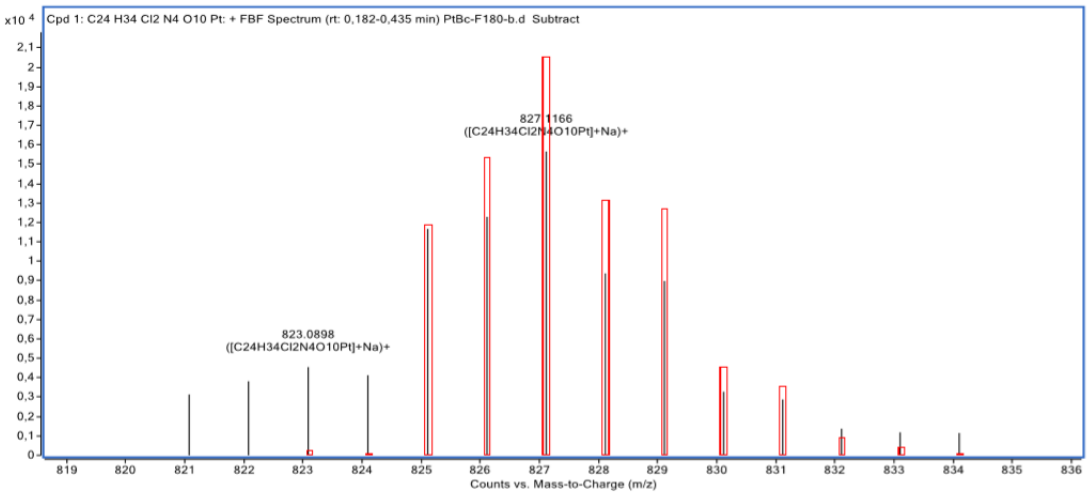
Annexe **3.9**. HMBC NMR of complex **PtBC**.



Annexe **3.10**. FTIR of **PtBC**.

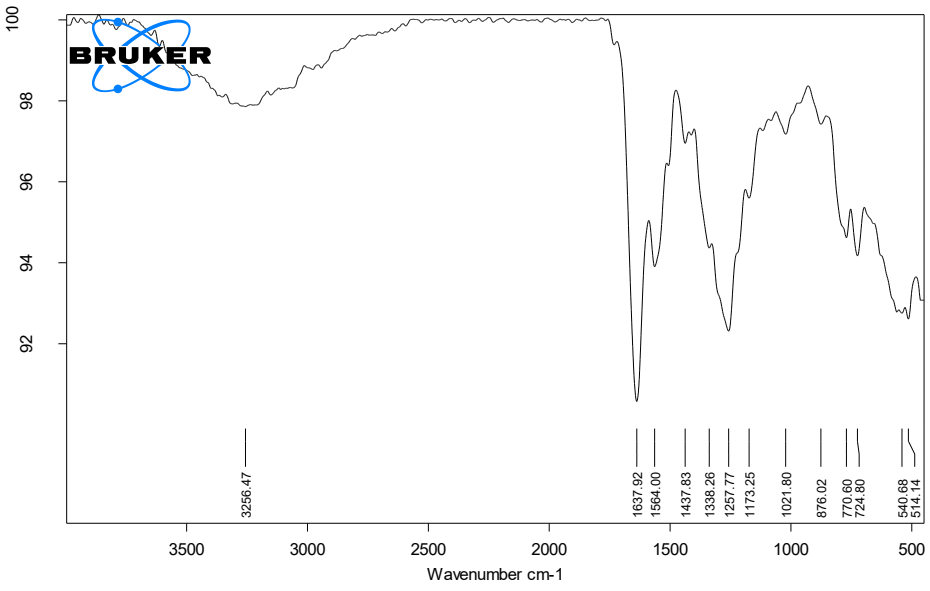


Annexe **3.11**. HRMS $[M+H]^+$ of complex **PtBC**.

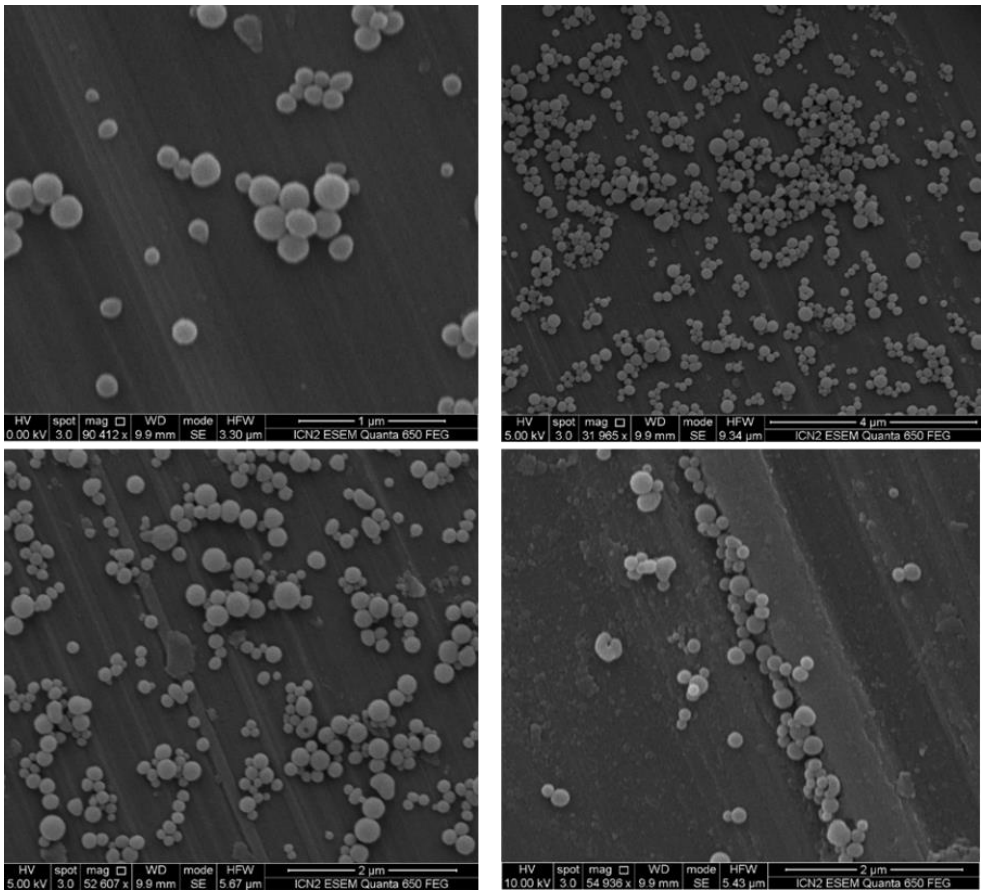


Annexe **3.12**. HRMS $[M+Na]^+$ of complex **PtBC**.

Characterisation of Polymeric Pt(IV) Bis-catechol NPs (pPtBC NP)

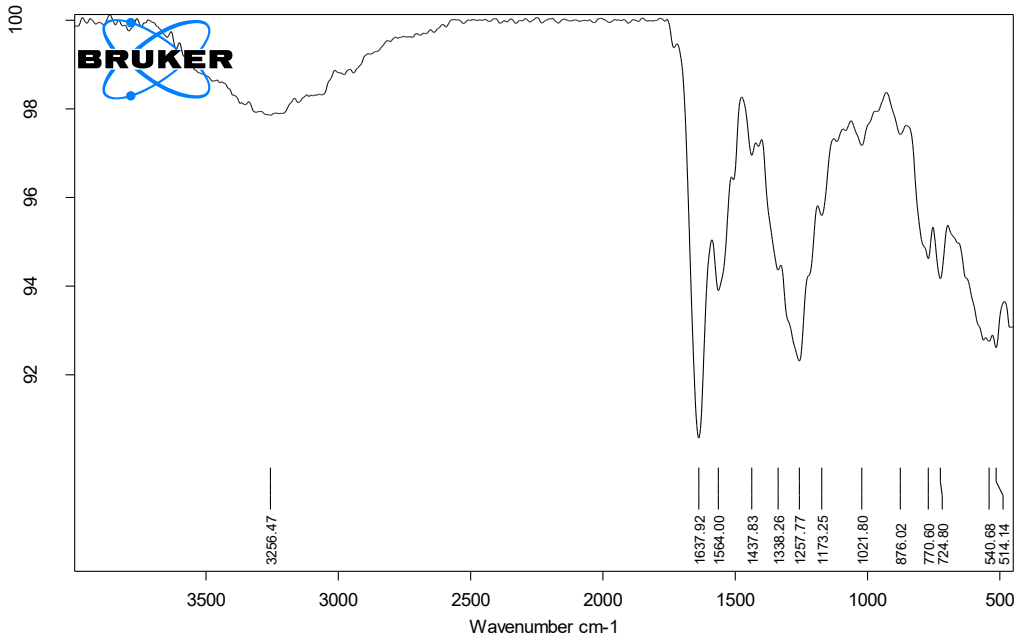


Annexe **3.13**. FTIR of **pPtBC NP**.

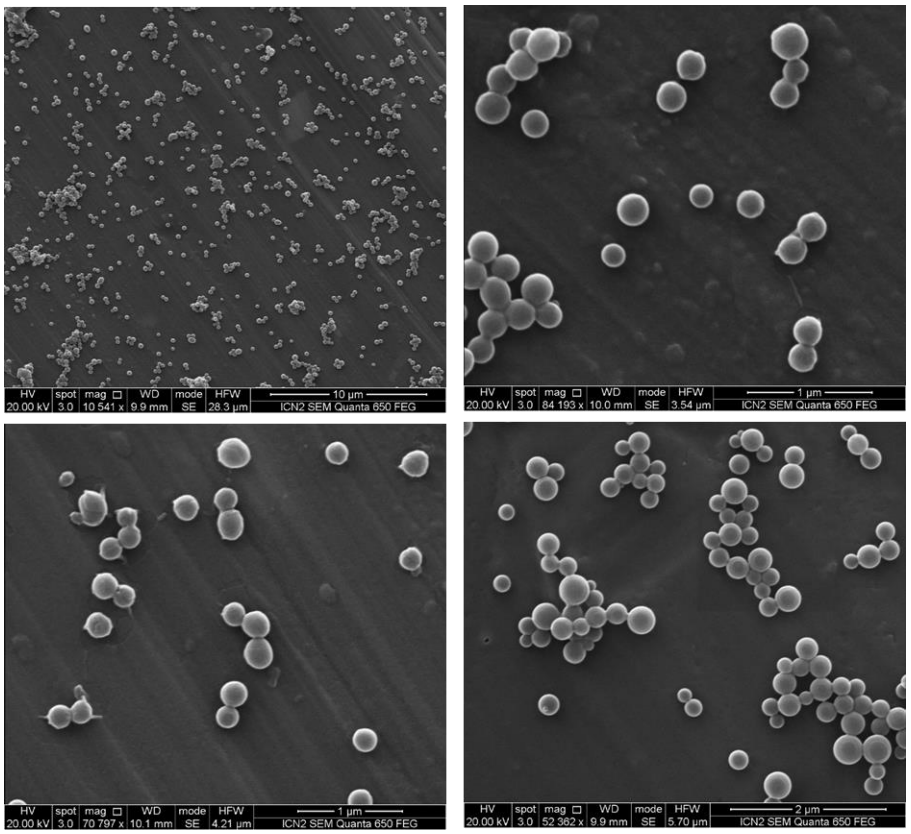


Annexe **3.14.** SEM imaging of **pPtBC NPs**.

Characterisation of Polymeric Nordihydroguaiaretic Acid NPs (pNDGA NPs)



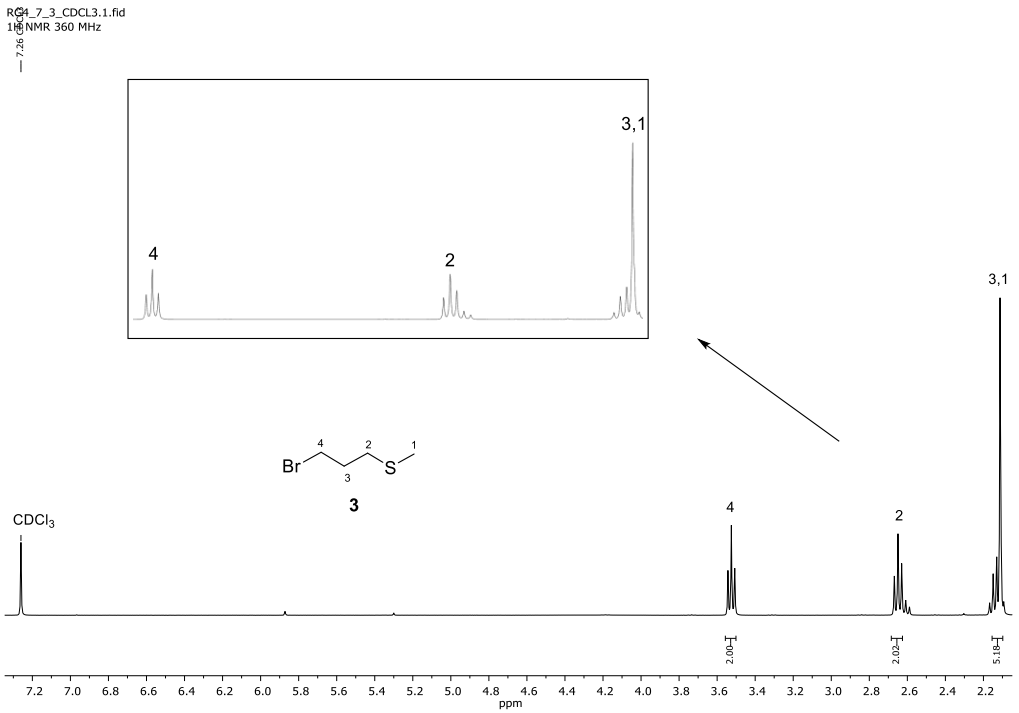
Annexe **3.15.** FTIR of **pNDGA NPs**.



Annexe **3.16**. SEM imaging of **pNDGA NPs**.

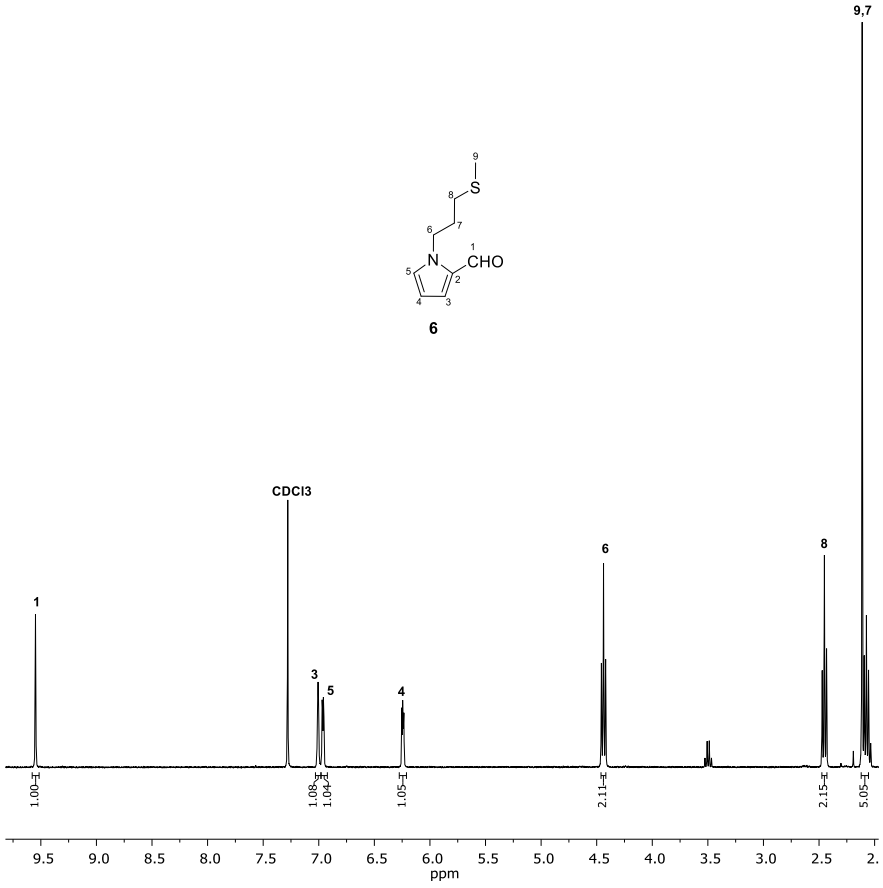
3.7.2. Supramolecular Photoactivatable Squaraine Pt(II) Nanoparticles

Characterisation of (3-bromopropyl)(methyl)sulfane (3)



Annexe **3.17**. ^{1}H-NMR of **3**.

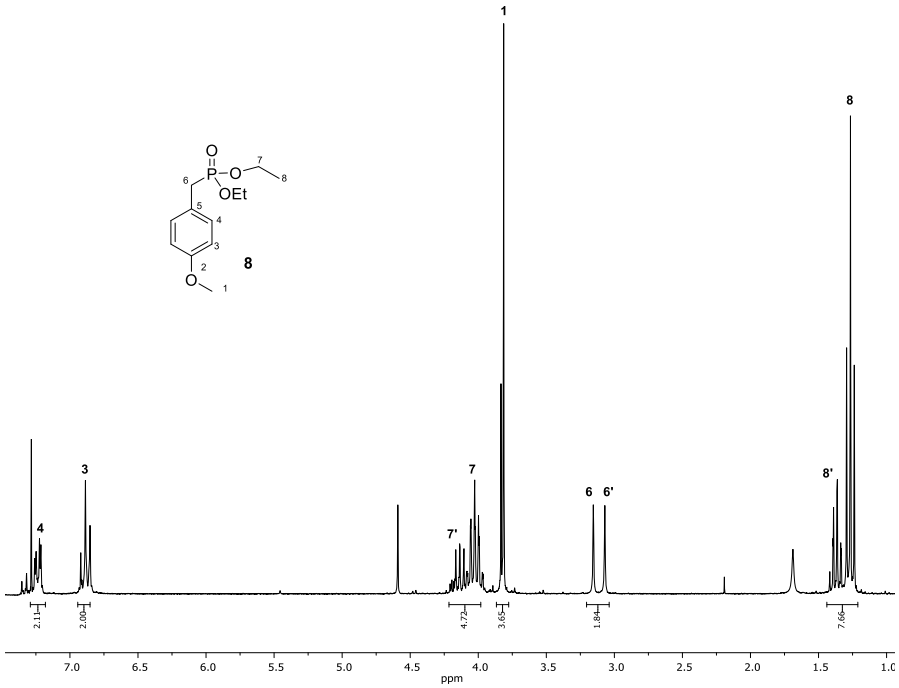
Characterisation of 1-(3-(methylthio)propyl)-1H-pyrrole-2-carbaldehyde (6)



6

Annexe **3.18**. ^{1}H-NMR of **6**.

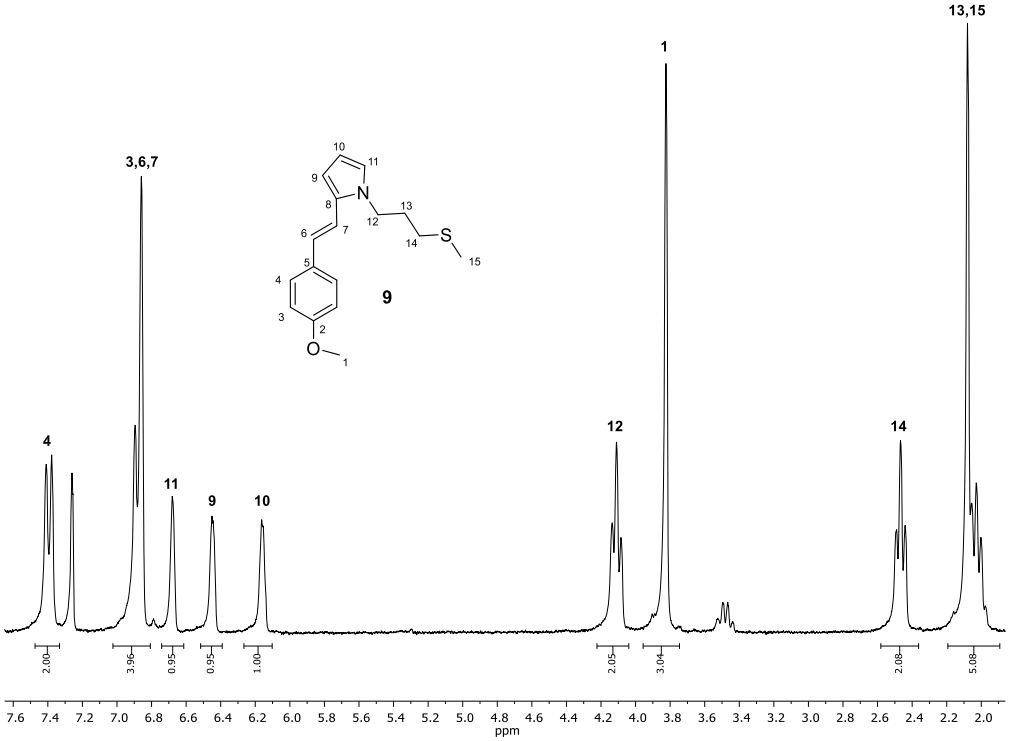
Characterisation of diethyl (4-methoxybenzyl)phosphonate (8)



8

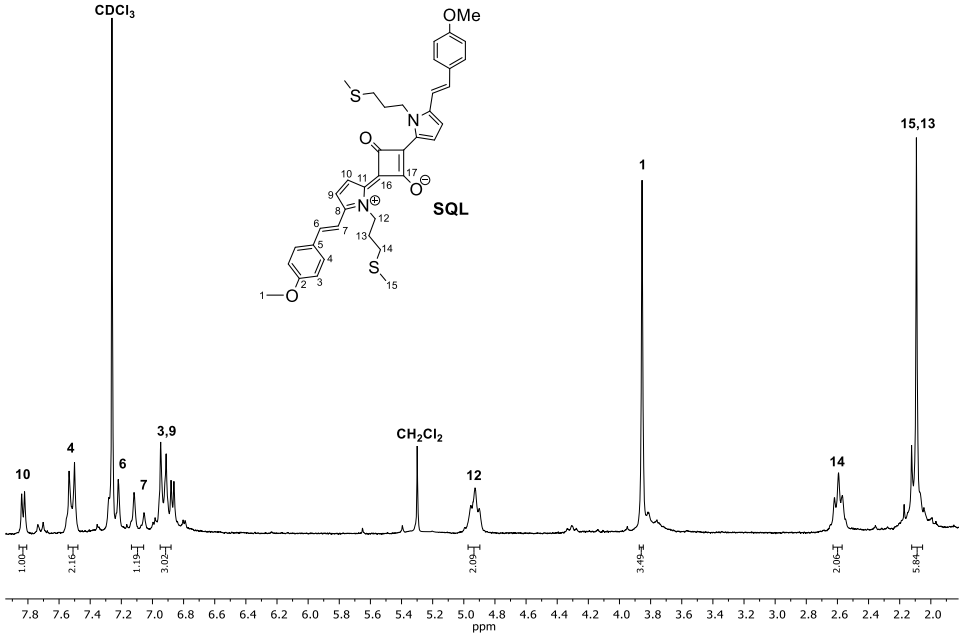
Annexe **3.19**. ^{1}H-NMR of **8**.

Characterisation of (E)-2-(4-methoxystyryl)-1-(3-(methylthio)propyl)-1H-pyrrole (9)

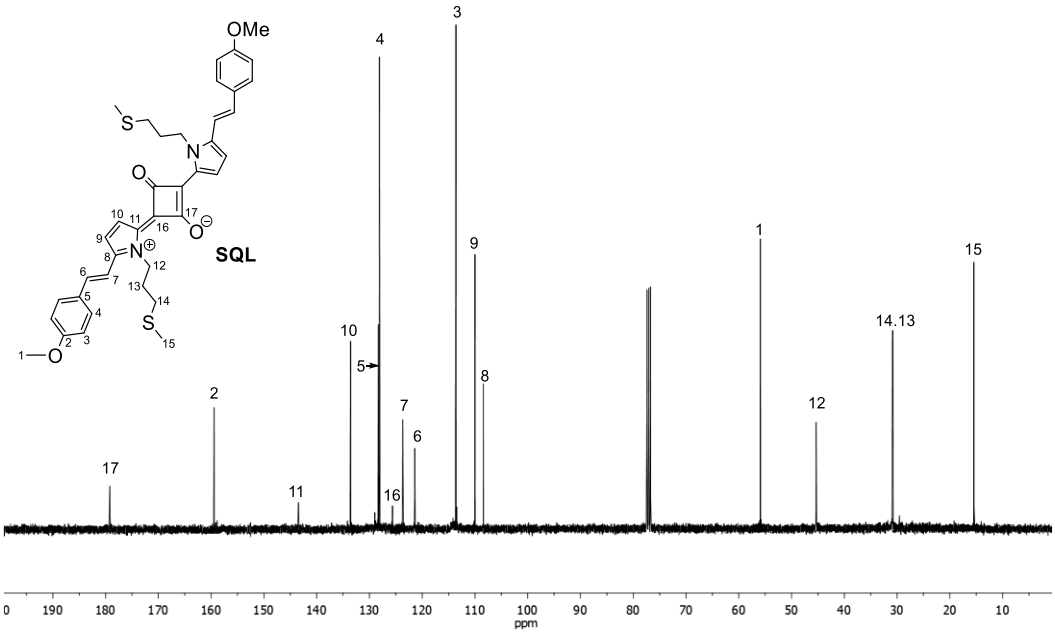


Annexe **3.20**. ^{1}H-NMR of **9**.

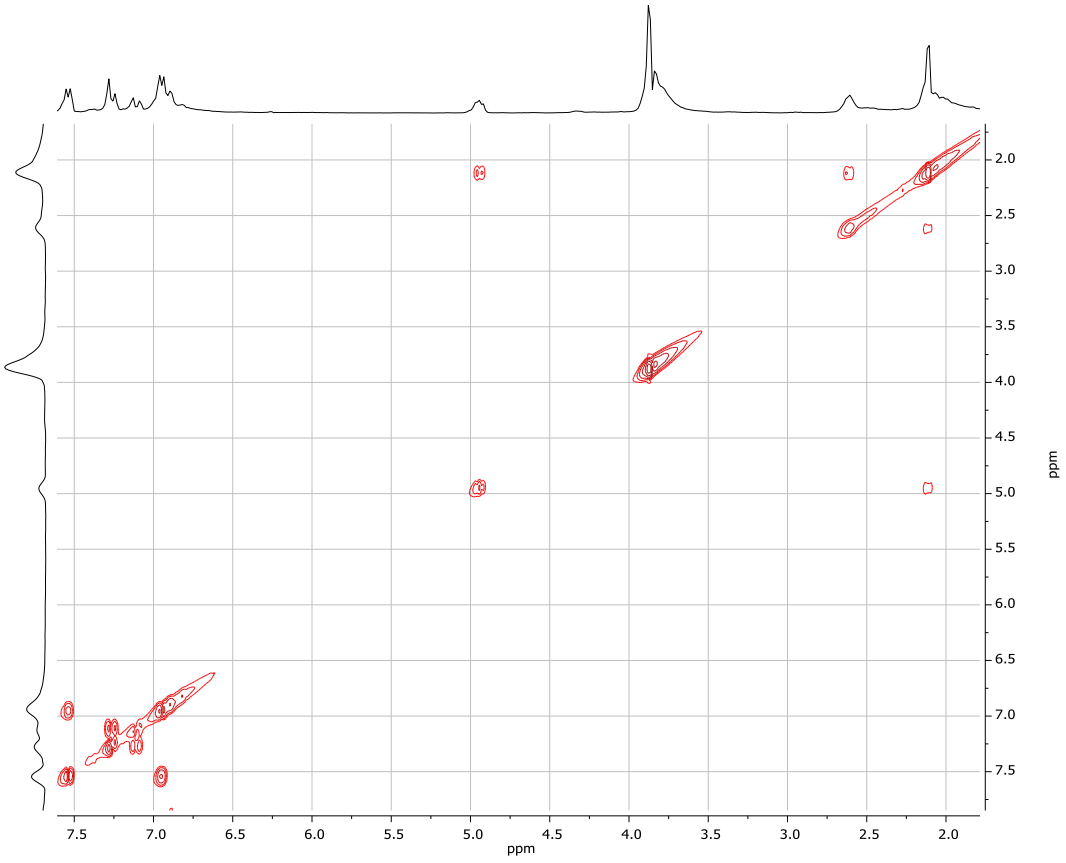
Characterisation of (E)-2-(5-((E)-4-methoxystyryl)-1-(3-(methylthio)propyl)- 1H-pyrrol-2-yl)-4-(5-((E)-4-methoxystyryl)-1-(3-(methylthio)propyl)-2H-pyrrol-1-ium-2-ylidene)-3-oxocyclobut-1-en-1-olate (SQL)



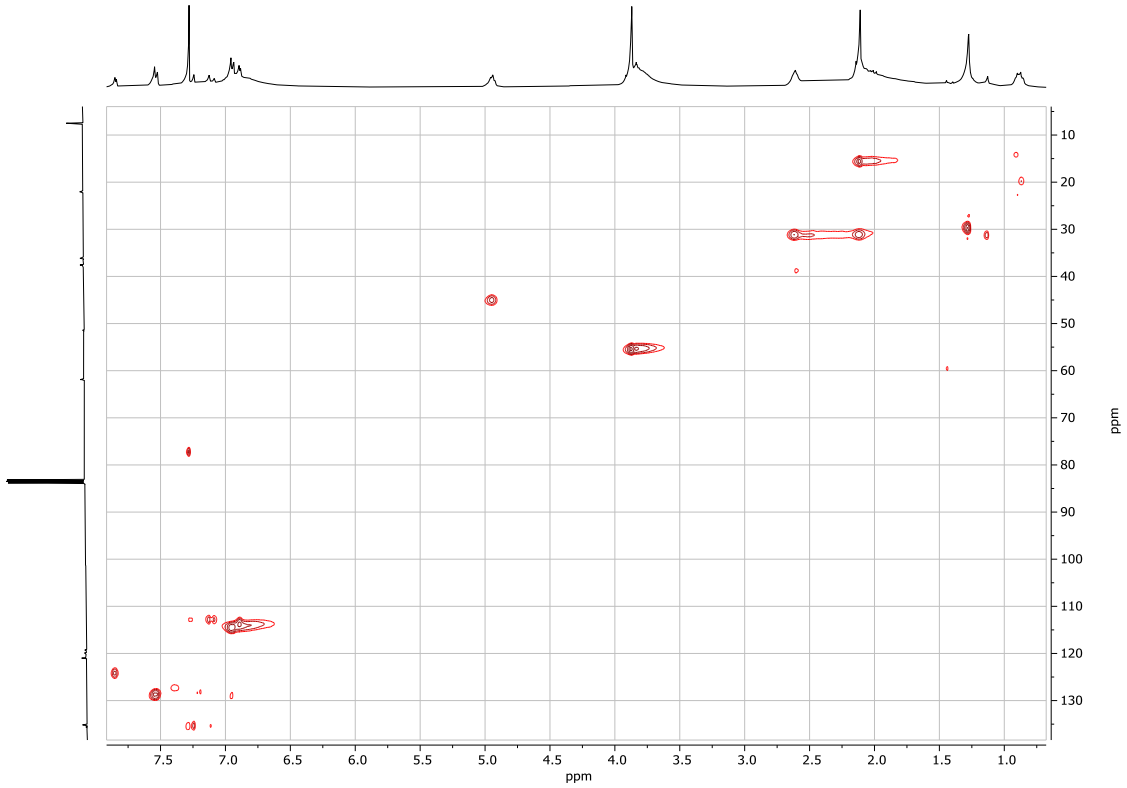
Annexe **3.21**. ^{1}H-NMR of **SQL**.



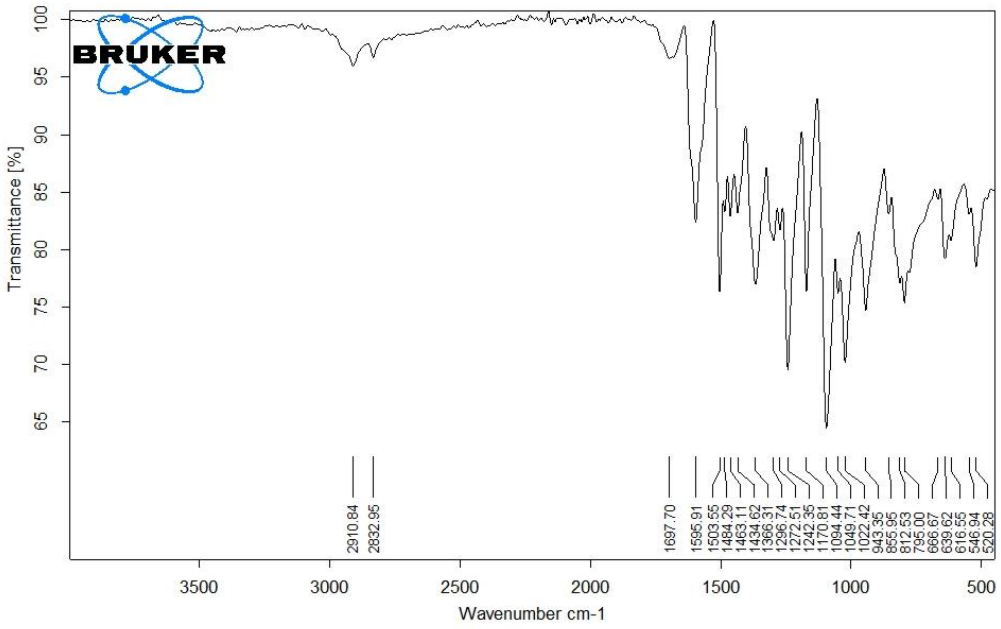
Annexe **3.22**. ^{13}C-NMR of **SQL**.



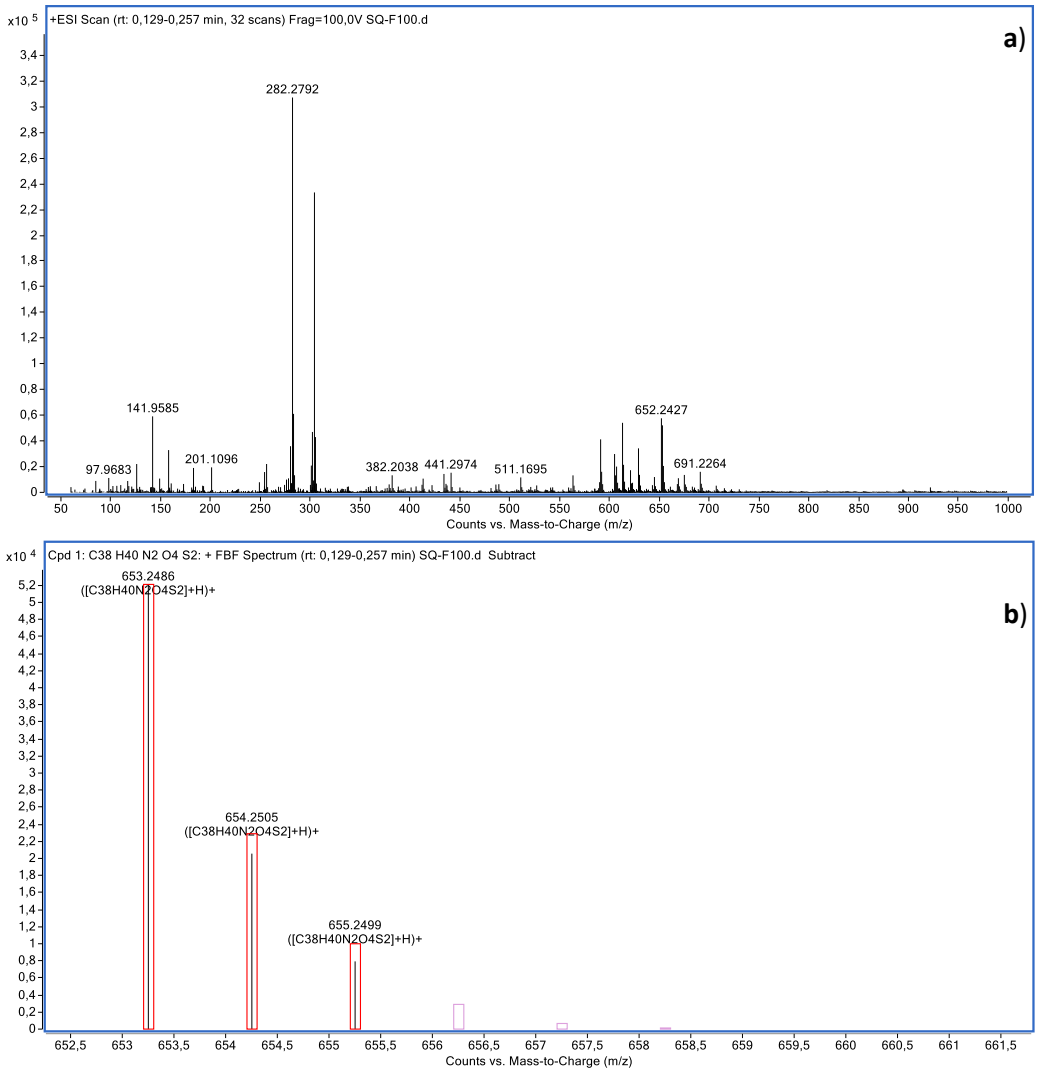
Annexe **3.23**. COSY of **SQL**.



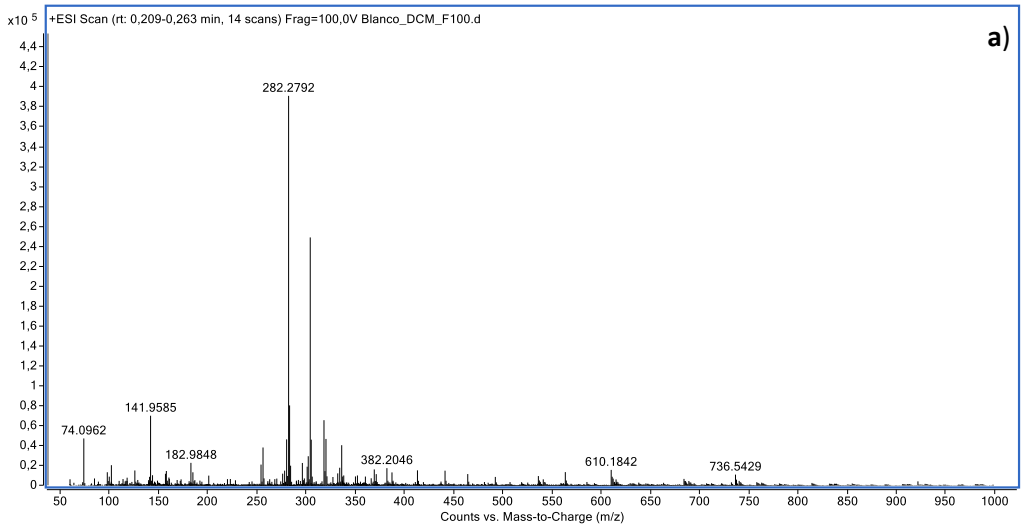
Annexe **3.24**. HSQC of **SQL**.

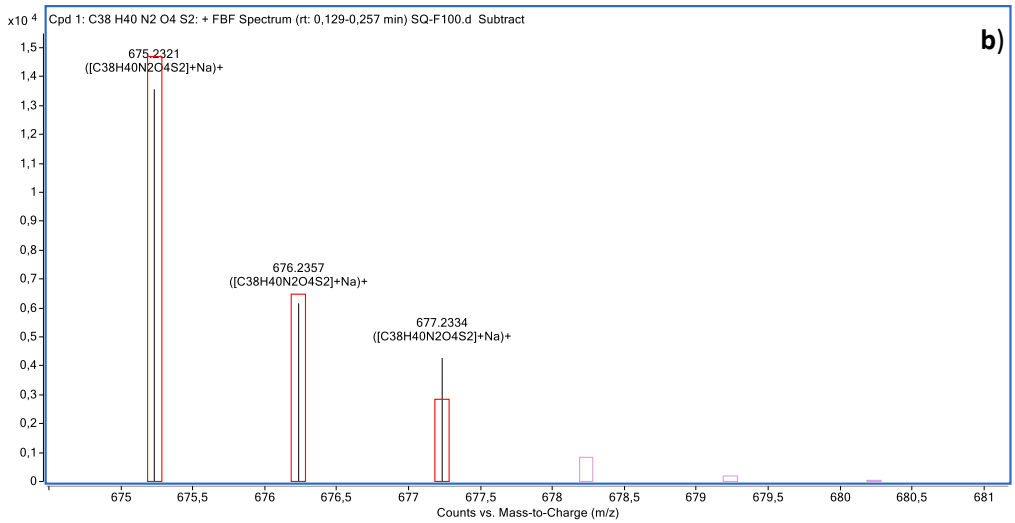


Annexe **3.25**. FTIR of **SQL**.



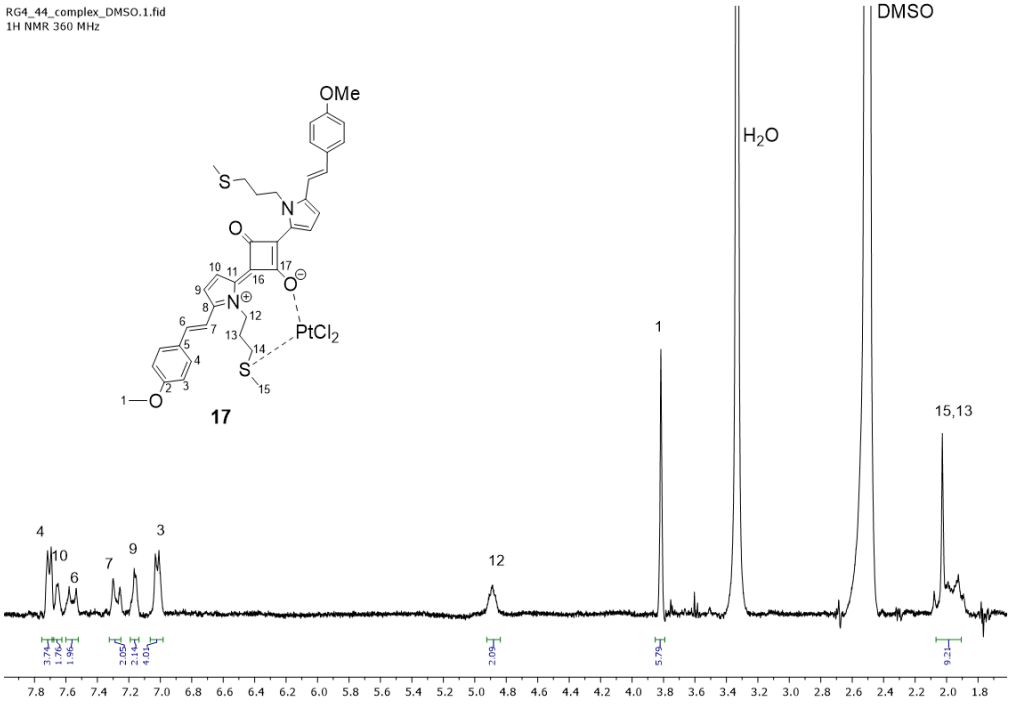
Annexe **3.26.** HRMS of **SQL** at **a)** with [M+H] entire scan **b)** [M+H] centered at SQL M value with theoretical values in red squares and real values in black lines.



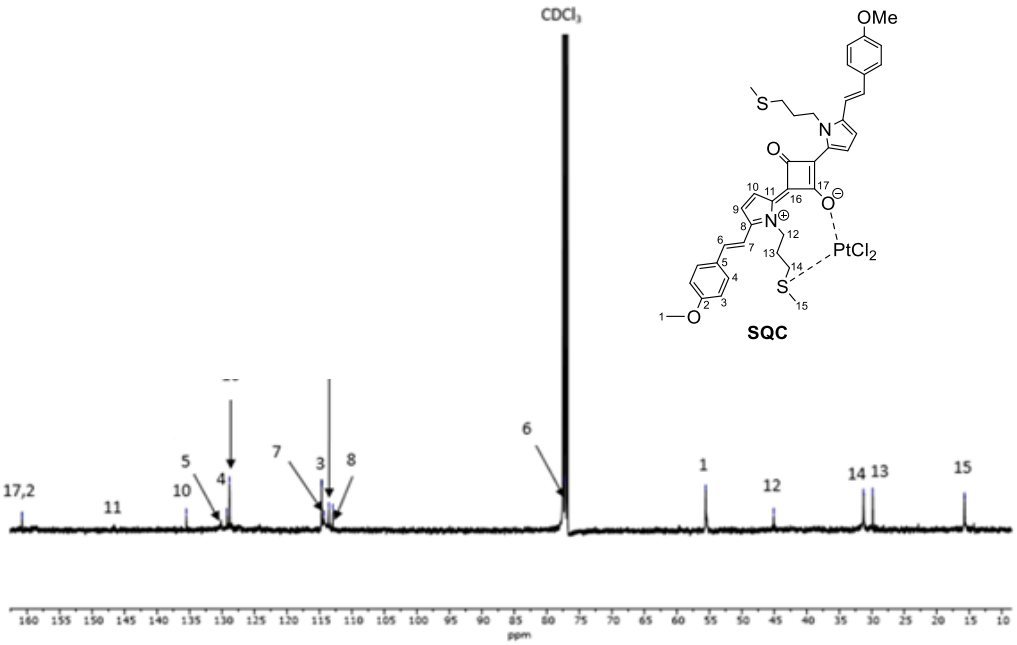


Annexe **3.27.** HRMS of **SQL** at **a**) with [M+Na] entire scan (**b**) [M+Na] centered at SQL M value with theoretical values in red squares and real values in black lines.

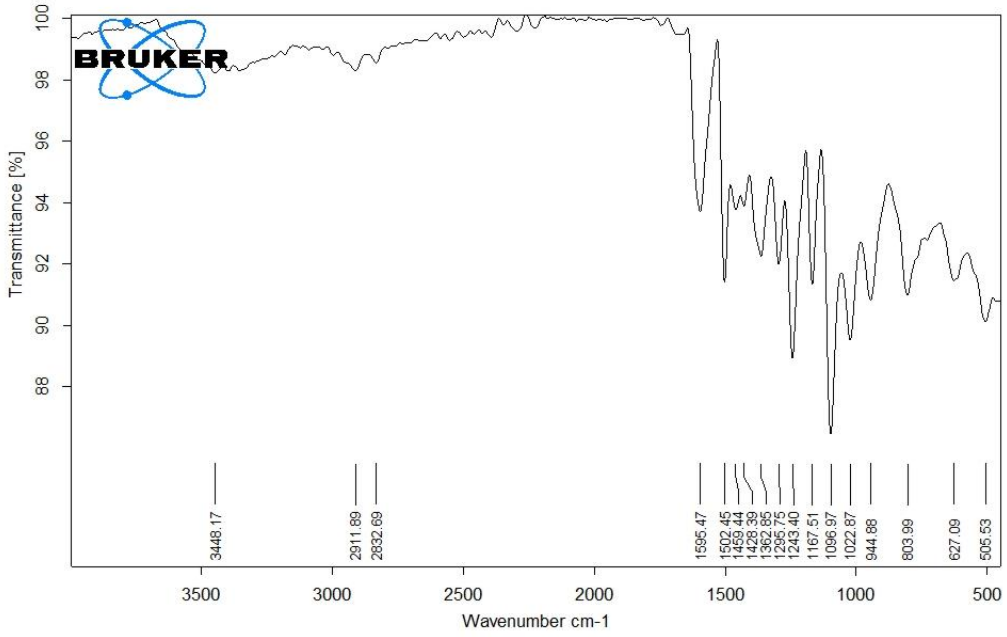
Characterisation of dichloro(((E)-2-(5-((E)-4-methoxystyryl)-1-(3-(methylthio)propyl)-1H-pyrrol-2-yl)-4-(5-((E)-4-methoxystyryl)-1-(3-(methylthio)propyl)-2H-pyrrol-1-ium-2-ylidene)-3-oxocyclobut-1-en-1-yl)oxy)platinate(II) (SQC)



Annexe **3.28**. ^{1}H-NMR of **SQC**



Annexe **3.29**. ^{13}C-NMR of **SQC**



Annexe **3.30**. FTIR of **SQC**

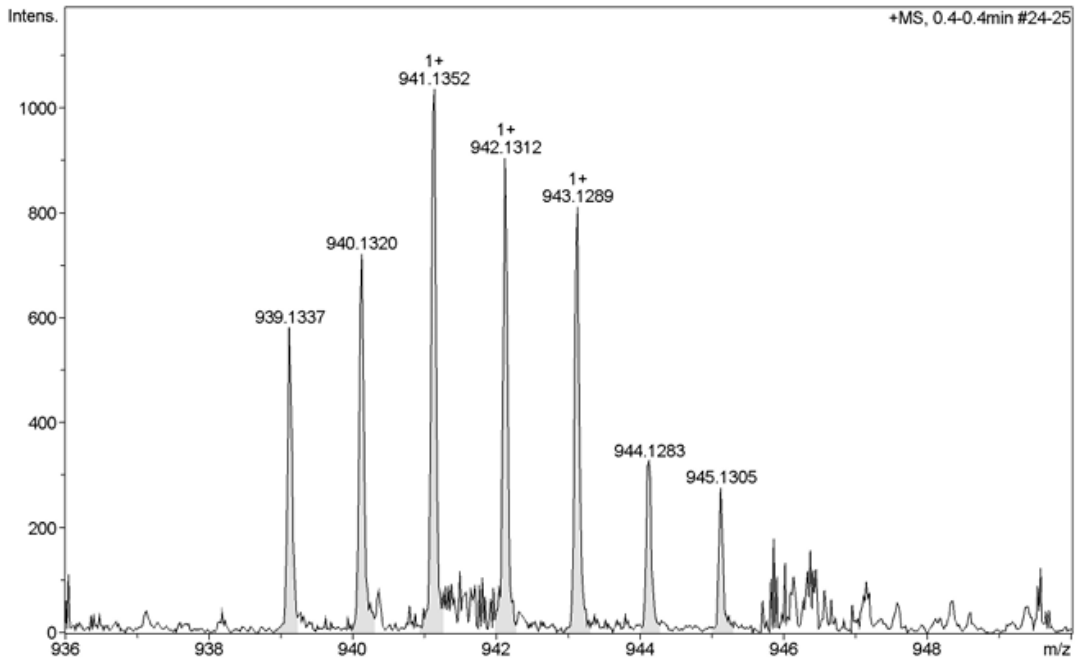
Servei d'Anàlisi Química **Universitat Autonoma de Barcelona**

Àrea de Cromatografia i Espectrometria de Masses

Registre d'alta resolució

Analysis Info

Analysis Name	20EM039(RG4-47-Complex)_1-B,4_01_27455.d	Acquisition Date	21/07/2020 13:47:04
Method	_FI_wide_pos_2016-06-20.m	Operator	SAQ
Sample Name	20EM039(RG4-47-Complex)	Instrument	micrOTOF-Q
Comment	OPR-MBR // ESI+ / Dó en MeCN µfiltrada // Química - Roger Gómez.		



#	m/z	I	I %
1	939.1337	582	56.2
2	940.1320	721	69.7
3	941.1352	1035	100.0
4	942.1312	905	87.5
5	943.1289	811	78.4
6	944.1283	328	31.7
7	945.1305	278	26.9

Annexe **3.31.** HRMS of **SQC** at with [M+Na]

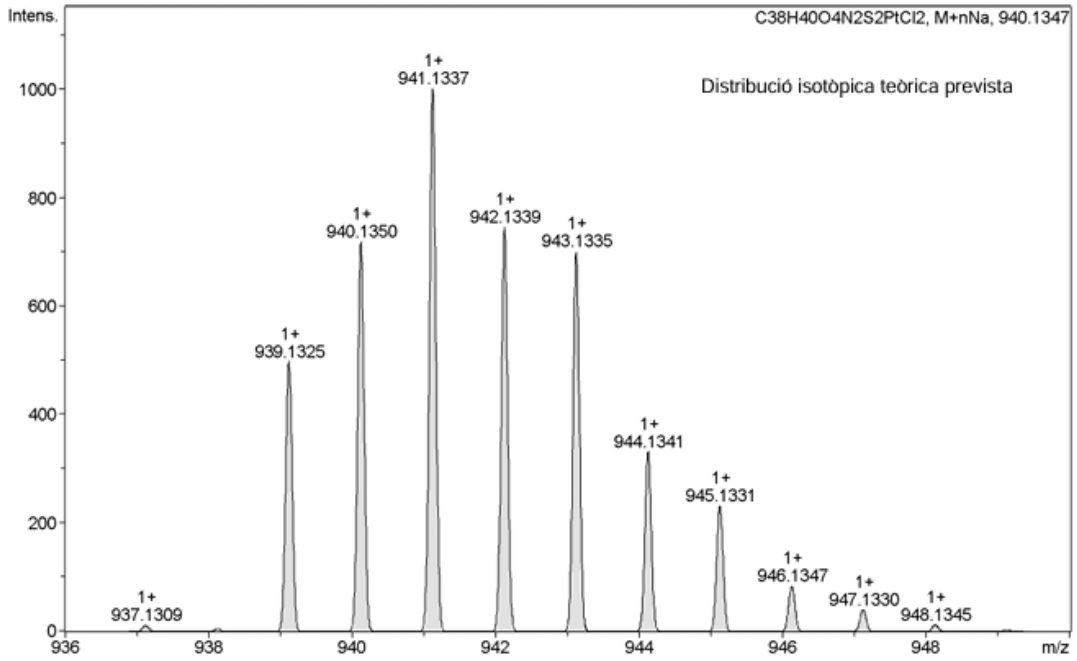
Servei d'Anàlisi Química **Universitat Autonoma de Barcelona**

Àrea de Cromatografia i Espectrometria de Masses

Registre d'alta resolució

Analysis Info

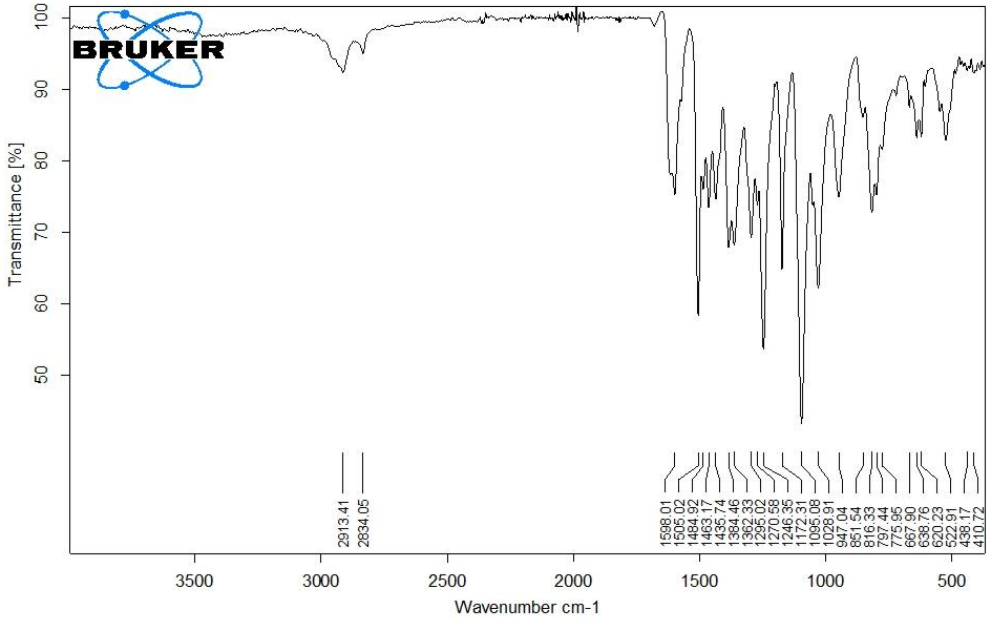
Analysis Name	20EM039(RG4-47-Complex)_1-B,4_01_27455.d	Acquisition Date	21/07/2020 13:47:04
Method	_FI_wide_pos_2016-06-20.m	Operator	SAQ
Sample Name	20EM039(RG4-47-Complex)	Instrument	micrOTOF-Q
Comment	OPR-MBR // ESI+ / Dó en MeCN µfiltrada // Química - Roger Gómez.		



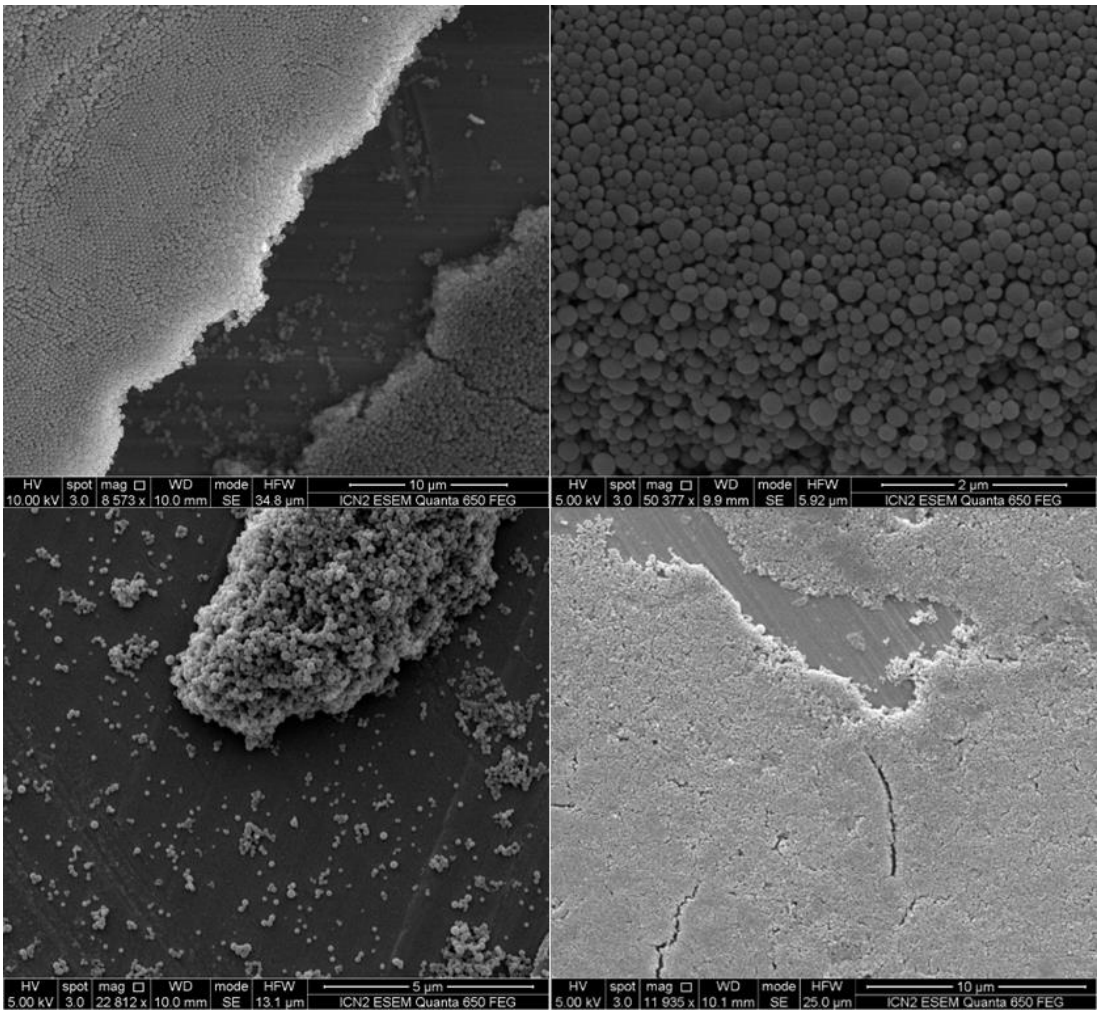
#	m/z	I	I %
1	937.1309	12	1.2
2	939.1325	496	49.6
3	940.1350	717	71.7
4	941.1337	1000	100.0
5	942.1339	744	74.4
6	943.1335	700	70.0
7	944.1341	331	33.1
8	945.1331	232	23.2
9	946.1347	84	8.4
10	947.1330	40	4.0
11	948.1345	12	1.2

Annexe **3.32.** HRMS of **SQC** at with theoretical values of [M+Na]

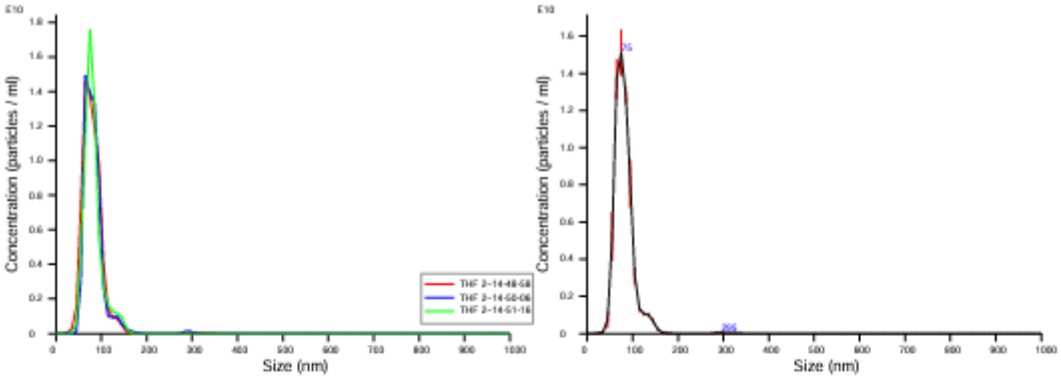
Characterisation of Squaraine Ligand Nanoparticles (SQL NP)



Annexe **3.33**. FTIR of **SQL NP**



Annexe **3.34.** SEM images of **SQL NP** under Pt 5 nm thin film layer.



FTLA Concentration / Size graph for Experiment:
THF 2 2022-09-14 14-48-36

Averaged FTLA Concentration / Size for Experiment:
THF 2 2022-09-14 14-48-36
Error bars indicate + / -1 standard error of the mean

Included Files

THF 2 2022-09-14 14-48-58
THF 2 2022-09-14 14-50-06
THF 2 2022-09-14 14-51-16

Details

NTA Version:	NTA 3.4 Build 3.4.4
Script Used:	SOP Standard Measurement 02-48-23PM 14~
Time Captured:	14:48:36 14/09/2022
Operator:	Amable Bernabe
Pre-treatment:	1:50
Sample Name:	THF 2
Diluent:	Milli- Q Water
Remarks:	

Capture Settings

Camera Type:	sCMOS
Laser Type:	Blue488
Camera Level:	12
Slider Shutter:	1200
Slider Gain:	146
FPS	25.0
Number of Frames:	1498
Temperature:	22.4 - 22.7 ºC
Viscosity:	(Water) 0.938 - 0.944 cP
Dilution factor:	5 x 10e1
Syringe Pump Speed:	50

Analysis Settings

Detect Threshold:	5
Blur Size:	Auto
Max Jump Distance:	Auto: 14.5 - 16.7 pix

Results

Stats: Merged Data

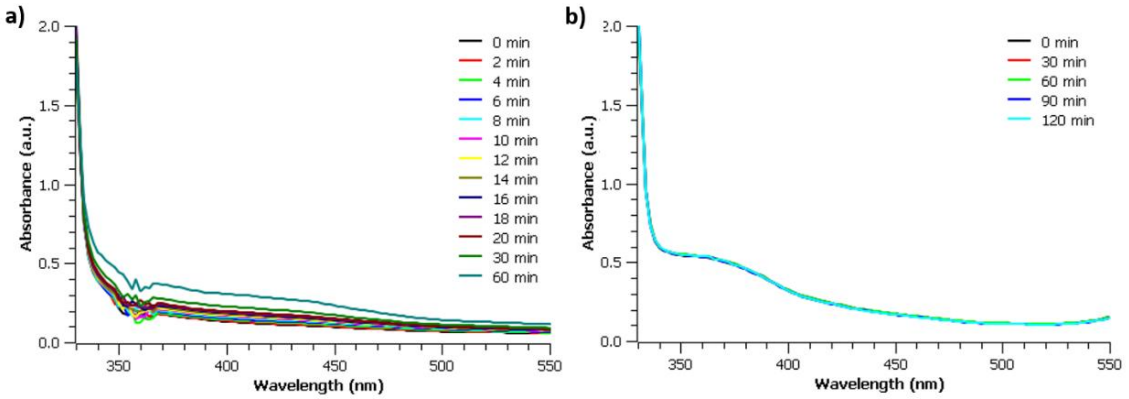
Mean:	81.2 nm
Mode:	73.8 nm
SD:	22.1 nm
D10:	60.2 nm
D50:	77.9 nm
D90:	104.2 nm

Stats: Mean +/- Standard Error

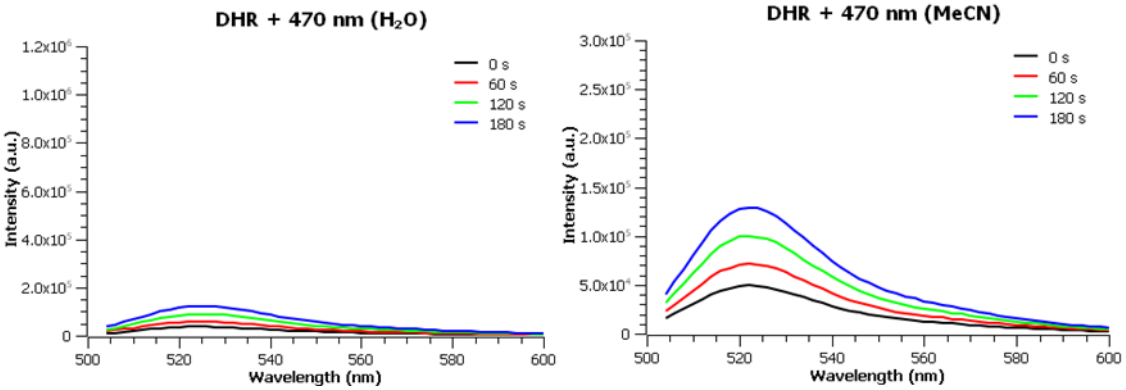
Mean:	81.2 +/- 0.8 nm
Mode:	71.4 +/- 2.2 nm
SD:	22.0 +/- 1.1 nm
D10:	59.6 +/- 1.7 nm
D50:	77.9 +/- 0.6 nm
D90:	104.4 +/- 1.4 nm
Concentration:	6.34e+10 +/- 2.09e+09 particles/ml
	69.3 +/- 2.3 particles/frame
	81.8 +/- 0.9 centres/frame

Annexe **3.35**. NTA analysis summary of **SQL NP**

*Fluorescence spectra of the photochemical study using the **DHN** probe for the determination of superoxide production.*

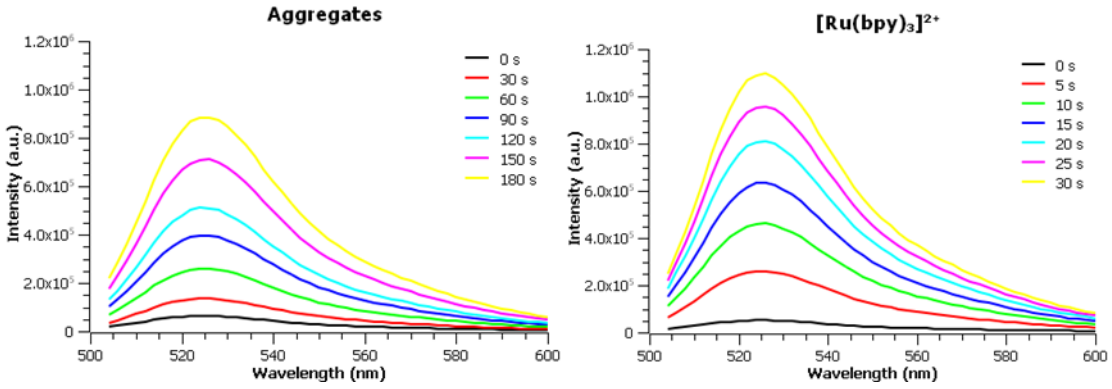


Annexe **3.36**. **a)** Evolution of the UV-vis spectrum of **DHN** upon blue light irradiation (470 nm, 51.4 mW·cm^{-2}) in the presence of **SQL NP** in water. **b)** Evolution of the UV-vis spectrum of **DHN** in the presence of **SQL NP** in water in dark conditions.

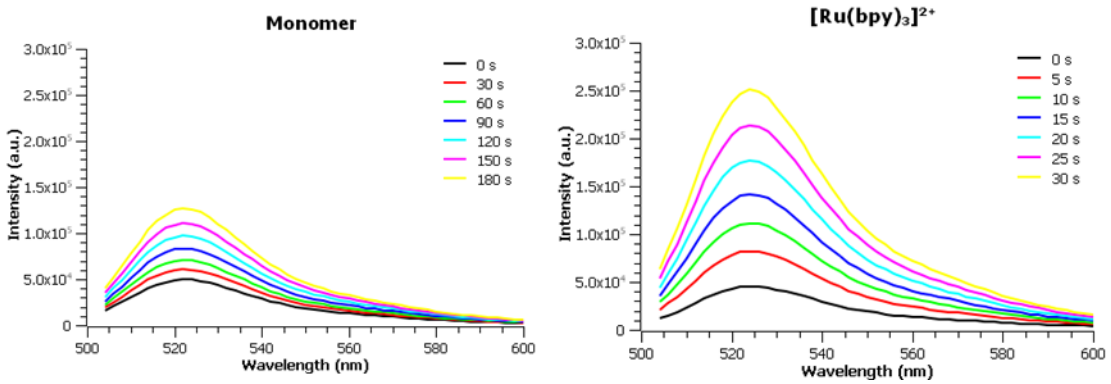


*Fluorescence spectra of the photochemical study using the **DHR123** probe for the determination of superoxide production.*

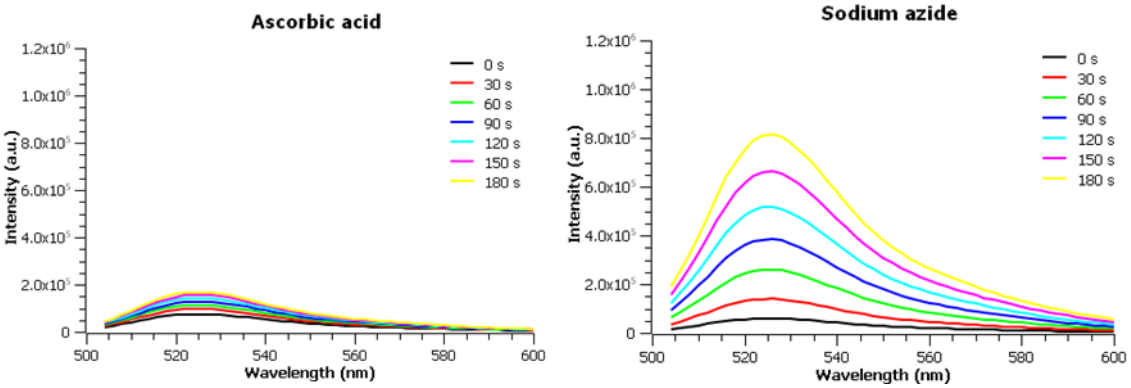
Annexe **3.37**. Evolution of the fluorescence spectra emission of DHR123 upon blue light irradiation (470 nm, 51.4 mW·cm^{-2}) without PS in water and ACN.



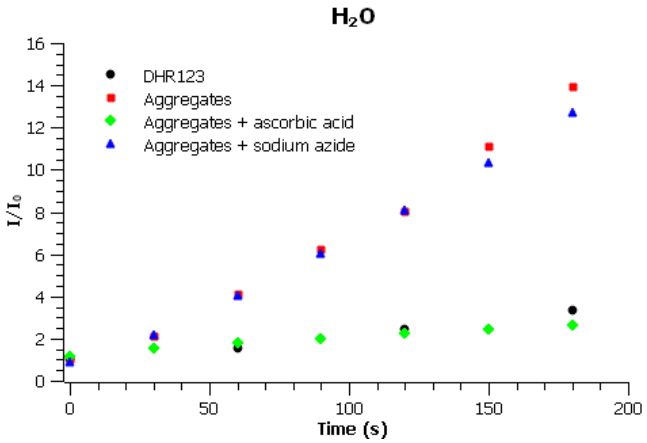
Annexe **3.38.** Evolution of the fluorescence spectra emission of DHR123 upon blue light irradiation (470 nm, 51.4 mW·cm^{-2}) with **SQL NP** and $[Ru(bpy)_3]^{2+}$ in water.



Annexe **3.39.** Evolution of the fluorescence spectra emission of DHR123 upon blue light irradiation (470 nm, 51.4 mW·cm^{-2}) with **SQL** and $[Ru(bpy)_3]^{2+}$ in ACN.



Annexe **3.40.** Evolution of the fluorescence spectra emission of DHR123 upon blue light irradiation (470 nm, 51.4 mW·cm^{-2}) with **SQL NP** and 100 equiv. of scavenger in water.

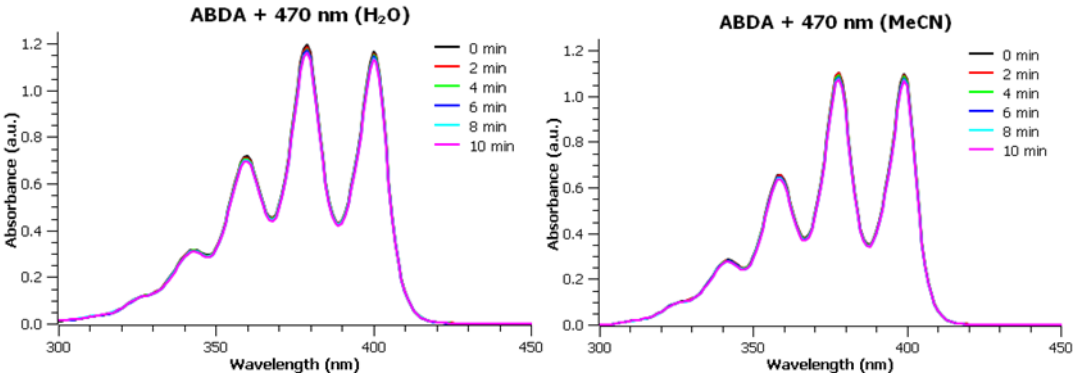


Annexe **3.41**. Comparative plots of I/I_0 as a function of time for the experiment of photooxidation of DHR123 under blue light irradiation (470 nm, 51.4 mW·cm^{-2}) in water in the presence of scavengers (ascorbic acid or sodium azide).

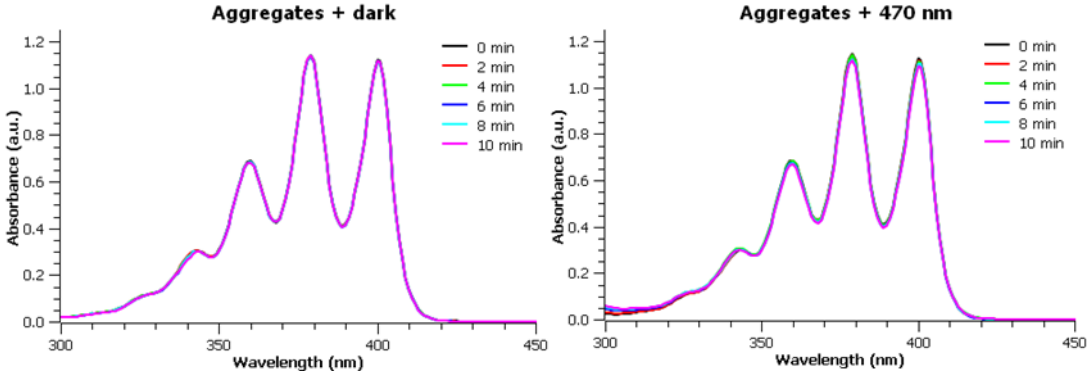
Annexe **3.42.** Slope (S) of I/I_0 vs time for the experiments of photooxidation of DHR123 upon blue light irradiation (470 nm, 51.4 mW·cm^{-2}) in water.

Compound	S
DHR123 control	0.0130
Aggregates	0.0723
Aggregates + Ascorbic acid	0.0080
Aggregates + Sodium azide	0.0666
$[Ru(bpy)_3]^{2+}$	0.6625

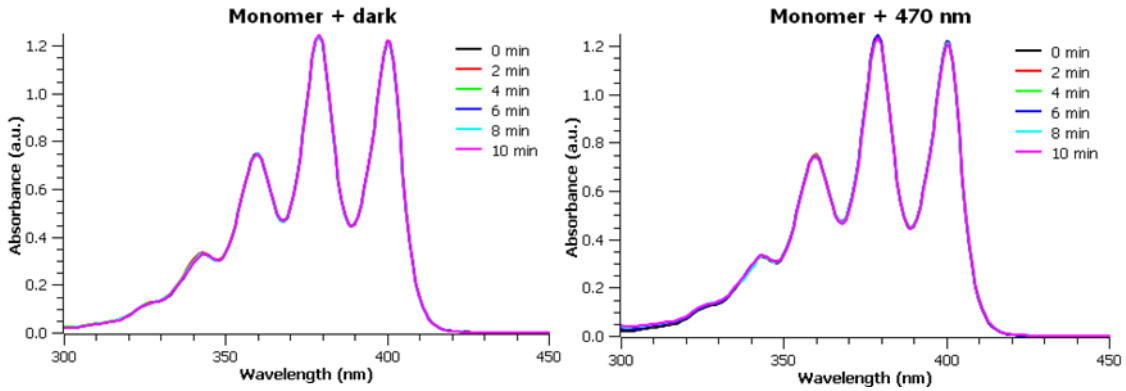
Fluorescence spectra of the photochemical study using the ABDA probe for the determination of SO.



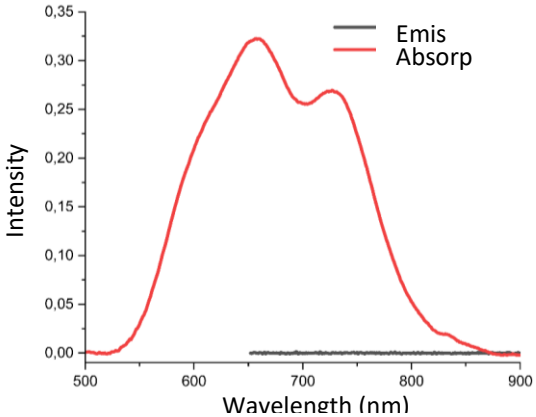
Annexe **3.43**. Evolution of the UV-vis spectra of ABDA without PS in water and ACN upon blue light irradiation (470 nm, 51.4 mW·cm^{-2}).



Annexe **3.44**. Evolution of the UV-vis spectra of ABDA with **SQL NP** in water in dark conditions and upon blue light irradiation (470 nm, 51.4 mW·cm^{-2}).

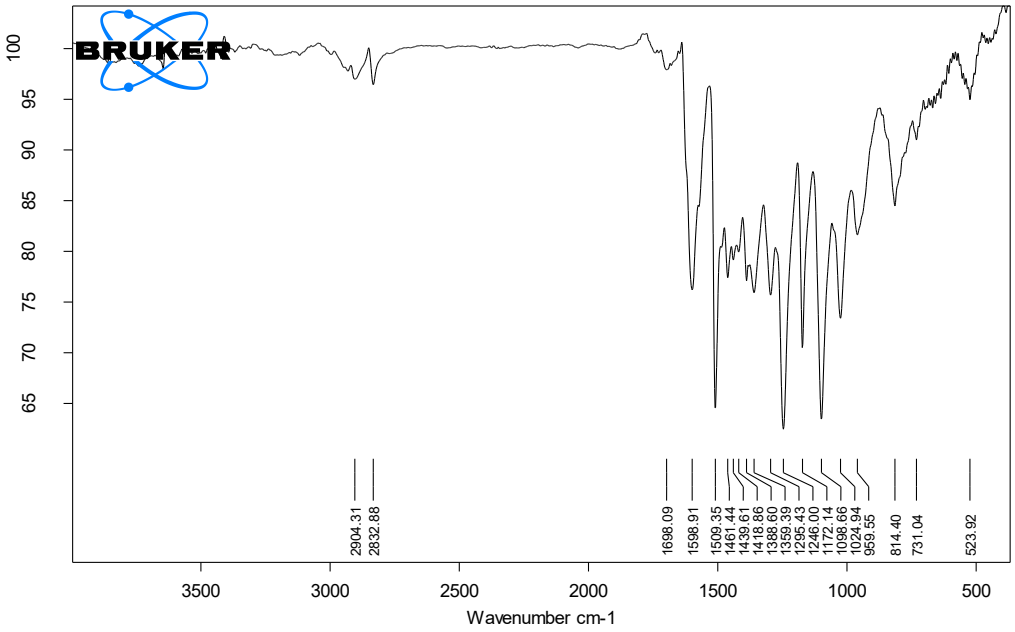


Annexe **3.45**. Evolution of the UV-vis spectra of ABDA with **SQL** in ACN in dark conditions and upon blue light irradiation (470 nm, 51.4 mW·cm^{-2}).

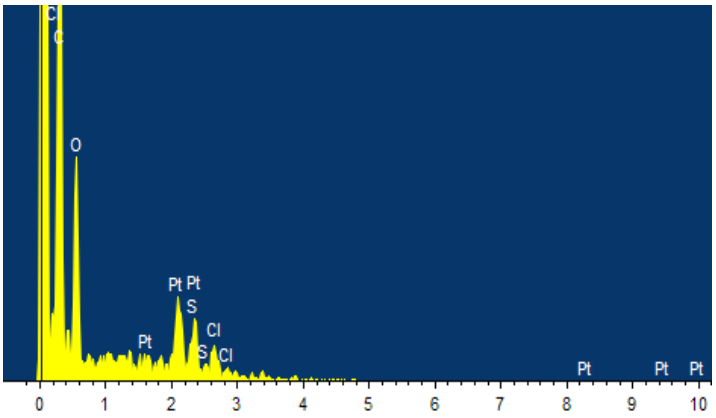


Annexe **3.46**. UV–vis absorption and fluorescence emission (under 675 nm excitation) of **SQL NPs** in water.

Characterisation of squaraine complex NPs (SQC NP)

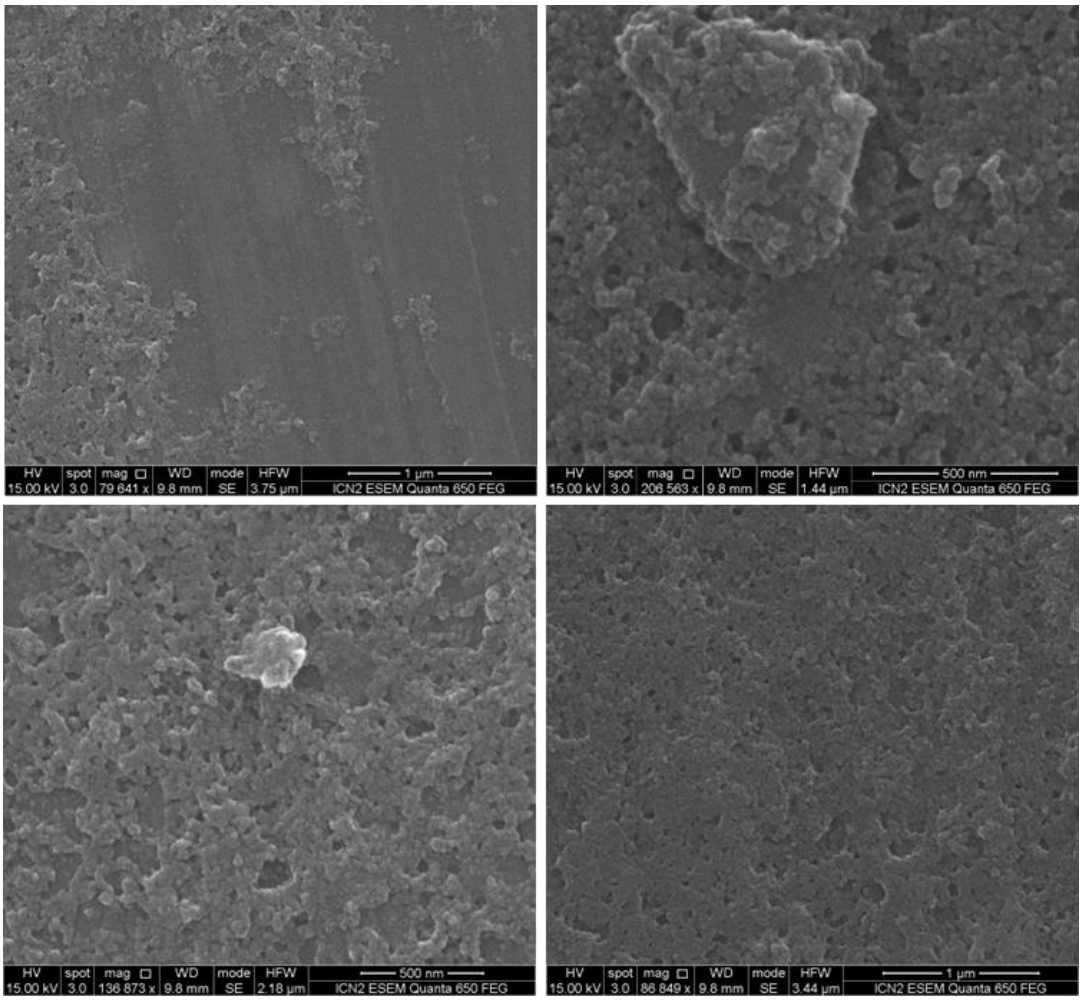


Annexe **3.47**. FTIR of **SQC NP.**



Element	Weight%	Atomic%
C K	54.21	79.28
O K	10.66	11.70
S K	7.32	4.01
Cl K	6.17	3.06
Pt M	21.65	1.95
Totals	100.00	

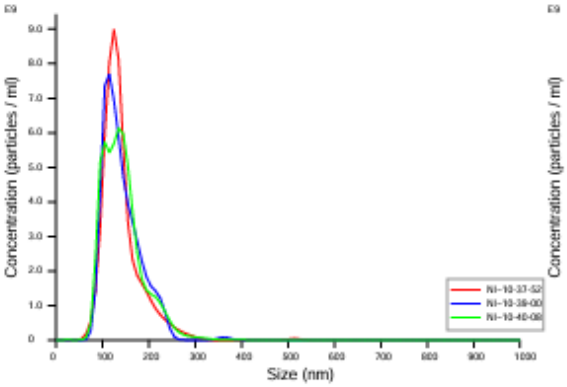
Annexe **3.48**. EDX of **SQC NP.**



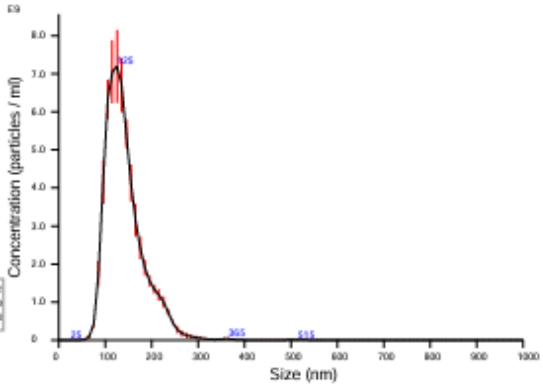
Annexe **3.49.** SEM images of **SQC NP** under 5 nm Pt thin film layer.

Annexe **3.50**. Total Pt release raw data of **SQC NP** under irradiation at 785 nm.

	Pt [He]	
Sample Name	Conc. [ppb]	Conc. RSD
RGA 0min	11.96	1.4
RGA 1min	7.19	0.9
RGA 2min	10.69	1.0
RGA 5min	14.23	0.8
RGA 10min	16.31	1.2
RGA 15min	31.62	0.6
RGA 20min	25.89	1.1
RGA 60min	32.18	0.8
RGA 1,5h	34.80	0.4
RGA 2h	31.21	0.9
RGA 3h	34.70	0.8
RGA 6h	39.26	1.3
RGA 8h	38.09	1.4
RGA 24h	40.66	1.0
ResiduoPt A	4807.97	0.9
ResiduoPt B	7937.86	0.3



FTLA Concentration / Size graph for Experiment:
NIC 15E-24h 2023-01-31 10-37-30



Averaged FTLA Concentration / Size for Experiment:
NIC 15E-24h 2023-01-31 10-37-30
Error bars indicate + / -1 standard error of the mean

Included Files

NIC 15E-24h 2023-01-31 10-37-52
NIC 15E-24h 2023-01-31 10-39-00
NIC 15E-24h 2023-01-31 10-40-08

Details

NTA Version:	NTA 3.4 Build 3.4.4
Script Used:	SOP Standard Measurement 10-37-18AM 31J~
Time Captured:	10:37:30 31/01/2023
Operator:	Amable Bernabe
Pre-treatment:	1:50
Sample Name:	NIC 15E-24h
Diluent:	water+2%DMSO
Remarks:	

Capture Settings

Camera Type:	sCMOS
Laser Type:	Blue488
Camera Level:	12
Slider Shutter:	1200
Slider Gain:	146
FPS	25.0
Number of Frames:	1498
Temperature:	14.4 - 14.6 °C
Viscosity:	(Water) 1.147 - 1.152 cP
Dilution factor:	5 x 10e1
Syringe Pump Speed:	50

Analysis Settings

Detect Threshold:	5
Blur Size:	Auto
Max Jump Distance:	Auto: 11.2 - 12.0 pix

Results

Stats: Merged Data

Mean:	141.7 nm
Mode:	122.3 nm
SD:	42.2 nm
D10:	98.5 nm
D50:	133.0 nm
D90:	199.5 nm

Stats: Mean +/- Standard Error

Mean:	141.7 +/- 0.7 nm
Mode:	125.2 +/- 7.0 nm
SD:	42.2 +/- 0.9 nm
D10:	98.7 +/- 1.6 nm
D50:	133.2 +/- 1.7 nm
D90:	199.6 +/- 2.2 nm
Concentration:	5.81e+10 +/- 2.37e+08 particles/ml
	63.4 +/- 0.3 particles/frame
	68.8 +/- 0.2 centres/frame

Annexe **3.51**. NTA analysis summary of **SQC NP.**

Chapter 4

Singlet Oxygen Storage and on-Demand Magnetic Induced Release for a Multi-Approach Therapy

In this Chapter, we will see the combination of a SPION core with a Zr-based coordination polymer shell that incorporates a functionalised 9,10-diphenylanthracene.

This combination allows heat generation with SO storage and release. On top of this, MRI was also studied, with impactful and evident improvements in *in vitro* settings against classical iron-based MRI CAs, and evidence of improvements in imaging at *in vivo* settings.

In a first step, colloidal stability, morphology, chemical composition and physicochemical interactions with magnetic fields of such platform were performed. Moreover, cellular transmission electron microscopy (TEM) imaging, *in vitro* cytotoxicity, *in vivo* tolerability, and biodistribution have been studied and reported in this work.

In a second step, the interaction of our system with light, coupled with the possible interactions between magnetic behaviour and optical properties, has been studied and applied to *in vitro* therapy approaches of these core-shell NP against the GL261 cell line.

In a third step, the development of a control platform based on a Zr-anthracene-based coordination polymer is reported and discussed. Despite the original purpose, *in vitro* cell viability assays display this platform as a potential activatable therapeutic platform for GBM therapy.

Results in this Chapter have been presented at the:

1. "14th International Conference on the Scientific and Clinical Applications of Magnetic Carriers" congress under the title "Development of Core-Shell Nanoparticles for Singlet Oxygen Storage and *in-situ* Release Through Magnetic Hyperthermia for a Multi-Approach Cancer Treatment".
2. "Nanomed Europe 2025" under the title "Hybrid Zirconia/Coordination Polymer Nanoparticles for Effective Hyperthermia in Glioblastoma Treatment".
3. "Spanish Conference on Biomedical Applications of Nanomaterials" under the title "Hybrid Iron Oxide-Zirconium MOF Core-Shell Nanoparticles with Enhanced T_2 Imaging Responses".
4. Manuscript in preparation under the title "Hybrid Iron Oxide-Zirconium CPN Core-shell NPs with enhanced T_2 MRI for Selective Bladder Targeting".

4.1. Introduction

4.1.1. Reactive Oxygen Species

As has been mentioned in Chapter 3, ROS comprise oxygen-based free radicals and non-radical species such as superoxide ($O_2^{\bullet-}$) anions or SO, being the latter an electronically excited form of molecular oxygen that differs from the electronic ground state (triplet oxygen) in its spin configuration. These reactive species often have short lifetimes, which makes them highly reactive in oxidative processes towards biological material.[1] As a result, ROS, and more often SO, have presented as a powerful tool with plenty of mechanisms that lead to cell death, allowing it to achieve great therapeutic efficacy with low generation yields.[2]

4.1.2. Photodynamic Therapy in Glioblastoma Treatment

PDT uses PSs that accumulate in tumour tissue and are activated only under light irradiation. The result of such interaction is the generation of cytotoxic ROS with spatiotemporal control that has enabled PDT to be presented as a selective tool to generate ablation of tumours while sparing healthy surrounding cells.[3,4] This spatial selectivity helps treat infiltrative tumour margins beyond surgical reach, with minimal systemic toxicity.[4,5]

However, PDT efficacy is limited by low PS delivery, hypoxic TME, and poor PS selectivity. NPs can address these issues by carrying PSs across the BBB, targeting tumour cells, and even carrying catalytic components to locally produce oxygen or additional ROS.[3-5] Recent examples of NPs targeting GBM treatment via PDT include the work by Zhao *et al.*, who report on an iron-bi oxide NP engineered for deep GBM PDT. NPs were cloaked in a fused macrophage/bacterial hybrid membrane and conjugated to a pH-sensitive anti-osteopontin antibody, enabling tumour targeting and BBB penetration, while under 660 nm light, generating Type I ROS via photocatalysis.[6] Another work, now from Jardón *et al.*, reports on titanium dioxide NPs functionalized with folic acid and loaded with zinc phthalocyanine as a PS. These NPs demonstrated targeting properties towards folic acid receptors overexpressed on GBM that, under a 385 nm light source, achieved ROS generation and induced phototoxicity in C6 glioma cells.[7] Or even further, the works from Zhang *et al.* report on lipid-based NPs loaded with indocyanine green as a NIR PS and embedded in glioma cell membranes. The resulting NPs achieved biomimetic targeting, resulting in an enhanced uptake by glioma cells *in vitro* and tumour accumulation in mice. This nanoparticulate system then triggered mitochondrial apoptosis based on ROS production under 808 nm irradiation, causing a 93% tumour growth suppression *in vivo.*[8]

4.1.3. Combination of Photodynamic Therapy and Platinum-Based Chemotherapy for Glioblastoma Treatment

Nanoparticulate platforms that combine Pt-based drugs with PDT approaches to GBM treatment represent an attractive modality in cancer treatment, as both modalities approach tumour death via complementary mechanisms. Pt drugs generate death via apoptosis-related mechanisms and immunogenic activation, whereas PDT generates cytotoxic ROS locally in light-exposed tumour

areas, sparing normal tissue. A combination of both therapies has often been sighted as a promising pathway that potentially yields synergistic cytotoxicity.[9]

Examples of such combinations can be found from Borah et al., who developed β-cyclodextrin-encapsulated Pt(II) complexes as fluorescent NPs for GBM PDT. The cyclometalated Pt(II) complex is inert in the dark, but under 390 nm irradiation, the NP photodecomposes, releasing Pt(II) ions and generating ROS.[10] Paul *et al.* report an amphiphilic PEG-polylactic acid (PLA) micelles co-loaded with chlorine e6 and a Pt(IV) diazido prodrug. Under 660 nm irradiation wavelength, this system induced an energy transfer between chlorine e6 and Pt(IV) that provoked the photoreduction to Pt(II) while generating azidyl radicals and oxygen (Figure 4.1).[11]

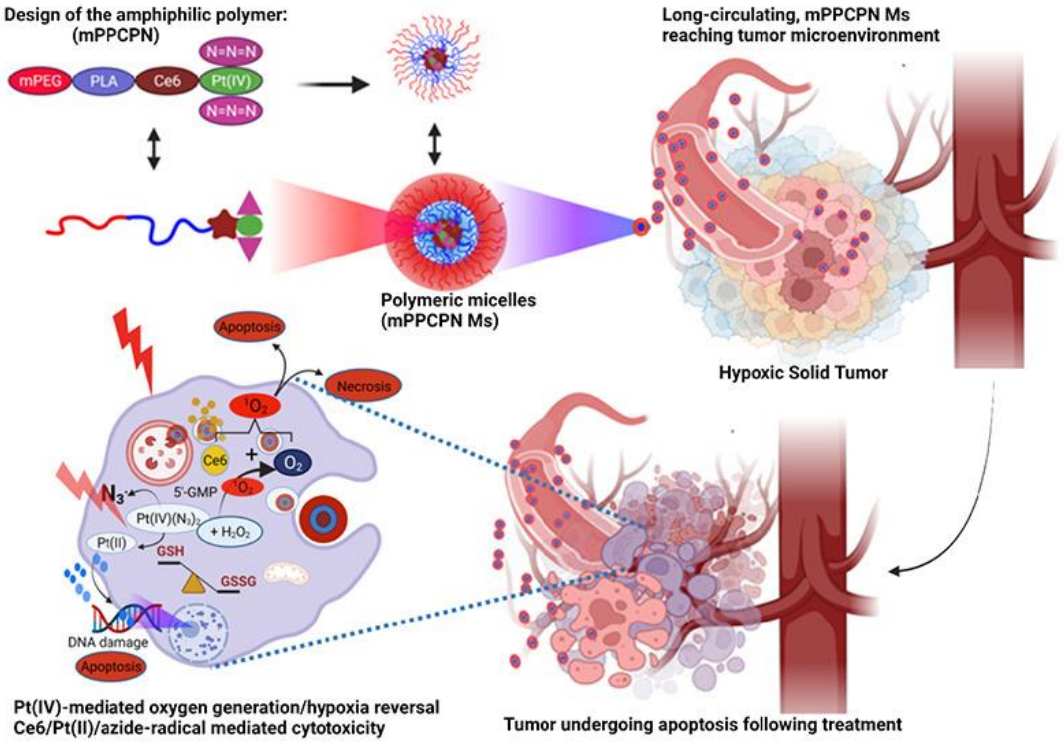


Figure **4.1.** Graphical representation of the dual action Pt(IV) PEG-PLA micelles' structure and intracellular processes as reported by Paul et al.[11]

Unfortunately, the advantages of targetable and activatable therapies like PDT and PACT are limited in GBM application due to poor PS delivery to the brain, tumour hypoxia which reduces oxygen for the photodynamic reaction, and limited light penetration into deep tissues.[12,13,]The human skull presents an important barrier to light itself, with radiation of the first biological window of application (i.e., 800 nm, 700 mW·cm^{-2}) only penetrating up to 4.24% of incident light.[14,15] When adding the scalp, cerebrospinal fluid, white matter, and grey matter, the energy fluence capable of reaching the deep brain target of GBM becomes null.[16] Reports on PDT-based therapies for GBM are often locally implemented intrathecal or post-surgery via optical fibres to treat beyond the resection cavity, which usually implies invasive and inadequate therapeutic approaches.[4]

4.1.4. Light-Independent ROS Generation Mechanisms

Although light-induced ROS generation is unviable in GBM settings due to the limited penetration of light, other alternative SO generation pathways can be used to overcome the biological tissue limitations. For example, rich manganese oxide-coated persistent luminescent NPs (Mn-ZGGOs) that can generate SO and hydroxyl radicals without external light have been reported by Ding *et al.*[17] These NPs decompose in the TME to release Mn^{3+}, which leads to the generation of SO and hydroxyl radicals. Or chemically induced electron exchange and Cherenkov radiation induced PDT from radionuclides (^{90}Y) and positron emission tomography (PET) imaging radionuclides (^{18}F, ^{68}Ga) and have been reported by Lioret *et al.*[18]

Other approaches showed how ultrasounds effectively activate sonosensitizers, leading to the generation of ROS, including SO.[19] ROS generation in this field is produced via mechanisms like cavitation, sonoluminescence, and pyrolysis, cascading into the generation of ROS.[20] A representative example of such therapy is the use of titanium oxide NPs for non-invasive sonodynamic therapy of cancer, as reported by You *et al.*[21]

Other methods generate ROS via chemical reactions induced by heat from PTT.[22,23] Examples in the literature of such phenomena come from thermal-responsive nanobombs. Wang *et al.* described thermally controlled ROS generation by calcium oxide when irradiated with NIR light.[24] Meng *et al.* reported iron-based nanocomposites that generated hydroxyl radicals based on the photothermal effect that enhances the Fenton reaction.[25] while Chen *et al.* detailed a **CDDP**-loaded metal-phenolic network able to photothermally trigger ROS generation after irradiation with a NIR light source (Figure **4.2**)[26].

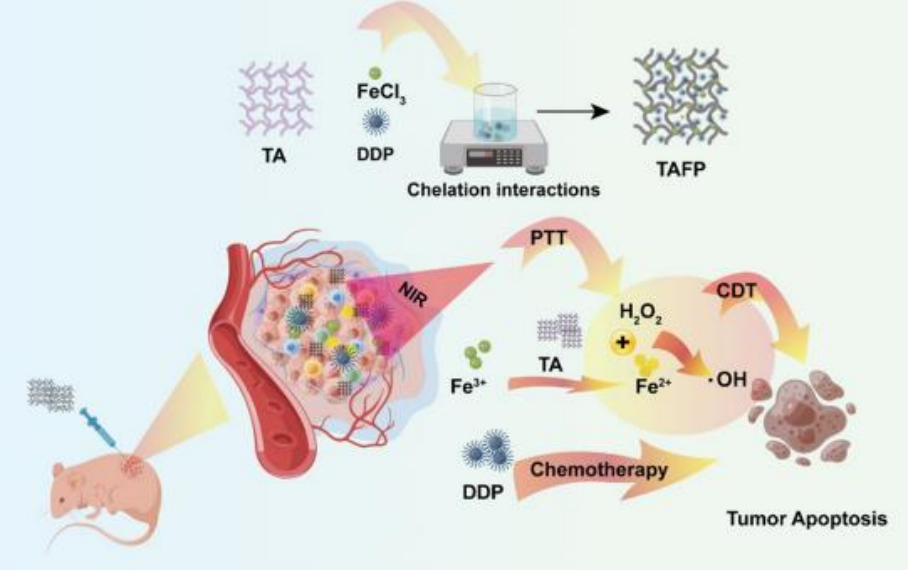


Figure **4.2**. Scheme illustration of the fabrication process of TAFP composites, and the antitumor procedure of TAFP composites via the PTT/chemodynamic therapy (CDT)/CT synergistic effect as reported by Chen *et al.* [22]

Nonetheless, such approaches are also limited in GBM settings because of the light permeability barrier to effectively reach the brain. Thus, considering this scenario, alternative sources of heat to produce heat-induced ROS generation were evaluated. One interesting option consisted of the use of MHT as a compatible tool that could enhance the efficacy of generated ROS in a synergetic combination therapy.[27]

4.1.4.1. MHT as a Source of Heat in the Generation of ROS

MHT is a clinical therapy for the treatment of diseases that exploits the heat generation capability of particles in the presence of an AMF that dates back to 1957.[26] It has been with the development of magnetic nanoparticles (MNPs) that this field has evolved to what is nowadays understood as MHT.[27] Hyperthermia means abnormally high body temperature, and it may be caused as part of a specific treatment, an infection, or exposure to heat. In terms of therapy, hyperthermia is a cancer treatment that uses heat to damage or kill cancer cells while causing minimal harm to normal tissue.[28]

*For a more in-depth understanding of the physicochemical properties of MNPs, a specific mechanistic explanation of the generation of heat of MNPs, and the advantages and limitations of MHT, the reader may direct their attention to the "**4.7.1.2 Hysteresis-Induced Heating Mechanisms**" section in the Conceptual Explanations in the Annexes of this Thesis.*

Overall, the flexibility and tunability of MNPs, particularly their ability to generate heat in the presence of deeply penetrating AMF, enable us to envision new therapeutic mechanisms for GBM treatment. Specifically, heat generation of MNPs under a magnetic field could be harnessed to trigger the generation of ROS through a thermally induced pathway. This combination would represent a novel advancement in the context of intracranial application, where light-based strategies such as PDT and PTT are limited by poor tissue penetration. Moreover, prior studies where MHT was used in combination with MNPs-loaded chemotherapeutic agents, such as CDDP-loaded systems,[29,30] have demonstrated synergistic antitumoral effects.

As is the underlying work of this Thesis, the possibility to incorporate Pt release with a ROS generation gives rise to a novel two-way combination therapy approach that we aim to explore. This system could use heat generation to trigger both effects, and although not the initial objective, there is the possibility of further combining this platform with MHT.

4.1.4.2. Precedents of Combination Therapies Between ROS and MHT

A combination of MHT with ROS generation or CT has been previously reported to be able to generate a synergistic enhancement of antitumor efficacy.[31] MHT can increase blood circulation and oxygenation, which decreases hypoxia and increases drug accumulation in tumours via efflux transporter inhibition.[32] MHT can independently induce the production of ROS, amplifying the oxidative stress effect.[33] Combination therapy allows for a cumulative cell death effect that leads to a lower energy heating transfer, lower NP accumulation, and lower chemotherapeutic efficacy required to achieve cell death.[34,35] Parallelly, ROS generation can trigger macrophages and T-cells, stimulating cytokine secretion, while MHT can enhance dendritic cells and natural killer cells for an immune response activation.[36-40] At the same time, MHT inhibits DNA repair pathways, thus enhancing ROS and antineoplastic-induced damage, enhancing cytotoxicity. [41-43] For example, Kurokawa *et al.* reported that MHT can increase the generation of mitochondrial ROS, sensitising cells via N-acetylcysteine (NAC) inhibition to PS hematoporphyrin dichloride for increased PDT toxicity.[44] Another recent example of successful combination therapy comes from Rivera *et al.*, who reported on an MHT, RT, and CT with TMZ combination therapy for the treatment of GBM that significantly and synergistically reduced cell viability with a remarkable increase in cell apoptosis. On top of that, it was evaluated that such a combination led to increased immune

activation.[45] Finally, one last example, from Hu *et al.,* displayed MNPs, functionalized with glucose oxidase enzymes, as able to generate MHT and amplify oxidative stress (Figure **4.3**).[46] Overall, combination therapies have been reported to show synergistic behaviour and enhanced efficacy with few drawbacks, enhancing drug efficacy.

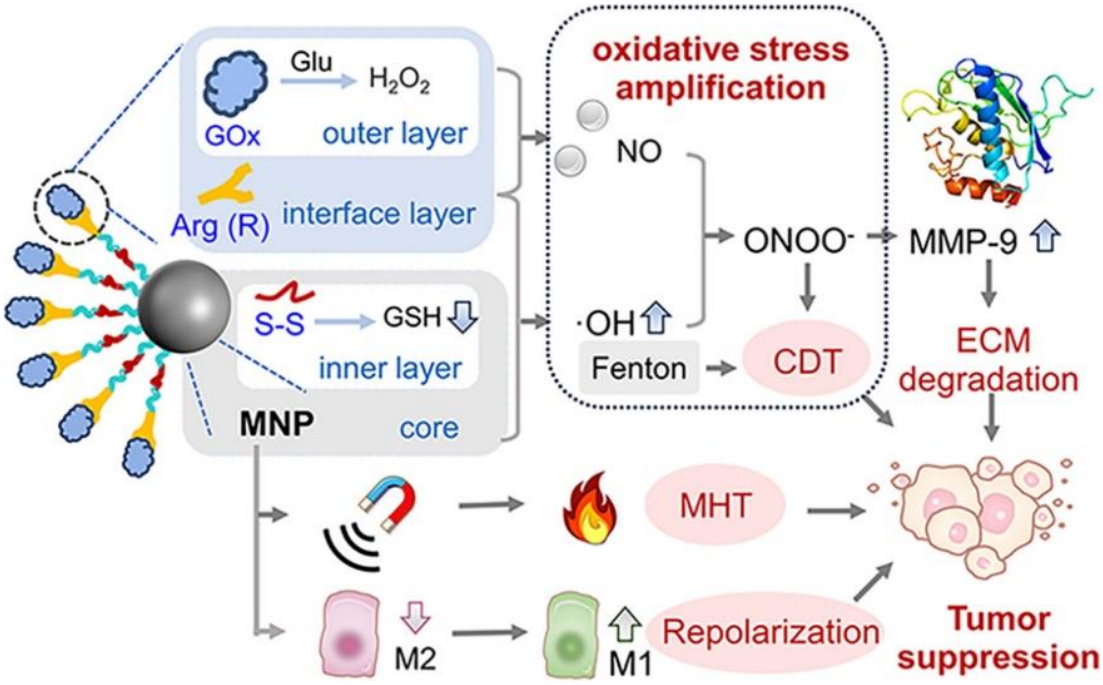


Figure **4.3**. Representative schematic from Hu *et al.* representing the modified MNP and the possible combination of pathways that lead to tumour suppression.[55]

4.1.5. Our Approach to ROS Generation via MHT

The power of ROS in cancer therapy remains unquestionably one of the most efficient tools in cancer therapy. However, classical generation of ROS through the well-known PDT mechanism is limited by the poor light penetration into the brain and a hypoxic tumour environment lacking freely available oxygen. To avoid these limitations, ROS can be generated through induced heat-dependent reactions.[22,23] Therefore, in this Chapter, we present MHT as an interesting tool that could generate and enhance the efficacy of generated ROS .[25]

For this purpose, in our research group, we envisioned the development of a core-shell NP (**pDPA-CNP@Fe NP**) that combines: i) The capability of generating heat via MHT from a SPION core, and ii) A shell composed of a coordination polymer capable of photosensitising and absorbing oxygen under UV irradiation pre-administration, and capable of releasing it on demand via MHT-triggered hyperthermia post-administration (Figure **4.4**). Furthermore, the well-known behaviour of iron oxide to act as a CA in MRI will allow us to explore further applications in theragnostic capabilities, developing a tri-functional particle that combines therapy and imaging.

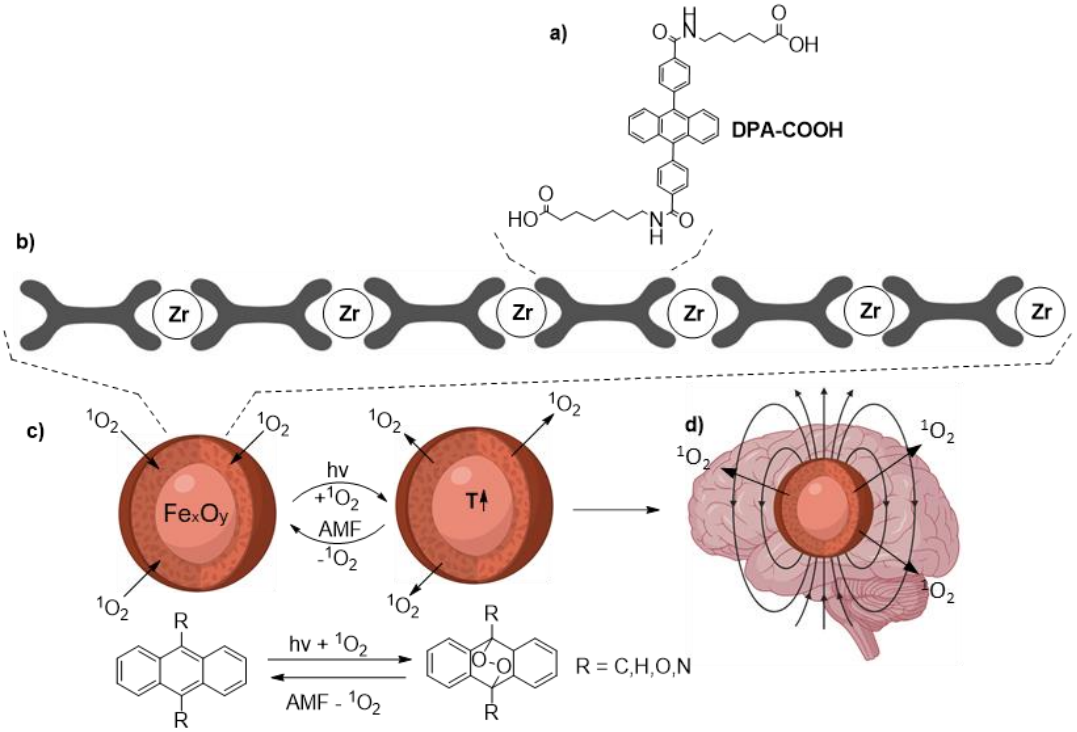


Figure **4.4**. Schematic representation of the proposed concept for the development of a core-shell NP with **a) DPA-COOH** as a monomer of **b)** a coordination polymer based on Zr coordination between **DPA-COOH** and Zr. Resulting in a **c) pDPA-CNP@Fe NP** based on a coordination polymer capable of absorbing SO under UV radiation, and a SPION core capable of generating heat in the presence of an AMF, which can be used to release SO back to the environment, **d)** within the concept of intra-brain applications.

This approach allows us to benefit from a dual effect treatment, overcoming light penetration limitations of PDT and the limitations related to the hypoxic tumour environment TME. Moreover, the intrinsic SPION properties that allow it to act as a CA allow us to evaluate the resulting nanoconstruct for theragnostic applications. Additionally, the coordination-based nature of the shell allows for the incorporation of chemotherapeutics (i.e. Pt-based drugs) to be used in combination with MNPs. This combination also represents a leap forward in therapy that we aim to explore. Consequently, we originally designed and evaluated the development of a Pt-based platform that incorporated chemotherapeutic drugs as part of the combination therapy approach (Figure **4.5**).

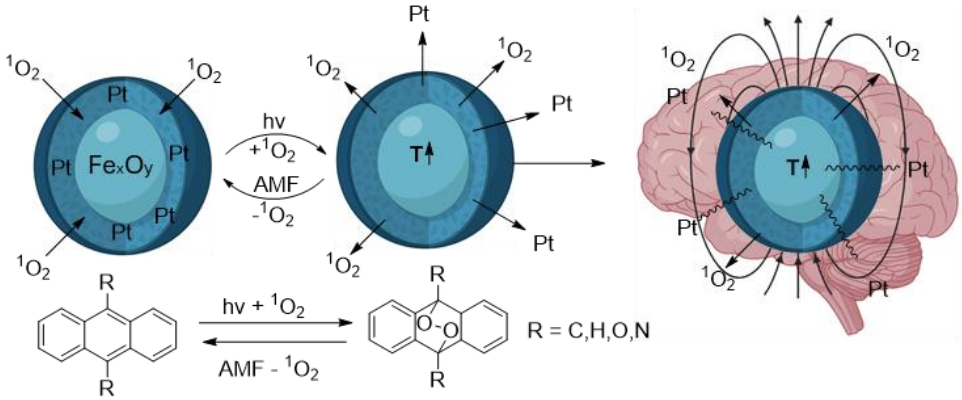


Figure **4.5**. Schematic representation of the proposed concept for the development of a Pt-loaded core-shell NP for a combination therapy approach.

4.1.5.1. Role and families of Core-Shell Nanoparticles in Biomedicine

Core-shell NPs are particles composed of a material coated with another material on top of it.[47] These NPs not only allow for the combination of different properties from different material composites, but also for the change of properties by shifting the core-to-shell ratio.[48] This behaviour also enables the modification of cytotoxicity via coating of the core with a non-toxic shell, while it also allows for the improvement of biostability for medicinal applications.[47,49] Core-shells have historically received plenty of applications in the field of optical imaging,[50–52] PET,[53] biosensors,[53,54] targeted gene delivery,[55,56] targeted drug delivery,[57-60] and MRI.[61-63]

For instance, Na *et al.* reported rhenium disulfide/mesoporous silica core-shell NPs as an effective pH-responsive platform for doxorubicin release in a combined CT and PTT.[64] Kaliaperumal *et al.* described a core-shell NP based on chitosan-tripolyphosphate core combined with an iodine shell as sensors for the diagnosis of salivary alpha amylase.[65] Examples in the field of MRI include the recent reports from Yue *et al.*, reporting on a SPION-based core carbon coated as a T_{2w} CA while presenting important magnetic behaviour.[63]

Core-shell NPs can be classified based on their core-shell material composition. As such, they can be classified as: i) Inorganic/inorganic core-shell NPs, encompassing silica and non-silica, lanthanide and semiconductor NPs, ii) Organic/organic core-shell NPs, iii) Multi-shell NPs, iv) Hollow NPs, and v) Inorganic/organic core-shell NPs, which encompass magnetic/organic core-shell NPs.[66] The proposed platform for this Chapter can thus be defined as an inorganic/organic core-shell NP, as it is composed of an inorganic SPION core and a coordination polymer shell.

4.1.5.1.1. Super Paramagnetic Iron Oxide Nanoparticles

As iron oxide cores, SPIONS show strong paramagnetic properties with a high saturation field and extra anisotropy contributions.[67] Among the different options, SPIONS are usually composed of two structural configurations: magnetite-Fe_3O_4, or maghemite–γ-Fe_2O_3, coated with a biocompatible polymer.[68] SPIONs accumulate in tumours through passive targeting by the EPR effect, or through active targeting with the help of targeting ligands.[69-71] Furthermore, the magnetite and maghemite cores of SPIONs are well known to be detected in MRI.[74] SPIONs improve image quality by altering the magnetic properties of surrounding tissues, resulting in clearer visualisation of abnormalities such as tumours.[74]

Over the last years, a plethora of different morphologies like nanospheres, plates, tetrahedrons, cubes, truncated octahedrons, octahedrons, concaves, octapods, and multibranched have been reported.[73] At the same time, protocols describing multicore synthesis have emerged, focusing on the generation of surface anisotropy via aggregation of spherical single-core aggregated particles.[74] Multicore SPIONs still retain the versatility in applications that standard SPION particles present in MRI, drug delivery, and MHT treatment.[75]

In this Chapter, two main strategies have been followed. On one hand, multicore, or clustered, SPIONs were proposed, which have a track record of success in medical applications for MHT in the brain, and boast of amplitude of field-related work and reproducibility.[68,76] On the other hand, iron nanocubes were presented as a more efficient nano-heater alternative, although these are usually associated with low reproducibility and low yields (Figure **4.6**).[77]

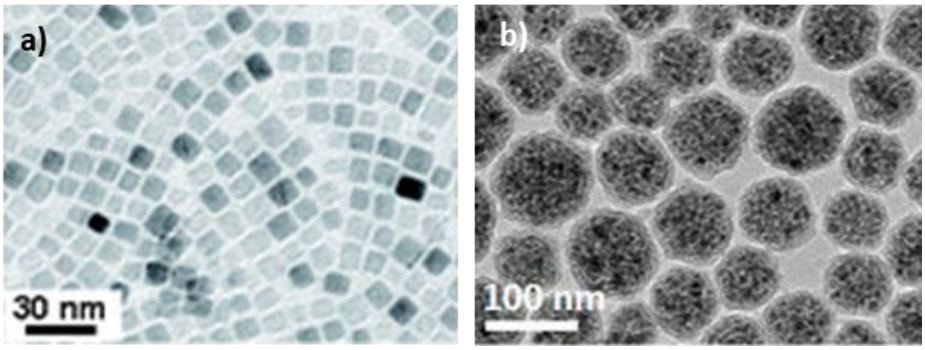


Figure **4.6**. **a)** TEM imaging of SPION nanocubes reported by Xu *et al*.[78] **b)** TEM imaging of SPION clusters reported by Nemec *et al.*[79]

4.1.5.1.2. Zirconium-Anthracene Coordination Polymer Shell for SO Capture and Delivery

The Zr-anthracene coordination polymer proposed consists of the coordination of Zr(IV) ions to the bridging ligand diphenyl anthracene 7-4-(10-(4-((5-carboxypentyl)carbamoyl)phenyl) anthracene-9-yl)benzamido)heptanoic acid (**DPA-COOH**) (Figure **4.4.a** and **4.4.b**).

On one hand, Zr(IV) was selected because of two main factors:

- **High biocompatibility and low toxicity**. The human body naturally contains small amounts of Zr as an essential biogenic element.[80] *In vivo* assays in rats of zirconyl (IV) acetate show a lethal dose comparable to those of iron at 4.1 $g \cdot kg^{-1}$.[81] In fact, Zr is commonly used in the development of zirconium dioxide-based dental biomaterials[82,83] or orthopaedic protheses.[84]
- **Chemical nature**. Zr naturally forms strong bonds with carboxylate ligands thanks to its hard Lewis acid properties. This leads to great chemical and mechanical stability to the coordination bonds,[85-87], which has an impact on the stability in physiological media for long periods of time.[88]

On the other side, anthracene compounds were chosen as they are well known for their capacity to absorb and release SO under UV and thermal stimulus, respectively.[89,90] This process is possible thanks to the formation of an endoperoxide functional group within the anthracene conjugated electronic structure (Figure **4.7**).[91] The main pathway for the synthesis of aromatic endoperoxides is the [4+2] cycloaddition reaction between molecular excited oxygen (i.e., SO) with the aromatic substrate.[92] Obtention of anthracene endoperoxide can be achieved via one-pot synthesis using light to photoexcite anthracene and lead to the formation of SO and subsequent Diels-Alder reaction.[92] The process that leads to the obtention of the original anthracene and molecular SO through a retro-Diels-Alder reaction is known as thermolysis.[93]

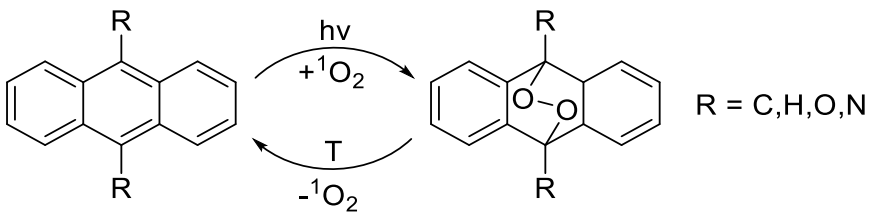


Figure **4.7**. Schematic representation of the SO loading of anthracenes under UV irradiation and SO release from anthracene endoperoxides under thermal stimulus.

This reaction has been exploited for many applications, like PTT-PDT combination therapy,[94] SO carriers to deliver SO in hypoxic tumour environments,[95] or even SO detectors.[96] This process, however, is not only specific to anthracenes, and can be observed with other aromatic compounds like benzene, naphthalene and phenolic compounds.[97-99]

However, under UV light, anthracenes can suffer [4+4] cycloaddition reactions (Figure **4.8**).[100,101]

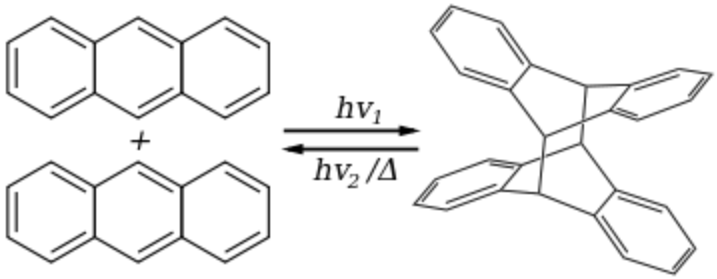


Figure **4.8**. Photodimerization of anthracene as reported by Han *et al.*[102]

To avoid this side reaction, a bulky group that induces steric hindrance into the molecule and avoids this dimerisation process was introduced. For this reason, in our proposed system, we used the molecule **DPA-COOH** (Figure **4.4.a**), which contains two phenyl moieties, to favour the formation of the endoperoxide and avoid the [4+4] cycloaddition side reactions. This is a result of **DPA-COOH** being unable to achieve effective overlapping of molecular orbitals due to steric hindrance, avoiding the [4+4] cycloaddition. [100,103]

*For a more in-depth understanding on the chemical behaviour of cycloaddition reactions in the context of SO loading and release the reader may direct their attention to the "**4.7.1.6. Singlet Oxygen and Endoperoxide Formation**" section in the Conceptual Explanations in the Annexes of this Thesis.*

4.2. Objectives

According to the previous sections, the main objective of this Chapter will be the development of a core-shell NP (**pDPA-CNP@Fe NP** and **pDPA/DSCP-CNP@Fe NP**) that combines a coordination polymer shell and a SPION core. This platform is envisioned to be used for GBM treatment as a theragnostic platform via ROS accumulation and thermal release via MHT, all of it combined with a potential CA for MRI.

For this purpose, the specific objectives are as follows:

1. Synthesis and Characterisation of pDPA-CNP@Fe NP

- Synthesis of a SPION core (**Fe-Clustered NP**) capable of undergoing MHT.
- Synthesis and characterisation of the monomer **DPA-COOH**.
- Design and coating of the **Fe-Clustered NP** with a functional coordination polymer based on a suitable **DPA-COOH** and Zr, forming **pDPA-CNP@Fe** (Figure **4.9**).
- Characterisation of **pDPA-CNP@Fe NP**'s: chemical, physical, and biological properties of the system.

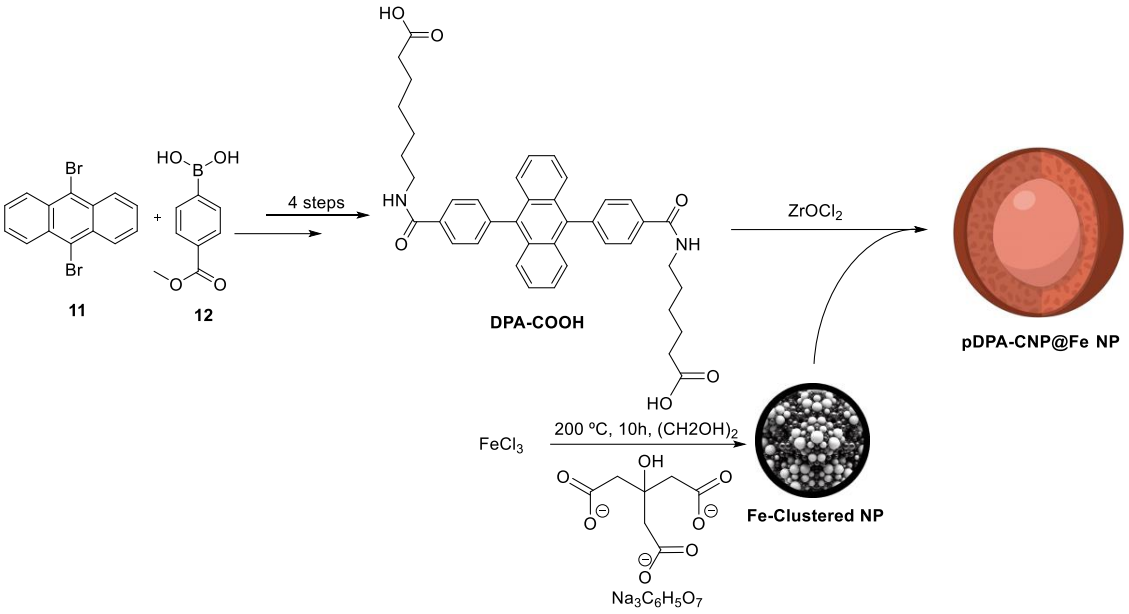


Figure **4.9**. Schematic representation of the preparation of target **DPA-COOH** monomer, **Fe-Clustered NP**, and **pDPA-CNP@Fe NP**.

2. Evaluation of Applications of pDPA-CNP@Fe NP in Imaging and Therapeutic Applications

To study the applicability of **pDPA-CNP@Fe NP** in the target fields of MRI, and GBM therapy, comprising of:

- Validation of the *in vitro* and *in vivo* capabilities of **pDPA-CNP@Fe NP** as a CA in MRI.
- Validation of the capability of **pDPA-CNP@Fe NP** to interact with AMF.
- Validation of the capability of **pDPA-CNP@Fe NP** to undergo SO loading and release under thermal stimulus and MHT triggered stimulus.
- Validation of the *in vitro* efficacy of **pDPA-CNP@Fe NP** against GBM cell culture.

3. Synthesis, Characterisation and Evaluation of Control Platform pDPA-CNP

To develop and study a control coordination polymer, **pDPA-CNP**, based on the Zr-based coordination polymer shell of **pDPA-CNP@Fe NP**, comprising:

- Synthesis of the functional Zr-based coordination polymer (**pDPA-CNP**).
- Validate the capability of **pDPA-CNP** to undergo SO storage under UV irradiation and release under external thermal stimulus. Such system must be biocompatible and stable in physiological conditions.
- Validation of the *in vitro* and *in vivo* capabilities of **pDPA-CNP** against GBM and comparison against **pDPA-CNP@Fe NP.**

4. Development of Core-Shell NP Based on SPION-Zr/Pt-Based Coordination Polymer for Triple Cancer Treatment Approach in MRI Theragnostic Settings

Development of a platform that combined controlled and sustained Pt release from previously developed Pt(IV) complex **DSCP** with the **pDPA-CNP@Fe NP** platform (Figure **4.10**).

To develop such target, the following objectives will be considered:

- Synthesis of suitable Pt(IV) complex **DSCP**, and incorporation into the coordination polymer shell during **pDPA-CNP@Fe NP** synthesis.
- Study and characterisation of the obtained NP, evaluation, and comparison with previous platforms of all aforementioned properties in the earlier sections.

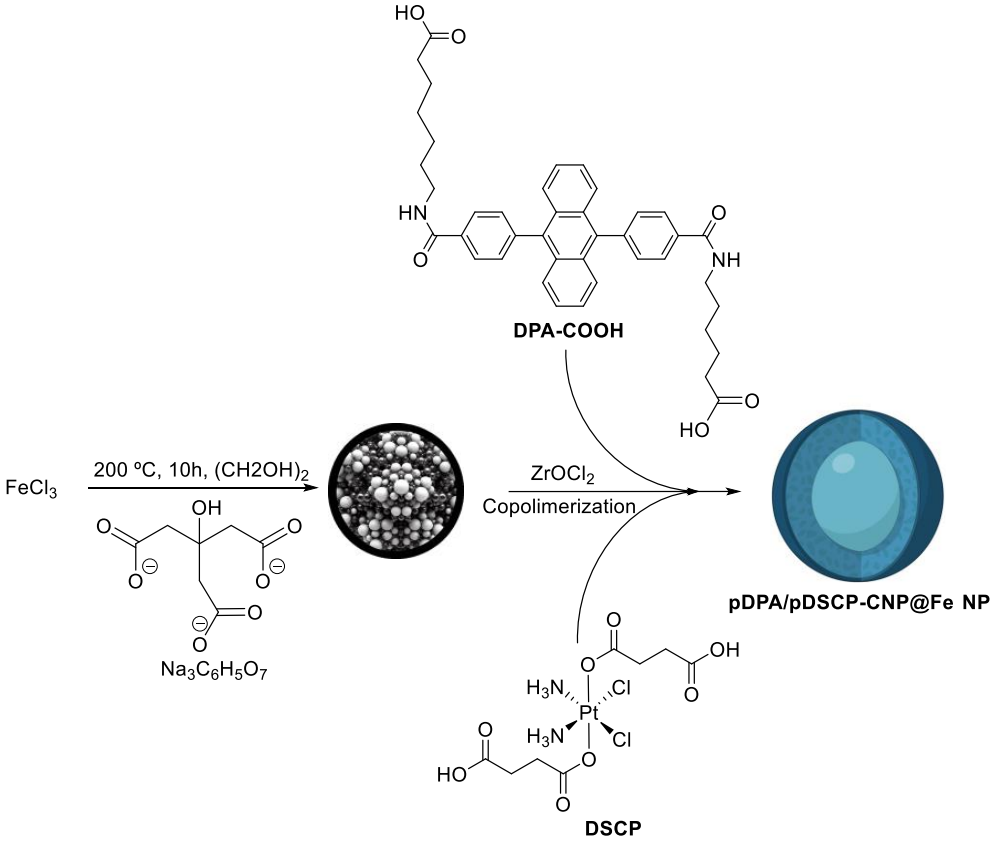


Figure **4.10**. Schematic illustration of the preparation of Pt(IV)-Zr(IV) coordination polymer-based core-shell NP.

4.3. Results and Discussions

Work on this Chapter has been carried out in collaboration with Dr. Pablo Guardia from *ICMAB*, who took a firsthand role in the study of magnetic-related physical properties such as hysteresis and MHT of our NPs. Dr. Jordi Arbiol from *ICN2*, whom we consulted for his expertise in crystallography-related inquiries. PhD student Núria Basanta from *ICN2* and *IBB-UAB*, whose expertise was key in the *in vitro* and *in vivo* studies. And Dr. Tamara Fernández from *IBB-UAB*, who assisted in the early stages of *in vitro* experimentation. Dr. Alejandro Gómez from *ICN2* provided the iron oxide nanocubes.

4.3.1. Core-shell pDPA-CNP@Fe NPs Platform

pDPA-CNP@Fe NP has two components required for its synthesis, a SPION core, and the coordination polymer shell composed of monomer **DPA-COOH** and Zr(IV). The first sections will discuss the synthesis of the required components before the synthesis of the core-shell platform.

4.3.1.1. Synthesis of DPA-COOH

Ligand **DPA-COOH** consists of a 9,10-diphenylahtracene functionalized at both *para* positions of the phenyls with amides that bond and extend a spacer to include a carboxylic acid at both ends. Such an arrangement allows for coordination with transition metals like Zr, making **DPA-COOH** a linker molecule with two coordination points suitable for coordination polymerisation. The synthesis of **DPA-COOH** was performed following a previous protocol, with some improving modifications, reported by a former PhD student from our research group, Dr. Junda Zhang.

DPA-COOH synthesis was based on a 5-step linear synthesis that used as starting material 9,10-dibromoanthracene (**11**). First steps of the synthesis started with a Suzuki coupling between anthracene **11** and organoborane **12**, yielding the diphenyl anthracene scaffold **13**. Second step of the synthesis undertakes anthracene **13** in a hydrolysis with potassium hydroxide to yield anthracene carboxylic acid **14**. The third and fourth steps use dicarboxylic acid **14** in a chlorination reaction, followed by an immediate substitution reaction with amine **15** to obtain anthracene amide **16**. This step incorporates an alkyl chain segment into our network, allowing for better flexibility and isolating the electronically conjugated region. The fifth and final step of the synthesis consists of a hydrolysis reaction of ester **16** to yield the target **DPA-COOH** monomer with an overall yield of 41.2% (Figure **4.11**).

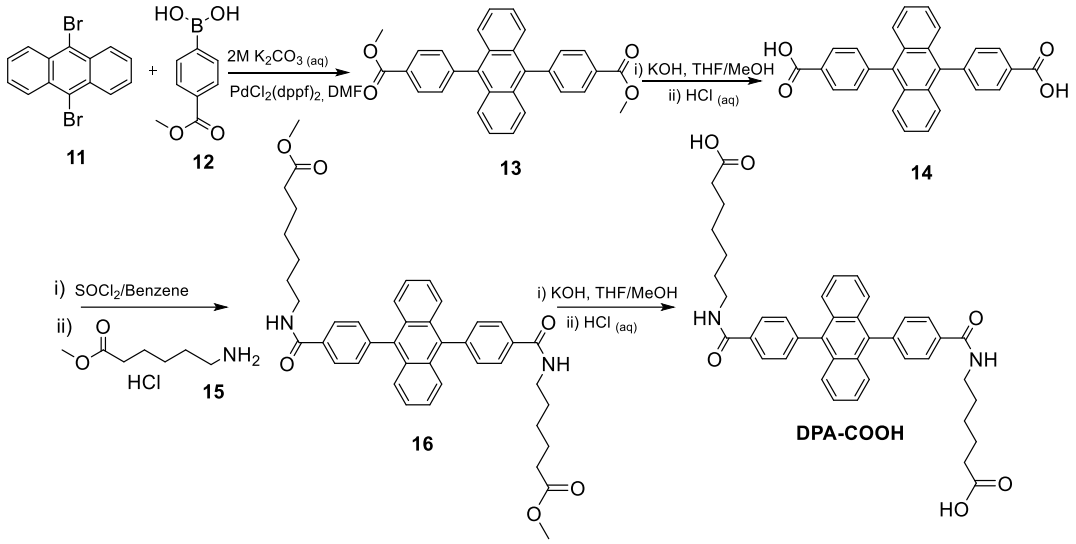


Figure **4.11**. Synthetic route taken to yield **DPA-COOH** from commercially available starting materials.

4.3.1.2. Synthesis of the Super Paramagnetic Iron Oxide NP Core

Two different strategies were followed in the design of the SPION core, clustered iron oxide NPs and iron oxide nanocubes (Figure **4.12**).

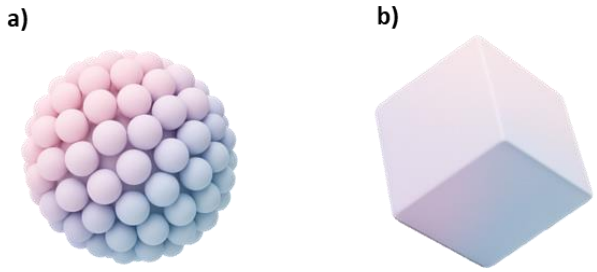


Figure **4.12**. Different geometries of iron oxide NP used: **a)** raspberry-like conformation and **b)** nanocubes.

Iron oxide nanocubes were chosen as a platform due to their monodispersity and general uniformity, providing highly controlled sizes and shapes. Therefore, leading to reproducible magnetic properties,[104,105] and high magnetic anisotropy.[105] On the other hand, multi-clustered iron oxide NPs were chosen due to their cooperative magnetic behaviour of single magnetic cores resulting in enhanced magnetic susceptibility,[106] higher relaxivity in MRI and improved hyperthermic efficiency.[106] Moreover, they also benefit from large porous structures that allow to enhance the formation of coatings and surface functionalization,[106,107] as well as presenting better cell interaction due to increased surface area.[108]

4.3.1.2.1. Synthesis and Characterisation of Fe-Clustered NPs

The spherical clustered iron oxide NPs (**Fe-Clustered NPs**) were obtained following a procedure already described in the literature by Shun Shen *et al.* through a solvothermal synthesis.[109] In a typical synthesis $FeCl_3$, sodium citrate and sodium acetate were mixed in ethylene glycol. Then, the mixture was heated to 200 °C in a stainless-steel autoclave for 10 hours. The resulting final product, a magnetic pellet, was washed first with water and finally with ethanol. The resulting product was stored in ethanol in the fridge (Figure **4.13**).

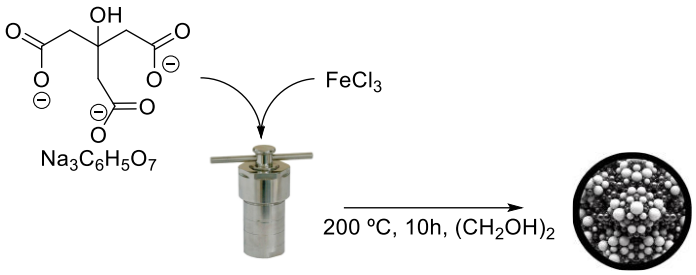


Figure **4.13.** Synthesis of **Fe-Clustered NPs** through a solvothermal process from sodium citrate and $FeCl_3$.

FTIR of such systems presents simple, as the only signals present in the spectrum above the fingerprint region are the ones originating from the citrate with a broad O-H stretching and a fairly wide C=O stretching at 3372 cm^{-1} and 1597 cm^{-1}, respectively. Meanwhile, the C-O stretching from the carboxylic acids is also observable at 1384 cm^{-1}. Finally, the presence of Fe-O stretching band at 541 cm^{-1} is also indicative of NP formation (Figure **4.14**). The original spectrum can be found in Annexe **4.26**.

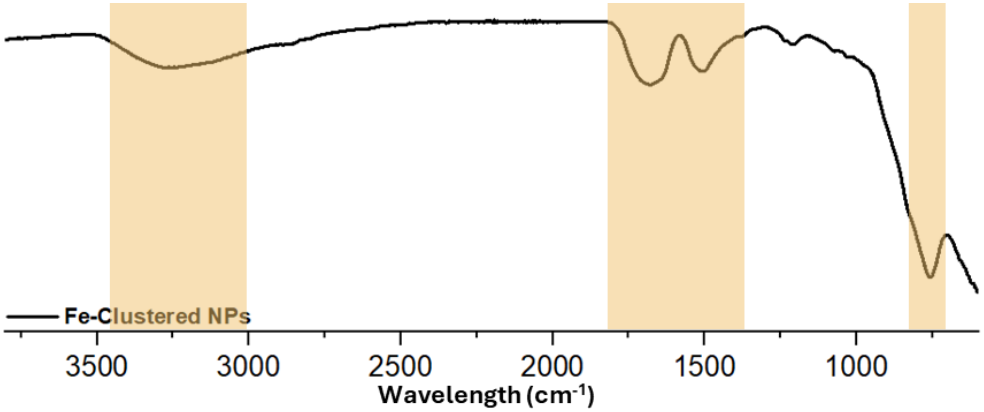


Figure **4.14**. FTIR of **Fe-Clustered NPs**.

The hydrodynamic size and ζ-potential of the **Fe-Clustered NPs** were measured using DLS (Figure **4.15**) and NTA (Annexe **4.32**), respectively. Our **Fe-Clustered NPs** showed sizes of 221.3 ± 1.8 nm with a reasonable PDI of 0.120 ± 0.037 and a ζ-potential of -7.6 ± 0.3 mV at DLS. At NTA, the particles presented sizes of 165.9 ± 1.6 nm. The low ζ-potential results indicate colloidal instability in water due to a low electrostatic repulsion.

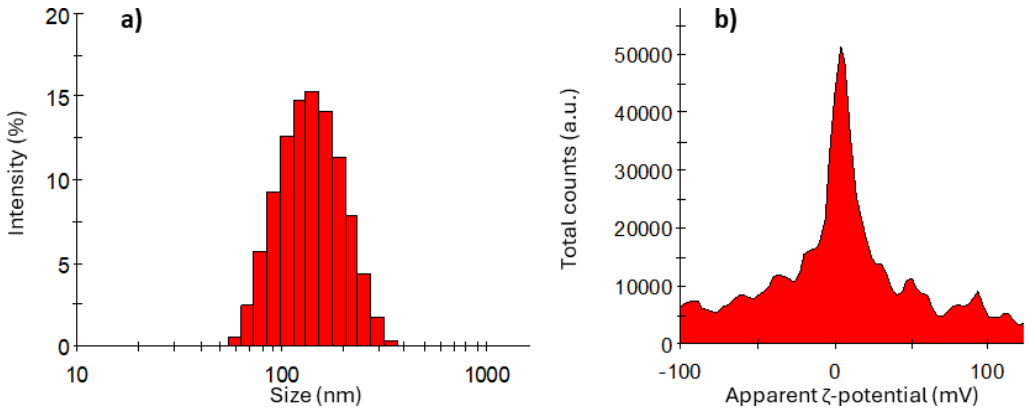


Figure **4.15**. **a)** Size intensity distribution by DLS and **b)** representative ζ-potential of **Fe-Clustered NPs** in water.

Fe-Clustered NPs morphology has also been studied using SEM imaging and scanning transmission electron microscopy (STEM) imaging (Figure **4.16**). These images show a multi-cluster aggregation with a raspberry-like shape morphology and an average size of 184.0 ± 6.1 nm. These results fall in accordance with the ones obtained by NTA analysis.

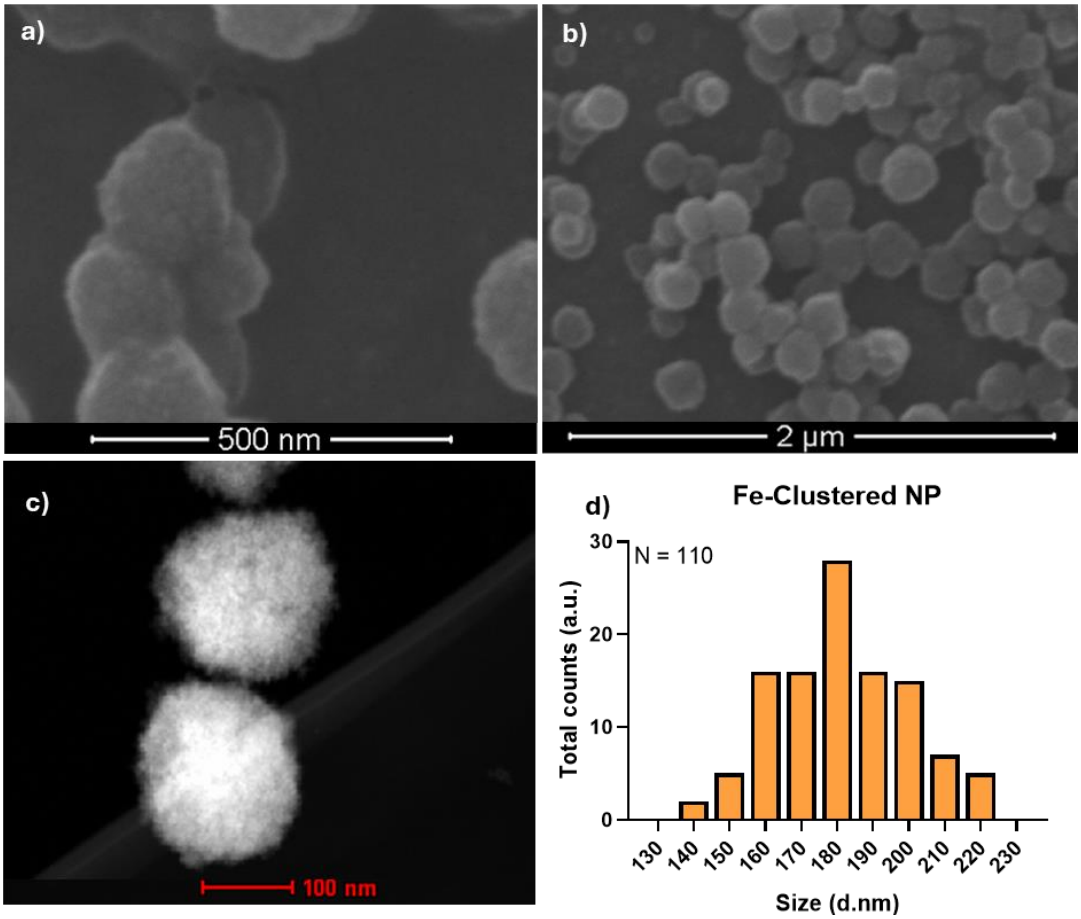


Figure **4.16. a-b)** Representative SEM images of **Fe-Clustered NPs** under a 5 nm Pt thin film coating for imaging. **c)** Representative STEM imaging at high-angle annular dark-field (HAADF) detector mode of **Fe-Clustered NPs**. **d) Fe-Clustered NPs** size distribution by SEM image size counting.

Elemental mapping of the sample, performed at the ALBA synchrotron facilities, showed a clear presence of iron and oxygen from the core formulation, as well as carbon and sodium from the stabilising sodium citrate (Figure **4.17**).

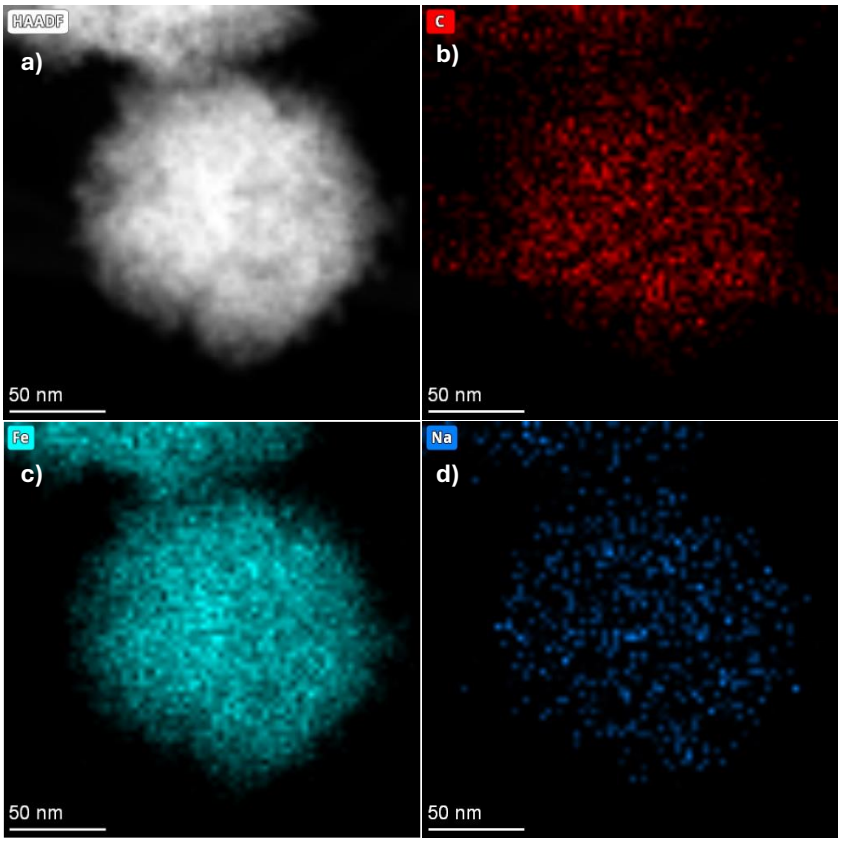


Figure **4.17**. **a)** Representative STEM imaging at HAADF detector mode of **Fe-Clustered NPs**. Elemental maps of **Fe-Clustered NPs** obtained via EDX 2-dimensional mapping of **b)** carbon, **c)** iron, and d) sodium.

ICP-MS was performed to determine the iron content of the **Fe-Clustered NP**, showing an Fe w/w content of 65.2 ± 2.3% (Annexe **4.27**). Thermogravimetric analysis (TGA) also displayed a matching value of inorganic material ranging between 56 to 73% (Annexe **4.29**). Powder X-ray diffraction (XRD) corroborated the typical XRD pattern for the superparamagnetic magnetite Fe_3O_4 (Figure **4.18**).[110]

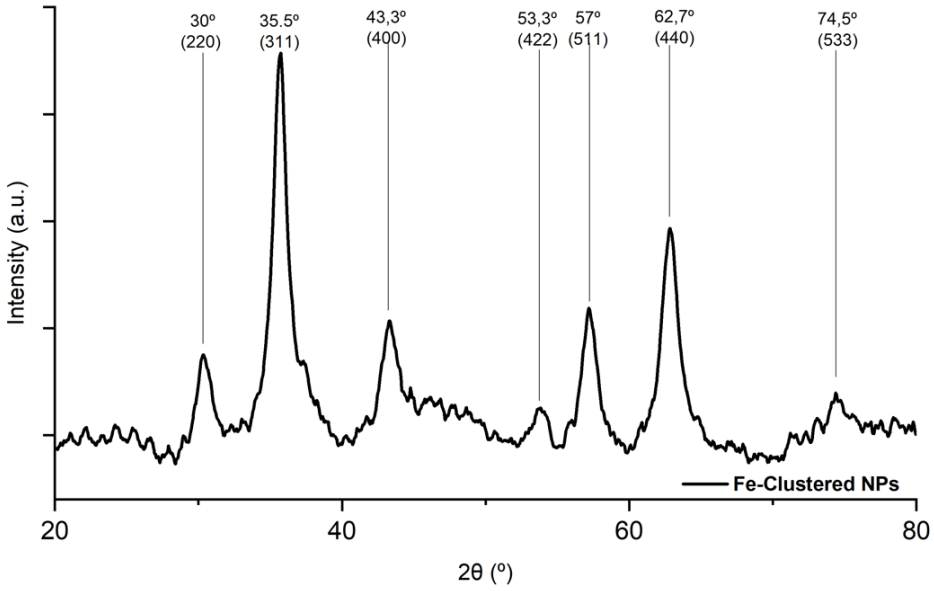


Figure **4.18**. Room temperature XRD measurement for **Fe-Clustered NPs.** Overlayed the theoretical 2θ XRD magnetite values as reported in the literature.

However, magnetite is a crystalline structure consisting of a network of Fe(II) and Fe(III).[111] Synthesis of pure magnetite has always been of interest due to its multiple applications as a superparamagnetic material. However, it has been observed that, in attempts to synthesise magnetite, impurities of Fe_2O_3 can be present. Fe_2O_3 can adopt four different crystalline polymorphs: hematite (α-Fe_2O_3), β-Fe_2O_3, maghemite (γ-Fe_2O_3), and ε-Fe_2O_3.[112] Moreover, magnetite's Fe(II) components present a natural tendency to oxidise to Fe(III) maghemite. As a result, such processes can reduce the superparamagnetic behaviour of such NPs. Nonetheless, both phases present very similar XRD patterns, so even though our XRD measurements present the characteristic pattern of magnetite,[113] only Mössbauer spectroscopy could define it.

4.3.1.2.2. Characterisation of Iron Oxide Nanocubes

The iron oxide nanocubes, provided by Dr. Alejandro Gómez, were briefly characterised. While the **Fe-Clustered NP** prepared at our laboratory used sodium citrate as the NP stabiliser, the iron oxide nanocubes used poly(maleicanhydride-alt-1-octadecene) (PMAO), with an average Mn of 30000-50000, as the stabiliser agent. Such change in the stabilising agent can be clearly observed at the FTIR spectrum (Figure **4.19**).

The spectrum shows strong signals at 2911 and 2843 cm^{-1} that belong to the aliphatic C-H stretching. Furthermore, signals belonging to the C=O anhydride bond stretching can also be observed at 1554 cm^{-1}. In the fingerprint region, the signal at 1364 cm^{-1} could be identified as the C-O-C stretching. Finally, at 544 $cm^{-1,}$ we observe the typical band for Fe-O. The original spectrum can be found in Annexe **4.22**.

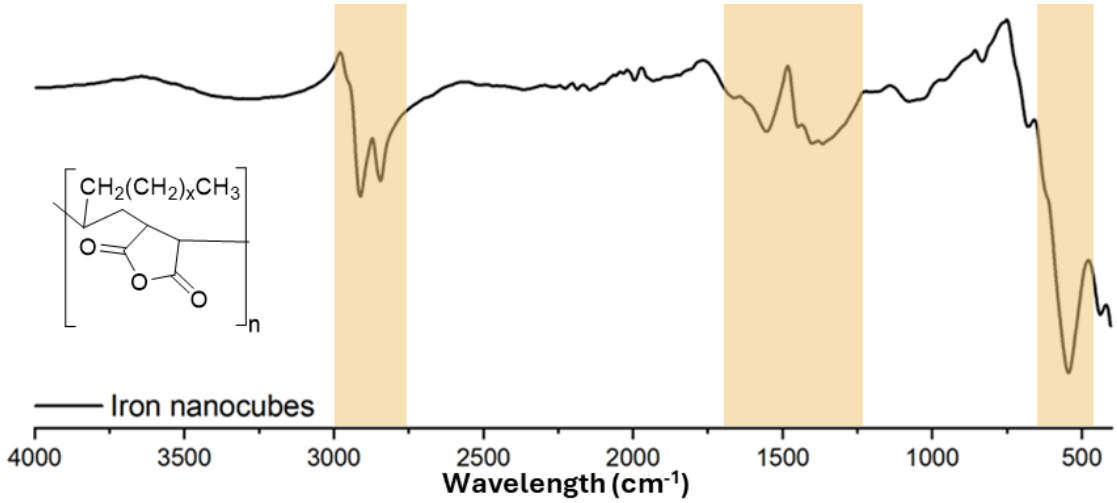


Figure **4.19**. FTIR of the iron oxide nanocubes.

DLS of the iron oxide nanocubes in water showed clear aggregation, presenting sizes of 282.4 ± 3.7 nm with a PDI of 0.425 ± 0.019. The ζ-potential revealed a value of -49.2 ± 0.3 mV (Figure **4.20**). NTA analysis showed an average size of 105.7 ± 0.6 nm and PDI of 0.072 ± 0.005 (Annexe **4.24**).

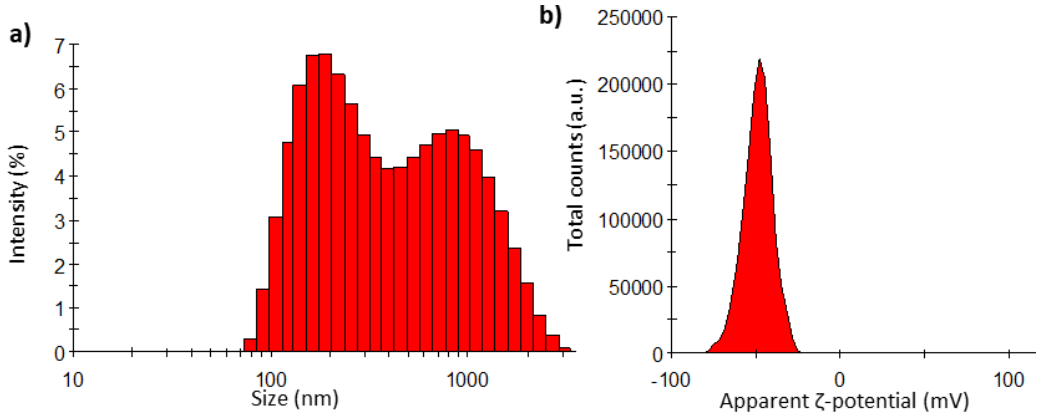


Figure **4.20**. **a)** Size intensity distribution by DLS and **b)** representative ζ-potential of the iron oxide nanocubes.

SEM imaging displayed the aggregation hinted at by DLS results. Only in the higher resolution STEM can the individual shapes of the iron oxide nanocubes be spotted (Figure **4.21**).

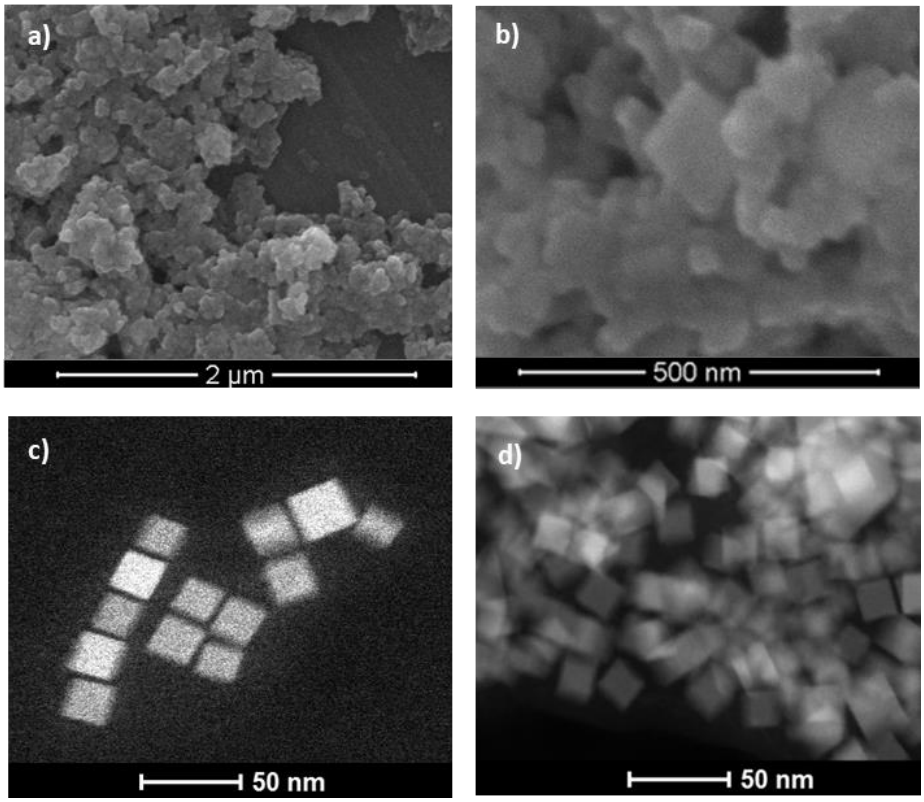


Figure **4.21**. Electronic microscopy images of the iron oxide nanocubes; **a-b)** Representative SEM images of the iron oxide nanocubes under a 5 nm Pt thin film coating for imaging, and **c-d)** Representative STEM images at HAADF detector mode of the iron oxide nanocubes.

4.3.1.3. Synthesis and Characterisation of pDPA-CNP@Fe NPs

Conceptually, the preparation of **pDPA-CNP@Fe NPs** is simple. From an already existing core, the next step to follow will consist of growing a coordination polymer, based on **DPA-COOH** and Zr(IV), on the particle surface, yielding a **pDPA-CNP@Fe NPs**.

The procedure for the synthesis of our core-shell NPs was performed for both available metal cores, iron oxide nanocubes and **Fe-Clustered NPs**.

In a typical synthesis, the **Fe-Clustered NPs**/iron oxide nanocubes were washed and suspended in DMF. **DPA-COOH** and $ZrCl_2O\cdot(H_2O)_6$ were also dissolved in DMF and mixed with the iron core. After sonication and ensuring proper suspension of all reagents, the solution was heated to 90 °C for 4 hours without stirring. The final core-shell NPs were obtained and washed with DMF and water. Finally, core-shell NPs were suspended in water for storage (Figure **4.22**).

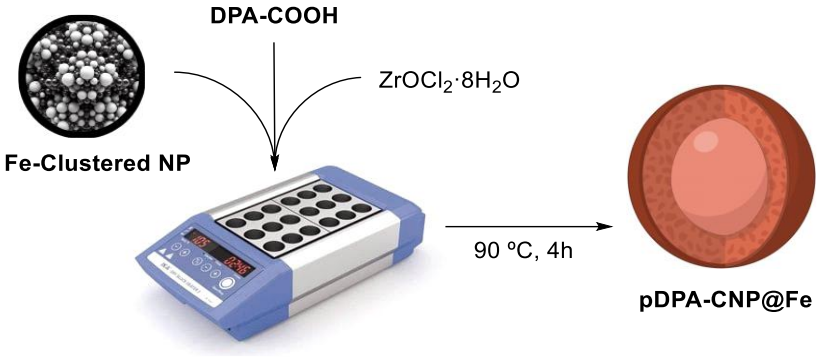


Figure **4.22**. Synthesis representation of **pDPA-CNP@Fe** using **Fe-Clustered NPs** as starting material.

FTIR of both coated iron oxide nanocube (**pDPA-CNP@Nanocube NPs**) and coated **Fe-Clustered NPs** (**pDPA-CNP@Fe NPs**) present similar. The spectra are looking mostly like that of **DPA-COOH** and their respective iron cores since they are now major components of the NP system. Both systems present slight O-H broad bands around 3300 cm^{-1}, C=C and C-C stretching at 2932 and 2859 cm^{-1}, as well as an array of C=O stretching from all the functional groups in our system between 1637 and 1443 cm^{-1} (Figure **4.23**). This homogenization of FTIR spectra is to be expected as, functionally speaking, both NP systems are very similar and only differ in the stabilising agent of the NP. Moreover, the only other major difference is the morphology of the iron core, which FTIR, as a tool to analyse bond energy, is unable to differentiate. The original spectra can be found in Annexes **4.36**, **4.38**, and **4.20**.

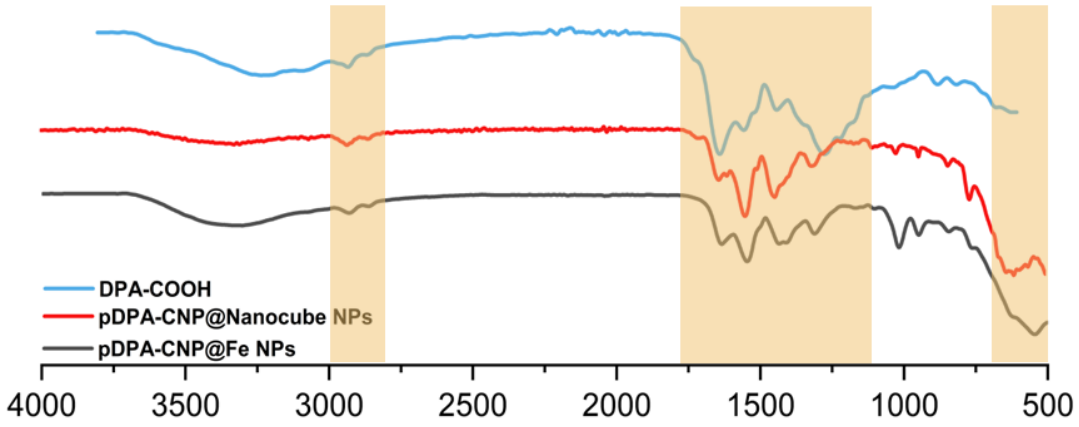


Figure **4.23**. FTIR comparative between **DPA-COOH** (blue), **pDPA-CNP@Nanocube NPs** (red), and **pDPA-CNP@Fe NPs** (black).

The formation of the CNP coating can be determined and studied using STEM imaging. In STEM imaging, two differentiated phases are observed, one from the electron-dense metallic iron core and another from the amorphous coordination polymer (Figure **4.24**). From the images obtained, we could distinctly observe that the coating of both iron cores was achieved. As observed, **pDPA-CNP@Nanocube NP**'s coating is proved irregular, with amorphous shapes and

iron aggregation, resulting in unreproducible and unreliable. On the other hand, **pDPA-CNP@Fe NP**'s coating showed much more homogeneous and efficient, generating well-rounded NPs and presenting only one single iron core incorporated for each shell. The coordination polymer also looks smooth and without irregularities.

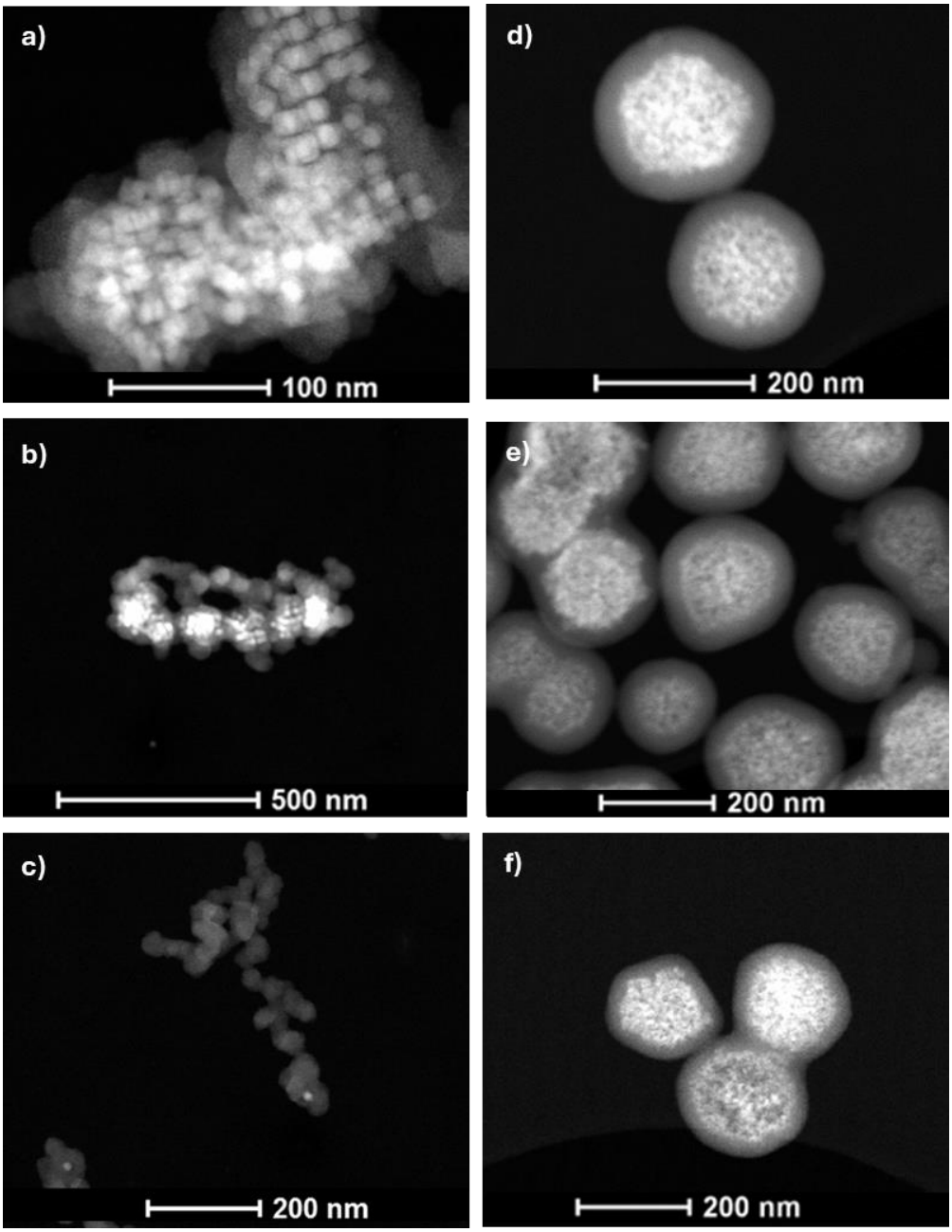


Figure **4.24.** Representative STEM imaging at HAADF detector mode of **a-c) pDPA-CNP@Nanocube NPs**, and **d-f) pDPA-CNP@Fe NPs**.

The differences between irregular shapes and morphology in **pDPA-CNP@Nanocube NPs** versus the well-defined and homogeneous **pDPA-CNP@Fe NPs** can be clearly observed in particle size analysis using DLS. Hydrodynamic size and ζ-potential studies using DLS revealed that our **pDPA-CNP@Fe NPs** had sizes of 288.0 ± 2.0 nm, with a PDI of 0.132 ± 0.041 and a ζ-potential of 43.6 ± 0.6 (Figure **4.25.a-b**). However, **pDPA-CNP@Nanocube NPs** presented hydrodynamic sizes of 296.6 ± 4.0 nm, with a PDI of 0.429 ± 0.031 and a ζ-potential of -49.2 ± 0.3 (Figure **4.25.c-d**).

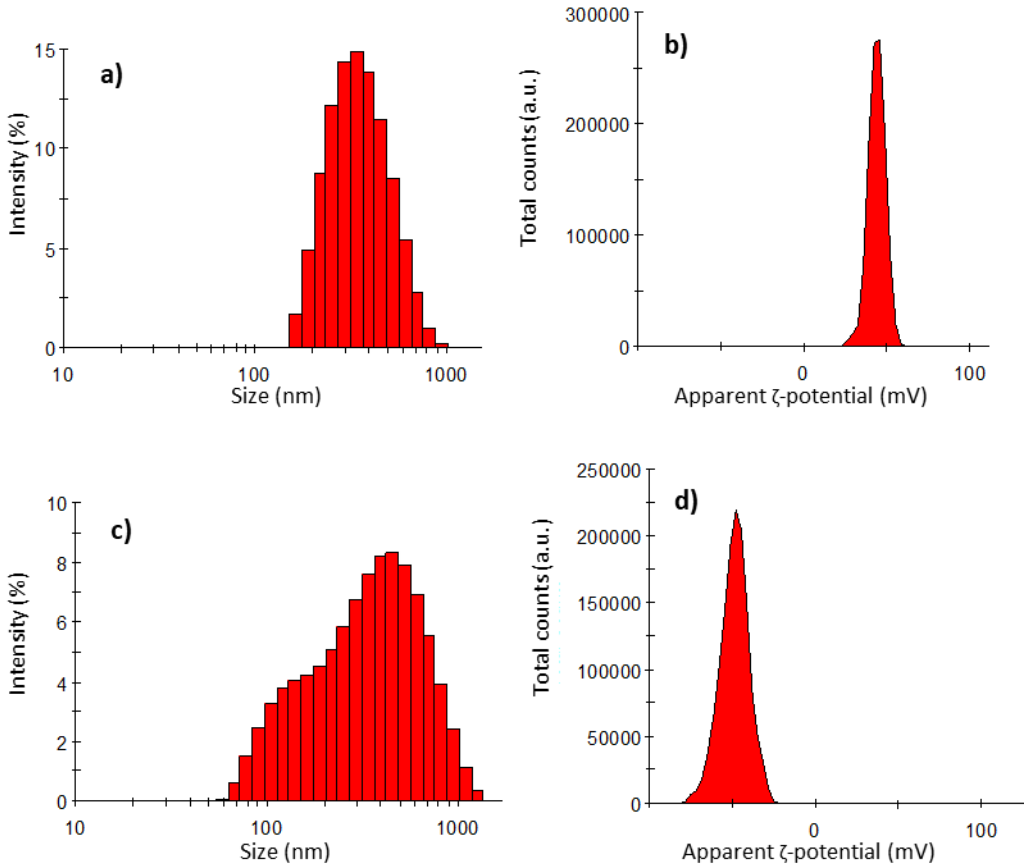


Figure **4.25**. **a)** Size intensity distribution by DLS and **b)** representative ζ-potential of **pDPA-CNP@Fe NPs**. **c)** Size intensity distribution by DLS and **d)** representative ζ-potential of **pDPA-CNP@Nanocube NPs**.

The irregular PDI and sizes from the **pDPA-CNP@Nanocube NPs** represented a barrier for any biological applications where a dose-dependent response is required.[114] Big polydispersity means big size disparity between different NP populations that will behave differently in terms of transport. Depending on the size and density of NPs, different processes like sedimentation, diffusion and settling dictate NP transport, and a poor PDI indicate poor control and reproducibility over such transport processes.[114] The same concept applies to a NP's shape.[115,116] Due to the problems arising from the **pDPA-CNP@Nanocube NPs** system, we decided to abandon this nanoconstruct and focus the *in vitro* studies on **pDPA-CNP@Fe NPs** as they present more homogeneous and thus more reproducible. Thereafter, we will exclusively study from here the **pDPA-CNP@Fe NP** system.

SEM imaging again confirms the findings of STEM imaging (Figure **4.24**) for pDPA-CNP@Fe NPs, showing spherical NPs with well-distributed homogeneity (Figure **4.26**).

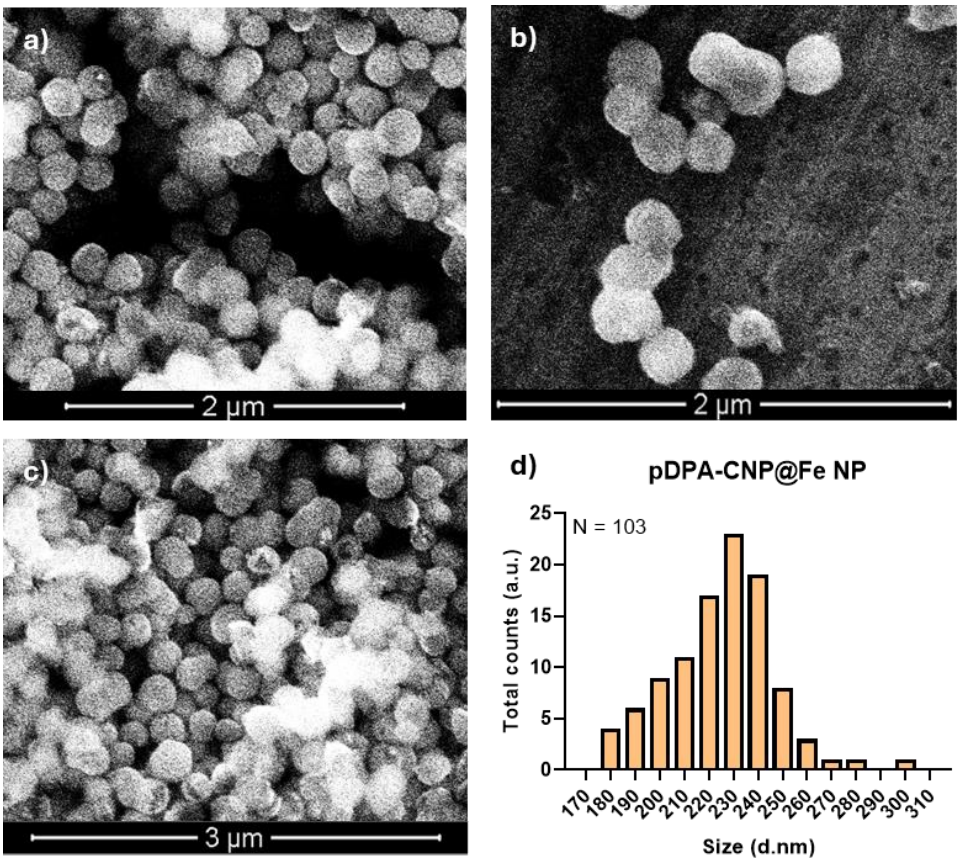


Figure **4.26. a-c)** Representative SEM images of **pDPA-CNP@Fe NPs** under a 5 nm Pt thin film coating for imaging. **d) pDPA-CNP@Fe NPs** size distribution by SEM image size counting.

ICP-MS of **pDPA-CNP@Fe NPs** showed an iron loading of 15.5% (Annexe **4.39**). Elemental mapping at the ALBA synchrotron facility gave information about the core-shell nature of **pDPA-CNP@Fe NPs** (Figure **4.27**). Samples showed a very clear distribution of zirconium and carbon all around the NP, but only the presence of iron in the centre of the NP. We also observe a sparse corona of sodium at the edge of the shell.

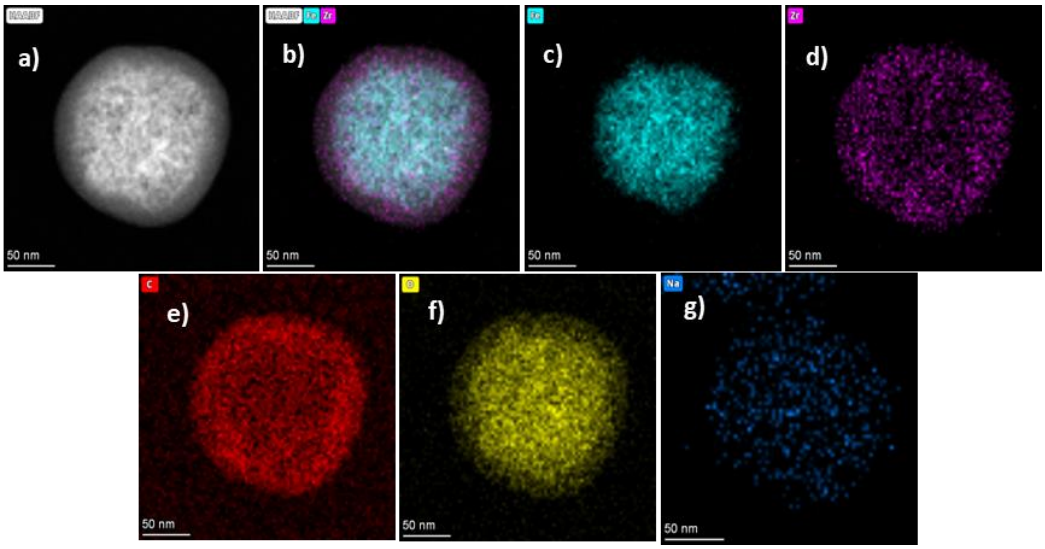


Figure **4.27**. **a)** Representative STEM imaging at HAADF detector mode of **pDPA-CNP@Fe NPs.** Elemental maps of **pDPA-CNP@Fe NPs** obtained via EDX 2-dimentional mapping of; **b)** overlay between zirconium (purple) and iron (blue) **c)** iron, **d)** zirconium, **e)** carbon, **f)** oxygen, and **g)** sodium.

The core-shell system **pDPA-CNP@Fe NP** has, until now, shown considerably large sizes either via **DLS** (Figure **4.25**) or **NTA** (Annexe **4.42**). As mentioned in Chapter 3, NPs that present sizes bigger than 200 nm face important challenges in cell internalisation as well as distributing through the body and reaching the target brain tumours.[117-119] However, surface charge plays an important role in these calculations, as positive charges generally benefit from better cellular internalisation.[120] Fortunately, the ζ-potential of our **pDPA-CNP@Fe NPs** is considerably high, at 44.2 mV (Figure **4.25**). As a result, warranting the continued study of this platform in further steps.

4.3.1.4. *In vitro* Characterisation of pDPA-CNP@Fe NPs

4.3.1.4.1. Study of pDPA-CNP@Fe NP's Colloidal Stability

Positively charged NPs tend to agglomerate faster when compared to negatively charged NPs in physiological media, which can lead to lower internalisation efficiency because of RES clearance.[121] This is especially crucial to us, since, as observed, our platform presents a strongly positive surface charge potential.

Supramolecular colloidal stability test in physiological concentrations of PBS-BSA will allow us to assess if any aggregation is happening, giving us information that can be of use during *in vitro* cytotoxicity studies. For this purpose, an experiment was set where a suspension of **pDPA-CNP@Fe NPs** was dispersed in a PBS-BSA solution at a concentration of 0.05 mg Fe·mL^{-1}. The size of the NPs was then tracked via DLS over a period of 72 hours with 24-hour intervals between measurements (Figure **4.28**).

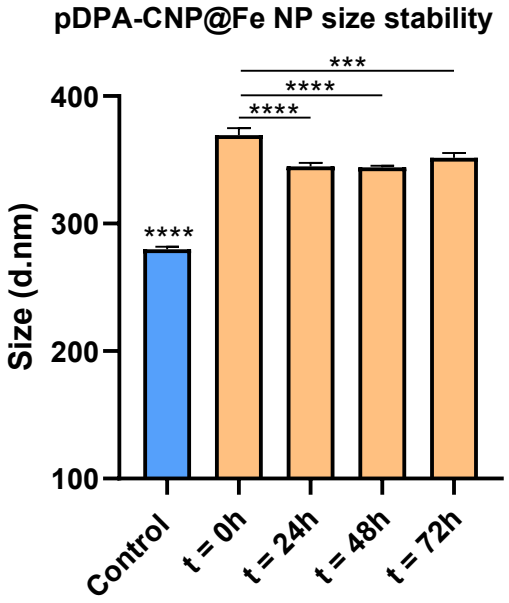


Figure **4.28**. Evolution of size distribution as given by DLS overtime of **pDPA-CNP@Fe NPs** in PBS containing 42 mg·mL^{-1} of BSA. All groups contain a control group in MilliQ® water. Data represent the mean ± SE, n=3. Statistical differences were calculated using one-way ANOVA, followed by Turkey's multiple comparison test, where (*) denotes P < 0.05, (**) denotes P < 0.01, (***) denotes P < 0.001, and (****) denotes P < 0.0001. Statistical differences between samples are marked with a line, otherwise it denotes same grade of significance against all samples.

A clear increase in size is observable at 0 hours, from 280 ± 1 to 369 ± 3 nm. Such an increase was attributed to the formation of a protein corona. Among the NP parameters which affect the protein corona, the surface properties, such as hydrophobicity and surface charge, have the biggest impact.[122] As a matter of fact, it has been reported that by increasing the surface charge density of NPs, protein corona adsorption increases.[123] Karmali *et al.*[124] studied strongly positively charged lipoplexes and polyplexes binding with albumin and hypothesise that this size increase is the result of the affinity of the opposite charge from the NPs with the negatively charged BSA proteins. Consequently, it comes as no surprise that the strong positive charge of our **pDPA-CNP@Fe NPs** strongly interacts with negatively charged proteins of BSA. However, over the period of 72 hours, protein corona decreases in size and stabilises to sizes of 351 ± 2 nm.

4.3.1.4.2. Cytotoxicity Studies of pDPA-CNP@Fe NPs

pDPA-CNP@Fe NP's cytotoxicity over a 24- and 72-hour period was tested against a GL261 GBM cell line (Figure **4.29**). The choice of cells was decided on the basis of presenting as close a model as possible to our target of GBM cancer treatment and possible pre-clinical animal model studies. At the same time, the non-coated **Fe-Clustered NP**'s cytotoxicity was also studied for comparison purposes.

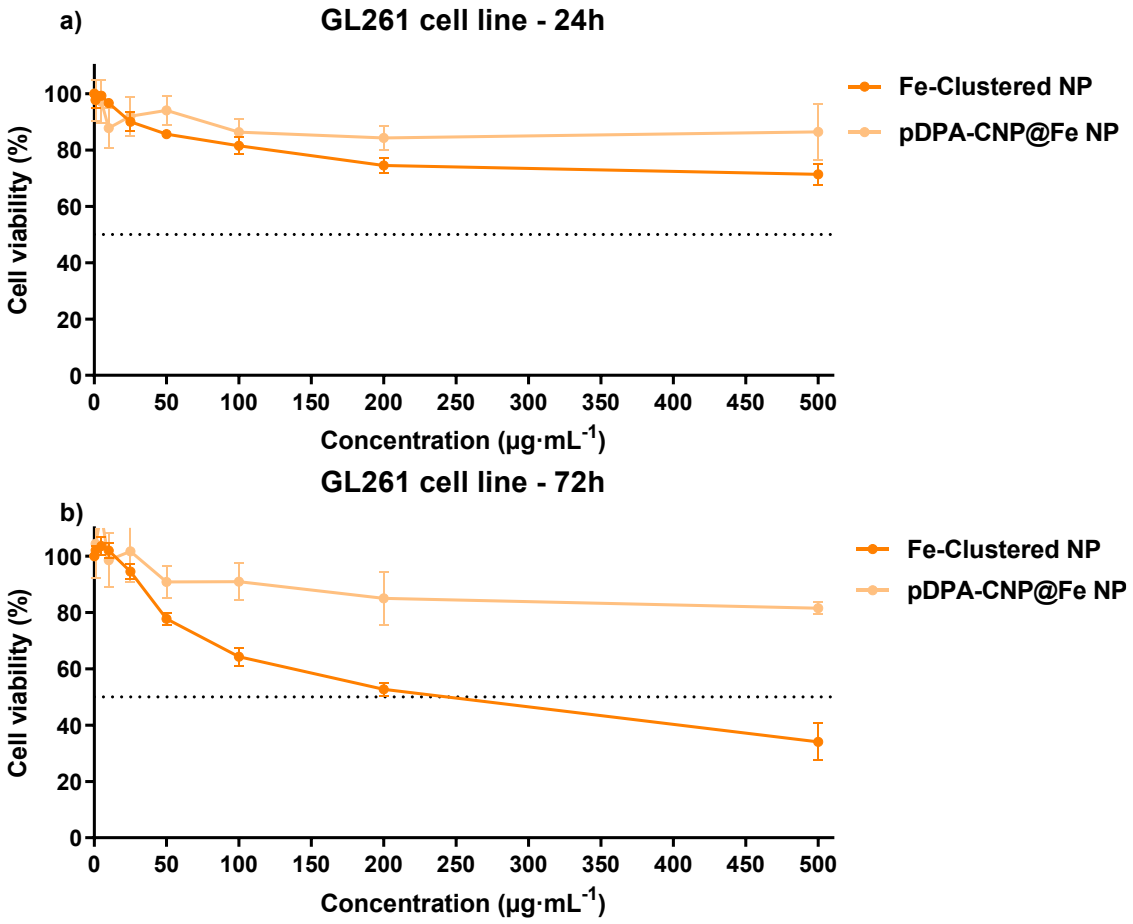


Figure **4.29**. Effects on cell viability of **pDPA-CNP@Fe NPs** in GL261 cell line at concentrations of 0, 1, 5, 10, 25, 50, 100, 200, 500 µg·mL^{-1} after **a)** 24- and **b)** 72- hour time periods. Data represents the mean ± SE, n=3.

The results from the assay showed no cytotoxicity within the concentration ranges studied (0-500 μg·ml^{-1} in terms of Fe content) at any time interval for **pDPA-CNP@Fe NPs**, ensuring biocompatibility. Nonetheless, the most interesting result comes from **Fe-Clustered NP**. In the 24-hour period, **Fe-Clustered NPs** present only a slight decrease in cell viability at high concentration ranges between 100 to 500 μg·mL^{-1} in relation to Fe content. On the other hand, at a 72-hour time period, the cytotoxicity is relatively higher and increase notably in the 100-500 μg·ml^{-1} range, with a IC_{50} value of 221 ± 40 μg·mL^{-1}. These results indicate that the formation of a shell around the SPION core contributes to its insulation and prevent it from any possible cytotoxic effect, demonstrating **pDPA-CNP@Fe NPs** are biocompatible and safe in the non-activated state.

4.3.2. pDPA-CNP@Fe NP in Magnetic Resonance Imaging

4.3.2.1. Magnetic Resonance Imaging by SPIONs

The role and properties of a CA in MRI are very closely related to the fundamental properties of this technique and the possible magnetic relaxation rates of excited nuclear spins in longitudinal relaxation (T_1) and transverse relaxation (T_2) (Figure **4.30**).[125]

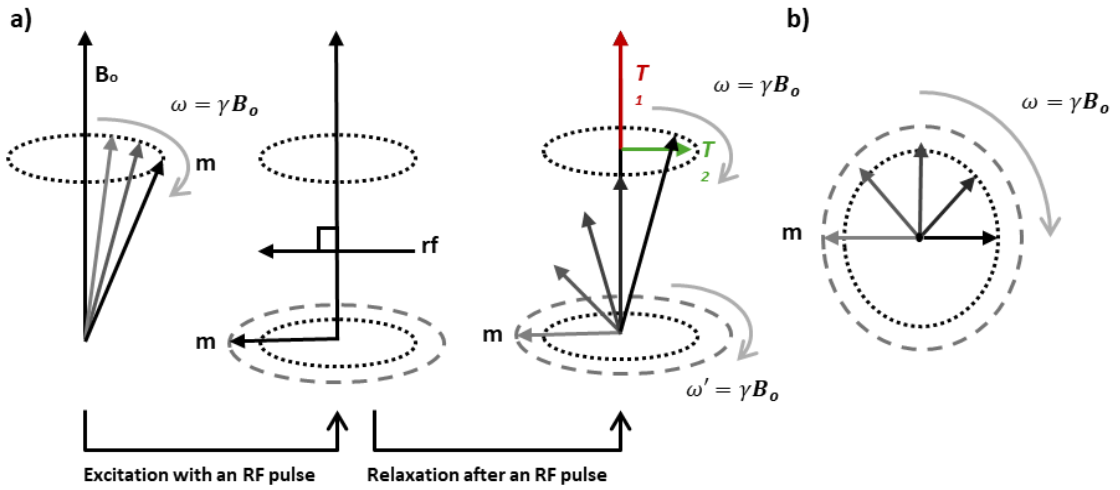


Figure **4.30**. **a)** Basics of the magnetic resonance phenomenon. After the application of radio frequency pulses through a transversal $\mathbf{B_o}$, magnetisation aligns with the applied radio frequency. Relaxation can then be tracked by decomposition of the magnetisation into the two spherical vectorial component directions: T_1 and T_2. The change in intensity of these two vectors, until relaxation to the equilibrium of the magnetic spins takes place, gives rise to what is detected in MRI. **b)** Top view of the T_2 process.

In proton-based MRI (^{1}H-MRI), the intensity of a given signal depends on multiple parameters, which include the proton density, T_1 and T_2 relaxation times, and the cellular microenvironment.[126] Classical MRI presents limited contrast between tissues with similar intrinsic properties. Thereafter, differentiating tumours based solely on unenhanced MRI can be challenging. To address this, CAs are employed to improve image resolution by altering proton relaxation behaviour in targeted regions. These agents shorten relaxation times, leading to positive enhancement (i.e., brighter images) in T_1-weighted (T_{1w}) scans and negative enhancement (i.e., darker images) in T_{2w} scans.[127] Current CA complexes used in the medical field, like Gd-based Dotarem™, have presented little specificity, as well as being linked to toxicity issues tracked to unexpected Gd release.[128]

The lack of MRI specificity and safety can be rectified using gold-based NPs or iron oxide NPs (i.e., SPIONs).[129-131] Paramagnetic NPs, when placed in the magnetic field, disturb the field, causing faster water ^{1}H relaxation, thus enabling detection with MRI.[132] SPIONS typically present a transversal relaxivity (r_2) much higher than the longitudinal relaxivity (r_1), yielding high r_2/r_1 ratios. As such, SPIONs are classically classified as a highly efficient T_2 agent. Examples of SPIONs as T_2 CAs can be found in the reports from Lee *et al.*, who report on a manganese-enriched SPION that present as a T_{2w} CA with r_2 values of 1193 $mM^{-1}{\cdot}s^{-1}$ and r_2/r_1 of 208 while also displaying strong MHT properties in *in vivo* settings for the treatment of GBM.[133] As well as other reports from Jacqmarcq *et al.*, who report on SPION-based systems for MRI-based microthrombi detection in stroke, displaying mussel-inspired iron oxide clusters that displayed r_2 values of 388 $mM^{-1}{\cdot}s^{-1}$ and r_2/r_1 values of 239.[134]

Direct comparisons with commercial and standard of care CA, like Gd complexes, are hard to find as they are mainly focused on dual-mode MRI CAs, meaning, CAs that present optimal properties to perform as either T_1 or T_2 CA. Moreover, the standard Dotarem™ presents as a T_{1w} CA with very low r_2/r_1 ratios of 1.13. Overall, it is common for SPIONs to outperform Gd-based drugs or other molecular T2 drugs; their main limitation, however, lies in the lack of research regarding SPION-based systems reaching clinical trials.[134]

4.3.2.2. *In vitro* Magnetic Resonance Imaging Phantoms

To evaluate **pDPA-CNP@Fe NPs** as a platform for MRI, the r_1 and r_2 values were determined by T_{1w} and T_{2w} image acquisition of a NP suspension at different concentrations with respect to the total metal concentration. For this assay, **pDPA-CNP@Fe NPs** were suspended in a H_2O-agarose 1% solution at pH = 7.4, and measured as phantoms in an MRI Biospec of 7 T. H_2O-agarose 1% solutions allow measuring phantoms in an environment that simulates the viscosity and consistency of biological tissues, mimicking the behaviour of water in physiological environments. r_1 and r_2 were then obtained via the slope of the plot of inverse relaxation values versus the concentration of Fe. This agarose-based method has been widely used in the literature to obtain the relaxivity parameters of several commercial CAs.[136] Phantom T_{2w} images are presented in Figure **4.31,** and the obtained r_1 and r_2 values are summarised in Table **4.1**.

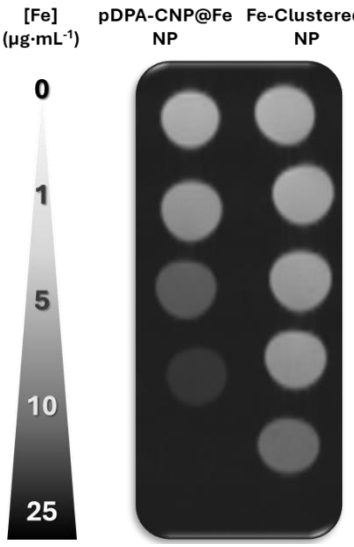


Figure **4.31**. T_{2w} images acquired for **pDPA-CNP@Fe NPs** and **Fe-Clustered NPs** at decreasing metal concentration (25, 10, 5, 1 and 0 $\mu g{\cdot}mL^{-1}$).

Table **4.1.** *In vitro* simulated settings for r_1 and r_2 parameters for **Fe-Clustered NPs** and **pDPA-CNP@Fe NPs**.

	Medium	***r_1 ($mM^{-1}\cdot s^{-1}$)***	***r_2 ($mM^{-1}\cdot s^{-1}$)***	***r_2/r_1***
Fe-Clustered NP	Agarose 1%	0.31 ± 0.02	59.03 ± 3.51	193.10 ± 17.73
pDPA-CNP@Fe		1.12 ± 0.12	1007.23 ± 21.17	852.47 ± 99.81

The r_1 values were determined to be 0.31 ± 0.02 $mM^{-1}\cdot s^{-1}$ for **Fe-Clustered NPs**, and 1.12 ± 0.12 $mM^{-1}\cdot s^{-1}$ for **pDPA-CNP@Fe NPs**. Iron oxide NPs are well known to be T_{2w} relaxation agents, with high r_2 and low r_1.[137] This is precisely the case for our **Fe-Clustered NP** and **pDPA-CNP@Fe NPs**, with values around or lower than 1 $mM^{-1}\cdot s^{-1}$. Generally, good r_1 CAs are considered to be good if they present high r_1 values, typically >3-5 $mM^{-1}\cdot s^{-1}$.[137] For comparison purposes, a good T_{1w} CA like the commercial Gd-based GdDTPA presents r_1 values of 4.5 ± 0.4 $mM^{-1}\cdot s^{-1}$ and r_2 values of 4.6 ± 0.7 $mM^{-1}\cdot s^{-1}$.[138] In this context, we can clearly see that no NP system we hold presents comparable r_1 values good enough to be considered a T_{1w} CA.

On the other hand, r_2 values were determined to be 59.03 ± 3.51 $mM^{-1}\cdot s^{-1}$ for **Fe-Clustered NPs**, and 1007.23 ± 21.17 $mM^{-1}\cdot s^{-1}$ for **pDPA-CNP@Fe NPs**. A good T_{2w} CA, especially for iron oxide NPs, has r_2 values of 100 to 300 $mM^{-1}\cdot s^{-1}$, with the most efficient iron-based CAs reported displaying r_2 values of 528, 761, 719, and 470 $mM^{-1}\cdot s^{-1}$.[137,139,140] Within these guidelines, **pDPA-CNP@Fe NPs** demonstrates great potential as a T_{2w} CA.

The increase in r_2 values of **pDPA-CNP@Fe NPs** when compared to the **Fe-Clustered NP** comes as no surprise. It is well known that surface chemistry of a nanomaterial substantially influences the contrast of such material. In coordination polymers and metal organic frameworks (MOFs), the high porosity and supramolecular interactions with water allow for water penetration and entrapment, effectively facilitating rapid water exchange with the iron core.[141] Such reports are relevant since water interaction with a CA facilitates and accelerates the ^1H proton relaxation times, resulting in a positive enhancement.[142] Moreover, hydrodynamic sizes are also an important factor in $r_{1/2}$; the strong surface charge of the coordination polymer part of **pDPA-CNP@Fe NPs** allows for effective non-specific water interactions that yield big hydrodynamic sizes that lead to increased values of $r_{1/2}$.[143]

The behaviour of CAs under relies on the relaxivity ratio (r_2/r_1). Broadly, a material behaves as a T_{2w} CA if r_2/r_1 is greater than 10, and as a T_{1w} CA if r_2/r_1 is smaller than two.[144] **pDPA-CNP@Fe NPs** greatly outperforms this definition, as it presents a value of r_2/r_1 almost two orders of magnitude higher at 852.47 ± 99.81. For example, magnetoferritin (ferritin protein loaded with Fe_3O_4) measured at 7 T displays $r_1 \approx 1.50$ $mM^{-1}\cdot s^{-1}$ and $r_2 \approx 528$ $mM^{-1}\cdot s^{-1}$ ($r_2/r_1 \approx 352$).[137] Similarly, PHySIOMIC particles (PDA-encased SPION clusters) in a 7 T phantom had $r_1 \approx 0.50$ and $r_2 \approx 119.6$ ($r_2/r_1 \approx 239$).[145] Finally, when we account for r_2 values, **pDPA-CNP@Fe NPs** within the field of SPIONs outmatches most of the reported and commercially available CA (Figure **3.32**).

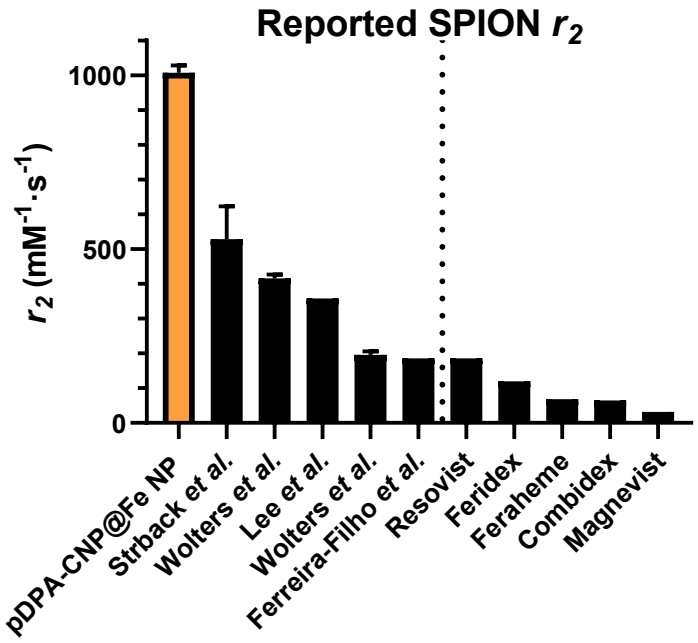


Figure **3.32**. Comparison between reported SPION-based CA from Wolters *et al.,*[146] Lee *et al.,*[147] Ferreira-Filho *et al.,*[148] and commercially available Resovist,[149] Feridex,[149] Combidex,[149] and Magnevist.[149]

These results display that the **DPA-COOH-Zr** coordination polymer used for our **pDPA-CNP@Fe NPs** platform enhances the **Fe-Clustered NP** to display improved relaxation times and potential as a T_{2w} CA. Moreover, the results obtained display increased relaxation times, almost orders of magnitude higher than those of concurring cutting-edge SPION particles reported in recent literature. Therefore, we have increased hopes for applicability as a good CA in *in vivo* MRI studies.

4.3.2.3. *In vivo* Magnetic Resonance Imaging Evaluation

Given the excellent *in vitro* phantoms s results, we aim to bring our systems to pre-clinical *in vivo* MRI assays. Furthermore, any information obtained during the following studies can be used in prospective therapy-focused applications of **pDPA-CNP@Fe NPs**.

Firstly, studies previous to *in vivo* MRI evaluation consisted of the determination of safety and tolerability (to evaluate the MTD) of **pDPA-CNP@fe NPs**. Then, using the data obtained, *in vivo* MRI was conducted. Finally, biodistribution from the mice treated for imaging followed.

For *in vivo* studies, C57BL/6J female mice of 10-12 weeks of age, with body weights of 20.2 ± 0.6 g, were used. In MRI CA and biodistribution studies, GL261 GBM tumour-bearing mice were used. Tumour implantation protocols can be found at the *"**4.5. Materials and Experimental Methods**"* section of this Chapter.

To ensure that all experimentation follows adequate ethical practices, *in vivo* experimentation was performed in collaboration with PhD student Núria Basanta from *ICN2* and *IBB-UAB*, who possesses the knowledge and certification required to perform such assays.

4.3.2.3.1. Tolerability Studies of pDPA-CNP@Fe NPs

The experiment was designed following the guidance on dose level selection for regulatory general toxicology studies in pharmaceuticals.[150] In a typical assay, two groups of three mice each, control and **pDPA-CNP@Fe NPs** treatment groups, were randomly assigned. The treatment group received increasing doses of **pDPA-CNP@Fe NPs** in i.v. administrations via tail vein, starting from 0.002 mmol Fe·kg^{-1}, and doubling concentration until reaching 0.24 mmol Fe·kg^{-1}. A 72-hour rest period was stablished between administrations. On the other hand, control group received vehicle administrations consisting of saline buffer supplemented with 0.5 mM murine serum albumin (MSA). Welfare parameters like behaviour and body weight were monitored during and after 30 days following the final administration to detect any signs of distress or adverse effects. Under these conditions, a dose of 0.24 mmol Fe·kg^{-1} of **pDPA-CNP@Fe NPs** proved safe, and no body weight loss or toxicity symptoms observed during, and neither for the 30-day period after administration (Figure **4.33**).

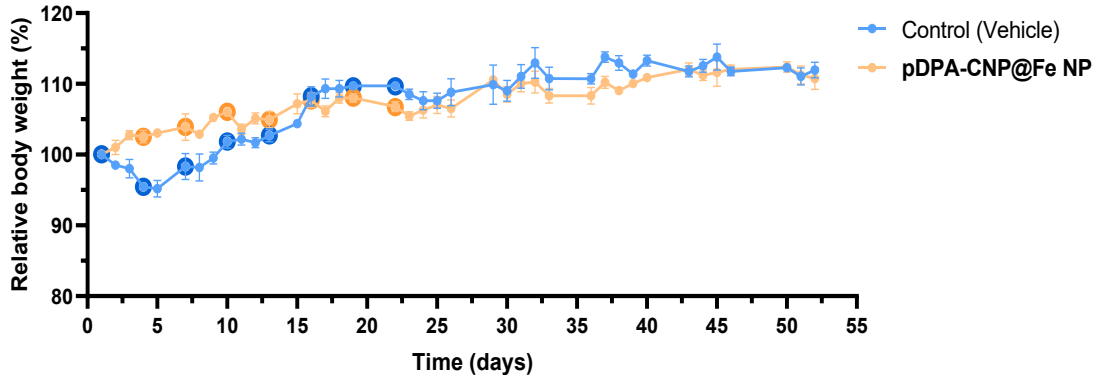


Figure **4.33**. Relative body weight of C57BL/6J female mice with n=3 for each group. Control mice (blue) were i.v. administered with vehicle (PBS with 0.5 mM MSA), and treated mice (orange) were i.v. administered with increasing concentrations of **pDPA-CNP@Fe NP** in the same vehicle as control group (PBS with 0.5 mM MSA). A 72-hour rest period was stablished between administrations (highlighted points). Data is shown as mean ± SE. Initial mice weight measured at first day pre **pDPA-CNP@Fe NPs** i.v. administration is considered as 100%.

Tolerability indicated that no toxicity was observed with any of the concentrations administered, no behavioural change was spotted, and the body weight of mice between control and treated mice displayed no significant differences throughout the experiment. Despite testing concentrations of up to 0.24 mmol Fe·kg^{-1}, the administered **pDPA-CNP@Fe NP** dosage in biodistribution and *in vivo* MRI experiments will consist of 0.12 mmol Fe·kg^{-1}, well below the maximum dose tested, and well tolerated by the treated cohort. Thirdly, this value perfectly matches the safety administration ranges for Fe-based NPs, which are established up to a 0.6 mmol Fe·kg^{-1}.[151-153] This result gives an added value to **pDPA-CNP@Fe NPs** in comparison with Gd-based CAs, which, although widely used in clinical settings, are often associated with undesired side effects.[154]

4.3.2.3.2. In vivo Magnetic Resonance Imaging Evaluation

For the *in vivo* CAs study, GL261 GBM tumour-bearing mice after 19.5 ± 1.5 days post tumour implantation, and with tumour volume of 66.2 ± 23.8 mm^3, were used. MRI scans for brain as well as full body, were performed to track any significant change in contrast of any section of treated mice. Tumour-bearing mice were i.v. administrated with **pDPA-CNP@Fe NPs**, as a CA, at a dose of 0.12 mmol Fe·kg^{-1} in 100 µL of PBS containing 0.5% MSA. T_{1w} and T_{2w} images, as well

as T_{1w} and T_{2w} maps in the case of whole-body mice images, were continuously acquired before the administration, immediately and up to 2 hours after administration, and again at 24 hours post-administration (the complete description of the procedure and acquisition parameters are detailed in the *"4.3 Materials and Experimental Methods"* section). Relative contrast enhancement (RCE) in kidney renal cortex and renal medulla, liver, bladder, and brain tumour were obtained via normalization against mice muscle/brain and pre-administration data. To process the brain MRI data ROIs were defined in both T_{1w} and T_{2w} images. Two ROIs were manually defined, one within the tumour area and the other within the contralateral normal brain tissue. To process the whole-body MRI data related to the CA, ROIs were defined in both T_{1w} and T_{2w} map images for the organs of interest. T_{1w} and T_{2w} relaxation times, and absolute signal intensities for both T_{1w} and T_{2w} maps sequences were obtained. One map image was obtained before CA administration (pre-administration) and multiple were acquired after CA administration (post-administration). Due to the inability of **pDPA-CNP@Fe NP** to act as a T_{1w} CA we will proceed to describe only T_{2w} results (Figure **4.34**), data on acquired T_{1w} images can be found in Annexe **4.51** to **4.53**.

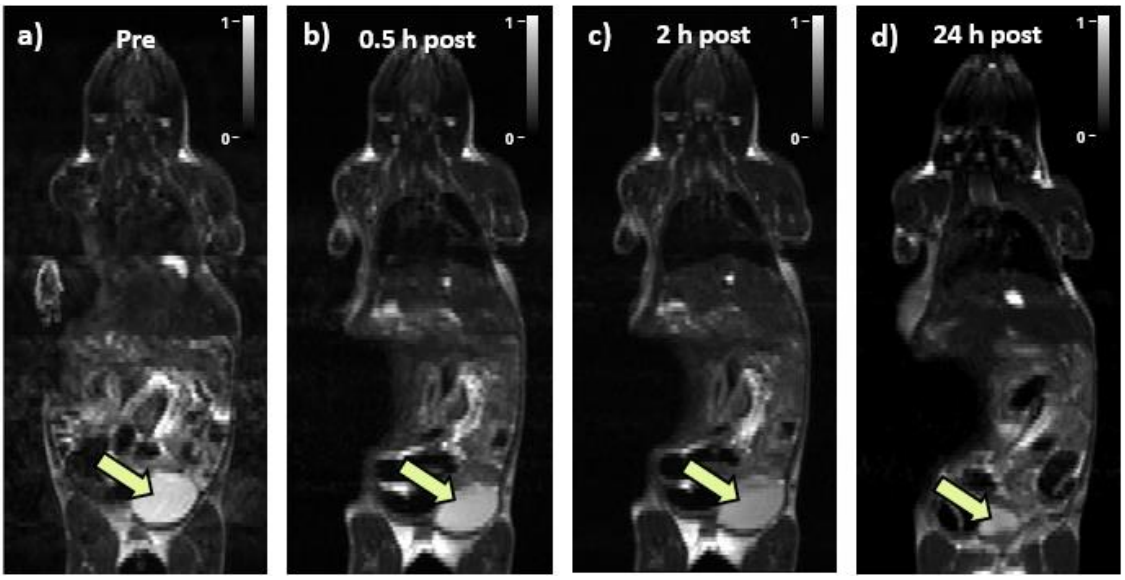


Figure **4.34**. Representative example of *in vivo* study of GL261 GBM tumour-bearing mice (mouse number C2116) administered with **pDPA-CNP@Fe NP** (0.12 mmol Fe·kg^{-1}). From left to right, T_{2w} MRI images obtained **a)** pre-administration, **b)** 0.5 hours post-administration, **c)** 2 hours post-administration, **d)** 24 hours post-administration. Light green arrows indicate the bladder.

RCE values for post-administration images were calculated for each time point. For reference, RCE value for pre-administration images was set to 100% in T_{2w} relaxation and saturation times, and 0% in T_{1w} relaxation and saturation times. In this case, the RCE values give information about contrast improvement before and after CA administration. T_{2w} RCE relaxation times can be observed in Figure **4.35**, T_{2w} saturation times and T_{1w} relaxation and saturation times can be found in Annexe **4.52** and Annexe **4.53**.

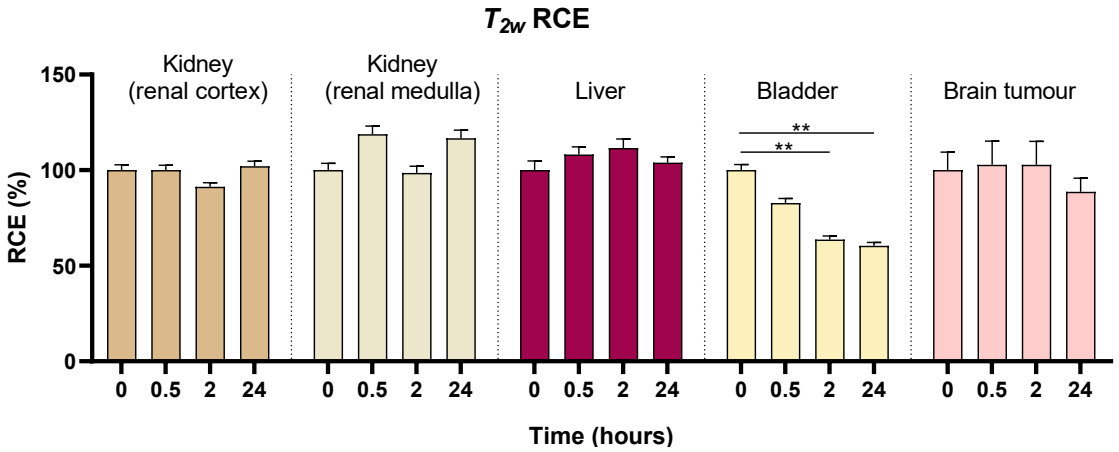


Figure **4.35**. T_{2w} *in vivo* RCE for **pDPA-CNP@Fe NP** in treated GL261 GBM tumour-bearing mice in kidney renal cortex and renal medulla, liver, bladder, and brain tumour. The 100% RCE is the normalised reference value corresponding to pre-administrated MRI. Data represents the mean ± SE, n=2. Statistical differences were calculated using two-way ANOVA, followed by Dunnett's multiple comparison test, where (*) denotes P < 0.05, (**) denotes P < 0.01, (***) denotes P < 0.001, and (****) denotes P < 0.0001.

Significant RCE was clearly observed in the bladder with a remarkable decrease, especially from the mean minimum RCE value observed at 24-hour post-administration (60.4 ± 1.7%). Brain tumour displayed no statistical significance of RCE values at the 24-hour post-administration time frame, although only minor (88.7 ± 7.2%) and with a high error margin. In comparison with previously developed Fe-based CAs within our research group, we have the reports of Suárez *et al.* with a coordination polymer based on iron that reaches a T_{2w} RCE in mice tumour of 73.7 ± 14.4%.[155] In comparison, for brain imaging, our **pDPA-CNP@Fe NPs** fall considerably. Nonetheless, our highest RCE is observed in the bladder, with clear statistical significance. Most RCE values for bladder reported in the literature come from T_{1w} studies with Gd. The few examples that can be found on SPIONs report presenting a T_{2w} RCE value in the bladder of 27%, as reported by Ding *et al.,* but only at *in vitro* settings, and Tyagi *et al.,* who reports on total signal loss from anemia treatment drug ferumoxytol, however, using a very high 5 mM with regards to Fe concentration.[156,157] Furthermore, administration in these settings is intravesical, requiring a highly invasive administration, while we achieved our results from i.v. administration.

RCE values seem not to recover over the 24-hour time period, which suggests bioaccumulation in those tissues. However, such accumulation, when taking tolerability data into account, seems not to be enough to cause any health-related issues in treated mice.

Overall, although the initial target of GBM MRI CA, **pDPA-CNP@Fe NP** presents as a possible prospect of CA in bladder-related tumours, further evaluation and research in this application is required. Nonetheless, the slight increase in RCE in tumour, still gives hope to the applicability in the originally intended field. Nonetheless, it is also evident that for any GBM theragnostic applications, future work requires to finetune properties like size and targeting to increase selectivity towards brain, and more specifically brain tumours. Furthermore, alternative administration methods may also be employed to enhance targeting, like IN administration as explored in Chapter 3.

4.3.2.3.3. Biodistribution Studies of pDPA-CNP@Fe NPs

Given **pDPA-CNP@Fe NPs**, with a mean size of 288.0 ± 0.2 nm, we would expect the NPs to accumulate in the spleen or liver, with a smaller chance in the kidneys. Accumulation in the brain would only be expected with a big enough tumour that ensures formation of a leakier BTB, as was the case in our current settings. Nonetheless, experimental MRI RCE data shows accumulation specifically in the bladder. These results seem counterintuitive, as it is reported that particles between and larger than 100 to 200 nm are usually captured within the spleen and liver via phagocytosis by liver Kupffer cells and splenic macrophages, leading to RES clearance. And only particles smaller than 6 nm are rapidly cleared via the kidneys into the urinary track.[158,159]

In this context, biodistribution of **pDPA-CNP@Fe NPs** was evaluated at 2- and 24-hours post i.v. tail administration in GL261 GBM tumour-bearing mice after 19.5 ± 1.5 days post tumour implantation with tumour volume of 66.2 ± 23.8 mm^3, with the same mice evaluated in MRI. **pDPA-CNP@Fe NP** biodistribution was quantified via determination of Fe and Zr levels within different organs using ICP-MS (Figure **4.36** and **4.37**). Results are based on normalization of Fe or Zr content in µg Fe·mg^{-1} protein or µg Zr·mg^{-1} protein.

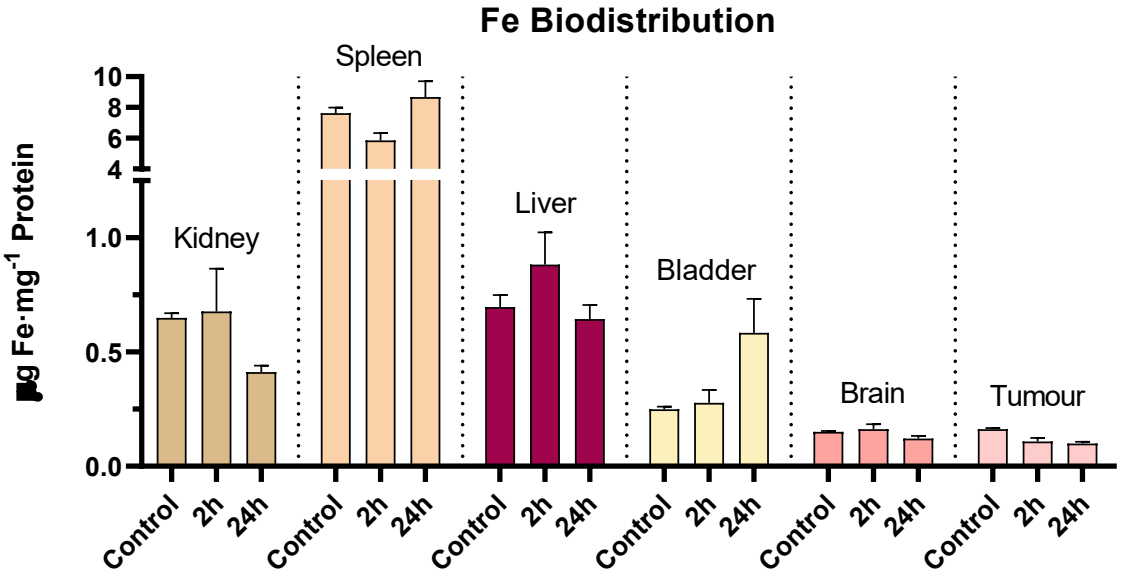


Figure **4.36**. Biodistribution of Fe correlated to **pDPA-CNP@Fe NP** in mice organs. **pDPA-CNP@Fe NP** was administrated i.v. with a dosage of 0.12 mmol Fe·kg^{-1} body weight. The concentration of Fe in different tissues was detected by ICP-MS at various points post administration. Data represents the mean ± SE, n=3.

In terms of Fe biodistribution (Figure **4.36**), results point to the accumulation pattern observed in MRI. **pDPA-CNP@Fe NP**, or fragments of it, seem to accumulate in bladder, especially at the 24-hour period. Besides bladder, no other accumulation pattern seems to form (i.e., no increase in basal Fe levels was observed). As a result of the low **pDPA-CNP@Fe NP** concentration administered for our assays, Fe quantification proves challenging, as it easily falls within the noise levels of the natural-occurring Fe content in mice. Opposite to Fe, Zr is present at lower concentrations within the mice body, typically at trace elements level. This makes Zr an excellent element tracer for our **pDPA-CNP@Fe NP**, providing a clearer picture of NP accumulation (Figure **4.37**).[160]

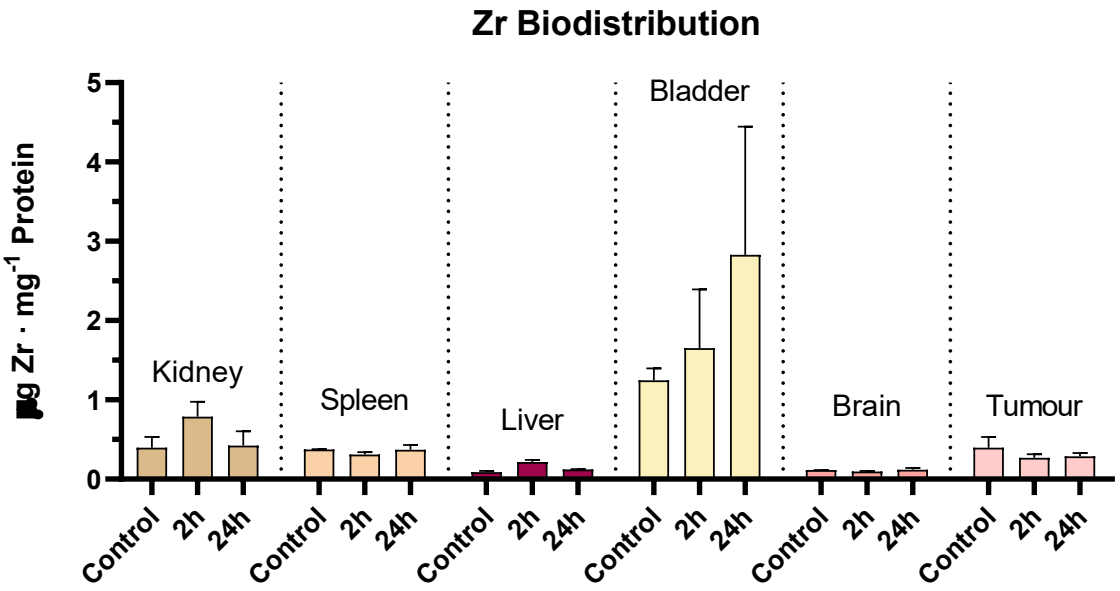


Figure **4.37**. Biodistribution of Zr correlated to **pDPA-CNP@Fe NP** in mice organs. **pDPA-CNP@Fe NP** was administered i.v. with a dosage of 0.12 mmol Fe·kg^{-1} body weight. The concentration of Zr in different tissues was detected by ICP-MS at various points post administration. Data represents the mean ± SE, n=3.

Results from biodistribution tracking Zr reinforce the observed data from Fe biodistribution. As Zr and Fe are both present inside the **pDPA-CNP@Fe NP**, the correlation between both biodistribution results is a good indicator of the NPs' fate inside mice. Thereafter, the accumulation pattern in bladder, observed in both elements, hints towards the selective targeting of this organ, as no other accumulation pattern is observed within the selected organs. While statistical significance was not achieved, a trend towards significance was. These results are consistent with high variability at *in vivo* assays and suggest that expanding the cohort and reducing deviation may be needed for clearer outcomes.

As for the fate of **pDPA-CNP@Fe NPs**, most studies display that NPs bigger than the renal cut-off (6 nm) remain out of the urinary track (i.g., bladder) after i.v. administration, while accumulating in liver or spleen.[161] Nonetheless some recent examples have utilised transcytosis across peritubular capillaries into tubule cells to display intact 140 nm PEGylated Fe_3O_4 NPs into the bladder.[162] Therefore, displaying alternative pathways NPs can follow to reach the bladder, and pointing at possible causes of selective contrast in bladder.

All in all, even at the low experimental NP concentrations, when data from Fe and Zr measurements are compared, the results strongly support a consistent accumulation pattern. Furthermore, biodistribution and MRI clearly demonstrate selective accumulation in the bladder, with no appreciable retention in other major organs. This outcome suggests that, although bladder targeting was not the initial aim, **pDPA-CNP@Fe NPs** represent a promising candidate for a selective T_2 bladder CA, capable of generating strong MRI contrast even at very low doses, displaying very high sensitivity.

4.3.3. pDPA-CNP@Fe NP as a Platform in Glioblastoma Treatment

We have evaluated the efficacy of **pDPA-CNP@Fe NPs** as a CA in GBM, and observed that its applicability was more suitable in bladder. Despite the poor selectivity towards the brain, alternative administration routes can enhance delivery to this tissue. For example, IN and intrathecal administration have recently been revisited as administration of drugs in GBM treatment.[163] Thereafter, **pDPA-CNP@Fe NP** as a platform for GBM treatment will still be studied in this Thesis, while also understanding that future work needs to address the targeting and accumulation issue if GBM remains the target of this platform.

However, we first must assess the storage under UV-irradiation and the release of SO under an MHT-triggered stimulus.

4.3.3.1. Characterisation of Optical Properties of pDPA-CNP@Fe NPs

DPA-COOH is a polycyclic aromatic hydrocarbon, and consequently it is also capable to undergo endoperoxide formation via cycloaddition (Figure **4.38**). Precisely also because of the repercussion of endoperoxide formation on the UV-vis and fluorescence spectra, they present as a tool to follow and study the formation and trapping of molecular oxygen.

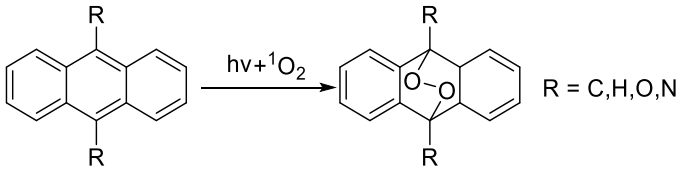


Figure **4.38**. Template reaction of anthracene with SO through a [4+2] Diels-Alder cycloaddition.

Because of this, UV-vis spectrum of **DPA-COOH** in DMF, and the **pDPA-CNP@Fe NPs** in water**,** were recorded (Figure **4.39**). As expected for anthracenes, both showed strong absorption bands near the UV region with maximums of absorbance (λ_{Abs}) at 356 nm for **DPA-COOH**, and 362 nm the **pDPA-CNP@Fe NPs**. The ε for the NPs is harder to determine since scattering and non-specific interactions play an important interference in UV-vis spectrum of such. Therefore, ε was only studied for molecular **DPA-COOH** and was found to be $1.37 \cdot 10^4$ $M^{-1} \cdot cm^{-1}$.

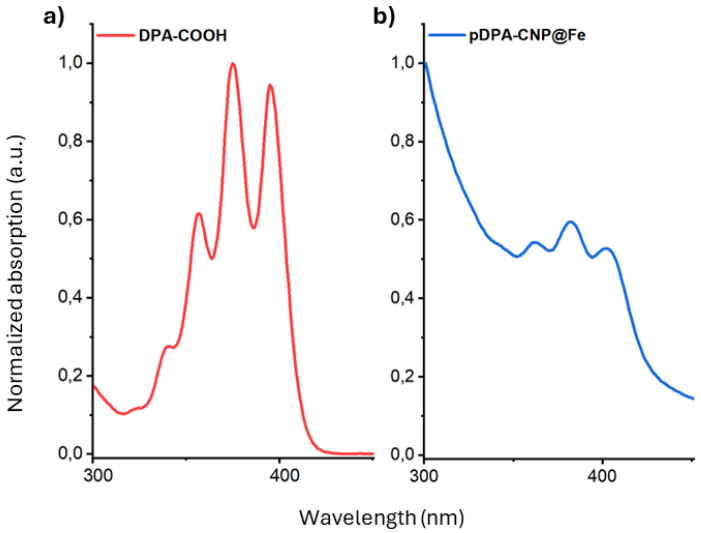


Figure **4.39**. UV-vis spectrum of **a) DPA-COOH** in DMF (red), and **b) pDPA-CNP@Fe NPs** in water (blue).

Absorption of both compounds fall within proximity of each other, since formation of the **pDPA-CNP@Fe NPs** does not affect the conjugation of **DPA-COOH**, which is the biggest contributor to such spectrum. Furthermore, the absorption spectrum of **DPA-COOH** in DMF solutions resemble those reported for the parent non-modified 9,10-Diphenylanthracene (**DPA**) (λ_{Abs}=375 nm), showing that functionalization did not significantly affect the optical properties and the electronic state energies.[164] The appearance of a baseline for **pDPA-CNP@Fe NPs** can be mainly attributed to the scattering effect NPs experience, which also coincides with the biggest scattering at higher energy frequencies.[165] Scattering increases as the wavelength approaches the particle size, usually NPs are small enough not to matter, but in our case, size of our nanoparticulate system is big enough to perceive an impact. Furthermore, the iron from the core also increases the widening and baseline contribution of **pDPA-CNP@Fe NPs** as a result of the iron core absorption spectrum, which is wide, and engulfs most of the entire range.

Polycyclic aromatic hydrocarbons are also known to present strong fluorescence, which can be used to study any structural change that may be observed in the polycyclic aromatic region of **DPA-COOH**.[166] As such, fluorescence excitation and emission spectra of **DPA-COOH** ,and the **pDPA-CNP@Fe NPs** were recorded using an emission wavelength of 495 nm and an excitation wavelength of 375 nm (Figure **4.40**).

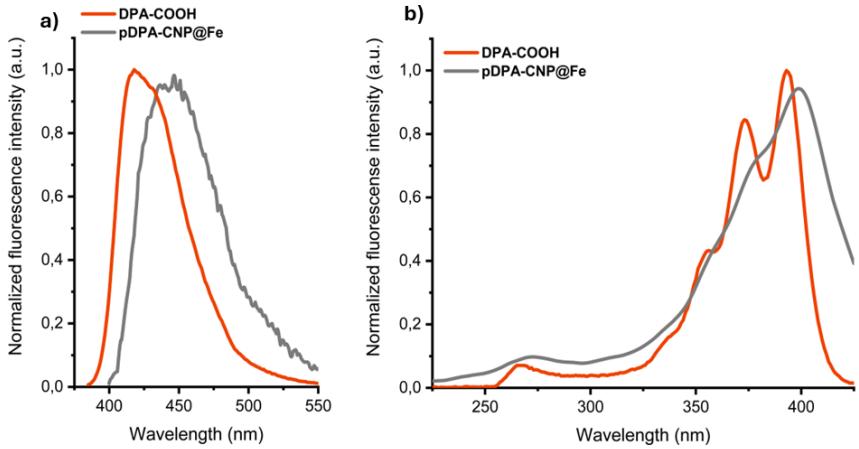


Figure **4.40**. Fluorescence emission spectrum of **DPA-COOH** in DMF (orange) and **pDPA-CNP@Fe NPs** in water (grey) recorded at **a)** 495 nm and **b)** 375 nm.

The fluorescence excitation maxima (λ_{exc}) for **DPA-COOH** and **pDPA-CNP@Fe NPs** were recorded at 375 nm, and observed to be 393 and 400 nm, respectively. While the emission maxima for **DPA-COOH**, and **pDPA-CNP@Fe NPs** were found at 418 and 447 nm respectively. FQYs were recorded of 98.9% with λ_{exc}=375 nm for **DPA-COOH**; and 1.26% with λ_{exc}=375 nm for **pDPA-CNP@Fe NPs**.

Fluorescence intensity and FQY of the nanoparticulate system were, as expected, of much less intensity than **DPA-COOH**. Most probably, due to the self-quenching of energy emission of NPs, effectively reducing fluorescence intensity by absorbing light of the same energy they are emitting.[167] Moreover, the iron oxide core presents a broad absorption spectrum that overlaps with the excitation wavelength used to observe fluorescence. This results in an effective loss of energy due to energy transfer to the **Fe-Clustered NPs**.

4.3.3.1.1. Loading and Release

It is expected that, when polycyclic aromatic hydrocarbons in solution are irradiated by light at their absorption wavelengths, they react with molecular oxygen dissolved in the solvent, acting as a PS and generating SO. Consequently, reaction with the same SO generated forms endoperoxides. This is the result of a 1,4-cycloaddition with molecular SO [4+2].[168] Endoperoxide formation of such compounds breaks conjugation of their system and, as a result, the maxima of the absorption and fluorescence spectra decrease due to a change in their electronic structure.[169] Anthracene endoperoxides also have the possibility to decompose thermally (i.e., retro-Diels-Alder reaction), regenerating the original aromatic compound, releasing SO in the process and recovering their original spectrum.

To prove that such phenomena is occurring in our system we need to observe three different things happening; i) A decrease in signal in the UV-vis spectra as a result of endoperoxide formation, ii) A recovery of UV-vis signal because of induced release of SO through retro Diels-Alder reaction, and iii) A release of SO as a result of the reverse reaction. (Figure **4.41**)

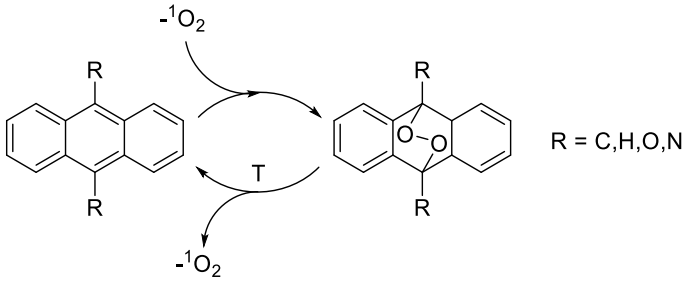


Figure **4.41**. Template reaction of anthracene with SO through a [4+2] Diels-Alder cycloaddition, forming an endoperoxide, and reverse cycloelimination reaction.

Decrease of absorption in the UV-vis spectrum was observed for **DPA-COOH**, and **pDPA-CNP@Fe NPs** under UV at 365 nm irradiation, as well as an increase of absorption intensity during thermal-induced recovery (Figure **4.42**), correlating to the behaviour described in Figure **4.41**.

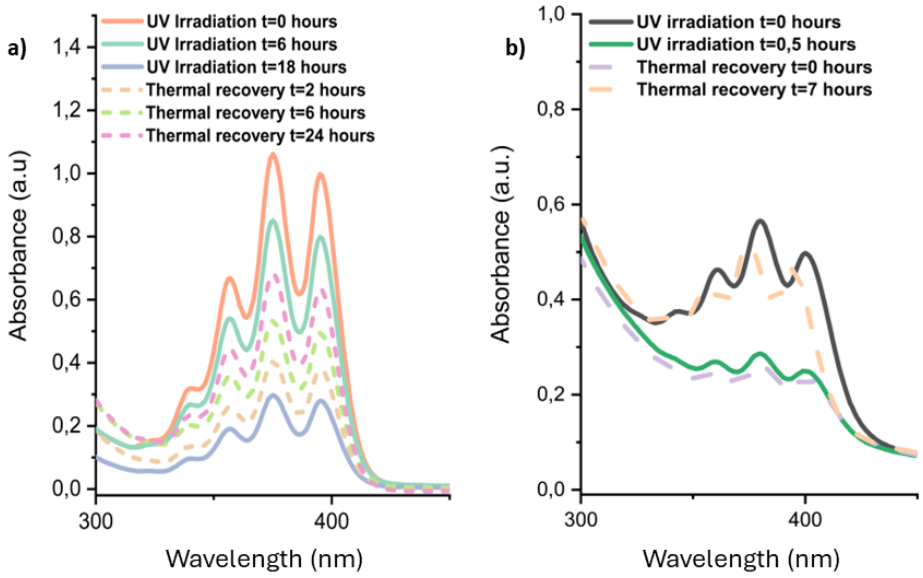


Figure **4.42**. UV-vis spectra under irradiation with a 365 nm UV lamp source (continuous line) and thermal recovery at 90 °C (dashed line) of **a) DPA-COOH** and **b) pDPA-CNP@Fe NPs**.

Absorption spectra recovery can be seen to be almost total for **DPA-COOH** and to a lesser degree for **pDPA-CNP@Fe NPs**, with small shifts in the absorption bands of this compound. Possible explanation for such phenomena is the fact that thermal decomposition of polycyclic aromatic hydrocarbons endoperoxides can follow two distinct reaction pathways. One follows a reverse cycloaddition (i.e., retro-Diels-Alder reaction) and yields the starting material (i.e., recovery of UV signal observed). The second pathway generates homolytic cleavage of the O-O bond yielding products of side reactions with such cleavage (Figure **4.43**).[170]

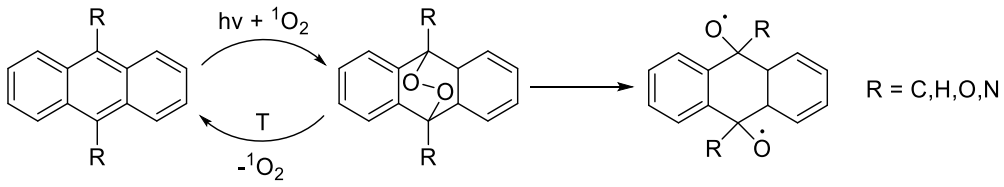


Figure **4.43**. Template reaction of anthracene with SO through a [4+2] Diels-Alder cycloaddition and reverse cycloelimination reaction with the alternative homolytic bond cleavage reaction path.

The same endoperoxide formation and reverse reaction was also followed using the fluorescence emission of **DPA-COOH** and **pDPA-CNP@Fe NPs** under a 375 nm excitation wavelength (Figure **4.44**).

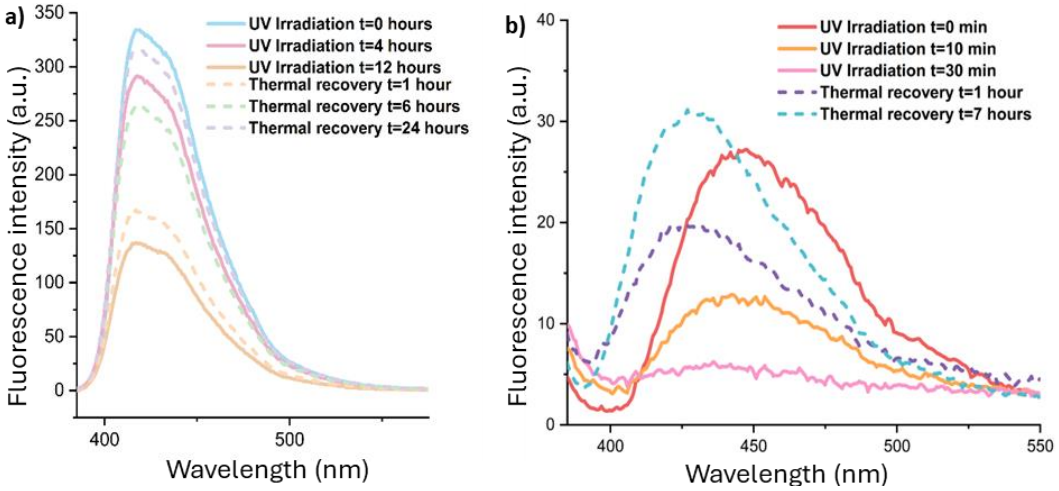


Figure **4.44**. Fluorescence emission spectra at 375 nm under irradiation with a 365 nm UV lamp source (continuous line) and thermal recovery at 90 °C (dashed line) of **a) DPA-COOH** and **b) pDPA-CNP@Fe NPs**.

Behaviour like that of the UV-vis spectra was observed here, with **DPA-COOH** recovering much closer to the original fluorescence emission spectra, whereas **pDPA-CNP@Fe NPs** recovers not only to higher intensities, but also slightly shifted to higher energies. We attribute the hypsochromic shift to the same behaviour as before, which stems from the change in nature of some of the **pDPA-COOH** molecules.

Under irradiation, [2+4] endoperoxide formation is not the only possible reaction to occur. It has long been known that [4+4] cycloaddition of two anthracenes is a possible outcome when photoactivating this process through irradiation of such molecules.[171] The study of the possible outcome of such reactions will be studied further in the "***4.3.4.5. Singlet Oxygen Load and Unload in pDPA-CNP***" section of this Chapter.

Finally, to assess whether SO was being released from our **pDPA-CNP@Fe NPs** during the thermal recovery phase, we used a singlet oxygen sensor green (SOSG) dye commercialised from Fisher Scientific (USA). SOSG consists of a fluorescent probe sensitive to SO, gaining fluorescence when in contact with such. In this experiment our **pDPA-CNP@Fe NPs** to be studied where separated into two samples, both were irradiated, but only one was subjected to a thermal recovery phase. The recovery phase consisted of an external heat source that subjected the sample to 100 °C for 8 hours. SOSG was then added to both suspensions (Figure **4.45**).

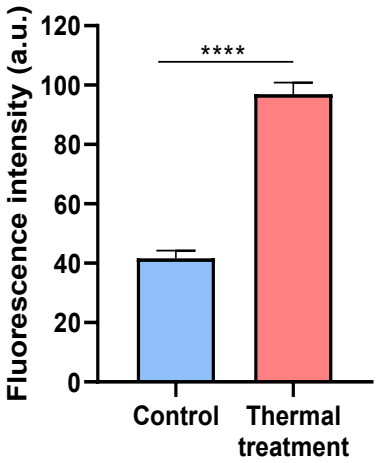


Figure **4.45**. Fluorescence intensity of **pDPA-CNP@Fe NPs** at 540 nm in the presence of SOSG after irradiation for 10 minutes under a UV-lamp source at 365 nm; with a 90 °C thermal treatment for 1 hour (pink), and control group without thermal treatment (blue). Data represents the mean ± SE, n=3. Statistical differences were calculated using a t test of unpaired groups, while (*) denotes P < 0.05, (**) denotes P < 0.01, (***) denotes P < 0.001, and (****) denotes P < 0.0001.

Fluorescence of our probe demonstrated SO presence (fluorescence signal increase) in the samples that had been thermally treated. At the same time, samples that were not thermally treated showed no fluorescence. These results clearly indicate that **pDPA-CNP@Fe NPs** can release SO under thermal stimulus, and although some side reactions may be occurring to our NPs during this phase, we still achieve the release of our target oxidative species.

4.3.3.2. MHT as a Trigger for SO Release in pDPA-CNP@Fe NP

Next steps evaluated the feasibility of using MHT as source of heat to release SO cargo. How suitable a material is for MHT is strongly dictated by the interactions of such materials to a magnetic field.[173] Therefore, we first characterised the magnetic properties of **pDPA-CNP@Fe NPs** and afterwards the magnetically induced SO release.

4.3.3.2.1. Magnetic Characterisation of pDPA-CNP@Fe NPs

pDPA-CNP@Fe NPs showed a magnetic saturation (MST) of 100 emu·g^{-1} and a specific absorption rate (SAR) of 13 W·g^{-1} when measured at 100 Oe (Figure **4.46**). In general, for MHT applications, particles with high SAR and low MST are favoured. For reference, SAR values for SPIONS usually range from 10 to 400 W·g^{-1}, although data must be taken carefully as the strength of the applied magnetic field yields different SAR intensities.[172] MST and SAR give an idea of how strong a magnetic field must be to completely align all magnetic domains of a NP and how much heat our **pDPA-CNP@Fe NPs** are capable of transferring to their environment, respectively.[173] While MST

correlates to the maximum magnetisation achieved when magnetic moments are fully aligned with an external field, SAR refers to the energy loss as a result of hysteresis-induced heating mechanisms.

*For a more in-depth understanding of MST and SAR and their physical context in magnetisation, the reader may direct their attention to the "**4.7.1.1. Physicochemical Properties of Magnetic Nanoparticles**" section in the Conceptual Explanations in the Annexes of this Thesis.*

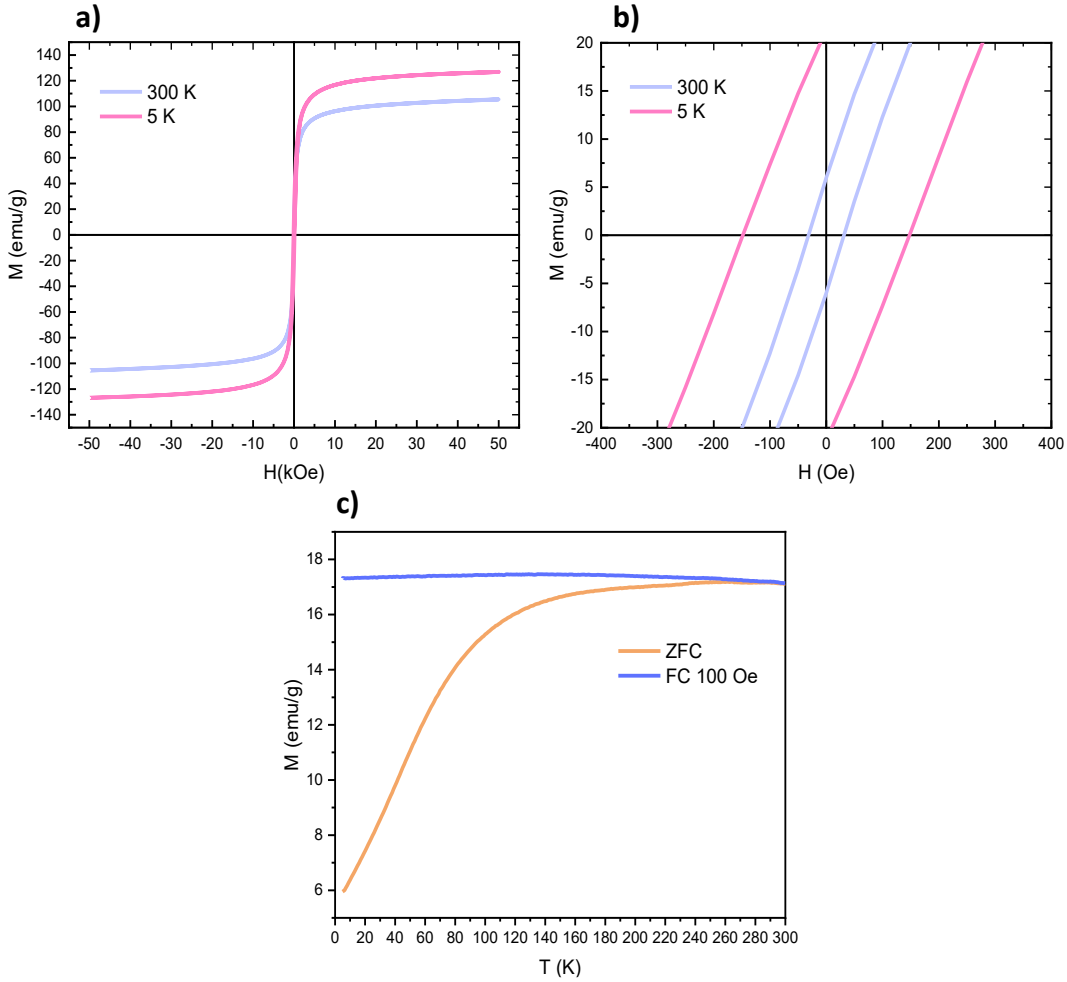


Figure **4.46**. **a)** Magnetic hysteresis curves measured results for **pDPA-CNP@Fe NPs** at 5 K and 300 K, **b)** zoom of the low magnetic field region of measured magnetic hysteresis curves**. c)** Zero-field cooling (ZFC) and field cooling (FC) magnetisation of **pDPA-CNP@Fe NPs** as a function of temperature measured at a field of 100 Oe.

All in all, the poor SAR raises concerns for enough heat generation to reach a combined therapeutic approach of hyperthermia with ROS generation. However, although heat generation may not be enough to generate bulk heating to the solvent, it may still exhibit enough local surface heating to induce the retro-Diels-Alder reaction and SO release (Figure **4.41**).

4.3.3.2.2. Magnetically Induced SO Release

To evaluate if our system was capable of releasing SO in MHT, **pDPA-CNP@Fe NPs** already SO loaded after UV lamp irradiation at 365 nm, were treated under MHT conditions, subjecting them to a 16 mT and 366 kHz AMF. Aliquots of the magnetically treated samples were taken over time, and the presence of SO was tested via fluorescence using the SOSG probe (Figure **4.47**).

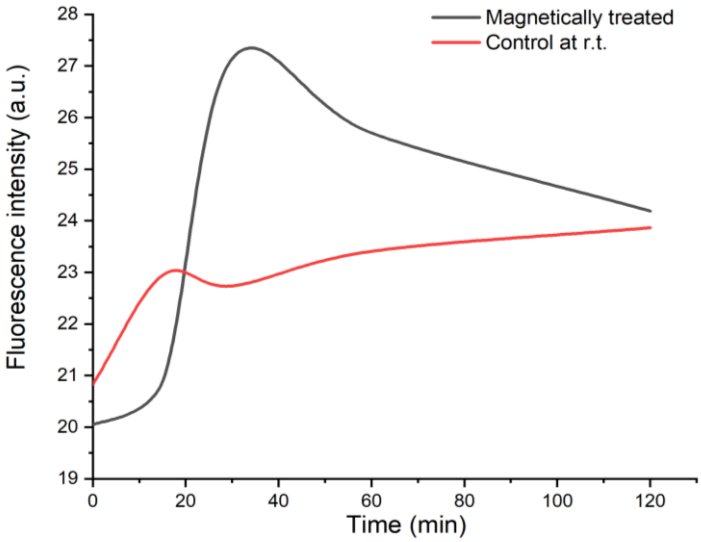


Figure **4.47**. Fluorescence emission intensity of SOSG in the presence **pDPA-CNP@Fe NPs**, after UV irradiation for 30 minutes at 365 nm, and subjected to MHT at 16 mT and 366 kHz AMF (black)), and control group (red) over time at 540 nm with excitation source at 490 nm.

Data from this assay shows a clear burst release of SO over a short period of time, saturating, and then losing signal due to SO effusion out of the sample container. This data conclusively shows that our system is capable of storing and releasing SO on its own using MHT in a burst release. Moreover, these results demonstrate that, even with poor magnetic properties for bulk MHT, we achieve a local surface heating strong enough to undergo a retro-Diels-Alder reaction and release our cytotoxic cargo.

4.3.3.2.3. Therapeutic SO Loaded pDPA-CNP@Fe NP Stability

To achieve effective GBM treatment, it is important that nanocarriers do not lose therapeutic cargo prematurely before reaching the tumour site.[174] To ensure that slow and passive diffusion is not occurring, we decided to incubate SO-loaded **pDPA-CNP@Fe NPs** at different temperatures and observe the release of SO over time (Figure **4.48**). Overall, the results of such experiment display a clear tendency to retain the oxygen loaded within the **pDPA-CNP@Fe NPs** at room temperature and at cell incubating temperatures, whereas only at high, artificially induced, temperatures release of SO was observed

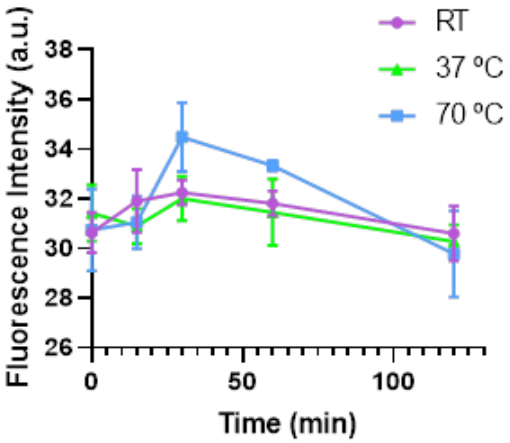


Figure **4.48**. Fluorescence emission intensity at 540 nm of **pDPA-CNP@Fe NPs** subjected to 30 minutes irradiation under a UV lamp source at 365 nm and different temperatures: room temperature or RT (purple), 37 °C (green), 70 °C (blue), over time.

Therefore, the current nanoparticulate system allows to load and avoid passive release, while achieving a fast complete release of the cytotoxic cargo over small periods of time under AMF.

4.3.3.3. *In vitro* Cell Viability Assays of pDPA-CNP@Fe NP

The aim of our research from here will be to try and observe whether our **pDPA-CNP@Fe NPs** present significant differences in survivability between SO-loaded and unloaded **pDPA-CNP@Fe NPs**, as well as significant differences with their different components, **Fe-Clustered NPs** and, later on, in the following sections, the control platform **pDPA-CNP**.

In short, tested NPs were taken to a concentration according to iron content of 0.5 mg·mL^{-1} in the presence of GL261 cells suspended in cell culture medium. The suspended mixture of NPs and GL226 cells were then subjected to MHT in an AMF generator (magnetherm MAGFORCE Ltd.) equipped with an 18-turn coil (366 kHz, 16 mT) for two periods of 30 minutes, with a pause of 10 minutes in between. Cells were then diluted and seeded on a 96-well plate at 5,000 cells/well, bringing the NPs concentration according to Fe content, down to 0.05 mg·mL^{-1}. The effect on cell viability was determined by a PrestoBlue® method, collecting data at both 24- and 72-hour intervals (Figure **4.49**). Fe content concentration for cell viability assays was chosen on a comparative basis against the literature standard for Fe-based MHT studies.[133,175,176] Field intensity and frequency to which cells had been exposed had been chosen as to follow standard regulatory MHT patient settings, following the MagForce Phase II trial settings (2.5-18.8 mT, 100 kHz).[177] Furthermore, the 30-minute exposure periods had been taken to avoid the possible expression of heat shock proteins that could dampen the effects on cell viability.[178]

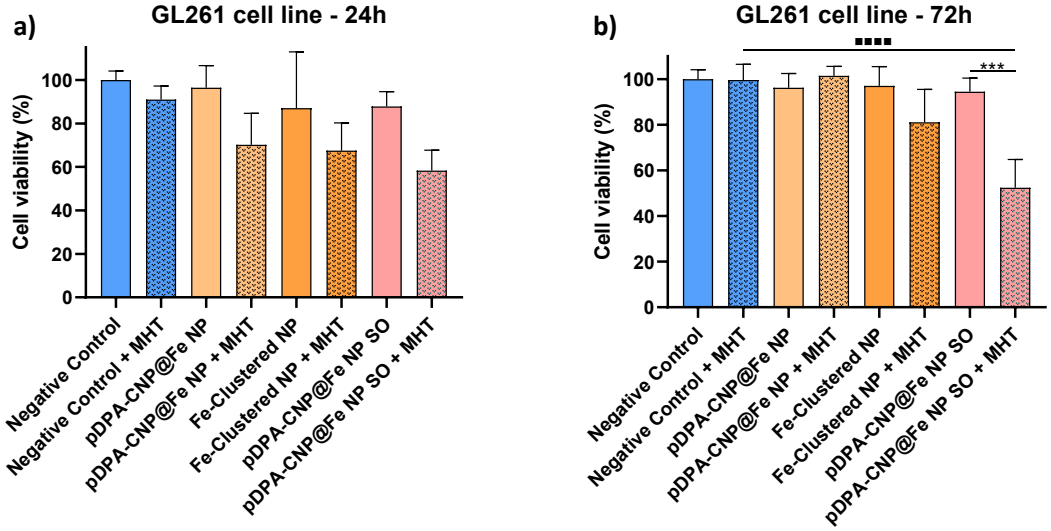


Figure **4.49**. Cell viability of **pDPA-CNP@Fe NPs** (0.05 mg Fe·mL^{-1}), **Fe-Clustered NPs**, and **pDPA-CNP@Fe NPs** (0.05 mg Fe·mL^{-1}) SO loaded under no-MHT and MHT treatment in GL261 cell line after 24 hours and 72 hours. Untreated cells were used as controls. Data represents the mean ± SE, n=3. Statistical differences were calculated using two-way ANOVA, followed by Sidak's multiple comparison test (*) and Dunnett's multiple comparison test (▪), where (* or ▪) denotes P < 0.05, (** or ▪▪) denotes P < 0.01, (*** or ▪▪▪) denotes P < 0.001, and (**** or ▪▪▪▪) denotes P < 0.0001.

Overall, MHT treated **pDPA-CNP@Fe NPs** (SO-loaded and non-loaded), and **Fe-Clustered NPs** display better activity against GL261 cell line than the non-MHT treated counterparts. However, only statistical relevance is found in the 72-hour assay for SO-loaded **pDPA-CNP@Fe NPs**. A summary of cell viability data can be found in Table **4.2** and Table **4.3**

Table **4.2**. Summary of 24-hour cell viability assay data.

		Negative Control	**Fe-Clustered NP**	**pDPA-CNP@Fe NP**	**pDPA-CNP@Fe NP** SO
Cell viability	Non-MHT treated	100 ± 17.4	87.1 ± 44.7	96.5 ± 17.9	87.8 ± 20.5
	MHT treated	91 ± 17.4	67.5 ± 26.8	70.2 ± 25	58.3 ± 30.4

Table **4.3**. Summary of 72-hour cell viability assay data.

		Negative Control	**Fe-Clustered NP**	**pDPA-CNP@Fe NP**	**pDPA-CNP@Fe NP** SO
Cell viability	Non-MHT treated	100 ± 17.4	97 ± 20.6	96.2 ± 11.3	94.5 ± 21.2
	MHT treated	99.6 ± 11.9	81.1 ± 31.3	101.4 ± 7.2	52.4 ± 31.5

In general terms, we observe that 24-hour viability is lower than that at the 72-hour assay, except for the SO-loaded sample **pDPA-CNP@Fe NPs**. We expect this difference to take root in the two different possible cell death mechanisms occurring. While only the SO-loaded **pPDA-CNP@Fe NP** can release the cytotoxic cargo under thermal stimulus, all other samples only produce cell death via MHT heating. Over the next 24- and 72-hours cells that experienced no SO release recover, while cells that underwent simultaneous MHT and SO release do not. Therefore, a different onset of action of SO versus MHT is observed. While MHT achieves most of the cytotoxic activity in short periods of time, SO is capable of retaining such efficacy over longer periods. This difference in the onset of action of SO versus MHT can, at the same time, explain why no statistical significance is found in cell viability at the 24-hour assay for **pDPA-CNP@Fe NPs**, but as SO starts to influence, a statistical significance rises in the 72-hour assay.

Results from cell viability demonstrate that **pDPA-CNP@Fe NPs**, after SO loading and MHT treatment, cell viability drops to almost 52.4 ± 31.5% with a clear benefit of combination therapy between MHT and SO release.

Despite the poor magnetic behaviour of our **pDPA-CNP@Fe NPs** as characterised before, in these settings, we have observed and discussed MHT as a source of cell death. This is because some MHT experiments have been reported in the literature to show substantial cellular damage without observing a macroscopic temperature change. The damage reported has ranged from cell membrane destruction to DNA transformation to growth factor activation.[179-181] Such phenomena have received the name of "Cold Hyperthermia", and although some causes have been pointed out, no general rule has been observed among all cases reported.[27] Nonetheless, the general line of thinking has focused on the case study of high temperature gradients on NPs surfaces as the source of such phenomena.[182] Experiments showing such gradients have been reported for some time, using targeted temperature-sensitive reactions like double-stranded DNA melting, expression of heat shock protein promoters, heterogeneous catalysis of Fisher-Tropsch reaction and, more relevant to our case, retro-Diels-Alder reactions.[181,183,184] The seminal work of Pellegrino *et al.* has also reported local temperatures of tens of kelvin higher on the NPs surface than on the bulk using local temperature probing in Azo-functionalised iron oxide NPs.[180]

Since then, many more studies have shown such behaviour, like the work from Dorota et al., who reported on iron oxide MNPs to achieve drug release using a heat-triggered retro-Diels-Alder reaction while avoiding bulk heating.[185] Some examples directly link the cold hyperthermia of citric acid-coated iron oxide NPs to delayed-onset cellular apoptosis.[186] At the same time, the work of Mar *et al.* has also shown that the belief that temperature must be raised above 43 °C to kill cancer cells is not always applicable, by showing EGFR-targeted iron oxide NPs that killed cancer cells without perceptible temperature rise.[187]

4.3.4. Synthesis, Characterisation and Evaluation of Control Platform pDPA-CNP

For comparison purposes, a control NP platform (**pDPA-CNP**) exclusively consisting of the coordination polymer shell, not as a core-shell NPs, was developed. **DPA-COOH** polymerisation capability in coordination polymerisation is independent of the presence of the iron oxide core we used in the **pDPA-CNP@Fe NP** synthesis. As such, this allows us to test the polymerisation capability of **DPA-COOH** with Zr, while at the same time yielding a NP that can be used for testing and comparison purposes against **pDPA-CNP@Fe NP**.

4.3.4.1. Synthesis and Characterisation of pDPA-CNP

For the CNP synthesis, **DPA-COOH** and zirconyl chloride octahydrate in excess amounts were mixed in DMF under constant and vigorous stirring while heated at 90 °C. After allowing the reaction to evolve for 6 hours, the final **pDPA-CNPs** were isolated and washed with DMF and water by centrifugation, obtaining **pDPA-CNPs** as a white-pale pellet (Figure **4.50**).

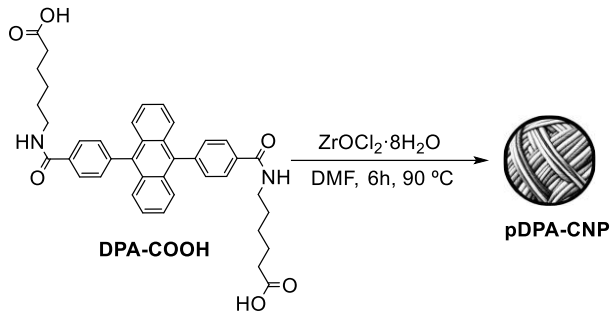


Figure **4.50.** Synthesis of **pDPA-CNP** from **DPA-COOH**

4.3.4.1.1. Chemical Characterisation

FTIR characterisation of **pDPA-CNP** presents itself very similar to that of molecular **DPA-COOH** (Figure **4.51**). Both present the expected signals from the two carbon-oxygen double bonds of the carbonyl groups at 1616 and 1541 cm^{-1}, and 1635 and 1549 cm^{-1}, respectively. Both **pDPA-CNP** and **DPA-COOH** systems also present the aliphatic C-H stretching signals at 2936 and 2926 cm^{-1}. The most remarkable difference outside the fingerprint region is the decrease in the O-H stretching broad band intensity. Such result is the consequence of the **pDPA-CNP** coordination reaction removing an important contribution from carboxyl O-H bonds from the carboxyl groups, showing a decrease in signal at 3308 cm^{-1} for **pDPA-CPN** and 3226 cm^{-1} for **DPA-COOH**. In general lines, the IR spectra changed homogeneously as with the core-shell systems, which is expected, as the main contributor in both cases to IR came from the coordination shell, in this case, **pDPA-CNP**. The original spectra can be found in Annexe **4.58** and Annexe **4.20**.

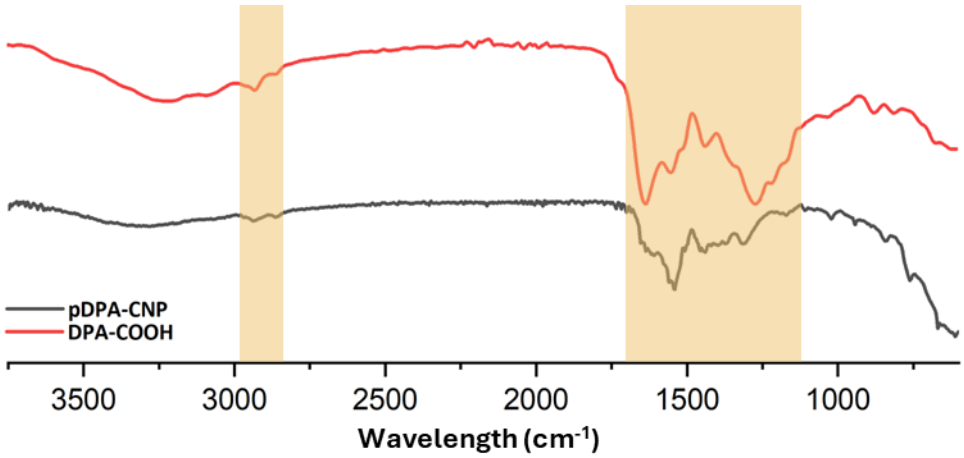


Figure **4.51**. FTIR comparative between **pDPA-CNP** (black) and **DPA-COOH** (red).

ICP-MS was performed to determine the Zr load in the NPs (Annexe **4.59**). With a Zr coordination number of 6, the theoretical value of Zr w/w in the NP was of 4.50% and was found to be, in early studies and mild digestion conditions, 3.18 ± 1.45%. These results fall within the expected margins of a coordination polymer not following a perfect coordination pattern, but close to it. However, we will explain later how these results were reevaluated in further studies.

4.3.4.1.2. Morphological and surface characterisation

Hydrodynamic size and ζ-potential of **pDPA-CPN** were measured using DLS (Figure **4.52**), and size measurements were also made with NTA (Annexe **4.69**). Particles obtained showed hydrodynamic sizes of 135.9 ± 4.6 nm with a low PDI of 0.102 ± 0.008 and a ζ-potential of 42.5 ± 0.5 mV via DLS and a size of 138.0 ± 1.1 nm via NTA, showing conformity between both measurements.

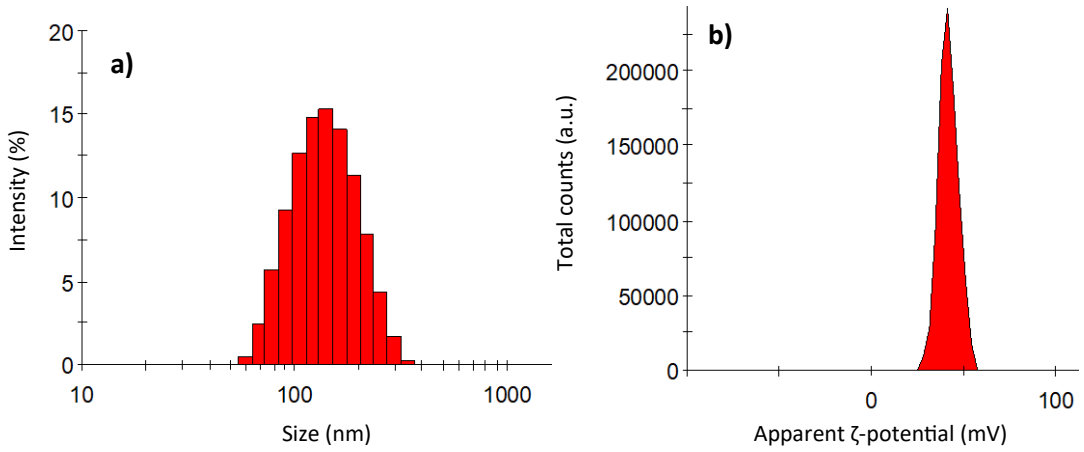


Figure **4.52**. **a)** Size intensity distribution by DLS and **b)** representative ζ-potential of **pDPA-CNP**.

ζ-potential measurements showed a very positive charge that may result from counterions of the carboxylic acids surrounding the NP or amide interactions with the solvent. We can expect that the surface charge had to be similar to that of the **pDPA-CNP@Fe NP** as the shell presents the biggest contribution to solvent-to-surface interactions from the final NP. Furthermore, low PDI ensures, just as we explained earlier, that no big size disparity between NP populations is

present, ensuring homogeneous transport and reproducibility, which was not ensured with **pDPA-CNP@Fe NP**.

Colloidal stability of **pDPA-CNP** in physiological conditions was then studied, tracking the change in size of the system over time. For this purpose, an experiment was set where a suspension of **pDPA-CNP,** with the same concentration as the *in vitro* studies that will be carried out, was prepared in a PBS-BSA solution. The size of the NPs was tracked via DLS over a period of 72 hours with 24-hour intervals between measurements (Figure **4.53**).

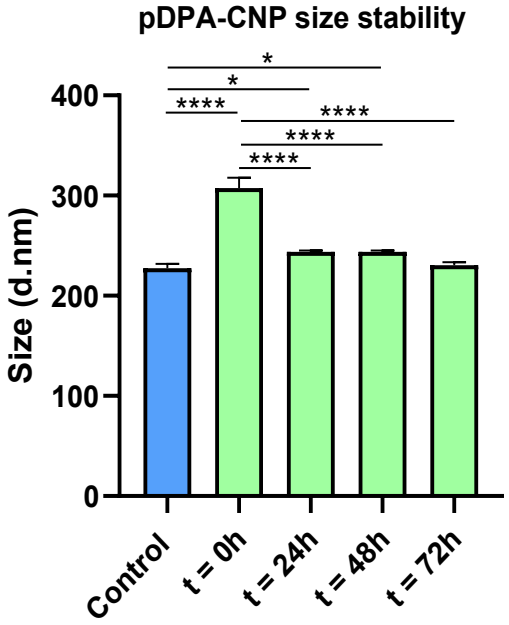


Figure **4.53**. Evolution of size distribution as given by DLS overtime of **pDPA-CNP** in PBS with 42 mg·mL^{-1} of BSA. All groups contain a control group in MilliQ® water. Data represent the mean ± SE, n=3. Statistical differences were calculated using one-way ANOVA, followed by Turkey's multiple comparison test, where (*) denotes P < 0.05, (**) denotes P < 0.01, (***) denotes P < 0.001, and (****) denotes P < 0.0001.

As observed with the previous system **pDPA-CNP@Fe NPs**, **pDPA-CNP** displays a clear increase in size at time 0 hours, from 228.1 ± 3.3 to 307.4 ± 6.1 nm. Such an increase was attributed not to aggregation, but to protein corona formation. The very strong positive charges attract negatively charged proteins strongly, forming big protein coronas around our NPs. Over the period of 72 hours, however, protein corona stabilised to sizes of 230.8 ± 2.2 nm.

The parameters that impact protein corona have already been discussed with **pDPA-CNP@Fe NP** system, and still apply the same here, mostly because the same surface chemistry from the previous platform repeats. We present the same coordination polymer as the shell, which is the component that performs surface-related interactions with solvent, salts, and biomolecules present. Thereafter, it comes to no surprise that the strong positive charge of our NPs strongly interacts with the negatively charged proteins from BSA. This interaction then results in what we observe as the formation of a big protein corona, stabilising over time. This result, at the same time, also hints at good biocompatibility as this set of NPs gets stabilised and coated in biocompatible proteins.

pDPA-CPN morphology was studied using SEM imaging (Figure **4.54**). **pDPA-CPN** presented themselves as very spherical and homogeneous across all samples. Size characterised via imaging with SEM yielded sizes of 144.4 ± 20.2 nm, which fell in accordance with all the previous results from the different methods employed. The shape and size of NPs play an important role in the internalisation capabilities of such systems, and we can start seeing an indication of a spherical NP formation. More importantly, the homogeneous shape avoids the problems from differently shaped subpopulations having different behaviour, ensuring, again, reproducibility.

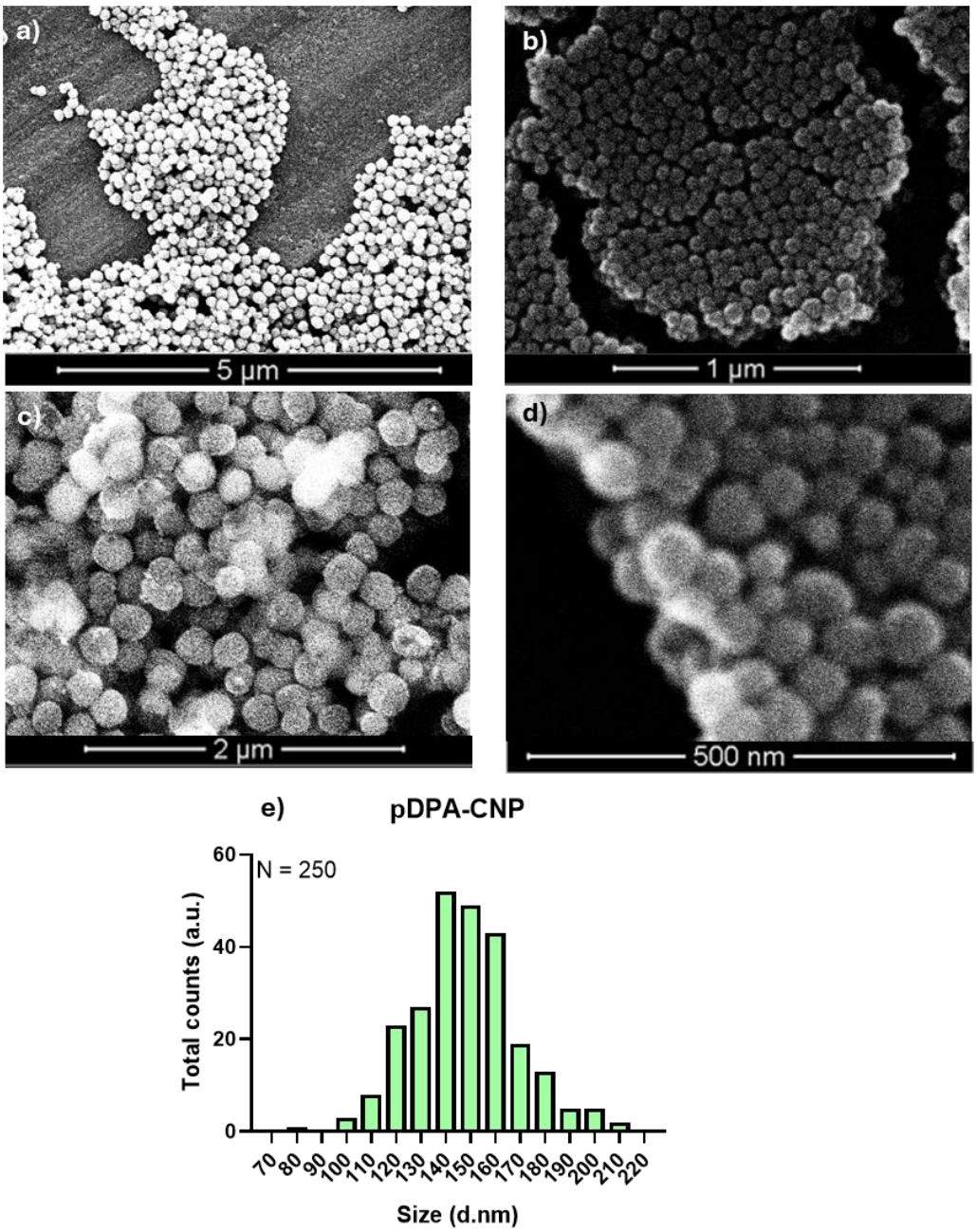


Figure **4.54. a-b)** Representative SEM images of **pDPA-CNPs** under a 5 nm Pt thin film coating. **c-d)** Representative STEM imaging at HAADF detector mode of **pDPA-CNP. e) pDPA-CNPs** size distribution by SEM image size counting.

4.3.4.1.3. Optical Characterisation

pDPA-CNP presented the same anthracene based strong absorption near the UV region, with maximum of absorbance (λ_{Abs}) at 362 nm, same as the recorded for **pDPA-CNP@Fe NPs**. Again,

we observe, just as happened with **pDPA-CNP@Fe NP**, an important base-line contribution to the UV-vis spectra. This contribution can, following the same line of thought as for **pDPA-CNP@Fe NP**, originate from light scattering of the NP system. The UV-vis spectra of **DPA-COOH** and **pDPA-CNP@Fe NP** have been added for comparison (Figure **4.55**).

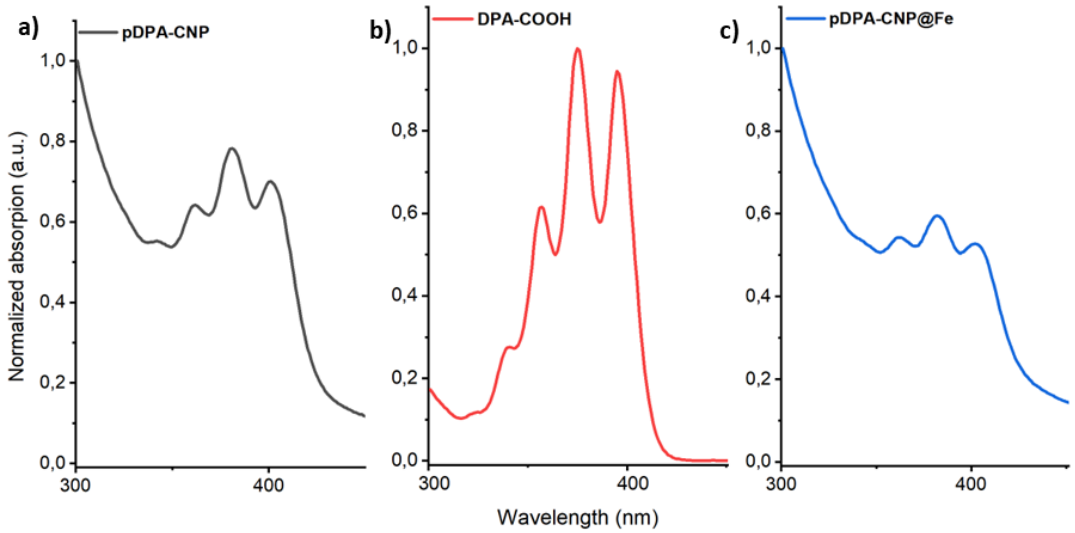


Figure **4.55**. UV-vis spectra of **a) pDPA-CNPs** in water (black), **b) DPA-COOH** in DMF (red), and **c) pDPA-CNP@Fe NPs** in water (blue).

The fluorescence spectrum of **pDPA-CNP** was also recorded. Fluorescence excitation and emission spectra of **pDPA-CNPs** were recorded using an emission wavelength of 495 nm and an excitation wavelength of 375 nm, the same spectra of **DPA-COOH** and **pDPA-CNP@Fe NP** have been added for comparison purposes (Figure **4.56**).

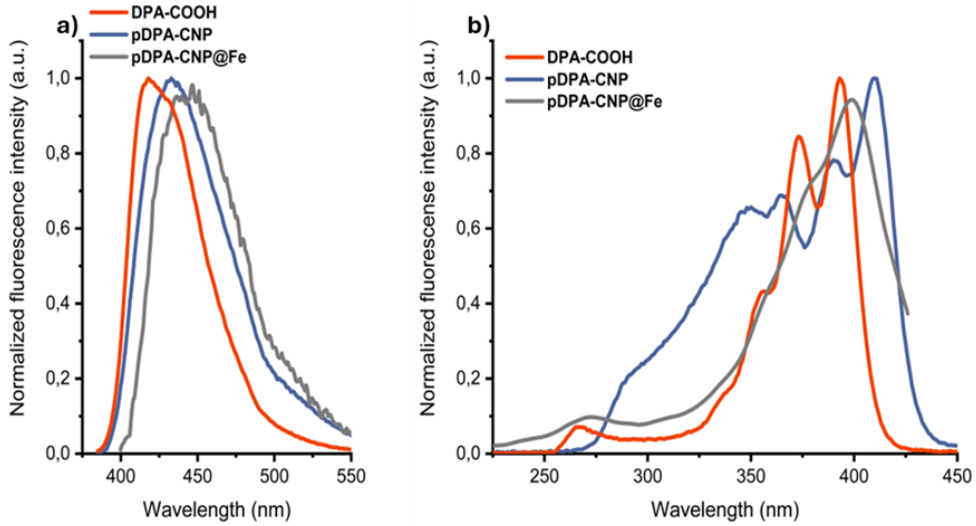


Figure **4.56**. **a**) Fluorescence emission spectra recorded at 495 nm of **DPA-COOH** in DMF (orange), **pDPA-CNPs** in water (blue), and **pDPA-CNP@Fe NPs** in water (grey). **b**) Fluorescence excitation spectra recorded at 375 nm of **DPA-COOH** in DMF (orange), **pDPA-CNPs** in water (blue), and **pDPA-CNP@Fe NPs** in water (grey).

The fluorescence excitation maximum (λ_{exc}) for **pDPA-CNP** was recorded at 375 nm and observed to be 410 nm. While the emission maximums for **pDPA-CNP**, was found at 433 nm. FQY was of 59.1 % with λ_{exc} = 375 nm for **pDPA-CNP**. We observe again that fluorescence intensity and

quantum yield of **pDPA-CNP** were much less intense than **DPA-COOH** (98.9% at 375 nm). This is mostly hypothesised to be due to self-quenching of energy emission of NPs, effectively reducing fluorescence intensity by absorbing light of the same energy they are emitting, but less so than that of **pDPA-CNP@Fe NP**, probably due to energy transfer to Fe that **pDPA-CNP** cannot perform.[188]

4.3.4.1.4. Magnetic Properties

Although expecting a diamagnetic behaviour from **pDPA-CNP**, the magnetic properties were evaluated and used as a comparison against those of **pDPA-CNP@Fe NP** (Figure **4.57**). As expected from a zirconium oxide, **pDPA-CNP** displayed a complete diamagnetic behaviour, with no magnetisation or interaction with the magnetic field.

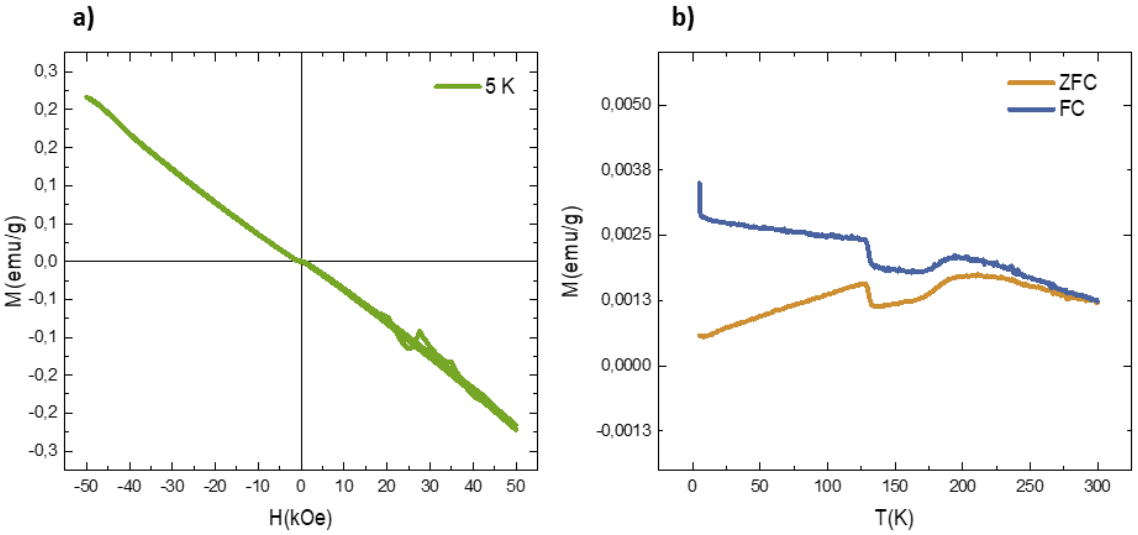


Figure **4.57**. **a)** Magnetic hysteresis curves. measured results for **pDPA-CNP** at 5 K. **b)** ZFC and FC magnetisation of **pDPA-CNP** as a function of temperature measured at a field of 50 Oe.

Furthermore, morphological changes because of interactions with AMFs were tracked. Thereafter, **pDPA-CNP** was submitted to the same AMF treatment conditions as the *in vitro* cell viability assays and its morphology was studied via SEM imaging (Figure **4.58**). We observe that NPs retain the same morphology and roughly the same size as the non-MHT-treated samples. With sizes ranging from 147.8 ± 20.9 nm in non-MHT treated samples and 143.0 ± 17.6 nm for MHT treated samples, as analysed histologically via SEM imaging. Therefore, concluding AMFs do not alter the NPs morphology.

Coordination bonds formed by Zr with carboxylate ligands are known to be strong due to the hard Lewis acid presentation of the Zr atoms interacting with another hard Lewis acid from the carboxylate moieties.[85-87] Accordingly, we then expect such bonds to have great chemical and mechanical stability.

One final indicator of NP degradation that was tracked came from Zr release into the media. As the coordination metal node of our polymeric network, the release of water-soluble Zr species could be linked to NP degradation. However, after analysis using the dialysis bag method of MHT-treated **pDPA-CNP** samples, no release of Zr was observed in ICP-MS. (Annexe **4.68**).

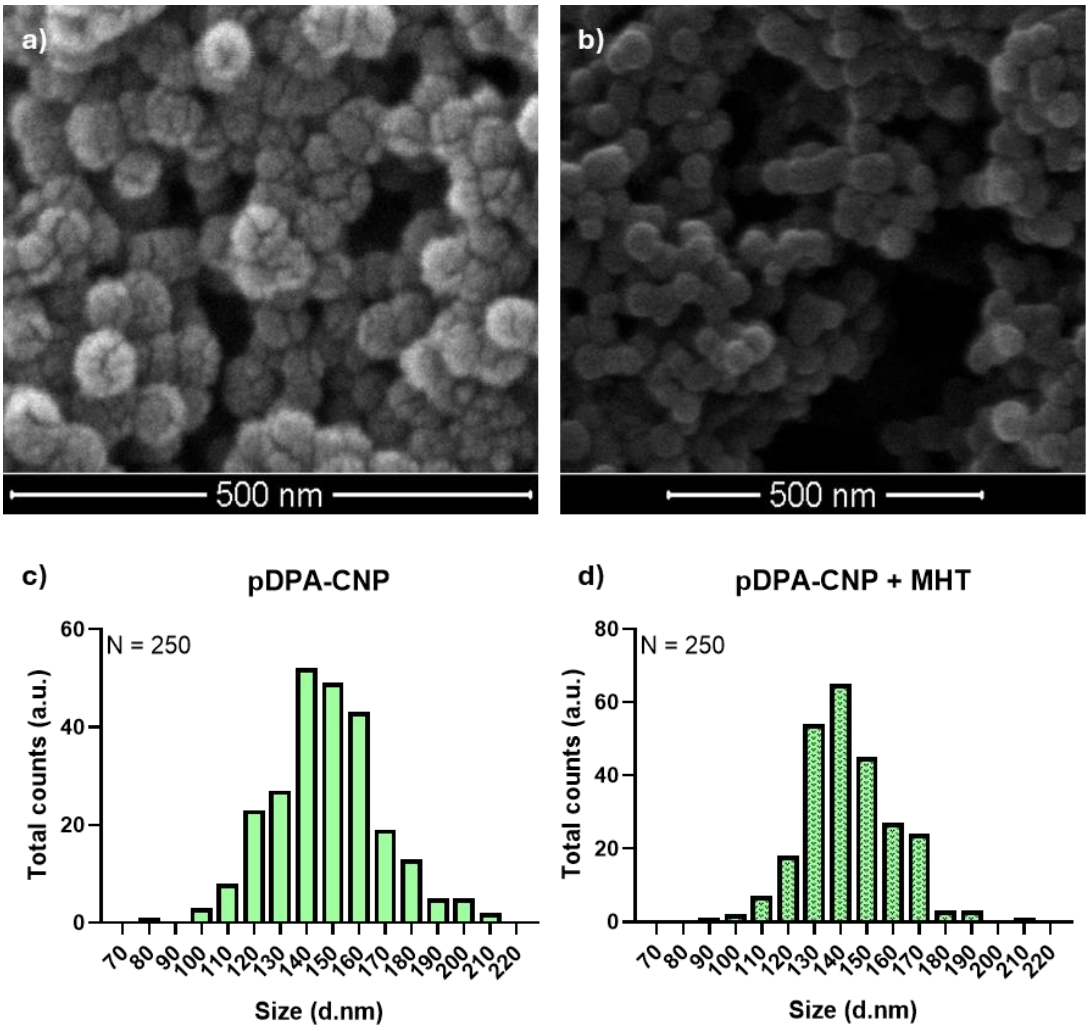


Figure **4.58.** Representative SEM images of **pDPA-CNP** under a 5 nm Pt thin film coating for imaging after **a)** no MHT treatment and **b)** 60 minutes subjection to an AMF (366 kHz, 16 mT) in a magnetherm (MAGFORCE Ltd.) calorimetric hyperthermia device equipped with an 18-turn coil. And SEM histogram of **pDPA-CNP** after **c)** no MHT treatment and **d)** 60 minutes subjection to an AMF (366 kHz, 16 mT) in a magnetherm (MAGFORCE Ltd.) calorimetric hyperthermia device equipped with an 18-turn coil.

4.3.4.1.5. Phantom Contrast Agent

Finally, the platform **pDPA-CNP** was also tested as possible CA. However, no impact over T_{1w} or T_{2w} was observed. A summary of r_1 and r_2 values can be found in Table **4.4**.

Table **4.4.** *In vitro* simulated settings for r_1 and r_2 parameters for **pDPA-CNP**.

	Medium	***r_1 ($mM^{-1}\cdot s^{-1}$)***	***r_2 ($mM^{-1}\cdot s^{-1}$)***	***r_2/r_1***
pDPA-CNP	Agarose 1%	0.11 ± 0.04	-0.63 ± 0.23	-5.65 ± 2.82

With the previous results from the magnetic characterisation, it was expected that **pDPA-CNP** presented very poor contrast capabilities. **pDPA-CNP** presents diamagnetic behaviour and has no capability on its own to be used as an MRI CA. Furthermore, Zr is usually only reported in the literature as a stabilising agent aimed to improve safety profile of already existing MRI CAs.[189,190]

4.3.4.2. *In vitro* Studies of pDPA-CNP

4.3.4.2.1. Cell Internalisation

Studies on the uptake of **pDPA-CNP** will allow us to partially understand the fate of our NPs and where they are accumulating. Thereafter, GL261 cell line was seeded in a six-well plate, allowed to grow and adhere for 24 hours and treated with a concentration of 0.1 mg·mL^{-1} of **pDPA-CNP** at different time intervals. The media was then removed and stored for analysis, while the cells were lysed in PBS with 1% SDS, collected and stored for analysis. **pDPA-CNP NPs** concentration was then determined via fluorescence spectroscopy (Figure **4.59**).

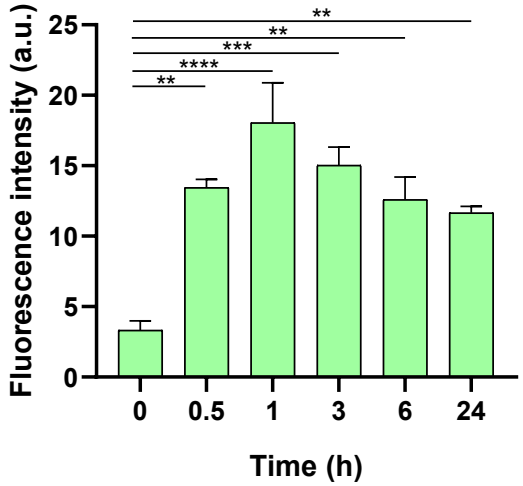


Figure **4.59**. **pDPA-CNP** internalisation (0.1 mg·mL^{-1}) in GL261 cell line after 0, 0.5, 1, 3, 6, 24 hours. Data represents the mean ± SE, n=3. Statistical differences were calculated using one-way ANOVA, followed by Turkey's multiple comparison test, where (*) denotes P < 0.05, (**) denotes P < 0.01, (***) denotes P < 0.001, and (****) denotes P < 0.0001.

The most evident and clear observation from **pDPA-CNP** internalisation studies is the increase of fluorescence intensity (attributed to an increase of intracellular concentration of **pDPA-CNP**) over a 1-hour time period, followed by a decrease over the next hours (attributed to a decrease in intracellular concentration of **pDPA-CNP**). The maximum intracellular concentration was determined to be of 4.0 ± 0.5 µg·mL^{-1}, accounting for 2.6% of the entire **pDPA-CNP** population administered, at 1-hour time mark. Different conclusions can be drawn from this behaviour: i) Possible metabolic pathways are degrading **pDPA-CNP** after internalisation, resulting in a decrease of **pDPA-CNP** intracellular concentration after 1 hour. ii) At first glance, uptake of **pDPA-CNP** could be minor.

The increase and then decrease of **pDPA-CNP** intracellular concentration means that a dynamic equilibrium between metabolism and exocytosis governs the intracellular concentration of **pDPA-CNP**. Moreover, internalisation of **pDPA-CNP** could be governed by the extracellular concentration of NPs. During the first few hours, the extracellular concentration of **pDPA-CNP** would be high enough to present a higher internalisation rate than degradation rate, leading to accumulation. However, at later time periods, extracellular concentration would be lower, and as such, internalisation rates would be slower, leading to a higher degradation/exocytosis rate, resulting in a decrease in intracellular concentration.

Therefore, when getting the results of internalisation, we can only give affirmation of how much **pDPA-CNP** is present at a given specific time, but cannot affirm how much has been totally uptaken until that specific time period. These results are a snap picture that cannot consider all past **pDPA-CNP** that has been uptaken and afterwards degraded/extruded before the sample was analysed.

Extracellular **pDPA-CNP** concentration was also followed using the same fluorescence spectroscopy but due to the requirement of UV light needed and the cell culture media interference, no conclusive data could be taken from it (Annexe **4.74**).

4.3.4.2.2. In vitro Cytotoxicity

Cytotoxicity of **DPA-COOH** and $ZrOCl_2$ were tested. In this context, GL261 cell line in exponential growth were seeded in a 96-well plate, allowed to adhere for 24 hours, and treated at ranging concentrations of **DPA-COOH** and $ZrOCl_2$ from 0 to 500 $\mu g \cdot mL^{-1}$. Plates were then incubated for 24 and 72 hours, treated with PrestoBlue®, and read using fluorescence spectroscopy at an emission wavelength of 572 nm and an excitation wavelength of 530 nm (Figure **4.60**). Since **DPA-COOH** required 1% DMSO in cell culture medium to reach total solubility, a control group under the same conditions was included in the measurements.

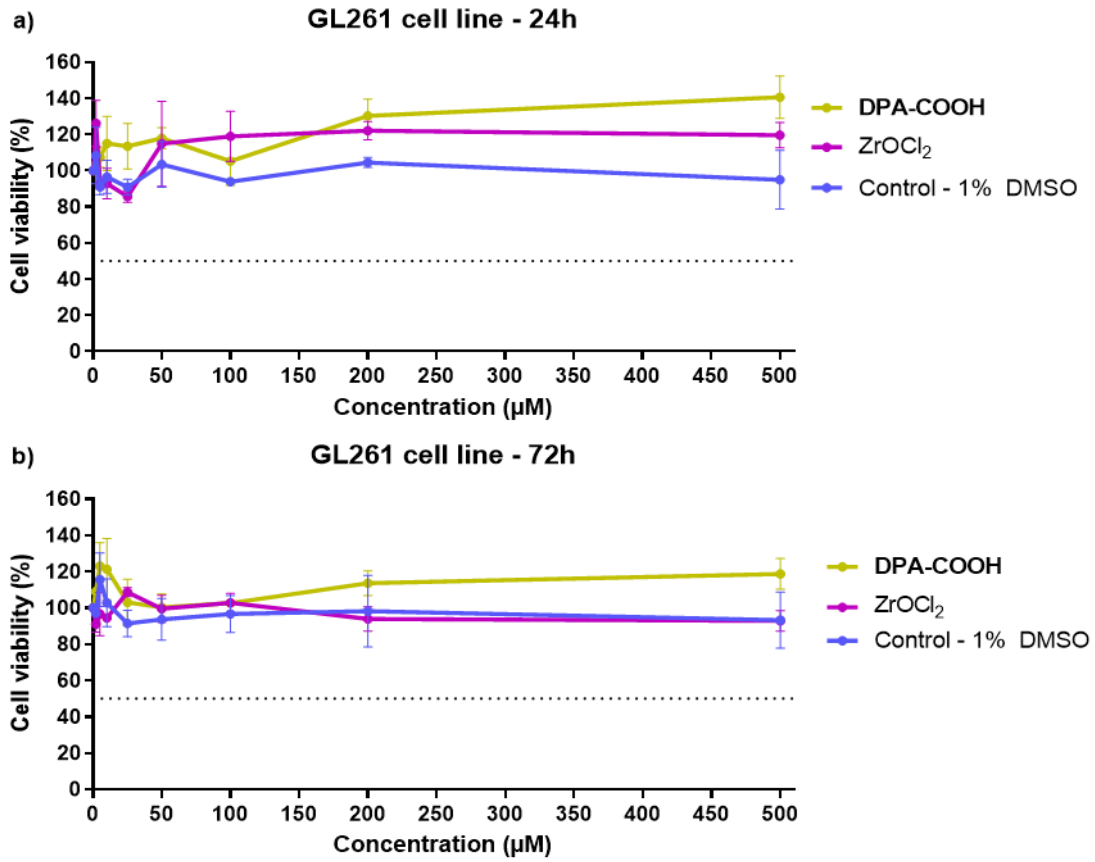


Figure **4.60**. Effects on cell viability of **DPA-COOH** (green) and $ZrOCl_2$ (purple) in GL261 cell line at concentrations of 0, 1, 5, 10, 25, 50, 100, 200, 500 µM after **a)** 24- and **b)** 72-hour time periods. Data represents the mean ± SE, n=3.

Results from the effects on cell viability of the monomeric components of **pDPA-CNP** are evident; Neither compound displays any cytotoxicity within the working ranges that were tested. Such results do not come as a surprise for the Zr metal complex, as it enjoys from plethora of scientific

evidence displaying the good biocompatibility of plenty of salts, complexes, metallic allotropic structures, oxide-based clusters, ceramics, and nanostructures based on such compound.[191-193] This well-reported behaviour in the literature was also precisely the reason why such a metal complex was chosen for the coordination polymerisation of our NPs.

A more surprising result was that of **DPA-COOH.** Anthracenes are well known as PSs in the field of PDT; however, they are usually associated with dark toxicities, meaning they present an inherent toxicity even when under no light irradiation.[194,195] One could expect such planar molecules to easily intercalate within DNA strands, leading to cell death. Nonetheless, it is true that modifications on the 9,10- positions have successfully led to decreased toxicity of such species. In the case of **DPA-COOH**, the phenyl groups, the flexible aliphatic chain, and the carboxyl groups at the end can perform steric hindrance that results in DNA intercalation not occurring. This, in turn, results in **DPA-COOH** reversing the original expectations and showing biocompatibility with the treated GL261 cell line.

The effect on cell viability of **pDPA-CNP** was also studied. To this aim, the same protocol as before, but now with **pDPA-CNP**, was performed to obtain the relationship between NPs concentration and cell viability (Figure **4.61**).

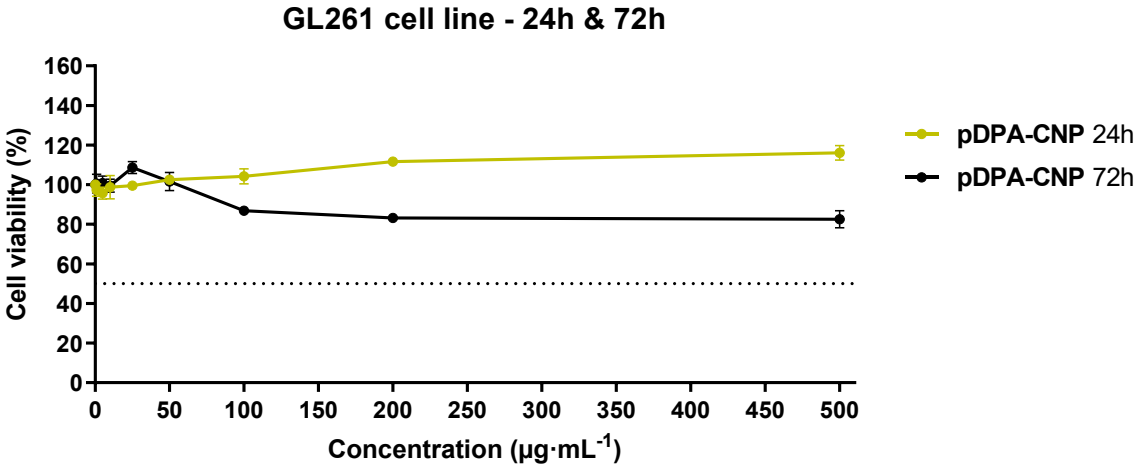


Figure **4.61.** Effects on cell viability of **pDPA-CNP** in GL261 cell line at concentrations of 0, 1, 5, 10, 25, 50, 100, 200, 500 µg·mL^{-1} after 24- (green) and 72- (black) hour time periods. Data represents the mean ± SE, n=3.

pDPA-CNP displayed no appreciable cytotoxicity within the concentration working ranges studied. This result also links to those of cytotoxicity from **pDPA-CNP@Fe NPs** and **Fe-Clustered NPs** (Figure **4.31**), which found that coating of the **Fe-Clustered NPs** with the CNP shell enhanced biocompatibility.

4.3.4.2.3. In vitro Cell Viability Assays Under Alternating Magnetic Fields

Tested **pDPA-CNP** were taken to a concentration according to Zr to 1 mg·mL^{-1} (as it corresponded to the shell mass of the **pDPA-CNP@Fe NPs** counterpart) in the presence of GL261 cell line suspended in cell culture medium. The suspended mixture of **pDPA-CNP** and GL261 cell line was then subjected to MHT in an AMF generator (magnetherm MAGFORCE Ltd.) equipped with an 18-turn coil (366 kHz, 16 mT) for two periods of 30 minutes, with a pause of 10 minutes in between.

Cells were then diluted and seeded on a 96-well plate at a 5,000-cell density, bringing the concentration according to Zr of **pDPA-CNPs** down to 0.1 mg Zr·mL^{-1} for **pDPA-CNPs**. The effect on cell viability was determined by a PrestoBlue® method, collecting data at both 24- and 72-hour intervals (Figure **4.62**).

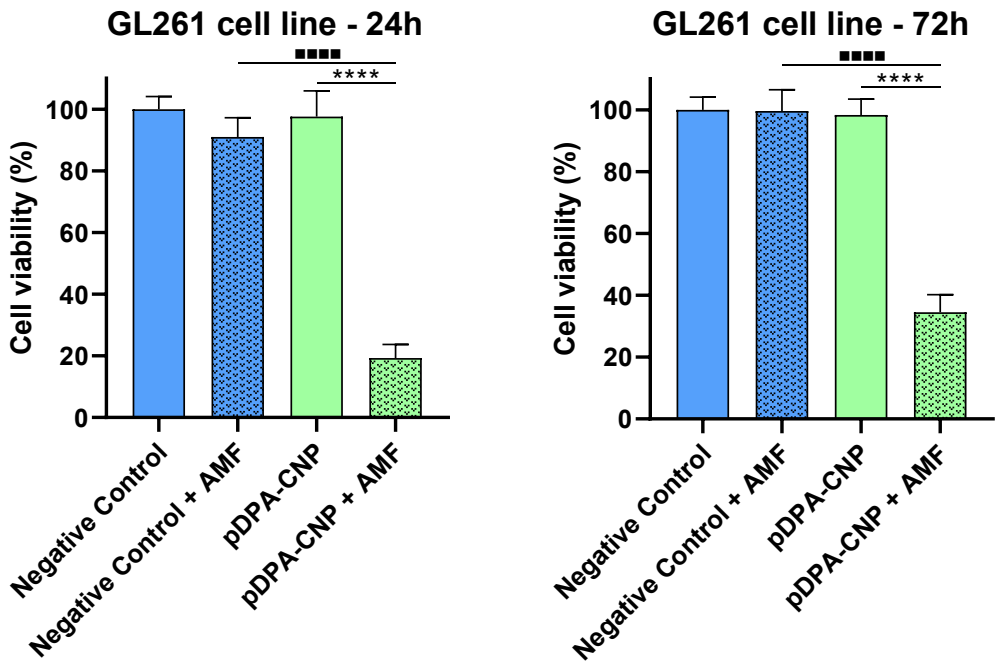


Figure **4.62**. Cell viability of **pDPA-CNP** (0.1 mg·mL^{-1}) in GL261 cell line under no-MHT and MHT treatment after 24 hours and 72 hours. Untreated cells were used as controls. Data represents the mean ± SE, n=3. Statistical differences were calculated using two-way ANOVA, followed by Sidak's multiple comparison test (*) and Dunnett's multiple comparison test (▪), where (* or ▪) denotes P < 0.05, (** or ▪▪) denotes P < 0.01, (*** or ▪▪▪) denotes P < 0.001, and (**** or ▪▪▪▪) denotes P < 0.0001.

Opposite to what we observed from **pDPA-CNP@Fe NPs**, **pDPA-CNP**'s results, and very surprisingly to us, here paint a different picture. **pDPA-CNP** clearly shows a triggered behaviour by AMF, with clear and dramatic GL261 cell line death observed for AMF-treated samples. **pDPA-CNP** AMF-treated samples showed a 19.3 ± 10.7% survival in 24-hour assays, and then 34.5 ± 17.3% in the 72-hour assays. A summary of cell viability data can be found in Table **4.5** and Table **4.6**.

Table **4.5**. Summary of 24-hour cell viability assay data.

		Negative Control	**pDPA-CNP**
Cell viability	Non-AMF treated	100 ± 17.4	97.6 ± 17.9
	AMF treated	91 ± 17.4	19.3 ± 10.7

Table **4.6**. Summary of 72-hour cell viability assay data.

		Negative Control	**pDPA-CNP**
Cell viability	Non-AMF treated	100 ± 17.4	98.3 ± 14.4
	AMF treated	99.6 ± 11.9	34.5 ± 17.3

The underlying results from cell viability for **pDPA-CNP** treated samples are that; i) We have a statistically strong and significant difference between **pDPA-CNP** samples treated with AMF and **pDPA-CNP** samples that have not. ii) That **pDPA-CNP** samples that have been treated with AMF also present statistically significant differences with negative control and negative control AMF treated. iii) No statistically significant differences between negative control and samples with non-MHT treated **pDPA-CNP** were observed.

Thereafter, any effect that may be causing cell death is not a result of **pDPA-CNP** own toxicity, as this has previously been assessed in cytotoxicity assays. Neither has the AMF taken a role in cell death, as the negative control disproves such approach. However, we can observe that toxicity is induced via AMFs, and that such toxicity must be a result of interaction between AMF and **pDPA-CNP.** Nonetheless, MHT can be discarded, as **pDPA-CNP** displays clear diamagnetic behaviour.

In summary, **pDPA-CNP** presents very positive and significantly high cell death on AMF-treated samples. Cell death seems to be triggered by AMFs and, surprisingly, presents much higher cell death than that of the original platform **pDPA-CNP@Fe NPs** (Figure **4.49**). These results raise some more questions that need be answered, and will shape the *in vitro* assays that will be performed; *why does **pDPA-CNP**, an amorphous coordination polymer, interact with the magnetic field? And why does the interaction with the AMF from **pDPA-CNP** lead to cell death? And why is the effect of MHT-triggered **pDPA-CNP** cell death so strong?*

4.3.4.2.4. *In vitro* Cellular Transmission Electron Microscopy Imaging

Further proof of the exacerbated cellular death was observed in cellular TEM imaging. TEM imaging of **pDPA-CNP** and **pDPA-CNP@Fe NPs** on GL261 fixated cells was performed. For this, just as in the cell viability protocol, GL261 cell line in exponential growth was suspended in cell culture medium, lifted, and **pDPA-CNP** or **pDPA-CNP@Fe NPs** were added to a concentration of 1 mg Zr·mL^{-1} and 0.5 mg Fe·mL^{-1}, respectively. The resulting suspensions were magnetically treated in an AMF generator (magnetherm MAGFORCE Ltd.), equipped with an 18-turn coil (366 kHz, 16 mT) for two periods of 30 minutes, with a pause of 10 minutes in between.

Afterwards, cell samples were centrifuged, and the medium removed. Immediately, cell fixation and dehydration were carried until samples were prepared for epoxy resin embedding. Ultrathin sections (70 nm) were cut using a Leica Ultramicrotome EM UC6 or Boeckeler PowerTomePC Ultramicrotome (Wetzlar, Germany) and stained. The sections obtained were imaged using a Jeol JEM-1400 (120 kV) TEM. Cellular TEM imaging unravelled interesting data as detailed next. Firstly, however, we must explain the different samples that were chosen for analysis.

For cellular TEM imaging, samples ranged from; i) Two control groups consisting of GL261 cell line magnetically treated and non-AMF treated, that will be used to compare cellular stress and physiology of treated groups and conditions, ii) Two **pDPA-CNPs** samples with GL261 cell line groups, one AMF treated and one non-AMF treated, and iii) Two **pDPA-CNP@Fe NPs** with GL261 cell line groups, one MHT treated and one non-MHT treated, that will be used to compare and corroborate the cold hyperthermia hypothesis formulated earlier for this platform.

Cells from both control groups, magnetically treated and non-magnetically treated, showed well-defined cellular morphologies, cellular interconnection between individuals, and even the

cellular organelle. We do not observe spherically shaped cells or stressed cells (Figure **4.63**). Such results pointed out to no cell damage.

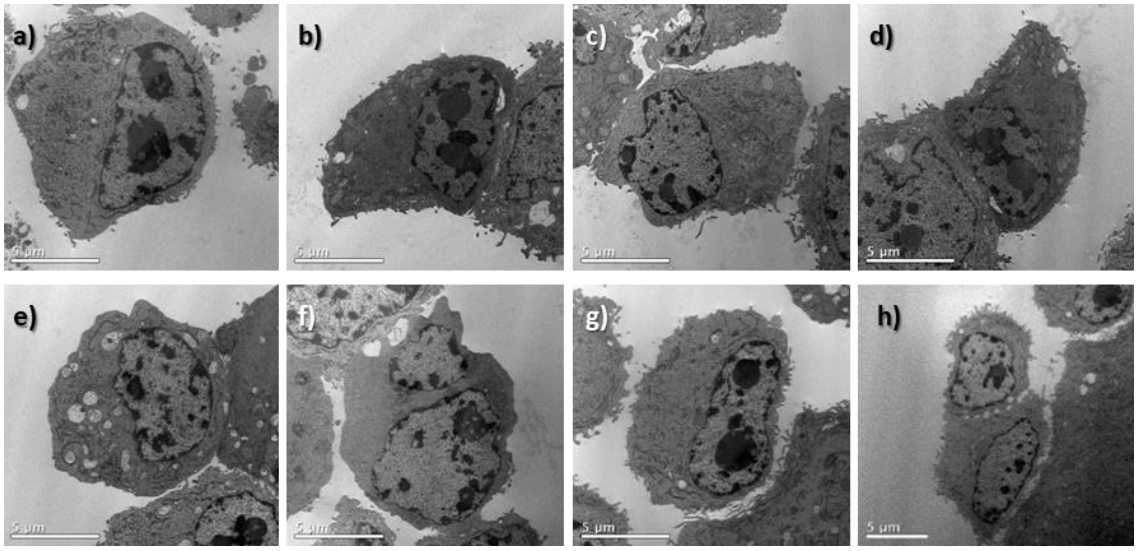


Figure **4.63**. TEM images showing GL261 cells at 4000x increments of **a-d)** non-MHT treated, and **e-h)** MHT treated control cell. Both displaying normal morphology.

Images of non-AMF-treated samples with **pDPA-CNP** already display a clear cellular membrane selectivity of the NPs, with clear accumulation patterns around those. **pDPA-CNP** is not observed randomly dispersed along the entire sample, but only around either cellular membrane or cellular material, displaying clear affinity towards cells. Cellular morphology follows quite closely that of the observed in the control groups, which is to be expected as **pDPA-CNP** without AMF does not induce cellular death (Figure **4.64**).

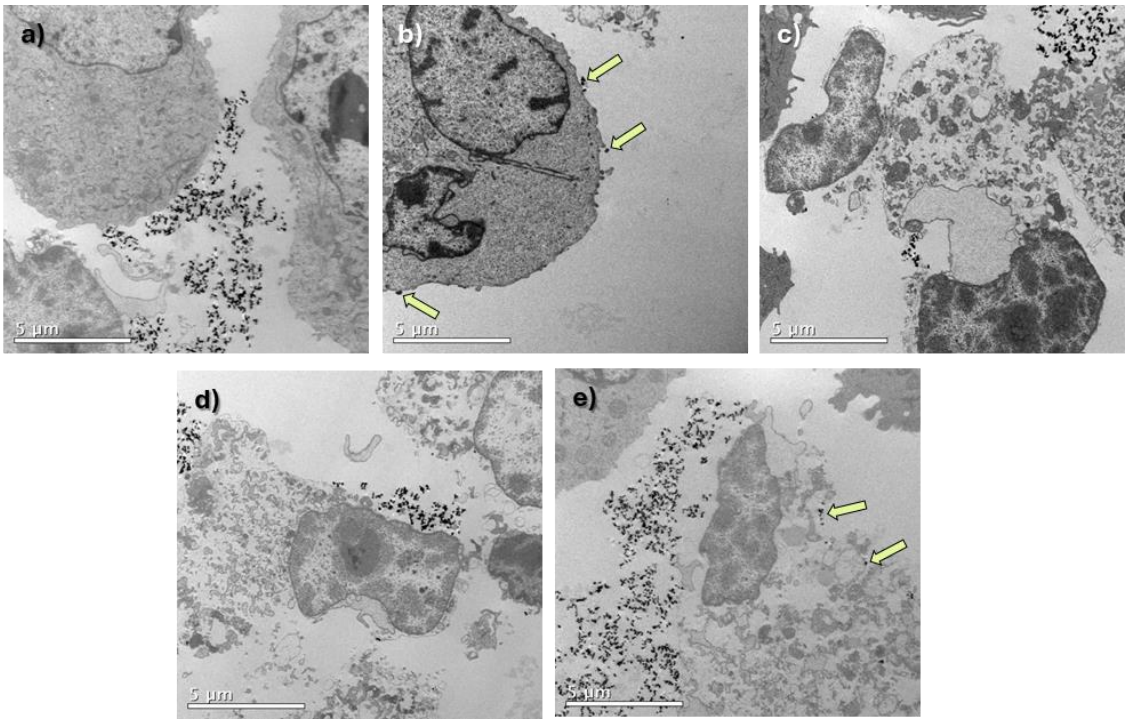


Figure **4.64**. TEM images showing GL261 cells interacting with **pDPA-CNP** at 4000x increments. Light green arrows indicate single **pDPA-CNP**.

Especially relevant is the case of poorly contrasted cell membranes like Figure **4.64.e**, the accumulation pattern of **pDPA-CNP** follows along the cell membrane, making it possible to trace an outline. Moreover, little internalisation was observed overall, which is supported by the internalisation observed during *in vitro* studies. At higher augmentation, NP interaction with the cell membrane or biologic material can be observed very clearly, as shown in the cell membrane interaction behaviour (Figure **4.65**).

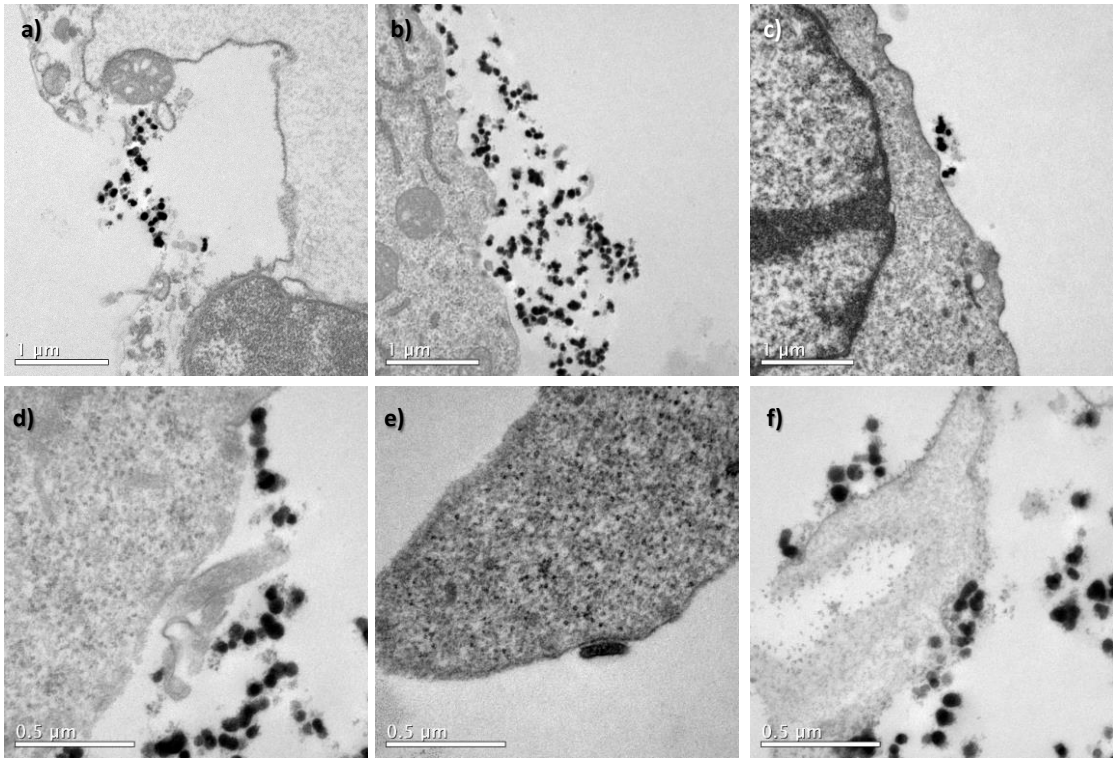


Figure **4.65**. TEM images showing GL261 cells with **pDPA-CNP** at: **a-c)** 20000x increments and **d-f)** 50000x increments.

Magnetically treated **pDPA-CNPs** also follow the same accumulation pattern on the cell membrane (Figure **4.66**).

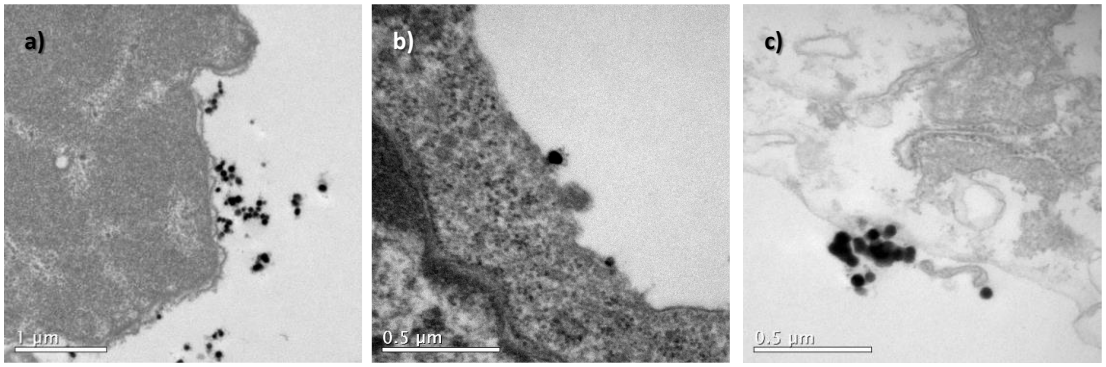


Figure **4.66**. TEM images showing GL261 cells with **pDPA-CNP** MHT treated at: **a)** 20000x increments and **b-c)** 50000x increments.

Though from here on, we can start to observe the pathway that led to the increased cell death in **pDPA-CNP** MHT-treated samples. As **pDPA-CNP** accumulate and AMF is triggered, the proximity to the cell membrane induces the formation of cell membrane damage in the form of cavitation (Figure **4.67**).

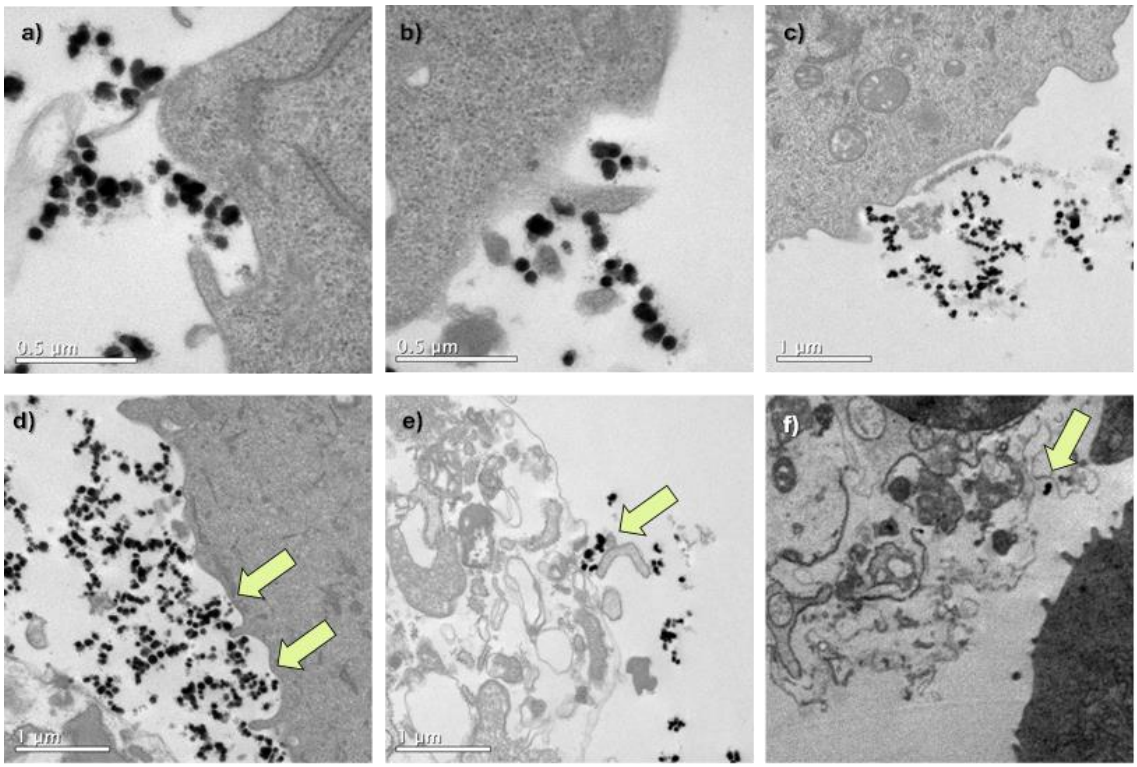


Figure **4.67**. TEM images showing GL261 cells with **pDPA-CNP** MHT treated at: **a-b)** 50000x increments and **c-f)** 20000x increments. Light green arrows indicate cavitation formation in the cell membrane.

While **pDPA-CNPs** interact with the magnetic field, cell membrane damage keeps occurring. This process leads to an eventual breaking and extravasation of cell cytosolic media, which in turn attracts and interacts with **pDPA-CNPs** in the media (Figure **4.68**).

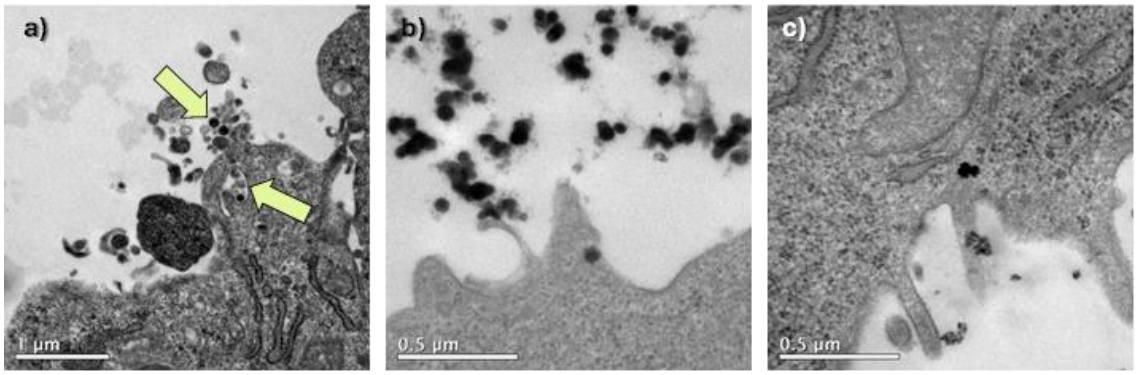


Figure **4.68**. TEM images showing GL261 cells with **pDPA-CNP** MHT treated at: **a-b)** 20000x increments and **c-f)** 50000x increments. Light green arrows indicate **pDPA-CNPs**.

Interestingly, only in the case of cells that are suffering from this cell membrane breaking, **pDPA-CNPs** can be observed internalised (Figure **4.69**). Such findings suggest that the high affinity, combined with the membrane cleavage, introduces a venue for **pDPA-CNP** internalisation, although still small in comparison to the main bulk of the sample.

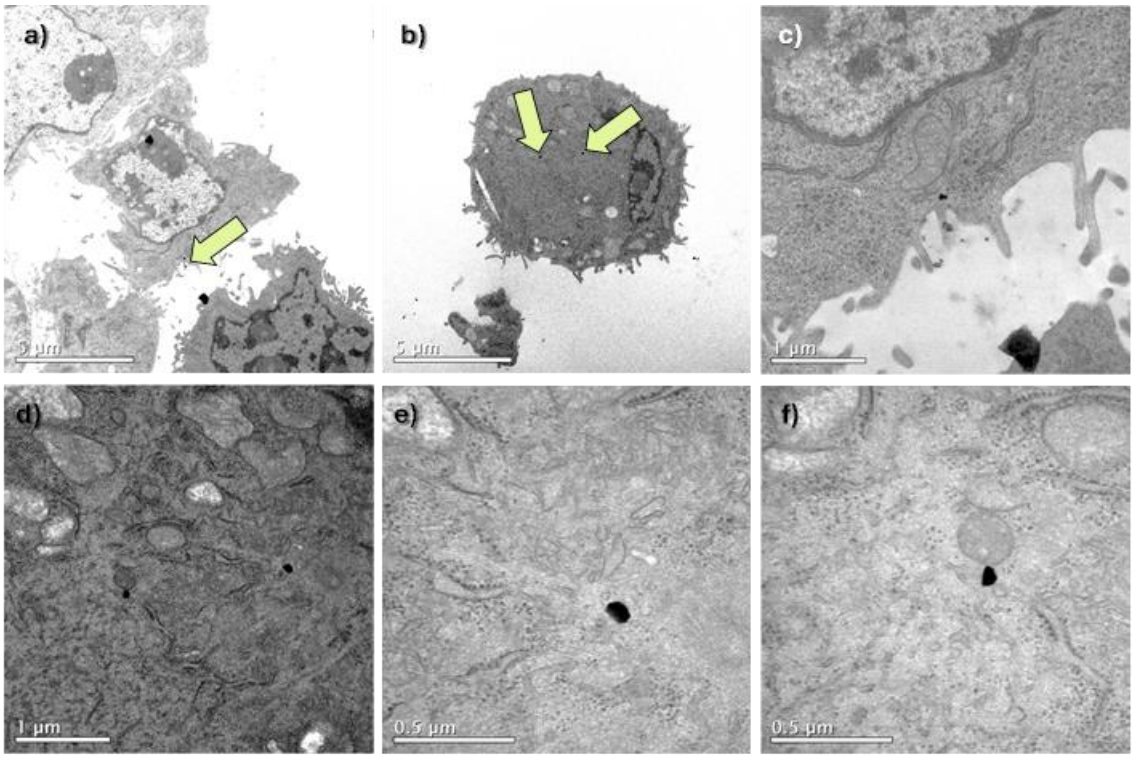


Figure **4.69**. TEM images showing GL261 cells with **pDPA-CNP** MHT treated at: **a-b)** 5000x increments, **c)** increased picture of a) at 20000x increments **d)** increased picture of b) at 20000x, and **e-f)** 50000x increments. Light green arrows indicate **pDPA-CNPs**.

Nonetheless, such observations are rare, as in most of the cases the **pDPA-CNP** accumulation is much bigger than just a couple of NPs. Accordingly, the damage produced to the cells is proportionally bigger, leading to total cell collapse before any internalisation occurs (Figure **4.70**).

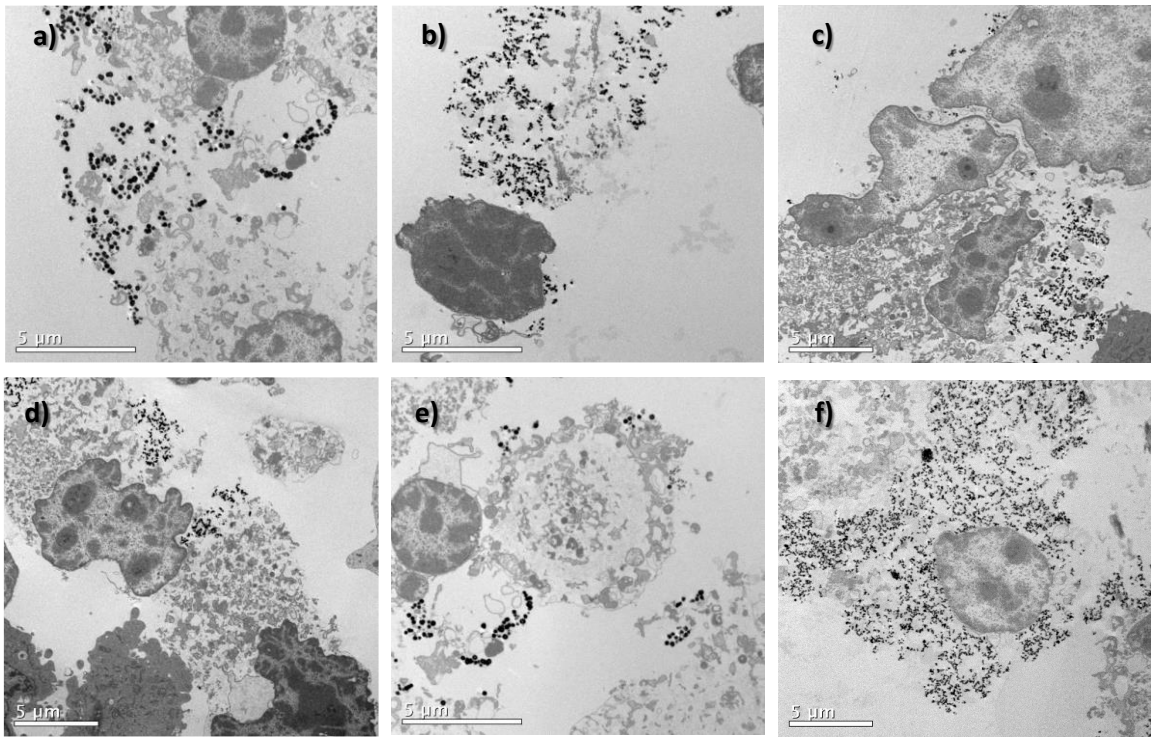


Figure **4.70**. TEM images showing GL261 cells with **pDPA-CNP** MHT treated at **5000**x increments.

The impact of **pDPA-CNP** is evident when inspecting the whole group of cells. High membrane affinity, followed by membrane damaging leading to extravasation of the cytosolic media is hypothesised to be the main mechanism of cell death. Interestingly, cell death and membrane rupturing leads to complete elimination of the cell, except for the cell nucleus, which can be readily observed in all cell death images. Another interesting pattern is the accumulation of NPs on what we could suspect to be the extravasated cytosol, in some cases allowing to imagine the original cell shape or membrane structure.

Even surviving cells of the **pDPA-CNP** AMF treated group seem to be slightly modified. Cells in this group present as rounder, with less interconnections between cells, or morphologically stressed (Figure **4.71**).

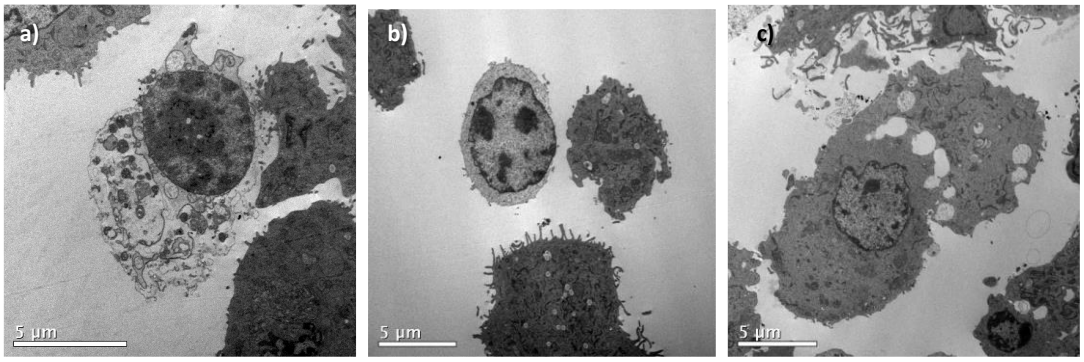


Figure **4.71**. TEM images showing GL261 cells with **pDPA-CNP** MHT treated at **5000**x increments.

The **pDPA-CNP@Fe NPs** also follow the same general pattern than **pDPA-CNP,** but with less cell death observed. Overall, non-MHT-treated **pDPA-CNP@Fe NPs** display no significant cell stress; however, they show the same accumulation patterns as **pDPA-CNP** (Figure **4.72**).

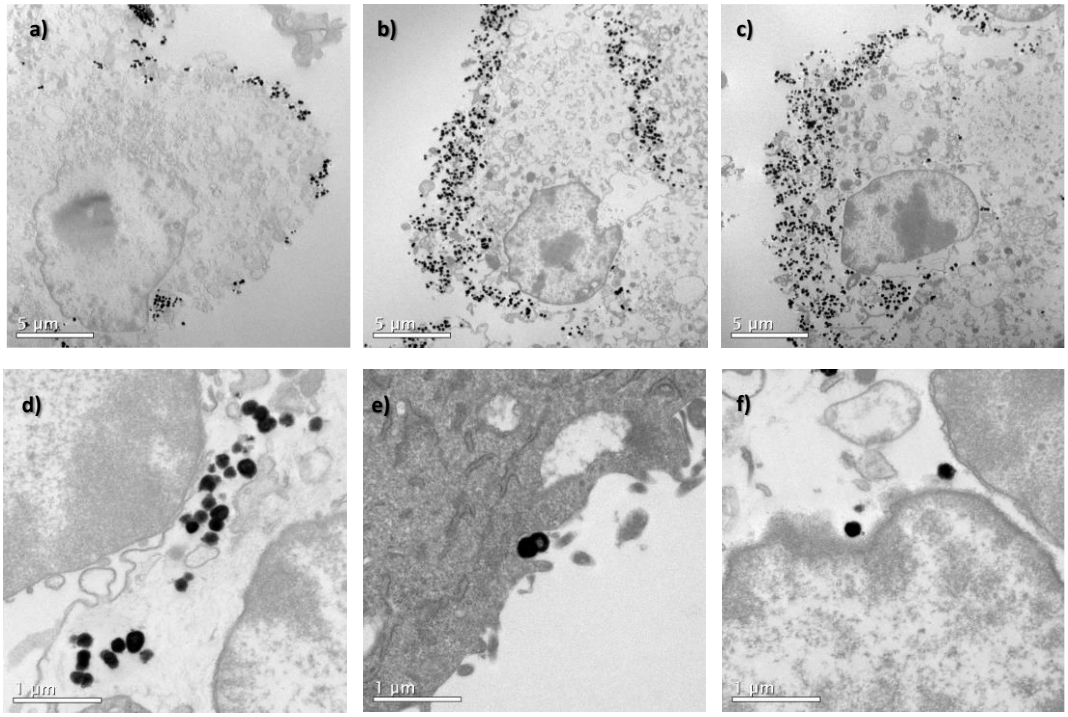


Figure **4.72**. TEM images showing GL261 cells with **pDPA-CNP@Fe NPs** at: **a-c)** 5000x increments and **d-f)** 20000x increments.

In the presence of MHT treatment, **pDPA-CNP@Fe NPs** also show cellular death, although to a lesser extent than **pDPA-CNP** (Figure **4.73**).

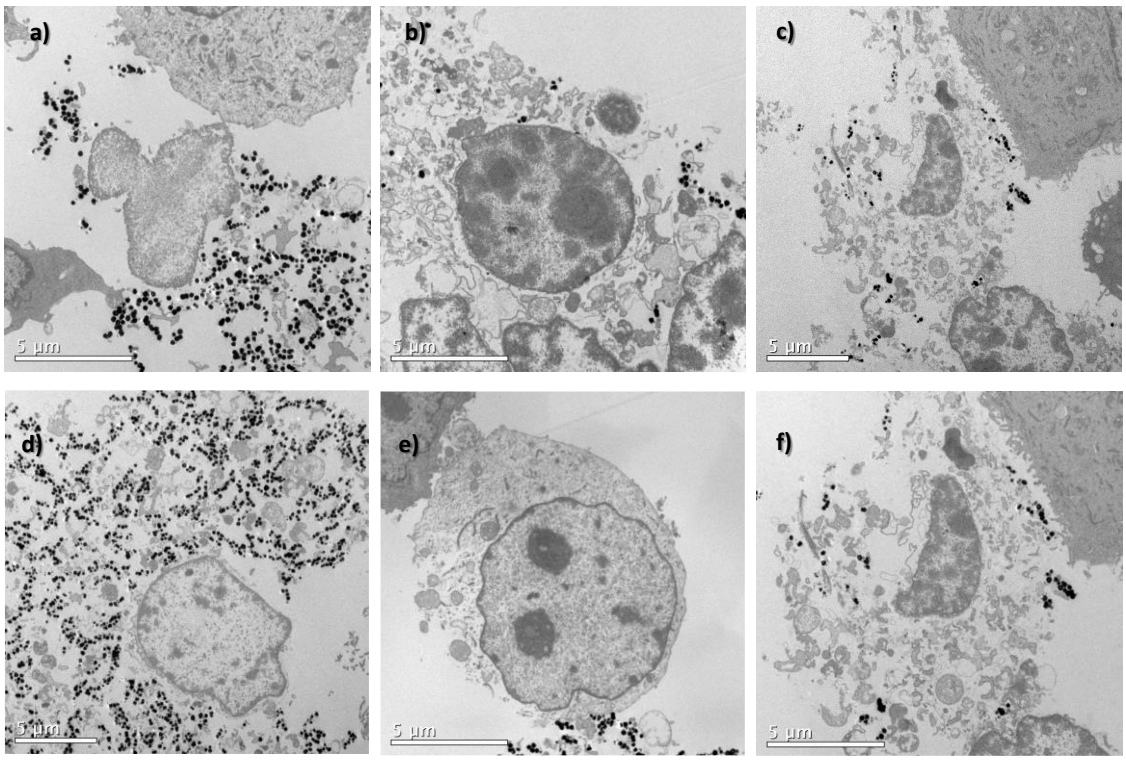


Figure **4.73**. TEM images showing GL261 cells with **pDPA-CNP@Fe NPs** MHT treated at: 5000x increments.

Cellular TEM imaging of **pDPA-CNP@Fe NPs** and **pDPA-CNP** allows us to explain the behaviour of both systems.

On one hand, when previously discussing **pDPA-CNP@Fe NPs** cell viability results, we built a hypothesis around cold hyperthermia. A case of cold hyperthermia builds strongly on local gradients of heat as a leading source of cell death; thereafter, close proximity to cells is required for such a hypothesis to be possible. Findings from TEM imaging on **pDPA-CNP@Fe NPs** show that such required patterns of accumulation on the cell membrane for cold hyperthermia occur. **pDPA-CNP@Fe NPs** accumulates on cell membranes and, under MHT treatment, damages the cell membrane until leaking causes cytosolic extravasation, leading to cell death.

On the other hand, for **pDPA-CNP**, we also observe an AMF-dependant behaviour, as well as important cell membrane interaction and adhesion, just as **pDPA-CNP@Fe**. We also have insight that any mechanisms cannot be realistically pointed to an MHT behaviour as **pDPA-CNP** is diamagnetic, nor to inherent NP toxicity. Therefore, any potential cell death mechanism seems to be related to local interactions, which, although small in impact, the close proximity to cells might produce a strong enough effect to cause cell membrane damage (Figure **4.74**).

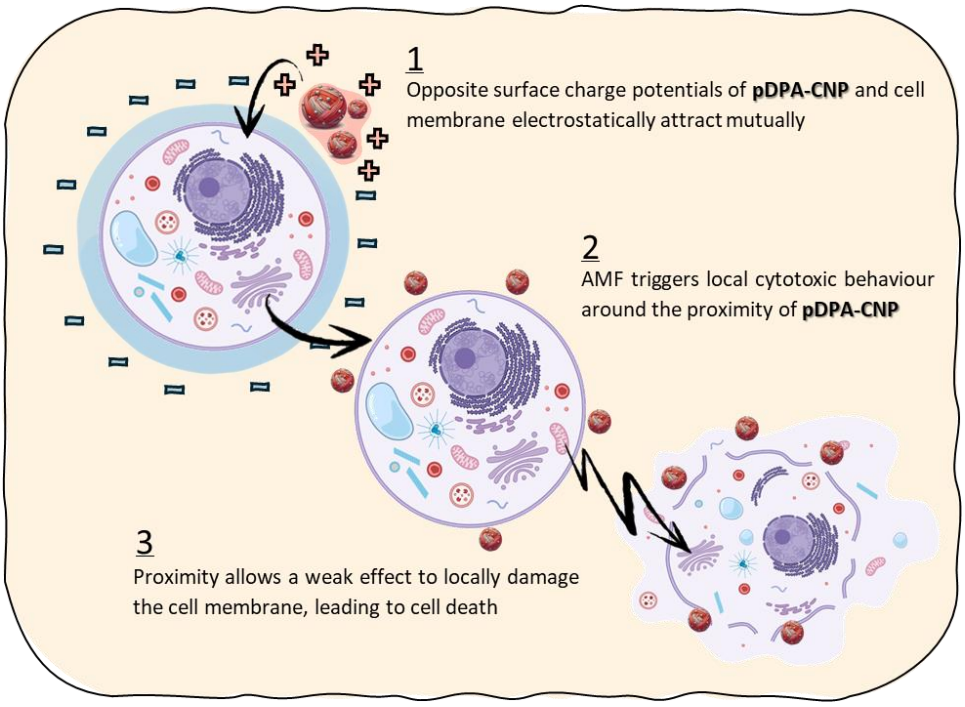


Figure **4.74**. Infographic describing possible cold hyperthermia cellular death mechanism of **pDPA-CNP**.

The use of highly opposite surface charges to achieve maximal interaction with the negatively charged cell membrane is something already reported in the literature. For example, we have already described in the introduction the case of magnetite-coated cationic liposomes that exploit electrostatic interactions with negatively charged phospholipids in the cell membrane to achieve better MHT results than otherwise. [196-198]

With the compiled evidence of **pDPA-CNP** MHT turn-on effect, and the unexpectedly good cell viability results, the focus shifted from a control platform to a valid approach to cancer treatment. However, before postulating this platform for such a purpose, we need to further understand the behaviour behind the cell death mechanism.

4.3.4.3. Origin of the Interaction with AMFs

A diamagnetic Zr-based coordination polymer consisting of isolated Zr coordination nodes that link with organic bridging ligands should, in principle, not show interaction with a magnetic field. Moreover, Zr^{4+} presents no unpaired d-orbital electrons, which leads to Zr presenting only diamagnetism as observed in our measurements. Therefore, to better formulate a hypothesis on why our **pDPA-CNPs** are interacting with the AMF, more information on our system was required.

The first approach taken was the elemental analysis (EA) of our **pDPA-CNPs** to elucidate the molecular composition of our system. Results from EA showed the presence of % C at 31.13 ± 0.26, % N 1.53 ± 0.12, % O 14 ± 0.35, % H 3.42 ± 0.09 (Annexe **4.61**). Such mass is expected to come entirely from the organic components of the **pDPA-CNPs** and adds to a total of 50.08 ± 0.25%. Interestingly, if we also add the Zr mass, based on the ICP reported earlier (% Zr at 3.18 ± 1.45%), we can only barely account for a total mass of the entire system of 54%. Such result presents an interesting aspect, as it shows that nearly 46% of the total mass of the system is unaccounted for in the form of metals/metal oxides, and other halogen-based compounds, that elude EA analysis and still contribute to the total mass of the system.

TGA is a tool that not only provides information on the different melting points, degradation, and reactions that our sample may experience under augmenting temperature changes, it also provides an idea on the composition of a sample. When **pDPA-CNP** is subjected to temperatures rising to 800 °C, total remaining mass in the sample accounts for 52% (Annexe **4.70**). At such high temperatures, organic mass in the sample will have combusted, and only inorganic compounds would remain. These results match with the EA results of total inorganic mass and made us reevaluate some of the data we obtained before, and formulated a hypothesis based on the chemistry of Zr.

ICP measurements of Zr requires complete and total digestion of the sample for quantitative analysis. As such, most analytical laboratories follow a standard procedure, with minor modifications between different laboratories, for microwave-assisted digestion for transition metals. However, Zr, and especially Zr oxides, stabilise and become hard to digest when compared to regular oxides.[199]

Our hypothesis:

With this information, we formulated the hypothesis that zirconium dioxide or zirconia (ZrO2) could be forming inside our polymeric NP, decreasing the total organic weight obtained in EA, and increasing the inorganic weight obtained in TGA. The data obtained from ICP until now would account for the theoretical value from the coordination polymer, which matches nicely with the expected, if the total mass of the NP were composed only of a coordination polymer. While the inorganic ZrO_2 had not been digested and eventually removed via filtration before injection into the detector during ICP-MS analysis.

The presence of ZrO_2 entrapped into our **pDPA-CNP** plays an important role in understanding why our NP is capable of interacting with AMFs during the cell viability assays. In many oxide materials, the introduction of defects like oxygen vacancies can significantly alter the magnetic properties of such materials.[200-202] This is also true for ultra-small NPs, where properties can change dramatically due to quantum confinement and high surface-to-volume ratios.[203,204] Typically, ZrO_2 is a non-reducible oxide, meaning the generation of oxygen vacancies is very thermodynamically unfavourable.[205] The capability to reduce such materials is one of the properties that can be modified, going from bulk to nanostructured ZrO_2. ZrO_2 NPs have been experimentally, as well as computationally, studied to form NPs with sizes that can range from 1.5 to 5 nm in size, as well as 50 nm in size.[206-208] Moreover, Zr atoms forming part of such latices can still present coordinating capability, allowing them to be flexible and easily incorporated into polymers/surface via coordination.[209,210]

Then the question to answer is: *why is this hybrid material formed?* ZrO_2 NPs are usually synthesised by mixing a Zr^{4+} metal salts in a high temperature reaction vessel and left stirring for periods of time that range from a few hours to over-night conditions.[211,212] Such conditions are also the ones we subject our zirconium salt $ZrOCl_2$ in the **pDPA-CNP** synthesis. This could mean that, through a one pot reaction, and since the reaction media contains an excess of Zr metal ions, formation of both spices are happening simultaneously, coordinating and integrating inside of the coordination polymer structure.

As we mentioned, macroscopic ZrO_2 materials have a hard time reducing themselves and generating oxygen vacancies. However, non-stoichiometric synthesis in rations of Zr:O different to 1:2 required for perfect crystalline NP structure lead to intrinsic oxygen deficiencies.

Having formulated a theory based on the presence of ZrO_2 NPs inside our **pDPA-CNP**, we first need to prove that, indeed, we have a higher-than-expected Zr inside the NP. For this purpose, after ensuring proper digestion protocol for our **pDPA-CNPs** the results obtained from ICP-MS for % Zr were found to be 15.8 ± 0.8% (Annexe **4.60**).

We may have showed that we have the presence of extra Zr into our **pDPA-CNP**, but still require demonstrating that such Zr is in the form of ZrO_2. A good indicative tool for such study can be powder XRD, as we would expect to observe a pattern that resembles that of ZrO_2 (Figure **4.75**).

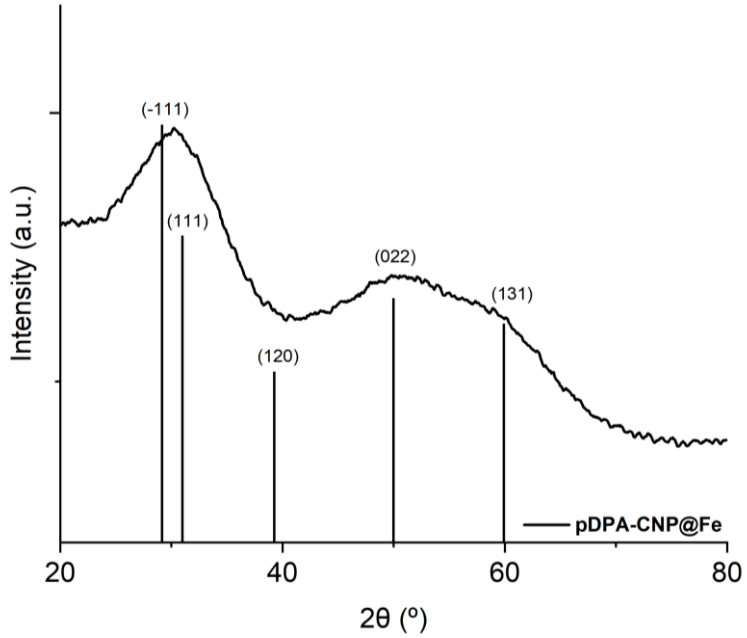


Figure **4.75**. Room temperature XRD measurement for **pDPA-CNP**. Overlayed the theoretical 2θ XRD ZrO_2 nanostructures spectra at the same relative strength as reported in the literature.[213]

Due to the amorphous nature of our coordination polymer, we would never expect to get very well-defined Bragg peaks like that of crystalline ZrO_2. The amorphous composition of our coordination polymer diffracts radiation in non-uniform patterns that average among all the possible diffraction-available angles. However, we can use such techniques as an indicative tool that qualitatively shows an envelope that overlaps with the signals that would be expected from a sample containing ZrO_2.

4.3.4.3.1. Electron Microscopy Imaging

We thus far have good indicators to the presence of ZrO_2 NPs, but the best tool to prove that we do indeed have the incorporation of such NPs is electron microscopy.

Until now we have obtained SEM data via imaging of samples recovered by a thin layer of Pt for imaging purposes. To obtain proper surface morphology information, acquisition of electron-backscatter of unmetallized samples can be used (Figure **4.76**).

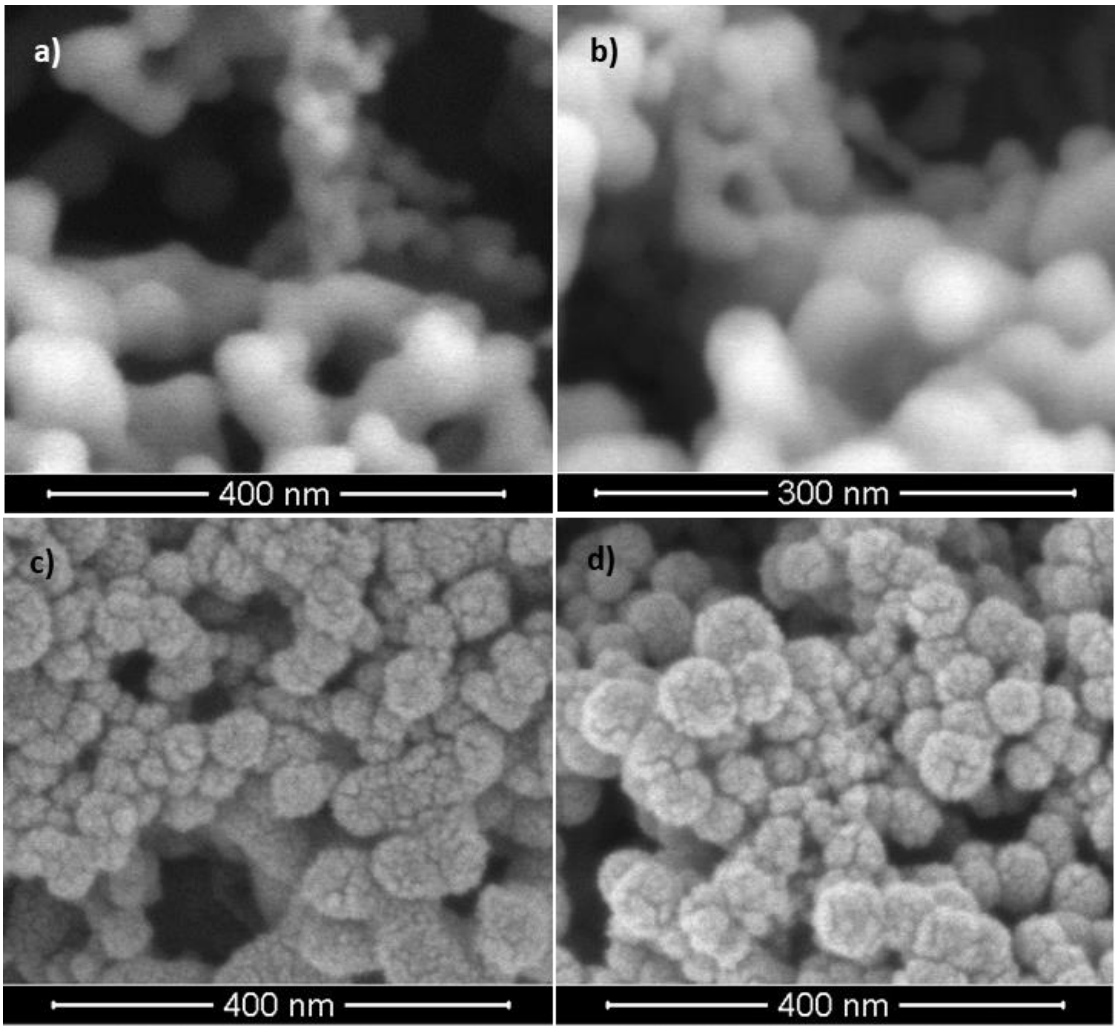


Figure **4.76**. Representative SEM images of **pDPA-CNPs** of **a-b)** electron backscatter of unmetallized samples and **c-d)** regular SEM imaging of **pDPA-CNPs** under a 5 nm Pt thin film coating for imaging.

Electron backscatter of unmetallized **pDPA-CNPs** displays clear smooth surface morphology, contrary to what we could expect at the beginning from Pt-metalised samples, which display granular and irregular surfaces. Such morphological information is crucial, as the expected sizes of the ZrO_2 NPs range around the 5 nm mark, and could easily be mistaken for cavitation, rugosity or granulation on the **pDPA-CNPs** surface during STEM imaging.

Knowing that the morphology of our pDPA-CNPs is a smooth and spherical NP, we can more confidently use data obtained from STEM and TEM imaging, as they provide information on the **pDPA-CNP** structure (Figure **4.77**).

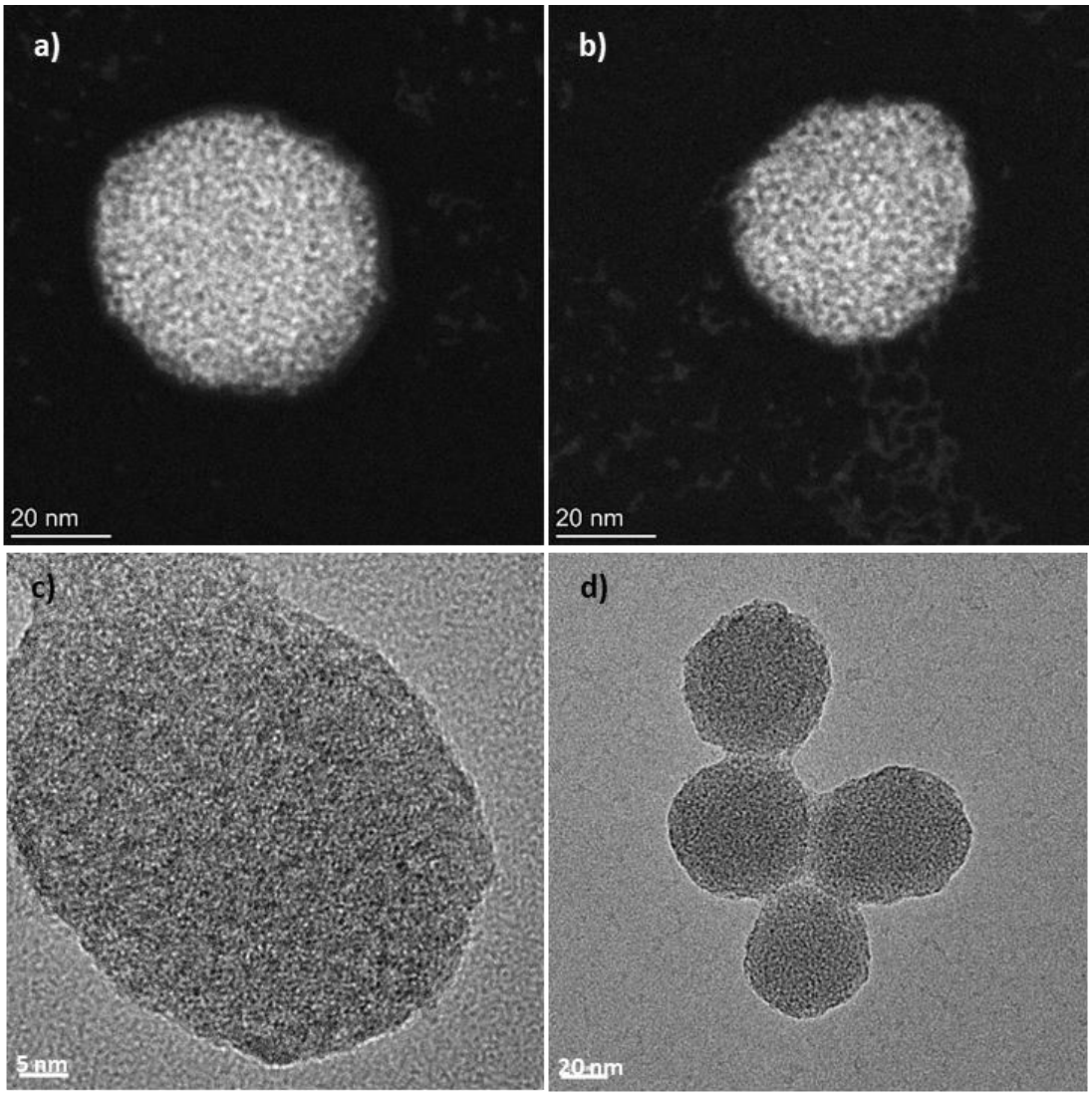


Figure **4.77**. **a-b)** Representative high-resolution STEM images of **pDPA-CNP** at HAADF detector mode. **c-d)** Representative TEM images of **pDPA-CNP** at HAADF detector mode.

Amorphous polymers and metallic or crystalline NPs will display differently in STEM and TEM imaging, as the electron density transmitting through them will vary. As such, we expect two different possible outcomes when inspecting TEM and STEM imaging. Either no ZrO_2 NPs are present, in which case a completely smooth and homogeneous NP image should be obtained. Or ZrO_2 NPs are present, in which case we expect to see a granular NP with brighter spots scattered into the NP as higher electron density travels through the ZrO_2 NPs than the organic and amorphous coordination polymer. As can be clearly observed in our detector modes, we have a very granular NP, which we know is not due to surface morphology interference. Such granularity can be attributed to different electron density paths that give rise to different contrast within the NP. Moreover, grain size within the NP matches with the tentative ZrO_2 NPs size.

Cross section EDX of **pDPA-CNP** was also performed and displayed higher Zr counts on brighter spots, corresponding to STEM imaging taken (Annexe **4.67**). However, the most definitive proof of ZrO_2 NPs presence within our sample came from performing electron energy loss spectroscopy (EELS) mapping of **pDPA-CNP** at the ALBA synchrotron facilities (Figure **4.78**).

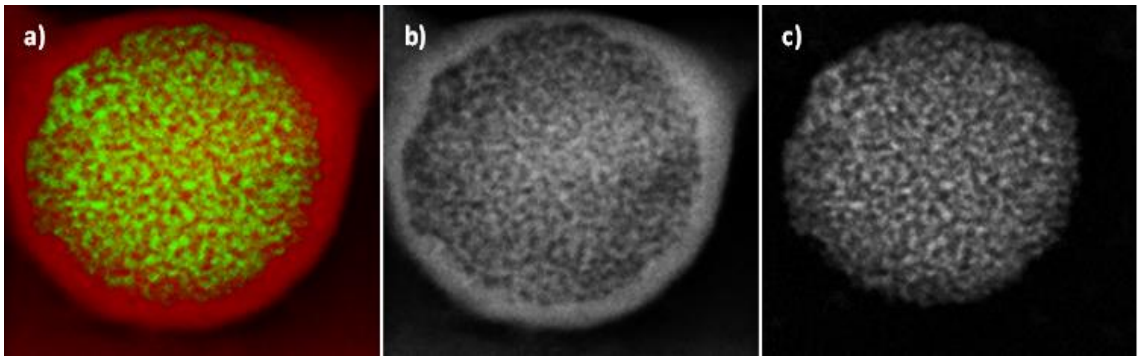


Figure **4.78**. Representative STEM imaging of **pDPA-CNP** elemental mapping via EELS 2-dimensional mapping of; **a)** overlay of carbon (red) and zirconium (green), **b)** carbon, and **c)** zirconium.

EELS mapping of Zr and carbon shows a clear accumulation of bright Zr spots that correspond to higher density Zr within the sample. Interestingly, bright spots of Zr in EELS mapping correlate to dark spots in the EELS carbon mapping, which indicates that such bright Zr spots do not correlate to homogeneously distributed Zr in the coordination polymer network, but to NPs occupying cavities in the carbon network.

4.3.4.3.2. X-ray Photoelectron Spectroscopy

X-ray photoelectron spectroscopy (XPS) is a surface-sensitive quantitative spectroscopic technique that, using X-ray irradiation of a sample, provides information on the bond energy of the molecules forming the analyte. As such, XPS reveals specific energies that are unique to interactions between specific atoms. **pDPA-CNP** was thus analysed via XPS (Figure **4.79**).

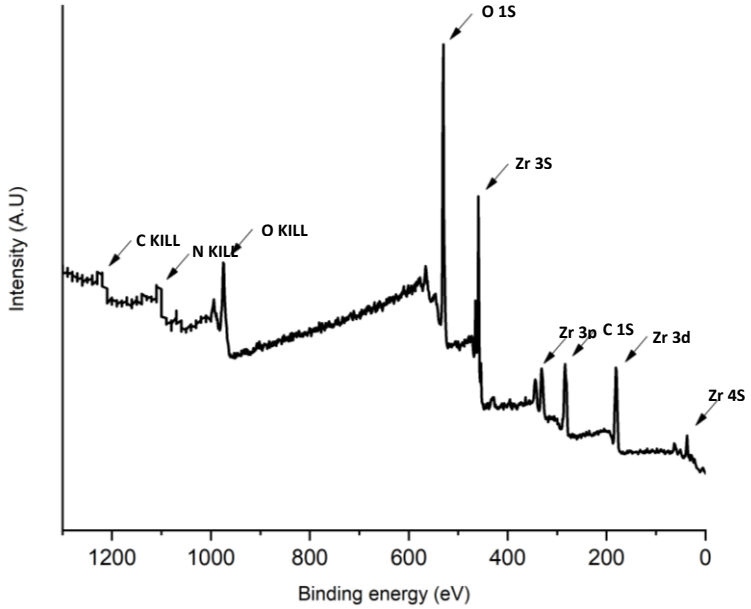


Figure **4.79**. Full spectrum of XPS measurements recorded at room temperature (298 K) of **pDPA-CNP** he peaks corresponding to Si 2p and O 1s are due to the silicon substrates used for the deposition of the samples.

Overall, the XPS spectrum shows an atomic composition based on the binding energy intensity of 4.0% Zr, 47.0% O, 1.6% N, and 33.2% C. Such result, when accounted to sample mass, becomes in agreement with the results from EDX (Annexe **4.63**), EA (Annexe **4.61**), as well as ICP analysis (Annexe **4.60**).

Deconvolution of the total intensity count observed for the region of the spectrum that correlates to Zr 3d energy orbitals shows three different energy peaks (Figure **4.80**).

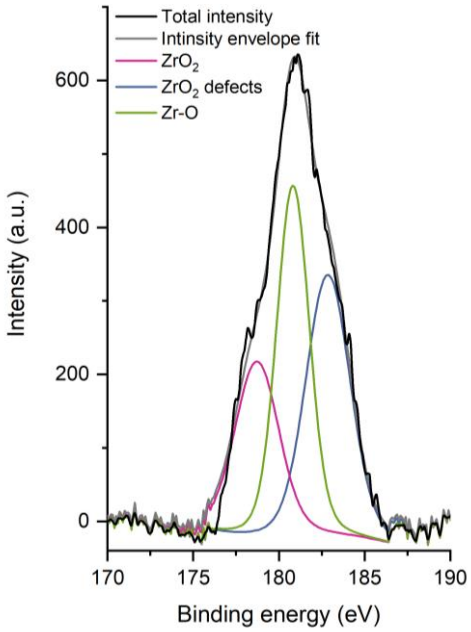


Figure **4.80**. Curve-fitting results for Zr 3d high-resolution XPS spectrum for **pDPA-CNP** and the corresponding deconvolution.

This peaks match with; i) Zr oxides, with a theoretical value of 182.3 eV and an experimental value of 182.7 eV, ii) Zirconium suboxides, which could arise from imperfections of the zirconium oxide cluster, or as a result of interactions/interferences with the coordination polymer, with theoretical values that range between 179-180.5 eV and an experimental value of 179 eV, and iii) Zr coordination contributions with **DPA-COOH**, forming the backbone of the coordination polymer with Zr-O coordination bonding with no reported theoretical value and an experimental value of 180.8 eV. This may be definitive evidence that **pDPA-CNP** contains ZrO_2 NPs that are heterogeneously distributed within our NPs. As well as having a strong indicator of oxygen vacancy formation in the ZrO_2 NPs.

4.3.4.3.3. Determination of Oxygen Vacancies Presence

As observed in XPS, the presence of different suboxides in the ZrO2 NPs can be an indication of oxygen vacancy formation. Energy loss near edge structure (ELNES) provides a tool to cross-reference the results from XPS. ELNES measures the electric dipole transitions from core-orbital to unoccupied states specific of each element and oxidation state. For this purpose, ELNES was performed at the ALBA synchrotron and data was interpreted with the help of Dr. Aziz Genç from *ICN2*.

ELNES structure of Zr changes according to the oxidation state, which modifies L-edge transitions (transitions from 2p electron orbitals to higher energy states) (Figure **4.81**). $L_{2,3}$ energy transitions will thus depend on Zr oxidation state, where the modifications are particularly visible in the L_3 edge (first peak) and the intensity ratio between L_3 and L_2 (second peak) edges.

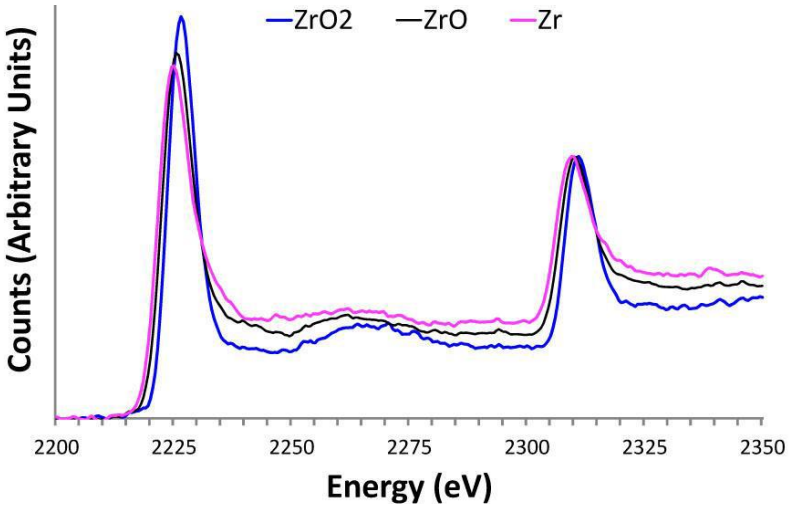


Figure **4.81**. Zr $L_{3,2}$ ELNES obtained from the ZrO_2, ZrO and Zr samples by Kirsty *et al.*[214]

The oxidation states of the Zr can then be obtained by measuring the L_3/L_2 ratios (Figure **4.82**).

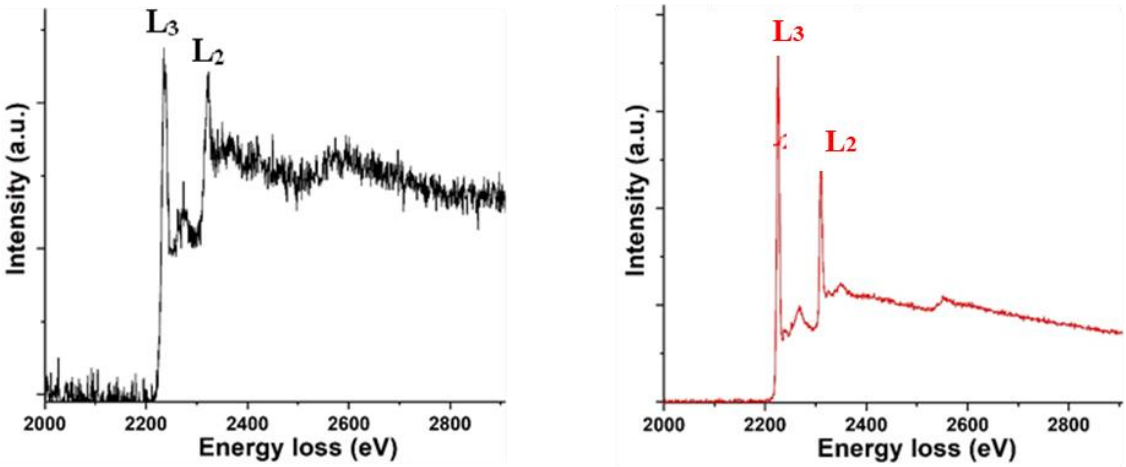


Figure **4.82**. **a)** Experimentally obtained Zr $L_{3,2}$ ELNES, and **b)** reference data from the EELS Atlas.[215]

Reference data was used to have an indirect idea about the oxidation state of Zr. As observed, the L_3 and L_2 ratios of the experimentally obtained and reference data are quite different, suggesting a difference in the oxidation states. The ratios of the L_3/L_2 in both spectra were calculated by taking the second derivatives of the signals to normalise the effects of white-line intensities in different spectra.[216] L_3/L_2 ratio was 2.088 for the reference Zr spectrum and found to be 2.070 in the experimental spectrum. A ratio being slightly lower than the reference may suggest that not all the Zr in the sample has a +4 oxidation state, further pushing the oxygen vacancy hypothesis.

4.3.4.4. Zirconium Oxide Catalysed ROS Generation

With all the previous information, we can now try to formulate a more appealing hypothesis to explain possible mechanisms for the MHT-triggered cell death of **pDPA-CNP**. Among them, amorphous ZrO_2 NPs have been reported to be able to act as "peroxidase-like" catalysts. ZrO_2 NPs have shown the capability to decompose hydrogen peroxide into reactive radicals. An example of this has been reported by Kamila Sobańska *et al.*, with amorphous ZrO_2 surfaces converting H_2O_2 into superoxide ($O_2^{-}\cdot$) and hydroxyl (·OH) radicals.[217]

In our case, we hypothesise that although ZrO_2 NPs in our system have proven to be non-magnetic, with strong diamagnetic behaviour, AMFs can induce weak electric fields and ionic motion. For instance, exposure of membrane-tethered ferritin-TRPV1 constructs to an AMF has been reported to increase intracellular ROS by 30% and extracellular ROS by 140% via activation of membrane NADPH oxidase. These findings suggest that AMFs can trigger cellular oxidases to generate superoxides at the membrane. If such activation occurred, local H_2O_2 could be converted by adjacent ZrO_2 into $O_2^{-}\cdot$ and ·OH. [217]

Localisation of ROS generation on the cell membrane could fall in accordance with the already observed behaviour from cellular TEM imaging for **pDPA-CNP** (Figure **4.64 to 4.71**). Moreover, ROS generation at the cell surface can severely damage membranes and trigger apoptosis. Membrane lipid peroxidation is the result of ROS interaction on the cell membrane lipids, breaking down into cytotoxic aldehydes and additional radicals. This results in the propagation of oxidative stress deeper into the cell.[218] Local extensive peroxidation can lead to membrane rupture or form pore-like lesions like observed in our cellular TEM imaging. Thus, ROS produced on the outside can easily initiate cell death by attacking the membrane, leading to intracellular oxidative stress. This behaviour could match ZrO_2 NPs antitumoral cytotoxic reports associated to ROS apoptotic marker capase-9, and Bax autophagy signalling.[219]

4.3.4.4.1. Estimation of ROS Formation

To prove the last hypothesis, ROS formation was tracked via fold-change of a ROS-sensitive fluorescent probe.

For this, cells were seeded, incubated for 24 hours, and treated with DCFCDA. After internalisation of the fluorescent probe, DCFCDA cells were then treated with **pDPA-CNP** and MHT-treated **pDPA-CNP** at a final concentration of 0.1 $mg \cdot mL^{-1}$, allowed to react with DCFCDA fluorescent dye for 4 hours and measured using fluorescence spectroscopy (Figure **4.83**).

Overall, we observe that **pDPA-CNPs** that are not loaded with SO do not present any statistically significant ROS generation when compared against the control group. However, **pDPA-CNP** that had been AMF-treated showed a slight increase in ROS when compared to control or **pDPA-CNP** not treated with AMF. Nonetheless, the difference cannot be classified as statistically significant, although it presents a trend towards significance. However, the experiment design might have underestimated the total ROS generation. In this assay, ROS generation has been evaluated in cell culture media only after **pDPA-CNP** had been subjected to an AMF and then added to the cell culture. Hence, the combination of AMF, cells, and **pDPA-CNP** had not been studied together. Therefore, ROS generation could be higher than studied until now, but further work needs to optimise the experimental settings and finally prove the underlying hypothesis.

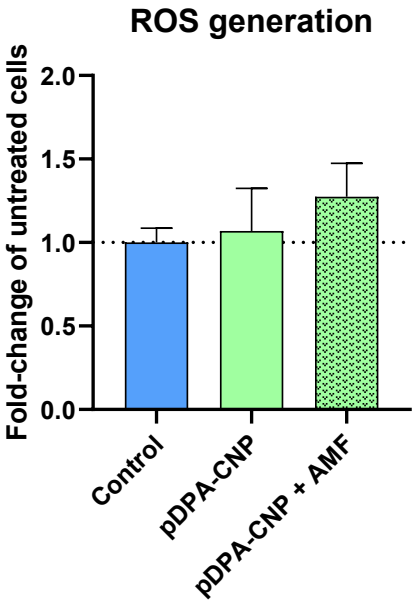


Figure **4.83**. ROS generation, **pDPA-CNP** (0.1 mg·mL^{-1}) in GL261 cell line after 4 hours. Data is represented as a fold increase of base line control fluorescent prove DCFCDA measured at excitation 485 nm and emission 535 nm. H_2O_2 0.1 mM positive control was performed as a test for fluorescent dye proper activity but excluded for representation purposes. Data represents the mean ± SE, n=3. Statistical differences were calculated using one-way ANOVA, followed by Turkey's multiple comparison test, where (*) denotes P < 0.05, (**) denotes P < 0.01, (***) denotes P < 0.001, and (****) denotes P < 0.0001.

4.3.4.5. Singlet Oxygen Load and Unload in pDPA-CNP

Finally, we will explore whether **pDPA-CNP** undergoes the same SO loading and release profile as **pDPA-CNP@Fe NPs**. To prove it, we need to observe the same three processes as before studied (decrease in UV-vis and fluorescence signal under UV radiation, recovery of UV-vis and fluorescence signal under thermal stimulus, and release of SO). In this context, UV-vis and fluorescence both followed a direct decrease in signal intensity under 375 nm UV irradiation. Decrease in signal intensity repeated the pattern of **pDPA-CNP@Fe NP**, taking only 30 minutes to almost present total conversion of **pDPA-CNP**. Then, clear signal strength recovery was observed over a period of 24 hours at 90 °C (Figure **4.84**). These results hint again that retro-Diels-Alder reaction was occurring. With the same shifts in the absorption and fluorescence bands of **pDPA-CNP** after thermal recovery, like **pDPA-CNP@Fe NPs** present. With the same underlying explanation, of thermal decomposition of polycyclic aromatic hydrocarbons endoperoxides, it is still the most plausible.

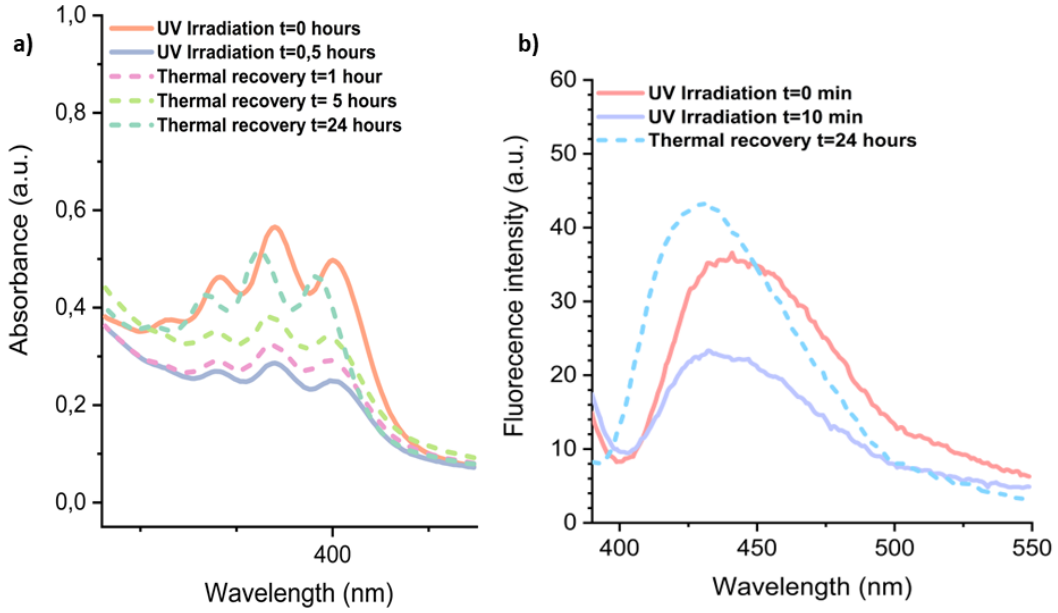


Figure **4.84**. **a)** UV-vis spectra and **b)** fluorescence emission spectra at 375 nm of **DPA-CNP** under irradiation with a 365 nm UV lamp source (continuous line) and thermal recovery at 90 °C (dashed line).

To ensure that no other side reactions, aside from the intended endoperoxide formation, is occurring during irradiation, different absorption/emission studies in hypoxic and open to atmosphere environments were performed (Figure **4.85**). In such approach we can analyse the oxygen dependency of the [2+4] endoperoxide formation and discard other side reactions such as [4+4] cycloaddition reactions of anthracene moieties.

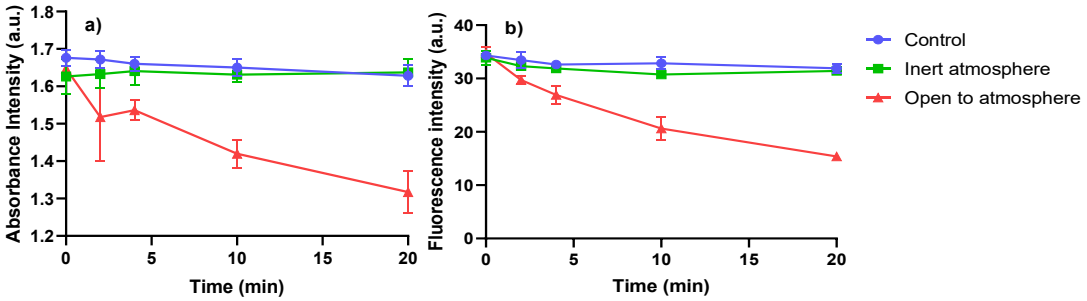


Figure **4.85**. **a)** UV-vis absorption intensity, and **b)** fluorescence emission intensity at 450 nm with excitation wavelength set at 380 nm of **pDPA-CNP** at 378 nm (control, blue), **pDPA-CNP** after irradiation with a UV-lamp source at 365 nm (red), **pDPA-CNP** after irradiation with a UV-lamp in the absence of oxygen (green). Data represents the mean ± SE, n=3.

The results of such experiments proved very satisfactory. Thus, under no irradiation (control group) and irradiation under inert atmosphere (hypoxic environment) the absorption intensity in the UV-vis spectra as well as the fluorescence intensity of **pDPA-CNPs** remained constant. However, intensity under irradiation at atmospheric exposure showed a clear declining tendency in both UV-vis and fluorescence, indicating that the UV photoactivated process was oxygen-dependent.

Finally, we assessed the SO release from **pDPA-CNP** during thermal recovery. For this, we will follow the same SOSG method. In this experiment, **pDPA-CNP** was separated into two samples, both were irradiated, but only one was subjected to a thermal recovery phase. The recovery

phase consisted of an external heat source that subjected the sample to 100 °C for 8 hours. SOSG was then added to both suspensions (Figure **4.86**).

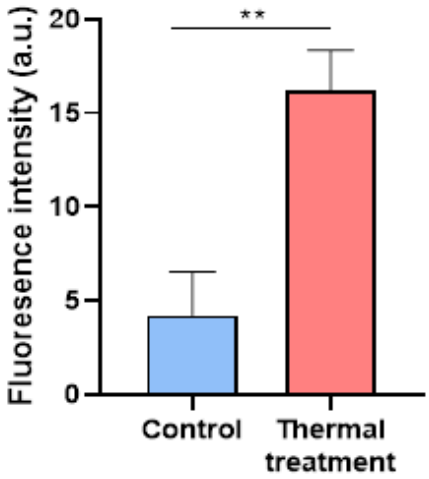


Figure **4.86**. Fluorescence intensity of **pDPA-CNP NPs** at 540 nm in the presence of SOSG after irradiation for 10 minutes under a UV-lamp source at 365 nm; with a 90 °C thermal treatment for 1 hour (red), and control group without thermal treatment (blue). Data represents the mean ± SE, n=3. Statistical differences were calculated using a t test of unpaired groups, where (*) denotes $P < 0.05$, (**) denotes $P < 0.01$, (***) denotes $P < 0.001$, and (****) denotes $P < 0.0001$.

In this instance, we once again observe SO release from the coordination polymer as a result of the retro-Diels-Alder reaction. Overall, we observed that **pDPA-CNP** are a capable system to absorb SO, as observed with the changes in the UV-vis spectrum, and release it, as seen in the fluorescence of the SO probe.

4.3.4.5.1. Estimation of ROS Formation from AMFs in the Presence of SO Loaded pDPA-CNP

Having observed that **pDPA-CNP** is also capable of loading and unloading SO under UV irradiation and respective thermal stimulus, ROS generation under MHT-triggered settings was studied. For this assay, cells were seeded, incubated for 24 hours, and treated with DCFCDA. After internalisation of the fluorescent probe, DCFCDA cells were then treated with **pDPA-CNP** (in combinations of magnetically and SO-loaded groups) at a final concentration of 0.1 $mg \cdot mL^{-1}$, allowed to react with DCFCDA fluorescent dye for 4 hours and measured using fluorescence spectroscopy (Figure **4.87**). Previous ROS assay results from non-SO loaded NPs are plotted for comparison purposes.

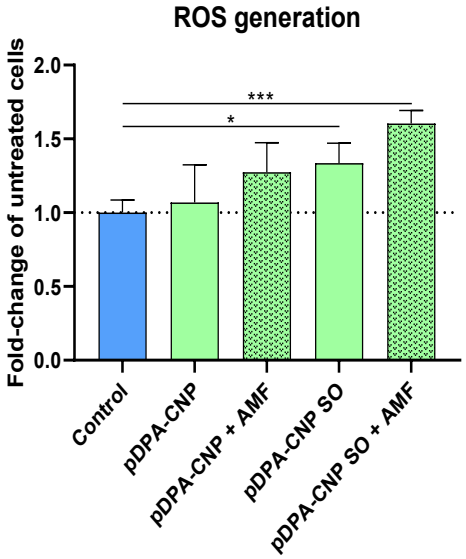


Figure **4.87**. ROS generation, **pDPA-CNP and pDPA-CNP SO** (0.1 mg·mL^{-1}) in GL261 cell line after 4 hours. Data is represented as a fold increase of base line control fluorescent prove DCFCDA measured at excitation 485 nm and emission 535 nm. H_2O_2 0.1 mM positive control was performed as a test for fluorescent dye proper activity but excluded for representation purposes. Data represents the mean ± SE, n=3. Statistical differences were calculated using one-way ANOVA, followed by Turkey's multiple comparison test, where (*) denotes $P < 0.05$, (**) denotes $P < 0.01$, (***) denotes $P < 0.001$, and (****) denotes $P < 0.0001$.

In general, all samples of **pDPA-CNP** loaded with SO present statistically significant higher ROS generation, from which three different conclusions can be taken; i) the hypothesis that UV light was capable to load SO to our **pDPA-CNP** was, once again, proven correct, ii) ROS being detected without AMF could indicate that, either the fluorescent prove is reacting with endoperoxide groups from the SO loaded **pDPA-CNP** or, despite what was observed previously, SO is being released at incubating temperatures of 37 °C, and iii) SO release is significantly higher under AMF treatment. Hence, proving that SO loading enhances the ROS generation profile under MHT.

Despite all these suggestive results, as was underlined previously, ROS generation assays need to be reevaluated and is left for future work.

4.4. Conclusions

Although the final goal of developing a core-shell particle that combined Pt in its structure was not achieved, the **pDPA-CNP@**Fe NPs and **pDPA-CNP** proved to be remarkably successful.

Regarding **pDPA-CNP@Fe NP**, we conclude that the platform demonstrated outstanding properties in in vitro phantoms as a T_{2w} CA. When translated *in vivo*, it showed specific accumulation in the bladder while maintaining excellent tolerability. In terms of cytotoxicity, **pDPA-CNP@Fe NP** exhibited synergistic effects between MHT and ROS, resulting in effective and sustained cell death under external stimuli, enabling selective activation as a therapeutic agent.

A summary of the landmarks of this work is:

- Successfully establishing the synthesis of the component parts of the core-shell nanocostruct **pDPA-CNP@Fe NPs** (**pPDA-COOH** and **Fe-Clustered NP**).
- Three nanostructured platforms were synthesised with well-controlled sizes and dispersities: **pDPA-CNP@Fe NPs** (288.0 ± 2.0 nm, PDI 0.132 ± 0.041), **pPDA-CNP** (135.9 ± 4.6 nm, PDI 0.102 ± 0.008), and **Fe-Clustered NP** (221.3 ± 1.8 nm, PDI 0.120 ± 0.037).
- **pDPA-CNP@Fe** exhibited adequate magnetothermal properties, albeit with SAR values on the lower end of the superparamagnetic spectrum.
- Optical and spectroscopic studies (UV-vis, fluorescence, SO probe assays) confirmed that both **pDPA-CNP** and **pDPA-CNP@Fe NPs** are capable of photoactivated SO uptake via endoperoxide formation and subsequent release via thermally driven retro-Diels–Alder reactions.
- Colloidal stability assays of **pDPA-CNP** and **pDPA-CNP@Fe NPs** suggested the formation of a protein corona in physiological-like media, suggesting favourable interactions for potential *in vivo* applications.
- *In vitro* studies on GL261 murine GBM cell line demonstrated that SO-loaded **pDPA-CNP@Fe NPs** exhibited enhanced cytotoxicity upon MHT exposure. Results underlined a clear benefit of combination therapy between ROS and MHT when compared to control groups.
- *In vitro* phantom studies of **pDPA-CNP@Fe NPs** displayed optimal relaxation times as a T_{2w} CA as a result of the shell coordination polymer enhancing the iron oxide core relaxivity. *In vivo* studies of **pDPA-CNP@Fe NP** unfortunately did not yield the expected results for GBM imaging, but gave way to applications as a highly sensitive CA in the bladder.
- *In vivo* biodistribution confirmed the claims of **pDPA-CNP@Fe NP** as a bladder CA with a clear accumulation pattern and selectivity towards this organ over the studied ones.

On the side of **pDPA-CNP**, although initially intended as a control platform, this structure achieved excellent cytotoxicity in GBM settings with AMF-triggered behaviour, which allows for controlled activation. The origin of the cytotoxicity of the platform is only hypothesised, but points towards *in situ* ROS generation.

A summary of the landmarks of this work is:

- **pDPA-CNPs** displayed as a structurally robust structure that does not degrade under AMFs, as observed in SEM imaging.

- **pDPA-CNPs** demonstrated biocompatibility in cytotoxicity assays, coupled with good colloidal stability in physiological media. Additionally, testing of the monomeric components showed no cytotoxicity upon internalisation and degradation, supporting the safety of the system.
- *In vitro* viability displayed **pDPA-CNP** as a perfect candidate for a turn-on platform to achieve cancer cell death, activated only under AMF stimulus.
- Through cellular TEM imaging of **pDPA-CNP** and **pDPA-CNP@Fe NP,** it was observed high surface cell membrane interaction and attachment.
- Nanostructured ZrO_2 with oxygen vacancies in the network of **pDPA-CNP** was determined to be present.

Future efforts should focus on:

- Elucidating the origin of the interactions with AMF from **pDPA-CNPs**.
- Elucidating the role of ROS in cell death mechanisms caused by **pDPA-CNPs**.
- Assessing the *in vivo* pharmacokinetics, biodistribution, and therapeutic index in relevant GBM models of **pDPA-CNPs** and **pDPA-CNP@Fe NPs**.

4.5. Materials and Experimental Methods

4.5.1. Materials

Solvents and starting materials were purchased from Merck (Germany) and used as received without further purification. Deuterated solvents were purchased from Eurisotop (Germany). PBS tablets and SOSG were purchased from Thermo Scientific (USA). DCFCDA was purchased from Merck (Germany).

4.5.2. Characterisations

Nuclear magnetic resonance (NMR) spectra were registered at *Servei de Ressonància Magnètica Nuclear at the Universitat Autònoma de Barcelona*. ^{1}H-NMR were registered at Bruker DPX (250 MHz), Bruker DPX360 (360 MHz) and Bruker ARX400 (400 MHz). Chemical shifts of protons are described in ppm using the residual deuterated solvent signals as internal reference (chloroform-d_1; 7.26 ppm). ^{13}C-NMR were registered at Bruker ARX400 (100 MHz), chemical shifts of carbons are described in ppm using the residual deuterated solvent signals as internal reference (chloroform-d_1; 77.16 ppm). 2D COSY, HSQC and HMBC spectra were recorded at Bruker DPX360 (360 MHz) and Bruker ARX400 (400 MHz), chemical shifts of protons and carbons are described in ppm using the residual deuterated solvent signals as internal reference (chloroform-d_1; ^{1}H 7.56 ppm or ^{13}C 77.16 ppm). All spectra have been registered at room temperature.

Abbreviations used to describe signal multiplicities have been: s (singlet), d (doublet), q (quadruplet), qt (quintuplet), bs (broad singlet), m (multiplet) and J to indicate coupling constants (Hz).

Infrared spectrometry (IR) was performed using an MKII Golden gate spectrometer equipped with golden gate singlet reflection diamond ATR (attenuated total reference). Each spectrum was acquired between 400 and 4000 cm^{-1} at a spectral resolution of 2 cm^{-1}. Samples were measured in powder with Golden gate singlet reflection diamond ATR or pelletised with anhydrous $KBr_{(s)}$. Peaks were described in cm^{-1} and intensity described as strong (s), medium (m), and weak (w).

Electron absorption spectrometry (UV-vis) was performed using a Cary 4000 and Cary 600 spectrophotometers (Agilent, USA), in the 200−800 nm wavelength range, using a matched pair (one for the solvent blank and one for the sample) of quartz cuvettes of 1 cm optical path length, and solvents quality HPLC. Molar absorptivity of samples was obtained by plotting absorption at different concentrations of a sample within the linear range of absorptivity and extracting the linear fit, isolating absorptivity value from the linear fit equation.

Fluorescence spectra were measured on a HORIBA PTI QuantaMaster 8000 Spectrofluorometer (Horiba, Japan) at a wavelength range of 300-900 nm in a 1 cm optical path long quarts cuvettes in DMF or water.

Fluorescence quantum yield (FQY) was measured on a Hamamatsu C9920-02G fluorimeter using an integration sphere in a 1 cm optical path long quarts cuvettes in DMF or water.

Electrospray ionization mass spectroscopy (ESI-MS) has been performed at *Servei d'Anàlisi Química at Universitat Autònoma de Barcelona* using a 1200 RR (Agilent Technologies) – mass spectrometer triple-quadrupole–time of flight (QTOF) microTOF-Q (Bruker Daltoniks, USA).

Inductively coupled plasma mass spectrometry (ICP-MS) was performed at *Parque Científico Tecnológico* of the *Universidad de Burgos,* using an Agilent 8900 ICP-MS/MS with automatic sampler and octupole detector. Measurements were recorded using ^{56}Fe as Fe tracer and ^{90}Zr as Zr tracer.

Solid dry samples were digested via a closed beaker digestion in the ETHOS SEL Milestone microwave in a 35:65 $HCl:HNO_3$ suspension for a total of 30 minutes while temperature was kept at 170 °C.

Liquid aqueous samples that did not require digestion were stored in a 2% HNO_3 solution and directly injected for analysis.

Elemental analysis (EA) was performed at *Servei d'Anàlisi Química at Universitat Autònoma de Barcelona* or at *Parque Científico Tecnológico* of the *Universidad de Burgos*, using a Flash EA 2000 CHNS (Thermo Scientific, USA), in both cases for determination of % C, N, H, S, O.

Dynamic light scattering (DLS) for hydrodynamic size distribution and zeta surface charge potential of NPs (0.5 $mg \cdot mL^{-1}$) were measured using a ZetasizerNano 3600 instrument (Malverm Instruments, UK), with a size range limit from 0.6 nm to 6 nm. NPs were dispersed in water or PBS-30 $mg \cdot mL^{-1}$ BSA to study colloidal stability in physiological conditions.

Nanoparticle tracking analysis (NTA) was performed at *Institut de Ciència de Materials de Barcelona* at the *Soft Materials Service,* using a Nanosight NS300 (Malvern Instruments, UK)

Scanning electron microscopy (SEM) images were obtained using a scanning electron microscope (FEI Quanta 650 FEG or Magellan 400L XHR) at an acceleration voltage of 5–20 KV, high-vacuum mode, and an electron gun distance to the sample of 5 mm. SEM samples were prepared by drop-casting the corresponding dispersions of NPs on aluminium tape followed by solvent evaporation under room temperature conditions. Before analysis, the samples were metalised with a thin layer of platinum (thickness of 5 nm) using a sputter coater (Emitech K550).

Transmission electron microscopy (TEM) images were obtained using JEM-1400 (120 kV) at the *Institut Català de Nanociència i Nanotecnologia* main building facilities or a Thermo Scientific Spectra 300 double-corrected (S)TEM at the ALBA synchrotron facilities.

Samples were prepared by drop casting of water suspensions consisting of the target study NPs onto a copper thin grid (TED PELLA inc, USA) which was afterwards dried in vacuum.

ImageJ (Copyright (C) 1989, 1991 Free Software Foundation, Inc.) analytical software was used form SEM imaging NPs size analysis using the integrated particle analysis software from binary file images taken from 8-bit format files from SEM imaging.

Elemental mapping (EM) images were obtained using a double aberration corrected transmission electron microscope (Thermo Scientific Spectra 300 (S)TEM) equipped with Super-X windowless EDX detector operated at 200 kV at the ALBA synchrotron facilities.

Electron energy loss spectroscopy (EELS) was performed with a Thermo Scientific Spectra 300 double-corrected (S)TEM on a Gatan GIF Continuum K3 energy filter for EELS and EFTEM applications (>3000 spectra per second at >95% duty cycle), with Low-noise, high dynamic range CMOS 1069.EXUP (30-300 kV) detector and the K3 electron counting direct detector (80-300 kV) at the alba synchrotron facilities.

Powder X-ray diffraction (XRD) patterns were recorded on PANanlytical X'pert PRO MRD (Multipurpose Diffractometer) equipped with a CuKα radiation source (λ=1.54184 Å) with goniometer (320 mm radius) in a four-circle geometry. Detector consisted of a Pixcel 1D, a fast X-ray detector based on Medipix2 technology. The measurement conditions were 2θ range (10-45°); step size 0.03°; counting time/time per step = 14 seconds.

X-ray photoelectron spectroscopy (XPS) measurements were performed with a Phoibos 150 analyser in ultra-high vacuum conditions (based pressure 10^{-10} mbar). Monochromatic AlKα as X-ray source (1486.6 eV). Electron energy analyser operated at pass energy of 50 eV perpendicular to the sample surface. All data was treated with CasaXPS version 2.3.17PR1.1 (Casa Software LTD, UK) software.

Thermogravimetric analysis (TGA) and **Differential scanning calorimetry (DSC)** measurements were carried out using a NETZSCH-STA 449 F1 Jupiter under $N_{2(g)}$ atmosphere in aluminium holding crucibles. Measurements were carried out at a scan rate of 10 K·min^{-1}, from 25 to 900 °C. DSC was measured using the same equipment with a cryostat under the same condition range.

Magnetic characterisation of pDPA-CNP@Fe was carried out in a Quantum Design SQUID magnetometer. Hysteresis loops M(H) were measured under a maximum applied field of 100 kOe at 5 K, in order to evaluate the coercive field (H_C), and saturation magnetisation (M_H). Saturation magnetisation was obtained by extrapolating to zero field the experimental M(H) curve from the high-field range where the magnetisation varies linearly with H. Hysteresis loops were normalised to the total iron mass according to ICP-MS results. ZFC and FC magnetisation curves were measured at 100 Oe in the temperature range 5-300 K.

Zr drug release from pDPA-CNP was evaluated using the dialysis method. Concentrated **pDPA-CNP** (1 mg·mL^{-1}) was reconstituted in 1 mL of MilliQ® water and placed in dialysis bags (MWCO=6,000–8,000 Da). The bags were then immersed in sealed beakers containing 100 mL of PB buffer with pH values set at 7.4 The beakers were then kept at 37 °C. At predetermined time points, a 1 mL aliquot was withdrawn from the dialysate and immediately replaced with an equal volume of fresh buffer. Samples were then taken to, and stored, in a 10 mL 2% a HNO_3 solution. The quantity of released Zr was determined using ICP-MS.

Estimation of singlet oxygen generation of pDPA-CNP@Fe and pDPA-CNP under external heating

Two iron core shell, or coordination polymer, NP solutions in MilliQ® water where prepared (2 mL, 0.01 mg·mL^{-1} related to iron for **pDPA-CNP@Fe** or 2 mL, 0.05 mg·mL^{-1} related to total mas for **pDPA-CNP**). One solution was irradiated for 30 minutes until complete endoperoxide formation, followed by UV-vis. Both, irradiated and non-irradiated solutions were heated in the oven at 110 °C for 12 hours. A stock solution of SOSG was prepared (5 mM) and 4 µL were added to each solution, reaching the final working concentration at 10 µM of SOSG. Both solutions were

allowed to evolve over a period of 15 minutes and their emission fluorescence spectra at 540 nm was recorded with an excitation source at 490 nm.

Estimation of singlet oxygen generation of pDPA-CNP@Fe under magnetic hyperthermia

From a **pDPA-CNP@Fe NPs** stock solution at 0.3 mg Fe·mL^{-1}, two samples were prepared by taking 400 µL of stock solution and brought to 1 mL of 100 mM pH 7.5 tris buffer in water, yielding a final working concentration of 0.12 mg Fe·mL^{-1}. Both samples were then oxygen loaded under irradiation at 365 nm under a laboratory UV lamp for 20 minutes. One sample is then placed in a magnetherm (MAGFORCE Ltd.) calorimetric hyperthermia device equipped with an 18 turn coil, and exposed to an AMF at 366 kHz, 16 mT. The other sample was kept at room temperature and used as a negative control.

125 µL aliquots of both samples were then withdrawn at t=0, 15, 30 minutes, 1, 2, 4 hours and diluted to a total volume of 2 mL of 100 mM pH 7.5 tris buffer in MilliQ® water, reaching the final measuring concentration of 0.0075 mg Fe·mL^{-1}. To this, 4 µL of a previously prepared SOSG stock solution (3 mg·mL^{-1}) were added. The dye was left to react for 15 minutes, their emission fluorescence spectra at 540 nm was recorded with an excitation source at 490 nm.

Quantitative magnetic resonance imaging phantoms (MRI-Phantoms)

From **pDPA-CNP@Fe, Fe-clustered NPs, pDPA-CNP** stock solutions at 100 µg Fe·mL^{-1} and 100 µg Zr·mL^{-1} respectively, five samples for each system were prepared at different metal concentrations (25, 10, 5, 1 and 0 µg Fe·mL^{-1}). The NPs were then dispersed in 2 mL of 1% agarose in MilliQ® water at 37 °C, sample was sonicated to ensure a good colloidal suspension, and then solidified at room temperature.

Subsequently, r_1 and r_2, along with the corresponding acquisitions sequences for NP's gelations studies, were measured under a 7 T (300 MHz) magnetic field using a Bruker Biospec 70/30 SUR spectrometer (Bruker BioSpin GmbH, Germany), equipped with a mini-imaging gradient set (400 mT·m^{-1}). MRI acquisitions were performed at the co-managed NMR facility of the *Universitat Autònoma de Barcelona* and *Centro de Investigación Biomédica en Red–Bioingeniería, Biomateriales y Nanomedicina* (Spain), Unit 25 of NANBIOSIS, http://www.nanbiosis.es.

For *in vitro* studies MRI, a 72 mm inner diameter quadrature volume coil was used as both transmitter and receiver. MRI data were acquired and processed on a Linux workstation using ParaVision 5.1 software (Bruker BioSpin GmbH, Germany).

For T_{1w} images were acquired with a RARE-variable repetition time (VTR) sequence with TR = 100 ms, TE=6 ms, flip angle (FA) = 180°, TA=3 min 24 s 800 ms, FOV=9 x 4.5 cm^2, MTX=256 x 128, ETL=1, number of excitations (NEX)=16, NS=3, ST=4 mm, and IT=7 mm. For T_{2w} images were acquired with a RARE sequence with TR=4200 ms, TE=12 ms, TE_{eff}=36 ms, FA=180°, TA=1 min 40 s 800 ms, FOV=9 x 4.5 cm^2, MTX=256 x 128, ETL=1, NEX=2, NS=3, ST=4 mm, and IT=7 mm. For T_1 maps were acquired with a RARE-VTR sequence with TR list=50, 80, 120, 160, 200, 250, 300, 360, 420, 500, 650, 850, 1100, 1600, 2200, 3000, 5000, and 10000 ms, TE=6 ms, FA=180°, TA=2 min 37 s 670 ms, FOV=9 x 4.5 cm^2, MTX=128 x 64, ETL=1, NEX=1, NS=3, ST=4 mm, and IT=7 mm. For T_2 maps were acquired with multi-slice multi-echo (MSME) sequence with TR=3000 ms, TE=10 ms, TE_{eff}=600 ms, FA=180°, TA=6 min 2 s 450 ms, FOV=9 x 4.5 cm^2, MTX=128 x 64, ETL=1, NEX=1, NS=3, ST=4 mm, and IT=7 mm.

After processed, the obtained inverse $T_{1\text{-}2w}$ values were plotted versus the concentrations of Fe. The slope was then used to get the $r_{1\text{-}2}$. The relaxivity ratio was obtained by division between relaxivity rates (r_2/r_1).

4.5.3. *In vitro* assays

Cell line culture

Murine GBM GL261 cell line was obtained from the American Type Culture Collection (ATCC; USA). GL261 was cultured in Dulbecco's modified eagle medium enriched with 4.5 $g{\cdot}L^{-1}$ D-glucose (DMEM (1X) + GlutaMAX™-), 10% heat-inactivated FBS, and 1% penicillin-streptomycin. The cells were grown as adherent monolayer in 75 cm^2 cell-culture flask (Nunclon™ Delta Surface, Merck, Germany) and maintained in an incubator (HERAcell, 150i, Thermo Scientific, USA) at 37 °C in 5% CO_2 with a relative humidity of 95%. Cell culture media, FBS, antibiotics, PBS, trypsin, Trypan Blue and material were procured from Thermo Scientific (USA).

To subculture or collect cells, cells must be in the logarithmic phase growth, which is achieved at around 75% confluence. Once this confluence was reached, the culture medium was removed from the flask. Then, 5 mL of sterile PBS were added to the flask to wash the cells and remove any residual medium. After removing the PBS and repeating again the same process, 3 mL of trypsin were added, the flask was then returned to incubator for 3 minutes. If upon observing the cells under the microscope ≥ 90% of the cells were detached, 6 mL of fresh medium were added to neutralize the trypsin and facilitate cell collection. The cell suspension was then transferred to a 15 mL Falcon tube (Falcon, Cultek, Spain) and centrifuged (Thermo Scientific, USA) at 1200 rpm for 5 minutes to collect the cells. The supernatant was discarded, and the cell pellet resuspended in fresh medium to the desired dilution factor. Then, 1 mL of this resuspension was added to a flask containing 13 mL of fresh medium. To seed the required amount, a cell count was performed, and the necessary number of cells were seeded into the corresponding plate for each experiment.

Cell counting

Cell counting was performed using a Neubauer hemocytometer and Trypan Blue for cell viability assessment. Trypan Blue is a dye that differentiates living cells from dead ones, as dead cells cannot extrude Trypan Blue due to a lack of necessary energy-dependant mechanisms. An aliquot of 10 µL of the cell suspension to be studied was mixed with 10 µL of Trypan Blue. Next, 10 µL of the mixture were placed into the Neubauer hemocytometer, and the number of living cells were counted using an optical microscope.

Reactive oxygen species (ROS) determination

GL261 cell line was seeded in a black 96-well plate (Sudelab, Spain) at a density of 20,000 cells/well, to ensure full confluence, in a final volume of 100 µL. After 24 hours, the medium was removed, and the cells were rinsed with serum-free medium. Subsequently, serum-free medium containing the fluorescent probe DCFCDA (Merck, Germany) at a final working concentration of 25 µM was added, and the cells were incubated in the dark for 30 minutes. Once the probe was internalised, the medium containing the probe was replaced with either medium (negative

control) or media-containing the analytes to be studied (**pDPA-CNP** in all combinations of SO loaded and MHT treated) at a final concentration of 0.5 $mg \cdot mL^{-1}$.

SO loaded samples were irradiated at 365 nm under a laboratory UV lamp for 20 minutes. While MHT treated samples (one SO loaded and one non-SO loaded) were then placed in a magnetherm (MAGFORCE Ltd.) calorimetric hyperthermia device equipped with an 18-turn coil and exposed to an AMF at 366 kHz, 16 mT. The other compounds were kept at room temperature. A positive control with 0.1 mM H_2O_2 was included.

Following a 4-hour incubation, the fluorescence of each well was measured at emission 535 nm with excitation at 485 nm using a microplate reader (Victor3, Perkin Elmer, USA). All experiments were conducted in triplicate in three independent experiments and normalised based on the negative control loaded with dye. The data was processed using GraphPad Prism software (version 8.0).

Cellular internalization studies

GL261 cell line in exponential growth phase was seeded in a six-well plate (Sudelab, Spain) at a density of 500,000 cells/well, in a final volume of 1 mL of cell culture media. Following a 24-hour incubation, the old media was replaced with 1 mL of fresh media with or without **pDPA-CNP** at a concentration of 0.1 $mg \cdot mL^{-1}$. The treated cells were allowed to internalise the compound for 0, 0.5, 1, 3, 6 and 24 hours in the incubator. The media was removed and stored, and the cells were washed twice with cold PBS to remove any remaining compound outside the cells. Subsequently, 1 mL of cold PBS with 1% of SDS was added to each well to lyse the cells. The cells were then collected and stored. The standard curve matrix was prepared by addition of **pDPA-CNP** at 0.02, 0.04, 0.06, 0.08 and 0.1 $mg \cdot mL^{-1}$ after lysing the cells. Samples were analysed using fluorescence spectroscopy at an emission wavelength set at 433 nm and an excitation wavelength set at 393 nm. All experiments were conducted in triplicate in three independent experiments, and the data were processed using GraphPad Prism software (version 8.0).

***In vitro* cytotoxicity assays**

GL261 cell line in exponential growth was seeded in a 96-well plate (Sudelab, Spain) at a density of 5,000 cells/well in a final volume of 100 µL. After 24 hours of incubation, 100 µL of fresh media containing compound (**DPA-COOH**, $ZrOCl_2 \cdot 8H_2O$ and **pDPA-CNP**, or **pDPA-CNP@Fe NPs** and **Fe-Clustered NPs**) at different concentrations (0, 1, 5, 10, 25, 50, 100, 200, 500 µM or 0, 1, 5, 10, 25, 50, 100, 200, 500 $\mu g \cdot mL^{-1}$ respectively) was added. The plates were then incubated for an additional 24 or 72 hours. For sample preparation, **DPA-COOH** was dissolved in medium with 1% DMSO to a concentration of 1 $mg \cdot mL^{-1}$. **pDPA-CNP**, and $ZrOCl_2 \cdot 8H_2O$ were also dissolved in medium to a concentration of 1 $mg \cdot mL^{-1}$. The required concentrations of the control were added using medium containing 1% DMSO.

After 24- and 72-hour post-treatment, 10 µL of PrestoBlue® (0.15 $mg \cdot mL^{-1}$, Thermo Scientific, USA) were added to each treated well with and without cells (as a blank), as well as to three wells containing only medium. The plates were incubated at 37 °C for about 4 hours, and measurements were performed using the Victor3 microplate reader (Perkin Elmer, USA) at emission of 572 nm with excitation at 530 nm. The relative cell viability (%) of each sample related to the control (cells without compound) was calculated. All experiments were conducted

in triplicate in three independent experiments, and the data were processed using GraphPad Prism software (version 8.0).

Viability assays

Two stock solution at 2.3 mg Fe·mL^{-1} of **pDPA-CNP@Fe** were prepared. One of them remained untreated, while the other was irradiated at 365 nm under a laboratory UV lamp for 20 minutes. Moreover, one stock solution at 10 mg·mL^{-1} of **pDPA-CNP** and one stock solution at 2.3 mg Fe·mL^{-1} of **Fe-Clustered NPs** were prepared. All samples, except SO-loaded samples, were sterilised by autoclave at 121 °C for 15 minutes.

GL261 cell line in exponential growth was lifted, counted and brought to a total cell count of 1,000,000 cells for each working condition to be studied. Cells were then brought to a final volume of 50 µL with the previous addition of 11 µL of compound (**pDPA-CNP**, **pDPA-CNP@Fe**, **pDPA-CNP@Fe** SO loaded, **Fe-Clustered NPs**), reaching a final cell concentration of 20.000.000 cells/mL and a final compound concentration of either 0.5 mg Fe·mL^{-1} or 2.2 mg **pDPA-CNP**·mL^{-1}. Cell control condition was brought to a final volume of 50 µL. Then, one sample of each condition was placed in magnetherm (MAGFORCE Ltd.) calorimetric hyperthermia device equipped with an 18-turn coil and exposed to an oscillating magnetic field (366 kHz, 16 mT), and exposed to an AMF for two periods of 30 minutes, with a pause of 10 minutes in between. The second sample of each condition was kept at room temperature for the same amount of time.

Subsequently, all samples were individually diluted to 1 mL of media were seeded to a 96-well plate at a density of 5,000 cells/well. After 24- and 72-hour incubation, 10 µL of PrestoBlue® (0.15 mg·mL^{-1}, Thermo Scientific, USA) were added to each condition well, as well as to three wells containing only medium. The plates were incubated at 37 °C for about 4 hours, and measurements were performed using the microplate reader (Victor3, Perkin Elmer, USA) at emission of 572 nm with excitation at 530 nm. The cell viability (%) for each sample related to the control (cells without compounds) was calculated. All experiments were conducted in triplicate in three independent experiments, and the data were processed using GraphPad Prism software (version 8.0).

Cellular transmission electron microscopy imaging

One stock solution at 2.3 mg Fe·mL^{-1} of **pDPA-CNP@Fe** and one stock solution at 10 mg·mL^{-1} of **pDPA-CNP** were prepared and sterilised by autoclave at 121 °C for 15 minutes.

GL261 cell line in exponential growth phase was lifted, counted and brought to a total cell count of 1,000,000 cells for each working condition to be studied. Cells were then brought to a final volume of 50 µL with the previous addition of 11 µL of stock solution, reaching a final cell concentration of 20.000.000 cells/mL, and a final compound concentration of either 0.5 mg Fe·mL^{-1} or 2.2 mg **pDPA-CNP**·mL^{-1}. Cell control condition was brought to a final volume of 50 µL. Then, one sample of each condition was placed in magnetherm (MAGFORCE Ltd.) calorimetric hyperthermia device equipped with an 18-turn coil and exposed to an AMF (366 kHz, 16 mT). Samples were then exposed to an AMF for two periods of 30 minutes with a pause of 10 minutes in between. The second sample of each condition was kept at room temperature for the same amount of time.

Afterwards, cell samples were centrifuged at 1200 rpm for 5 min, and the medium removed. Immediately, 2 mL of 0.1 M PB solution containing 2.5% glutaraldehyde at 4 °C was added for fixation. After 1 hour, cells were then rinsed 3 times with PBS. The cellular pellet was postfixed in 0.1 M PB solution containing 1% osmium tetroxide potassium ferricyanide solution at 4 °C for 1 hour, rinsed with PBS and distilled H_2O, and dehydrated in a graded series of ethanol containing solutions (30, 60, 70, 80 and 100%), and exposed for 15 minutes to each concentration. Finally, warm epoxy resin was mixed with ethanol (1:1) for infiltration for a total time of 1 hour, and fresh epoxy resin was used for cell embedding (60 °C, 48 hours). Ultrathin sections (70 nm) were cut using a Leica Ultramicrotome EM UC6 or Boeckeler PowerTomePC Ultramicrotome (Germany) and stained with 5% uranyl acetate in 50% ethanol and 2% aqueous lead citrate solution. The sections obtained were imaged using a Jeol JEM-1400 (120 kV) TEM. Resin embedding, ultrathin sections and images were sectioned and obtained at *Servei de Microscòpia i Difracció de Raigs X* at the *Universitat Autònoma de Barcelona*.

Statistical analyses

Data were analysed using GraphPad Prism (version 8.0) and values are represented as the mean ± SE of three independent experiments. Statistical differences were calculated using one-way ANOVA, followed by Turkey multiple comparison test. Except the case of cell viability where statistical differences were calculated using two-way ANOVA, followed by Sidak's multiple comparison test and Dunnett multiple comparison test. The significance threshold for all tests was set at $p < 0.05$.

4.5.4. *In vivo* assays

Animal studies

All animal studies were approved by the local ethics committee (*Comitè d'Ètica en la Recerca*, CERec, https://www.uab.cat/ca/etica-recerca accessed on June 25th 2025) and according to the regional and state legislation (protocol CEEAH-4859). C57BL/6J female mice of 10-12 weeks of age, with body weights 20.2 ± 0.6 g (n=15) were purchased from Charles River Laboratories (Charles River Laboratories International, USA), and housed in the *Universitat Autònoma de Barcelona*'s animal facilities (*Servei d'Estabulari*, www.uab.cat/ca/servei-estabulari accessed on June 25th 2025). All animals were maintained in consistent housing and controlled conditions: 12-hours light/12-hours dark cycles (light from 8 am to 8 pm), temperature 22 ± 2 °C, relative humidity 55 ± 10%, water and standard food access *ad libitum*, and enriched environment. Animal experiments and care were conducted in collaboration with duly accredited personnel.

Preclinical model generation

Except for tolerability studies, GL261 tumour-bearing mice were used. Tumours were induced by stereotactic intracranial injection of 10^5 murine GBM GL261 cell line, obtained from the American Type Culture Collection (ATCC, USA), in caudate nucleus. For this, analgesia (meloxicam at 4.0 $mg \cdot kg^{-1}$, Meloxidyl, Ceva, USA) and anaesthesia, a mixture of ketamine (Ketamidor at 125 $mg \cdot kg^{-1}$, Richer pharma, Austria) and xylazine (Xilagesic at 15 $mg \cdot kg^{-1}$, Calier, Barcelona), were administrated subcutaneously and intraperitoneally, respectively. Once mice no longer responded to the toe pinch reflex, they were immobilised in a stereotaxic holder (Kopf Instruments, USA) in a prone position. Then, the incision area was shaved and sterilised, and a

1 cm incision was made to expose the skull. A 1 mm hole was drilled 0.1 mm posterior to Bregma and 2.32 mm to the right of the midline using a microdrill (Fine Science Tools, Germany). Then, a 26G Hamilton syringe (USA) positioned on a digital push-pull microinjector (Harverd Apparatus, USA) was used for the injection of 4 µL of 10^5 GL261 cell line in medium at a depth of 3.35 mm from the skull surface, at a rate of 2 µL·min^{-1}. After the injection, the Hamilton syringe remained in place for 2 minutes to minimize cell reflux, then was slowly and carefully withdrawn. Finally, the incision was closed with 6.0 silk suture (Braun, Spain) and disinfected with povidone-iodine (Betadine, Vemedia Pharma, Spain). Mice were actively monitored until fully recovered and were re-administered intraperitoneal analgesia after 24 hours.

***In vivo* MRI studies**

Mice were subjected to non-invasive brain MRI scans to measure the volumes, localization, and evolution of the tumour. All MRI studies were performed at the co-managed NMR facility of the *Universitat Autònoma de Barcelona* and *Centro de Inverstigación Biomédica en Red–Bioingeniería, Biomateriales y Nanomedicina* (Spain), Unit 25 of NANBIOSIS, http://www.nanbiosis.es. The 7 T Bruker Biospec 70/30 USR spectrometer (Bruker BioSpin GmbH, Germany) equipped with a mini-imaging gradient set (400 mT·m^{-1}) was used for MR acquisitions.

For brain MRI of mice, a 72 mm inner diameter linear volume coil served as the transmitter, a dedicated quadrature surface coil designed for the mouse brain was used as the receiver. For whole-body MRI of mice, a 72 mm inner diameter quadrature volume coil was used as both transmitter and receiver. MRI data were acquired and processed on a Linux workstation using ParaVision 5.1 software (Bruker BioSpin GmbH, Germany). During imaging, mice were placed in a dedicated imaging bed equipped with an integrated heating system to maintain body temperature (37-38 °C) and allow for administration of anaesthesia (1-1.5% isoflurane in O_2 at 1 L·min^{-1}). Respiratory rate was monitored using a pressure probe (SA Instrumetns, Inc., USA) and maintained between 60–80 breaths per minute.

MRI tumour progression monitoring

To monitor tumour progression in GL261 tumour-bearing mice, high-resolution T_{2w} MRI was performed using RARE sequence for brain tumour visualization.

The imaging parameters were as follows: TR=4200 ms, TE=12 ms, TE_{eff}=36 ms, FA=180°, TA=6 min 43 s 200 ms, FOV=19.2 x 19.2 cm^2, MTX=256 x 256, ETL=8, NEX=4, NS=10, ST=0.5 mm, and IT=0.1 mm.

Tumour volumes were calculated from MRI scans by delineated ROIs in each slice using ParaVision 5.1 software to measure tumour area. Subsequently, mice tumour volumes were computed using the following Equation **4.1**:

$$TV\ (mm^3) = \left[(AS_1\ x\ ST) + \left(\sum_2^{10} AS\ x\ (ST + IT)\right)\right] x\ 0.075^2 \qquad \text{Equation } \mathbf{4.1}$$

where TV is the tumour volume, AS indicates the number of pixels within the ROI defined by tumour boundaries in each MRI slice, ST is the slice thickness (0.5 mm), IT is the inter-ST (0.1 mm), and 0.075^2 signifies the individual pixel surface area in mm².

MRI *in vivo* contrast agent data acquisition

For CA imaging, GL261 tumour-bearing mice (n=6), after 19.5 ± 1.5 days post tumour implantation, and with tumour volume of 66.2 ± 23.8 mm^3, were used.

Tumour-bearing mice were i.v administrated with **pDPA-CNP@Fe NPs**, as a CA, at a dose of 0.12 mmol Fe·kg^{-1} in 100 µL of PBS containing 0.5% MSA. T_{1w} and T_{2w} images, as well as T_{1w} and T_{2w} maps in the case of whole-body mice images, were continuously acquired before the administration, immediately and up to 2 hours after administration, and again at 24 hours post-administration.

Two types of MRIs sequences were performed, for brain and for whole-body mice. For brain MRI of mice: For T_{1w} images were acquired with a RARE sequence with TR=200 ms, TE=8.5 ms, FA=180°, TA=51 s 200 ms, FOV=192.2 x 192.2 cm^2, MTX=128 x 128, ETL=1, NEX=2, NS=5, ST=1 mm, and IT=1.1 mm. For T_{2w} images were acquired with a RARE sequence with TR=4200 ms, TE=12 ms, TE_{eff}=36 ms, FA=180°, TA=50 s 400 ms, FOV=192.2 x 192.2 cm^2, MTX=128 x 128, ETL=8, NEX=1, NS=5, ST=1 mm, and IT=1.1 mm. For whole-body MRI of mice, T_{1w} and T_{2w} scout images were initially performed to be used as reference images for prescribing the final coronal sections through the main organs of interest (kidneys, liver, bladder and muscle). For T_{1w} images were acquired with a MSME sequence with TR=400 ms, TE=10 ms, FA=180°, TA=1 min 42 s 400 ms, FOV=9 x 3 cm^2, MTX=256 x 128, ETL=1, NEX=2, NS=12, ST=1 mm, and IT=1.2 mm. For T_{2w} images were acquired with a RARE sequence with TR=4000 ms, TE=12 ms, TE_{eff}=36 ms, FA=180°, TA=1 min 36 s 0 ms, FOV=9 x 3 cm^2, MTX=256 x 128, ETL=4, NEX=1, NS=12, ST=1 mm, and IT=1.2 mm. For T_1 maps were acquired a RARE-VTR sequence with TR list=350, 500, 1000, 2000, 3000 ms, TE=7.5 ms, FA=180°, TA=5 min 52 s 800 ms, FOV=9 x 3 cm^2, MTX=128 x 128, ETL=2, NEX=1, NS=12, ST=1 mm, and IT=1.2 mm. For T_2 maps were acquired with MSME sequence with TR=3000 ms, TE=7.5, TE_{eff}=225 ms, FA=180°, TA=4 min 48 s 0 ms, FOV=9 x 3 cm^2, MTX=128 x 128, ETL=1, NEX=1, NS=12, ST=1 mm, and IT=1.2 mm.

MRI data processing and post-processing

To process the brain MRI data related to the CA, ROIs were defined in both T_{1w} and T_{2w} images. Specifically, two ROIs were manually defined in each slice, one within the tumour area and the other within the contralateral normal brain tissue. Absolute signal intensities for both T_{1w} and T_{2w} sequences were obtained from several slices of multiple images acquired at different time points. Three images were obtained before CA administration (pre-administration) and multiple were acquired after CA administration (post-administration) at 30 minutes, 2 hours and 24 hours. The RCE was computed using the following Equation **4.2**:

$$RCE\ (\%)_{Brain} = \frac{S_t}{S_c}\ x\ 100 \qquad \text{Equation } \mathbf{4.2}$$

where RCE represents the relative contrast enhancement in the brain, S_t indicates the absolute signal intensity of the tumour, and S_c indicates the absolute signal intensity of the contralateral normal brain tissue.

For reference, RCE value for pre-administration images was set to 100% RCE for T_{2w} and to 0% RCE for T_{1w}. From this reference, values for post-administration images were then calculated for each time point: 30 minutes, 2 hours, and 24 hours after CA administration.

To process the whole-body MRI data related to the CA, ROIs were defined in both T_1 and T_2 map images. Specifically, different ROIs were manually defined in each slice, selecting the organs of interest: kidneys (renal cortex and renal medulla), liver, bladder and muscle. T_{1w} and T_{2w} and absolute signal intensities for both T_{1w} and T_{2w} maps sequences were obtained from several slices of multiple images acquired at different time points. One map image was obtained before CA administration (pre-administration) and multiple were acquired after CA administration (post-administration) at 30 minutes, 2 hours and 24 hours. The RCE for each organ was computed using the following Equation **4.3**:

$$RCE\ (\%)_{Organ} = \frac{S_o}{S_m}\ x\ 100 \qquad \text{Equation } \mathbf{4.3}$$

where RCE represents the relative contrast enhancement in each organ, S_o indicates the absolute signal intensity of the organ, and S_m indicates the absolute signal intensity of the muscle tissue.

For reference, RCE value for pre-administration images was set to 100% RCE for T_2 and to 0% RCE for T_1. From this reference, values for post-administration images were then calculated for each time point: 30 minutes, 2 hours, and 24 hours after CA administration.

Tolerability assay

C57BL/6J female mice of 10 weeks of age and with body weights 20.0 ± 0.4 g (n = 6), were randomly assigned to two groups: control and **pDPA-CNP@Fe NPs**, with three mice in each group. The treatment group received increasing i.v. doses of **pDPA-CNP@Fe NPs**, ranging from 0.002 to 0.24 mmol Fe·kg^{-1}, doubling with each administration. A 72-hour interval was maintained between administrations. The control group received vehicle administrations consisting of saline buffer supplemented with 0.5 mM MSA. Body weight and additional welfare parameters were monitored for 30 days following the final administration to detect any clinical signs of distress or adverse effects. No higher doses were evaluated.

Biodistribution assay

Biodistribution of **pDPA-CNP@Fe NPs** was evaluated at 2- and 24-hours post i.v. tail administration in C57BL/6J female mice. For this, GL261 tumour-bearing mice after 19.5 ± 1.5 days post tumour implantation with tumour volume of 66.2 ± 23.8 mm^3 (n=9), were randomly assigned to three groups: control, **pDPA-CNP@Fe NPs** 2 hours and **pDPA-CNP@Fe NPs** 24 hours, with three mice in each group. **pDPA-CNP@Fe NPs** groups received i.v. tail administration of 0.012 mmol Fe·kg^{-1} in 100 µL of PBS containing 0.5% MSA, the same dose that will be used in MRI assays. After 2- or 24-hours post administration, the mice were euthanised and the organ tissues of interest (brain, tumour, kidneys, liver, spleen and bladder) excised, weighted, and stored at -80 °C.

Organ tissues were placed directly on the RINO 1.5 mL screw cap tubes with 100 µL of 0.5 mm zirconium oxide beads from Sigma-Aldrich (Merck, Spain) and variably volumes of tissue protein extraction reagent (T-PER™, Thermo Scientific, USA), specifically twice the volume of every tissue volume was added. The organ tissues were then homogenised for 5 minutes at power level 8, except for the kidney at power level 12, using the Bullet Blender® (Next Advanced, USA). Finally, the homogenate was collected in Eppendorf tubes.

ICP-MS analysis was performed at *Parque Científico Tecnológico* of the *Universidad de Burgos,* using an Agilent 8900 ICP-MS/MS with automatic sampler and octupole detector. Measurements were recorded using ^{56}Fe and ^{90}Zr as Fe and Zr tracer. All samples were digested via a closed beaker digestion in the ETHOS SEL Milestone microwave in a 1:7 H_2O_2:HNO_3 suspension for a total of 30 minutes while temperature was kept at 170 °C. Protein quantification was performed using a Bradford kit protocol (Quick Start Bradford Dye reagent X1, Bio-Rad, USA). All samples were diluted 1:100 with PBS.

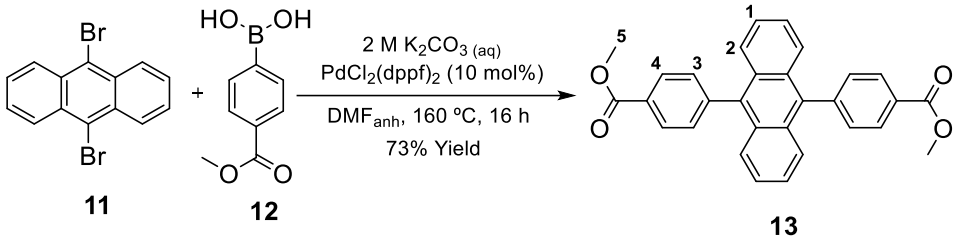
Finality, **pDPA-CNP@Fe NP** biodistribution was quantified via determination of Fe levels within different organs and normalised them with corresponding protein (μg Fe·mg^{-1} protein of tissue) and weight (μg Fe·mg^{-1} organ tissue).

Statistical analysis

Data were analysed using GraphPad Prism (version 8.0) and values are represented as the mean ± SE of independent experiments. Statistical differences were calculated using two-way ANOVA, followed by Dunnett multiple comparison test for MRI data. Statistical differences were calculated using two-way ANOVA, followed by Turkey multiple comparison test for biodistribution assay. The significance threshold for all tests was set at $p < 0.05$, and values falling between 0.05 and 0.1 were regarded as a "trend toward significance".

4.5.5. Synthesis procedures

Synthesis of dimethyl 4,4'-(anthracene-9,10-diyl)dibenzoate (13)



Scheme **4.1.** synthesis of 4,4'-(anthracene-9,10-diyl)dibenzoate (**13**) from 9,10-dibromoanthracene (**11**) and 4-(methoxycarbonyl) phenyl) boronic acid (**12**).

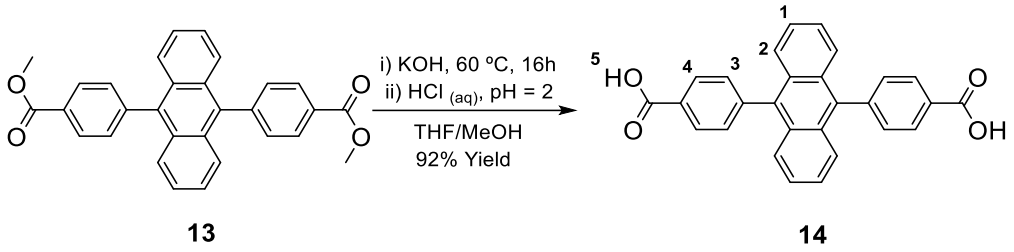
A solution of 9,10-dibromoanthracene (**11**) (375 mg, 1.11 mmol), 4 - (methoxycarbonyl) phenyl) boronic acid (**12**) (502.5 mg, 2.79 mmol) and $PdCl_2(dppf)_2$ in catalytic proportions (81 mg, 0.111 mmol) were prepared in 30 ml of anhydrous and degassed $DMF_{(anh)}$. Then, and while in constant and vigorous stirring, a solution of $K_2CO_{3(aq)}$ (15 mL, 2 M) was added to the first solution. The resulting mixture was then allowed to react at 160 °C for 16 hours, obtaining a viscous yellow oil.

The resulting crude product was then purified by column chromatography (silica gel, CH_2Cl_2), affording the diphenyl anthracene ester **13** as an off-white solid (376.4 mg, 0.84 mmol, 73.0% yield)

Spectroscopic information of **13**:

^{1}H-NMR (400 MHz, Chloroform-*d*) δ 8.30 (d, $J_{4,3}$ = 8.6 Hz, 4H), 7.62 (m, 4H), 7.58 (d, $J_{1,2}$ = 6.8Hz, 4H), 7.38 – 7.32 (m, 4H), 4.03 (s, 6H).

Synthesis of 4,4'-(anthracene-9,10-diyl)dibenzoic acid (14)



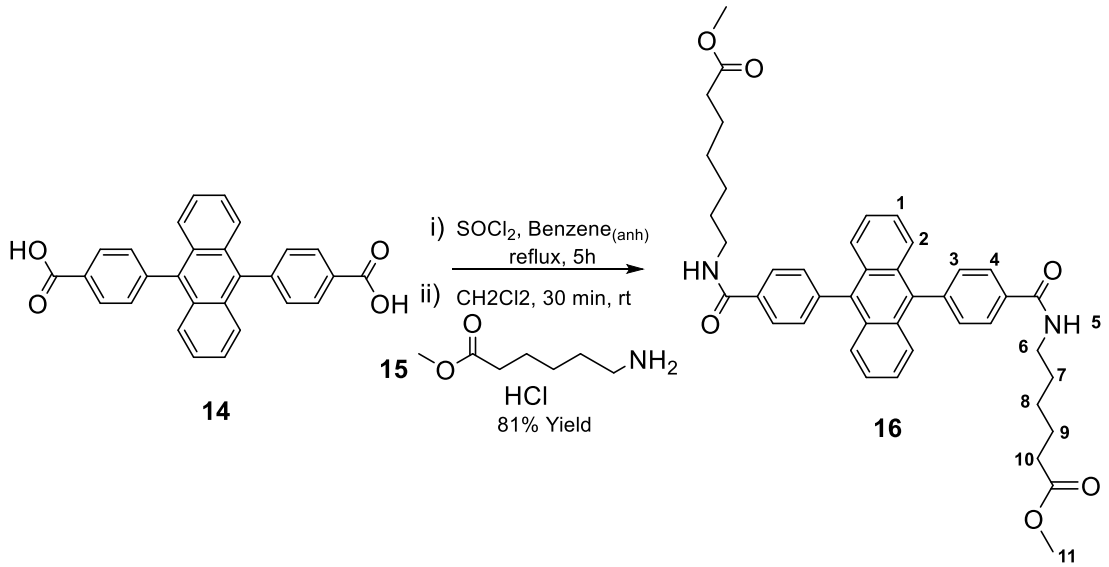
Scheme **4.2.** Synthesis of 4,4'-(anthracene-9,10-diyl)dibenzoic acid (**14**) from 4,4'-(anthracene-9,10-diyl)dibenzoate (**13**).

The diphenyl anthracene ester **13** (347.2 mg, 0.77 mmol) was suspended in a 1:1 MeOH:THF solution (50 mL). While under vigorous stirring, KOH(aq) (15 mL, 2 M) was added, and the resulting solution was refluxed at 60 °C for 16 hours. The reaction was then allowed to cool down to room temperature, and $HCl_{(aq)}$ (8 M) was used to bring down the pH to 2. The resulting precipitate was isolated and rinsed with water and THF to afford the anthracene carboxylic acid **14** as a white powder solid (297.2 mg, 0.71 mmol, 92.3% yield)

Spectroscopic information of **14**:

^{1}H-NMR (400 MHz, DMSO-d_6) δ 13.12 (s, 2H), 8.17 (d, $J_{4,2}$ = 8.2 Hz, 4H), 7.56 (d, $J_{2,4}$ = 8.2 Hz, 4H), 7.57-7.51 (m, 4H), 7.43-7.38 (m, 4H).

Synthesis of *dimethyl 4,4'-((4,4'-(anthracene-9,10-diyl)bis(benzoyl))bis-(azanediyl))dibutyrate (16)*



Scheme **4.3.** Synthesis of 4,4'-((4,4'-(anthracene-9,10-diyl)bis(benzoyl))bis-(azanediyl))dibutyrate (**16**) from 4,4'-(anthracene-9,10-diyl)dibenzoic acid (**14**).

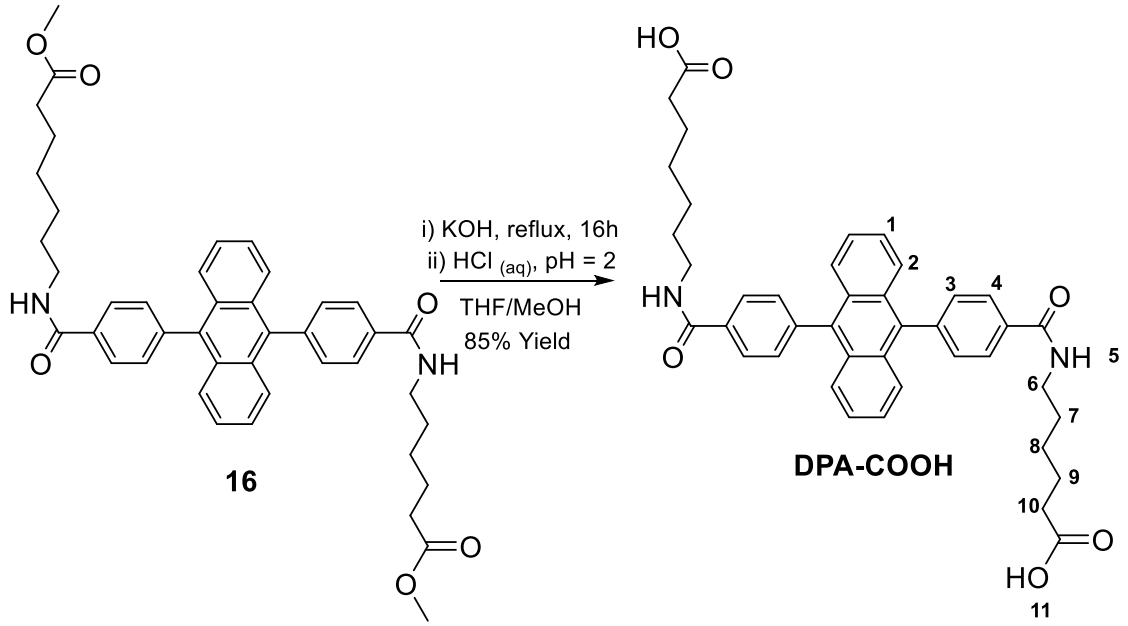
The anthracene carboxylic acid **14** (120 mg, 0.29 mmol) was suspended in anhydrous benzene (10 mL) under an inert atmosphere. Thionyl chloride (21 µL, 0.29 mmol) was then added, and the resulting solution was refluxed for 5 hours in the presence of a catalytic quantity of DMF (50 µL). Benzene and excess thionyl chloride were then removed under reduced pressure evaporation.

The resulting off-yellow residue was diluted in anhydrous CH_2Cl_2, and methyl 4-aminobutanoate hydrochloride (49 mg, 0.29 mmol) was added. The mixture was then allowed to evolve at room temperature for 30 minutes. The resulting precipitate was isolated by filtration and washed several times with CH_2Cl_2, affording ester **16** as a white powder solid (157 mg, 0.23 mmol, 81.1% yield).

Spectroscopic information of **16**:

^{1}H-NMR (400 MHz, Chloroform-*d*) δ 8.04 (d, $J_{4,3}$=8.2 Hz 4H), 7.65 (dd, $J_{1,2\text{-}1,3}$ = 6.8, 3.3 Hz, 4H), 7.59 (d, $J_{3,4}$=8.2 Hz, 4H), 7.37 (dd, $J_{2,1\text{-}2,3}$ = 6.8, 3.3 Hz, 4H), 6.41 (t, $J_{5,6}$ = 5.8 Hz, 2H), 3.71 (s, 6H), 3.60 (q, $J_{6,7\text{-}6,5}$ = 6.7, Hz, 4H), 2.40 (t, $J_{10,9}$ = 7.3 Hz, 4H), 1.80 – 1.72 (m, 8H), 1.56 – 1.47 (m, 4H).

Synthesis of 7-(4-(10-(4-((5-carboxypentyl)carbamoyl)phenyl)anthracen-9-yl)benzamido)heptanoic acid (DPA-COOH)



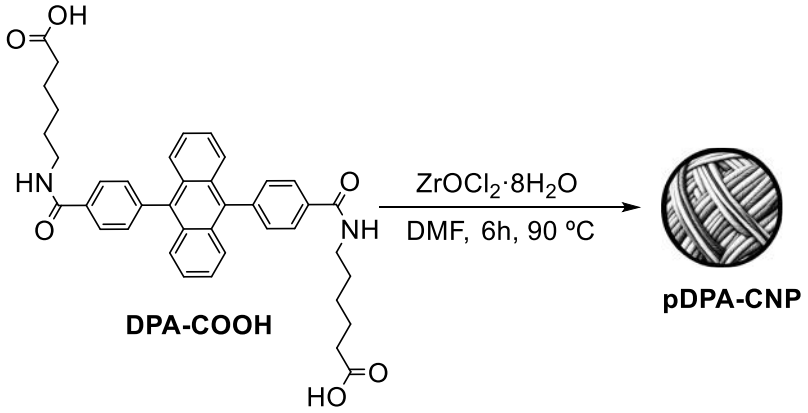
Scheme **4.4.** Synthesis of 7-(4-(10-(4-((5-carboxypentyl)carbamoyl)phenyl)anthracen-9- yl)benzamido)heptanoic acid (**DPA-COOH**) from 4,4'-((4,4'-(anthracene-9,10-diyl)bis(benzoyl))bis-(azanediyl))dibutyrate (**16**).

Ester **16** (157 mg, 0.23 mmol) was dissolved in MeOH:1,4-dioxane 1:1 to a total volume of 60 mL. To this solution, and under vigorous stirring, $KOH_{(aq)}$ (2 M, 30 mL) was added. The resulting solution was then refluxed at 60 °C for 16 hours. Afterwards, the reaction was allowed to cool down to room temperature and $HCl_{(aq)}$ (8 M) was used to bring the pH down to 2. The resulting precipitate was isolated by filtration and rinsed with water, MeOH and 1,4-dioxane to afford the final product **DPA-COOH** (129.1 mg, 19.6 mmol, 85.1% yield) as an off-white powder.

Spectroscopic information of **DPA-COOH**:

^{1}H-NMR (400 MHz, N, N-dimethyl-formamide-d_7) δ 12.35 (s, 2H), 8.75 (t, $J_{5,6}$ = 5.7 Hz, 2H), 8.32 (d, $J_{2,1}$= 8.1 Hz, 4H), 7.73 – 7.62 (m, 8H), 7.51 (dd, $J_{1,2\text{-}1,3}$ = 6.9, 3.2 Hz, 4H), 3.51 (q, $J_{6,5\text{-}6,7}$ = 6.7 Hz, 5H), 2.36 (t, $J_{10,9}$ = 7.3 Hz, 4H), 1.78 – 1.63 (m, 8H), 1.51 (m, 4H). IR ν 3228 (m), 3087 (w), 2926 (w), 2862 (w), 1633 (s), 1549 (w), 1435 (w), 1268 (s), 1216 (w), 875 (w), 809 (w), 670 (m) cm^{-1}. MS-ESI (m/z) [M]$^-$ Calcd. for $C_{40}H_{40}N_2O_6$ 643.28, found 643.28.

Synthesis of polymeric Zr-based diphenyl-anthracene coordination nanoparticle (pDPA-CNP)



Scheme **4.5.** Synthesis **of pDPA-CNP** from 7-(4-(10-(4-((5-carboxypentyl)carbamoyl)phenyl)anthracen-9-yl)benzamido)heptanoic acid (**DPA-COOH**).

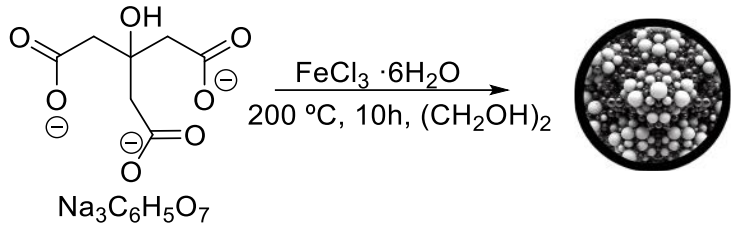
Zirconyl chloride octahydrate ($ZrCl_2 \cdot 8H_2O$) (11.0 mg) and **DPA-COOH** (4.0 mg) were dissolved in 1 mL DMF each separately. Sonication was performed until both spices were totally dissolved. The **DPA** solution was then added to the $ZrCl_2 \cdot 8H_2O$ one. DMF (2 mL) was added to the resulting solution, bringing the final volume to 4 mL. The mixture was then heated to 90 °C under vigorous stirring for a total of 4 hours. The white suspension of **pDPA-NPs** formed was then isolated by centrifugation and washed multiple times with DMF and water. The sample was resuspended in water for storage, yielding **pDPA-NPs** as a pale white suspension in a 4.1 mg yield.

Spectroscopic information of **pDPA-CNP**:

IR v: 3308 (m), 2936 (m), 2862 (w), 1616 (w), 1541 (s) , 1438 (w), 1436 (s), 1373 (w) 1312 (m), 1171 (w), (w), 1020 (w), 843 (w), 761 (w), 668 (w) cm^{-1}; Z-Ave (H_2O) 135.9 ± 4.60 nm; PDI (H_2O) 0.102 ± 0.008 ; ζ-pot 42.5 ± 0.458 mV; ICP-MS Zr (%(w/w)) calcd. 4.50% found 15.8% XPS (Zr) fit calcd. 182.7, 179, 180.8 eV.

Synthesis of superparamagnetic iron oxide nanoparticle (Fe-Clustered NP)

Synthesis of Fe-Clustered NPs followed reported procedure from the literature with minor modifications.[141]



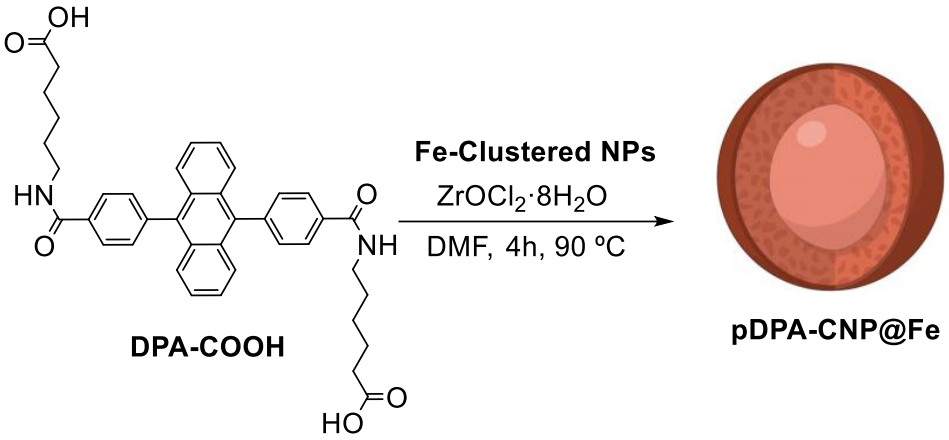
Scheme **4.6.** Synthesis of **Fe-Clustered NPs** from sodium citrate and Fe(III) chloride hexahydrate.

$FeCl_3 \cdot 6H_2O$ (0.31 g), $C_8H_3Na_3O_7 \cdot 2H_2O$ (0.12 g), and NaOAc (0.60 g) were dissolved in 10 mL of ethylenglycol under vigorous stirring for 30 minutes. The reaction was then transferred to a stainless-steel autoclave and heated to 200 °C for 10 hours. The reaction was then allowed to cool down to room temperature. The resulting suspension was then isolated magnetically and washed with water and ethanol. Yielding the final SPION core Fe-Clustered NPs as a magnetically active brown pellet that was resuspended in ethanol for further use.

Spectroscopic information of **Fe-Clustered NPs**:

IR v: 3378 (m), 1589 (s) , 1389 (s), 1054 (w), 541 (s) cm^{-1}; Z-Ave (H_2O) 221.3 ± 1.8 nm; PDI (H_2O) 0.120 ± 0.037; ζ-pot -7.60 ± 0.28 mV; ICP-MS Fe (%(w/w)) found 65.2 ± 2.3% XRD 2θ: 30º, 35.5º, 43.3º, 53.3º, 57º, 62.7º, 74.5º.

Synthesis of polymeric Zr-based diphenyl-anthracene on Fe-based Super Paramagnetic Iron Oxide Core Shell Nanoparticle (pDPA-CNP@Fe NP)



Scheme **4.7.** Synthesis of **pDPA-CNP@Fe NP** from **Fe-Clustered NPs** and 7-(4-(10-(4-((5-carboxypentyl)carbamoyl)phenyl)anthracen-9- yl)benzamido)heptanoic acid (**DPA-COOH**).

Zirconyl chloride octahydrate (ZrCl2·8H2O) (11.0 mg), **DPA-COOH** (4.0 mg) and the SPION core NPs (1.0 mg) are dissolved/suspended in 1 mL DMF. Sonication was performed until all spices were totally dissolved/suspended. The **DPA-COOH**'s and **Fe-Clustered NPs** solutions were then added to the ZrCl2·8H2O one. DMF (1 mL) was added to the resulting solution, bringing the final volume to 4 ml. The mixture was then heated in the oven without stirring at 50 °C for 15 minutes and then brought to 90 °C for 4 hours. At that point, the solution will have passed from dark brown to orange. The orange suspension of **pDPA-CNP@Fe NPs** was then isolated by centrifugation and washed with DMF and water magnetically. The sample was then resuspended in water for storage, yielding the iron core shell NPs as a pale orange suspension in a 2.3 mg yield.

Spectroscopic information of **pDPA-CNP@Fe NP**:

IR v: 3302 (s), 2930 (w), 2863 (w), 1634 (s), 1545 (s), 1435(s), 1410(s), 1312 (m), 1169 (s), 1102 (w), 1018 (s), 949 (m), 844 (w), 546 (s); Z-Ave (H_2O) 288.0± 2.0 nm; PDI (H_2O) 0.132 ± 0.041 nm; ζ-pot 43.6 ± 0.6mV; ICP-MS Fe (%(w/w)) found 15.0%.

4.6. References

1. Sosa V, Moliné T, Somoza R, Paciucci R, Kondoh H, LLeonart ME. Oxidative stress and cancer: An overview. *Ageing Res Rev.* **2013**;12(1). doi:10.1016/j.arr.2012.10.004
2. Maharjan PS, Bhattarai HK. Singlet Oxygen, Photodynamic Therapy, and Mechanisms of Cancer Cell Death. *J Oncol.* **2022**;2022. doi:10.1155/2022/7211485
3. Bhanja D, Wilding H, Baroz A, et al. Photodynamic Therapy for Glioblastoma: Illuminating the Path toward Clinical Applicability. *Cancers*. **2023**;15(13). doi:10.3390/cancers15133427
4. Kim HS, Lee DY. Nanomedicine in Clinical Photodynamic Therapy for the Treatment of Brain Tumors. *Biomed.* **2022**;10(1). doi:10.3390/biomedicines10010096
5. Aldhubiab B, Almuqbil RM. Polymeric Nanoparticle-Mediated Photodynamic Therapy: A Synergistic Approach for Glioblastoma Treatment. *Pharm*. **2025**;18(7):1057. doi:10.3390/ph18071057
6. Zhao X, Zhao R, Nie G. Nanocarriers based on bacterial membrane materials for cancer vaccine delivery. *Nat Protoc*. **2022**;17(10). doi:10.1038/s41596-022-00713-7
7. Jardón-Guadarrama G, Manríquez-Ramírez ME, Rodríguez-Pérez CE, et al. TiO2-ZnPc nanoparticles functionalized with folic acid as a target photosensitizer for photodynamic therapy against glioblastoma cells. *J Mater Sci Mater Med*. **2024**;35(1):51. doi:10.1007/s10856-024-06823-w
8. Zhang F, Wen C, Peng Y, et al. Biomimetic lipid nanoparticles for homologous-targeting and enhanced photodynamic therapy against glioma. *Eur. J. Pharm. Sci.* **2023**;190. doi:10.1016/j.ejps.2023.106574
9. Baglo Y, Sorrin AJ, Liang BJ, Huang HC. Harnessing the Potential Synergistic Interplay Between Photosensitizer Dark Toxicity and Chemotherapy. *Photochem Photobiol*. **2020**;96(3). doi:10.1111/php.13196
10. Borah ST, Mondal A, Das B, Saha S, Das Sarma J, Gupta P. β-Cyclodextrin Encapsulated Platinum(II)-Based Nanoparticles: Photodynamic Therapy and Inhibition of the NF-κB Signaling Pathway in Glioblastoma. *ACS Appl Bio Mater.* **2025**;8(4):3331-3342. doi:10.1021/acsabm.5c00103
11. Paul M, Itoo AM, Ghosh B, Biswas S. Hypoxia alleviating platinum(IV)/chlorin e6-based combination chemotherapeutic-photodynamic nanomedicine for oropharyngeal carcinoma. *J Photochem Photobiol B.* **2023**;238:112627. doi:10.1016/j.jphotobiol.2022.112627
12. Shi L, Sordillo LA, Rodríguez-Contreras A, Alfano R. Transmission in near-infrared optical windows for deep brain imaging. *J Biophotonics*. **2016**;9(1-2). doi:10.1002/jbio.201500192
13. Jacques SL. Optical properties of biological tissues: A review. *Phys Med Biol.* **2013**;58(11). doi:10.1088/0031-9155/58/11/R37
14. Lapchak PA, Boitano PD. Transcranial near-infrared laser therapy for stroke: How to recover from futility in the NEST-3 clinical trial. In: *Acta Neurochir. Suppl*. Vol 121. **2016**. doi:10.1007/978-3-319-18497-5_2
15. Lapchak PA, Boitano PD, Butte P V., et al. Transcranial near-infrared laser transmission (NILT) profiles (800 nm): Systematic comparison in four common research species. *PLoS One*. **2015**;10(6). doi:10.1371/journal.pone.0127580
16. Wang EB, Kaur R, Fierro M, Austin E, Jones LR, Jagdeo J. Safety and penetration of light into the brain. In: Photobiomodulation in the Brain: Low-Level Laser (Light) *Ther. Neurol. Neurosci*. **2019**. doi:10.1016/B978-0-12-815305-5.00005-1
17. Ding D, Feng Y, Qin R, et al. Mn 3+ -rich oxide/persistent luminescence nanoparticles achieve light-free generation of singlet oxygen and hydroxyl radicals for responsive imaging and tumor treatment *Theranostics.* **2021**;11(15). doi:10.7150/thno.62437
18. Lioret V, Bellaye PS, Bernhard Y, et al. Cherenkov Radiation induced photodynamic therapy - repurposing older photosensitizers, and radionuclides. *Photodiagnosis Photodyn Ther*. **2023**;44. doi:10.1016/j.pdpdt.2023.103816
19. Canaparo R, Foglietta F, Barbero N, Serpe L. The promising interplay between sonodynamic therapy and nanomedicine. *Adv Drug Deliv Rev*. **2022**;189. doi:10.1016/j.addr.2022.114495
20. Ding X, Chang M. Catalytically Active NaNbO3 Nanorods for Sonodynamic Cancer Therapy. doi:10.48550/arXiv.2310.11793
21. You DG, Deepagan VG, Um W, et al. ROS-generating TiO2 nanoparticles for non-invasive sonodynamic therapy of cancer. *Sci Rep*. **2016**;6. doi:10.1038/srep23200
22. Chen X, Wang L, Liu S, Luo X, Wang K, He Q. Cisplatin-loaded metal–phenolic network with photothermal-triggered ROS generation for chemo-photothermal therapy of cancer. *Cancer Nanotechnol*. **2022**;13(1). doi:10.1186/s12645-022-00149-4
23. Meng X, Chen L, Lv R, Liu M, He N, Wang Z. A metal-phenolic network-based multifunctional nanocomposite with pH-responsive ROS generation and drug release for synergistic chemodynamic/photothermal/chemo-therapy. *J Mater Chem B*. **2020**;8(10). doi:10.1039/d0tb00008f
24. Wang L, Yang M, Gao R, et al. Thermal responsive nanobombs generating reactive oxygen species for synergistic anticancer therapy. *J Colloid Interface Sci*. **2025**;687:607-616. doi:10.1016/j.jcis.2025.02.091

25. Anilkumar TS, Lu YJ, Chen HA, Hsu HL, Jose G, Chen JP. Dual targeted magnetic photosensitive liposomes for photothermal/photodynamic tumor therapy. *J Magn Magn Mater*. **2019**;473. doi:10.1016/j.jmmm.2018.10.020

26. GILCHRIST RK, MEDAL R, SHOREY WD, HANSELMAN RC, PARROTT JC, TAYLOR CB. Selective inductive heating of lymph nodes. *Ann Surg*. **1957**;146(4). doi:10.1097/00000658-195710000-00007

27. Blanco-Andujar C, Teran FJ, Ortega D. Current Outlook and Perspectives on Nanoparticle-Mediated Magnetic Hyperthermia. In: IIron Oxide Nanopart. *Biomed. Appl*.. **2018**. doi:10.1016/b978-0-08-101925-2.00007-3

28. Kok HP, Kotte ANTJ, Crezee J. Planning, optimisation and evaluation of hyperthermia treatments. *Int. J. Hyperthermia*.. **2017**;33(6):593-607. doi:10.1080/02656736.2017.1295323

29. Jiménez-López MC, Moreno-Maldonado AC, Martín-Morales N, et al. Novel cisplatin-magnetoliposome complex shows enhanced antitumor activity via Hyperthermia. *Sci Rep*. **2025**;15(1). doi:10.1038/s41598-025-88533-z

30. Omidian S, Nazarpak MH, Bagher Z, Moztarzadeh F. Vanadium ferrite-doped mesoporous bioactive glass-ceramics: controlled cisplatin delivery in chemohyperthermia. *RSC Adv*. **2025**;15(23):18657-18669. doi:10.1039/d5ra01999k

31. Di Corato R, Béalle G, Kolosnjaj-Tabi J, et al. Combining magnetic hyperthermia and photodynamic therapy for tumor ablation with photoresponsive magnetic liposomes. *ACS Nano*. **2015**;9(3). doi:10.1021/nn506949t

32. Huang WC, Shen MY, Chen HH, et al. Monocytic delivery of therapeutic oxygen bubbles for dual-modality treatment of tumor hypoxia. *J. Control. Release*.. **2015**;220. doi:10.1016/j.jconrel.2015.09.016

33. Ma X, Wang Y, Liu XL, et al. Fe3O4-Pd Janus nanoparticles with amplified dual-mode hyperthermia and enhanced ROS generation for breast cancer treatment. *Nanoscale Horiz*. **2019**;4(6). doi:10.1039/c9nh00233b

34. Yan H, Shang W, Sun X, et al. "All-in-One" Nanoparticles for Trimodality Imaging-Guided Intracellular Photo-magnetic Hyperthermia Therapy under Intravenous Administration. *Adv Funct Mater*. **2018**;28(9). doi:10.1002/adfm.201705710

35. Curcio A, Silva AKA, Cabana S, et al. Iron oxide nanoflowers @ cus hybrids for cancer tri-therapy: Interplay of photothermal therapy, magnetic hyperthermia and photodynamic therapy. *Theranostics*. **2019**;9(5). doi:10.7150/thno.30238

36. Arnaut LG, Pereira MM, Dąbrowski JM, et al. Photodynamic therapy efficacy enhanced by dynamics: The role of charge transfer and photostability in the selection of photosensitizers. *Chem. Eur. J.*. **2014**;20(18). doi:10.1002/chem.201304202

37. Frey B, Weiss EM, Rubner Y, et al. Old and new facts about hyperthermia-induced modulations of the immune system. *Int. J. Hyperthermia*.. **2012**;28(6). doi:10.3109/02656736.2012.677933

38. Firczuk M, Nowis D, Gołb J. PDT-induced inflammatory and host responses. Photochem. Photobiol. Sci.. **2011**;10(5). doi:10.1039/c0pp00308e

39. Kim YK, Lee JY, Suh HN. Cytokine-Induced JAK2-STAT3 Activates Tissue Regeneration under Systemic or Local Inflammation. *Int J Mol Sci.* **2022**;23(4). doi:10.3390/ijms23042262

40. Zhang HG, Mehta K, Cohen P, Guha C. Hyperthermia on immune regulation: A temperature's story. *Cancer Lett.* **2008**;271(2). doi:10.1016/j.canlet.2008.05.026

41. Oei AL, Vriend LEM, Crezee J, Franken NAP, Krawczyk PM. Effects of hyperthermia on DNA repair pathways: One treatment to inhibit them all. *Radiat. Oncol*.. **2015**;10(1). doi:10.1186/s13014-015-0462-0

42. Hou CH, Lin FL, Hou SM, Liu JF. Hyperthermia induces apoptosis through endoplasmic reticulum and reactive oxygen species in human Osteosarcoma cells. *Int J Mol Sci*. **2014**;15(10). doi:10.3390/ijms151017380

43. Krishnaswami V, Natarajan B, Sethuraman V, Natesan S, RajSelvaraj B. Nano based photodynamic therapy to target tumor microenvironment. *Nano Trends*. **2023**;1. doi:10.1016/j.nwnano.2023.100003

44. Kurokawa H, Ito H, Terasaki M, Matsui H. Hyperthermia enhances photodynamic therapy by regulation of HCP1 and ABCG2 expressions via high level ROS generation. *Sci Rep*. **2019**;9(1). doi:10.1038/s41598-018-38460-z

45. Rivera D, Bouras A, Mattioli M, et al. Magnetic hyperthermia therapy enhances the chemoradiosensitivity of glioblastoma. *Sci Rep*. **2025**;15(1). doi:10.1038/s41598-025-95544-3

46. Hu A, Pu Y, Xu N, et al. Hierarchically decorated magnetic nanoparticles amplify the oxidative stress and promote the chemodynamic/magnetic hyperthermia/immune therapy. *Acta Biomater*. **2024**;173. doi:10.1016/j.actbio.2023.11.023

47. Chatterjee K, Sarkar S, Jagajjanani Rao K, Paria S. Core/shell nanoparticles in biomedical applications. *Adv Colloid Interface Sci.* **2014**;209. doi:10.1016/j.cis.2013.12.008

48. Oldenburg SJ, Averitt RD, Westcott SL, Halas NJ. Nanoengineering of optical resonances. *Chem Phys Lett*. **1998**;288(2-4). doi:10.1016/S0009-2614(98)00277-2

49. Allen C. The question of toxicity of nanomaterials and nanoparticles. *J. Control. Release*.. **2019**;304. doi:10.1016/j.jconrel.2019.06.008

50. Yeo RJ, Yeo JCC, Yu Tan S, et al. Core-Shell Micro- and Nano-Structures for The Modification of Light-Surface Interactions. *Adv Opt Mater*. **2024**;12(4). doi:10.1002/adom.202301955

51. Gerasov N, Shandura M, Kovtun Y, Losytskyy M, Negrutska V, Dubey I. Fluorescent labeling of proteins with amine-specific 1,3,2-(2H)-dioxaborine polymethine dye. *Anal Biochem*. **2012**;420(2). doi:10.1016/j.ab.2011.09.018

52. Wang Y, Li Y, Cui Y, et al. Duplex SYBR Green I-based real-time PCR assay for the rapid detection of canine kobuvirus and canine astrovirus*. J Virol Methods*. **2021**;290. doi:10.1016/j.jviromet.2021.114066

53. Li Q, Li C, Wang Y, et al. Bimagnetic Core/Shell Nanoprobes with Tunable Exchange Coupling for High Resolution and Sensitive Magnetic Particle Imaging. *Angew. Chem. Int. Ed.*. **2025**;64(6). doi:10.1002/anie.202418015

54. Awiaz G, Lin J, Wu A. Recent advances of Au@Ag core–shell SERS-based biosensors. *Exploration*. **2023**;3(1). doi:10.1002/EXP.20220072

55. Casper J, Nicolle L, Willimann M, et al. Core–Shell Structured Chitosan-Polyethylenimine Nanoparticles for Gene Delivery: Improved Stability, Cellular Uptake, and Transfection Efficiency. *Macromol Biosci*. **2023**;23(1). doi:10.1002/mabi.202200314

56. Cheng B, Ahn HH, Nam H, et al. A Unique Core–Shell Structured, Glycol Chitosan-Based Nanoparticle Achieves Cancer-Selective Gene Delivery with Reduced Off-Target Effects. *Pharmaceutics*. **2022**;14(2). doi:10.3390/pharmaceutics14020373

57. Yang Z, Xie Y, Song J, et al. Self-Assembly of Biocompatible Core-Shell Nanocapsules with Tunable Surface Functionality by Microfluidics for Enhanced Drug Delivery. *Adv Funct Mater*. **2024**;34(44). doi:10.1002/adfm.202407112

58. Shi Y, Zhang Y, Zhu L, Miao Y, Zhu Y, Yue B. Tailored Drug Delivery Platforms: Stimulus-Responsive Core–Shell Structured Nanocarriers. *Adv Healthc Mater*. **2024**;13(1). doi:10.1002/adhm.202301726

59. Liu Y, Chen X, Lin X, et al. Electrospun multi-chamber core–shell nanofibers and their controlled release behaviors: A review. Wiley *Interdiscip Rev Nanomed Nanobiotechnol*. **2024**;16(2). doi:10.1002/wnan.1954

60. Akila B, Kogularasu S, Vasu D, et al. Bio-waste derived hierarchical hydroxyapatite core–Shell manganese ferrite ceramic biomaterial: Structural, morphological characterization, and controlled drug release properties. *Ceram Int*. **2025**;51(16):22698-22706. doi:10.1016/j.ceramint.2024.12.317

61. Abdolrahimi M, Vasilakaki M, Slimani S, et al. Magnetism of nanoparticles: Effect of the organic coating. *Nanomaterials.* **2021**;11(7). doi:10.3390/nano11071787

62. Zheltova V, Vlasova A, Bobrysheva N, et al. Fe3O4@HAp core–shell nanoparticles as MRI contrast agent: Synthesis, characterization and theoretical and experimental study of shell impact on magnetic properties. *Appl Surf Sci.* **2020**;531. doi:10.1016/j.apsusc.2020.147352

63. Yue H, Zhao D, Tegafaw T, et al. Core-Shell Fe3O4@C Nanoparticles as Highly Effective T2 Magnetic Resonance Imaging Contrast Agents: In Vitro and In Vivo Studies. *Nanomaterials*. **2024**;14(2). doi:10.3390/nano14020177

64. Na H, Carrier J, Oyon S, Lai CY. Fabrication of Rhenium Disulfide/Mesoporous Silica Core-Shell Nanoparticles for a pH-Responsive Drug Release and Combined Chemo-Photothermal Therapy. *ACS Appl Bio Mater*. **2024**;7(5):3337-3345. doi:10.1021/acsabm.4c00291

65. Kaliaperumal K, Subramanian K, Seenivasan A, et al. Development of smart core-shell nanoparticles-based sensors for diagnostics of salivary alpha-amylase in biomedical and forensics. *E-Polymers*. **2024**;24(1). doi:10.1515/epoly-2023-0051

66. Sathiyaseelan A, Saravanakumar K, Mariadoss AVA, Wang MH, Manikandan M, Shajahan A. Core-shell silver nanoparticles: Synthesis, characterization, and applications. In: Green Synthesis of Silver Nanomaterials. Elsevier; **2022**:75-97. doi:10.1016/B978-0-12-824508-8.00007-1

67. Friedrich RP, Janko C, Unterweger H, Lyer S, Alexiou C. SPIONs and magnetic hybrid materials: Synthesis, toxicology and biomedical applications. *Phys. Sci*. Rev.. **2023**;8(8):1435-1464. doi:10.1515/psr-2019-0093

68. Maheshwari S, Singh A, Verma A, et al. Superparamagnetic iron oxide nanoparticles (SPIONs) in targeting brain tumors: advances and challenges. Med. *Oncol..Springer*. **2025**;42(8). doi:10.1007/s12032-025-02913-z

69. Chandrasekharan P, Tay ZW, Hensley D, et al. Using magnetic particle imaging systems to localize and guide magnetic hyperthermia treatment: Tracers, hardware, and future medical applications. *Theranostics*. **2020**;10(7). doi:10.7150/thno.40858

70. Bulte JWM. Superparamagnetic iron oxides as MPI tracers: A primer and review of early applications. *Adv Drug Deliv Rev*. **2019**;138. doi:10.1016/j.addr.2018.12.007

71. Rubia-Rodríguez I, Santana-Otero A, Spassov S, et al. Whither magnetic hyperthermia? A tentative roadmap. *Materials*. **2021**;14(4). doi:10.3390/ma14040706

72. Li K, Nejadnik H, Daldrup-Link HE. Next-generation superparamagnetic iron oxide nanoparticles for cancer theranostics. *Drug Discov Today*. **2017**;22(9). doi:10.1016/j.drudis.2017.04.008

73. Girardet T, Venturini P, Martinez H, Dupin JC, Cleymand F, Fleutot S. Spinel Magnetic Iron Oxide Nanoparticles: Properties, Synthesis and Washing Methods. *Appl. Sci*.. **2022**;12(16). doi:10.3390/app12168127

74. Yoon TJ, Lee H, Shao H, Hilderbrand SA, Weissleder R. Multicore assemblies potentiate magnetic properties of biomagnetic nanoparticles. *Adv. Mater*.. **2011**;23(41). doi:10.1002/adma.201102948

75. Krasia-Christoforou T, Socoliuc V, Knudsen KD, Tombácz E, Turcu R, Vékás L. From single-core nanoparticles in ferrofluids to multi-core magnetic nanocomposites: Assembly strategies, structure, and magnetic behavior. *Nanomaterials*. **2020**;10(11). doi:10.3390/nano10112178

76. Gamarra L, Silva AC, Oliveira TR, et al. Application of hyperthermia induced by superparamagnetic iron oxide nanoparticles in glioma treatment. *Int J Nanomedicine*. **2011**. doi:10.2147/ijn.s14737

77. Kolosnjaj-Tabi J, Di Corato R, Lartigue L, et al. Heat-generating iron oxide nanocubes: Subtle "destructurators" of the tumoral microenvironment. *ACS Nano*. **2014**;8(5). doi:10.1021/nn405356r

78. Xu Z, Shen C, Tian Y, Shi X, Gao HJ. Organic phase synthesis of monodisperse iron oxide nanocrystals using iron chloride as precursor. *Nanoscale*. **2010**;2(6). doi:10.1039/b9nr00400a

79. Nemec S, Kralj S, Wilhelm C, Abou-Hassan A, Rols MP, Kolosnjaj-Tabi J. Comparison of iron oxide nanoparticles in photothermia and magnetic hyperthermia: Effects of clustering and silica encapsulation on nanoparticles' heating yield.*Appl. Sci.* **2020**;10(20). doi:10.3390/app10207322

80. Lee DBN, Roberts M, Bluchel CG, Odell RA. Zirconium: Biomedical and nephrological applications. *ASAIO Journal*. **2010**;56(6). doi:10.1097/MAT.0b013e3181e73f20

81. The MAK Collection for Occupational. doi:10.34865/mb744067vere6_2ad

82. Lin H, Yin C, Mo A. Zirconia Based Dental Biomaterials: Structure, Mechanical Properties, Biocompatibility, Surface Modification, and Applications as Implant. *Front. Dent. Med*.. **2021**;2. doi:10.3389/fdmed.2021.689198

83. Jung S, Moser MM, Kleinheinz J, Happe A. Biocompatibility of lithium disilicate and zirconium oxide ceramics with different surface topographies for dental implant abutments. *Int J Mol Sci*. **2021**;22(14). doi:10.3390/ijms22147700

84. Tang J, Yang H, Qian B, et al. TWIP-assisted Zr alloys for medical applications: Design strategy, mechanical properties and first biocompatibility assessment. *J Mater Sci Technol*. **2024**;184. doi:10.1016/j.jmst.2023.09.051

85. Decoste JB, Peterson GW, Jasuja H, Glover TG, Huang YG, Walton KS. Stability and degradation mechanisms of metal-organic frameworks containing the Zr6O4(OH)4 secondary building unit. *J Mater Chem A Mater*. **2013**;1(18). doi:10.1039/c3ta10662d

86. Mondloch JE, Katz MJ, Planas N, et al. Are Zr6-based MOFs water stable? Linker hydrolysis vs. capillary-force-driven channel collapse. *Chem. Commun*.. **2014**;50(64). doi:10.1039/c4cc02401j

87. Jiang HL, Feng D, Wang K, et al. An exceptionally stable, porphyrinic Zr metal-organic framework exhibiting pH-dependent fluorescence. *J Am Chem Soc*. **2013**;135(37). doi:10.1021/ja406844r

88. Ruyra A, Yazdi A, Espín J, et al. Synthesis, culture medium stability, and in vitro and in vivo zebrafish embryo toxicity of metal-organic framework nanoparticles. *Chem. Eur. J*.. **2015**;21(6). doi:10.1002/chem.201405380

89. Aubry JM, Pierlot C, Rigaudy J, Schmidt R. Reversible binding of oxygen to aromatic compounds. *Acc Chem Res*. **2003**;36(9). doi:10.1021/ar010086g

90. Abdel-Shafi AA, Worrall DR. Mechanism of the excited singlet and triplet states quenching by molecular oxygen in acetonitrile. *J Photochem Photobiol A Chem*. **2005**;172(2). doi:10.1016/j.jphotochem.2004.12.006

91. Societies and Academies. *Nature*. **1926**;118(2962). doi:10.1038/118214a0

92. Clennan EL. Aromatic Endoperoxides†. *Photochem Photobiol*. 2023;99(2). doi:10.1111/php.13674

93. Drews W, Shimidt R, Brauer HD. The Photolysis Of The Endoperoxide Of 9,10-Diphenylanthracene. *Chem Phys Lett*. **1980**;70(1). doi:10.1016/0009-2614(80)80065-0

94. Zhu J, Zou J, Zhang J, Sun Y, Dong X, Zhang Q. An anthracene functionalized BODIPY derivative with singlet oxygen storage ability for photothermal and continuous photodynamic synergistic therapy. J Mater Chem B. **2019**;7(20). doi:10.1039/c9tb00180h

95. He YQ, Tang JH. Anthracene-Based Endoperoxides as Self-Sensitized Singlet Oxygen Carriers for Hypoxic-Tumor Photodynamic Therapy. *Adv Healthc Mater.John Wiley and Sons Inc*. **2025**;14(2). doi:10.1002/adhm.202403009

96. Bresolí-Obach R, Nos J, Mora M, Sagristà ML, Ruiz-González R, Nonell S. Anthracene-based fluorescent nanoprobes for singlet oxygen detection in biological media. *Methods.* **2016**;109. doi:10.1016/j.ymeth.2016.06.007

97. Lerdal D, Foote CS. Chemistry of singlet Oxygen. XXVII. Directing effect of methoxy group in additions to methoxystyrenes. *Tetrahedron Lett.* **1978**;19(35). doi:10.1016/S0040-4039(01)85600-8

98. Pawle RH, Haas TE, Müller P, Thomas SW. Twisting and piezochromism of phenylene-ethynylenes with aromatic interactions between side chains and main chains. *Chem Sci.* **2014**;5(11). doi:10.1039/c4sc01466a

99. Imran M, Chen MS. Self-Sensitized and Reversible O2Reactivity with Bisphenalenyls for Simple, Tunable, and Multicycle Colorimetric Oxygen-Sensing Films. *ACS Appl Mater Interfaces*. **2022**;14(1). doi:10.1021/acsami.1c16033

100. Hemming K. Organic Chemistry. By J. P. Clayden, N. Greeves, S. Warren, and P. D. Wothers; Oxford University Press, 2001, ISBN 0 19 850346 6, 53 Chapters, 1508 pages. *Chem. Educ*.. **2001**;6(6). doi:10.1007/s00897010513a

101. Kastrati A, Oswald F, Scalabre A, Fromm KM. Photophysical Properties of Anthracene Derivatives. *Photochem*. **2023**;3(2). doi:10.3390/photochem3020015

102. Han D, Lu H, Li W, Li Y, Feng S. Light- and heat-triggered reversible luminescent materials based on polysiloxanes with anthracene groups. *RSC Adv*. **2017**;7(89). doi:10.1039/c7ra12201b

103. Wasserman HH, Scheffer JR. Singlet Oxygen Reactions from Photoperoxides. *J Am Chem Soc*. **1967**;89(12). doi:10.1021/ja00988a064

104. Arias LS, Pessan JP, Vieira APM, De Lima TMT, Delbem ACB, Monteiro DR. Iron oxide nanoparticles for biomedical applications: A perspective on synthesis, drugs, antimicrobial activity, and toxicity. *Antibiotics*. **2018**;7(2). doi:10.3390/antibiotics7020046

105. Mandriota G, Avugadda SK, Sadeghi E, et al. Magnetic nanosheets: from iron oxide nanocubes to polydopamine embedded 2D clusters and their multi-purpose properties. *Nanoscale Horiz*. **2025**;10(6):1140-1158. doi:10.1039/D4NH00566J

106. Krasia-Christoforou T, Socoliuc V, Knudsen KD, Tombácz E, Turcu R, Vékás L. From Single-Core Nanoparticles in Ferrofluids to Multi-Core Magnetic Nanocomposites: Assembly Strategies, Structure, and Magnetic Behavior. *Nanomaterials*. **2020**;10(11):2178. doi:10.3390/nano10112178

107. Zhao S, Yu X, Qian Y, Chen W, Shen J. Multifunctional magnetic iron oxide nanoparticles: An advanced platform for cancer theranostics. *Theranostics.* **2020**;10(14). doi:10.7150/thno.42564

108. Neumann S, Kuger L, Arlt CR, Franzreb M, Rafaja D. Influence of the hierarchical architecture of multi-core iron oxide nanoflowers on their magnetic properties. *Sci Rep*. **2023**;13(1). doi:10.1038/s41598-023-31294-4

109. Shen S, Wang S, Zheng R, et al. Magnetic nanoparticle clusters for photothermal therapy with near-infrared irradiation. *Biomaterials*. **2015**;39. doi:10.1016/j.biomaterials.2014.10.064

110. Atrei A, Mahdizadeh FF, Baratto MC, Scala A. Effect of citrate on the size and the magnetic properties of primary fe3o4 nanoparticles and their aggregates. *Appl. Sci.* **2021**;11(15). doi:10.3390/app11156974

111. Niculescu AG, Chircov C, Grumezescu AM. Magnetite nanoparticles: Synthesis methods – A comparative review. *Methods*. **2022**;199. doi:10.1016/j.ymeth.2021.04.018

112. Tuček J, Zboril R, Petridis D. Maghemite nanoparticles by view of Mössbauer spectroscopy. *J Nanosci Nanotechnol*. **2006**;6(4). doi:10.1166/jnn.2006.183

113. Tadic M, Panjan M, Damnjanovic V, Milosevic I. Magnetic properties of hematite (α-Fe 2 O 3) nanoparticles prepared by hydrothermal synthesis method. *Appl Surf Sci*. **2014**;320. doi:10.1016/j.apsusc.2014.08.193

114. Rodriguez-Lorenzo L, Rothen-Rutishauser B, Petri-Fink A, Balog S. Nanoparticle polydispersity can strongly affect in vitro dose. *Part. Part. Syst. Charact*.. **2015**;32(3). doi:10.1002/ppsc.201400079

115. Dasgupta S, Auth T, Gompper G. Shape and orientation matter for the cellular uptake of nonspherical particles. *Nano Lett.* **2014**;14(2). doi:10.1021/nl403949h

116. Truong NP, Whittaker MR, Mak CW, Davis TP. The importance of nanoparticle shape in cancer drug delivery. *Expert Opin Drug Deliv.* **2015**;12(1). doi:10.1517/17425247.2014.950564

117. Moghimi SM, Hunter AC, Murray JC. Long-circulating and target-specific nanoparticles: Theory to practice. *Pharmacol Rev.* **2001**;53(2). doi:10.1016/s0031-6997(24)01494-7

118. Jhaveri AM, Torchilin VP. Multifunctional polymeric micelles for delivery of drugs and siRNA. *Front Pharmacol*. **2014**;5 APR. doi:10.3389/fphar.2014.00077

119. Jain RK, Stylianopoulos T. Delivering nanomedicine to solid tumors. *Nat Rev Clin Oncol*. 2010;7(11). doi:10.1038/nrclinonc.2010.139

120. Sinha S, Jing H, Sachar HS, Das S. Role of plasma membrane surface charges in dictating the feasibility of membrane-nanoparticle interactions. *Appl Phys Lett*. **2017**;111(26). doi:10.1063/1.5011208

121. Izak-Nau E, Voetz M, Eiden S, Duschl A, Puntes VF. Altered characteristics of silica nanoparticles in bovine and human serum: The importance of nanomaterial characterization prior to its toxicological evaluation. *Part Fibre Toxicol*. **2013**;10(1). doi:10.1186/1743-8977-10-56

122. Hajipour MJ, Safavi-Sohi R, Sharifi S, et al. An Overview of Nanoparticle Protein Corona Literature. *Small.John Wiley and Sons Inc*. **2023**;19(36). doi:10.1002/smll.202301838

123. Landry MP. Protein Corona Formation on Hard and Polymeric Nanoparticles – Towards Understanding Biocompatibility, Biodistribution, and Efficacy. ECS Meeting Abstracts. **2022**; MA2022-01(8):707-707. doi:10.1149/ma2022-018707mtgabs

124. Karmali PP, Simberg D. Interactions of nanoparticles with plasma proteins: Implication on clearance and toxicity of drug delivery systems. *Expert Opin Drug Deliv***. 2011**;8(3). doi:10.1517/17425247.2011.554818

125. Haynes H, Holmes W, Holmes WM. The Emergence of Magnetic Resonance Imaging (MRI) for 3D Analysis of Sediment Beds The Emerging Use of Magnetic Resonance Imaging (MRI) for 3D Analysis of Sediment Structures and Internal *Flow Processes*. doi:10.1002/adfm.20242528

126. Peng YK, Lui CNP, Chen YW, et al. Engineering of Single Magnetic Particle Carrier for Living Brain Cell Imaging: A Tunable T1-/T2-/Dual-Modal Contrast Agent for Magnetic Resonance Imaging Application. *Chem. Mater.* **2017**;29(10). doi:10.1021/acs.chemmater.7b00884

127. Jun YW, Lee JH, Cheon J. Chemical design of nanoparticle probes for high-performance magnetic resonance imaging. *Angew. Chem. Int. Ed*.. **2008**;47(28). doi:10.1002/anie.200701674

128. Xie W, Guo Z, Gao F, et al. Shape-, size-and structure-controlled synthesis and biocompatibility of iron oxide nanoparticles for magnetic theranostics. *Theranostics*. **2018**;8(12). doi:10.7150/thno.25220

129. Meola A, Rao J, Chaudhary N, Sharma M, Chang SD. Gold nanoparticles for brain tumor imaging: A systematic review. *Front Neurol*. **2018**;9(MAY). doi:10.3389/fneur.2018.00328

130. Shevtsov M, Multhoff G. Recent Developments of Magnetic Nanoparticles for Theranostics of Brain Tumor. *Curr Drug Metab.* **2016**;17(8). doi:10.2174/1389200217666160607232540

131. Mao Q, Gu M, Hong C, et al. A Contrast-Enhanced Tri-Modal MRI Technique for High-Performance Hypoxia Imaging of Breast Cancer. *Small*. **2024**;20(28). doi:10.1002/smll.202308850

132. Blasiak B, Van Veggel FCJM, Tomanek B. Applications of nanoparticles for MRI cancer diagnosis and therapy. *J Nanomater.* **2013**;2013. doi:10.1155/2013/148578

133. Lee J, Na YR, Na CM, et al. 7-nm Mn0.5 Zn0.5Fe2O4 superparamagnetic iron oxide nanoparticle (SPION): a high-performance theranostic for MRI and hyperthermia applications. *Theranostics*. **2025**;15(7):2883-2902. doi:10.7150/thno.103503

134. Jacqmarcq C, Picot A, Flon J, et al. MRI-based microthrombi detection in stroke with polydopamine iron oxide. *Nat Commun.* **2024**;15(1). doi:10.1038/s41467-024-49480-x

135. Estelrich J, Sánchez-Martín MJ, Busquets MA. Nanoparticles in magnetic resonance imaging: From simple to dual contrast agents. *Int J Nanomedicine*. **2015**;10. doi:10.2147/IJN.S76501

136. Sanchez LM, Arciniegas L, Alvarez VA, Gonzalez JS. Phantom gels towards medicine improvement: Uses for magnetic device tests and enhancements on magnetic-dependent clinical techniques. *Mater. Biomed. Eng*.. **2019**. doi:10.1016/B978-0-12-816913-1.00014-3

137. Strbak O, Balejcikova L, Kmetova M, et al. Longitudinal and transverse relaxivity analysis of native ferritin and magnetoferritin at 7 T MRI. *Int J Mol Sci*. **2021**;22(16). doi:10.3390/ijms22168487

138. Kim HK, Lee GH, Chang Y. Gadolinium as an MRI contrast agent. *Future Med Chem*. **2018**;10(6). doi:10.4155/fmc-2017-0215

139. Lee N, Choi Y, Lee Y, et al. Water-dispersible ferrimagnetic iron oxide nanocubes with extremely high r 2 relaxivity for highly sensitive in vivo MRI of tumors. *Nano Lett*. **2012**;12(6). doi:10.1021/nl3010308

140. Gossuin Y, Martin E, Vuong QL, et al. Characterization of commercial iron oxide clusters with high transverse relaxivity. *J Magn Reson Open*. **2022**;10-11. doi:10.1016/j.jmro.2022.100054

141. McLeod SM, Robison L, Parigi G, et al. Maximizing Magnetic Resonance Contrast in Gd(III) Nanoconjugates: Investigation of Proton Relaxation in Zirconium Metal-Organic Frameworks. *ACS Appl Mater Interfaces*. **2020**;12(37). doi:10.1021/acsami.0c13571

142. Zhen Z, Xie J. Development of manganese-based nanoparticles as contrast probes for magnetic resonance imaging. *Theranostics*. **2012**;2(1):45-54. doi:10.7150/thno.3448

143. Ahmadpoor F, Masood A, Feliu N, Parak WJ, Shojaosadati SA. The Effect of Surface Coating of Iron Oxide Nanoparticles on Magnetic Resonance Imaging Relaxivity. *Frontiers in Nanotechnology.* **2021**;3. doi:10.3389/fnano.2021.644734

144. Hamilton N, Allen C, Reynolds S. The effect of gadolinium contrast agent on T1 and T2 relaxation of brain in live and fixed zebrafish MRI. In: *Joint Annual Meeting ISMRM-ESMRMB ISMRT 31st Annual Meeting. ISMRM*; **2022**. doi:10.58530/2022/2332

145. Jacqmarcq C, Picot A, Flon J, et al. MRI-based microthrombi detection in stroke with polydopamine iron oxide. *Nat Commun.* **2024**;15(1). doi:10.1038/s41467-024-49480-x

146. Rahman M. Magnetic Resonance Imaging and Iron-oxide Nanoparticles in the era of Personalized Medicine. *Nanotheranostics*. **2023**;7(4). doi:10.7150/ntno.86467

147. Lee D, Sohn J, Kirichenko A. Quantifying Liver Heterogeneity via R2*-MRI with Super-Paramagnetic Iron Oxide Nanoparticles (SPION) to Characterize Liver Function and Tumor. *Cancers*. **2022**;14(21). doi:10.3390/cancers14215269

148. Ferreira-Filho VC, Morais B, Vieira BJC, et al. Influence of SPION Surface Coating on Magnetic Properties and Theranostic Profile. *Molecules.* **2024**;29(8). doi:10.3390/molecules29081824

149. Wang YXJ. Superparamagnetic iron oxide based MRI contrast agents: Current status of clinical application. *Quant Imaging Med Surg.* **2011**;1(1). doi:10.3978/j.issn.2223-4292.2011.08.03

150. Robinson, Sally (AstraZeneca L, Chapman K (NC3Rs, Hudson S (Compliance SI, et al. Guidance on Dose Level Selection for Regulatory General Toxicology Studies for Pharm.; **2009**.

151. Funk F, Ryle P, Canclini C, Neiser S, Geisser P. The new generation of intravenous iron: chemistry, pharmacology, and toxicology of ferric carboxymaltose. *Arzneimittelforschung*. **2010**;60(6 a). doi:10.1055/s-0031-1296299

152. Cheng W, Ping Y, Zhang Y, Chuang KH, Liu Y. Magnetic resonance imaging (MRI) contrast agents for tumor diagnosis. *J Healthc Eng.* **2013**;4(1). doi:10.1260/2040-2295.4.1.23

153. Lapusan R, Borlan R, Focsan M. Advancing MRI with magnetic nanoparticles: a comprehensive review of translational research and clinical trials. Nanoscale *Adv. RSC*. **2024**;6(9):2234-2259. doi:10.1039/d3na01064c

154. Iyad N, S.Ahmad M, Alkhatib SG, Hjouj M. Gadolinium contrast agents- challenges and opportunities of a multidisciplinary approach: Literature review. *Eur J Radiol Open*. **2023**;11. doi:10.1016/j.ejro.2023.100503

155. Suárez-García S, Arias-Ramos N, Frias C, et al. Dual T1/ T2 Nanoscale Coordination Polymers as Novel Contrast Agents for MRI: A Preclinical Study for Brain Tumor. *ACS Appl Mater Interfaces*. **2018**;10(45). doi:10.1021/acsami.8b15594

156. Shen S, Ding W, Ahmed S, et al. Ultrasmall superparamagnetic iron oxide imaging identifies tissue and nerve inflammation in pain conditions. *Pain Medicine*. **2018**;19(4). doi:10.1093/pm/pnx267

157. Ding C, Wu K, Wang W, et al. Synthesis of a cell penetrating peptide modified superparamagnetic iron oxide and MRI detection of bladder cancer. *Oncotarget*. **2017**;8(3). doi:10.18632/oncotarget.13578

158. Hickey JW, Santos JL, Williford JM, Mao HQ. Control of polymeric nanoparticle size to improve therapeutic delivery. J. Control. Release. **2015**;219. doi:10.1016/j.jconrel.2015.10.006

159. Soo Choi H, Liu W, Misra P, et al. Renal clearance of quantum dots. *Nat Biotechnol*. **2007**;25(10). doi:10.1038/nbt1340

160. Abou DS, Ku T, Smith-Jones PM. In vivo biodistribution and accumulation of 89Zr in mice. *Nucl Med Biol*. **2011**;38(5). doi:10.1016/j.nucmedbio.2010.12.011

161. Waegeneers N, Brasseur A, Van Doren E, et al. Short-term biodistribution and clearance of intravenously administered silica nanoparticles. *Toxicol Rep*. **2018**;5. doi:10.1016/j.toxrep.2018.05.004

162. Naumenko V, Nikitin A, Kapitanova K, et al. Intravital microscopy reveals a novel mechanism of nanoparticles excretion in kidney. *J. Control. Release*. **2019**;307. doi:10.1016/j.jconrel.2019.06.026

163. Singh E, Gurses ME, Costello MC, et al. Intrathecal chemotherapy for leptomeningeal disease in high-grade gliomas: a systematic review. *J Neurooncol*. **2024**;167(1). doi:10.1007/s11060-024-04582-w

164. Boens N, Qin W, Basarić N, et al. Fluorescence lifetime standards for time and frequency domain fluorescence spectroscopy. *Anal Chem*. **2007**;79(5). doi:10.1021/ac062160k

165. Becker J. Light-Scattering and -Absorption of Nanoparticles. **2012**. doi:10.1007/978-3-642-31241-0_2

166. Rivera-Figueroa AM, Ramazan KA, Finlayson-Pitts BJ. Fluorescence, Absorption, and Excitation Spectra of Polycyclic Aromatic Hydrocarbons as a Tool for Quantitative Analysis. *J Chem Educ*. **2004**;81(2). doi:10.1021/ed081p242

167. Stenspil SG, Laursen BW. Photophysics of fluorescent nanoparticles based on organic dyes - challenges and design principles. *Chem Sci.RSC*. **2024**;15(23):8625-8638. doi:10.1039/d4sc01352b

168. Zander M. Polycyclic Hydrocarbons. Band I, Von E. Clar . Academic Press, London-New York und Springer-Verlag, Berlin-Göttingen-Heidelberg 1964. 1. Aufl., XXVIII, 488 S., 80 Abb., 8 Tab., Ln. DM 70.–. . *Angewandte Chemie*. **1965**;77(19). doi:10.1002/ange.19650771941

169. Sakai KI, Ohshima S, Uchida A, Oonishi I, Fujisawa S, Nagashima U. Theoretical study on photooxygenation of large Polycyclic Aromatic Hydrocarbons by semiempirical molecular orbital methods. *J Phys. Chem*.. **1995**;99(16). doi:10.1021/j100016a027

170. Rigaudy J, Breliere C, Scribe P. Photochemistry of 9,10-diphenylanthracene endoperoxide. *Tetrahedron Lett*. 1978;19(7). doi:10.1016/S0040-4039(01)85367-3

171. Greene FD, Leslie Misrock S, Wolfe JR. The Structure of Anthracene Photodimers. *J Am Chem Soc*. **1955**;77(14). doi:10.1021/ja01619a051

172. El-Sherbiny IM, El-Sayed M, Reda A. Superparamagnetic Iron Oxide Nanoparticles (SPIONs) as Multifunctional Cancer *Theranostics*. **2020**. doi:10.1007/978-3-030-39923-8_6

173. Heating Mechanisms of Magnetic Nanoparticles for Hyperthermia. *J. Inst. Electr. Eng. Jpn*. **2023**;143(8):500-503. doi:10.1541/IEEJJOURNAL.143.500

174. Hauck M, Hellmold D, Kubelt C, et al. Localized Drug Delivery Systems in High-Grade Glioma Therapy—From Construction to Application. *Adv Ther*. **2022**;5(8). doi:10.1002/adtp.202200013

175. Zarif Attalla K, Hassan DH, Teaima MH, et al. Enhanced Intranasal Delivery of Atorvastatin via Superparamagnetic Iron-Oxide-Loaded Nanocarriers: Cytotoxicity and Inflammation Evaluation and In Vivo, In Silico, and Network Pharmacology Study for Targeting Glioblastoma Management. *Pharm.* **2025**;18(3). doi:10.3390/ph18030421

176. Rego GN de A, Mamani JB, Souza TKF, Nucci MP, Silva HR da, Gamarra LF. Therapeutic evaluation of magnetic hyperthermia using Fe3O4-aminosilane-coated iron oxide nanoparticles in glioblastoma animal model. *Einstein*. **2019**;17(4). doi:10.31744/einstein_journal/2019AO4786

177. Mahmoudi K, Bouras A, Bozec D, Ivkov R, Hadjipanayis C. Magnetic hyperthermia therapy for the treatment of glioblastoma: a review of the therapy's history, efficacy and application in humans. *Int. J. Hyperthermia*.. **2018**;34(8). doi:10.1080/02656736.2018.1430867

178. Somu P, Mohanty S, Basavegowda N, Yadav AK, Paul S, Baek KH. The Interplay between Heat Shock Proteins and Cancer Pathogenesis: A Novel Strategy for Cancer Therapeutics. *Cancers*. **2024**;16(3). doi:10.3390/cancers16030638

179. N'Guyen TTT, Duong HTT, Basuki J, et al. Functional Iron Oxide Magnetic Nanoparticles with Hyperthermia-Induced Drug Release Ability by Using a Combination of Orthogonal Click Reactions. Angew. Chem. **2013**;125(52). doi:10.1002/ange.201306724

180. Riedinger A, Guardia P, Curcio A, et al. Subnanometer local temperature probing and remotely controlled drug release based on Azo-functionalized iron oxide nanoparticles. *Nano Lett*. **2013**;13(6). doi:10.1021/nl400188q

181. Dias JT, Moros M, Del Pino P, Rivera S, Grazú V, De La Fuente JM. DNA as a molecular local thermal probe for the analysis of magnetic hyperthermia. *Angew. Chem. Int. Ed*. **2013**;52(44). doi:10.1002/anie.201305835

182. Hemery G, Garanger E, Lecommandoux S, et al. Thermosensitive polymer-grafted iron oxide nanoparticles studied by in situ dynamic light backscattering under magnetic hyperthermia. *J Phys D Appl Phys*. **2015**;48(49). doi:10.1088/0022-3727/48/49/494001

183. Chen F, Cai W. Nanomedicine for targeted photothermal cancer therapy: Where are we now? *Nanomedicine*. **2015**;10(1). doi:10.2217/nnm.14.186

184. He X, Zhang S, Tian Y, Cheng W, Jing H. Research Progress of Nanomedicine-Based Mild Photothermal Therapy in Tumor. *Int J Nanomedicine*. **2023**;18. doi:10.2147/IJN.S405020

185. Nieciecka D, Celej J, Żuk M, et al. Hybrid system for local drug delivery and magnetic hyperthermia based on spions loaded with doxorubicin and epirubicin. *Pharmaceutics*. **2021**;13(4). doi:10.3390/pharmaceutics13040480

186. Blanco-Andujar C, Ortega D, Southern P, Nesbitt SA, Thanh NTK, Pankhurst QA. Real-time tracking of delayed-onset cellular apoptosis induced by intracellular magnetic hyperthermia. *Nanomedicine*. **2016**;11(2). doi:10.2217/nnm.15.185

187. Creixell M, Bohórquez AC, Torres-Lugo M, Rinaldi C. EGFR-targeted magnetic nanoparticle heaters kill cancer cells without a perceptible temperature rise. *ACS Nano*. **2011**;5(9). doi:10.1021/nn201822b

188. Viger ML, Live LS, Therrien OD, Boudreau D. Reduction of self-quenching in fluorescent silica-coated silver Nanoparticles. *Plasmonics*. **2008**;3(1). doi:10.1007/s11468-007-9051-x

189. Yon M, Gineste S, Parigi G, et al. Hybrid Polymeric Nanostructures Stabilized by Zirconium and Gadolinium Ions for Use as Magnetic Resonance Imaging Contrast Agents. *ACS Appl Nano Mater*. **2021**;4(5). doi:10.1021/acsanm.1c00495

190. Amanda Anderson, Jos Laurie Campbell, Vipul Bansal. US20230138790A1. Published online August 2, **2022**:1-33.

191. Gautam C, Joyner J, Gautam A, Rao J, Vajtai R. Zirconia based dental ceramics: structure, mechanical properties, biocompatibility and applications. *Dalton Trans*.. **2016**;45(48). doi:10.1039/c6dt03484e

192. Pereverzyev V. Osseointegration and Biocompatibility of Zirconia Implants. Vol 1.; 2021.

193. Suh DW, Kim YK, Yi YJ. A review of biocompatibility of zirconia and bioactivity as a zirconia implant: In vivo experiment. *J. Korean Acad. Prosthodont.*. **2019**;57(1):88. doi:10.4047/jkap.2019.57.1.88

194. Oris JT, Giesy JP, Allred PM, Grant DF, Landrum PF. Photoinduced toxicity of anthracene in aquatic organisms: An environmental perspective. In: Studies in Environmental Science. Vol 25. **1984**. doi:10.1016/S0166-1116(08)72143-5

195. Brack W, Altenburger R, Küster E, Meissner B, Wenzel KD, Schüürmann G. Identification of toxic products of anthracene photomodification in simulated sunlight. *Environ Toxicol Chem*. **2003**;22(10). doi:10.1897/02-450

196. Hanini A, Lartigue L, Gavard J, et al. Thermosensitivity profile of malignant glioma U87-MG cells and human endothelial cells following γ-Fe2O3 NPs internalization and magnetic field application. *RSC Adv*. **2016**;6(19). doi:10.1039/c5ra22960j

197. Kurczewska J, Dobosz B. Recent Progress and Challenges Regarding Magnetite-Based Nanoparticles for Targeted Drug Delivery. *Appl. Sci*.. **2024**;14(3). doi:10.3390/app14031132

198. Pacheco ARF, Cardoso BD, Pires A, et al. Development of pH-Sensitive Magnetoliposomes Containing Shape Anisotropic Nanoparticles for Potential Application in Combined Cancer Therapy. *Nanomaterials*. **2023**;13(6). doi:10.3390/nano13061051

199. Jayabun S, Sengupta A. Development of Methodologies for the Chemical Quality Control of Zircon, A Precursor for Zirconium Production. *Chem. Select*.. **2021**;6(3). doi:10.1002/slct.202003464

200. Ji H, Peng J, Yang M, et al. Oxygen Vacancy-Induced Room-Temperature Ferromagnetism in a Layered Aluminosilicate *Material. Nano Lett*. **2025**;25(12):4939-4945. doi:10.1021/acs.nanolett.5c00253

201. Niu G, Hildebrandt E, Schubert MA, et al. Oxygen vacancy induced room temperature ferromagnetism in Pr-doped CeO2 thin films on silicon. *ACS Appl Mater Interfaces*. **2014**;6(20). doi:10.1021/am502238w

202. Nakai I, Sasano M, Inui K, et al. Oxygen vacancy and magnetism of a room temperature ferromagnet Co-doped TiO2. *J. Korean Phys. Soc*.. **2013**;63(3). doi:10.3938/jkps.63.532

203. Alivisatos AP. Semiconductor clusters, nanocrystals, and quantum dots. *Science* **1996**;271(5251). doi:10.1126/science.271.5251.933

204. Majetich SA, Jin Y. Magnetization directions of individual nanoparticles. *Science*. **1999**;284(5413). doi:10.1126/science.284.5413.470

205. Gionco C, Paganini MC, Giamello E, Burgess R, Di Valentin C, Pacchioni G. Cerium-doped zirconium dioxide, a visible-light-sensitive photoactive material of third generation. *J. Phys. Chem. Letters*. **2014**;5(3). doi:10.1021/jz402731s

206. Pacchioni G. Role of Nanostructuring on the Properties of Oxide Materials: The Case of Zirconia Nanoparticles. *Eur J Inorg Chem*. **2019**;2019(6). doi:10.1002/ejic.201801314

207. Rahman MA, Rout S, Thomas JP, McGillivray D, Leung KT. Defect-Rich Dopant-Free ZrO2 Nanostructures with Superior Dilute Ferromagnetic Semiconductor Properties. *J Am Chem Soc*. **2016**;138(36). doi:10.1021/jacs.6b06949

208. Chen L, Iwamoto C, Omurzak E, et al. Synthesis of zirconium carbide (ZrC) nanoparticles covered with graphitic “windows” by pulsed plasma in liquid. *RSC Adv*. **2011**;1(6). doi:10.1039/c1ra00194a

209. Chen GH, He YP, Zhang SH, Zhang L. A series of zirconium-oxo cluster complexes based on arsenate or phosphonate ligands. *Inorg Chem Commun*. **2018**;97:125-128. doi:10.1016/j.inoche.2018.09.013

210. Malaestean IL, Kutluca M, Speldrich M, Ellern A, Kögerler P. Macrocycles based on magnetically functionalized zirconium oxide clusters. Inorganica *Chim Acta*. **2012**;380(1). doi:10.1016/j.ica.2011.08.061

211. Modi SK, Nehra M, Kumar S, Mange PL, Modi KB, Dubey S. Synthesis, Characterization, and Performance of Zirconia Nanoparticulates as an Antibacterial, Antifungal, and Anticancer Activity Agent. *Bionanoscience*. **2024**;14(3):2529-2540. doi:10.1007/s12668-024-01483-0

212. Chitoria AK, Mir A, Shah MA. A review of ZrO2 nanoparticles applications and recent advancements. *Ceram Int*. **2023**;49(20). doi:10.1016/j.ceramint.2023.06.296

213. Mangla O, Roy S. Monoclinic Zirconium Oxide Nanostructures Having Tunable Band Gap Synthesized under Extremely Non-Equilibrium Plasma Conditions. **2018**. doi:10.3390/iocn_2018-1-05486

214. Annand KJ, Maclaren I, Gass M. Utilising DualEELS to probe the nanoscale mechanisms of the corrosion of Zircaloy-4 in 350°C pressurised water. *J. Nucl. Mater.*. **2015**;465. doi:10.1016/j.jnucmat.2015.06.022

215. https://eels.info/atlas/zirconium accessed 26/07/2025.

216. BRYDSON R. Probing the local structure and bonding at interfaces and defects using EELS in the TEM. *J Microsc*. **1995**;180(3). doi:10.1111/j.1365-2818.1995.tb03683.x

217. Sobańska K, Pietrzyk P, Sojka Z. Generation of Reactive Oxygen Species via Electroprotic Interaction of H2O2 with ZrO2 Gel: Ionic Sponge Effect and pH-Switchable Peroxidase- and Catalase-Like Activity. *ACS Catal*. 2017;7(4). doi:10.1021/acscatal.7b00189

218. Mundell JW, Brier MI, Orloff E, Stanley SA, Dordick JS. Alternating magnetic fields drive stimulation of gene expression via generation of reactive oxygen species. *iScience*. **2024**;27(3). doi:10.1016/j.isci.2024.109186

219. Shang Y, Wang Q, Li J, et al. Zirconia Nanoparticles Induce HeLa Cell Death Through Mitochondrial Apoptosis and Autophagy Pathways Mediated by ROS. *Front Chem*. **2021**;9. doi:10.3389/fchem.2021.522708

220. Chikazumi S, Graham, Jr CD. Physics of Ferromagnetism.; **1997**. doi:10.1093/oso/9780198517764.001.0001

221. Dennis CL, Ivkov R. Physics of heat generation using magnetic nanoparticles for hyperthermia. *Int. J. Hyperthermia*.. **2013**;29(8). doi:10.3109/02656736.2013.836758

222. Krycka KL, Booth RA, Hogg CR, et al. Core-shell magnetic morphology of structurally uniform magnetite nanoparticles. *Phys Rev Lett.* **2010**;104(20). doi:10.1103/PhysRevLett.104.207203

223. Noh SH, Na W, Jang JT, et al. Nanoscale magnetism control via surface and exchange anisotropy for optimized ferrimagnetic hysteresis. *Nano Lett*. **2012**;12(7). doi:10.1021/nl301499u

224. Dormann JL, Fiorani D, Tronc E. Magnetic Relaxation in Fine-Particle Systems. **1997**. doi:10.1002/9780470141571.ch4

225. Maeda H. Toward a full understanding of the EPR effect in primary and metastatic tumors as well as issues related to its heterogeneity. *Adv Drug Deliv Rev*. **2015**;91. doi:10.1016/j.addr.2015.01.002

226. Byrne JD, Betancourt T, Brannon-Peppas L. Active targeting schemes for nanoparticle systems in cancer therapeutics. *Adv Drug Deliv Rev.* **2008**;60(15). doi:10.1016/j.addr.2008.08.005

227. Liu X, Zhang Y, Wang Y, et al. Comprehensive understanding of magnetic hyperthermia for improving antitumor therapeutic efficacy. *Theranostics*. **2020**;10(8). doi:10.7150/thno.40805

228. Racca L, Cauda V. Correction to: Remotely Activated Nanoparticles for Anticancer Therapy. *Nano-Micro Letters*, **2021**, 13, 1, (11), 10.1007/s40820-020-00537-8). Nanomicro Lett. 2021;13(1). doi:10.1007/s40820-020-00553-8

229. Datta NR, Ordóñez SG, Gaipl US, et al. Local hyperthermia combined with radiotherapy and-/or chemotherapy: Recent advances and promises for the future. *Cancer Treat Rev*. **2015**;41(9). doi:10.1016/j.ctrv.2015.05.009

230. Graham W, Torbett-Dougherty M, Islam A, Soleimani S, Bruce-Tagoe TA, Johnson JA. Magnetic Nanoparticles and Drug Delivery Systems for Anti-Cancer Applications: A Review. *Nanomaterials*. **2025**;15(4). doi:10.3390/nano15040285

231. Adeeyo AO, Alabi MA, Oyetade JA, et al. Magnetic Nanoparticles: Advances in Synthesis, Sensing, and Theragnostic Applications. Magnetochemistry. *Multidisciplinary.* **2025**;11(2). doi:10.3390/magnetochemistry11020009

232. Yang X, Kubican SE, Yi Z, Tong S. Advances in magnetic nanoparticles for molecular medicine. *Chem. Commun*.. **2025**;61(15):3093-3108. doi:10.1039/d4cc05167j

233. Kievit FM, Zhang M. Surface engineering of iron oxide nanoparticles for targeted cancer therapy. *Acc Chem Res.* **2011**;44(10). doi:10.1021/ar2000277

234. Fernández M, Javaid F, Chudasama V. Advances in targeting the folate receptor in the treatment/imaging of cancers. *Chem Sci*. **2018**;9(4). doi:10.1039/c7sc04004k

235. Peeken JC, Vaupel P, Combs SE. Integrating hyperthermia into modern radiation oncology: What evidence is necessary? *Front Oncol*. **2017**;7(JUN). doi:10.3389/fonc.2017.00132

236. Yang SJ, Huang CH, Wang CH, Shieh MJ, Chen KC. The synergistic effect of hyperthermia and chemotherapy in magnetite nanomedicine-based lung cancer treatment. *Int J Nanomedicine*. **2020**;15. doi:10.2147/IJN.S281029

237. Jabalera Y, Sola-Leyva A, Carrasco-Jiménez MP, Iglesias GR, Jimenez-Lopez C. Synergistic photothermal-chemotherapy based on the use of biomimetic magnetic nanoparticles. *Pharmaceutics*. **2021**;13(5). doi:10.3390/pharmaceutics13050625

238. Tavakoli M, Maghsoudian S, Rezaei-Aderiani A, et al. Synergistic effects of paclitaxel and platelet-superparamagnetic iron oxide nanoparticles for targeted chemo-hyperthermia therapy against breast cancer. *Colloids Surf B Biointerfaces*. **2025**;251. doi:10.1016/j.colsurfb.2025.114584

239. Yi GY, Kim MJ, Kim HI, Park J, Baek SH. Hyperthermia Treatment as a Promising Anti-Cancer Strategy: Therapeutic Targets, Perspective Mechanisms and Synergistic Combinations in Experimental Approaches. *Antioxidants*. **2022**;11(4). doi:10.3390/antiox11040625

240. Cai Y, Kang X, Zhou L, et al. Multifunctional Superparamagnetic Copper Iron Oxide Nanoparticles for Synergistic Cancer Therapy via Magnetic Hyperthermia, Oxidative Stress and Immune Reprogramming. *Adv Funct Mater*. n/a(n/a):2425286. doi:10.1002/adfm.202425286

241. Jędrzak A, Grześkowiak BF, Golba K, et al. Magnetite nanoparticles and spheres for chemo-and photothermal therapy of hepatocellular carcinoma in vitro. *Int J Nanomedicine*. **2020**;15. doi:10.2147/IJN.S257142

242. Ryu JH, Koo H, Sun IC, et al. Tumor-targeting multi-functional nanoparticles for theragnosis: New paradigm for cancer therapy. *Adv Drug Deliv Rev.* **2012**;64(13). doi:10.1016/j.addr.2012.06.012

243. Lee SY, Fiorentini G, Szasz AM, Szigeti G, Szasz A, Minnaar CA. Quo Vadis Oncological Hyperthermia. *Front Oncol*. **2020**;10. doi:10.3389/fonc.2020.01690

244. Hildebrandt B, Wust P, Ahlers O, et al. The cellular and molecular basis of hyperthermia. *Crit Rev Oncol Hematol*. **2002**;43(1). doi:10.1016/S1040-8428(01)00179-2

245. Nuzhina J V., Shtil AA, Prilepskii AY, Vinogradov V V. Preclinical Evaluation and Clinical Translation of Magnetite-Based Nanomedicines. *J Drug Deliv Sci Technol*. **2019**;54. doi:10.1016/j.jddst.2019.101282

246. Andreozzi A, Brunese L, Cafarchio A, Netti P, Vanoli GP. Effects of magnetic nanoparticle distribution in cancer therapy through hyperthermia. *Int. J. Therm. Sci*.. **2025**;208. doi:10.1016/j.ijthermalsci.2024.109428

247. Pandhare AB, Mulik S V., Patil SS, Smotraiev R V., Patil RP, Delekar SD. Functional mixed metal oxide nanomaterials: a comprehensive review of their hyperthermic potential in cancer therapy. *RSC*. **2025**;49(12):4735-4754. doi:10.1039/d4nj02783c

248. Meenach SA, Vogt FG, Anderson KW, Zach Hilt J, McGarry RC, Mansour HM. Design, physicochemical characterization, and optimization of organic solution advanced spray-dried inhalable dipalmitoylphosphatidylcholine (DPPC) and dipalmitoylphosphatidylethanolamine poly(ethylene glycol) (DPPE-PEG) microparticles and nanoparticles for targeted respiratory nanomedicine delivery as dry powder inhalation aerosols. *Int J Nanomedicine*. **2013**;8. doi:10.2147/IJN.S30724

249. Ramirez-Nuñez AL, Jimenez-Garcia LF, Goya GF, Sanz B, Santoyo-Salazar J. In vitro magnetic hyperthermia using polyphenol-coated Fe3O4γFe2O3 nanoparticles from Cinnamomun verum and Vanilla planifolia: The concert of green synthesis and therapeutic possibilities. *Nanotechnology*. **2018**;29(7). doi:10.1088/1361-6528/aaa2c1

250. Hamdous Y, Chebbi I, Mandawala C, et al. Biocompatible coated magnetosome minerals with various organization and cellular interaction properties induce cytotoxicity towards RG-2 and GL-261 glioma cells in the presence of an alternating magnetic field. *J Nanobiotechnology*. **2017**;15(1). doi:10.1186/s12951-017-0293-2

251. Ramezani Farani M, Azarian M, Heydari Sheikh Hossein H, et al. Folic Acid-Adorned Curcumin-Loaded Iron Oxide Nanoparticles for Cervical Cancer. *ACS Appl Bio Mater*. **2022**;5(3). doi:10.1021/acsabm.1c01311

252. De Cuyper M, Caluwier D, Baert J, Cocquyt J, Van Der Meeren P. A successful strategy for the production of cationic magnetoliposomes. *Zeitschrift Fur Physikalische Chemie*. Vol 220. **2006**. doi:10.1524/zpch.2006.220.1.133

253. Ribeiro RSG, Ketkar-Atre A, Yin T, et al. Improved labeling of pancreatic islets using cationic magnetoliposomes. *J Pers Med.* **2018**;8(1). doi:10.3390/jpm8010012

254. Le Renard PE, Jordan O, Faes A, et al. The in vivo performance of magnetic particle-loaded injectable, in situ gelling, carriers for the delivery of local hyperthermia. *Biomaterials*. **2010**;31(4). doi:10.1016/j.biomaterials.2009.09.091

255. Häring M, Schiller J, Mayr J, Grijalvo S, Eritja R, Díaz DD. Magnetic gel composites for hyperthermia cancer therapy. Gels. **2015**;1(2). doi:10.3390/gels1020135

256. Shevtsov MA, Nikolaev BP, Ryzhov VA, et al. Ionizing radiation improves glioma-specific targeting of superparamagnetic iron oxide nanoparticles conjugated with cmHsp70.1 monoclonal antibodies (SPION-cmHsp70.1). *Nanoscale*. **2015**;7(48). doi:10.1039/c5nr06521f

257. Shinkai M, Yanase M, Honda H, Wakabayashi T, Yoshida J, Kobayashi T. Intracellular hyperthermia for cancer using magnetite cationic liposomes: In vitro study. *Jpn. J. Cancer Res*.. **1996**;87(11). doi:10.1111/j.1349-7006.1996.tb03129.x

258. Wang L, Fu H, Zhao J, et al. Cascade Magnetic Hyperthermia Therapy for Biofilm Eradication and Bone Regeneration via Dual Osteoimmuno-regulation. *ACS Nano*. **2025**;19(23):21679-21695. doi:10.1021/acsnano.5c04595

259. Yang M, Yu Y, Ge T, et al. Unlocking the Promise of Antitumor Hyperthermia-Immunotherapy with Spiky Surface Topology. *Advanced Science*. **2025**;12(14). doi:10.1002/advs.202415868

260. Wang X, Hui H, Han J, et al. A CLDN18.2-Targeted Nanoplatform Manipulates Magnetic Hyperthermia Spatiotemporally for Synergistic Immunotherapy in Gastric Cancer. *Advanced Science*. **2025**;12(16). doi:10.1002/advs.202413913

261. Chen L, Zhang G, Shi Y, Qiu R, Khan A. Neuropilin-1 (NRP-1) and Magnetic Nanoparticles, a Potential Combination for Diagnosis and Therapy of Gliomas. *Curr Pharm Des*. **2015**;21(37). doi:10.2174/1381612821666150917092658

262. Brusentsova NA, Pirogovb YA, Polyanskiyc VA, et al. Magnetohydrodynamic thermochemotherapy and MRI of malignant tumorigenesis. In: Solid State Phenomena. Vol 190. **2012**. doi:10.4028/www.scientific.net/SSP.190.717

263. Xie L, Jin W, Zuo X, et al. Construction of small-sized superparamagnetic Janus nanoparticles and their application in cancer combined chemotherapy and magnetic hyperthermia. *Biomater Sci*. **2020**;8(5):1431-1441. doi:10.1039/c9bm01880h

264. Taylor A, Krupskaya Y, Krämer K, et al. Cisplatin-loaded carbon-encapsulated iron nanoparticles and their in vitro effects in magnetic fluid hyperthermia. *Carbon N Y*. **2010**;48(8). doi:10.1016/j.carbon.2010.03.009

265. Poodat M, Divsalar A, Ghalandari B, Khavarinezhad R. A new nano-delivery system for cisplatin using green-synthesized iron oxide nanoparticles. *J. Iranian Chem. Soc*.. **2023**;20(3). doi:10.1007/s13738-022-02706-5

266. Lu J, Yu C, Du K, Chen S, Huang S. Targeted delivery of cisplatin magnetic nanoparticles for diagnosis and treatment of nasopharyngeal carcinoma. Colloids Surf. *B Biointerfaces*.. **2025**;245. doi:10.1016/j.colsurfb.2024.114252

267. Shestovskaya M V., Luss AL, Bezborodova OA, et al. Iron Oxide Nanoparticles as Enhancers for Radiotherapy of Tumors. *ACS Appl Bio Mater*. **2025**;8(3):2535-2547. doi:10.1021/acsabm.4c01978

268. Maier-Hauff K, Rothe R, Scholz R, et al. Intracranial thermotherapy using magnetic nanoparticles combined with external beam radiotherapy: Results of a feasibility study on patients with glioblastoma multiforme. *J Neurooncol*. **2007**;81(1). doi:10.1007/s11060-006-9195-0

269. van Landeghem FKH, Maier-Hauff K, Jordan A, et al. Post-mortem studies in glioblastoma patients treated with thermotherapy using magnetic nanoparticles. *Biomaterials*. **2009**;30(1). doi:10.1016/j.biomaterials.2008.09.044

270. Maier-Hauff K, Ulrich F, Nestler D, et al. Efficacy and safety of intratumoral thermotherapy using magnetic iron-oxide nanoparticles combined with external beam radiotherapy on patients with recurrent glioblastoma multiforme. *J Neurooncol.* **2011**;103(2). doi:10.1007/s11060-010-0389-0

271. Sauer J. Diels-Alder reactions II: The Reaction Mechanism. *Angew. Chem. Int. Ed*.. **1967**;6(1). doi:10.1002/anie.196700161

272. Filatov MA, Senge MO. Molecular devices based on reversible singlet oxygen binding in optical and photomedical applications. *Mol Syst Des Eng*. **2016**;1(3). doi:10.1039/c6me00042h

273. FUDICKAR W, LINKER T. Applications of Endoperoxides derived from Acenes and Singlet Oxygen. In: Patai's Chemistry of Functional Groups. **2014**. doi:10.1002/9780470682531.pat0872

274. Pierlot C, Rataj V, Aubry JM. Chapter 3. Water-Soluble Carriers of Singlet Oxygen for Biological Media. **2016**. doi:10.1039/9781782622208-00047

275. Zehm D, Fudickar W, Linker T. Molecular switches flipped by oxygen. *Angew. Chem. Int. Ed*.. **2007**;46(40). doi:10.1002/anie.200700443

276. Li M, Xu Y, Peng X, Kim JS. From Low to No O2-Dependent Hypoxia Photodynamic Therapy (hPDT): A New Perspective. *Acc Chem Res*. **2022**;55(22). doi:10.1021/acs.accounts.2c00531

277. Yu Y, Wu S, Zhang L, et al. Cationization to boost both type I and type II ROS generation for photodynamic therapy. *Biomaterials*. **2022**;280. doi:10.1016/j.biomaterials.2021.121255

278. Kolemen S, Ozdemir T, Lee D, et al. Remote-Controlled Release of Singlet Oxygen by the Plasmonic Heating of Endoperoxide-Modified Gold Nanorods: Towards a Paradigm Change in Photodynamic Therapy. *Angew. Chem. Int. Ed*.. **2016**;55(11). doi:10.1002/anie.201510064

279. Sarkar D, Bera N, Ghosh S. [2+2] Photochemical Cycloaddition in Organic Synthesis. *European J Org Chem*. **2020**(10). doi:10.1002/ejoc.201901143

280. Sieburth SMN, Cunard NT. The [4 + 4] cycloaddition and its strategic application in natural product synthesis. *Tetrahedron*. **1996**;52(18). doi:10.1016/0040-4020(95)01077-7

281. Lowry RJ. The Novel Double [6 + 4] Cycloaddition of Tropone to Dimethylfulvene. *J Am Chem Soc*. **1970**;92(21). doi:10.1021/ja00724a077

282. Kennedy CR, Zhong H, MacAulay RL, Chirik PJ. Regio- and Diastereoselective Iron-Catalyzed [4+4]-Cycloaddition of 1,3-Dienes. *J Am Chem Soc.* **2019**;141(21). doi:10.1021/jacs.9b02443

283. Mose R, Preegel G, Larsen J, Jakobsen S, Iversen EH, Jørgensen KA. Organocatalytic stereoselective [8+2] and [6+4] cycloadditions. *Nat Chem*. **2017**;9(5). doi:10.1038/nchem.2682

284. Zhou Z, Tian R, Wang Z, et al. Artificial local magnetic field inhomogeneity enhances T2 relaxivity. *Nat Commun*. **2017**;8. doi:10.1038/ncomms15468

285. Zhao Z, Zhou Z, Bao J, et al. Octapod iron oxide nanoparticles as high-performance T 2 contrast agents for magnetic resonance imaging. *Nat Commun*. **2013**;4. doi:10.1038/ncomms3266

4.7. Annexes

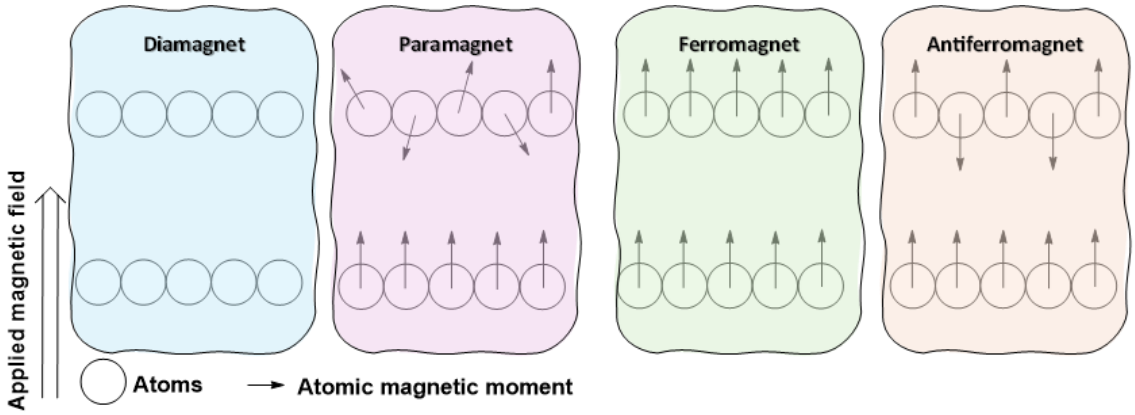
4.7.1. Conceptual explanations

4.7.1.1. Physicochemical Properties of Magnetic Nanoparticles

For particles to undergo heat generation with an applied AMF they first must be able to interact with such field. And, in summary, present themselves some sort of magnetic behaviour.

Magnetism comes from the interaction among orbital spin motions of electrons within atoms, which produce an atomic magnetic moment. With this definition all materials should be considered magnetic. However, to experience macroscopically detectable magnetism, an exchange interaction has to be effective between atomic components of a material, aligning their atomic magnetic moment.[220] If a material has all electrons paired (diamagnets) the spin pairing cancels out any momentum they may atomically generate, resulting in weak interactions. If spin pairing does not cancel out the atomic magnetic momentum, but the exchange interaction between atoms is very low (paramagnets), although they present individual atomic magnetic moments, unless an external magnetic field is applied, the atomic magnetic moments will remain randomized and cancel each other.[221]

On the other hand, if a strong exchange interaction is present, neighbouring atoms align their atomic magnetic moments in parallel (ferromagnets) resulting in a strong magnetisation, even without external magnetic field, or in antiparallel (antiferromagnets) in which case no macroscopic magnetisation is observable (Annexe **4.1**).[221]



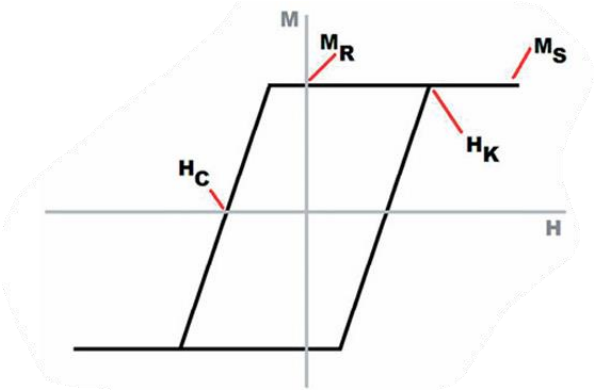
Annexe **4.1**. Schematic representation of magnetic atomic moments behaviour in the absence and presence of an applied external magnetic field from diamagnets (blue), paramagnets (purple), ferromagnets (green), and antiferromagnets (orange).

In addition to displaying atomic magnetic moment, magnetic materials also display several key characteristics when an external magnetic field is applied (Annexe **4.2**);[221]

- **Saturation magnetisation (M_s).** The maximum magnetisation achieved when magnetic moments are fully aligned with the external field.
- **Remanent magnetisation (M_r).** The residual magnetisation that remains when the external field is removed.

- **Coercivity (H_c).** The strength of the magnetic field required to reduce the magnetisation to zero after achieving saturation.
- **Anisotropy energy density (H_k).** The energy required to reorient the magnetisation referred to the preferred direction.

Characteristic response time. The time it takes for a magnetic moment to adjust to the changes in the applied field.

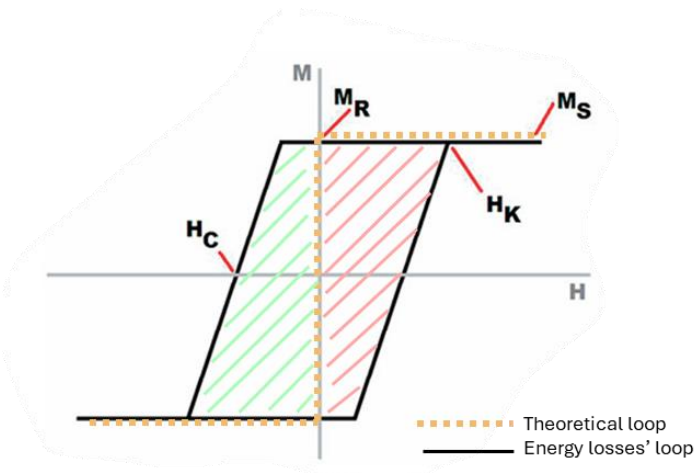


Annexe **4.2**. Schematic of a hysteresis loop showing the important parameters as reported by Dennis *et al*.[221]

With this brief summary of magnetic properties of materials, we can start to understand how they are capable to generate heat with the interaction of time-varying fields.

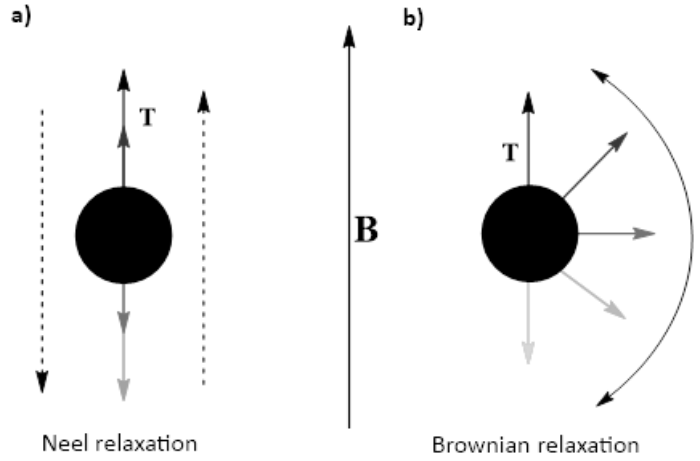
4.7.1.2. Hysteresis-Induced Heating Mechanisms

Magnetic moments of materials have their own magnitude and direction, as they form domains of parallel oriented magnetic moments. When an external magnetic field is applied, the atomic magnetic moments align with the field. However, the extent of alignment depends on both the strength of the field and the material's intrinsic properties (anisotropy H_k, saturation M_s). As the external field's polarity changes, the atomic moments adjust to the changing field. Nonetheless, if the field changes at high frequencies, the magnetic moments can lag behind the field applied. This lag results in a hysteresis loop. When plotting magnetisation versus the applied field, the magnetisation does not follow the same path during increasing and decreasing field cycles. This lag leads to energy losses, which are dissipated as heat (Annexe **4.3**).[222–224]



Annexe **4.3**. Representation of a theoretical hysteresis loop with no energy loss (dotted line) versus a realistic hysteresis loop (black line). Green and pink represent potential energy in the system. As a AMF is applied, magnetic atomic moments start aligning with the field, taking time and incurring lagging behind the alternating field applied.

Heat dissipation in these cases can occur via two different mechanisms; i) Brownian relaxation, the entire domain/NP rotates in response to the external magnetic field, and ii) Néel Relaxation, internal reorientation of the magnetic moment within the NP/domain, instead of the particle physically rotating (the magnetic moment overcomes the anisotropy energy barrier and flips its direction) (Annexe **4.4**).[224]



Annexe **4.4.** Schematic representation of **a)** Neel's relaxation **b)** Brownian relaxation. B represents the direction of the applied field and T represents the direction of the material magnetic moment.

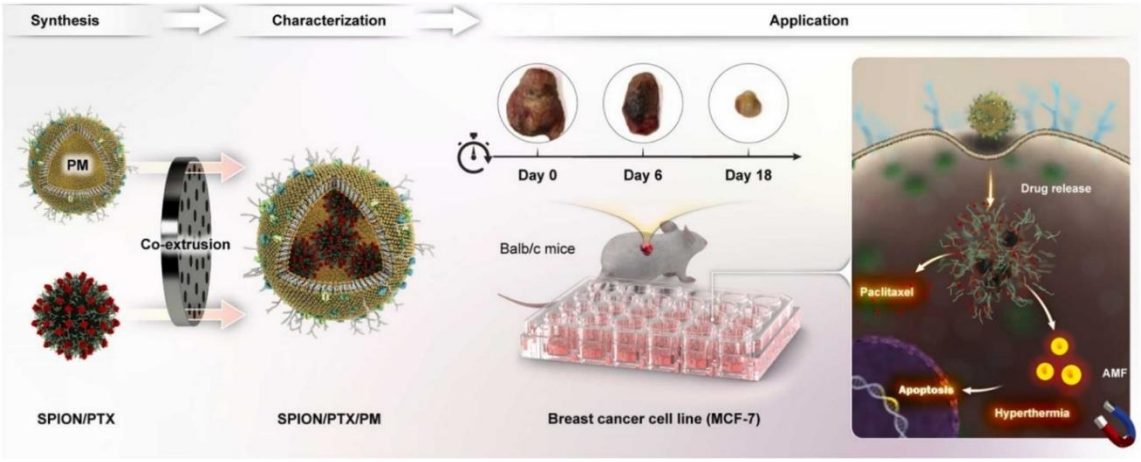
4.7.1.2.1. Advantages of Magnetic Hyperthermia

MHT rises some interesting unique advantages that are noteworthy to mention.

As happens from any NP-based therapy, the EPR effect allows for accumulation of particles towards neoplastic tissue.[225,226] This, in turn, allows for selective and localised heating, as these particles can only generate heat locally to the accumulated region, raising exclusively the temperature at the tumour site.[227–229]

Beyond hyperthermia, MNPs can provide as a platform for drug carriers, gene, or protein therapies, as well as be used in roles as theragnostic drugs, showing as a versatile tool for combination therapies.[230–232]

Coating with polymers or ligands also allow these platforms to benefit from enhanced biocompatibility and active targeting.[233,234] Moreover, MHT can act as an adjunctive treatment by enhancing the effectiveness of CT and RT. The heat generated can improve tumour blood flow, thereby increasing drug penetration and oxygenation, synergistically improving chemotherapeutic drug therapies.[235–237] As an example of the before mentioned advantages, Tavakoli *et. al.* displayed synergistic effects by coating iron oxide-based NPs with platelet membranes for carrying Paclitaxel, achieving synergistic chemotherapy with hyperthermia and increased biocompatibility (Annexe **4.5**).[238]



Annexe **4.5**. Schematic illustration of nano formulation presented by Tavakoli *et al.,* from preparation and illustration of AMF induced hyperthermia and paclitaxel release.[238]

Importantly to us, also, are the findings that suggest synergistic effects and sensitization to ROS that MHT has displayed in combination therapies. Enhancing the effect of ROS on cancer cells can happen either by inducing cellular stress, that allow to more easily induce mitochondrial dysfunction, or by combination therapy with ROS generating agents.[239] For example, Cai *et al.* reports on multifunctional superparamagnetic copper iron oxide NPs that synergistically interact in cancer therapy via MHT induced oxidative stress and sensitization.[240]

Characteristically, MHT is less dependent on tissue transparency, making it suitable for deep-seated tumours where light penetration is challenging, like GBM in our case. [241,242]

4.7.1.3. Current Challenges and Limitations of MHT

Currently, no oncological definition for hyperthermia exists, which leads to inconsistent methodologies, and makes comparison between different studies difficult.[243,244] Moreover, synthesis of the most used NPs (magnetite NPs) remains a technical challenge, with results that lack consistency across different reported procedures.[71] Furthermore, most MNPs MHT-based systems have not progressed beyond early clinical trials. Difficulties in accurately delivering and controlling the magnetic field, along with challenges in reproducible NP synthesis have hampered their advance in this field.[245]

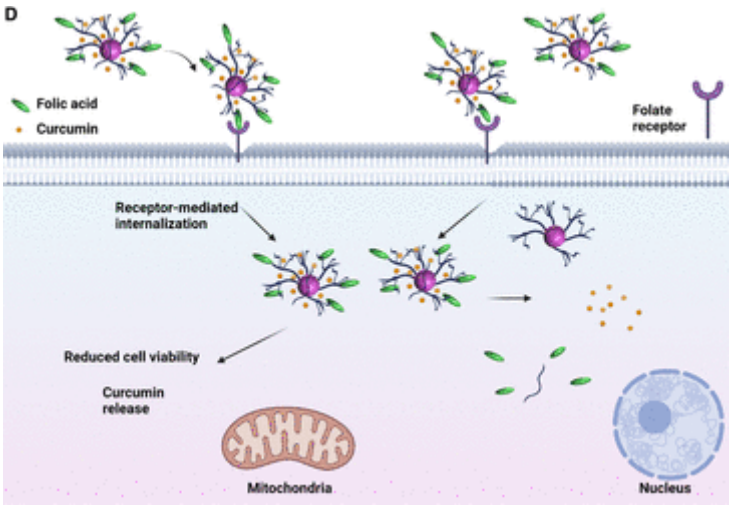
4.7.1.4. Examples of MHT in GBM Models

Since the first reports of MHT back in 1957, plenty of new studies have emerged in this field. The very bast majority of reports focus on iron-based NPs for cancer treatment, although here we will focus mainly in GBM treatment.

4.7.1.4.1. MNPs-Induced Hyperthermia at *In Vitro* GBM Models

As is expected, *in vitro* approaches to GBM treatment have plenty of examples in the literature. While most focus on the use of iron oxides for the generation of heat[246–249], we can already find some that are functionalizing iron-based NPs using drug conjugation. Examples with chitosan as a drug coating to magnetosome minerals can be observed reported by Hamdous *et al.*, who use such platform to induce cytotoxicity towards GL261 GBM cell line via combination therapy with good biocompatibility as tested with fibroblast 3T3 cells while at the same time presenting important bactericidal properties.[250] With more drugs conjugation, we have the reports from

Ramezani *et. al.*, who report on curcumin and folic acid loaded iron oxide NPs for cervical cancer, showing the development of high loading and delivery of anticancer drug curcumin, with promising results against HeLa cells while also achieving a good MRI CA for theragnostic purposes (Annexe **4.6**).[251]



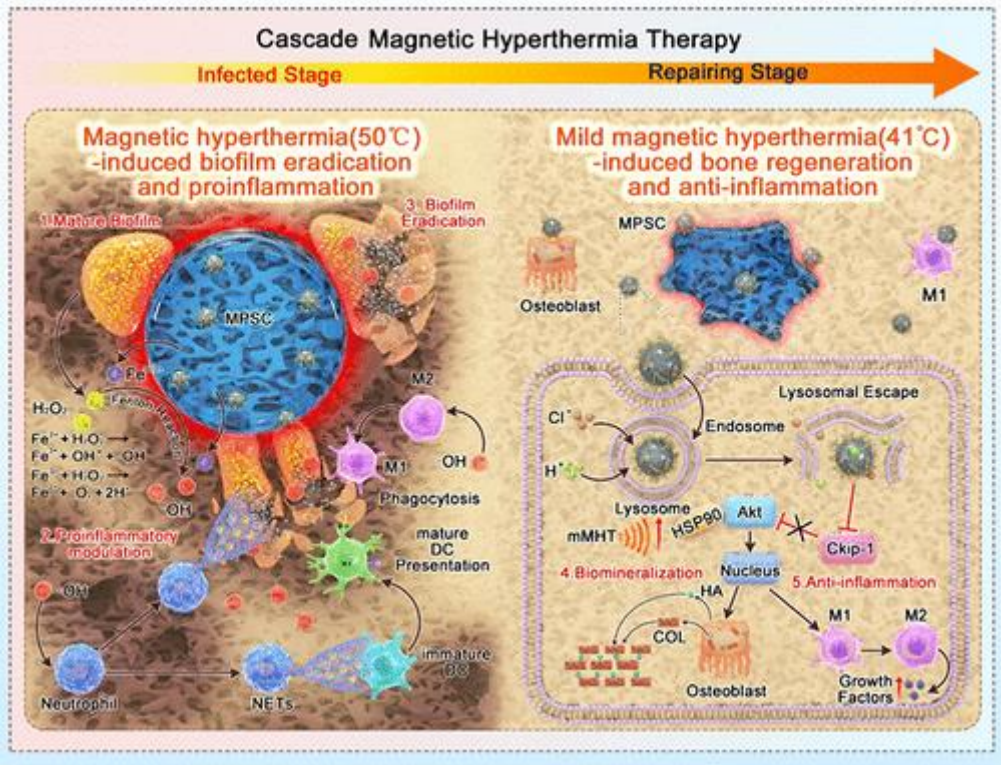
Annexe **4.6**. Schematic representation of FA-adorned HPG IONPs in internalizing in cells and release of curcumin for cervical cancer therapy as reported by Ramezani *et al.*[251]

Some other coatings focus on improving targeting of the iron oxide NPs on cell membranes, decreasing the distance gap between NPs and cells to achieve more efficient heat transfer to cancer cells.[130,196] An example of this comes from Cuyper *et al.*, who report on a successful preparation of magnetite-coated cationic liposomes owing to their enhanced cellular affinity due to their electrostatic interactions with the negatively charged phospholipids in the cell membrane, forming a seminar work that has started sparked the development of this delivery strategy.[252] Later evolving into more recent examples like Ribeiro *et al.* in applications for pancreatic islets treatment.[253]

Aside from these, other strategies have been developed, alternative to the use of MNPs, are the application of magnetic gel composites embedded into polymer hydrogel matrices for cancer treatment reaching preclinical models, as reported by Renadr *et al.*[254] However, examples are plentiful as reviewed by Häring *et al.*[255] Immunogenic therapies have also been studied by association of iron oxides with Hsp70-specific antibodies.[256]

4.7.1.4.2. MNPs-Induced Hyperthermia at *In Vivo* GBM Models

The first *in vivo* model of glioma using MHT for treatment was developed in 1997[257], and since then we have observed the rise in research of hyperthermia-induced antitumor immune response[258] and the increase in selectivity of tumour targets by nano-conjugation with antigens and antibodies.[259–261] As well as the combination of hyperthermia with chemotherapy.[262–266] Recent examples of this include the reports from Shestovskaya *et al.* of iron oxide NPs as enhancers of RT using heparinised iron oxide NPs in combination with radiation therapy in *in vivo* settings (Annexe **4.7**).[267]



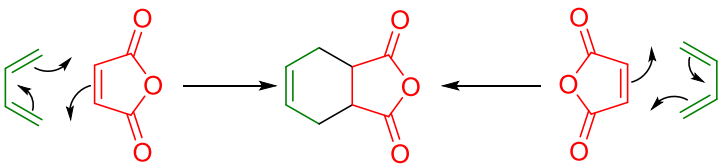
Annexe **4.7**. Schematic illustration from Lingtan *et al.* representing infected bone defects (IBDs). Treatment in femoral condyles under treatment by cascade MHT therapy-triggered immune response activation and treatment.[267]

4.7.1.4.3. MNPs-Induced Hyperthermia in Clinical Studies

The potential of MNPs in MHT has been proven numerous times in clinical studies, all in combination with RT. With the first one taking place in 2003[268], and since then proving an increase in survival rate of treated patients with few side effects and no serious complications.[269,270]

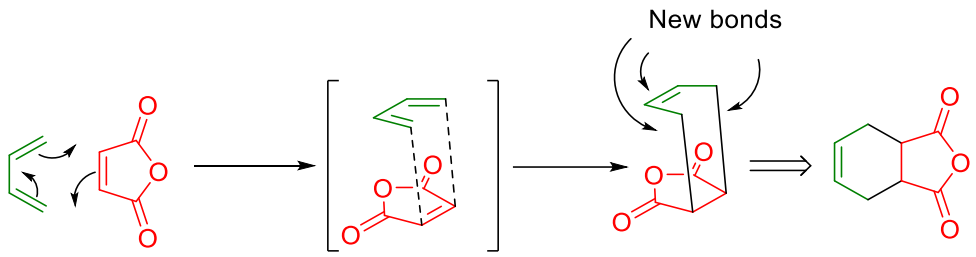
4.7.1.5. SO and Endoperoxide Formation

[4 + 2] cycloadditions, or more commonly known as Diels-Alder reactions, are a type of pericyclic cycloaddition that revolve around the formation of a cyclic product through a concerted mechanism. Diels-Alder reactions occur between a conjugated diene and dienophile and can be regarded as a rearrangement of the electronic conjugated structure of the involved reagents (Annexe **4.8**).[271]



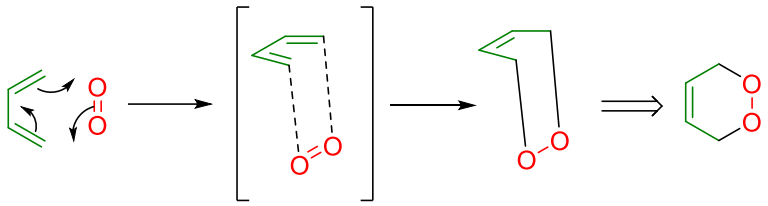
Annexe **4.8**. Electron rearrangement of a Diels-Alder [4+2] cycloaddition between a diene (green) and a dienophile (red).

The Diels-Alder reaction is stereospecific. Diels-Alder reactions follow a concerted mechanism that requires effective π -orbital overlap between the HOMO electron orbital of the diene and the LUMO of the dienophile. This geometry leads to the rearrangement of three π bonds to two new σ-bonds and one new π-bond (Annexe **4.9**).[100]



Annexe **4.9**. Schematic representation of the stereospecific mechanism of a Diels-Alder [4+2] cycloaddition between a diene (green) and a dienophile (red).

And following is an example of the Diels-Alder reaction for the endoperoxide formation with molecular oxygen (Annexe **4.10**).



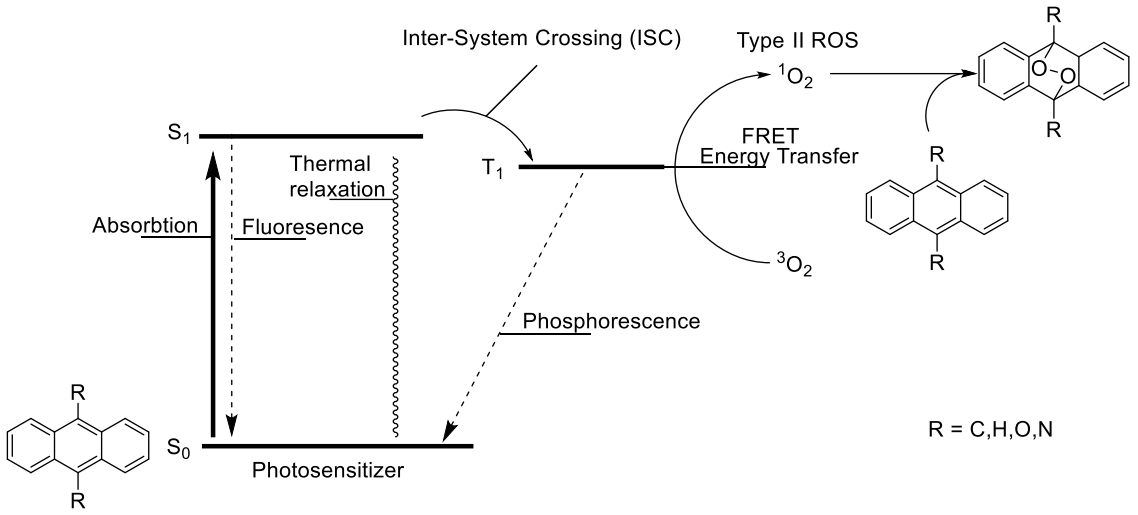
Annexe **4.10**. Schematic representation of the reaction mechanism of a Diels-Alder [4+2] cycloaddition between a diene (green) and oxygen (red).

We will, however, not enter into the frontier orbital description of cycloadditions as well as the regioselectivity of such reactions as it falls outside of the scope of this Chapter.

The requirement of effective orbital overlap leads us to one of the first requirements of the endoperoxide formation. Molecular oxygen is found in the electronic triplet spin ground state ($^3O_2$), whereas organic molecules are mostly found in the electronic singlet spin ground state (S_0). Electron orbital overlap and subsequent electron transfer between different spin orbitals are known as spin-forbidden transitions. Molecules can experience changes in their energy levels as long as they maintain their spin, and can change spin as long as they retain their energy levels, but not both at the same time.[103,272–274]

An easy way to circumvent such limitation is the use of electronically exited oxygen to their electronic spin singlet state ($^1O_2$), or SO. In this configuration, electron spin matches between interacting molecular orbitals, leading to effective orbital overlap and electron transfer.[169,275]

Just like in PDT, excitation of molecular oxygen to the SO exited state ($^1O_2$) requires the use of a photosensitizer. Briefly, and using our own anthracene as example; a photosensitizer, anthracene in our case, can undergo a light induced transition from the ground state (S_0) to the excited singlet state (S_1). Since energy levels between S_1 and triplet excited state (T_1) of a PS are similar, the ISC (change of electronic orbital spin) is not spin-forbidden.[95] At this stage, the photosensitizer can interact with molecular oxygen (matching electron spin orbitals) to promote the ground state orbital to an exited SO (photochemical Type II reaction), which in turn can then react with the anthracene photosensitizer to undergo the Diels-Alder reaction (Annexe **4.11**).[276,277]

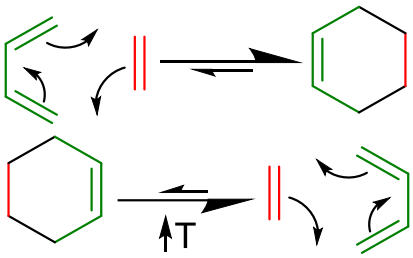


Annexe **4.11**. Schematic representation of the role of a generic anthracene as a PS, displaying the excitation pathways of anthracene to higher electronic excited states (S_1) as well as the available relaxation pathways photon emission via fluorescence or phosphorescence and thermal relaxation. As well as the available path of ISC to achieve a different spin excited state (T_1) from which Type II ROS can be achieved through electronic energy transfer to molecular oxygen, and subsequent reaction with anthracene to form the target endoperoxide functional group.

4.7.1.6. Endoperoxide Cleavage and SO Release

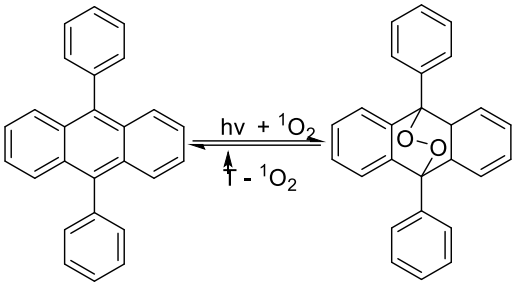
Having understood how we can load SO in our **DPA-COOH** monomer through an endoperoxide formation, we have to start explaining how we can achieve release of such highly reactive oxygen.

Diels-Alder reaction are reversible reactions that thermodynamically reach an equilibrium between products and reagents. Although formation of cyclic products is spontaneous and much more favoured than the reverse reaction, under harsh conditions such processes are possible to be reversed (Annexe **4.12**).[92]



Annexe **4.12**. Schematic representation of the preferred equilibria direction of Diels-Alder reaction and retro-Diels-Alder reaction.

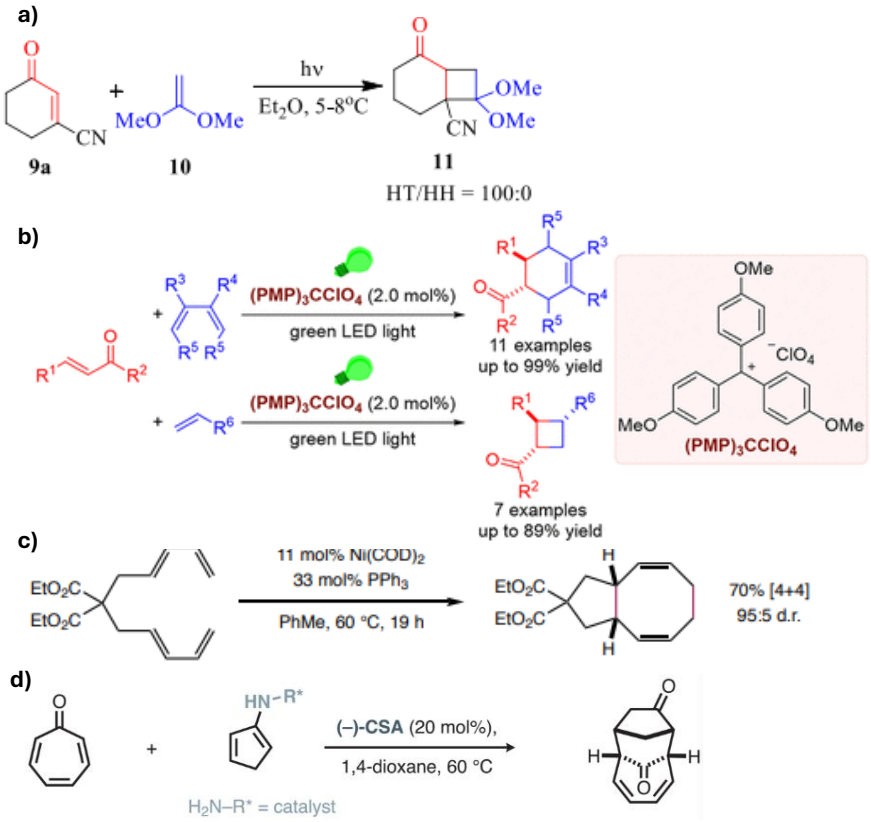
Such reactions are known as retro-Diels-Alder and leads to the recovery of the original reagents. In the case of anthracenes and endoperoxide functional groups, such reactions lead to the obtention of the original anthracene and molecular SO.[93] The process by which such reverse reactions occur are known as thermolysis, as the cleavage and obtention of the original molecule requires high temperatures to be applied. **DPA-COOH** can be classified in the family of 9,10-diphenylantrhacenes (**DPA**), as the core aromatic structure is shared among them. **DPA** was the first anthracenes in which such behaviour was discovered, back in 1967, and displayed yields of SO recovery around 60% under temperatures that can range between 60 to 100 °C (Annexe **4.13**).[103,278]



Annexe **4.13**. Endoperoxide formation from **DPA** under UV light irradiation and SO recovery under a thermolysis process.

4.7.1.6.1. Dimerization Reactions of 9,10-diphenylantrahcene

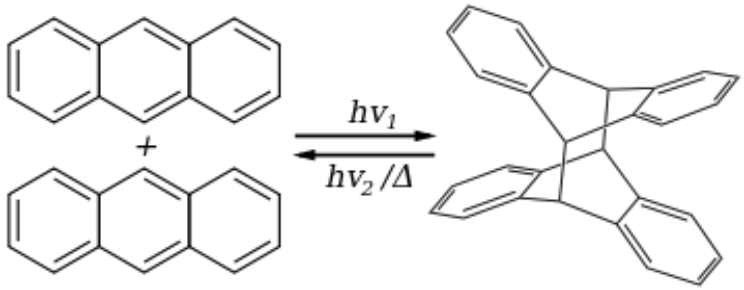
Diels-Alder, as we mentioned, is a cycloaddition reaction, but it is not the only possible cycloaddition that can occur. Just as Diels-Alder is a [4+2] cycloaddition (with the numbers referring to the total number of atoms of each component taking part) other combinations can also give cycloadditions, like [2+2][279], [4+4][280], [6+4][281] among other increasing number of atoms combinations (Annexe **4.14**).



Annexe **4.14**. Representative examples of **a)** [2+2] cycloaddition[279], **b)** [4+2] cycloaddition, **c)** [4+4] cycloaddition[282], **d)** [6+4] cycloaddition.[283]

However, not all electron combinations face the same activation mechanisms, and one must look at the Woodward-Hoffman rule to understand when a cycloaddition is thermally allowed or requires photoactivation to succeed.[100] For the sake of brevity, we will simplify the explanation behind the rules that govern activation of such reactions and simply use a mnemotechnic rule that tells us that [2+2], [4+4] … reactions require photoactivation to succeed, whereas [4+2], [6+2], [6+4] … are thermally allowed.[100]

Under such circumstances, and we go back to the structure of an anthracene molecule, the radiation needed to photoexcite the sensitizer and generate SO can be used for a [4+4] cycloaddition reaction between anthracene units (Annexe **4.15**).[101]



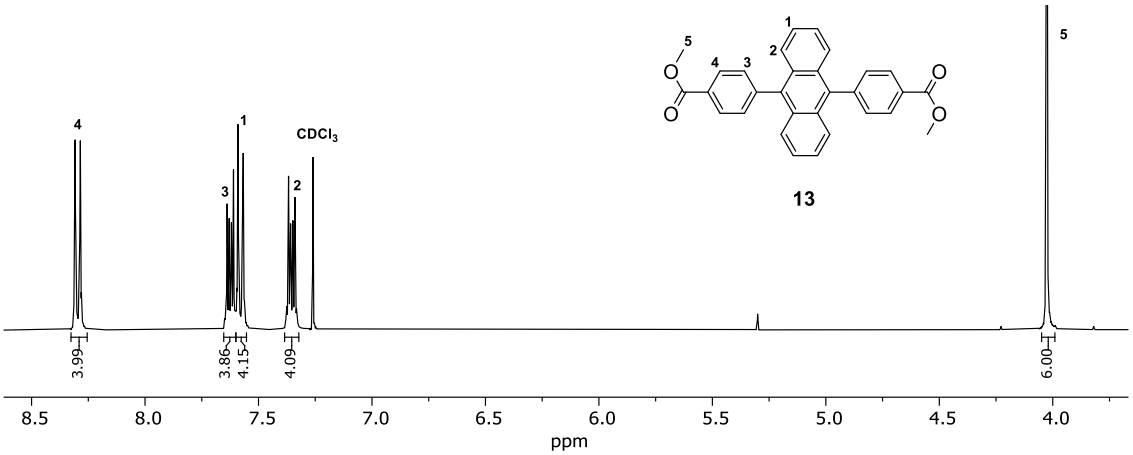
Annexe **4.15**. Photodimerization of anthracene as reported by Han *et al.*[102]

However, in the case of the chosen molecule for this Thesis, **DPA-COOH**, contains two phenyl moieties that introduce steric hindrance to the approach of two **DPA-COOH** molecules. As **DPA-COOH** cannot achieve effective overlapping of molecular orbitals due to steric hindrance it also cannot undergo such [4+4] cycloaddition. Thus, no reaction of dimerization occurs, ensuring the [4+2] cycloaddition is the only possible final outcome.[100,103]

Such behaviour, thus, allows to understand how anthracenes, or **DPA-COOH**, can be exploited to store and release SO on demand while avoiding side reactions that quench its storage. **DPA-COOH** allows to exploit molecular oxygen photoexcitation and heat induced thermolysis, or retro-Diels-Alder reaction in our system. While at the same time, providing the coordination capabilities of carboxylic acids to coordinate and polymerize to form a coordination polymer that will be exploited for the shell formation of our envisioned core-shell NP.

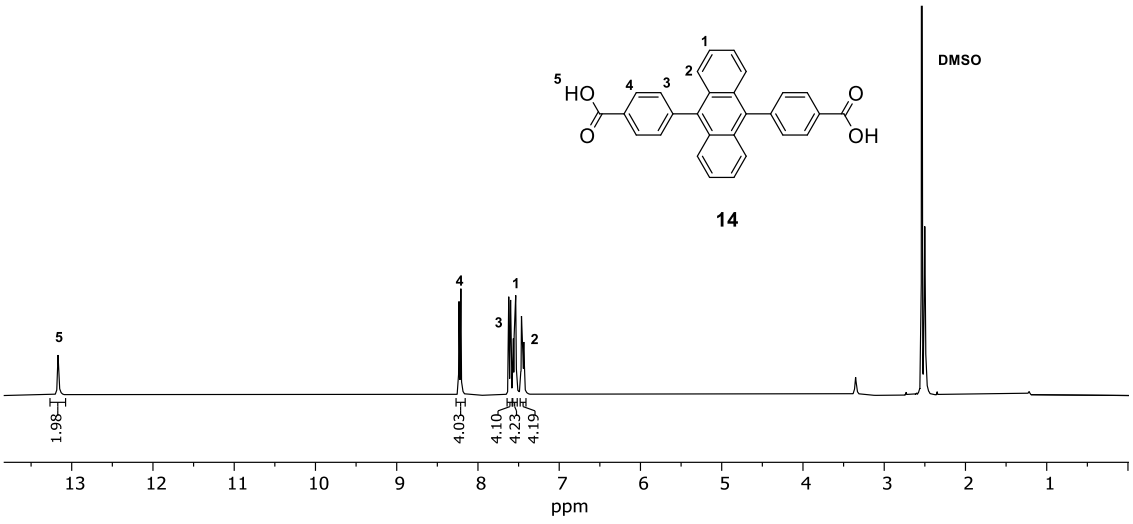
4.7.2. Experimental Data

Characterisation of Dimethyl 4,4'-(anthracene-9,10-diyl)dibenzoate (13)



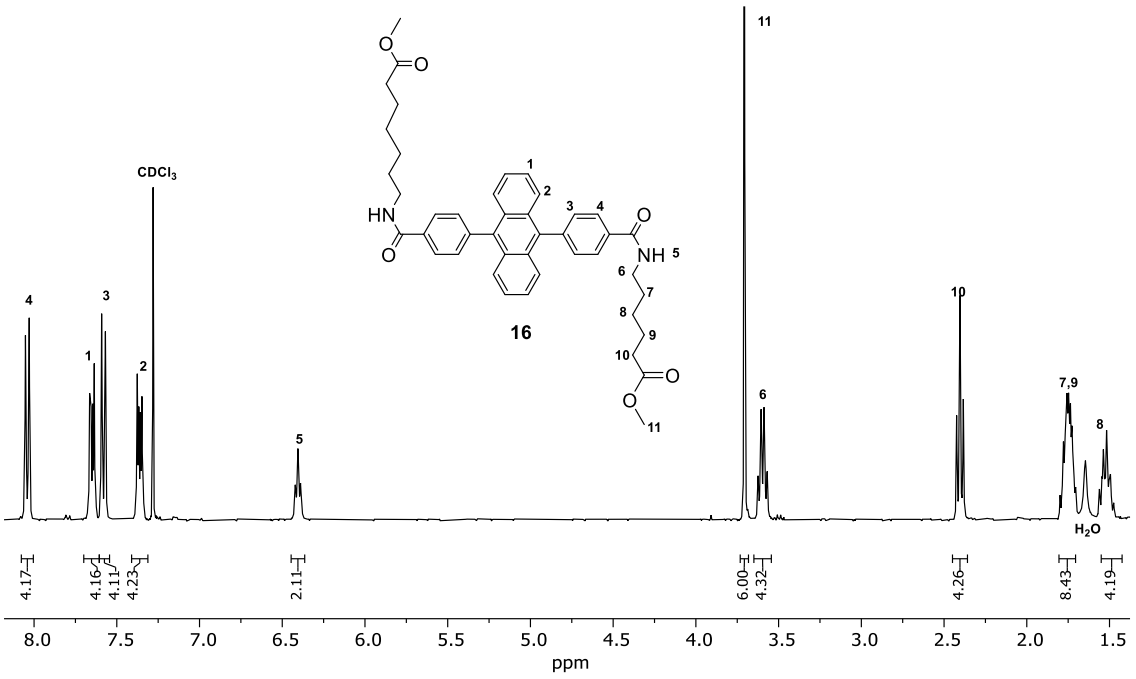
Annexe **4.16**. ^{1}H-NMR of **13**.

Characterisation of 4,4'-(anthracene-9,10-diyl)dibenzoic acid (14)



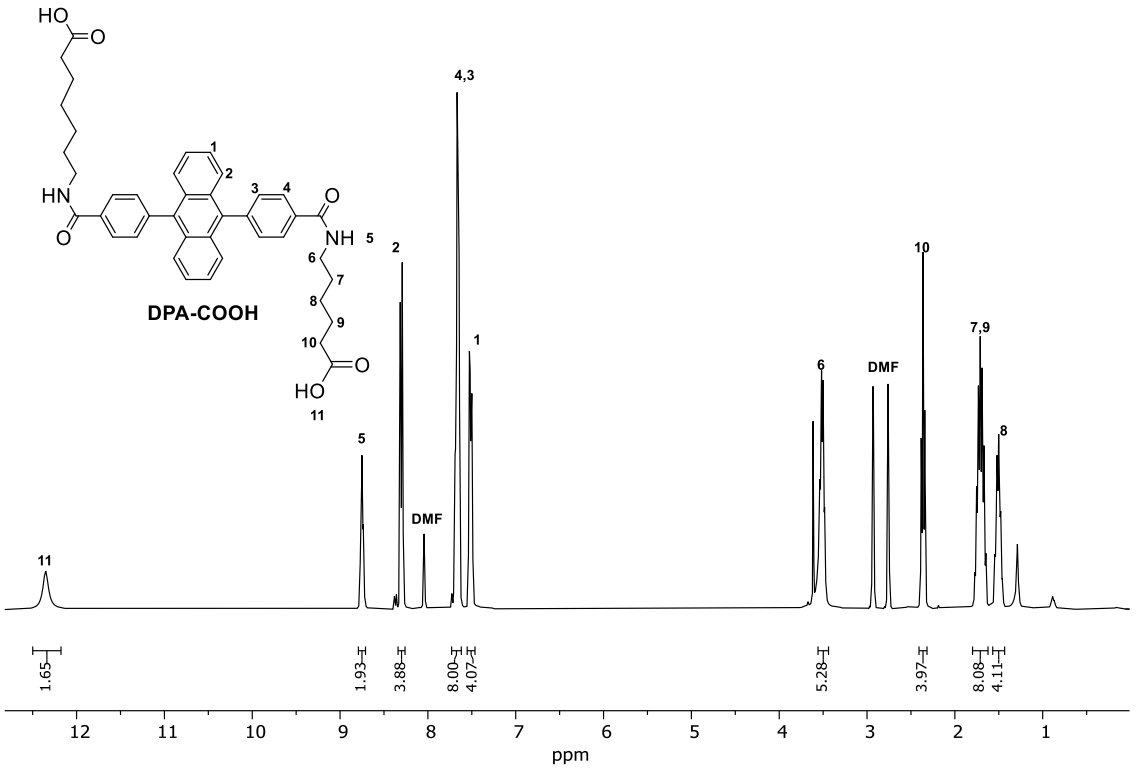
Annexe **4.17**. ^{1}H-NMR of **14**.

Characterisation of Dimethyl 4,4'-((4,4'-(anthracene-9,10-diyl)bis(benzoyl))bis-(azanediyl))dibutyrate (16)

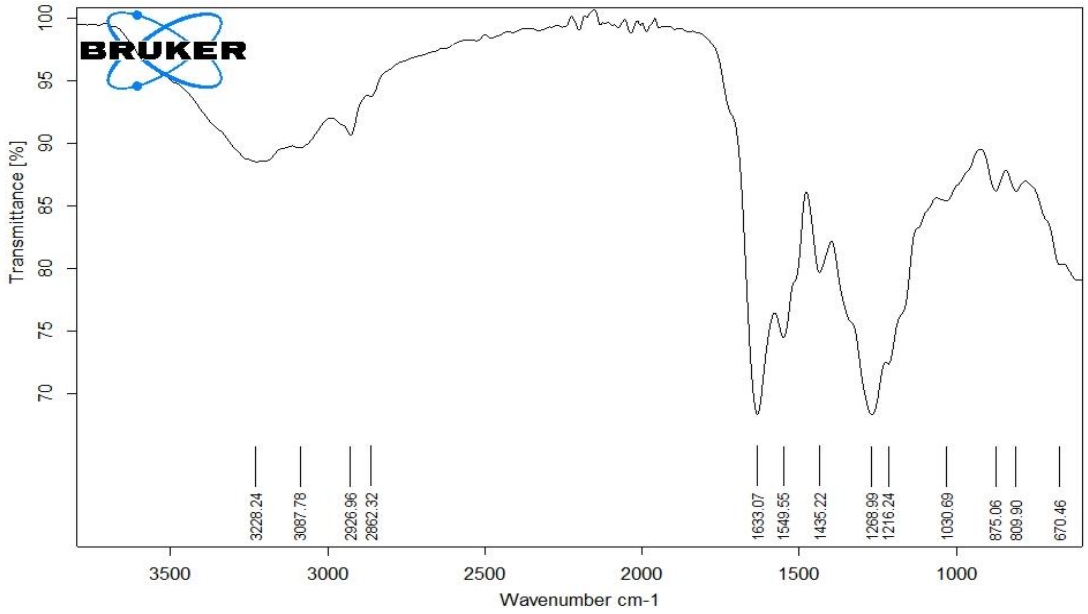


Annexe **4.18**. ^{1}H-NMR of **16**.

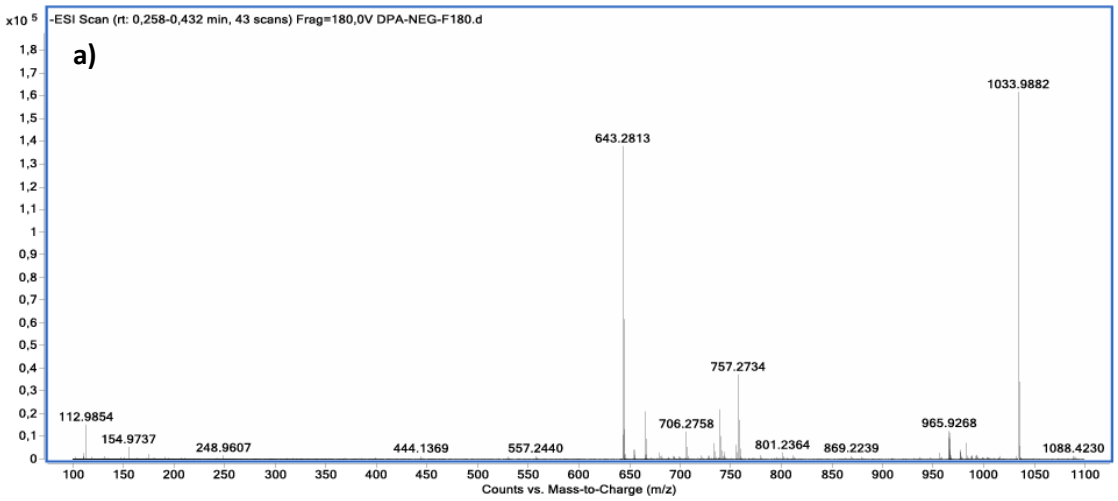
Characterisation of 7-(4-(10-(4-((5-carboxypentyl)carbamoyl)phenyl)anthracen-9-yl)benzamido)heptanoic acid (DPA-COOH)



Annexe **4.19**. ^{1}H-NMR of **DPA-COOH**.

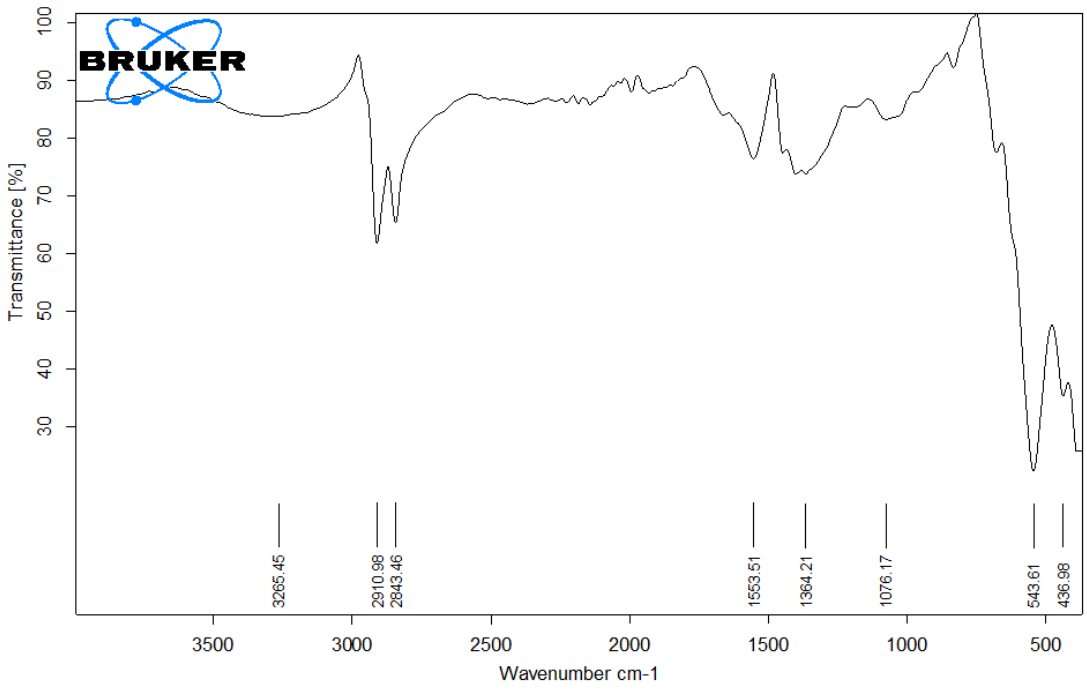


Annexe **4.20**. FTIR of **DPA-COOH**.

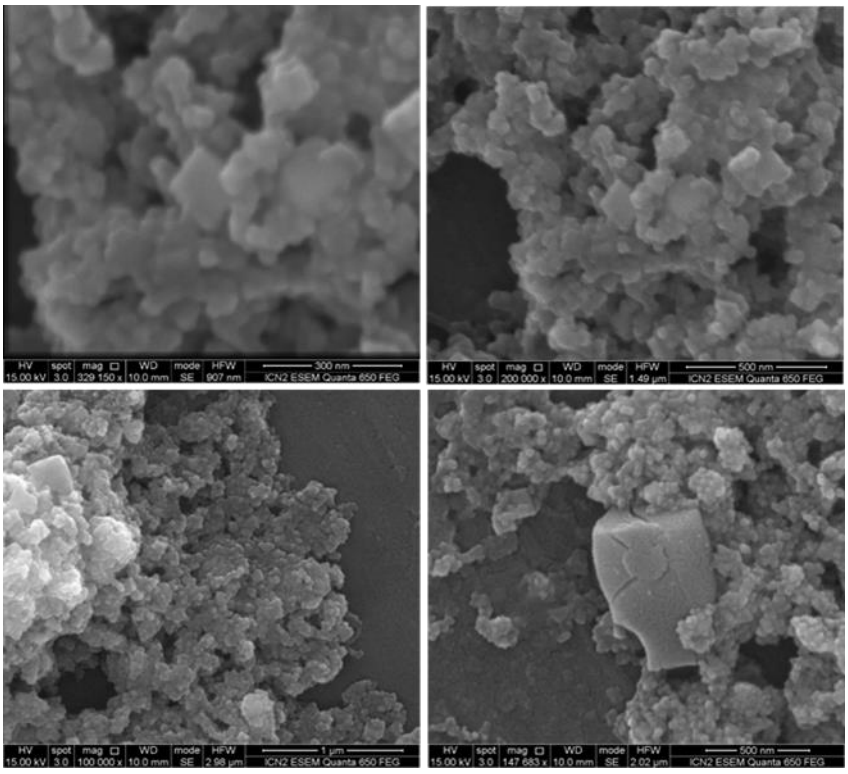


Annexe **4.21.** HRMS of SQL at **a**) with [M+Na] entire scan **b**) [M+Na] centered at **DPA-COOH** M value with theoretical values in red squares and real values in black lines.

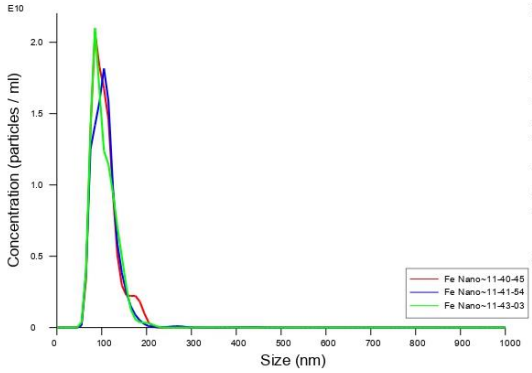
Characterisation of Iron Oxide Nanocubes



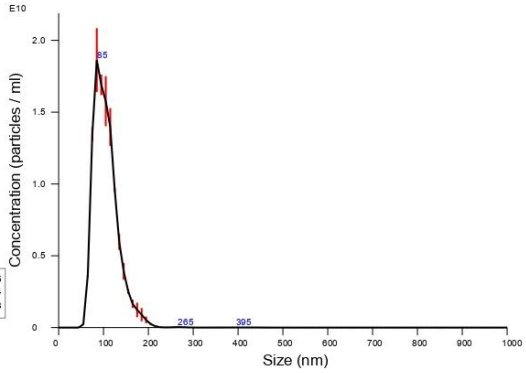
Annexe **4.22**. FTIR of iron oxide nanocubes.



Annexe **4.23.** SEM images of iron oxide nanocubes under a 5 nm Pt thin film layer imaging.



FTLA Concentration / Size graph for Experiment:
Fe Nanocubs 2023-04-25 11-40-32



Averaged FTLA Concentration / Size for Experiment:
Fe Nanocubs 2023-04-25 11-40-32
Error bars indicate + / -1 standard error of the mean

Included Files

Fe Nanocubs 2023-04-25 11-40-45
Fe Nanocubs 2023-04-25 11-41-54
Fe Nanocubs 2023-04-25 11-43-03

Details

NTA Version:	NTA 3.4 Build 3.4.4
Script Used:	SOP Standard Measurement 11-40-18AM 25A~
Time Captured:	11:40:32 25/04/2023
Operator:	Amable Bernabe
Pre-treatment:	1:100
Sample Name:	Fe Nanocubs
Diluent:	water
Remarks:	

Capture Settings

Camera Type:	sCMOS
Laser Type:	Blue488
Camera Level:	11
Slider Shutter:	890
Slider Gain:	146
FPS	25.0
Number of Frames:	1498
Temperature:	23.8 - 23.9 ºC
Viscosity:	(Water) 0.912 - 0.914 cP
Dilution factor:	1 x 10e2
Syringe Pump Speed:	50

Analysis Settings

Detect Threshold:	5
Blur Size:	Auto
Max Jump Distance:	Auto: 14.3 - 14.8 pix

Results

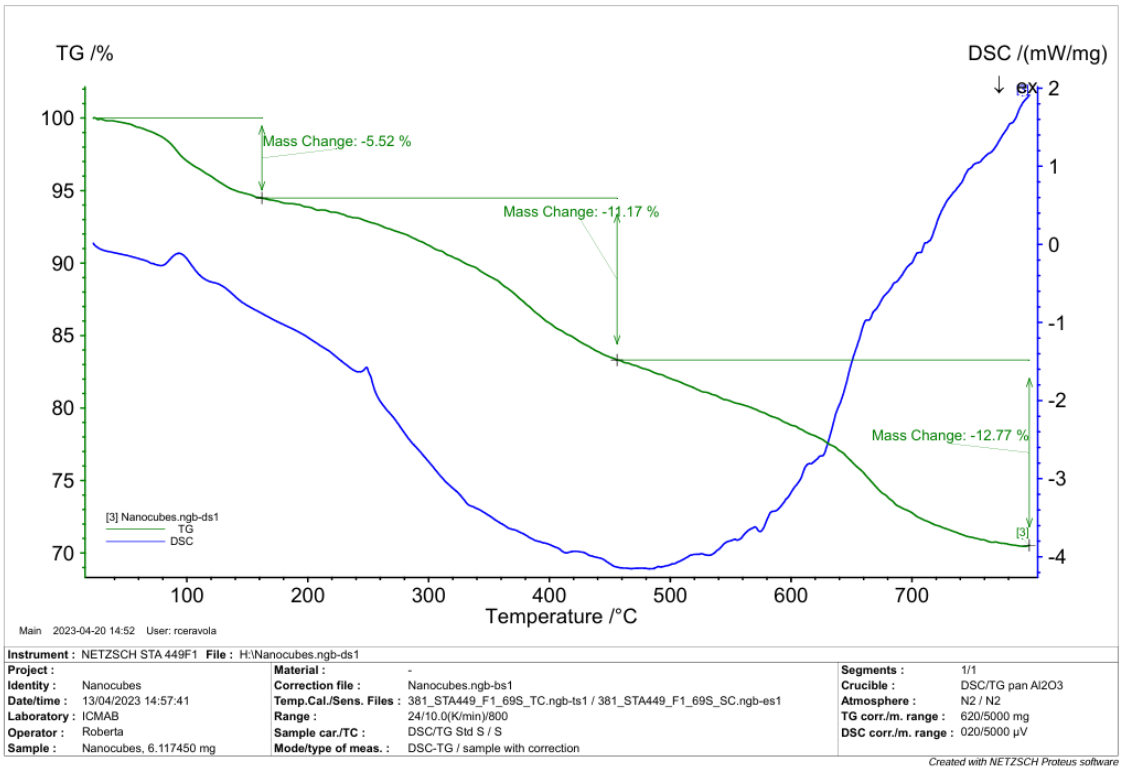
Stats: Merged Data

Mean:	105.7 nm
Mode:	87.5 nm
SD:	28.4 nm
D10:	75.2 nm
D50:	101.2 nm
D90:	141.0 nm

Stats: Mean +/- Standard Error

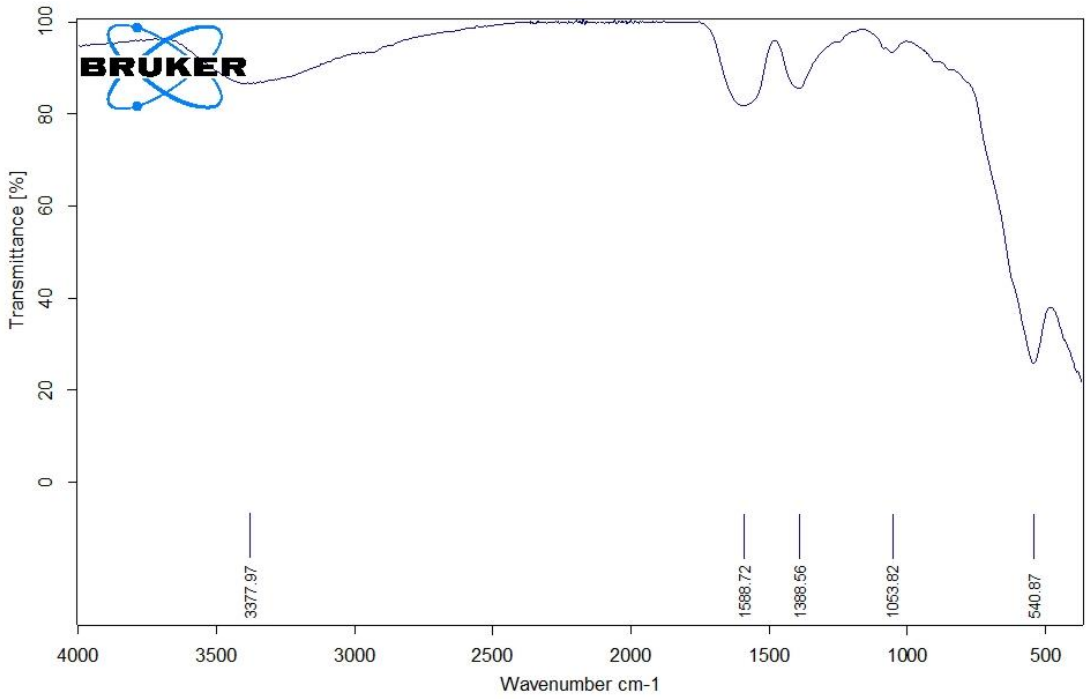
Mean:	105.7 +/- 0.6 nm
Mode:	92.9 +/- 6.1 nm
SD:	28.4 +/- 0.4 nm
D10:	75.2 +/- 0.3 nm
D50:	101.0 +/- 1.4 nm
D90:	141.5 +/- 1.7 nm
Concentration:	1.10e+11 +/- 2.84e+09 particles/ml
	59.9 +/- 1.6 particles/frame
	65.1 +/- 1.7 centres/frame

Annexe **4.24**. NTA analysis summary of iron oxide nanocubes.



Annexe **4.25**. TGA–DSC analysis of iron oxide nanocubes.

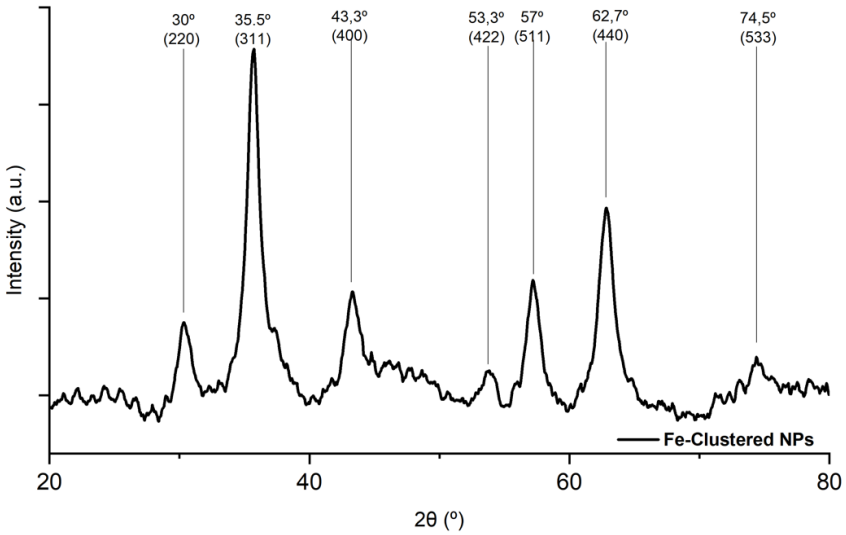
Characterisation of Fe-Clustered NP



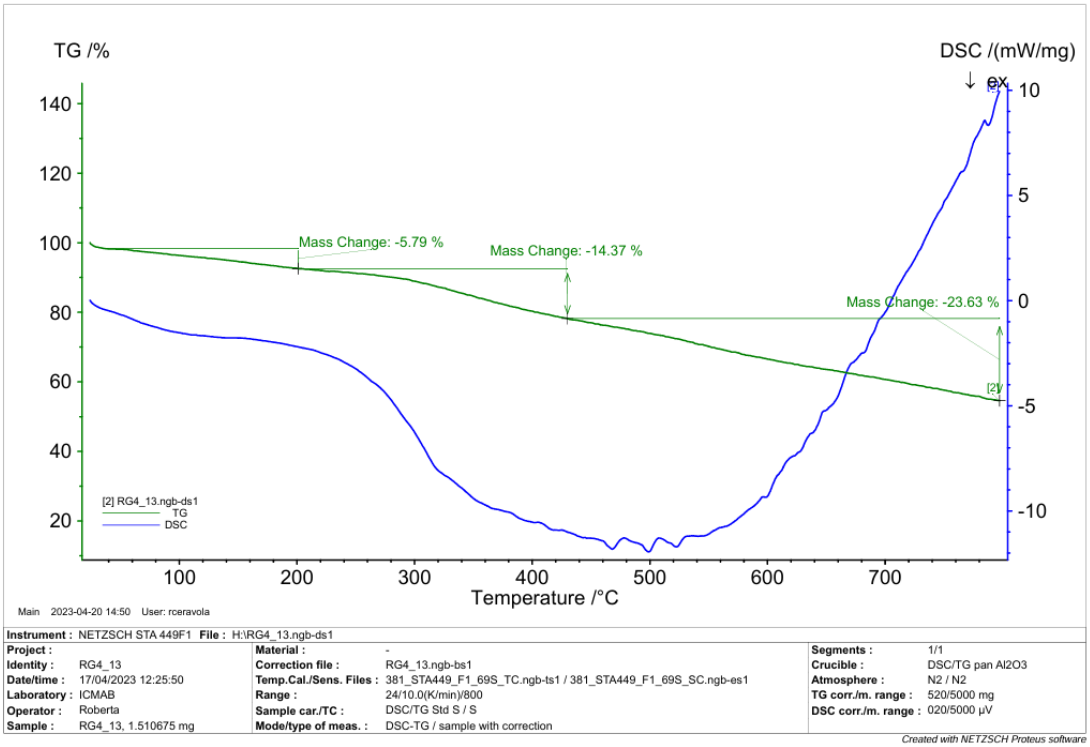
Annexe **4.26**. FTIR of **Fe-Clustered NPs**.

	Fe [He]	
Sample Name	Conc. [%]	Conc. RSD
FeOXide NP	65,20	2,3

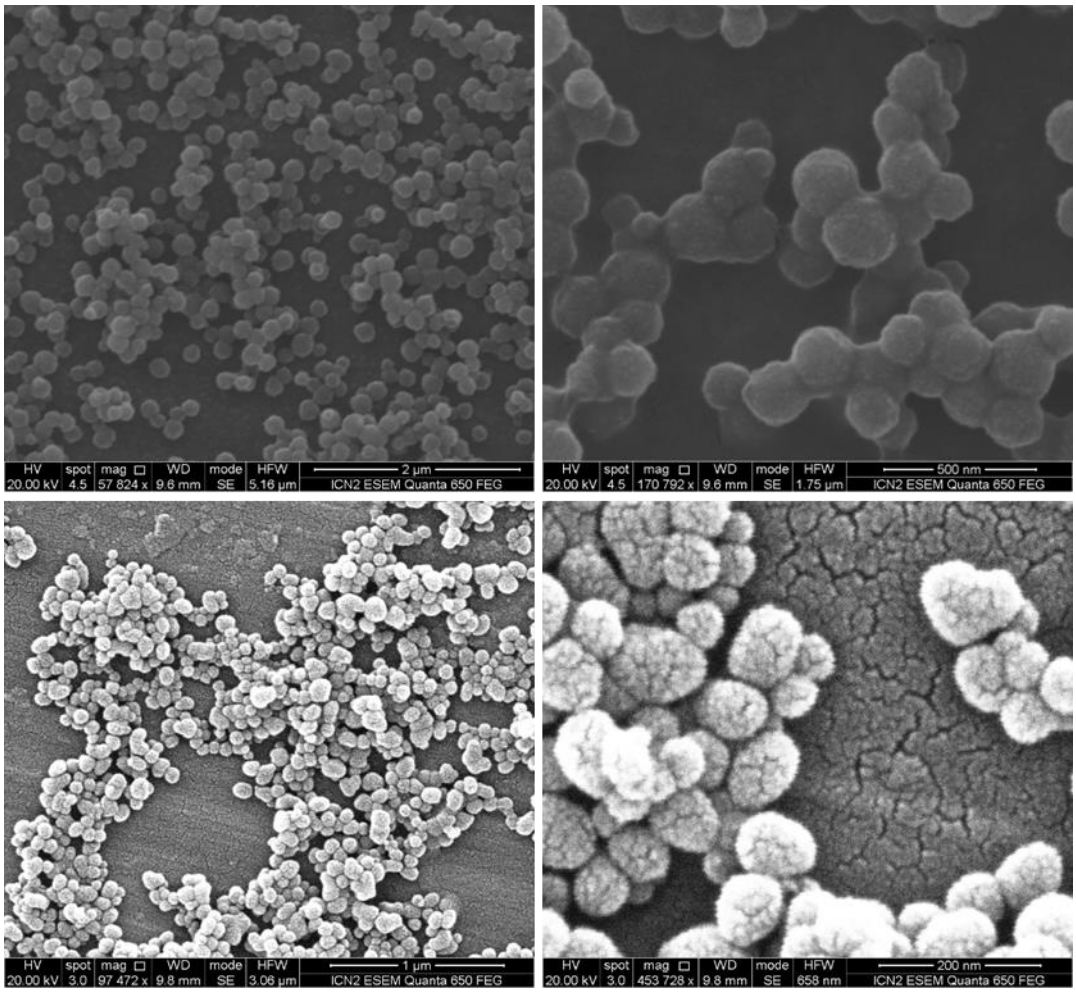
Annexe **4.27**. ICP-MS of Fe% in w/w in **Fe-Clustered NPs**.



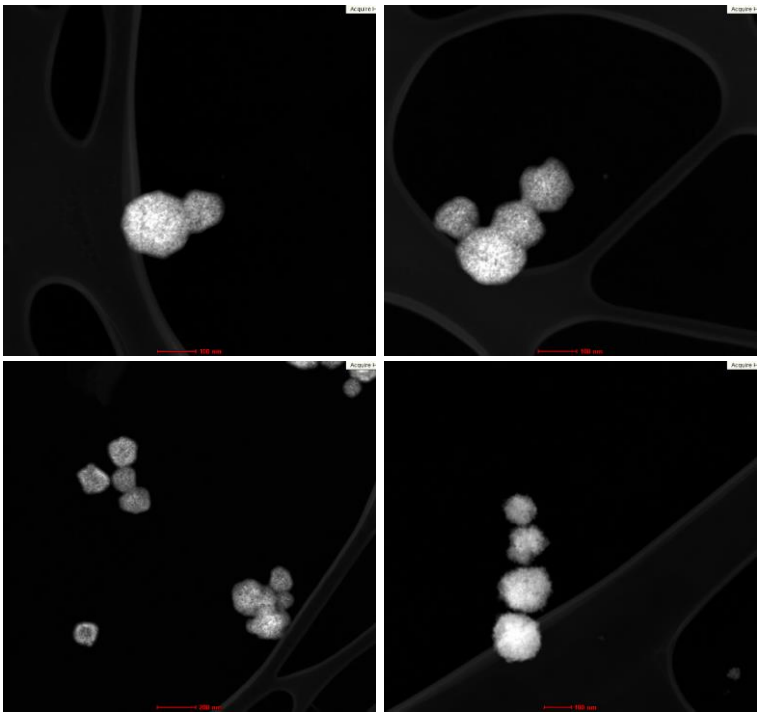
Annexe **4.28**. Room temperature XRD measurement for **Fe-Clustered NPs**.



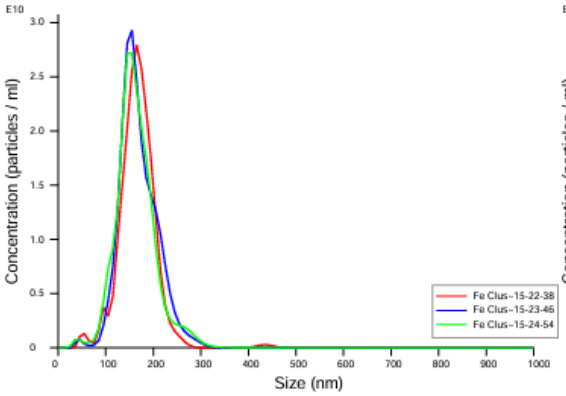
Annexe **4.29**. TGA-DSC analysis of **Fe-Clustered NPs**.



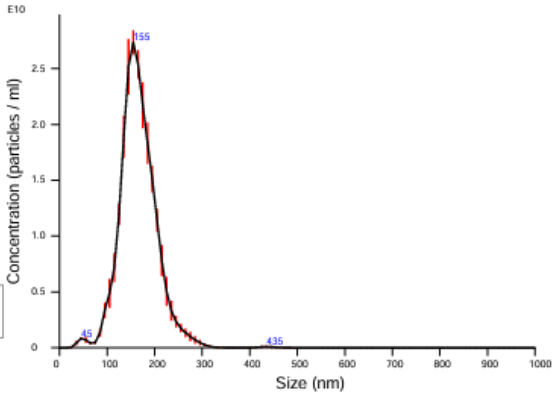
Annexe **4.30.** SEM images of **Fe-Clustered NP** under a 5 nm Pt thin film layer imaging.



Annexe **4.31.** STEM imaging at HAADF detector mode of **Fe-Clustered NP**.



FTLA Concentration / Size graph for Experiment:
Fe Cluster 2024-04-15 15-22-17



Averaged FTLA Concentration / Size for Experiment:
Fe Cluster 2024-04-15 15-22-17
Error bars indicate + / -1 standard error of the mean

Included Files

Fe Cluster 2024-04-15 15-22-38
Fe Cluster 2024-04-15 15-23-46
Fe Cluster 2024-04-15 15-24-54

Details

NTA Version:	NTA 3.4 Build 3.4.4
Script Used:	SOP Standard Measurement 03-22-01PM 15A~
Time Captured:	15:22:17 15/04/2024
Operator:	Amable Bernabe
Pre-treatment:	1:500
Sample Name:	Fe Cluster
Diluent:	Milli-Q water
Remarks:	

Capture Settings

Camera Type:	sCMOS
Laser Type:	Blue488
Camera Level:	8
Slider Shutter:	317
Slider Gain:	15
FPS	25.0
Number of Frames:	1498
Temperature:	25.7 - 25.8 °C
Viscosity:	(Water) 0.873 - 0.875 cP
Dilution factor:	5 x 10e2
Syringe Pump Speed:	30

Analysis Settings

Detect Threshold:	5
Blur Size:	Auto
Max Jump Distance:	Auto: 14.0 - 14.8 pix

Results

Stats: Merged Data

Mean:	165.9 nm
Mode:	155.3 nm
SD:	40.1 nm
D10:	121.9 nm
D50:	162.7 nm
D90:	213.5 nm

Stats: Mean +/- Standard Error

Mean:	165.9 +/- 1.6 nm
Mode:	155.8 +/- 4.8 nm
SD:	40.1 +/- 0.6 nm
D10:	121.8 +/- 2.9 nm
D50:	162.5 +/- 2.2 nm
D90:	212.9 +/- 3.8 nm
Concentration:	2.20e+11 +/- 4.85e+09 particles/ml
	24.0 +/- 0.5 particles/frame
	45.2 +/- 1.3 centres/frame

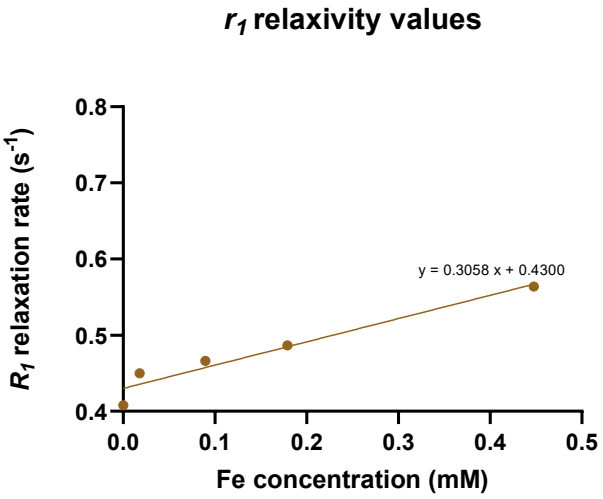
Annexe **4.32**. NTA analysis summary of **Fe-Clustered NP**.

Fe-Cluster

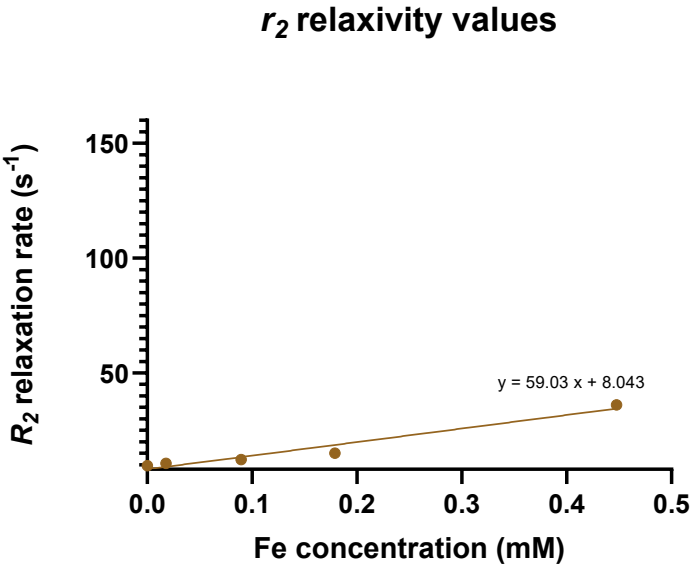
[Fe] (μg·mL^{-1})	T_1 (ms)	T_1 (s)	$R_1 = 1/T_1$ (s^{-1})
0	2452	2.45	0.4078
1	2222	2.22	0.4500
5	2145	2.15	0.4662
10	2055	2.06	0.4865
25	1774	1.77	0.5638

[Fe] (μg·mL^{-1})	T_2 (ms)	T_2 (s)	$R_2 = 1/T_2$ (s^{-1})
0	104.2	0.1042	9.597
1	94.0	0.0940	10.638
5	81.9	0.0819	12.215
10	66.5	0.0665	15.045
25	27.7	0.0277	36.058

Annexe **4.33**. Transversal T_1 and T_2 and their corresponding R_1 and R_2 values of **Fe-Clustered NP**.

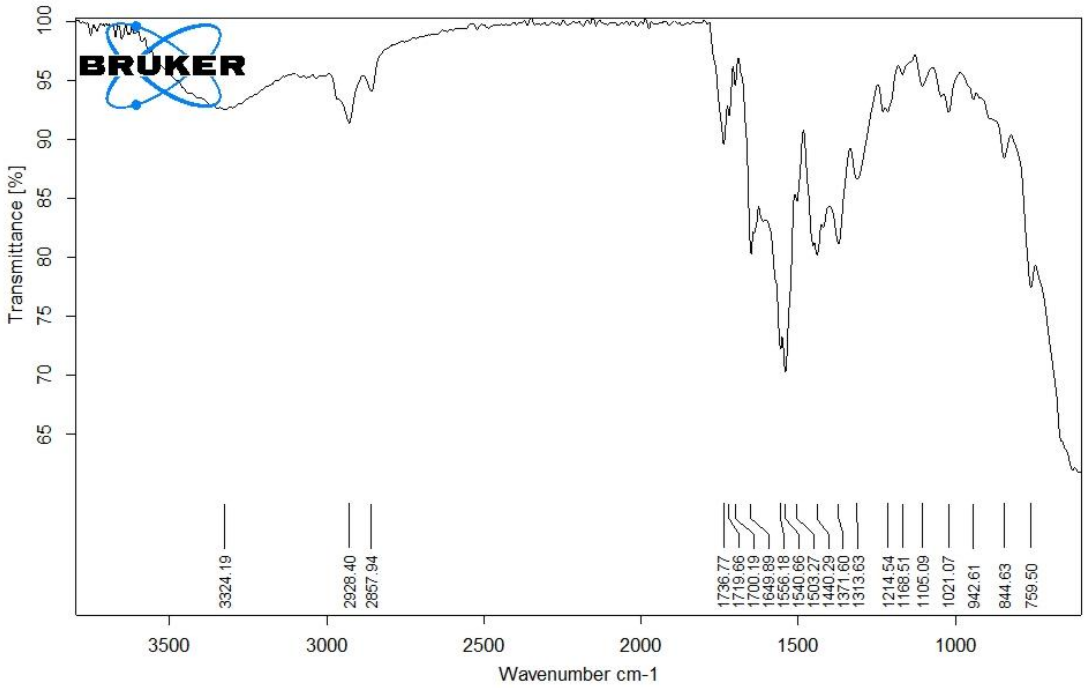


Annexe **4.34**. r_1 value of **Fe-clustered NP**.

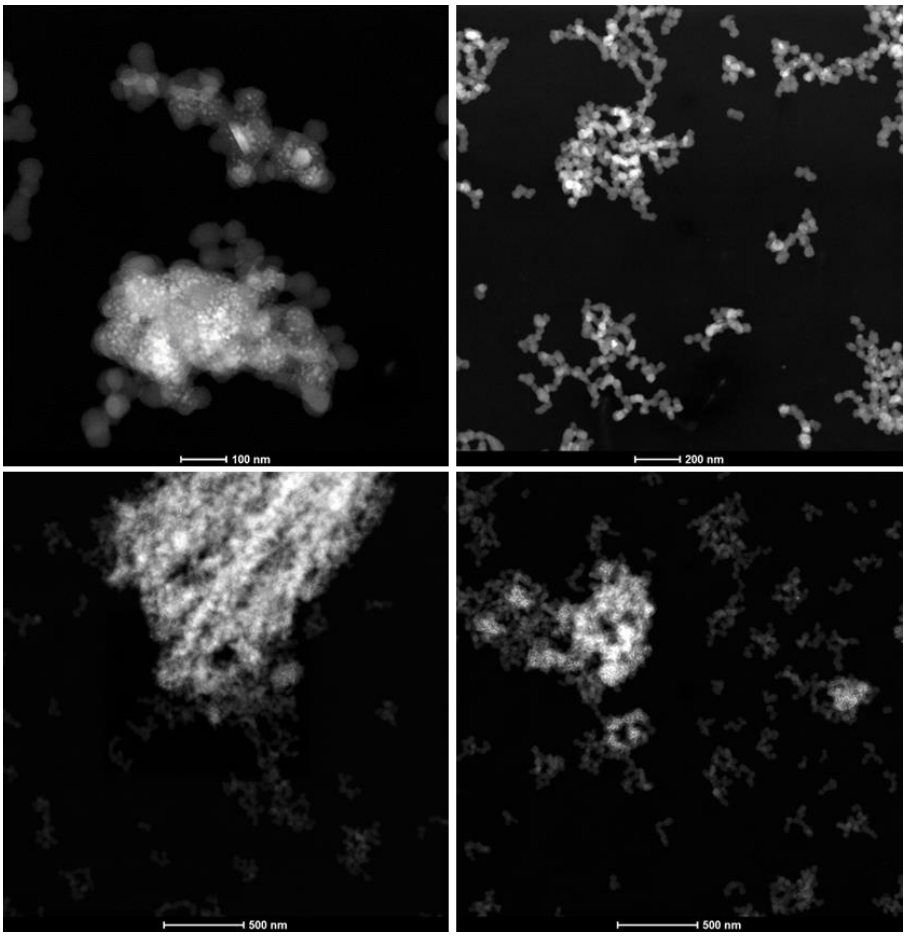


Annexe **4.35**. r_2 value of **Fe-Clustered NP**.

Characterisation of pDPA-CNP@Nanocube NPs

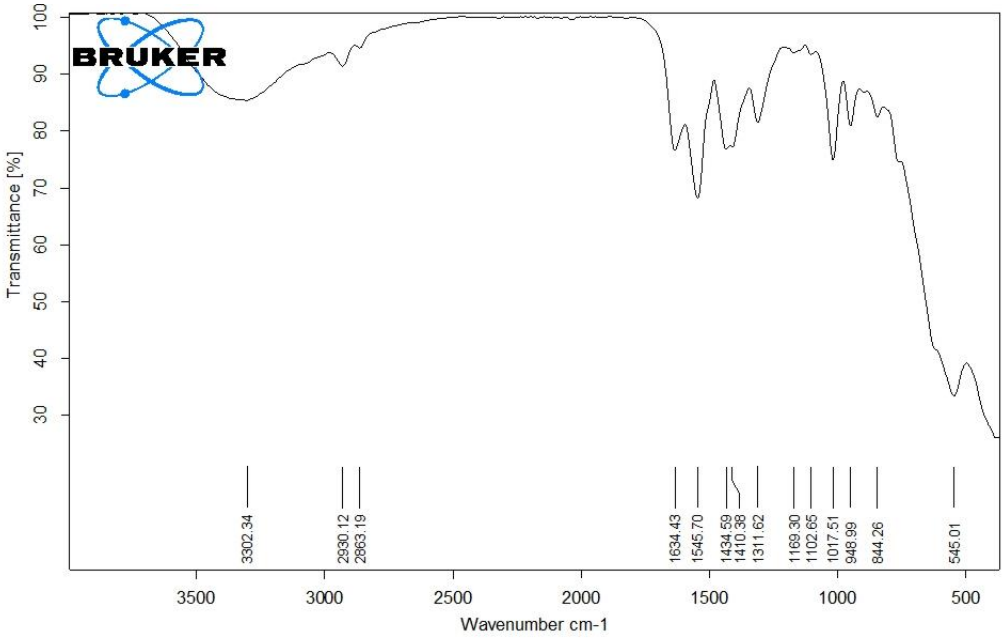


Annexe **4.36**. FTIR of **pDPA-CNP@Nanocube NPs**.



Annexe **4.37.** STEM imaging at HAADF detector mode of **pDPA-CNP@Nanocube NPs**.

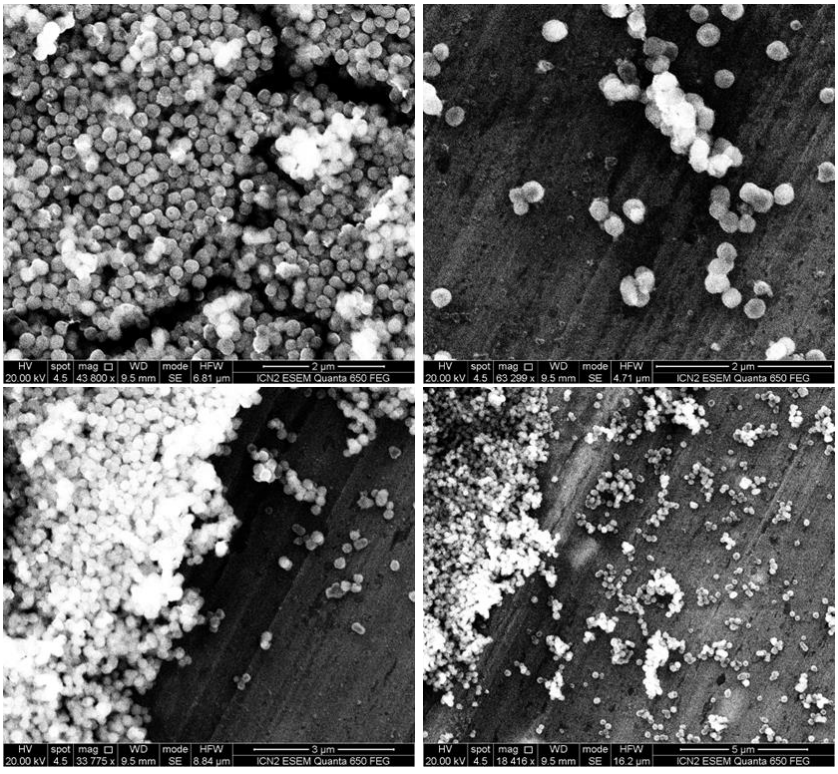
Characterisation of pDPA-CNP@Fe NPs



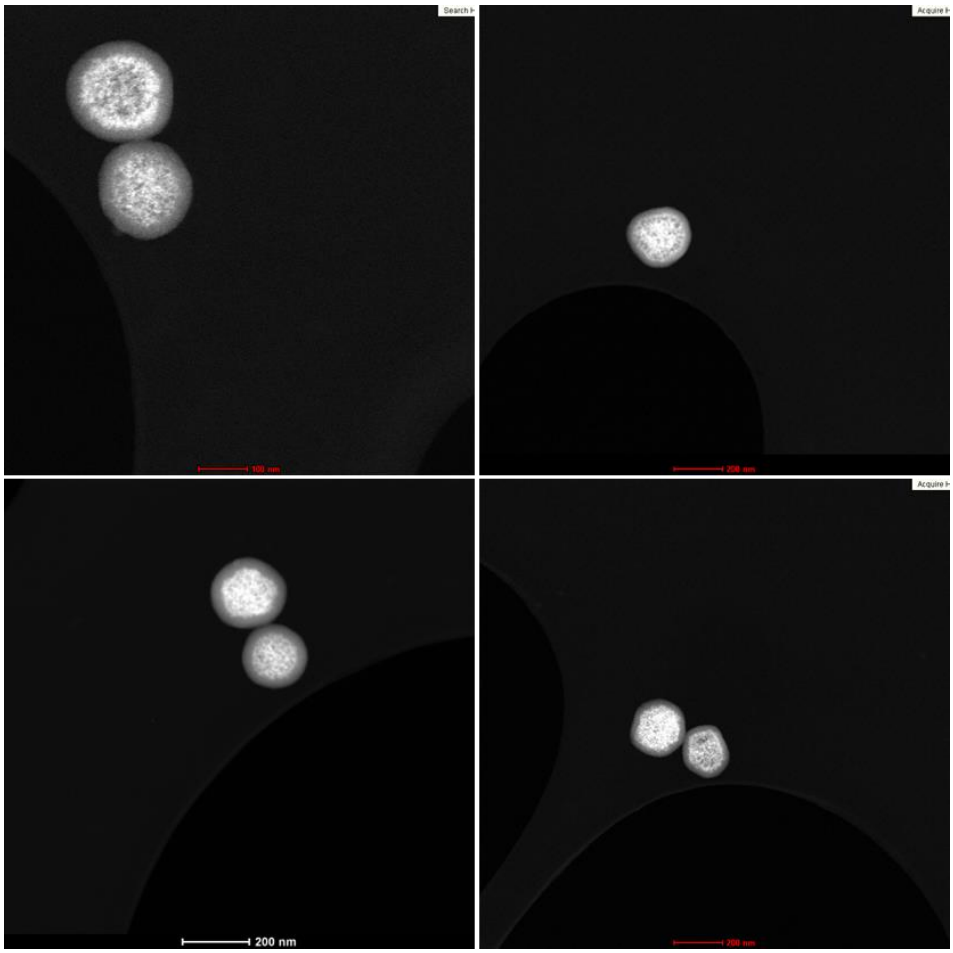
Annexe **4.38**. FTIR of **pDPA-CNP@Fe NPs**.

	Fe [He]	
Sample Name	Conc. [%]	Conc. RSD
FEDPA NP 5,4 A	13,80	2,8
FEDPA NP 5.4 B	17,22	3,0

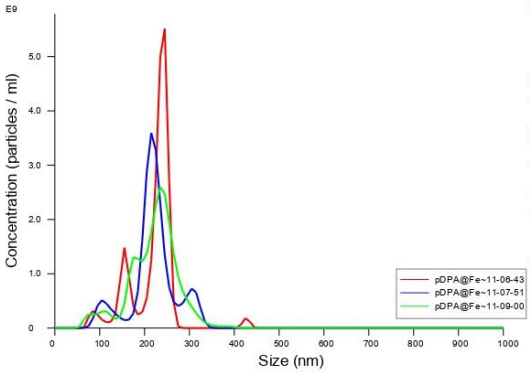
Annexe **4.39**. ICP-MS of Fe% in w/w in **pDPA-CNP@Fe NPs**.



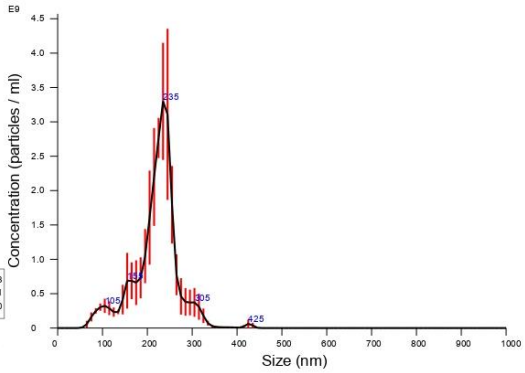
Annexe **4.40.** SEM images of **pDPA-CNP@Fe NPs** under a 5 nm Pt thin film layer imaging.



Annexe **4.41.** STEM imaging at HAADF detector mode of **pDPA-CNP@Fe NPs**.



FTLA Concentration / Size graph for Experiment:
pDPA@Fe 2025-04-08 11-06-32



Averaged FTLA Concentration / Size for Experiment:
pDPA@Fe 2025-04-08 11-06-32
Error bars indicate + / -1 standard error of the mean

Included Files

pDPA@Fe 2025-04-08 11-06-43
pDPA@Fe 2025-04-08 11-07-51
pDPA@Fe 2025-04-08 11-09-00

Details

NTA Version:	NTA 3.4 Build 3.4.4
Script Used:	SOP Standard Measurement 11-06-21AM 08A~
Time Captured:	11:06:32 08/04/2025
Operator:	Amable Bernabe
Pre-treatment:	1:50
Sample Name:	pDPA@Fe
Diluent:	water
Remarks:	

Capture Settings

Camera Type:	sCMOS
Laser Type:	Blue488
Camera Level:	7
Slider Shutter:	165
Slider Gain:	15
FPS	25.0
Number of Frames:	1498
Temperature:	21.6 - 21.7 ºC
Viscosity:	(Water) 0.959 - 0.961 cP
Dilution factor:	5 x 10e1
Syringe Pump Speed:	30

Analysis Settings

Detect Threshold:	5
Blur Size:	Auto
Max Jump Distance:	Auto: 11.8 - 12.8 pix

Results

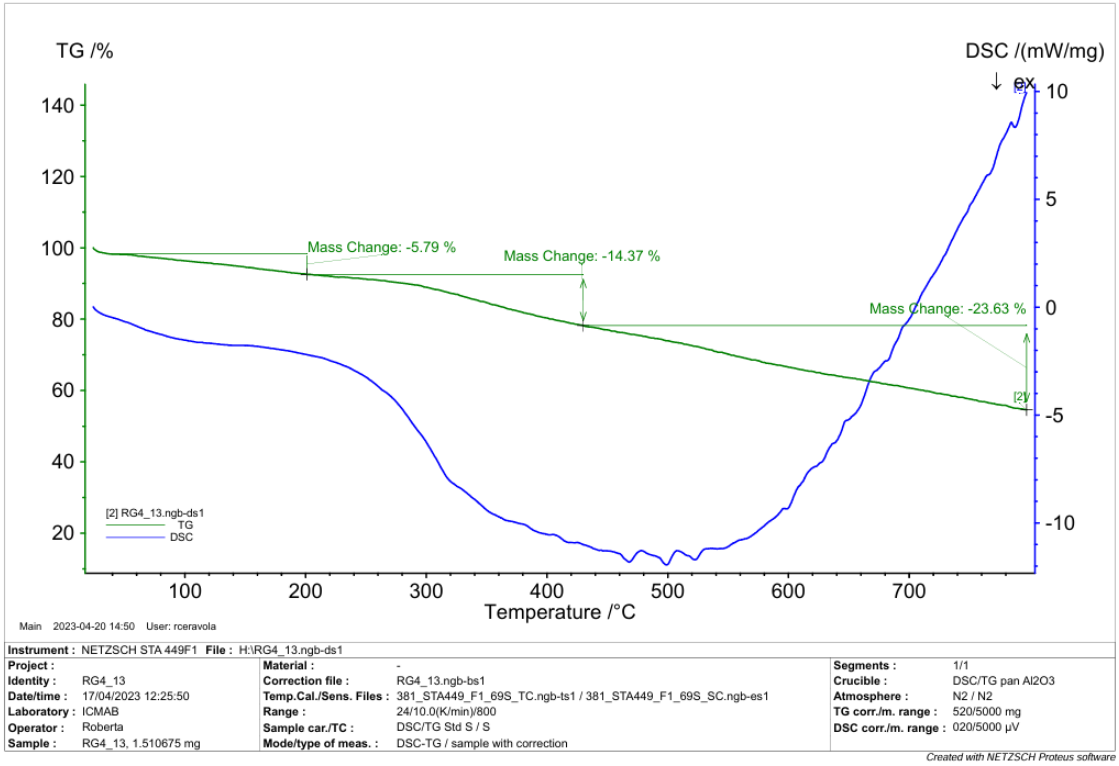
Stats: Merged Data

Mean:	220.0 nm
Mode:	237.4 nm
SD:	51.5 nm
D10:	151.9 nm
D50:	227.6 nm
D90:	269.5 nm

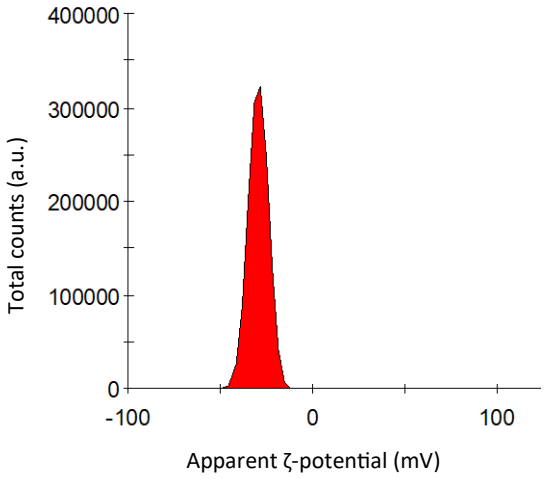
Stats: Mean +/- Standard Error

Mean:	220.0 +/- 0.2 nm
Mode:	231.9 +/- 7.6 nm
SD:	51.4 +/- 1.1 nm
D10:	151.3 +/- 3.0 nm
D50:	227.1 +/- 4.1 nm
D90:	275.4 +/- 11.2 nm
Concentration:	2.40e+10 +/- 3.95e+08 particles/ml
	26.2 +/- 0.4 particles/frame
	45.7 +/- 1.0 centres/frame

Annexe **4.42**. NTA analysis summary of **pDPA-CNP@Fe NPs**.



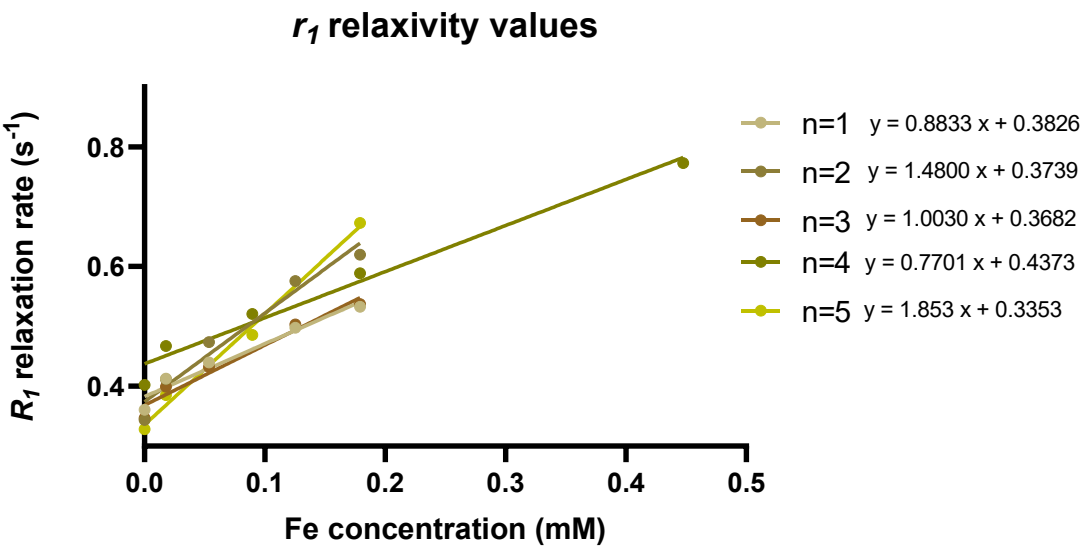
Annexe **4.43**. TGA – DSC analysis of **pDPA-CNP@Fe NPs**.



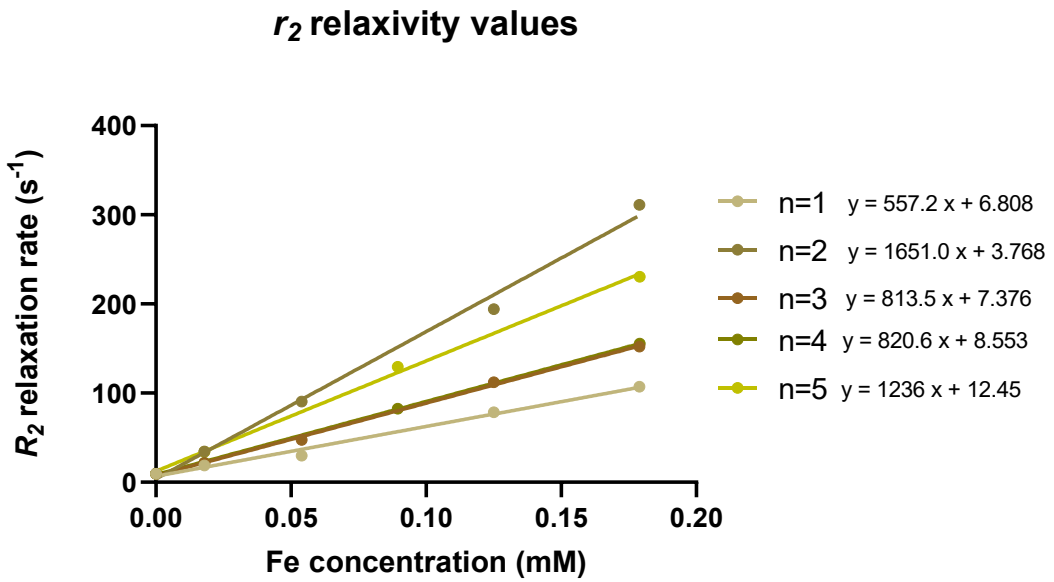
Annexe **4.44**. Representative ζ-potential of **pDPA-CNP@Fe NPs** after UV irradiation at 365 nm for 30 minutes.

n = 1				n = 1			
[Fe] (µg·mL^{-1})	T_1 (ms)	T_1 (s)	$R_1 = 1/T_1$ (s^{-1})	[Fe] (µg·mL^{-1})	T_2 (ms)	T_2 (s)	$R_2 = 1/T_2$ (s^{-1})
0	2770	2.77	0.361	0	105.5	0.1055	9.481
1	2423	2.42	0.413	1	53.2	0.0532	18.805
3	2274	2.27	0.440	3	33.7	0.0337	29.693
7	2007	2.01	0.498	7	12.8	0.0128	78.416
10	1877	1.88	0.533	10	9.3	0.0093	107.163
n = 2				**n = 2**			
[Fe] (µg·mL^{-1})	T_1 (ms)	T_1 (s)	$R_1 = 1/T_1$ (s^{-1})	[Fe] (µg·mL^{-1})	T_2 (ms)	T_2 (s)	$R_2 = 1/T_2$ (s^{-1})
0	2907	2.91	0.344	0	106.4	0.1064	9.401
1	2427	2.43	0.412	1	29.1	0.0291	34.420
3	2109	2.11	0.474	3	11.0	0.0110	90.580
7	1736	1.74	0.576	7	5.2	0.0052	194.109
10	1613	1.61	0.620	10	3.2	0.0032	311.107
n = 3				**n = 3**			
[Fe] (µg·mL^{-1})	T_1 (ms)	T_1 (s)	$R_1 = 1/T_1$ (s^{-1})	[Fe] (µg·mL^{-1})	T_2 (ms)	T_2 (s)	$R_2 = 1/T_2$ (s^{-1})
0	2884	2.88	0.3467	0	105.3	0.1053	9.496
1	2506	2.51	0.3990	1	46.3	0.0463	21.595
3	2313	2.31	0.4323	3	21.1	0.0211	47.505
7	1988	1.99	0.5031	7	8.9	0.0089	112.108
10	1862	1.86	0.5371	10	6.6	0.0066	152.064
n = 4				**n = 4**			
[Fe] (µg·mL^{-1})	T_1 (ms)	T_1 (s)	$R_1 = 1/T_1$ (s^{-1})	[Fe] (µg·mL^{-1})	T_2 (ms)	T_2 (s)	$R_2 = 1/T_2$ (s^{-1})
0	2487	2.49	0.402	0	105.2	0.1052	9.509
1	2143	2.14	0.467	1	45.6	0.0456	21.946
5	1921	1.92	0.521	5	12.1	0.0121	82.418
10	1697	1.70	0.589	10	6.4	0.0064	155.440
25	1293	1.29	0.773	25	NOISE		
n = 5				**n = 5**			
[Fe] (µg·mL^{-1})	T_1 (ms)	T_1 (s)	$R_1 = 1/T_1$ (s^{-1})	[Fe] (µg·mL^{-1})	T_2 (ms)	T_2 (s)	$R_2 = 1/T_2$ (s^{-1})
0	3046	3.05	0.328	0	103.6	0.1036	9.651
1	2598	2.60	0.385	1	29.3	0.0293	34.113
5	2058	2.06	0.486	5	7.7	0.0077	129.494
10	1485	1.49	0.673	10	4.3	0.0043	230.665

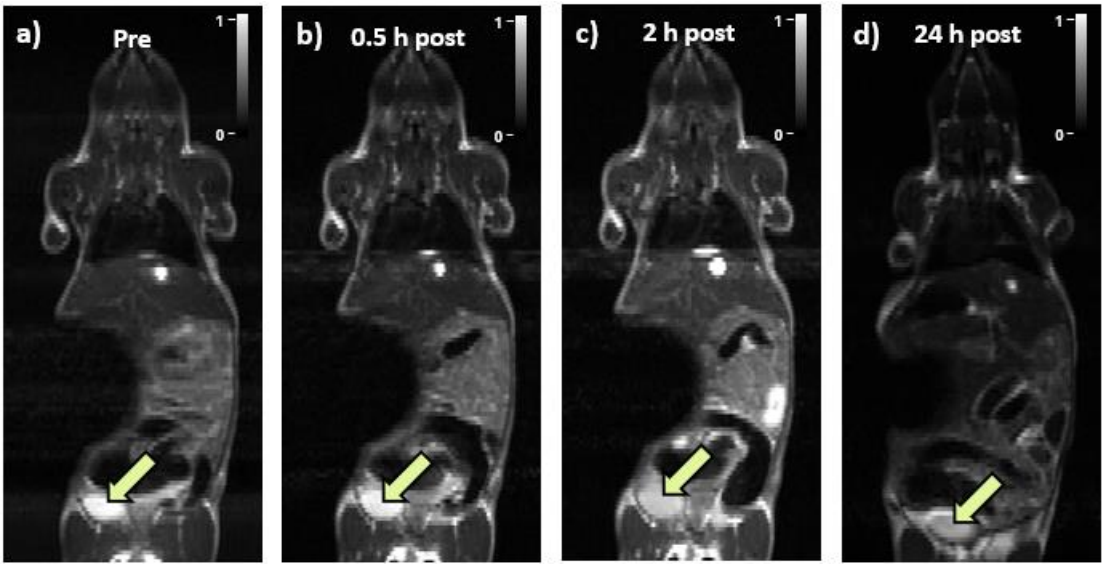
Annexe **4.45**. T_1 and T_2 and their corresponding R_1 and R_2 values of **pDPA-CNP@Fe NPs**.



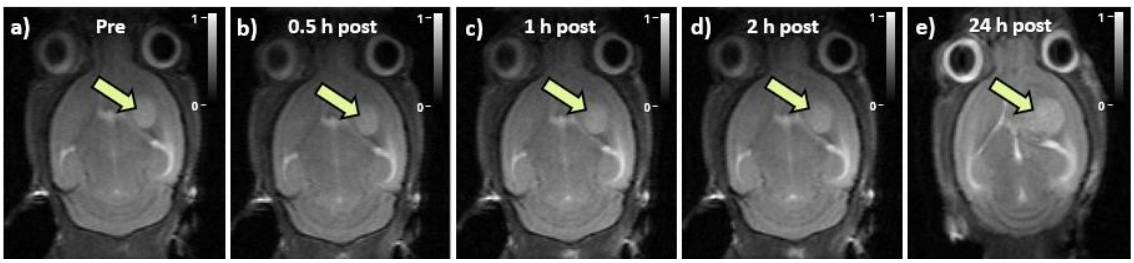
Annexe **4.46**. r_1 value of **pDPA-CNP@Fe NPs**.



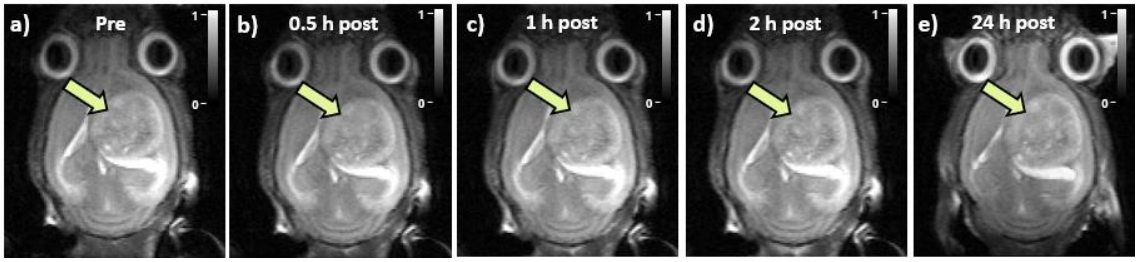
Annexe **4.47**. r_2 value of **pDPA-CNP@Fe NPs**.



Annexe **4.48**. Representative example of *in vivo* study of GL261 tumour-bearing mice (mouse number C2123) administered with **pDPA-CNP@Fe NP** (0.12 mmol Fe·kg^{-1}). From left to right, T_{2w} MRI obtained **a)** pre administration, **b)** 0.5 hours post administration, **c)** 2 hours post administration, **d)** 24 hours post administration. Light green arrows indicate the bladder.



Annexe **4.49**. Representative example of *in vivo* study of GL261 tumour-bearing mice (mouse number C2122) administered with **pDPA-CNP@Fe NP** (0.12 mmol Fe·kg^{-1}). From left to right, T_{2w} MRI obtained **a)** pre administration, **b)** 0.5 hours post administration, **c)** 1 hour post administration, **d)** 2 hours post administration, **e)** 24 hours post administration. Light green arrows indicate the tumour.

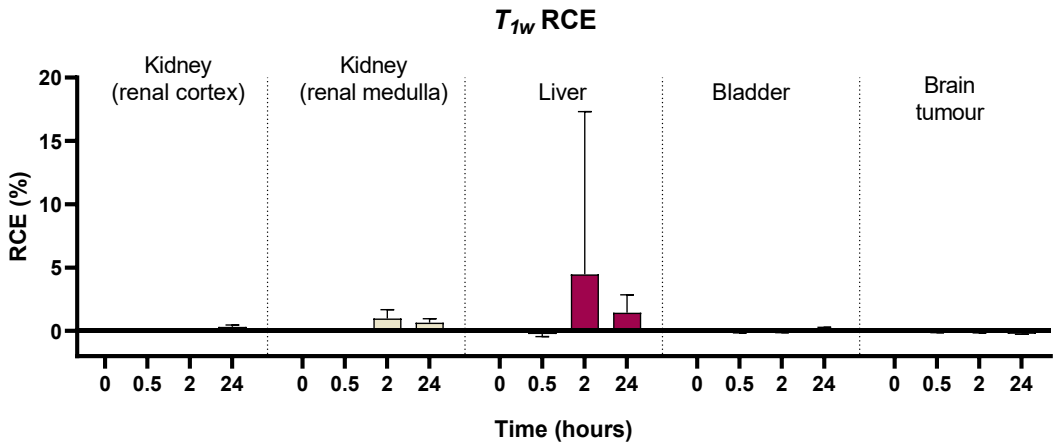


Annexe **4.50**. Representative example of *in vivo* study of GL261 tumour-bearing mice (mouse number C2125) administered with **pDPA-CNP@Fe NP** (0.12 mmol Fe·kg^{-1}). From left to right, T_{2w} MRI obtained **a)** pre administration, **b)** 0.5 hours post administration, **c)** 1 hour post administration, **d)** 2 hours post administration, **e)** 24 hours post administration. Light green arrows indicate the tumour.

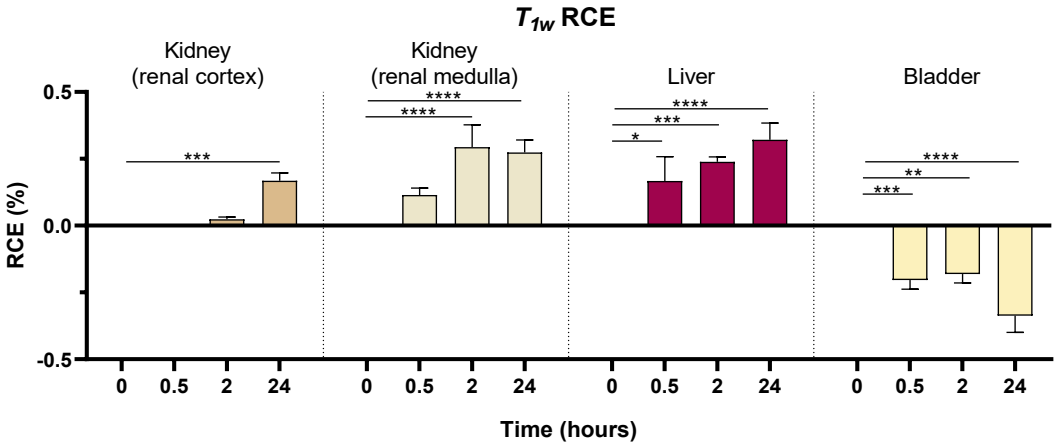
T1w	Relaxation time (ms)							
	Renal cortex		Renal medulla		Liver		Bladder	
	Mean	SD	Mean	SD	Mean	SD	Mean	SD
Pre	0,00	0,00	0,00	0,00	0,00	0,00	0,00	0,00
0.5 h	-0,09	-0,01	0,07	0,01	-0,25	-0,20	-0,13	-0,04
2 h	0,06	0,03	0,98	0,70	4,46	12,86	-0,06	-0,08
24 h	0,33	0,15	0,65	0,31	1,44	1,42	0,13	0,15

T1w	Saturation recovery (ms)							
	Renal cortex		Renal medulla		Liver		Bladder	
	Mean	SD	Mean	SD	Mean	SD	Mean	SD
Pre	0,00	0,00	0,00	0,00	0,00	0,00	0,00	0,00
0.5 h	0,00	0,00	0,11	0,03	0,17	0,09	-0,20	-0,03
2 h	0,02	0,01	0,29	0,08	0,24	0,02	-0,18	-0,03
24 h	0,17	0,03	0,27	0,05	0,32	0,06	-0,34	-0,06

Annexe **4.51.** T_{1w} relaxation time and saturation recovery of GL261 tumour-bearing mice in renal cortex (kidney exterior), renal medulla (kidney interior), liver, bladder, and brain tumour.



Annexe **4.52**. T_{1w} relaxation time % RCE of **pDPA-CNP@Fe NP** treated GL261 tumour-bearing mice in kidney, liver bladder and brain tumour. The 0% RCE is the normalised reference value corresponding to pre-administrated MRI. Data represents the mean ± SE of two independent experiments. Statistical differences were calculated using two-way ANOVA, followed by Dunnett multiple comparison test, where (*) denotes $P < 0.05$, (**) denotes $P < 0.01$, (***) denotes $P < 0.001$, and (****) denotes $P < 0.0001$.

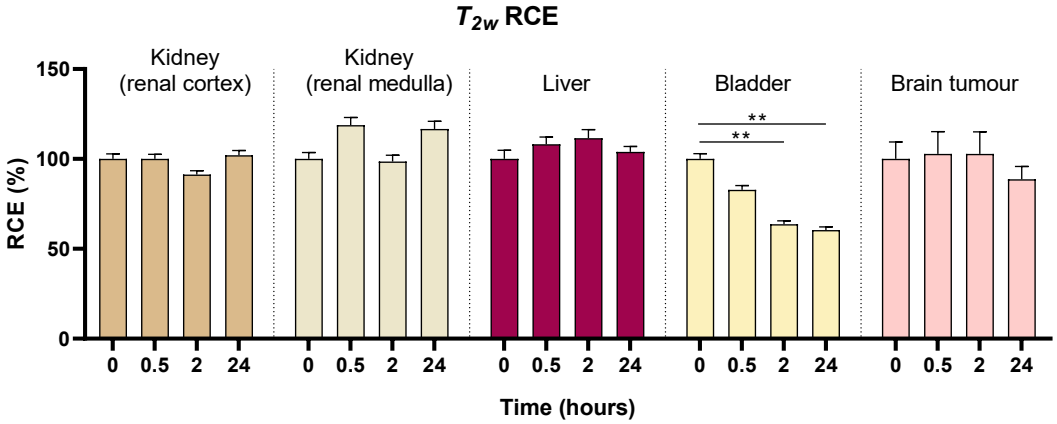


Annexe **4.53**. T_{1w} saturation time % RCE of **pDPA-CNP@Fe NP** treated GL261 tumour-bearing mice in kidney, liver bladder and brain tumour. The 0% RCE is the normalised reference value corresponding to pre-administrated MRI. Data represents the mean ± SE of two independent experiments. Statistical differences were calculated using two-way ANOVA, followed by Dunnett multiple comparison test, where (*) denotes P < 0.05, (**) denotes P < 0.01, (***) denotes P < 0.001, and (****) denotes P < 0.0001.

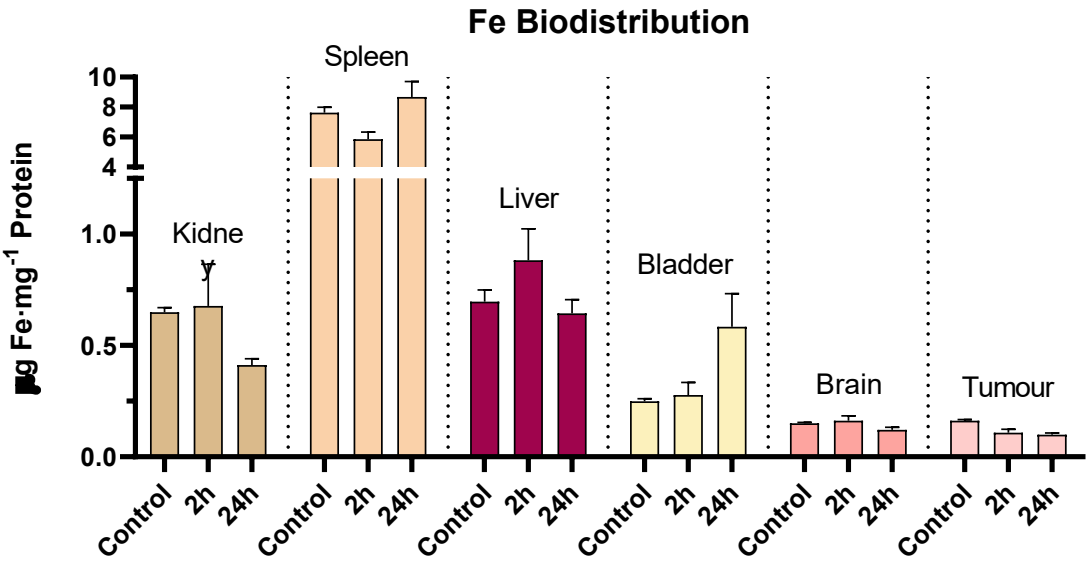
T2w	Relaxation time (ms)							
	Renal cortex		Renal medulla		Liver		Bladder	
	Mean	SD	Mean	SD	Mean	SD	Mean	SD
Pre	100,00	2,76	100,00	3,54	100,00	4,78	100,00	3,00
0.5 h	100,05	2,55	118,80	4,23	108,25	3,92	82,79	2,43
2 h	91,36	2,12	98,57	3,55	111,55	4,79	63,73	1,87
24 h	102,11	2,54	116,67	4,26	103,95	2,99	60,42	1,71

T2w	Saturation recovery (ms)							
	Renal cortex		Renal medulla		Liver		Bladder	
	Mean	SD	Mean	SD	Mean	SD	Mean	SD
Pre	100,00	19,69	100,00	35,40	100,00	25,40	100,00	18,08
0.5 h	90,40	25,14	106,13	39,23	96,59	22,61	85,52	19,66
2 h	91,09	20,16	111,59	39,05	101,55	18,52	67,09	13,40
24 h	106,32	27,18	128,87	45,46	89,10	16,26	73,78	8,32

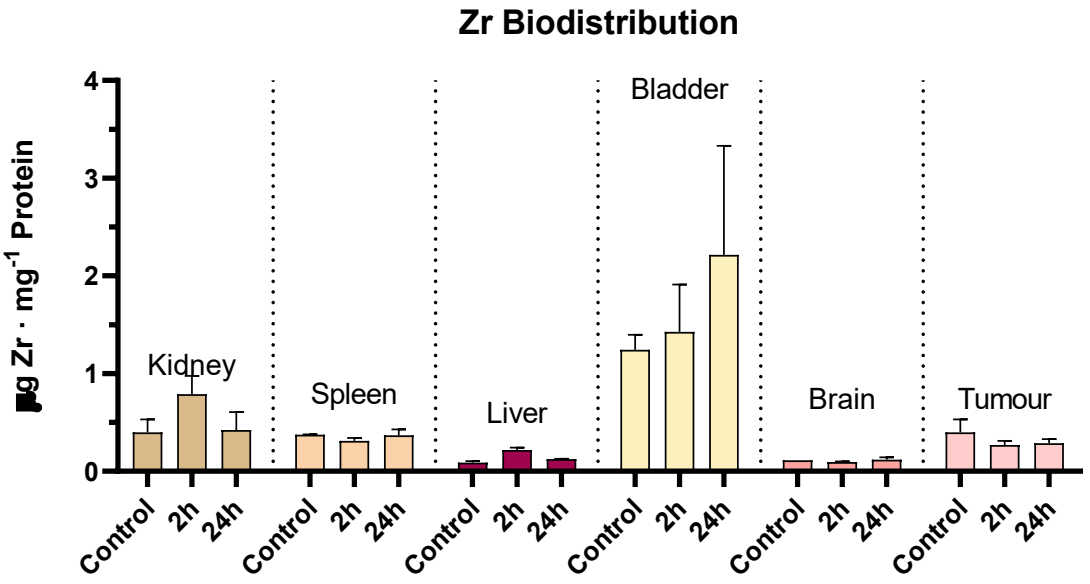
Annexe **4.54.** T_{2w} relaxation time and saturation recovery of GL261 tumour-bearing mice in renal cortex, renal medulla, liver, bladder, and brain tumour.



Annexe **4.55**. T_{2w} saturation time % RCE of **pDPA-CNP@Fe NP** treated GL261 tumour-bearing mice in kidney, liver bladder and brain tumour. The 100% RCE is the normalised reference value corresponding to pre-administrated MRI. Data represents the mean ± SE of two independent experiments. Statistical differences were calculated using two-way ANOVA, followed by Dunnett multiple comparison test, where (*) denotes P < 0.05, (**) denotes P < 0.01, (***) denotes P < 0.001, and (****) denotes P < 0.0001.

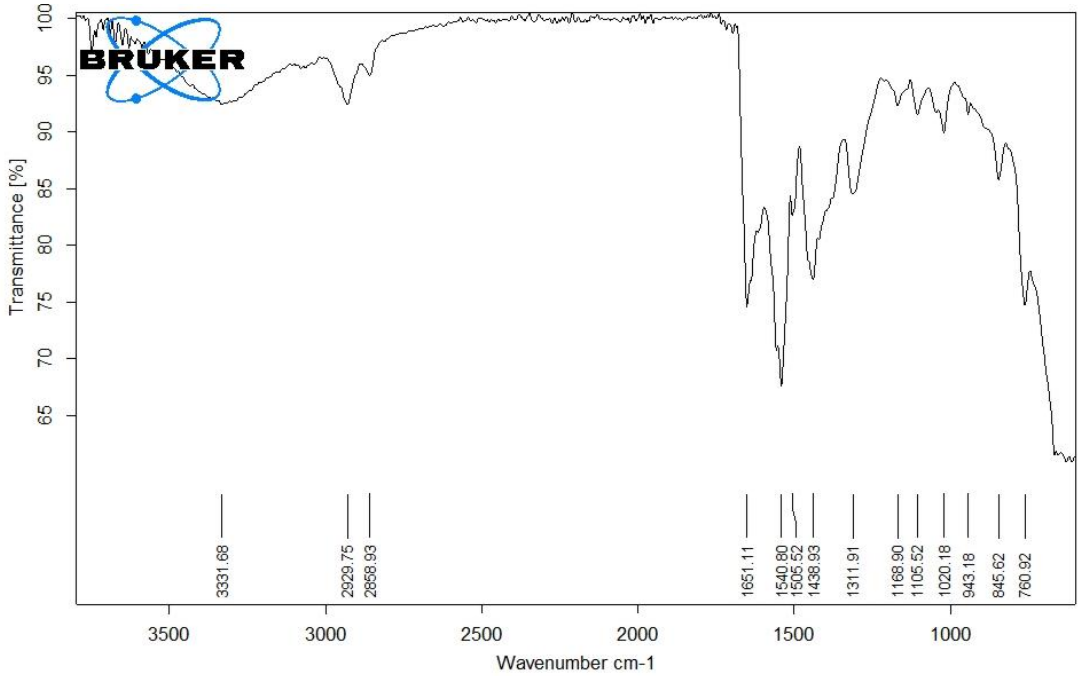


Annexe **4.56**. Biodistribution of Fe correlated to **pDPA-CNP@Fe NP** in mice organs. **pDPA-CNP@Fe NP** was administrated i.v. with a dosage of 0.12 mmol Fe·kg^{-1} body weight. The concentration of Fe in different tissues was detected by ICP-MS at various points post administration. Data is shown as mean ± SE.



Annexe **4.57**. Biodistribution of Zr correlated to **pDPA-CNP@Fe NP** in mice organs. **pDPA-CNP@Fe NP** was administrated i.v. with a dosage of 0.12 mmol Fe·kg^{-1} body weight. The concentration of Zr in different tissues was detected by ICP-MS at various points post administration. Data is shown as mean ± SE.

Characterisation of pDPA-CNP



Annexe **4.58**. FTIR of **pDPA-CNP**.

		Zr [He]	
Factor de dilución	Sample Name	Conc. [%]	Conc. RSD (%)
468400,5	pDPA Zr a dil2	3,15	2,3
525944,5	pDPA Zr b dil2	3,21	0,6

Annexe **4.59**. Preliminar ICP-MS of Zr% in w/w in **pDPA-CNP**.

Taula 1. Contingut de Zr en mostra

Codi SAQ	Zr (% (p/p))
25EAt012/001	15.8

Annexe **4.60**. ICP-MS of Zr% in w/w in **pDPA-CNP**.

Muestra: pDPA@Zr

1ª medida	%N: 1,65	%C: 30,92	%H: 3,52	%S: 0,00	%O: 13,90
2ª medida	%N: 1,54	%C: 31,06	%H: 3,39	%S: 0,00	%O: 14,37
3ª medida	%N: 1,42	%C: 31,42	%H: 3,36	%S: 0,00	%O: 13,68

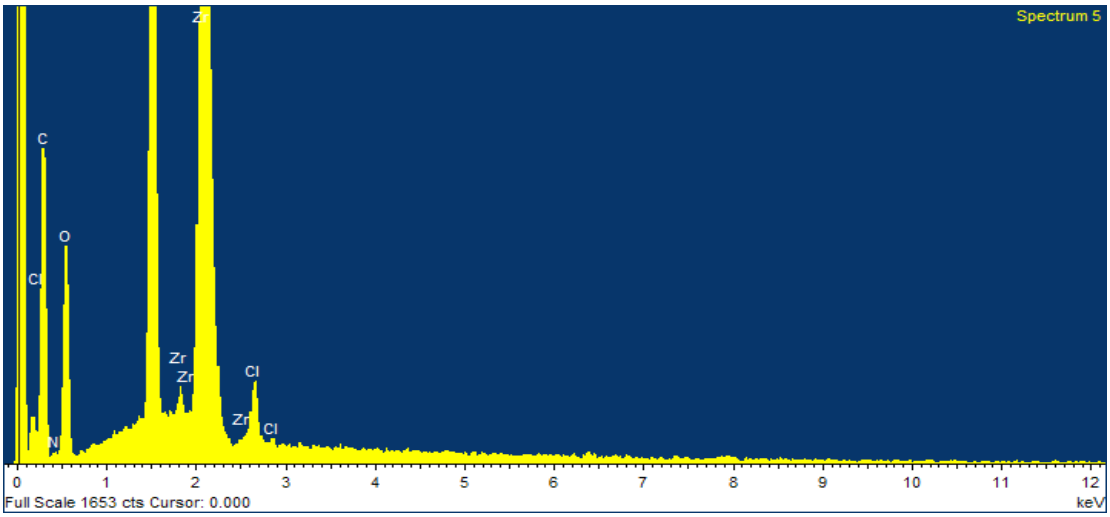
Annexe **4.61**. EA summary of **pDPA-CNP** as provided by *Parque Científico Tecnológico of the Universidad de Burgos*.

Codi Informe: 25AE005 - 21/1/2025

Resultats:

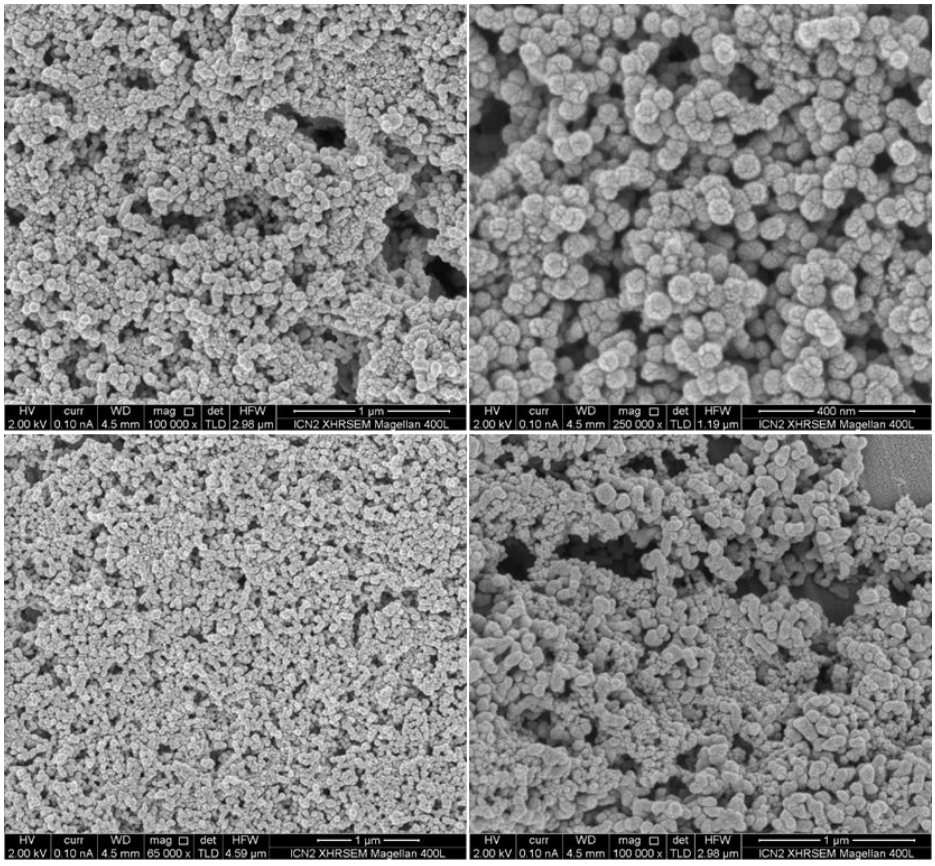
	% C	% H	% N	% S
teòric	30.90	3.50	1.65	-
experimental	30.09	3.54	1.64	0.13
	30.39	3.45	1.66	<0.1
	30.22	3.43	1.69	<0.1

Annexe **4.62**. EA summary of **pDPA-CNP** as provided by *Servei Anàlisis Química* from *Universitat Autònoma de Barcelona.*

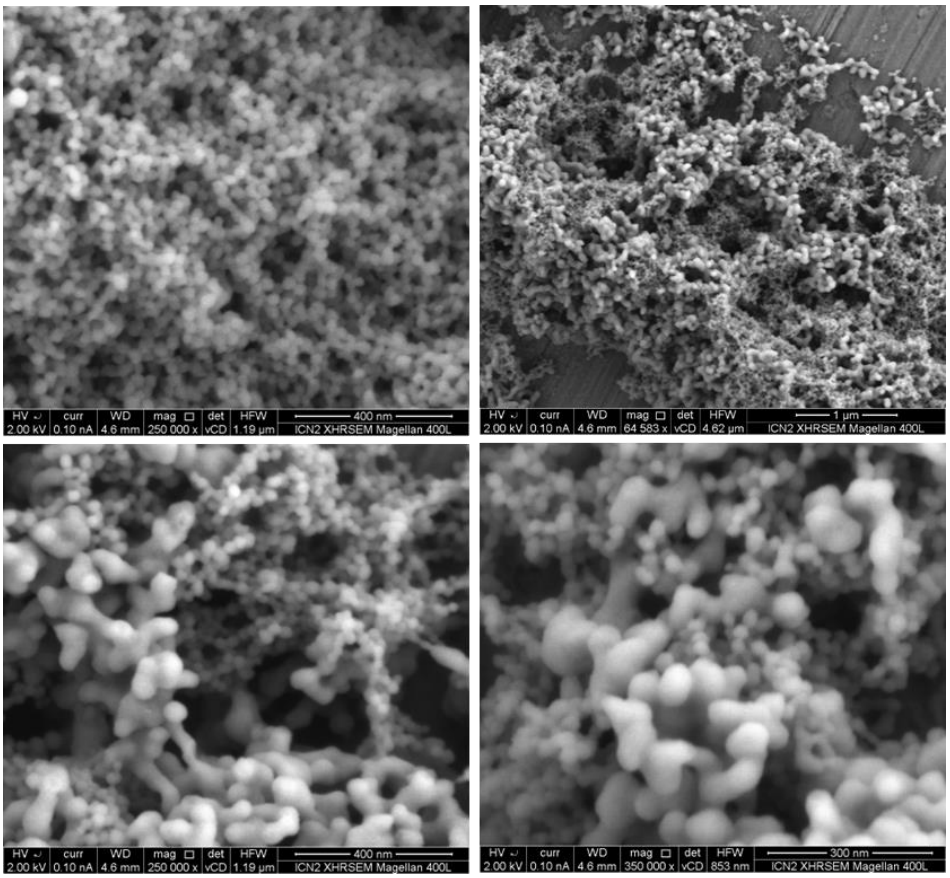


Element	Weight%	Atomic%
C K	47.82	67.85
N K	2.18	2.65
O K	22.50	23.97
Cl K	1.33	0.64
Zr L	26.17	4.89
Totals	100.00	

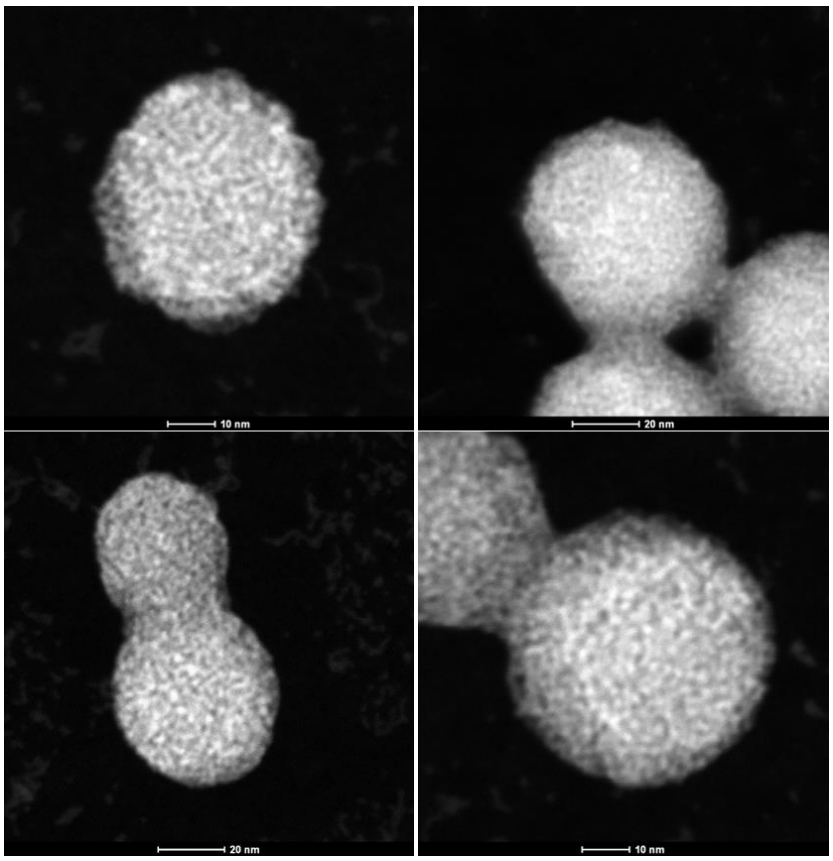
Annexe **4.63**. EDX of **pDPA-CNP**.



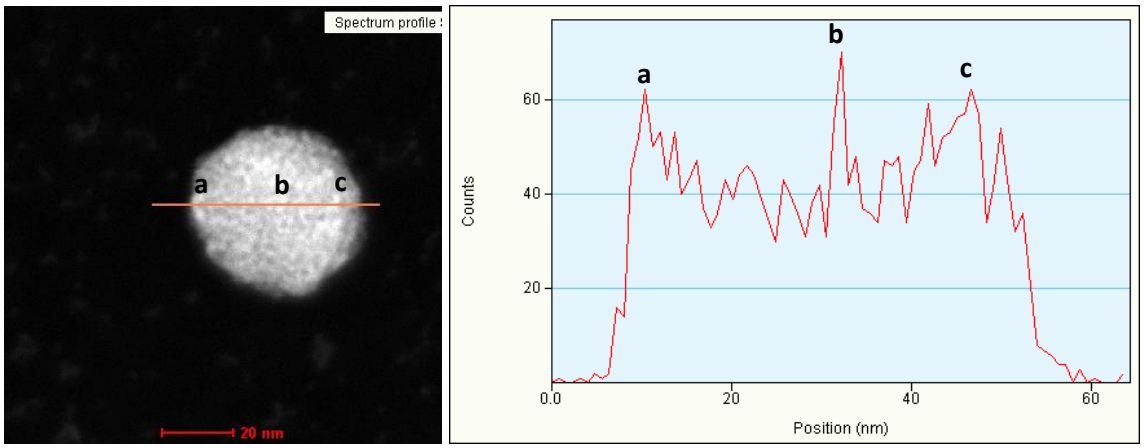
Annexe **4.64.** SEM images of **pDPA-CNP** under a 5 nm Pt thin film layer imaging.



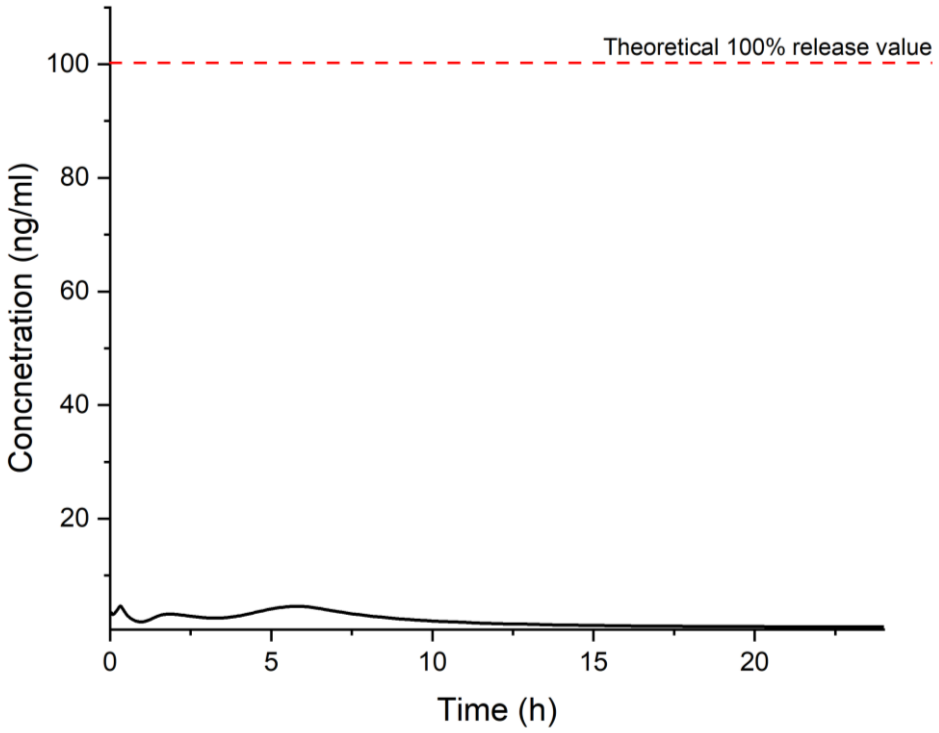
Annexe **4.65.** SEM images from the electron backscatter of **pDPA-CNP**.



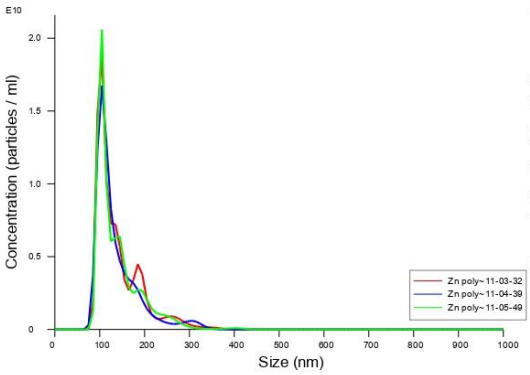
Annexe **4.66.** STEM imaging at HAADF detector mode of **pDPA-CNP**.



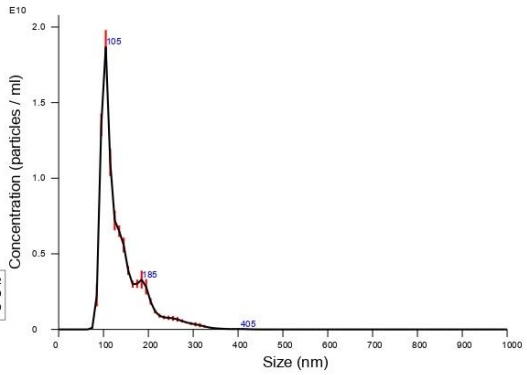
Annexe **4.67** XDR cross-section via STEM imaging of **pDPA-CNP**.



Annexe **4.68.** Zr release of **pDPA-CNP** after MHT treatment as analysed via ICP-MS.



FTLA Concentration / Size graph for Experiment:
Zn polymer 2023-04-25 11-03-17



Averaged FTLA Concentration / Size for Experiment:
Zn polymer 2023-04-25 11-03-17
Error bars indicate + / -1 standard error of the mean

Included Files

Zn polymer 2023-04-25 11-03-32
Zn polymer 2023-04-25 11-04-39
Zn polymer 2023-04-25 11-05-49

Details

NTA Version:	NTA 3.4 Build 3.4.4
Script Used:	SOP Standard Measurement 11-03-05AM 25A~
Time Captured:	11:03:17 25/04/2023
Operator:	Amable Bernabe
Pre-treatment:	1:100
Sample Name:	Zn polymer
Diluent:	water
Remarks:	

Capture Settings

Camera Type:	sCMOS
Laser Type:	Blue488
Camera Level:	11
Slider Shutter:	890
Slider Gain:	146
FPS	25.0
Number of Frames:	1498
Temperature:	22.5 - 22.6 ºC
Viscosity:	(Water) 0.938 - 0.941 cP
Dilution factor:	1 x 10e2
Syringe Pump Speed:	50

Analysis Settings

Detect Threshold:	5
Blur Size:	Auto
Max Jump Distance:	Auto: 12.5 - 12.9 pix

Results

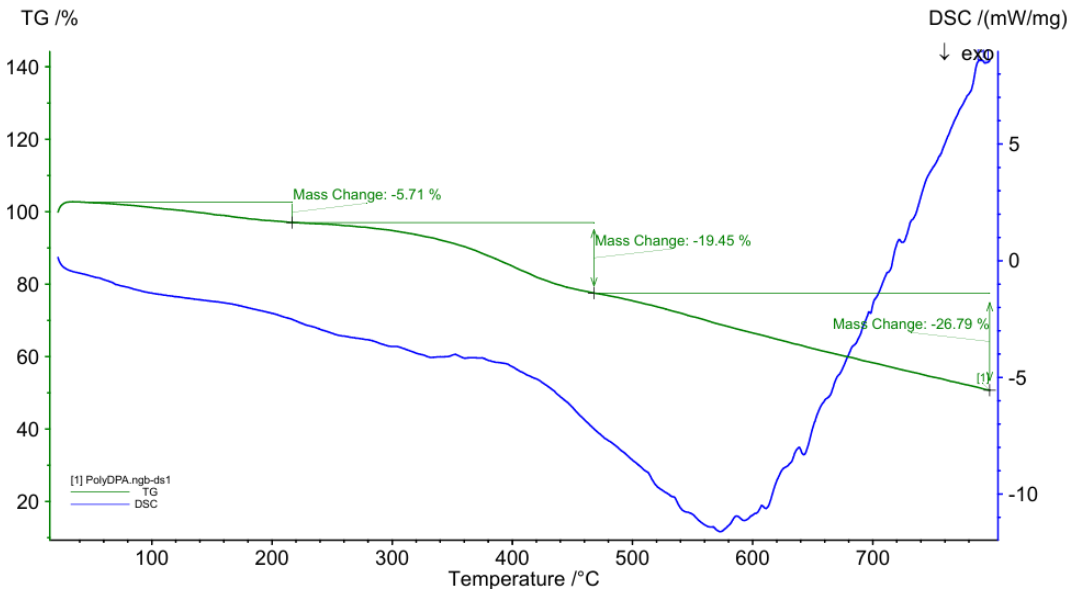
Stats: Merged Data

Mean:	138.0 nm
Mode:	104.0 nm
SD:	49.6 nm
D10:	94.9 nm
D50:	119.7 nm
D90:	203.0 nm

Stats: Mean +/- Standard Error

Mean:	138.0 +/- 1.1 nm
Mode:	104.2 +/- 0.6 nm
SD:	49.6 +/- 0.4 nm
D10:	94.9 +/- 0.5 nm
D50:	119.9 +/- 0.9 nm
D90:	202.7 +/- 2.5 nm
Concentration:	9.06e+10 +/- 1.71e+09 particles/ml
	49.5 +/- 0.9 particles/frame
	57.1 +/- 0.4 centres/frame

Annexe **4.69**. NTA analysis summary of **pDPA-CNP**.



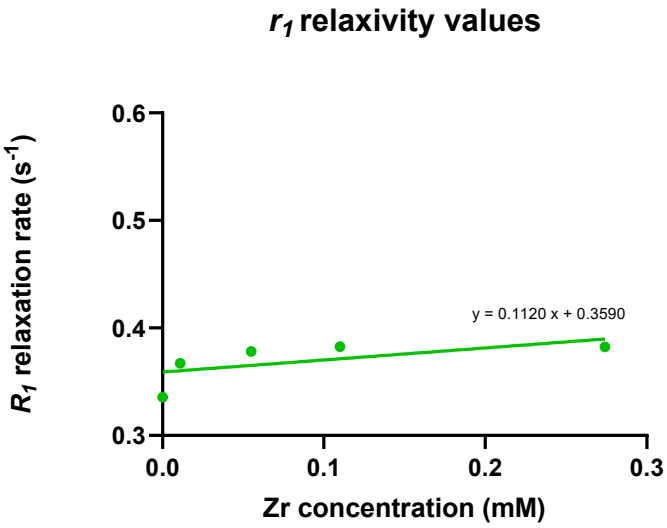
Annexe **4.70**. TGA–DSC analysis of **pDPA-CNP**.

pDPA-CNP

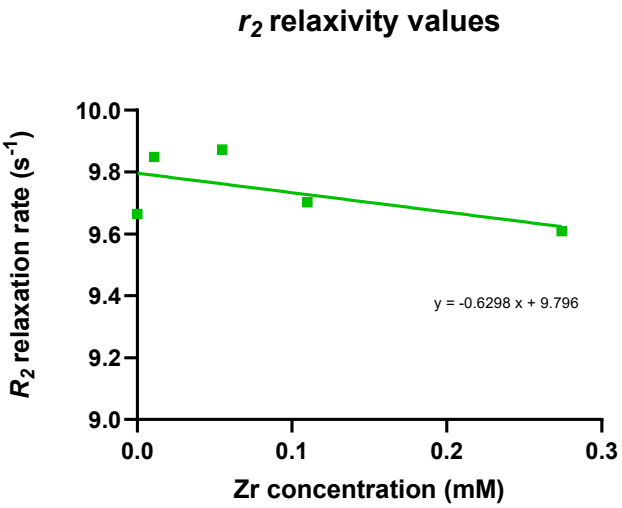
[Fe] (μg·mL^{-1})	T_1 (ms)	T_1 (s)	$R_1 = 1/T_1$ (s^{-1})
0	2980	2.98	0.3355
1	2724	2.72	0.3670
5	2645	2.65	0.3780
10	2613	2.61	0.3827
25	2616	2.62	0.3823

[Fe] (μg·mL^{-1})	T_2 (ms)	T_2 (s)	$R_2 = 1/T_2$ (s^{-1})
0	103.5	0.1035	9.665
1	101.5	0.1015	9.849
5	101.3	0.1013	9.873
10	103.1	0.1031	9.702
25	104.1	0.1041	9.609

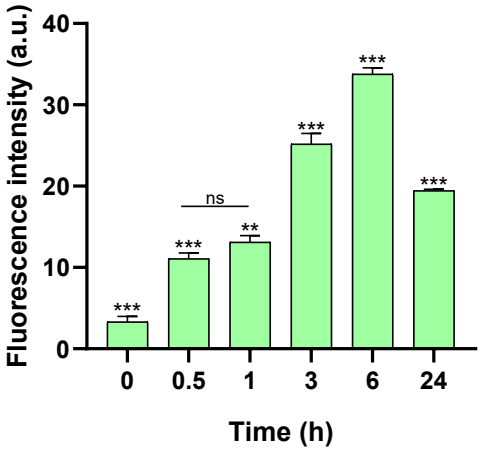
Annexe **4.71**. Transversal T_1 and T_2 and their corresponding R_1 and R_2 values of **pDPA-CNP**.



Annexe **4.72**. r_1 value of **pDPA-CNP**.



Annexe **4.73**. r_2 value of **pDPA-CNP**.



Annexe **4.74**. Extracellular, non-internalised, **pDPA-CNP** (0.1 mg·mL^{-1}) in murine GBM cell line GL261 after 0, 0.5, 1, 3, 6, 24 hours. Intensity is given by fluorescence measured at excitation 393 nm and emission at 433 nm. Data represents the mean ± SE, n=3. Statistical differences were calculated using one-way ANOVA, followed by Turkey's multiple comparison test, where (*) denotes P < 0.05, (**) denotes P < 0.01, (***) denotes P < 0.001, and (****) denotes P < 0.0001 and indicate the least statistical difference between all test groups.

Chapter 5

Development of Bioinspired Catechol-Based Pt(IV) Free-Standing Membranes for Post-Surgery Glioblastoma Treatment

In this Chapter, we present the development of a FSM derived from the previously studied monomer **PtBC**, envisioned as a therapeutic platform for post-surgical treatment of GBM within resection cavity sites.

The synthesis, physicochemical characterisation, and *in vitro* evaluation of the FSM are described, with comparative analyses to prior **PtBC**-based systems discussed in earlier Chapters. Furthermore, this Chapter also discusses the possible mechanisms for the formation of the developed FSMs, hinting at potential developments towards synergetic therapeutic combinations.

This work represents an open-ended stage of the research, with several avenues identified for further investigation and future development. Areas that require additional research have been identified, with future work outlined in those sections.

5.1. Introduction

As explained in the first Chapter of this Thesis, the standard clinical protocol for GBM treatment consists of three steps: maximum surgical resection, RT, and concomitant CT.[1-4]

In previous Chapters, we have discussed different nanostructured formulations that aim to improve the chemotherapeutic action in search of alternatives to replace the use of TMZ or to work with this drug synergistically. However, for this last Chapter, we aim to develop a material that can be used immediately after surgical resection and act as a local drug release system at the site of tumour extraction, while exerting a therapeutic effect through ROS generation.

The flexibility and versatility of the catechol-based formulations developed in the first Chapter of this Thesis allow us to exploit a designed advanced material to obtain functional TFs with well-defined composition, morphologies and therapeutic activity for GBM treatment.

5.1.1. Glioblastoma Surgical Resection

Surgical intervention is considered the cornerstone of GBM treatment. This intervention provides tissues for histopathological, genetic, and molecular analysis. Additionally, proper resection improves initial neurological status and contributes to better subsequent adjuvant treatment through cytoreductive surgery.[5] A comprehensive review of the literature and a meta-analysis of reported studies indicate that among patients who underwent surgical resection of the tumour mass, with a greater than 98% rate of treatment success, survival rates ranged from 52 to 86 weeks. In contrast, when such resection was lower, the range was from 35 to 64 weeks.[6–8]

These findings clearly indicate the importance of tumour resection in GBM therapy. Therefore, maximal surgical resection has become the goal of such interventions, as it reduces tumour burden and improves survival outcomes.[9] As expected, significant emphasis has been placed on this field to improve the surgeon's tools and their ability to efficiently remove tumour mass from patients without compromising neurological health. Such techniques include intraoperative magnetic resonance imaging (iMRI), fluorescence-guided surgery using the fluorescence probe 5-aminolevulinic acid (5-ALA), and neuronavigational systems, which allow for real-time visualisation of the tumour and surrounding healthy tissue (Figure **5.1**).[10,11]



Figure **5.1**. Representative pictures of **a)** neuronavigational surgery,[12] **b)** iMRI surgery,[13] and **c)** fluorescence-guided surgery.[14]

However, achieving total resection presents many challenges. GBM is a highly infiltrative tumour; the brain areas peripheral to the tumour are usually infiltrated by cancer cells.[5]

Moreover, the fast and aggressive nature of GBM means that by the time surgery is scheduled, the neoplasia visible in MRI at the time of diagnosis may already have invaded vital brain areas, making complete resection unfeasible. Finally, any benefit obtained from tumour resection becomes irrelevant if the procedure causes a greater neurological deficit than the preoperative one.[15,16] Even in the event of a successful and complete tumour mass resection, microscopic tumour cells often remain, particularly in the margins of the resection cavity. These can serve as a nidus for rapid tumour recurrence.[16,17] Precisely in this context, it has been observed that two-thirds of GBM recurrences happen within a 2 cm margin from the resection cavity, likely due to these residual infiltrative or peripheral cells.[17]

Hence, despite its critical role in GBM management, surgical resection alone is insufficient to prevent recurrence. These limitations underscore the necessity for innovative post-surgery strategies that target residual tumour cells at the resection site, aiming to reduce recurrence and improve patient outcomes.

5.1.2. Glioblastoma Post-Surgical Tumour Treatment

As we have seen, complete surgical resection, although a powerful tool, is not sufficient for complete GBM treatment. Surgical resection requires adjunctive therapies to avoid recurrence due to residual microscopic tumoral cells left after surgery.

Moreover, surgical resection triggers inflammatory and wound-healing responses in the tumour cavity. These processes accelerate the proliferation of residual GBM cells, making them more aggressive. Post-surgery therapy delivered within this window of opportunity helps outweigh this post-surgical stimulation.[18] For this reason, the standard clinical protocol was developed using a combination of post-surgery RT and TMZ.[1] Nonetheless, a plethora of other approaches have since been studied, such as tumour treating fields,[19] boron neutron capture therapy (Figure **5.2**),[20] anti-angiogenic therapy like bevacizumab[21] or nimotuzumab,[22] immunotherapy vaccination,[23,24] adoptive cell therapy,[25] checkpoint inhibition[26] or immunostimulants,[27] oncolytic virus therapy[28] or gene therapy.[29]

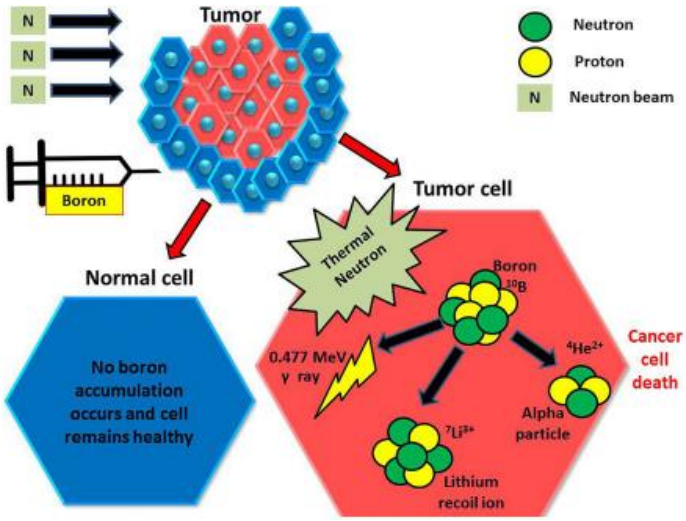


Figure **5.2**. Schematic depiction of boron neutron capture therapy as reported by Malouf et al.[20] The figure illustrates how boron compounds are preferentially localised in tumour cells, which are then irradiated with thermal neutrons. The boron then undergoes a reaction, giving an alpha particle and an inert lithium ion. The alpha particle then damages the tumour cell with a finite range.

Overall, however, any GBM drug-based therapy will face some commonly shared limitations. These include the presence of a TME network, a BBB that prevents drugs from reaching the brain, short half-lives that cause drugs to be metabolised and removed from the body before reaching their target, and a lack of tumour-specific targeting and selectivity, which can lead to systemic toxicities.[30,31]

To overcome these limitations, a novel tumour treatment strategy arises with interesting properties that allow it to bypass some of the main challenges by working synergistically with the surgical resection step. These approaches are based on the development of novel platforms for drug delivery.

5.1.3. Advanced Biomaterials

Advanced biomaterials are synthetic materials designed to induce a specific biological activity. The key difference between them and other materials is their characteristic ability to stay in a biological environment without damaging the surrounding tissues or degrading themselves in the process.[32,33]

The effectiveness of advanced biomaterials is rooted in several key properties: i) Good biocompatibility that ensures safe interaction with tissues, avoiding toxicity, inflammation, or immune rejection,[34] ii) Biofunctionality, meaning they not only provide structural support but also actively participate in biological processes (i.e., tissue regeneration, drug delivery, antimicrobial action, and biosensing),[35–37] iii) Customisability, allowing modulation of porosity, surface chemistry, degradation rate, and mechanical properties for patient-specific therapies,[38] and iv) Stimuli-responsiveness, enabling functional changes triggered by internal or external signals, including pH, enzymes, oxidative species, photostimulation, ultrasound, or magnetic fields.[39–44]

Advanced biomaterials have driven advancements in medical devices, diagnostic sensors, tissue engineering, and drug delivery systems.[45] Clinically approved examples include bioresorbable cardiovascular stents,[46] extracorporeal artificial organs,[47] tissue regenerative platforms,[48] and bioadhesives[49] which, most importantly for this Chapter, have found applications in drug delivery.

*For a more in-depth understanding of advanced biomaterials, the reader may direct their attention to the "**5.7.1.1 Advanced Biomaterials**" section in the Conceptual Explanations in the Annexes of this Thesis.*

5.1.3.1. Gliadel® Wafers in Initial Tumour Resection Surgery

A prominent drug delivery strategy in the post-surgery GBM setting employing advanced biomaterials comes in the form of a carmustine-loaded polifeprosan 20 polymeric network, known as Gliadel® wafers. Gliadel® wafers are biodegradable polymer wafers containing the 1,3-bis(2-chloroethyl)-1-nitrosurea (BCNU, carmustine) chemotherapeutic drug. Gliader® wafers first received FDA approval in 1997 for GBM treatment.[50] They are used as a form of interstitial CT in the treatment of recurrent malignant gliomas. The wafers are deposited into the tumour cavity after surgical resection and allow for the localised delivery of the drug to the surrounding brain tissue (Figure **5.3**).[51]

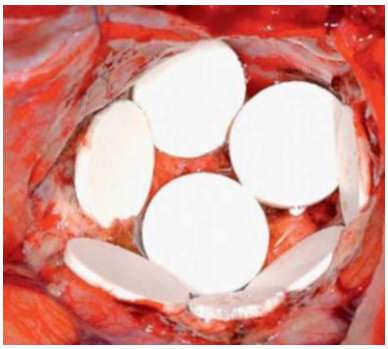


Figure **5.3**. Gliadel® wafers in the resection cavity, depicted by Jesse *et al.*[52]

These wafers consist of two main components:

- ***Carmustine***, a lipid-soluble and low-molecular-weight nitrosourea that received FDA approval for the treatment of GBM in 1977. Nonetheless, carmustine has since then been gradually replaced by TMZ as the standard of care on most applications.[53,54] However, carmustine remains the drug of choice in Gliader® wafers.
- ***Polifeprosan 20***, a copolymer of 1,3-bis-(p-carboxyphenoxy)propane and sebacic acid [p(CPP:SA)] in a 20:80 molar ratio, is considered a biomaterial. Both monomers are connected by anhydride bonds, forming a polymer that entraps carmustine via entanglement while exhibiting good biodegradation over time to release its payload.[55]

In Gliadel® wafers, carmustine is impregnated into the polymeric matrix, reaching a 3.85% drug loading.[51] Each wafer weighs 200 mg, thus packing 7.7 mg of carmustine. With a recommended carmustine drug dose in GBM treatment of 61.6 mg, eight wafers can be placed into the resection cavity during surgery.[55] The development of Gliadel® wafers and associated therapies represented a significant step forward. Gliadel® wafers allow direct delivery to the tumour bed with virtually no systemic toxicities while avoiding extra surgical interventions beyond standard surgical resection.[56] This approach circumvents the BBB and achieves high local drug concentrations within the brain.[55]

5.1.3.2. Limitations of Gliadel® Wafers

Although receiving FDA approval, reports on Gliadel® wafers are highly controversial. Meta-analysis reviews often provide conflicting or even contradictory findings on the factors under debate. Such data variability can partially be attributed to the lack of information on this topic, as research on Gliadel®-based wafers is scarce.

Surgical interventions are often a last resort in medical treatments. The risks in GBM intervention can range from brain damage, infections, bleeding, and edema to thrombosis.[57] However, since an effective GBM drug remains elusive to researchers, maximum tumour resection remains a must in GBM treatment. Furthermore, the introduction of Gliadel® wafers does come with additional risk factors during surgeries.[58] Serious intracranial infections because of interventions vary, depending on the review and statistical tools used to gather the data. Overall, however, there is consensus that an increase in such occurrences is observed, with rates ranging from 4% to a 28% increase.[10,59,60]

The application of Gliadel® wafers has also given rise to adverse effects not observed in placebo groups. The most notable are related to an increase in intracranial hypertension,[59] cyst formation in post-surgery tumour cavities associated with neurological worsening in 32% of patients,[59] and early post-surgery neurological deterioration, like post-surgery seizures (with a reported 2% to 25% increase),[61,62] aphasia,[63] visual field defects,[63] convulsions,[63] and hemiparesis.[60]

The survival benefit from the application of Gliadel® wafers is also controversial. The most recent studies generally agree that survival benefits are minimal, with a high rate of complications, [59] especially when compared to other treatment modalities like TMZ and radiation-based therapies.[64]

However, since the inception of Gliadel® wafers, no new drug other than carmustine has been clinically approved in these platforms, making them medically obsolete against more recent GBM drugs developed.[65] Overall, the introduction and approach of Gliadel® wafers offer an alternative venue and strategy for the treatment of recurrent GBM that, unfortunately, falls short of its initial expectations. However, since its first implementation, new materials and drugs have been developed. One such example comes from carmustine, which is no longer the standard drug for GBM treatment, and instead, TMZ is.[66,67] Moreover, Gliadel® wafers are limited by incomplete coverage of the tumour cavity surface due to the solid disc-shaped form and non-existent wet adhesion to the cavity walls. Therefore, there is a pressing need for the development of new platforms for more effective drug delivery that utilise more novel drug payloads and better adapt to the morphology of tumour resection cavities.

Based on this approach, in recent years, other materials for drug loading and release have been developed, and new platforms have been designed to overcome the challenges mentioned above.

5.1.4. Bioinspired Thin Films as Advanced Biomaterials

5.1.4.1. Overview of Thin Films as Advanced Biomaterials

TFs are bioadhesive biomaterials that have gained significant traction in recent years.[68] These thins, flexible polymeric layers are used in bio-applications to improve implant properties like biocompatibility and mechanical strength. Made from organic or ceramic materials, these coatings are designed to control cell adhesion, prevent infection, and enhance tissue engineering by providing a surface with tailored properties.[69]

TFs are commonly used as bioadhesives in medical applications, leveraging their ability to form biocompatible interfaces and provide controlled adhesion or release. Their properties are highly customizable through various fabrication techniques like spin-coating, plasma polymerisation, and physical deposition, which offer precise control over surface interactions. Materials such as chitosan-catechol and PEG-modified polymers, along with processes like laser ablation and layer-by-layer (LbL) assembly, allow for tailored film structures and improved performance. These TF adhesives are crucial for wound management, drug delivery, and tissue engineering.[69]

TFs can be applied as either sequentially deposited surface-bound coatings or as FSMs. The former are typically prepared using iterative LbL deposition, where polymers are adsorbed or

chemically bound to a surface. The latter are more robust and can range from several nanometres to micrometres thick, often prepared via hydrogen bonding, covalent interactions, or electrostatic assembly.[70]

A broad range of biocompatible polymers has been employed as TF backbones, including hydroxypropyl methylcellulose, carboxymethyl cellulose, hydroxypropyl cellulose, poly(vinylpyrrolidone), chitosan, gelatin, and sodium alginate, among many other examples.[71–73] TFs combine a polymeric backbone with the mechanical integrity of the substrate they coat, or act independently when free-standing. TFs can sometimes follow entirely aqueous preparation routes, favouring incorporation and stability of therapeutic cargo. This makes TFs well-suited as surface-mediated drug-release platforms, which is their main application (Figure **5.4**).[70,72]

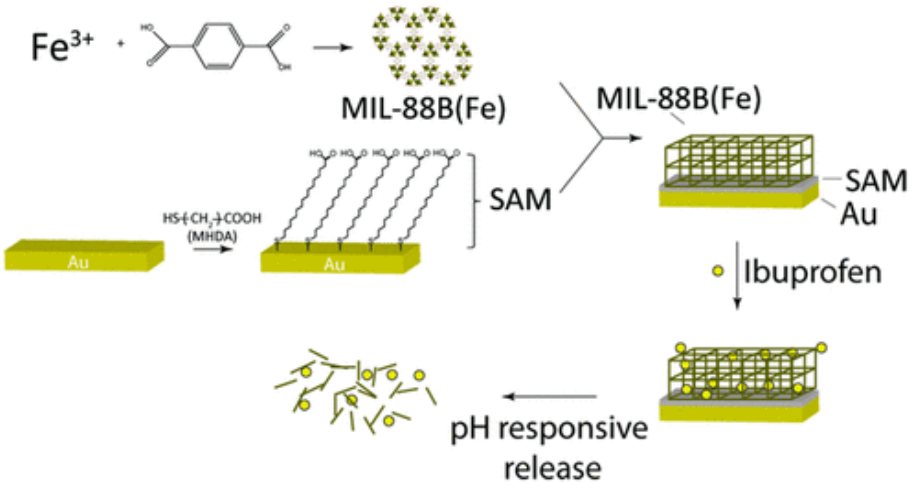


Figure **5.4**. Example of a pH-sensitive TFs based on MOF and ibuprofen as reported by Steven *et al.*[74]

The chemical tunability of polymer networks allows TFs to be engineered as stable materials that respond to chemical or physical stimuli, which in turn trigger degradation and/or controlled release, as well as surface-mediated delivery.[75] Using a TF as both an adhesive coating and a reservoir is an actively pursued strategy.[70] However, TFs are intrinsically thin and often relatively brittle or mechanically weak compared with bulk materials. Under physiological stresses (i.e., stretching, bending, and shear), they can crack, fatigue or delaminate from a substrate, which compromises their function.[68] TFs can also have a limited drug-loading capacity, especially for poorly soluble drugs, and tend to show significant initial “burst” release unless they are carefully engineered.[76] In moving tissues, in blood flow, or at interfaces with complex biomechanics (brain pulsation or joint movement), TFs can fail to conform, maintain adhesion, or permit controlled transport.[77] Finally, although LbL and composite strategies exist, it remains challenging to co-load large macromolecules, biologics or high loads of hydrophobic drugs while preserving film integrity and controlled release.[76]

Nonetheless, the FSM variation of TFs can overcome some of the limitations under careful design. FSMs can be considered a more robust form of TFs that have enough structural integrity to not require a substrate during their preparation, storage, and application.[78]

5.1.4.2. Mussels as a source of inspiration

A significant challenge for functional biomaterials is to endow them with bioadhesion capability, especially for their use in wet environments.[79,80] Water molecules in the interlayer between TFs or FSMs biomaterials and tissue can prevent the formation of strong interactions (specific or non-specific) with the target surface.[81,82] A solution to overcome this limitation comes from inspiration offered by marine mussels. These organisms can adhere strongly to diverse substrates in seawater using adhesive proteins rich in the modified amino acid L-3,4-dihydroxyphenylalanine (DOPA), which has inspired the development of synthetic biomaterials (e.g., adhesives, TFs, and FSMs) for biomedical uses.[83–87]

Biochemically, mussel foot proteins (Mfps) and related collagenous proteins are DOPA-containing families found in the mussel's foot (Figure **5.5**). Their compositions and roles (i.e., adhesion, cohesion, and structural integrity) have guided the design of synthetic materials in pH-sensitive hydrogels, tissue glues, and wet adhesives.[88–91]

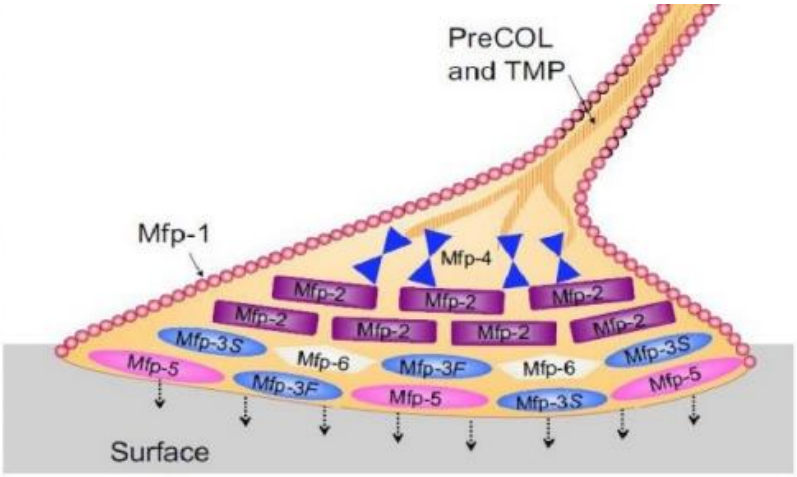


Figure **5.5**. Schematic distribution representation of as-studied proteins in a mussel foot. Reproduced from Waite *et al.*[92]

DOPA mediates multiple interaction mechanisms central to wet adhesion, including bidentate hydrogen bonding, π-π stacking, π-cation interactions, electrostatics, metal–catechol (e.g., Fe^{3+}) coordination, and covalent oxidative cross-linking, making it a versatile adhesive functional group that can interact with virtually any kind of surface (Figure **5.6**).[80,85,93–98]

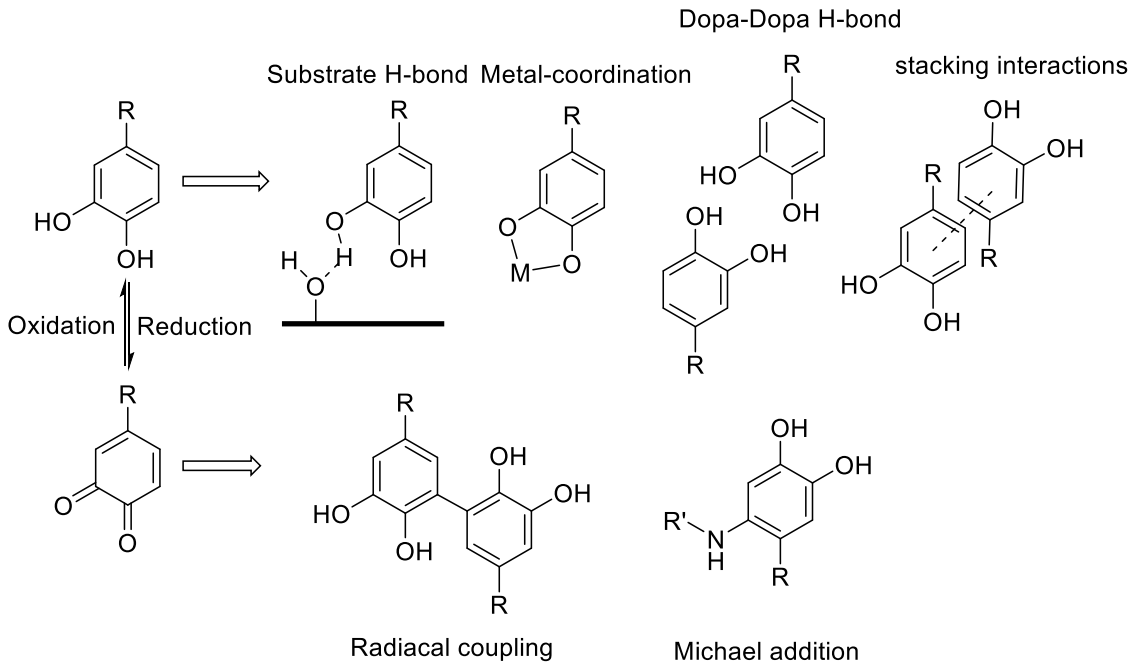


Figure **5.6.** Interaction mechanisms available for catechol functionalised molecules.[85]

Because mussels inhabit slightly basic seawater, DOPA chemistry and its dominant interaction modes are strongly pH-dependent. This includes Fe^{3+} coordination stoichiometry and hydrogen-bonding capacity, which are crucial factors that must be considered when adopting mussel-inspired adhesion into biomedical TFs.[87,92,93,99,100] Additionally, adhesion to organic biological surfaces has been demonstrated experimentally using organic TFs, where hydrogen bonding and hydrophobic interactions contribute to attachment.[101]

5.1.5. Catechol-Based Free-Standing Membranes

5.1.5.1. State of the Art on Catechol-Based FSMs

Based on the previous discussion, catechol-based FSMs, specifically those containing DOPA moieties, have been the subject of extensive research due to their excellent biocompatibility and strong adhesion. A prominent example is the rise of catechol-based TFs.[102,103] To date, most examples in the literature have reported the formation of coatings.[104] However, the need for substrates for their applicability could limit their implementation at the clinical level. For this reason, efforts are increasingly focused on the development of FSMs.

*For a more in-depth understanding of DOPA-containing examples in biomedical applications, the reader may direct their attention to the "**5.7.1.2 DOPA-Containing Biomaterials in Biomedical Applications**" section in the Conceptual Explanations in the Annexes of this Thesis.*

In addition to coatings, examples of such FSM platforms in the literature include the reports from Hong *et al.,* who demonstrated the development of stimuli-responsive catecholamine Janus-faced microfilms with excellent wet adhesion to skin.[105] Sousa *et al.* reported on cell-adhesive catechol-based FSMs for bone tissue engineering by introducing hyaluronic acid and chitosan.[106]

5.1.5.2. Our Approach to FSM Preparation

Our research group also boasts experience in FSM design, synthesis, evaluation and application. In this sense, a novel method has been developed based on a straightforward and green strategy using a substrate-free platform. This approach consists of using a bioinspired catechol precursor that, in the presence of specific amines, can induce a catechol-based oxidative polymerisation, leading to the formation of an FSM. This synthetic methodology can be performed in a one-pot, single-step procedure using green solvents and without the need for any substrate, yielding strong and malleable FSMs.

This approach has already proven a track record of success, resulting in multiple patent publications and research articles.[107] For example, Gabriel *et al.* demonstrated the capability of such systems to be deployed on skin and tissues when developing wearable mussel-inspired bioadhesive FSMs for use as sensors in battery-free devices for heat stroke prevention (Figure **5.7**).[108]

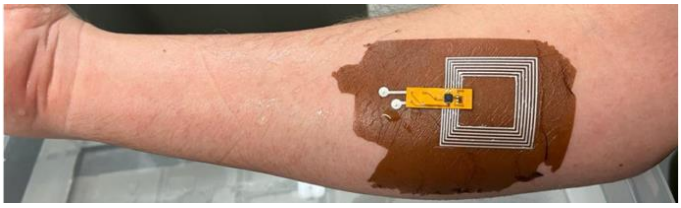


Figure **5.7**. Application of FSM on-skin for a battery-free sensor, as reported by Maroli *et al.*[108]

Bolaños *et al*.[109] recently reported on mussel-inspired bioadhesive FSMs as a patch for post-surgical GBM treatment. In this research, our group displays a family of polyphenol-based FSMs that displayed strong bioadhesion in wet environments and intrinsic antimicrobial activity. More notably, they demonstrated selective cytotoxicity against GBM LN229 cell line. The platform's cytotoxicity is reportedly attributed to ROS generation from the FSMs. The report also presents prominent ex vivo proof-of-concept evidence, demonstrating potential applicability and adhesion in pig brain cavities (Figure **5.8**).

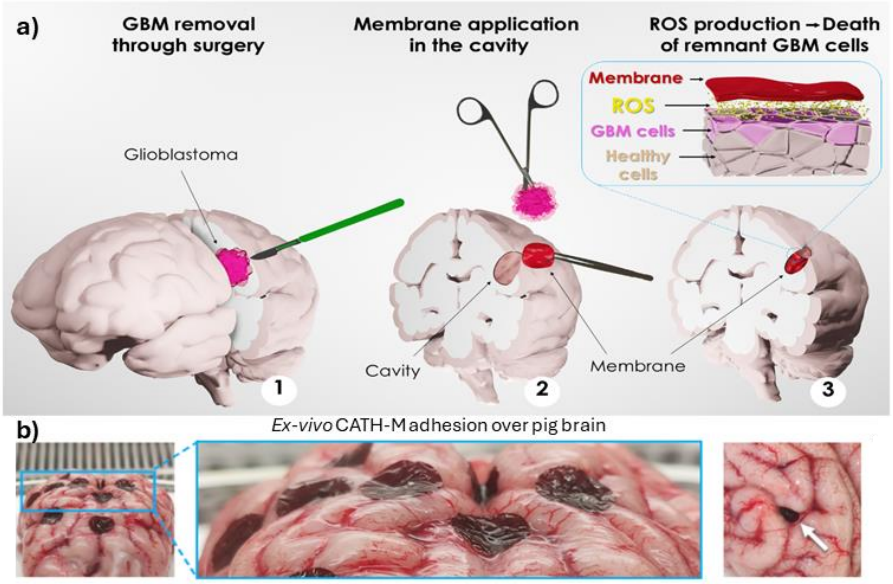


Figure **5.8**. **a)** Representation of the applicability of the reported amine-catechol FSM in GBM treatment. **b)** Representative images of pieces of reported amine-catechol FSM in an *ex vivo* pig brain and its ability to adapt with high conformability and remain attached to the different morphologies of this organ. As reported by Bolaños *et al.*[109]

These precedents in DOPA-inspired FSMs highlight their optimal suitability for GBM treatment through ROS generation. Moreover, earlier reports on DOPA-based adhesives and TFs highlight their potential for developing water-compatible adhesives that can encapsulate and deliver drugs at the adhesion site while maintaining biocompatibility.

Considering these precedents, and based on the previous study presented in ***Chapter 3*** of this Thesis, the possibility of combining the ROS generation of catechol-based FSMs with a chemotherapeutic drug was evaluated. Therefore, the aim was to focus on combining catechol-based FSMs with Pt-based prodrugs to generate a material with a dual therapeutic effect for post-surgery GBM treatment.

5.1.6. Bioinspired Catechol-Based Pt(IV) FSMs for Post-Surgery Glioblastoma Treatment

In this Chapter, we aim to develop a strategy for the incorporation of an active Pt-based drug into a well-suited catechol-based FSM platform.

5.1.6.1. The Rationale for the Selection of FSMs as a Platform

The choice of the FSM platform was evident, given the existing knowledge within our research group.

On one hand, catechol polymerisation and the preparation of catechol-based FSMs have been thoroughly studied due to their interesting wet adhesion properties. This research has led to the development of multiple applications, including bioadhesives and sealants,[110] bactericidal materials,[111] tissue regeneration,[107] and cancer treatment via ROS generation.[109] In summary, the use of catechol-based molecules and amines as linking ligands generates flexible block-copolymers that display excellent wet adhesion properties and ROS generation capabilities.[109]

On the other hand, the use of the reported bioinspired **PtBC** prodrug explored in Chapter 3 of this Thesis,[112] provides a chemotherapeutic species that can be integrated into FSMs.

PtBC presents suitable catechol functional groups for the formation of an oxidation-based polymer for FSM synthesis, closely related to that of **pPtBC NPs**, although incorporating linking amines into the structure (Figure **5.9**). The chemistry used in the development of **PtBC**-based FSM exploits the polymerisation capability of DA and catechol-like adducts, which has already been explained in "Chapter 3, **3.1.1.3. Oxidative polymerisation**", with a special focus now on linking amines' role in Michael-type addition mechanisms of oxidised quinones.

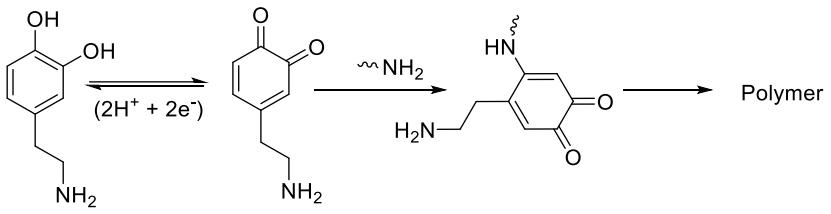


Figure **5.9**. Simplified reaction mechanism of catechol polymerisation based on amine nucleophilic Michael-like addition explained in Chapter 3.[113]

Furthermore, **PtBC** has previously displayed a capable drug for GBM treatment *in vitro*. **PtBC** has demonstrated comparable cytotoxicity to **CDDP** over long periods of time, allowing for sustained therapeutic efficacy.

5.1.6.2. Advantages of Incorporating a Pt(IV) Prodrug in FSMs

The use of FSMs as a platform for post-surgical GBM treatment is a new approach, with the only reported studies coming from our research group. Although different FSMs have been developed as drug delivery systems for cancer treatment[114,115], no examples of Pt loaded FSMs can be found in the literature. However, examples on catechol-based Pt(IV)-loaded NPs can be found, including the work previously described in this Thesis at in ***Chapter 3*** with the reported **pPtBC NPs**.[112]

While **pPtBC NPs** can show excellent tolerability and are somewhat capable of undergoing IN administration, the effectiveness in *in vivo* models has proven challenging, and in this Thesis, unfruitful. Delivery to the brain tumour is a difficult journey, and Pt-based drugs are limited by their poor capability to cross the BBB,[116] extensive off-target toxicities (i.e., nephrotoxicity and neurotoxicity),[117–120] and a narrow window of application.[120]

In a context where Pt is incorporated into an FSM and inserted into the post-surgery tumour cavity, the poor diffusion of Pt(II) and Pt(IV) through the BBB is no longer a concern. Since FSMs are locally administered to the site of interest, poor targeting of Pt drugs is also no longer an issue, as it allows for *in situ* release. This enables site-targeted therapy and local administration that can lead to a reduction in the well-known side effects of Pt drugs.

5.1.6.3. Design of Pt(IV)-based FSMs

Considering the advantages of catechol-based FSMs and the potential benefits of incorporating Pt-based drugs, our research group has aimed to develop a novel platform for the treatment of GBM's post-surgery surviving cells. This approach consists on the use of bioinspired **PtBC** prodrug, which was previously introduced in this Thesis. This prodrug has proven capable of releasing its cytotoxic Pt(IV)/Pt(II) cargo in reductive environments or in acid-triggered hydrolysis environments.

Under the right conditions, catechol-based **PtBC** in the presence of copolymeric amines can trigger polymerisation and the formation of an FSM. The resulting FSM is expected to retain wet adhesion properties from catechols while achieving Pt(IV) loading, capable of releasing its cytotoxic cargo over time, especially in tumour environments. Furthermore, the catechol moieties in the **PtBC** prodrug can act as an oxidative stress modulator and exhibit pro-oxidant activity.[121,122] In the appropriate polymerisation conditions, this can induce the generation of ROS as observed in a previously published work.[109]

Overall, **PtBC**-based FSMs serve as an ideal backbone for the development of an implantable platform to deliver effective medication in post-surgery settings (Figure **5.10**).

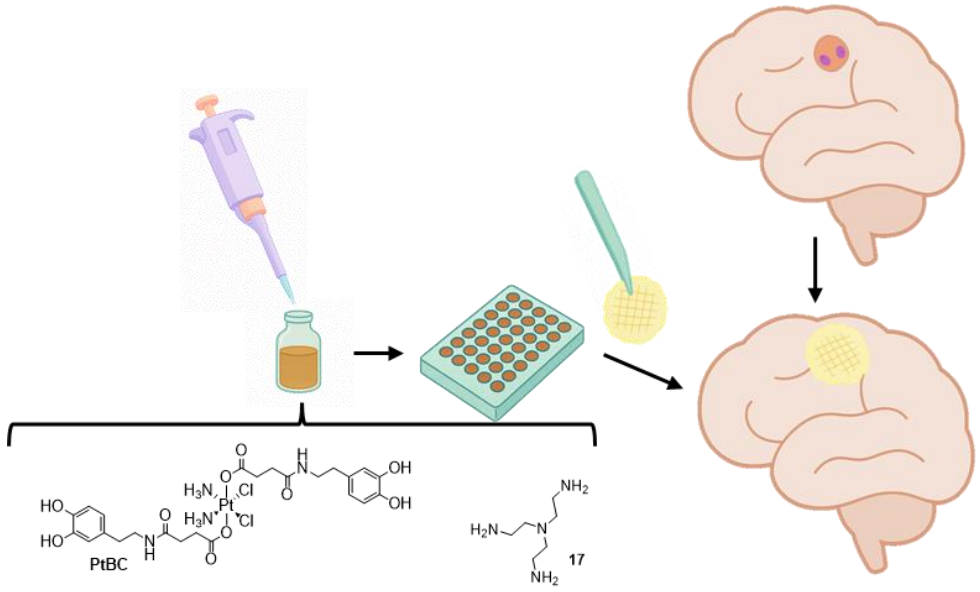


Figure **5.10**. Graphical abstract of the approach for post-surgical GBM treatment taken in this Chapter of the Thesis.

This aims to promote the elimination of surviving cancer cells in tumour resections. Furthermore, inserting the FSM into the tumour cavity circumvents the BBB, and prevents systemic distribution of cytotoxic cargo.

The integration of bioinspired catechol chemistry with **PtBC** prodrug in the form of an FSM represents a promising therapeutic strategy for post-surgery GBM management. This platform aims to overcome the limitations of current local delivery systems, such as those associated with Gliadel® wafers, by combining the adhesive and biofunctional features of catechol-based biomaterials with the cytotoxic and resistance-bypassing properties of Pt drugs. This novel platform has the potential to offer: i) Strong and biocompatible wet adhesion, ii) Localised and controlled Pt(IV) prodrug release, iii) ROS-mediated cytotoxicity, iv) Circumvention of systemic toxicity and BBB transport limitations, and v) Structural adaptability to irregular resection cavities (Figure **5.11**).

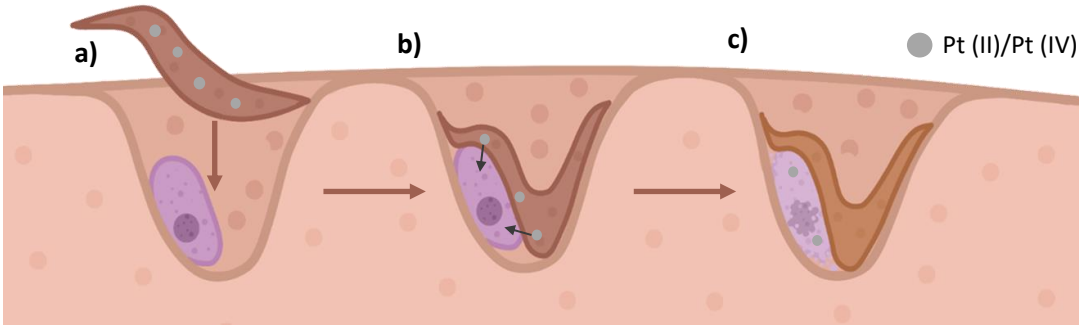


Figure **5.11**. Graphical representation of the approach followed in this Chapter. **a)** Survival of cancer cells in a tumour cavity post-surgical resection. An FSM is being placed in the tumour cavity. **b)** The FSM occupies the entire cavity and releases its cytotoxic cargo. **c)** Cell death as a result of interaction with alkylating-like drugs.

5.2. Objectives

In this Chapter, we envision the development of a biocompatible FSM that mimics mussel wet adhesion mechanisms. This material is anticipated to have medical value as a cytotoxic agent for post-surgery GBM treatment in tumour resection cavities. The work encompassed in this Chapter is considered a proof-of-concept.

For this purpose, the objectives of this Chapter are:

1. To develop, synthesise, and characterise a **PtBC**-based FSM capable of releasing Pt(IV) in physiological environments.
2. To validate the *in vitro* efficacy of the Pt-based FSM in GMB settings.

To achieve these objectives, the following steps will be carried out (Figure **5.12**):

- Synthesise a **PtBC** prodrug, following previously described protocols in this Thesis at section ***"3.3.1.1. Synthesis of the Precursor PtBC"***. This will result in a suitable melanin-like Pt(IV) molecule with DA moieties capable of oxidative co-polymerisation and mussel-like wet adhesion.
- Synthesise, optimise and characterise the FSM based on the oxidative co-polymerisation of Pt(IV) prodrug **PtBC** using a suitable amine-based co-monomer.
- Study the capability of the resulting **FSM-PtBC** to release Pt under physiological conditions.
- Develop and optimise cell seeding, adhesion, and protocols for cell viability assays.
- Study the *in vitro* cell viability of **FSM-PtBC** against a subset of cancer cells for GBM suitability assessment and comparison purposes.

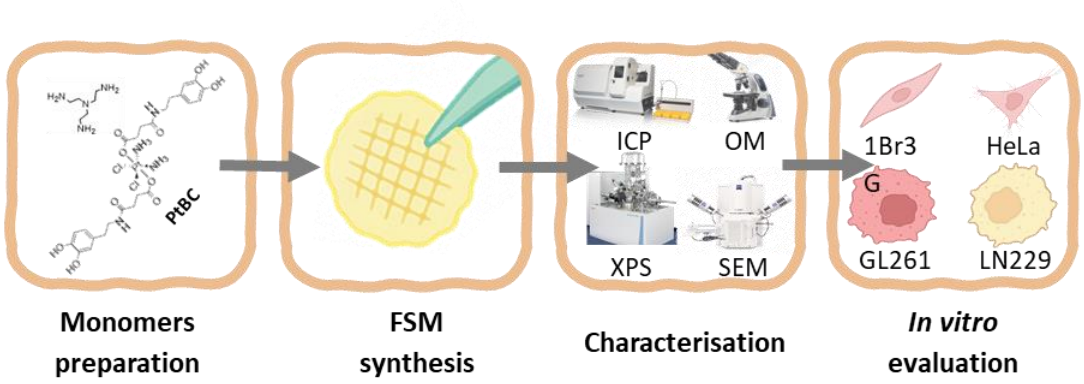


Figure **5.12**. Graphical abstract of the steps followed in this Chapter to achieve the objectives mentioned in this section.

5.3. Results and Discussions

The objective of this Chapter was to obtain an FSM intended for use as a post-surgery tumour cavity patch. This patch aims to prevent the proliferation of cancer cells and, as such, this platform is designed to display cytotoxic behaviour against cancer cells.

These materials have previously demonstrated their versatility as a functional platform with high stability in aqueous and physiological environments. FSM-based approaches have previously been successful in this area, though using different cytotoxic strategies.[109]

The polymeric network of the FSM will be based on the cross-linking between a well-known monomer in this Thesis, **PtBC**, and a tris-amine under mild oxidising conditions. Polymerisation in a controlled, basic, nucleophilic, and oxidative environment will be used for the polymerisation step and the obtaining of a free-standing **PtBC** membrane (**FSM-PtBC**).

Consequently, data from *in vitro* experimentation of previous Chapters using **PtBC** and **pPtBC NPs** will be used as a reference and benchmark against the resulting **FSM-PtBC** in cell viability assays.

Work on this Chapter has been carried out in collaboration with Prof. Victor Yuste from *Universitat Autònoma de Barcelona*.

5.3.1. Synthesis and Characterisation of FSM-PtBC

Synthesis of **FSM-PtBC** involves two clear steps: the synthesis of the **PtBC** monomer, and its subsequent oxidative polymerisation to form the **FSM-PtBC**. The synthesis and characterisation of **PtBC** have already been covered in previous Chapters and will not be addressed again here.

FSM-PtBC consists of a polymeric network based on catechol oxidative polymerisation. This network is composed of a catechol moiety, **PtBC**, and an amino-functionalised linker molecule. Reactions that exploit catechol polymerisation have historically used amine-based linkers, as they can mimic the reactivity of PDA polymerisation.[123,124] In our case, tris(2-aminoethyl)amine (**17**) was chosen as the linker, since it has the capability of binding with three different catechol moieties through Michael-like addition to generate the oxidised quinones of **PtBC**. At the same time, each **PtBC** contains two catechol moieties that can each react with two amine-based linkers. This arrangement of multiple reaction points on both components of the polymeric network gives rise to a very entangled and cross-linked system that helps shape a strong supramolecular material (Figure **5.13**).

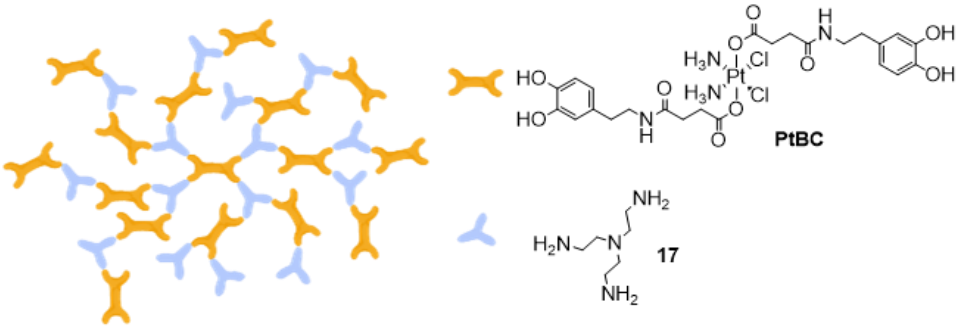


Figure **5.13**. Schematic illustration depicting a polymeric network composed via oxidative polymerisation between **PtBC** and tris(2-aminoethyl)amine (**17**).

In a typical synthesis of **FSM-PtBC**, catechol **PtBC** and tris(2-aminoethyl)amine linker (**17**) were dissolved in degassed methanol and degassed MilliQ® water, respectively, and mixed. The resulting mixture was aliquoted into a recipient with the desired final shape of the FSM. The mixture was then allowed to evolve in a vibration-free environment at 37 °C for 72 hours. The **FSM-PtBC** formed on the air-liquid interface as a result of oxidation of catechol moieties in the presence of atmospheric oxygen. The FSMs were then removed from the recipient and washed thoroughly with MilliQ® water (Figure **5.14**).

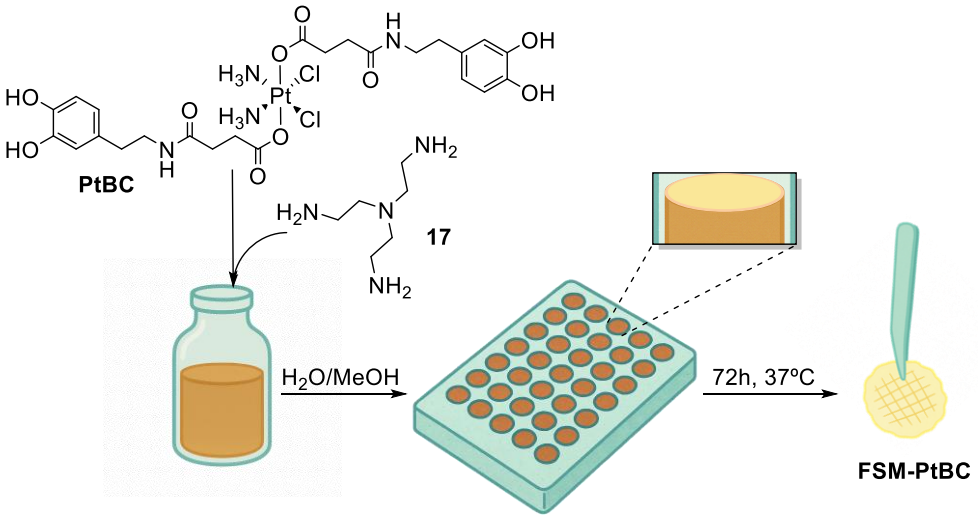


Figure **5.14**. Schematic representation of the procedure followed for the synthesis of **FSM-PtBC** via oxidation polymerisation.

Because **FSM-PtBC** adapt to the shape of the recipient, the use of 96-well plates provides the perfect size for future cell viability assays.

Attempts to synthesise the **FSM-PtBC** over a 24-hour period yielded brittle FSMs that broke easily during handling, washings, or *in vitro* experimentation. To generate more stable films, the reaction time was increased to 72 hours. Optical microscopy clearly shows the differences between FSMs formed over the two different time periods (Figure **5.15**).

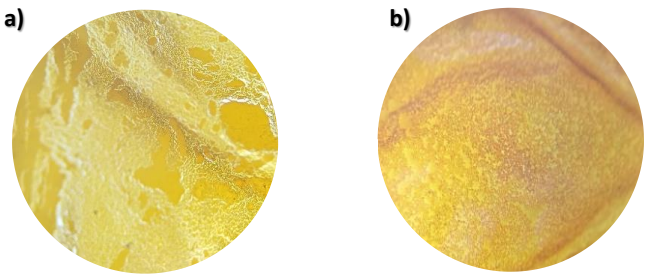


Figure **5.15**. Representative optical microscope imaging of **FSM-PtBC** after **a)** 24-hour, and **b)** 72-hour long synthesis, at 4x augmentations.

FSMs that underwent a 24-hour synthesis present as thin, with evident gaps, crevices and cracks in the network. In contrast, FSMs resulting from a 72-hour synthesis are much homogeneous and have fewer indentations or surface defects. Attempts at FSM formation under solvoneutral oxygen conditions yielded only a precipitate, indicating the importance of keeping the oxygen atmosphere. This precipitate formation was correlated to the formation of freely available **pPtBC**, as the polymeric capability of **PtBC** is well known to produce NP in bulk solvents when oxygen is present.

Spectroscopically, FTIR characterisation of the **FSM-PtBC** reveals many similarities to that of **pPtBC NPs** obtained in previous Chapters. Both materials exhibit characteristic peaks in the 1200-1400 cm^{-1} range, which are indicative of catechol moieties. A broadened peak at 1279 cm^{-1} is also present, resulting from oxidation products of DA. The increased broadening of the **FSM-PtBC** signals is expected due to the enhanced polymeric nature of the supramolecular material (Figure **5.16**). The original spectrum of **FSM-PtBC** can be found in Annexe **5.5**.

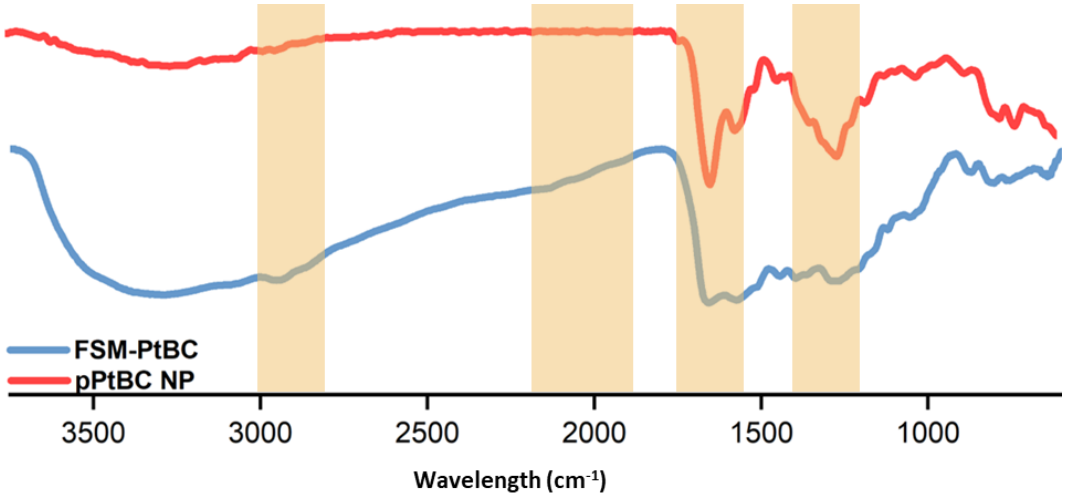


Figure **5.16**. FTIR comparison between **pPtBC NP** (red) and **FSM-PtBC** (blue).

Indeed, the similarities between **FSM-PtBC** and **pPtBC NPs** arise because they both share the same **PtBC** backbone molecule. The aliphatic component of this amine linker could lead to an increase in signal intensity in the C-H bands around 2800 cm^{-1}. The linker may also contribute to the small signals in the 2000 cm^{-1} region due to the vibrational contribution of N-H bonds. However, the significant broadening of the free -OH peak, either because of the amorphous polymerisation of **FSM-PtBC** or supramolecular hydrogen bonding, makes elucidation of the contributions to the 2800 cm^{-1} and 2000 cm^{-1} hard to determine.

Interestingly, **FSM-PtBC** reflectance gives valuable information about roughness and scattering of a sample, thus yielding valuable interface data (Figure **5.17**).

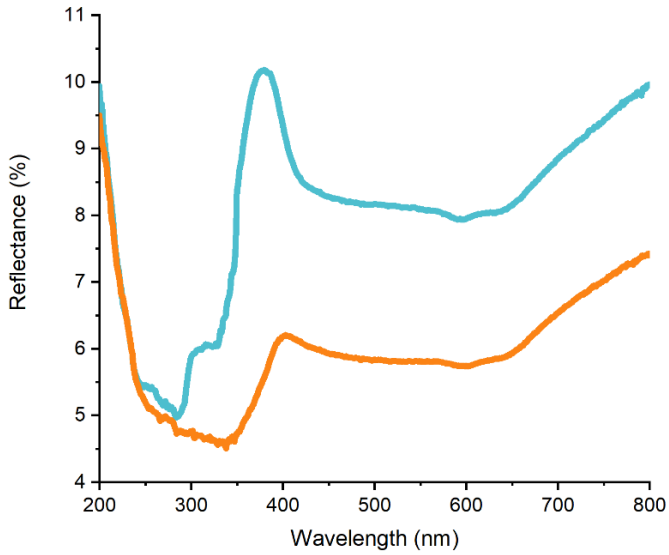


Figure **5.17**. Reflectance spectra of **FSM-PtBC** in dry conditions of both sides of the same FSM (one side orange, the other side blue).

The **FSM-PtBC** reflectance spectra present low reflectance (4 to 11%), which indicates that the material is generally absorptive in the studied ranges. Surface-wise, the low reflectance of the FSM is indicative of a rough surface, causing light to scatter diffusely rather than reflect directly. Interestingly, there is a notable difference in reflectance measurements depending on which side of the FSM was analysed. These variances are indicative of differences in surface morphology depending on the FSM side. At the same time, porous FSMs may also trap light and reduce specular reflectance. The baseline presents quite homogeneous, indicating a constant thickness across the film.[125]

Surface morphology was further examined using SEM imaging of **FSM-PtBC**, which corroborated the findings. The imaging displayed a Janus-like film, with one smooth side corresponding to the interface-to-air side, whereas the interface-to-solvent side of the film presented a rougher surface composed of spherical inlays, a behaviour known to be displayed in polycatechol-based FSMs.[108] The FSM also presents an average thickness of 2.7 ± 1.2 µm and high porosity, as observed via SEM imaging (Figure **5.18**).

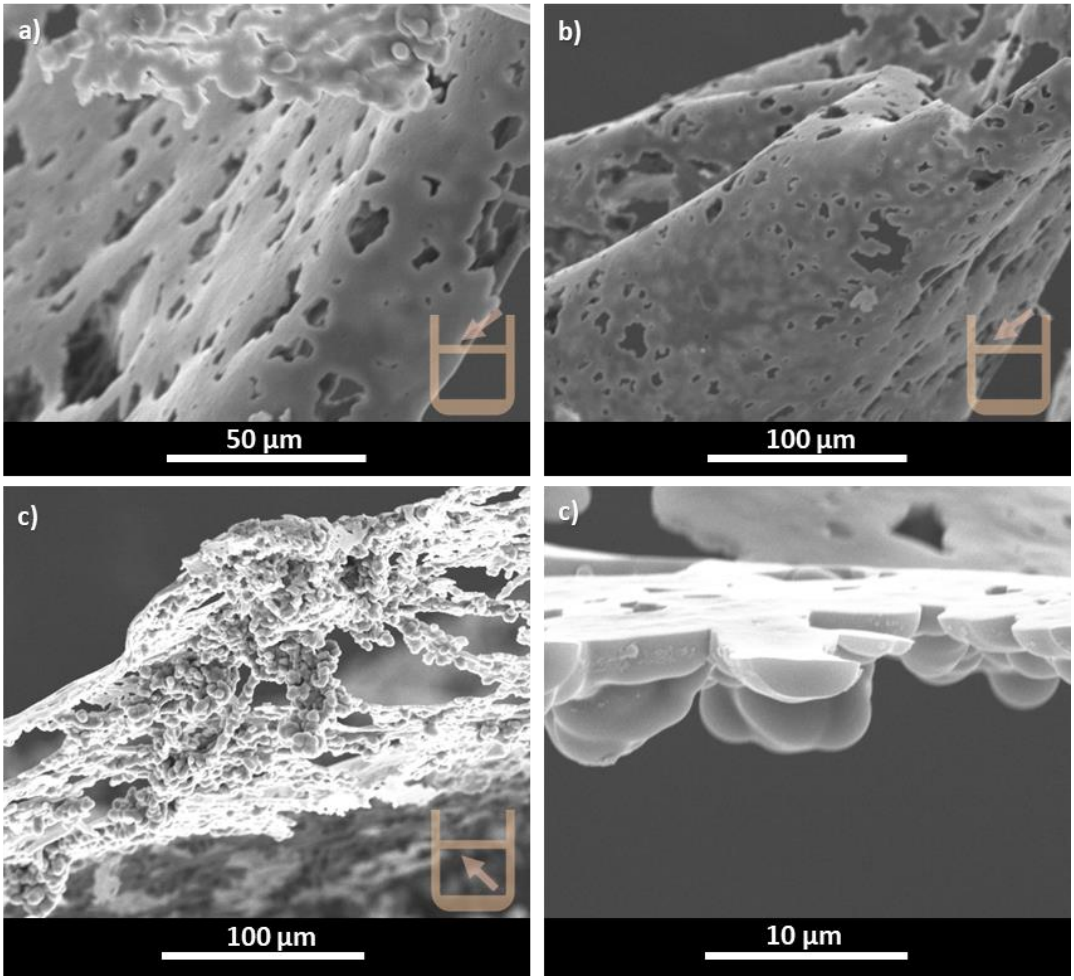


Figure **5.18**. Representative SEM image of **FSM-PtBC** under a 5 nm Pt thin film coating for imaging displaying **a-b)** interface-to-air side, **c)** interface-to-solvent side, and **d) FSM-PtBC** profile.

While reflectance measurements suggested a constant thickness and porosity of the **FSM-PtBC**, SEM imaging provided definitive proof of these homogeneous dimensions and morphology.

Apart from the formation of the TFs, a precipitate was also observed. The precipitate was attributed to a **pPtBC**-like coordination polymer formed as a result of coprecipitation during the synthesis of **FSM-PtBC**. Therefore, SEM images were taken from the precipitate residue to observe whether NP formation was indeed the root cause of the precipitation (Figure **5.19**).

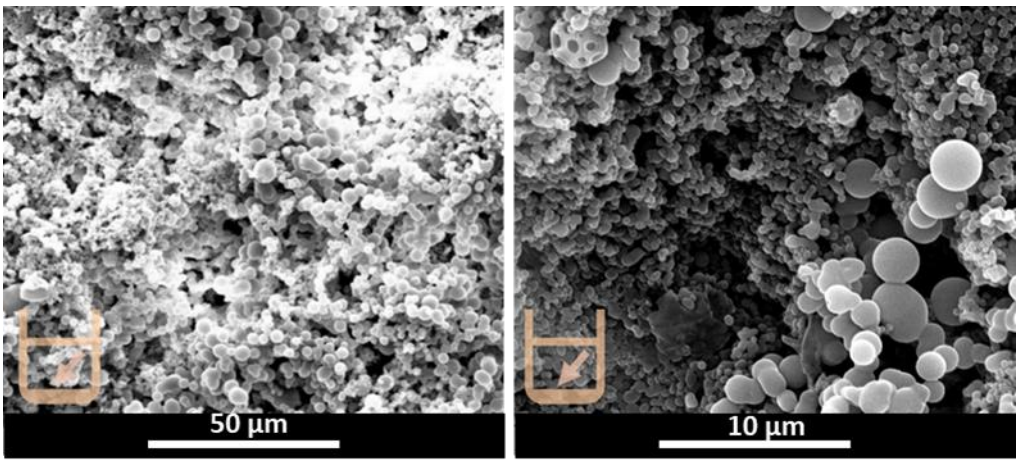


Figure **5.19**. Representative SEM image of precipitate NPs formed during **FSM-PtBC** synthesis under a 5 nm Pt thin film coating for imaging.

SEM imaging confirmed the formation of spherical NPs, which validates the hypothesis that **PtBC** monomer can also form NPs under the same conditions used for the synthesis of **FSM-PtBC** forms.

The NPs from the resulting precipitate presented an average size of 2535 ± 133 nm with a large PDI of 0.937 ± 0.07 and a ζ-potential of -9.44 ± 0.53 mV, as characterised by DLS (Figure **5.20**).

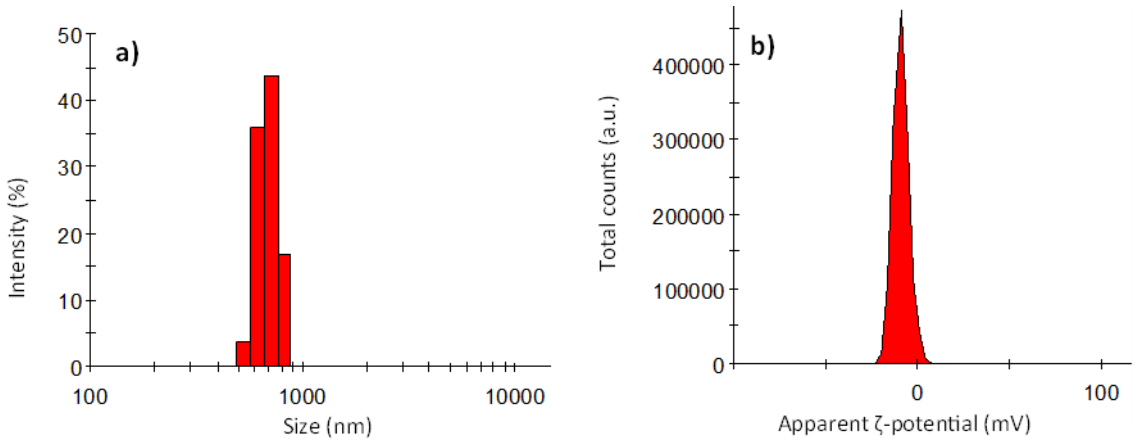


Figure **5.20**. **a)** Size intensity distribution by DLS of precipitated NPs formed during **FSM-PtBC** synthesis. **b)** Representative ζ-potential of precipitated NPs formed during **FSM-PtBC** synthesis.

As expected, a reaction without stirring can evolve into a non-homogeneous population of particles, tending towards larger sizes and non-homogeneous behaviour (i.e., indicated by a high PDI). The weak negative surface potential also indicates the capability of these NPs to aggregate, which could lead to the large particle sizes and agglomerates observed.

5.3.2. Studies on the Formation of FSM-PtBC

Given the Janus-like behaviour, the spherical inlays (or NP- loaded side) of the FSM, and the observation of a NP precipitate in SEM imaging, an interesting question arises: *Does the formation of **FSM-PtBC** require the initial formation of NPs?*

Evidence until now, supported by SEM imaging, indicates NP formation both in the solvent and as a component of the **FSM-PtBC**. The presence of NPs as a component of the FSM suggests that membrane formation is the result of an Oswalt ripening process. FSM could grow as NPs interact and agglomerate or fuse. However, to reach this situation, NPs must first form in solution or migrate to the surface, where they will compete in two possible processes: nucleation (i.e., the formation of new NPs) versus seed growth (i.e., increasing the size of existing NPs). These NPs then interact to form the **FSM-PtBC**. To gain a deeper understanding of the process involved in the preparation of **FSM-PtBC**, FSM formation was tracked in real time via optical microscopy (Figure **5.21**).

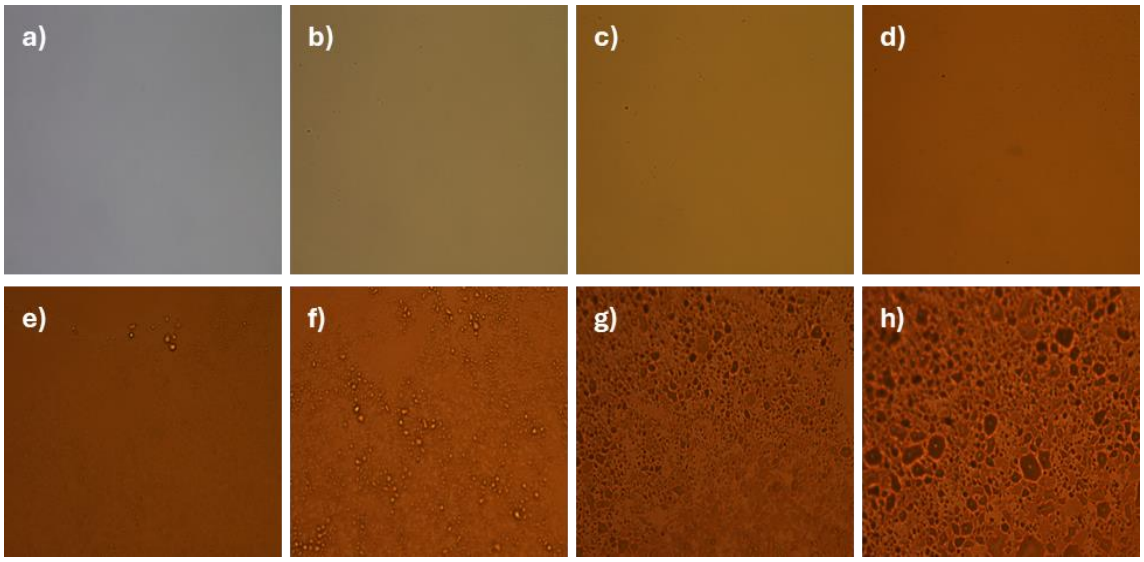


Figure **5.21**. **FSM-PtBC** formation through optical microscope at 50x augmentations at **a)** 0 hours, **b)** 3hours, **c)** 6 hours, **d)** 12 hours, **e)** 24 hours, **f)** 36 hours, **g)** 48 hours, and **h)** 72 hours.

Overall, from Figure **5.21**, we observe:

- **a-c)** The reaction vessel darkens, which can be attributed to the formation of oligomeric units of poly-**PtBC** that change the UV-vis absorptivity of the starting reagents.
- **c-d)** As time progresses, in the 6- to 12-hour periods, the formation of a granular layer at the interface becomes apparent. This granularity is attributed to the formation and accumulation of NPs on the surface.
- **d-e)** Up to the 24-hour mark, the granularity at the interface increases, while the sizes of individual grain-like particles remain constant. This indicates a more weighted preference for new seed formation in solution, while seed growth is already starting to occur.
- **f-h)** Finally, at the 36- to 72-hour timeframe, clear FSM formation is observed through fusion of granular units, resulting in a heterogeneous final FSM. This process clearly involves seed growth and fusion of clusters.

An interesting hypothesis can be formulated from the result of this assay. Nucleation and seed growth are common phenomena that occur in precipitation reactions. Both processes occur simultaneously, but each pathway is governed by different conditions. Overall, nucleation is considered the kinetically favoured pathway, while seed growth is seen as the thermodynamically favoured pathway.

In the context of **FSM-PtBC** formation, nucleation is the result of the reaction between different monomers of the **FSM-PtBC**, forming NPs (poly-**PtBC**). On the other hand, seed growth involves an increase in the size of those existing poly-**PtBC** NPs, or their fusion to form the **FSM-PtBC** platform. Since the solvent is saturated with reagents during the early stages of the reaction, this high concentration leads to rapid reaction between the reagents. Statistically, the most probable interactions at this point are between monomeric units, which favours the nucleation phase (Figure **5.21**.**a-c**, 0-6 hours), leading to the formation of oligomers. As the reaction evolves and reagents are depleted, these pre-formed oligomeric units begin to interact with either other oligomers or any remaining monomeric reagents, continuing the polymerisation process. Poly-DOPA reactions, for example, are known to form entanglement interactions with other oligomeric units, even without direct chemical bonding. This leads to the formation of the first NPs (Figure **5.21**.**c-d**, 6-12 hours).[126] As time progresses and reagents become scarcer (Figure **5.21**.**e-h**, 24-72 hours, NPs growth), the most probable interactions occur between existing NPs and other oligomers or other NPs, which eventually lead to seed growth and formation of **FSM-PtBC** (Figure **5.22**).

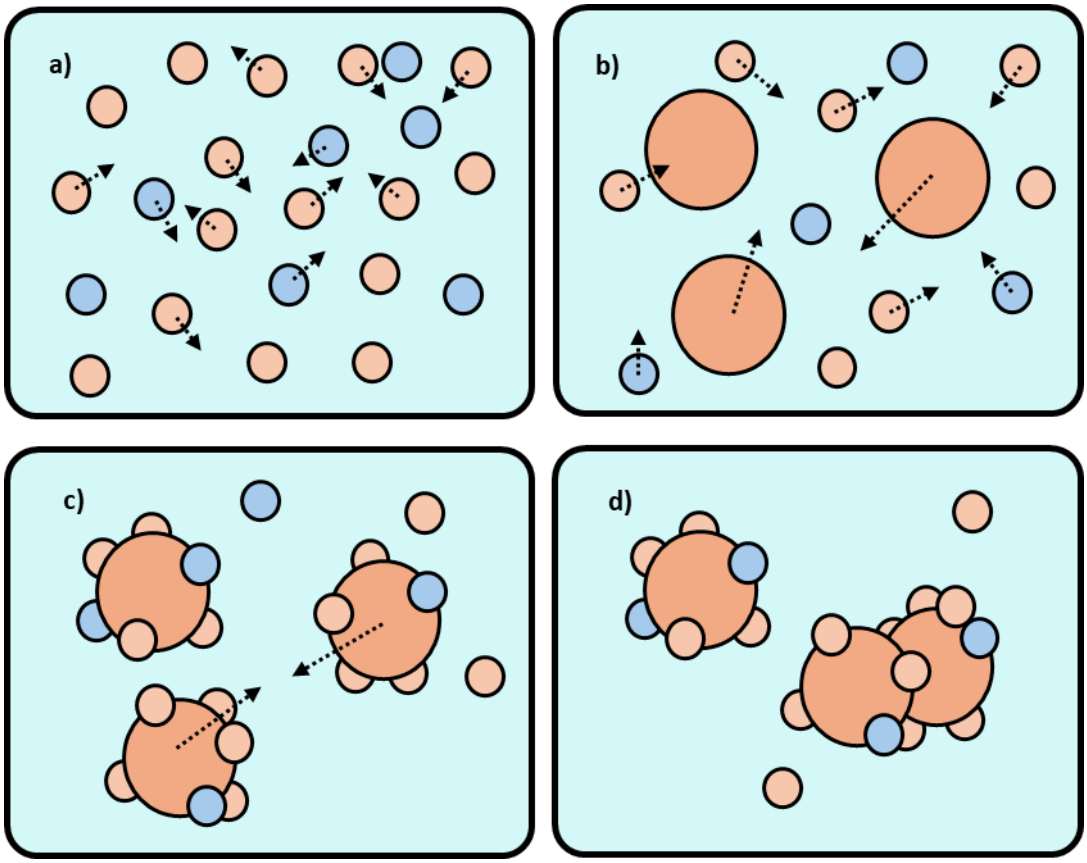


Figure **5.22**. Schematic representation of a reaction solution between amine **17** (blue) and **PtBC** (orange) at **a)** 0-hour time frame showing Brownian motion of dissolved monomers, **b)** 0- to 12-hour time frame, showing early oligomer and NP formation, and **c-d)** 24- to 72-hour time frame, showing NP growth from monomeric/oligomeric interactions and NP fusion respectively.

With the fundamental aspects of **FSM-PtBC** formation covered, other questions arise. *How do NPs accumulate at the interface? Why are the FSMs Janus-like? How do NPs interact together to form the **FSM-PtBC**?*

The Janus-like behaviour of the **FSM-PtBC** can be hypothesised as a result of the interactions between monomers, oligomers, and/or NPs reacting at the solvent-air interface. These interactions lead to *in situ* nucleation and eventual seed growth. Since no reagents are present in the atmospheric environment, the NPs can only grow toward the solvent, adopting a thermodynamically favourable shape (i.e., spherical) that minimises interactions with the solvent. These newly formed NPs are then incorporated into the growing FSM as other NPs accumulate at the interface, resulting in a smooth surface as the NPs fuse together (Figure **5.23**).

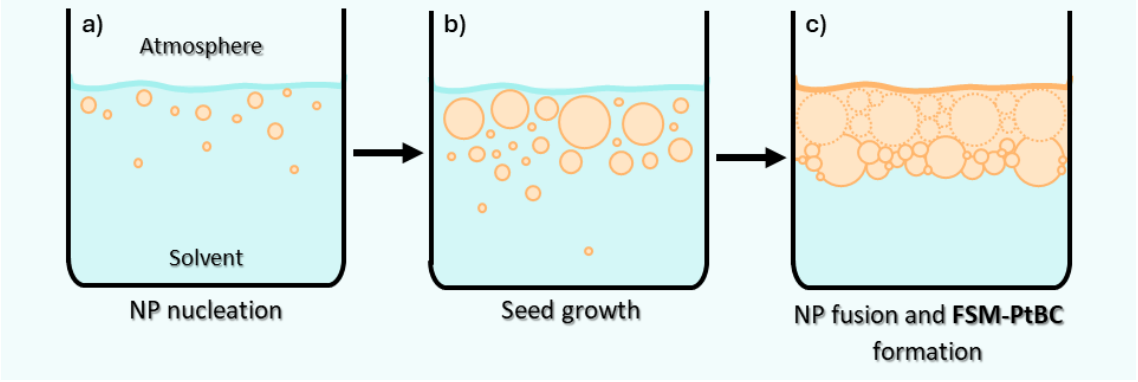


Figure 5.23. Schematic representation of the proposed process of FSM-PtBC formation, depicting: a) NP nucleation and seeding, b) NP accumulation at the air-solvent interface, and c) NP fusion and FSM-PtBC formation.

The accumulation of NPs at the interface can be attributed to a reagent gradient during the nucleation phase of **FSM-PtBC** formation. Because the polymerisation reaction requires oxidation, the higher concentration of oxygen at the interface leads to increased reaction kinetics. This results in a greater rate of NPs formation at the interface compared to the bulk solvent (Figure **5.24**). This hypothesis is supported by experimental observations showing a higher rate of NP and precipitate formation when oxygen availability to the solvent is uncontrolled, as opposed to synthesis in hypoxic environments, which displayed no reactivity.

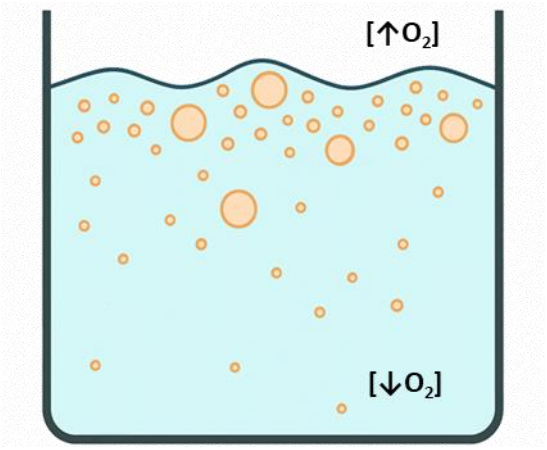


Figure **5.24**. Schematic representation of the proposed hypothesis of NP accumulation at the surface with reaction kinetics dictated by O_2 concentration.

The interaction and fusion between the NPs can also be explained in terms of hydrophobicity and surface charge. First, hydrophobic interactions drive the NPs to minimise the total surface area of the system in the aqueous environment and approach to each other (Figure **5.25.a**). Subsequently, reactive sites on the surface of one NP can chemically bond with reactive sites on another NP, leading to fusion. (Figure **5.25**.**b**).

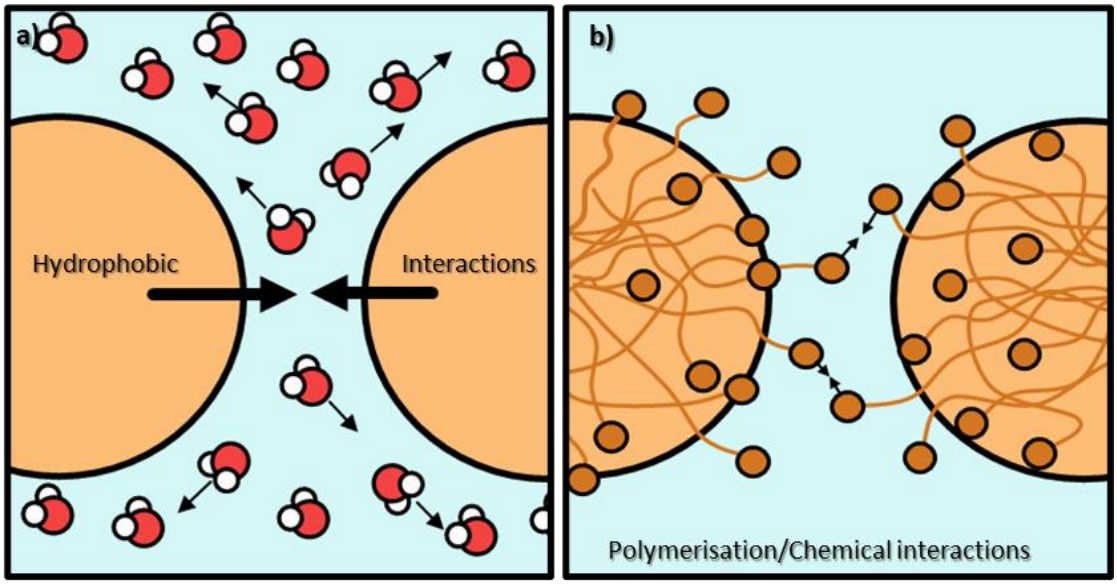


Figure **5.25**. Schematic representation of the hypothesised methods of particle interactions as; **a)** hydrophobic interactions, and **b)** chemical interactions as a result of oxidative polymerisation.

5.3.3. Platinum Content and Release Profile

Interestingly, from a compositional point of view, preliminary EDX analysis of the unmetallized **FSM-PtBC** sample yielded a high Pt loading, with a qualitative weight percentage of 13.44 ± 6.33% (Annexe **5.6**). This was later confirmed by a more reliable and accurate ICP-MS analysis, which measured a Pt content of 9.64 ± 0.55% (Annexe **5.7**). When compared to the Pt loading of the original **pPtBC NP** platform (17.02 ± 0.74%), the drop in Pt content can be correlated to the addition of amine bridging and crosslinking units, which decrease the relative weight of Pt loaded into the NP.

As the cytotoxicity of **FSM-PtBC** is expected to result, at least partially, from the release of alkylating-like Pt-based prodrugs (i.e., in the form of Pt(IV) or CDDP complexes), the total release of Pt into the surrounding environment was tracked via ICP-MS. To this aim, an **FSM-PtBC** of known mass was left in suspension in cell culture media for 24 hours, and aliquots were taken periodically. The Pt content was then analysed via ICP-MS and the results plotted over time (Figure **5.26**).

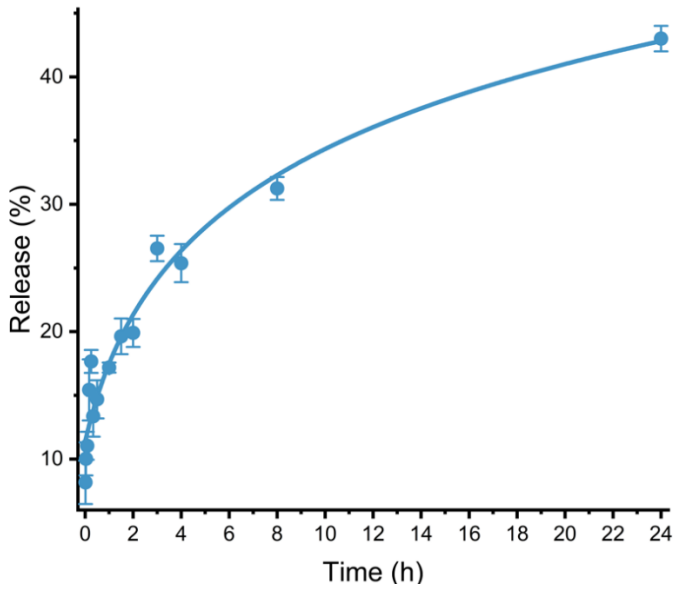


Figure **5.26**. Pt release of **FSM-PtBC** in a 24-hour period in cell culture media as analysed via ICP-MS. Data represents the mean ± SE, n=3.

In contrast to the Pt release profiles presented in previous Chapters, which employed the dialysis bag method for quantification, this study directly measured Pt release from the suspension medium. This was possible because the FSM maintained sufficient structural integrity to be left in suspension. The cell culture media were chosen as the solvent, as they represent a perfect match for the environment in which the *in vitro* experiments were carried out.

Under these settings, we can observe a clear release pattern with a quasi-logarithmic behaviour, indicating that total Pt release probably has not reached a plateau yet after the 24-hour mark. At the 24-hour mark, Pt release reaches a considerably high 43.0 ± 1.0% of the total Pt load. This information indicates that a sustained Pt release can be expected over long periods of time, allowing for longer-lasting therapies.

Interestingly, and contrary to what might be expected, the FSM retained structural integrity, showing no signs of mechanical stress, teardown, or degradation. Overall, Pt release was achieved in cellular media, which is promising for its applicability and for the release of Pt even without any externally required stimuli. Further studies need to be conducted to compare the release of Pt in acidic, reductive, and non-reactive environments (i.e., MilliQ® water) with the results from **pPtBC NPs**.

5.3.4. Development of Control Membrane FSM-TrisCat

Our research group has previously studied the behaviour of catechol-based FSMs, which generate ROS due to the incomplete oxidation of the catechol moiety during synthesis, particularly against GBM.[109]

For comparative purposes, a control FSM (**FSM-TrisCat**) was synthesised, which had been previously studied and characterised within our research group. This **FSM-TrisCat** is obtained by the reaction of tris(2-aminoethyl)amine (**17**) and pyrocatechol using the same protocol as **FSM-PtBC** (Figure **5.27**).[109] This FSM, without Pt complexes, was used as a reference to evaluate and compare the cytotoxic effect with the **FSM-PtBC**.

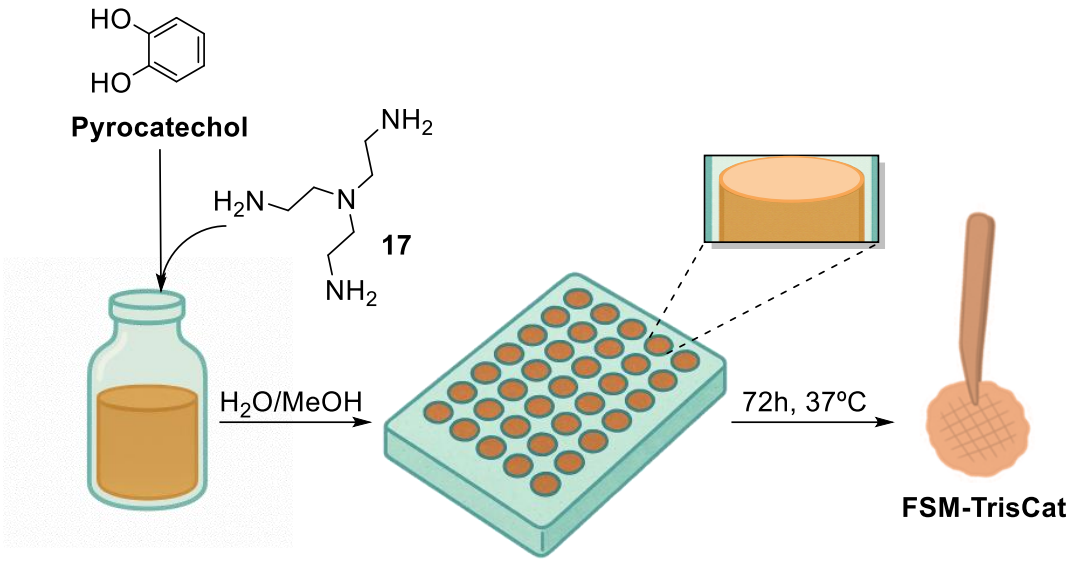


Figure **5.27**. Schematic representation of the procedure followed for the synthesis of **FSM-TrisCat** via oxidation polymerisation.

To ensure the correct preparation of **FSM-TrisCat**, FTIR spectrum and SEM images were recorded (Annexes **5.13** and **5.14**) and compared to the reported previous studies to confirm its successful preparation.[109] These control FSMs will help to isolate the effects of ROS generation and surface-related cell death mechanisms, as those are the only possible cell death mechanisms for **FSM-TrisCat**.

5.3.5. *In vitro* Cell Viability Evaluation

To evaluate the cytotoxic effect of **FSM-PtBC** and the control **FSM-TrisCat**, cell viability of the FSMs was tested against four cell lines: i) Murine GBM GL261 cell line, as they present a close model to our target GBM cancer treatment and a potential pre-clinical animal model, ii) Human cervical cancer cell line HeLa, as they present a generic cancer cell profile easily comparable to other studies, iii) Human epithelial GBM cancer cell line LN229, as they model the closest profile to human patient GBM, and iv) Non-malignant human fibroblast cell line 1Br3G as it presents as a healthy control. At the same time, 1Br3G, GL261, and HeLa cell models were also used in previous cytotoxicity studies of pPtBC NPs, allowing for a direct comparison between the two systems.

In a typical experiment, **FSM-PtBC** and **FSM-TrisCat** were washed with PBS-MilliQ® water and attached to the bottom of the well from a 96-well plate. Cells were then seeded on top of the FSMs, and viability was assessed after 24 hours post-treatment via the PrestoBlue™ method. Control cells were seeded in all experiments, receiving no treatment. **FSM-PtBC** and **FSM-TrisCat** were removed before the fluorescent measurements to avoid any possible interference from the FSMs.

The results from the cell viability experiment are presented in Figure **5.28**:

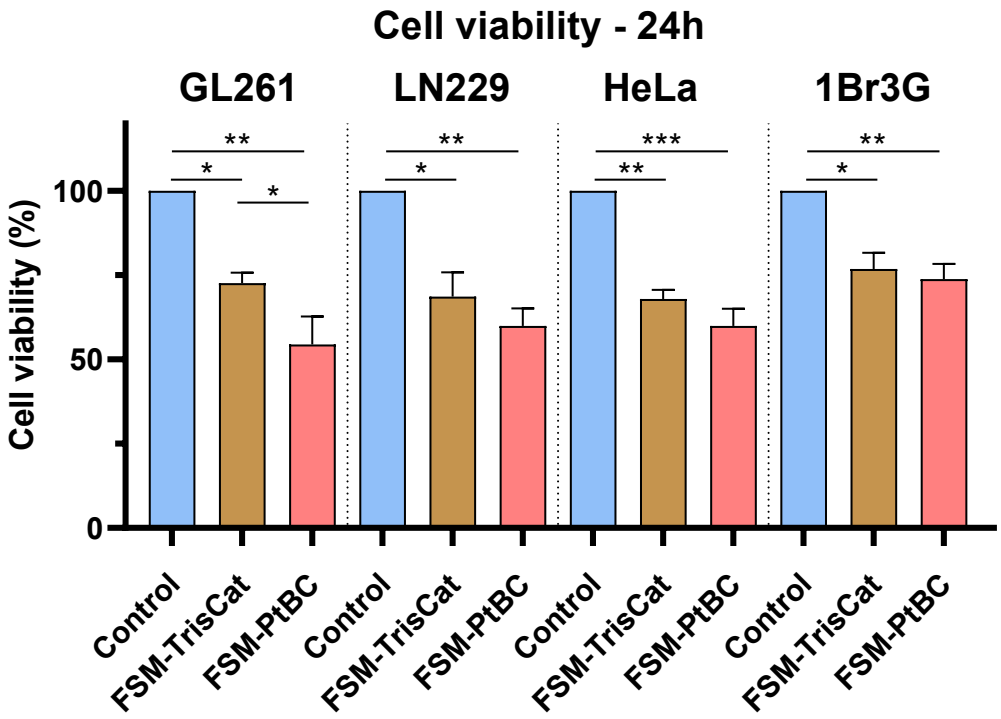


Figure **5.28**. Cell viability of **FSM-PtBC** and **FSM-TrisCat** in; **a)** Murine GBM GL261 cell line, **b)** Human epithelial GBM LN229 cell line, **c)** Human cervical HeLa cell line, and **d)** non-malignant human fibroblast 1Br3G cell line at 24 hours. All wells are treated with one FSM per well and include a negative control. Data represents the mean ± SE, n=3. Statistical differences were calculated using one-way ANOVA, followed by Turkey's multiple comparison test, where (*) denotes $P < 0.05$, (**) denotes $P < 0.01$, (***) denotes $P < 0.001$, and (****) denotes $P < 0.0001$.

Overall, the 24-hour cell viability studies highlight two key points:

- Firstly, seeding cells on the FSM, whether **FSM-PtBC** or **FSM-TrisCat**, impacts cell viability. This result is partially expected, as our research group has found that **FSM-TrisCat** can generate ROS, leading to cancer cell death.[109]

  As described in previous Chapters, DA and catechol-based functional groups can generate ROS through oxidation and prooxidative behaviour.[127] Our research group has characterised the transfer of these properties from the molecular to supramolecular structures in materials like **FSM-TrisCat**, especially in antimicrobial applications. Therefore, it is expected that some level of ROS generation and subsequent cell death would be induced by **FSM-TrisCat**, as observed. In the case of **FSM-PtBC**, there is a small increase in cytotoxicity that comes from the combination effect of ROS production and release of Pt.

  Interestingly, the ROS-generating capacity of **PtBC** and **pPtBC NPs**, as studied in section "***3.3.1.5.3. Determination of Reactive Oxygen Species Production"***, was found to be low. However, our previous protocol for the preparation of **pPtBC** used $NaIO_4$ as an oxidising reagent, which yielded complete oxidation of the monomeric components of the NP, decreasing their redox activity. In contrast, **FSM-PtBC** and **FSM-TrisCat** synthesis involve out-of-equilibrium reactions that can be stopped before complete reactivity of the component monomers is reached. Therefore, partial reactivity can still be retained after synthesis, leading to enhanced ROS generation when compared to the **pPtBC** platform.

Consequently, the slight increase in cytotoxicity of **FSM-PtBC** compared to **FSM-TrisCat** can be related to the combination of ROS generation and release of cytotoxic Pt species.

Future work in this Chapter will require ROS generation and evaluation to validate this finding.

- Secondly, **FSM-PtBC** presents a small, but statistically significant, decrease in cell viability compared to the control **FSM-TrisCat**.

  FSM-PtBC displays better results than the ROS control FSMs in all settings, which is especially significant in the GL261 cell line. At the same time, the increase in toxicity against healthy 1Br3G fibroblasts is kept to a minimum. Against the 1Br3G cell line, both **FSM-PtBC** and **FSM-TrisCat** present significantly lower cell death. This increase in cell viability is expected to be a result of the higher resistance of healthy cells towards ROS generation. This behaviour has been observed by our research group for **FSM-TrisCat**[109] and is also reported in the literature for other types of catechol-based coatings.[128]

  If we compare these results with the monomeric **PtBC** and **pPtBC NPs** from Chapter 3, a reduced toxicity in the 1Br3G cell line was also observed when compared to other cancer cells. This further contributes to explaining the overall decrease in toxicity in healthy fibroblasts and the low differentiation between ROS producer FSMs and ROS and Pt releaser FSMs.

In summary, we observe small toxicity from the Pt release of **FSM-PtBC** when compared to the control **FSM-TrisCat** at 24 hours. Furthermore, notable Pt release from **FSM-PtBC** at the 24-hour period (around 40%) is observed. However, the therapeutic effect based on Pt does not appear pronounced. This observation aligns with the results obtained for **PtBC** and **pPtBC NPs**. Both systems displayed fast cellular uptake, but slow DNA binding, tentatively attributed to the slow activation of Pt(IV) complexes to the active Pt(II) CDDP.

To evaluate the long-term chemotherapeutic effect, the same experiment was performed and the results analysed after 72 hours (Figure **5.29**). As observed, a different picture was obtained in the cell viability assay. Except for the healthy 1Br3G fibroblast cell line, a strong statistical significance was obtained when **FSM-PtBC** was compared to **FSM-TrisCat**. **FSM-PtBC** exhibited enhanced cytotoxicity, particularly in the HeLa cell line. The healthy 1Br3G fibroblast cells, on the other hand, show no statistical difference in terms of cell death.

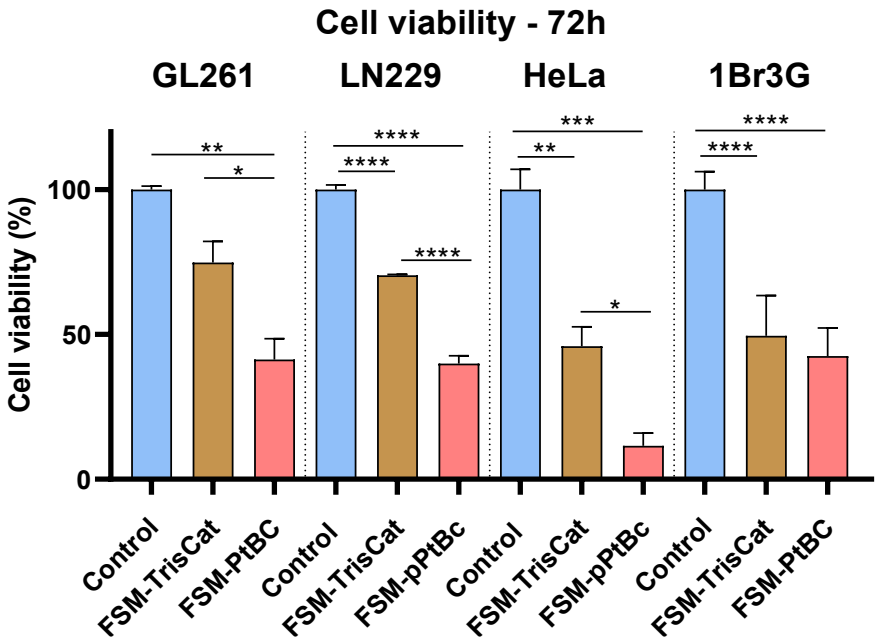


Figure **5.29**. Cell viability of **FSM-PtBC** and **FSM-TrisCat** in **a)** Murine GBM GL261 cell line, **b)** Human epithelial GBM LN229 cell line, **c)** Human cervical HeLa cell line, and **d)** non-malignant human fibroblast 1Br3G cell line at 72 hours. All wells are treated with one FSM per well and include a negative control. Data represents the mean ± SE, n=3. Statistical differences were calculated using one-way ANOVA, followed by Turkey's multiple comparison test, where (*) denotes $P < 0.05$, (**) denotes $P < 0.01$, (***) denotes $P < 0.001$, and (****) denotes $P < 0.0001$.

The low statistical difference between **FSM-PtBC** and **FSM-TrisCat** in the 24-hour cell viability assays suggests that ROS have a more immediate effect on cell viability, making this effect the leading cause of cytotoxicity. In accordance with the slow DNA-Pt binding affinity for **PtBC** and **pPtBC** studied in Chapter 3, a notable increase in cytotoxicity is expected over longer periods, which is what is observed in Figure **5.29** and also observed from data accrued for **PtBC** and **pPtBC**.

These results indicate that **FSM-PtBC** exhibits enhanced cytotoxic behaviour against cancer cells compared to previously developed FSMs from our research group, while maintaining a similar profile against healthy 1Br3G fibroblast cells. These findings are consistent with previous reports for **PtBC** and **pPtBC NPs** from Chapter 3, and boost the potential applicability of such FSMs as a drug delivery system for GBM treatment.

Overall, the considerable increase in cytotoxicity observed over the 72-hour cell viability assays for diverse tumoral cells, while maintaining the same profile against the healthy 1Br3G fibroblast cell line, represents a significant improvement for **FSM-PtBC** in FSM-based therapeutic approaches.

5.3.6. Post-*in vitro* Cell Viability FSM-PtBC Characterisation

The state of the FSMs was evaluated after cell viability assays to better understand the mechanisms influencing **FSM-PtBC** behaviour and possible degradability over time. As previously mentioned, during Pt release assays, the FSMs had not shown significant changes in structural integrity until the 24-hour mark. However, studies exceeding 24 hours in cell culture were conducted to ensure the chemical and morphological robustness of the FSMs.

5.3.6.1. Optical Analysis

FSM-PtBC was found to be structurally sound after 72-hour *in vitro* assays, with no apparent signs of degradation or rupturing. Further analysis via optical microscopy confirmed the macroscopic observations (Figure **5.30**).

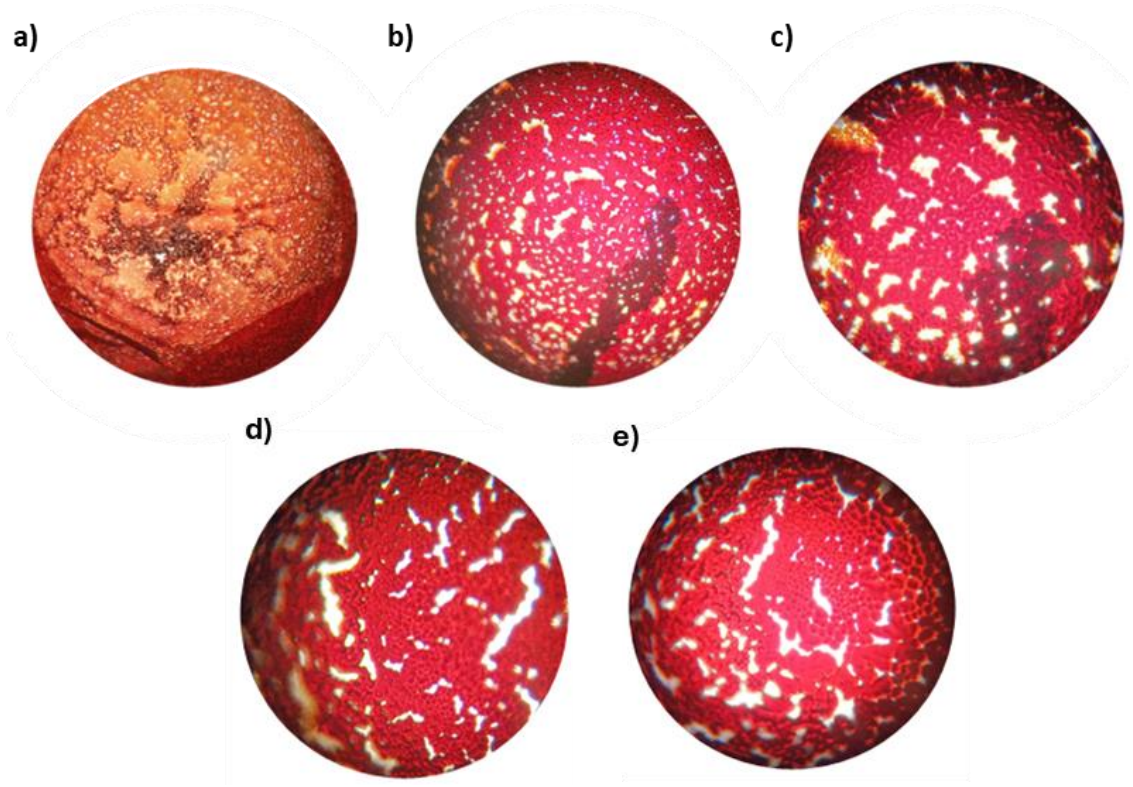


Figure **5.30**. Representative images of **FSM-PtBC** after 72-hour *in vitro* cell viability assay at **a)** 4x, **b)** 10x, and **c)** 20x augmentations and **d-f)** pre-cell viability assay at 10x augmentations.

While **FSM-TrisCat** shows a smooth and homogeneous surface (Annexe **5.15**), as expected from SEM imaging (Annexe **5.14**), **FSM-PtBC** presents a rugged and heterogeneous surface with porosity. This porosity allows cells to cross the FSM and reach the bottom of the well plate, an observation consistent with previous SEM imaging. Comparisons with observations from **FSM-PtBC** before cell viability assays displayed no significant differences.

5.3.6.2. Scanning Electron Microscopy Imaging

Changes in the surface morphology of **FSM-PtBC** were tracked via SEM imaging. After the cell viability assays were conducted, the FSMs were washed with MilliQ® water, dried, and sputter-coated with a 5 nm Pt thin film. SEM images were recorded (Figure **5.31**).

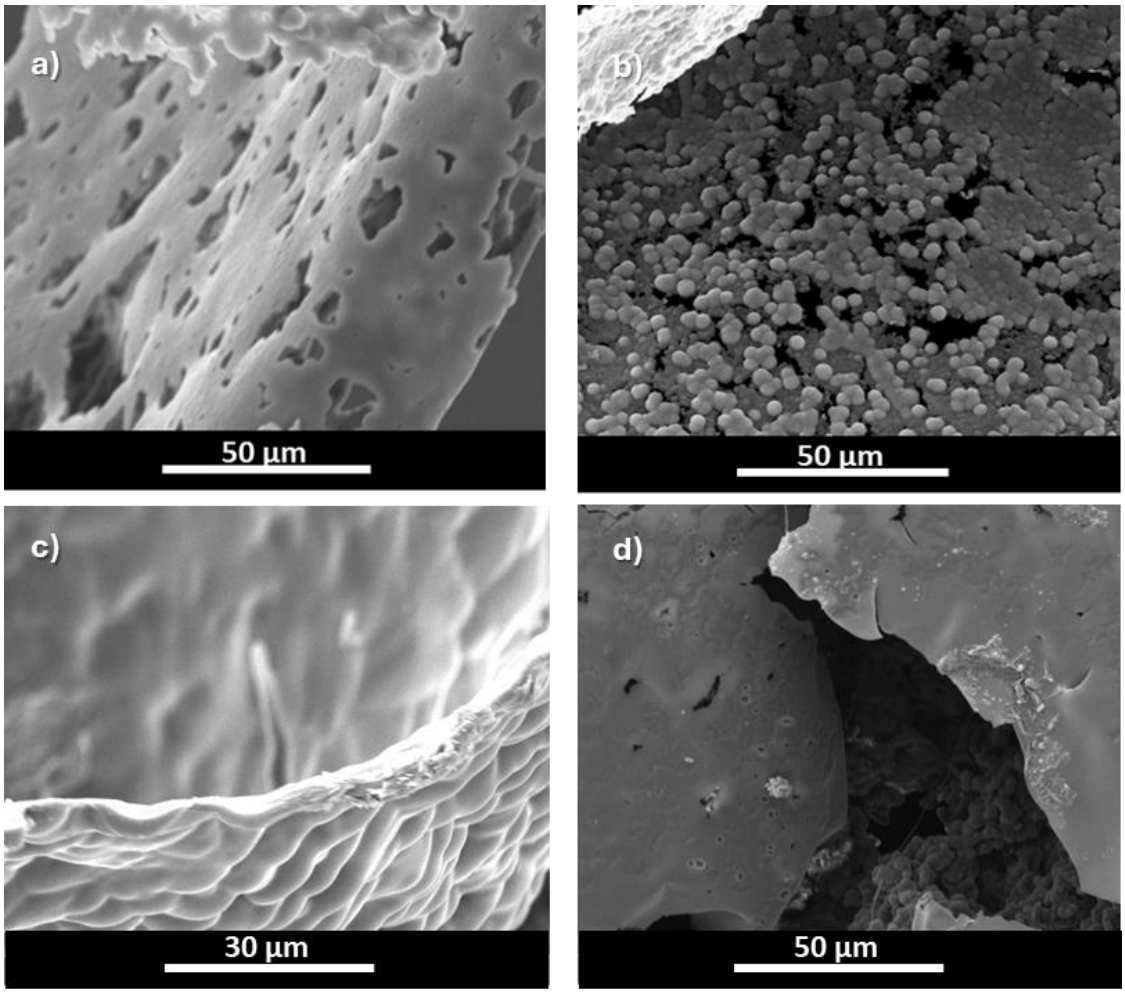


Figure **5.31** Representative SEM images of **FSM-PtBC**; **a-b)** pre-cell viability assays, and **c-d)** post-cell viability assays, under a 5 nm Pt thin film coating for imaging.

After cell viability assays, the SEM images show that **FSM-PtBC** retains its characteristic morphological features, including its Janus-like morphology with one smooth side and one rugged, NP-loaded side. The post-assay thickness of the FSM is approximately 2.9 ± 1.2 µm, which is roughly the same as the pre-assay thickness. Overall, **FSM-PtBC** demonstrates excellent stability and structural integrity, with no signs of breaking.

5.3.6.3. X-Ray Photoelectron Spectroscopy Analysis

XPS was used to study any chemical changes to the Pt present in the **FSM-PtBC** sample (Figure **5.32**). Their entire energy-range XPS spectra can be found in Annexe **5.8** and **5.9**.

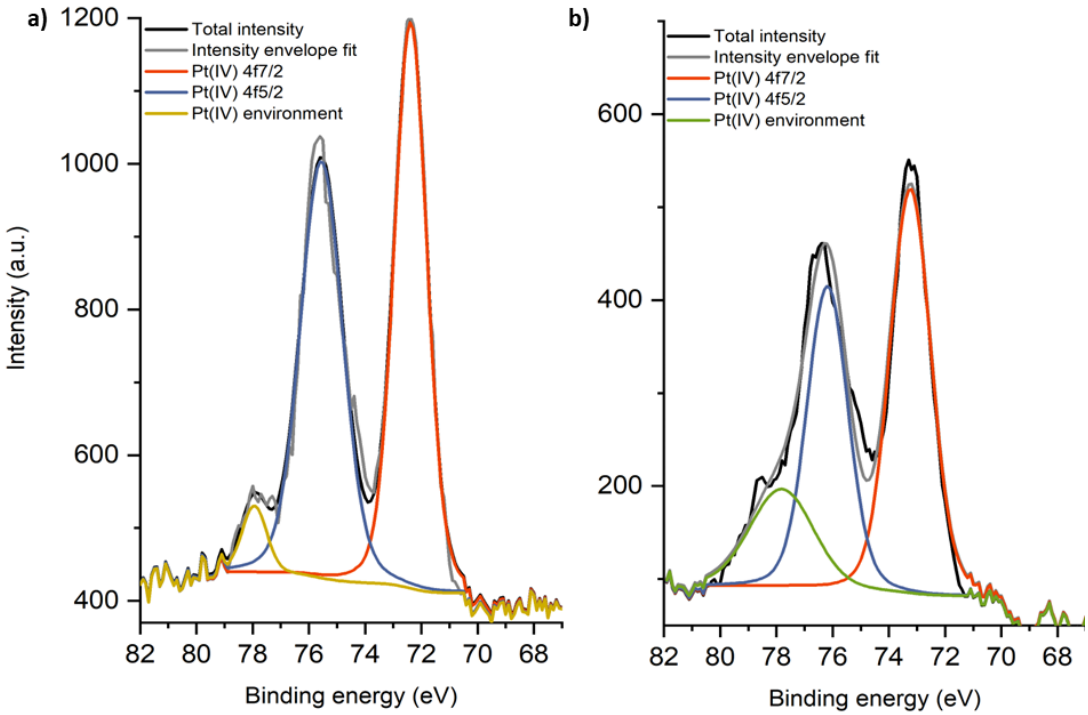


Figure 5.32. Curve-fitting results for Pt 4f high-resolution XPS spectra for **FSM-PtBC**; **a)** pre-cell viability assays, and **b)** post-cell viability assays, and the corresponding deconvolutions.

In XPS, Pt samples typically show two main peaks in the Pt 4f levels due to spin-orbit coupling, with a typical intensity ratio of 4:3. The binding energy of these peaks shifts depending on the oxidation state and chemical environment of the Pt.

Before cell viability assays (Figure **5.32.a**), two prominent peaks are centred at 73.3 and 76.5 eV. These findings are between those reported for Pt(II) (approximately 72.8 and 76.3 eV for CDDP) and Pt(IV) (approximately 74.5 and 77.8 eV for $PtCl_6^{2-}$).[129] Therefore, XPS supports the presence of Pt in a mixed oxidation state between Pt(II) and Pt(IV) species, especially given the broadened shape of the signals. The differences from the reference compounds are a result of different ligand environments, which are also evident in a third signal at higher binding energies. This signal is hypothesised to be a result of the multiple heteroatomic bonds (Pt-N, Pt-Cl and Pt-O) in the coordination polymer environment. However, this third signal is not indicative of Pt(0), as those peaks would appear at lower binding energies.

After cell viability assays (Figure **5.32.b**), Pt retains its binding energy shapes and values, but they present more broadened. This is partially expected due to the presence of redox-amphoteric catechols, which could slightly reduce Pt, broadening the peaks toward a more reduced Pt(II) contribution. Moreover, there is a relative increase in the contribution from the coordination polymer environment, which indicates that chemical changes are occurring during cell viability assays. However, the most significant change in the spectrum is the decrease in relative intensity. This behaviour indicates a clear loss of Pt from the sample, which is consistent with our Pt release studies.

5.3.7. Photothermal-Induced Heating of FSM-PtBC

While characterising **FSM-PtBC**, we had the opportunity to assess the photothermal conversion of our films, although it does not fall within our main scope of this Chapter.

Recent advances have demonstrated that FSMs and TFs loaded with photothermal agents, such as Prussian blue, and autophagy inhibitors can synergistically enhance tumour ablation efficacy. Specifically, these FSMs enable localised heating upon NIR irradiation and concurrently inhibit autophagic resistance mechanisms, leading to significantly improved tumour cell killing compared to PTT alone, while also offering controlled implantation and reduced systemic side effects.[130]

Therefore, the capability of catechol-based compounds to undergo photothermal conversion is well-established and extensively studied.[131–133] In this scenario, we aimed to determine the capacity of **FSM-PtBC** to display heat generation as a result of non-radiative heat loss after excitation with NIR light, and the potential of these TFs to act as a model of combined CT-PTT.

Catechol-based materials, such as catechol/polycatechol and related polymers, form extended π-conjugated systems that strongly absorb visible to NIR light and dissipate it as heat. Catechol units contain aromatic regions that, when polymerised, create broad electronic bands that absorb light from the UV to NIR ranges.[134,135] This behaviour was previously hinted at in the reflectance studies (Section ***5.3.1. Synthesis and Characterisation of FSM-PtBC***), and the dark colouration of the FSM also points to such a broad absorption spectrum. PDA in particular exhibits high fluorescence quenching, meaning that virtually every absorbed photon is eventually released as phonons (heat). The photothermal efficacy of conductive π-polymers relies on their post-excitation non-radiative relaxation pathways after excitation.[136]

A typical experiment involved irradiating a hydrated FSM with an 808 nm NIR laser at two different intensities: 580 mW and 1.7 W. This generated energy absorption densities of 2.05 $W \cdot cm^{-2}$ and 6.01 $W \cdot cm^{-2}$, respectively (Figure **5.33**).

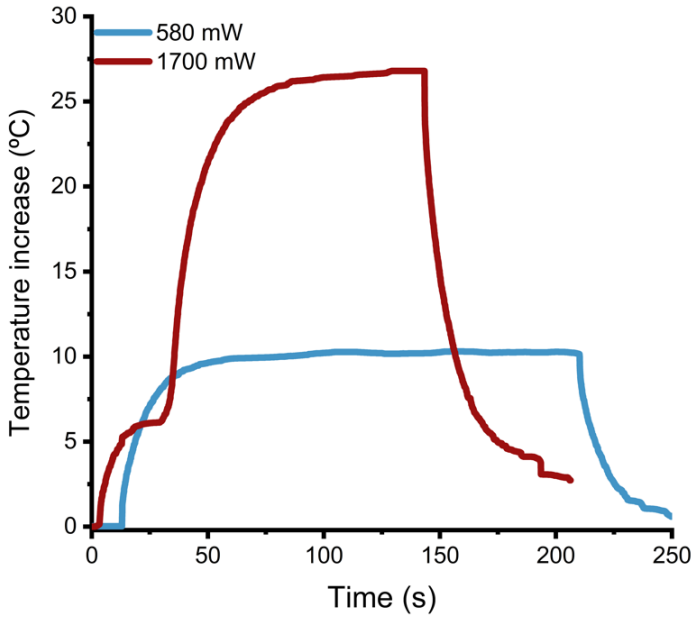


Figure **5.33**. Temperature change profile of **FMS-PtBC** in wet conditions under irradiation with free IR at 808 nm, and at different laser powers (580 mW and 1700 mW), and cooling under no irradiation.

Both settings yielded excellent photothermal conversion, resulting in a temperature increase from room temperature of 27 °C and 11 °C for the 580 mW and 1.7 W irradiation sources, respectively.

While these temperature increases are remarkably high, both light sources are well above the maximum tolerated energy dosage for PTT in skin cancer, which is 0.33 $W \cdot cm^{-2}$ for an 808 nm light source in clinical applications.[137] Nonetheless, further experimentation is required to fine-tune a more suitable light source and radiation wavelength. A comparison with the maximum tolerated energy dosage for GBM is not included because a clinically approved dosage has not been established as of the date of this Thesis.

The NPs formed during the synthesis of **FSM-PtBC** also displayed photothermal heating. However, due to time limitations, this behaviour was not fully characterised. Future experiments should focus on studying NPs' behaviour and conducting *in vitro* cell viability assays under PTT settings.

Notably, these results are promising for combining PTT with the initial goal of this Chapter, as the synergistic effect of combining PTT with CT could be a potential strategy to improve therapeutic outcomes against aggressive cancers, such as GBM.

5.4. Conclusions

This Chapter aimed to develop a mussel-inspired, catechol-based Pt(IV) **FSM-PtBC** for potential post-surgery GBM treatment.

As a result of work on this Chapter, we conclude that **FSM-PtBC** is a mechanically stable platform capable of sustained Pt release under physiological conditions. Its cytotoxicity results from combined effects of ROS and Pt release, delivering immediate toxicity via ROS generation and long-term therapeutic Pt effects. **FSM-PtBC** exhibits partial selectivity for cancer cells, showing limited impact on healthy fibroblasts. Additionally, **FSM-PtBC** has intrinsic photothermal conversion properties, offering potential for synergistic PTT and CT applications in GBM treatment.

A summary of the landmarks of this work is:

- Successful validation of the synthesis of **FSM-PtBC** via oxidative co-polymerisation from the reaction of **PtBC** prodrug with tris(2-aminoethyl)amine as a tridentate amine linker. The resulting product forms a robust, flexible, and shape-adaptable FSM.
- Characterisation suggested the formation of a highly crosslinked polymeric network with a Janus-like morphology, porosity, and constant thickness (2.7 ± 1.2 μm). Pt content was measured at 9.64 ± 0.55% (w/w).
- Mechanistic studies via *in situ* optical microscopy supported a nucleation–growth–fusion process for FSM formation.
- Pt release assays in cell culture media demonstrated a sustained Pt release profile, reaching 43.0 ± 1.0% at 24 hours, without loss of FSM integrity, suggesting feasibility for prolonged local CT.
- *In vitro* cytotoxicity assays against GL261, LN229, and HeLa cancer cell lines showed a statistically significant reduction in viability from **FSM-PtBC** compared to **FSM-TrisCat** controls, especially in 72-hour assays.
- Lower toxicity was observed in non-malignant 1Br3G fibroblasts in 24-hour cell viability assays, suggesting partial selectivity toward cancer cells, with 72-hour assays demonstrating no statistical difference from the control **FSM-TrisCat**.
- Comparison against the control **FSM-TrisCat** suggests that Pt incorporation is the main driver of enhanced cytotoxicity over 72-hour periods for **FSM-PtBC**, beyond surface-related or ROS-mediated effects.
- Preliminary photothermal conversion tests using 808 nm NIR irradiation demonstrated that **FSM-PtBC** generates significant heat, attributed to its extended π-conjugated catechol networks, indicating potential for combined CT-PTT.

Altogether, this work establishes the proof-of-concept for a bio-adhesive, drug-releasing TF tailored for post-surgical GBM therapy, with future work that should focus on:

- Exploring release behaviour under tumour-mimicking acidic/reductive conditions.
- Assessing *in vitro* photothermal-assisted cytotoxicity in GBM models.
- Evaluate and study ROS generation to validate findings from *in vitro* studies.

5.5. Materials and Experimental Methods

5.5.1. Materials

Solvents and starting materials were purchased from Merck (Germany) or TCI (Japan) and used as received without further purification.

5.5.2. Characterisations

Inductively coupled plasma mass spectrometry (ICP-MS) was performed at *Parque Científico Tecnológico* of the *Universidad de Burgos,* using an Agilent 8900 ICP-MS/MS with automatic sampler and octupole detector. Measurements were recorded using ^{194}Pt, ^{195}Pt, and ^{196}Pt as Pt tracers. Solid dry samples have been digested via a closed beaker digestion in the ETHOS SEL Milestone microwave in a 35:65 $HCl:HNO_3$ suspension for a total of 30 minutes while temperature was kept at 170 °C.

Infrared Spectrometry (IR) was performed using an MKII Golden gate spectrometer equipped each spectrum was acquired between 400 and 4000 cm^{-1} at a spectral resolution of 2 cm^{-1}. Samples were measured in direct transmittance mode through sample FSMs fixed in a holder.

Optical microscopy (OM) images were obtained using a Nikon ECLIPSE (Nikon, Japan) system equipped with 5x, 10x, 20x, 50x, and 100x magnification objectives and polarising filters. Sample solutions containing monomer **PtBC** and tris(2-aminoethyl)amine in H_2O/MeOH 1:1 were placed in 1 cm radius and height cylinders, occupying the total available volume of the vessel, and cantered to the imaging lenses. Pictures of the surface were then recorded at 0, 3, 6, 12, 24, and 72 hours. The resulting images were processed in ZEISS ZEN (Germany).

Dynamic light scattering (DLS) for hydrodynamic size distribution and zeta surface charge potential of NPs (0.5 $mg{\cdot}mL^{-1}$) were measured using a ZetasizerNano 3600 instrument (Malverm Instruments, UK), with a size range limit from 0.6 nm to 6 nm. NPs were dispersed in water to study colloidal stability in physiological conditions.

Scanning Electron Microscopy (SEM) images were obtained using a scanning electron microscope (FEI Quanta 650 FEG or Magellan 400L XHR) at an acceleration voltage of 5-20 KV. SEM samples were prepared by adhesion on double-sided carbon tape adhesives, followed by metallisation with a thin layer of Pt (thickness of 5 nm) using a sputter coater (Emitech K550). SEM pictures were acquired at accelerating voltages between 2 and 20 kV under a high-vacuum mode and an electron gun distance to the sample of 5 mm. FSM thickness was obtained by imaging of a sample prepared via perpendicular adhesion on a 90º SEM stub.

X-ray photoelectron Spectroscopy (XPS) measurements were performed with a Phoibos 150 analyser in ultra-high vacuum conditions (base pressure 10^{-10} mbar). Monochromatic AlKα as X-ray source (1486.6 eV). Electron energy analyser operated at pass energy of 50 eV perpendicular to the sample surface. All data was treated with CasaXPS version 2.3.17PR1.1 (Casa Software LTD, UK) software.

Reflectance spectroscopy of samples was measured using a Cary 4000 spectrophotometer (Agilent, USA), in the 200−800 nm wavelength range working in reflectance mode. Diffuse reflectance accessories module was used for acquisition of diffuse and specular reflectance of **FSM-PtBC**. Samples were placed in a size-adjusted holder, compatible with the module, for analysis.

Photothermal heating profile capacity was recorded using a NIR laser diode with a selected emission wavelength of 808 nm (L808P500MM, Thorlabs) driven by a laser diode controller (ITC4005, Thorlabs) equipped with an optical collimating and aligning system, and a thermal infrared camera (ETS320, FLIR) to monitor temperature variations at FSM surfaces. The irradiation incident power was set to 1.7 or 0.58 $W \cdot cm^{-2}$, and the temperature was monitored and recorded in real time during the assays. For an assay, **FSM-PtBC** was suspended and washed in MilliQ® water and then placed, while still wet, on a clean, level surface for data acquisition.

Pt drug release from FSM-PtBC was evaluated using direct sampling. **FSM-PtBC** was accurately weighted and suspended on 100 mL of cell culture media. The samples were then kept at 37 °C with gentle stirring throughout the study. At predetermined time points, 1 mL aliquots were withdrawn from the dialysate and immediately replaced with an equal volume of cell culture media. The quantity of released Pt was determined using ICP-MS.

5.5.3. *In vitro* assays

Cell line culture

Murine GBM GL261, human GBM LN229, human cervical cancer HeLa, and human fibroblast 1Br3G cell line were obtained from the American Type Culture Collection (ATCC; USA). GL261, LN299 and 1Br3G were cultured in Dulbecco's modified eagle medium enriched with 4.5 g/L D-glucose (DMEM (1X) + GlutaMAX™-) and 10% heat-inactivated FBS. HeLa was cultured in minimum essential medium (MEM Alpha) enriched with 10% heat-inactivated FBS and 1% GlutaMAX™-. The cells were grown as adherent monolayer in 75 cm^2 cell-culture flask (Nunclon™ Delta Surface) and maintained in an incubator (HERAcell, 150i, Thermo Scientific, USA) at 37 °C in 5% CO_2 with a relative humidity of 95%. Cell culture media, FBS, GlutaMAX™-, PBS, trypsin, Trypan Blue and material were procured from Thermo Scientific (USA).

To subculture or collect cells, cells must be in the logarithmic phase growth, which is considered to be achieved at around 75% confluence. Once this confluence was reached, the culture medium was removed from the flask. Then, 5 mL of sterile PBS was added to the flask to wash the cells and remove any residual medium. After removing the PBS and repeating again the same process, 3 mL of trypsin was added, the flask was then returned to incubator for 3 minutes. If, upon observing the cells under the microscope, ≥ 90% of the cells were detached, 6 mL of fresh medium was added to neutralize the trypsin and facilitate cell collection. The cell suspension was then transferred to a 15 mL Falcon tube (Cultek, Spain) and centrifuged (Thermo Scientific, USA) at 1200 rpm for 5 minutes to collect the cells. The supernatant was discarded, and the cell pellet was resuspended in fresh medium to the desired dilution factor. Then, 1 mL of this resuspension was added to a flask containing 13 mL of fresh medium. To seed the required amount, a cell count was performed, and the necessary number of cells were seeded into the corresponding plate for each experiment.

Cell counting

Cell counting was performed using a Neubauer hemocytometer and Trypan Blue for cell viability assessment. Trypan Blue is a dye that differentiates living cells from dead ones, as dead cells cannot extrude Trypan Blue due to a lack of necessary energy-dependent mechanisms. An aliquot of 10 µL of the cell suspension to be studied was mixed with 10 µL of Trypan Blue. Next, 10 µL of the mixture was placed into the Neubauer hemocytometer, and the number of living cells was counted using an optical microscope.

Cell viability assays

Stock of **FSM-TrisCat** and stock of **FSM-PtBC** were prepared and cleaned with sterile PBS-MilliQ® water. Then, the FSMs were adhered to the bottom of each well. To do this, 100 µL of PBS was added to each well, the FSM was carefully spread in the well, and then the PBS was removed.

GL261, LN299, HeLa and 1Br3G cells in exponential growth were seeded in a 96-well plate (Sudelab, Spain) on top of the FSMs or the control wells (without FSMs) and under optimal conditions. GL261 and LN299, HeLa, and 1Br3G cell lines were seeded at a density of 40,000, 10,000, and 15,000 cells/well, respectively, in a final volume of 200 µL. After 24- or 72-hours post-treatment, 10 µL of PrestoBlue® (0.15 mg·mL^{-1}, Thermo Scientific, USA) were added to each treated well, as well as to three wells containing only medium. The plates were then incubated at 37 °C for about 4 hours, and measurements were performed using the Victor 3 microplate reader (Perkin Elmer, USA) at emission of 572 nm with excitation at 530 nm. The cell viability (%) for each sample related to the control (without FSMs) was calculated. All experiments were conducted in triplicate, and the data were processed using GraphPad Prism software (version 8.0).

Statistical analyses

Data were analysed using GraphPad Prism (version 8.0) and values are represented as the mean ± SE of three independent experiments. Statistical differences were calculated using one-way ANOVA, followed by Turkeys multiple comparison test.

5.5.4. Synthesis procedures

Pt complex **PtBC** was obtained with the same methodology as described earlier and also reported as a result of the work in Chapter 3 of this Thesis.[112]

Synthesis of FSM-PtBC

A solution of Tris(2-aminoethyl)amine (7.5 µL, 0.052 mmol) in 0.5 mL of degassed water, and a solution of **PtBC** (24 mg, 0.031 mmol) in 0.25 mL of degassed methanol were mixed and immediately aliquoted in 100 µL aliquots in a 96-well plate. The resulting aliquoted mixture was then kept at 37 °C for 72 hours in the dark. Afterwards, the resulting TF formed on the liquid-air interface was detached from the well with a chirurgical biopsy punch, removed from the well, washed, and suspended with MilliQ® water, affording a dark brown FSM (0.4 mg) that displays buoyancy in water. Samples were then frozen while in

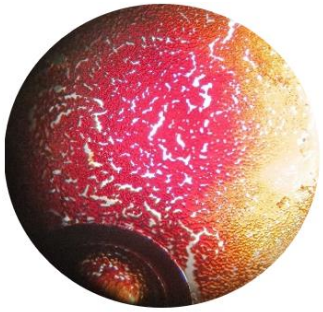


Figure **5.34**. Optical microscope representative images of **FSM-PtBC** at 4x augments.

suspension for storage and further use *in vitro* or lyophilised for characterisation.

Spectroscopic information of **FSM-PtBC**:

IR ν 3228 (m), 3087 (w), 2926 (w), 2862 (w), 1633 (s), 1549 (w), 1435 (w), 1268 (s), 1216 (w), 875 (w), 809 (w), 670 (m) cm^{-1}. ICP-MS Pt (%(w/w)) found 9.64 ± 0.55 %. XPS (Pt) fit calcd. 73.3, 76.5, 78.0 eV.

Synthesis of FSM-TrisCat

Synthesis of **FSM-TrisCat** followed an already reported procedure with minor modifications.[111]

A solution of Tris(2-aminoethyl)amine (30 µL, 0.2 mmol) in 4 mL of degassed water, and a solution of pyrocatechol (44 mg, 0.4 mmol) in 0.25 mL of degassed water were mixed and immediately aliquoted in 100 µL aliquots in a 96-well plate. The resulting aliquoted mixture was then kept at 37 °C for 72 hours in the dark. Afterwards, the resulting TF formed on the liquid-air interface was detached from the well with a chirurgical biopsy punch, removed from the well, washed, and suspended with MilliQ® water, affording a dark brown FSM (0.4 mg) that displays buoyancy in water. Samples were then frozen while in suspension for storage and further use *in vitro* or lyophilised for characterisation.

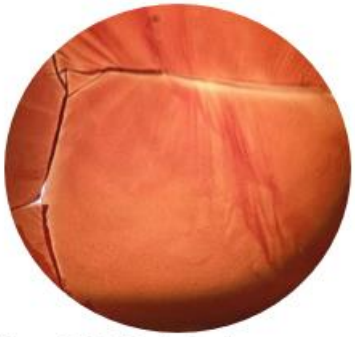


Figure **5.35**. Optical microscope representative images of **FSM-TrisCat** at 4x augments.

Spectroscopic information of **FSM-PtBC**:

IR ν 3249 (s), 2953 (m), 1548 (s), 1443 (w), 1353 (w), 1282 (s), 441 (s) cm^{-1}

5.6. References

1. Stupp R, Mason WP, van den Bent MJ, et al. Radiotherapy plus Concomitant and Adjuvant Temozolomide for Glioblastoma. *N. Engl. J. Med.* **2005**;352(10). doi:10.1056/nejmoa043330
2. Mnich K, Lhomond S, Wallace E, et al. Improving glioblastoma treatment with imaging, radiotherapy, drug delivery, and therapeutic systems. *Device.* **2025**;3(2):100685. doi:10.1016/j.device.2024.100685
3. Wu W, Klockow JL, Zhang M, et al. Glioblastoma multiforme (GBM): An overview of current therapies and mechanisms of resistance*. Pharmacol Res.* **2021**;171. doi:10.1016/j.phrs.2021.105780
4. Rodgers LT, Villano JL, Hartz AMS, Bauer B. Glioblastoma Standard of Care: Effects on Tumor Evolution and Reverse Translation in Preclinical Models. *Cancers*. **2024**;16(15):2638. doi:10.3390/cancers16152638
5. Revilla-Pacheco F, Rodríguez-Salgado P, Barrera-Ramírez M, et al. Extent of resection and survival in patients with glioblastoma multiforme: Systematic review and meta-analysis. *Medicine.* **2021**;100(25). doi:10.1097/MD.0000000000026432
6. Smets T, Lawson TM, Grandin C, Jankovski A, Raftopoulos C. Immediate post-operative MRI suggestive of the site and timing of glioblastoma recurrence after gross total resection: A retrospective longitudinal preliminary study. *Eur Radiol*. **2013**;23(6). doi:10.1007/s00330-012-2762-1
7. Kuhnt D, Becker A, Ganslandt O, Bauer M, Buchfelder M, Nimsky C. Correlation of the extent of tumor volume resection and patient survival in surgery of glioblastoma multiforme with high-field intraoperative MRI guidance. *Neuro Oncol.* **2011**;13(12). doi:10.1093/neuonc/nor133
8. Rossi M, Gay L, Ambrogi F, et al. Association of supratotal resection with progression-free survival, malignant transformation, and overall survival in lower-grade gliomas. *Neuro Oncol*. **2021**;23(5). doi:10.1093/neuonc/noaa225
9. Youngblood MW, Stupp R, Sonabend AM. Role of Resection in Glioblastoma Management. *Neurosurg Clin N Am*. **2021**;32(1). doi:10.1016/j.nec.2020.08.002
10. Hart MG, Garside R, Rogers G, Somerville M, Stein K, Grant R. Chemotherapy wafers for high grade glioma. *Cochrane Database Syst Rev*. **2011**;2011(3). doi:10.1002/14651858.CD007294.pub2
11. Young RM, Jamshidi A, Davis G, Sherman JH. Current trends in the surgical management and treatment of adult glioblastoma. *Ann Transl Med*. **2015**;3(9). doi:10.3978/j.issn.2305-5839.2015.05.10
12. https://healthcare-in-europe.com/en/news/benefits-of-ultrasound-in-neurosurgical-oncology.html.
13. https://www.cookchildrens.org/services/neurosciences/advanced-technology/intraoperative-magnetic-resonance-imaging/.
14. https://www.neurosurgery.pitt.edu/centers/image-guided-neurosurgery/fgs.
15. Pessina F, Navarria P, Cozzi L, et al. Maximize surgical resection beyond contrast-enhancing boundaries in newly diagnosed glioblastoma multiforme: is it useful and safe? A single institution retrospective experience. *J Neurooncol*. **2017**;135(1). doi:10.1007/s11060-017-2559-9
16. Rahman M, Abbatematteo J, De Leo EK, et al. The effects of new or worsened postoperative neurological deficits on survival of patients with glioblastoma. *J Neurosurg*. **2017**;127(1). doi:10.3171/2016.7.JNS16396
17. Campos B, Olsen LR, Urup T, Poulsen HS. A comprehensive profile of recurrent glioblastoma. *Oncogene*. **2016**;35(45). doi:10.1038/onc.2016.85
18. Waqar M, Trifiletti DM, McBain C, et al. Early Therapeutic Interventions for Newly Diagnosed Glioblastoma: Rationale and Review of the Literature. *Curr Oncol Rep*. **2022**;24(3). doi:10.1007/s11912-021-01157-0
19. Research progress of clinical application of tumor therapeutic electric field in glioblastoma. *Chin. Neurosurg. J.* **2021**;37(1). doi:10.3760/cma.j.cn112050-20200605-00330
20. Kageji T, Nagahiro S, Mizobuchi Y, Matsuzaki K, Nakagawa Y, Kumada H. Boron neutron capture therapy (BNCT) for newly-diagnosed glioblastoma: Comparison of clinical results obtained with BNCT and conventional treatment. *J. Med. Invest.* **2014**;61(3-4). doi:10.2152/jmi.61.254
21. Kreisl TN, Kim L, Moore K, et al. Phase II trial of single-agent bevacizumab followed by bevacizumab plus irinotecan at tumor progression in recurrent glioblastoma. *J Clin Oncol*. **2009**;27(5). doi:10.1200/JCO.2008.16.3055
22. Bai H, Harmanci AS, Erson-Omay EZ, et al. Integrated genomic characterization of IDH1-mutant glioma malignant progression. *Nat Genet*. **2015**;48(1). doi:10.1038/ng.3457
23. Del Vecchio CA, Li G, Wong AJ. Targeting EGF receptor variant III: Tumor-specific peptide vaccination for malignant gliomas. *Expert Rev Vaccines*. **2012**;11(2). doi:10.1586/erv.11.177
24. Gelao L, Criscitiello C, Esposito A, Goldhirsch A, Curigliano G. Immune checkpoint blockade in cancer treatment: A double-edged sword cross-targeting the host as an "innocent bystander." *Toxins*. **2014**;6(3). doi:10.3390/toxins6030914
25. Choi BD, Maus M V., June CH, Sampson JH. Immunotherapy for glioblastoma: Adoptive T-cell Strategies. *Clin Cancer Res*. **2019**;25(7). doi:10.1158/1078-0432.CCR-18-1625
26. Huang J, Liu F, Liu Z, et al. Immune checkpoint in glioblastoma: Promising and challenging. *Front Pharmacol*. **2017**;8(MAY). doi:10.3389/fphar.2017.00242

27. Sun S, Gu W, Wu H, et al. Immunostimulant In Situ Hydrogel Improves Synergetic Radioimmunotherapy of Malignant Glioblastoma Relapse Post-Resection. *Adv Funct Mater*. **2022**;32(43). doi:10.1002/adfm.202205038
28. Fukuhara H, Ino Y, Todo T. Oncolytic virus therapy: A new era of cancer treatment at dawn. *Cancer Sci*. **2016**;107(10). doi:10.1111/cas.13027
29. Begagić E, Bečulić H, Đuzić N, et al. CRISPR/Cas9-Mediated Gene Therapy for Glioblastoma: A Scoping Review. *Biomedicines*. **2024**;12(1). doi:10.3390/biomedicines12010238
30. Wang Z, Deng Z, Zhu G. Emerging platinum(iv) prodrugs to combat cisplatin resistance: From isolated cancer cells to tumor microenvironment. *Dalton Trans.* **2019**;48(8). doi:10.1039/c8dt03923b
31. Alfonso-Triguero P, Lorenzo J, Candiota AP, Arús C, Ruiz-Molina D, Novio F. Platinum-Based Nanoformulations for Glioblastoma Treatment: The Resurgence of Platinum Drugs? *Nanomaterials*. **2023**;13(10). doi:10.3390/nano13101619
32. Basu B, Nath S. Fundamentals of Biomaterials and Biocompatibility. *J. Biomater. Appl*. **2010**. doi:10.1002/9780470891315.ch1
33. Nkanga CI, Fisch A, Rad-Malekshahi M, et al. Clinically established biodegradable long acting injectables: An industry perspective. *Adv Drug Deliv Rev*. **2020**;167. doi:10.1016/j.addr.2020.11.008
34. Park J, Lakes RS. *Biomaterials: An Introduction: Third Edition*.; **2007**. doi:10.1007/978-0-387-37880-0
35. Rehman M, Madni A, Webster TJ. The era of biofunctional biomaterials in orthopedics: what does the future hold? *Expert Rev Med Devices*. **2018**;15(3). doi:10.1080/17434440.2018.1430569
36. Zhang L, Webster TJ. Nanotechnology and nanomaterials: Promises for improved tissue regeneration. *Nano Today*. **2009**;4(1). doi:10.1016/j.nantod.2008.10.014
37. Ripamonti U, Ferretti C, Teare J, Blann L. Transforming Growth Factor-β Isoforms and the Induction of Bone Formation. *J Craniofac Surg*. **2009**;20(5). doi:10.1097/scs.0b013e3181b09ca6
38. Aguado BA, Grim JC, Rosales AM, Watson-Capps JJ, Anseth KS. Engineering precision biomaterials for personalized medicine. *Sci Transl Med*. **2018**;10(424). doi:10.1126/scitranslmed.aam8645
39. Badeau BA, Deforest CA. Programming Stimuli-Responsive Behavior into Biomaterials. *Annu Rev Biomed Eng*. **2019**;21. doi:10.1146/annurev-bioeng-060418-052324
40. Gelmi A, Schutt CE. Stimuli-Responsive Biomaterials: Scaffolds for Stem Cell Control. *Adv Healthc Mater*. **2021**;10(1). doi:10.1002/adhm.202001125
41. Hu J, Zhang G, Liu S. Enzyme-responsive polymeric assemblies, nanoparticles and hydrogels. *Chem Soc Rev*. **2012**;41(18). doi:10.1039/c2cs35103j
42. Lu W, Wei S, Chen T. Stimuli-Responsive Fluorescent Polymeric Hydrogels. In: *Smart Stimuli-Responsive Polymers, Films, and Gels*. *Wiley*; **2022**:281-299. doi:10.1002/9783527832385.ch8
43. Chen J, Wang Y, Ma B, et al. Biodegradable hollow mesoporous organosilica-based nanosystems with dual stimuli-responsive drug delivery for efficient tumor inhibition by synergistic chemo- and photothermal therapy. *Appl Mater Today*. **2020**;19. doi:10.1016/j.apmt.2020.100655
44. Chen B, Xiang H, Pan S, Yu L, Xu T, Chen Y. Advanced Theragenerative Biomaterials with Therapeutic and Regeneration Multifunctionality. *Adv Funct Mater*. **2020**;30(34). doi:10.1002/adfm.202002621
45. Arne B, Yucang Li YX, Cuie W. Assessing the biocompatibility of biomaterials. *LAP*. **2017**;91.
46. Huang Y, Ding Z. Biomaterials for cardiovascular diseases. *Biomed. Technol.* **2024**;7:1-14. doi:10.1016/j.bmt.2024.05.001
47. Malchesky PS. Artificial Organs 2019: A year in review. *Artif Organs*. **2020**;44(3). doi:10.1111/aor.13650
48. Chang DK, Louis MR, Gimenez A, Reece EM. The Basics of Integra Dermal Regeneration Template and its Expanding Clinical Applications. *Semin Plast Surg*. **2019**;33(3). doi:10.1055/s-0039-1693401
49. Wu SJ, Zhao X. Bioadhesive Technology Platforms. *Chem Rev*. **2023**;123(24). doi:10.1021/acs.chemrev.3c00380
50. Ashby LS, Smith KA, Stea B. Gliadel wafer implantation combined with standard radiotherapy and concurrent followed by adjuvant temozolomide for treatment of newly diagnosed high-grade glioma: A systematic literature review. *World J Surg Oncol*. **2016**;14(1). doi:10.1186/s12957-016-0975-5
51. Westphal M, Ram Z, Riddle V, Hilt D, Bortey E. Gliadel® wafer in initial surgery for malignant glioma: Long-term follow-up of a multicenter controlled trial. *Acta Neurochir*. **2006**;148(3). doi:10.1007/s00701-005-0707-z
52. Wolinsky JB, Colson YL, Grinstaff MW. Local drug delivery strategies for cancer treatment: Gels, nanoparticles, polymeric films, rods, and wafers. *J. Control. Release.* **2012**;159(1). doi:10.1016/j.jconrel.2011.11.031
53. KAUR S, KENNEDY-SNODGRASS C, V. THOMAS S. A CASE OF LOMUSTINE-INDUCED PNEUMONITIS. *Chest*. **2022**;162(4). doi:10.1016/j.chest.2022.08.1481
54. Weiss RB, Issell BF. The nitrosoureas: carmustine (BCNU) and lomustine (CCNU). *Cancer Treat Rev*. **1982**;9(4). doi:10.1016/S0305-7372(82)80043-1
55. Bastiancich C, Malfanti A, Préat V, Rahman R. Rationally designed drug delivery systems for the local treatment of resected glioblastoma. *Adv Drug Deliv Rev*. **2021**;177. doi:10.1016/j.addr.2021.113951
56. Ohue S. Using BCNU wafers in the treatment of malignant gliomas. *Neurol Med Chir*. **2016**;25(11). doi:10.7887/jcns.25.882

57. Gulati S, Jakola AS, Nerland US, Weber C, Solheim O. The risk of getting worse: Surgically acquired deficits, perioperative complications, and functional outcomes after primary resection of glioblastoma. *World Neurosurg*. **2011**;76(6). doi:10.1016/j.wneu.2011.06.014

58. Perry J, Chambers A, Spithoff K, Laperriere N. Gliadel wafers in the treatment of malignant glioma: a systematic review. *Curr. Oncol*. **2007**;14(5). doi:10.3747/co.2007.147

59. Gkasdaris G, Berthiller J, Guyotat J, et al. Is Carmustine Wafer Implantation in Progressive High-Grade Gliomas a Relevant Therapeutic Option? Complication Rate, Predictors of Complications and Onco-Functional Outcomes in a Series of 53 Cases. *Cancers*. **2024**;16(20). doi:10.3390/cancers16203465

60. Valtonen S, Timonen U, Toivanen P, et al. Interstitial chemotherapy with carmustine-loaded polymers for high- grade gliomas: A randomized double-blind study. *Neurosurgery*. **1997**;41(1). doi:10.1097/00006123-199707000-00011

61. Della Puppa A, Denaro L, Rossetto M, et al. Postoperative seizure in high grade glioma patients treated with BCNU wafers. A mono-institutional experience. *J Neurooncol*. **2011**;105(2). doi:10.1007/s11060-011-0577-6

62. Brem H, Piantadosi S, Burger PC, et al. Placebo-controlled trial of safety and efficacy of intraoperative controlled delivery by biodegradable polymers of chemotherapy for recurrent gliomas. *The Lancet*. **1995**;345(8956). doi:10.1016/S0140-6736(95)90755-6

63. Ono T, Suzuki H, Nanjo H, Shimizu H. Clinical Course after Carmustine Wafer Implantation for Newly Diagnosed Adult-type Diffuse Gliomas; A controlled propensity matched analysis of a single center cohort. *J Neurooncol*. **2024**;168(3):393-404. doi:10.1007/s11060-024-04679-2

64. Champeaux-Depond C, Jecko V, Weller J, Constantinou P, Tuppin P, Metellus P. Recurrent high grade glioma surgery with carmustine wafers implantation: a long-term nationwide retrospective study. *J Neurooncol*. **2023**;162(2). doi:10.1007/s11060-023-04295-6

65. https://www.accessdata.fda.gov/scripts/cder/daf/index.cfm?event=BasicSearch.process. Published online September 5, **2025**.

66. Fisher JP, Adamson DC. Current FDA-approved therapies for high-grade malignant Gliomas. *Biomedicines*. **2021**;9(3). doi:10.3390/biomedicines9030324

67. Kleinberg L. Polifeprosan 20, 3.85% carmustine slow-release wafer in malignant glioma: Evidence for role in era of standard adjuvant temozolomide. *Core Evid*. **2012**;7. doi:10.2147/CE.S23244

68. Garg R, Gonuguntla S, Sk S, et al. Sputtering thin films: Materials, applications, challenges and future directions. *Adv Colloid Interface Sci*. **2024**;330:103203. doi:10.1016/j.cis.2024.103203

69. Maniruzzaman M, Boateng JS, Snowden MJ, Douroumis D. A Review of Hot-Melt Extrusion: Process Technology to Pharmaceutical Products. *ISRN Pharm*. **2012**;2012. doi:10.5402/2012/436763

70. Zelikin AN. Drug releasing polymer thin films: New era of surface-mediated drug delivery. *ACS Nano*. **2010**;4(5). doi:10.1021/nn100634r

71. Garg V, Jindal S. Buccal Bioadhesive Drug Delivery Systems and Their Applications. *Drug Deliv*. **2020**. doi:10.1002/9781119640240.ch8

72. Borges AF, Silva C, Coelho JFJ, Simões S. Oral films: Current status and future perspectives. *J. Control. Release.* **2015**;206. doi:10.1016/j.jconrel.2015.03.006

73. H J Y, Kulkarni GS, Paarak PM. Mucoadhesive Buccal Films. *JCPP*. **2023**;(35). doi:10.55529/jcpp.35.24.37

74. Guillen SG, Parres-Gold J, Ruiz A, et al. PH-Responsive Metal-Organic Framework Thin Film for Drug Delivery. *Langmuir*. **2022**;38(51). doi:10.1021/acs.langmuir.2c02497

75. Iqbal A, Naqvi SAR, Sherazi TA, Asif M, Shahzad SA. Thin films as an emerging platform for drug delivery. In: *J. Drug Deliv*. **2022**. doi:10.1016/B978-0-323-91376-8.00006-9

76. Park S, Han U, Choi D, Hong J. Layer-by-layer assembled polymeric thin films as prospective drug delivery carriers: Design and applications. *Biomater Res*. **2018**;22. doi:10.1186/s40824-018-0139-5

77. Radu ER, Voicu SI, Thakur VK. Polymeric Membranes for Biomedical Applications. *Polymer*. **2023**;15(3). doi:10.3390/polym15030619

78. Ponzio F, Ball V. Polydopamine deposition at fluid interfaces. *Polym Int*. **2016**;65(11). doi:10.1002/pi.5124

79. Lee BP, Messersmith PB, Israelachvili JN, Waite JH. Mussel-inspired adhesives and coatings. *Annu Rev Mater Res*. **2011**;41. doi:10.1146/annurev-matsci-062910-100429

80. Yu J, Wei W, Danner E, Ashley RK, Israelachvili JN, Waite JH. Mussel protein adhesion depends on interprotein thiol-mediated redox modulation. *Nat Chem Biol*. **2011**;7(9). doi:10.1038/nchembio.630

81. Petrone L, Kumar A, Sutanto CN, et al. Mussel adhesion is dictated by time-regulated secretion and molecular conformation of mussel adhesive proteins. *Nat Commun*. **2015**;6. doi:10.1038/ncomms9737

82. Wei W, Petrone L, Tan Y, et al. An Underwater Surface-Drying Peptide Inspired by a Mussel Adhesive Protein. *Adv Funct Mater*. **2016**;26(20). doi:10.1002/adfm.201600210

83. Waite JH, Andersen NH, Jewhurst S, Sun C. Mussel adhesion: Finding the tricks worth mimicking. *J Adhesion*. **2005**;81(3-4). doi:10.1080/00218460590944602

84. Williams R. Mimicking mussels. *Scientist*. **2013**;27(4).

85. Guo Q, Chen J, Wang J, Zeng H, Yu J. Recent progress in synthesis and application of mussel-inspired adhesives. *Nanoscale*. **2020**;12(3). doi:10.1039/c9nr09780e

86. Danner EW, Kan Y, Hammer MU, Israelachvili JN, Waite JH. Adhesion of mussel foot protein Mefp-5 to mica: An underwater superglue. *Biochemistry*. **2012**;51(33). doi:10.1021/bi3002538

87. Lu Q, Danner E, Waite JH, Israelachvili JN, Zeng H, Hwang DS. Adhesion of mussel foot proteins to different substrate surfaces. *J R Soc Interface*. **2013**;10(79). doi:10.1098/rsif.2012.0759

88. Liu Z, Ding Y, Ding Y, Wang W, Mao Z, Yu L. Gelatin-DOPA-knob/fibrinogen hydrogel inspired by fibrin polymerization and mussel adhesion for rapid and robust hemostatic sealing. *Biomaterials*. **2025**;317:123038. doi:10.1016/j.biomaterials.2024.123038

89. Xie C, Li Y, Guo X, Ding Y, Lu X, Rao S. Mussel-inspired adhesive hydrogels for local immunomodulation. *Mater Chem Front*. **2023**;7(5). doi:10.1039/d2qm01232d

90. Holten-Andersen N, Harrington MJ, Birkedal H, et al. pH-induced metal-ligand cross-links inspired by mussel yield self-healing polymer networks with near-covalent elastic moduli. *Proc Natl Acad Sci U S A*. **2011**;108(7). doi:10.1073/pnas.1015862108

91. Bhagat V, Becker ML. Degradable Adhesives for Surgery and Tissue Engineering. *Biomacromol.* **2017**;18(10). doi:10.1021/acs.biomac.7b00969

92. Waite JH. Mussel adhesion - Essential footwork. *J. Exp. Biol*. **2017**;220(4). doi:10.1242/jeb.134056

93. Yu J, Wei W, Menyo MS, Masic A, Waite JH, Israelachvili JN. Adhesion of mussel foot protein-3 to TiO2 surfaces: The effect of pH. *Biomacromol.* **2013**;14(4). doi:10.1021/bm301908y

94. Feinberg H, Hanks TW. Polydopamine: a bioinspired adhesive and surface modification platform. *Polym Int*. **2022**;71(5). doi:10.1002/pi.6358

95. Xu Z. Mechanics of metal-catecholate complexes: The roles of coordination state and metal types. *Sci Rep*. **2013**;3. doi:10.1038/srep02914

96. Xiang L, Zhang J, Wang W, et al. Nanomechanics of π-cation-π interaction with implications for bio-inspired wet adhesion. *Acta Biomater*. **2020**;117. doi:10.1016/j.actbio.2020.09.043

97. Kim S, Faghihnejad A, Lee Y, Jho YS, Zeng H, Hwang DS. Cation-π interaction in DOPA-deficient mussel adhesive protein mfp-1. *J Mater Chem B*. **2015**;3(5). doi:10.1039/c4tb01646g

98. Wilker JJ. The iron-fortified adhesive system of marine mussels. *Angew. Chem. Int. Ed.* **2010**;49(44). doi:10.1002/anie.201003171

99. Sánchez-Iglesias A, Grzelczak M, Altantzis T, et al. Hydrophobic interactions modulate self-assembly of nanoparticles. *ACS Nano*. **2012**;6(12). doi:10.1021/nn3047605

100. Yang B, Lim C, Hwang DS, Cha HJ. Switch of Surface Adhesion to Cohesion by Dopa-Fe3+ Complexation, in Response to Microenvironment at the Mussel Plaque/Substrate Interface. *Chem. Mater.* **2016**;28(21). doi:10.1021/acs.chemmater.6b03676

101. Green K. Mussel Adhesive Protein. In: *SURGICAL ADHESIVES and SEALANTS*. CRC Press; **2020**:19-27. doi:10.1201/9780429332500-4

102. Contreras-Pereda N, Suárez-García S, Pfattner R, Ruiz-Molina D. Melanin-inspired conductive thin films for multimodal-sensing wearable on-skin electronics. *Mater Today Chem*. **2024**;35. doi:10.1016/j.mtchem.2023.101855

103. Jalaber V, Del Frari D, De Winter J, et al. Atmospheric aerosol assisted pulsed plasma polymerization: An environmentally friendly technique for tunable catechol-bearing thin films. *Front Chem*. **2019**;7(APR). doi:10.3389/fchem.2019.00183

104. Ghosh A, Singh J, Lim S, Steele TWJ. Water activated catechol adhesive allows dip coated antimicrobial coatings. *Mater Today Adv*. **2023**;19. doi:10.1016/j.mtadv.2023.100398

105. Hong S, Schaber CF, Dening K, Appel E, Gorb SN, Lee H. Air/water interfacial formation of freestanding, stimuli-responsive, self-healing catecholamine janus-faced microfilms. *Adv. Mater*. **2014**;26(45). doi:10.1002/adma.201403259

106. Sousa MP, Mano JF. Cell-adhesive bioinspired and catechol-based multilayer freestanding membranes for bone tissue engineering. *Biomimetics*. **2017**;2(4). doi:10.3390/biomimetics2040019

107. Salvio SUÁREZ GARCÍA, Daniel RUIZ MOLINA, Javier SAIZ POSEU. US20240277896A1.

108. Maroli G, Rosati G, Suárez-García S, et al. Wearable, battery-free, wireless multiplexed printed sensors for heat stroke prevention with mussel-inspired bio-adhesive membranes. *Biosens Bioelectron*. **2024**;260. doi:10.1016/j.bios.2024.116421

109. Bolaños-Cardet J. *Mussel-Inspired Adv. Mater. for Biomedical Applications*. **2025.**

110. López-Moral A, Bolaños-Cardet J, Alibés R, et al. A bioinspired and environmentally sustainable polyphenol-based water adhesive. *J Colloid Interface Sci*. **2025**;680:987-996. doi:10.1016/j.jcis.2024.11.042

111. Bolaños-Cardet J, Ruiz-Molina D, Yuste VJ, Suárez-García S. Bioinspired phenol-based coatings for medical fabrics against antimicrobial resistance. *Chem. Eng*. **2024**;481. doi:10.1016/j.cej.2024.148674

112. Gómez-Herrera R, Alfonso-Triguero P, Mao X, et al. Bioinspired neuromelanin-like Pt(iv) polymeric nanoparticles for cancer treatment. *Nanotechnol Rev*. **2024**;13(1). doi:10.1515/ntrev-2024-0118

113. Yang J, Cohen Stuart MA, Kamperman M. Jack of all trades: Versatile catechol crosslinking mechanisms. *Chem Soc Rev*. **2014**;43(24). doi:10.1039/c4cs00185k

114. Sousa CFV, Monteiro LPG, Rodrigues JMM, Borges J, Mano JF. Marine-origin polysaccharides-based free-standing multilayered membranes as sustainable nanoreservoirs for controlled drug delivery. *J Mater Chem B*. **2023**;11(28). doi:10.1039/d3tb00796k

115. Moreira J, Vale AC, Alves NM. Spin-coated freestanding films for biomedical applications. *J Mater Chem B*. **2021**;9(18). doi:10.1039/d1tb00233c

116. Jacobs S, McCully CL, Murphy RF, Bacher J, Balis FM, Fox E. Extracellular fluid concentrations of cisplatin, carboplatin, and oxaliplatin in brain, muscle, and blood measured using microdialysis in nonhuman primates. *Cancer Chemother Pharmacol*. **2010**;65(5). doi:10.1007/s00280-009-1085-7

117. Гиневский ДА, Ижевский ПВ, Шейно ИН, Левитова ДГ. Modeling of pharmacokinetic processes of distribution of cisplatin in tumor tissues. *Nauchno-prakticheskii zhurnal «Medicinskaia genetika»*. **2020**;(6(215)):106-108. doi:10.25557/2073-7998.2020.06.106-108

118. Argyriou AA, Bruna J, Genazzani AA, Cavaletti G. Chemotherapy-induced peripheral neurotoxicity: Management informed by pharmacogenetics. *Nat Rev Neurol*. **2017**;13(8). doi:10.1038/nrneurol.2017.88

119. Kanat O, Ertas H, Caner B. Platinum-induced neurotoxicity: A review of possible mechanisms. *World J Clin Oncol*. **2017**;8(4). doi:10.5306/wjco.v8.i4.329

120. Research progress on the relationship between cisplatin ototoxicity and autophagy. *J Clin Otolaryngol Head Neck Surg.* **2020**;34(2). doi:10.13201/j.issn.1001-1781.2020.02.023

121. Andrés CMC, Pérez de la Lastra JM, Juan CA, Plou FJ, Pérez-Lebeña E. Polyphenols as Antioxidant/Pro-Oxidant Compounds and Donors of Reducing Species: Relationship with Human Antioxidant Metabolism. *Processes*. **2023**;11(9). doi:10.3390/pr11092771

122. Stoeva S, Hvarchanova N, Georgiev KD, Radeva-Ilieva M. Green Tea: Antioxidant vs. Pro-Oxidant Activity. *Beverages*. *MDPI*. **2025**;11(3). doi:10.3390/beverages11030064

123. Alfieri ML, Panzella L, Napolitano A. Multifunctional coatings hinging on the catechol/amine interplay. *European J Org Chem*. **2024**;27(1). doi:10.1002/ejoc.202301002

124. Lyu Q, Hsueh N, Chai CLL. The Chemistry of Bioinspired Catechol(amine)-Based Coatings. *ACS Biomater Sci Eng*. **2019**;5(6). doi:10.1021/acsbiomaterials.9b00281

125. Padera J. *Measuring Absorptance (k) and Refractive Index (n) of Thin Films with the PerkinElmer Lambda 950/1050 High Performance UV-Vis/NIR Spectrometers*.; **2013**.

126. Saiz-Poseu J, Sedõ J, García B, et al. Versatile nanostructured materials via direct reaction of functionalized catechols. *Adv. Mater.* **2013**;25(14). doi:10.1002/adma.201204383

127. Tao L, Park JY, Lambert JD. Differential prooxidative effects of the green tea polyphenol, (-)-epigallocatechin-3-gallate, in normal and oral cancer cells are related to differences in sirtuin 3 signaling. *Mol Nutr Food Res*. **2015**;59(2). doi:10.1002/mnfr.201400485

128. Forooshani PK, Meng H, Lee BP. Catechol Redox Reaction: Reactive Oxygen Species Generation, Regulation, and Biomedical Applications. In: *ACS Symposium Series*. Vol 1252. **2017**. doi:10.1021/bk-2017-1252.ch010

129. Romanchenko A, Likhatski M, Mikhlin Y. X-ray photoelectron spectroscopy (XPS) study of the products formed on sulfide minerals upon the interaction with aqueous platinum (IV) chloride complexes. *Minerals*. **2018**;8(12). doi:10.3390/min8120578

130. Mu J, Meng Z, Liu X, Guan P, Lian H. Implantable Nanofiber Membranes with Synergistic Photothermal and Autophagy Inhibition Effects for Enhanced Tumor Therapy Efficacy. *Adv. Fiber Mater*. **2023**;5(5). doi:10.1007/s42765-023-00311-6

131. Lee KK, Park KW, Lee SC, Lee CS. Perfluorocarbon-polyepinephrine core-shell nanoparticles as a near-infrared light activatable theranostic platform for bimodal imaging-guided photothermal/chemodynamic synergistic cancer therapy. *Theranostics*. **2025**;15(3):1077-1093. doi:10.7150/thno.102743

132. Chen X, Wang L, Liu S, Luo X, Wang K, He Q. Cisplatin-loaded metal–phenolic network with photothermal-triggered ROS generation for chemo-photothermal therapy of cancer. *Cancer Nanotechnol*. **2022**;13(1). doi:10.1186/s12645-022-00149-4

133. Wang Y, Wang J, Du H, et al. A dynamically cross-linked catechol-grafted chitosan/gelatin hydrogel dressing synergised with photothermal therapy and baicalin reduces wound infection and accelerates wound healing. *Int J Biol Macromol*. **2024**;273. doi:10.1016/j.ijbiomac.2024.132802

134. Zhang M, Mi M, Hu Z, et al. Polydopamine-Based Biomaterials in Orthopedic Therapeutics: Properties, Applications, and Future Perspectives. *Drug Des Devel Ther*.*Dove Medical Press Ltd*. **2024**;18:3765-3790. doi:10.2147/DDDT.S473007

135. Petropoulos V, Mordini D, Montorsi F, et al. Photochemical Pathways and Light-Enhanced Radical Scavenging Activity of 1,8-Dihydroxynaphthalene Allomelanin. *J Am Chem Soc*. **2025**;147(11):10031-10043. doi:10.1021/jacs.5c01855

136. Geng H, Lupton EJ, Ma Y, et al. Hybrid Polypyrrole and Polydopamine Nanosheets for Precise Raman/Photoacoustic Imaging and Photothermal Therapy. *Adv Healthc Mater*. **2023**;12(27). doi:10.1002/adhm.202301148

137. Roca AG, Lopez-Barbera JF, Lafuente A, et al. Iron oxide nanoparticles (Fe3O4, γ-Fe2O3 and FeO) as photothermal heat mediators in the first, second and third biological windows. *Phys Rep*. **2023**;1043. doi:10.1016/j.physrep.2023.10.003

138. Basu B, Katti DS, Kumar A. *Advanced Biomaterials: Fundamentals, Processing, and Applications*.; *Adv. Biomat*. **2010**. doi:10.1002/9780470891315

139. Vehof JWM, Haus MTU, De Ruijter AE, Spauwen PHM, Jansen JA. Bone formation in Transforming Growth Factor beta-1-loaded titanium fiber mesh implants. *Clin Oral Implants Res*. **2002**;13(1). doi:10.1034/j.1600-0501.2002.130112.x

140. Place ES, Evans ND, Stevens MM. Complexity in biomaterials for tissue engineering. *Nat Mater*. **2009**;8(6). doi:10.1038/nmat2441

141. Festas AJ, Ramos A, Davim JP. Medical devices biomaterials – A review. *Proceedings of the Institution of Mechanical Engineers, Part L: Proc. Inst. Mech. Eng. Pt. L J. Mater. Des. Appl*. **2020**;234(1). doi:10.1177/1464420719882458

142. Das SS, Chakraborti P. Development of Biomaterial for Total Hip Joint Replacement. In: *IOP Conf. Ser.: Mater. Sci. Eng.* Vol 377. **2018**. doi:10.1088/1757-899X/377/1/012177

143. Dziadek M, Stodolak-Zych E, Cholewa-Kowalska K. Biodegradable ceramic-polymer composites for biomedical applications: A review. *Mater. Sci. Eng. C.***2017**;71. doi:10.1016/j.msec.2016.10.014

144. Teo AJT, Mishra A, Park I, Kim YJ, Park WT, Yoon YJ. Polymeric Biomaterials for Medical Implants and Devices. *ACS Biomater Sci Eng*. **2016**;2(4). doi:10.1021/acsbiomaterials.5b00429

145. Yang Z, Yin G, Sun S, Xu P. Medical applications and prospects of polylactic acid materials. *iScience*.*Elsevier Inc.* **2024;**27(12). doi:10.1016/j.isci.2024.111512

146. S S, R G AP, Bajaj G, et al. A review on the recent applications of synthetic biopolymers in 3D printing for biomedical applications. *J Mater Sci Mater Med*. **2023**;34(12). doi:10.1007/s10856-023-06765-9

147. Oleksy M, Dynarowicz K, Aebisher D. Advances in Biodegradable Polymers and Biomaterials for Medical Applications—A Review. *Molecules*. **2023**;28(17). doi:10.3390/molecules28176213

148. Rezwan K, Chen QZ, Blaker JJ, Boccaccini AR. Biodegradable and bioactive porous polymer/inorganic composite scaffolds for bone tissue engineering. *Biomaterials*. **2006**;27(18). doi:10.1016/j.biomaterials.2006.01.039

149. Patel A, Mequanint K. Hydrogel Biomaterials. *BMEF*. **2011**. doi:10.5772/24856

150. Yuk H, Lu B, Zhao X. Hydrogel bioelectronics. *Chem Soc Rev*. **2019**;48(6). doi:10.1039/c8cs00595h

151. Wahane ARoyA, Karankal S, Sharma P, et al. Pharmaceutical Aspects on the Formulations of Hydrogel: An Update. *RJPDFT*. **2018**;10(2). doi:10.5958/0975-4377.2018.00012.5

152. Jin GZ, Kim HW. Effects of Type I Collagen Concentration in Hydrogel on the Growth and Phenotypic Expression of Rat Chondrocytes. *Tissue Eng Regen Med*. **2017**;14(4). doi:10.1007/s13770-017-0060-3

153. Wu S, Xu R, Duan B, Jiang P. Three-dimensional hyaluronic acid hydrogel-based models for in vitro human iPSC-derived NPC culture and differentiation. *J Mater Chem B*. **2017**;5(21). doi:10.1039/c7tb00721c

154. Heo DN, Hospodiuk M, Ozbolat IT. Synergistic interplay between human MSCs and HUVECs in 3D spheroids laden in collagen/fibrin hydrogels for bone tissue engineering. *Acta Biomater*. **2019**;95. doi:10.1016/j.actbio.2019.02.046

155. Hunt NC, Hallam D, Karimi A, et al. 3D culture of human pluripotent stem cells in RGD-alginate hydrogel improves retinal tissue development. *Acta Biomater*. **2017**;49. doi:10.1016/j.actbio.2016.11.016

156. Ho TC, Chang CC, Chan HP, et al. Hydrogels: Properties and Applications in Biomedicine. *Molecules*. **2022**;27(9). doi:10.3390/molecules27092902

157. Sgambato A, Cipolla L, Russo L. Bioresponsive hydrogels: Chemical strategies and perspectives in tissue engineering. *Gels*. **2016**;2(4). doi:10.3390/gels2040028

158. Qing W, Xing X, Feng D, Chen R, Liu Z. Indocyanine green loaded pH-responsive bortezomib supramolecular hydrogel for synergistic chemo-photothermal/photodynamic colorectal cancer therapy. *Photodiagnosis Photodyn Ther*. **2021**;36. doi:10.1016/j.pdpdt.2021.102521

159. Ghani M, Heiskanen A, Thomsen P, Alm M, Emnéus J. Molecular-Gated Drug Delivery Systems Using Light-Triggered Hydrophobic-to-Hydrophilic Switches. *ACS Appl Bio Mater*. **2021**;4(2). doi:10.1021/acsabm.0c01458

160. Abedi F, Davaran S, Hekmati M, Akbarzadeh A, Baradaran B, Moghaddam SV. An improved method in fabrication of smart dual-responsive nanogels for controlled release of doxorubicin and curcumin in HT-29 colon cancer cells. *J Nanobiotechnology*. **2021**;19(1). doi:10.1186/s12951-020-00764-6

161. Liang Y, He J, Guo B. Functional Hydrogels as Wound Dressing to Enhance Wound Healing. *ACS Nano*. **2021**;15(8). doi:10.1021/acsnano.1c04206

162. Ding C, Tian M, Feng R, Dang Y, Zhang M. Novel Self-Healing Hydrogel with Injectable, pH-Responsive, Strain-Sensitive, Promoting Wound-Healing, and Hemostatic Properties Based on Collagen and Chitosan. *ACS Biomater Sci Eng*. **2020**;6(7). doi:10.1021/acsbiomaterials.0c00588

163. Ying H, Zhou J, Wang M, et al. In situ formed collagen-hyaluronic acid hydrogel as biomimetic dressing for promoting spontaneous wound healing. *Mater. Sci. Eng. C.***2019**;101. doi:10.1016/j.msec.2019.03.093

164. Zhao Y, Song S, Ren X, Zhang J, Lin Q, Zhao Y. Supramolecular Adhesive Hydrogels for Tissue Engineering Applications. *Chem Rev*. **2022**;122(6). doi:10.1021/acs.chemrev.1c00815

165. Bordini EAF, Ferreira JA, Dubey N, et al. Injectable Multifunctional Drug Delivery System for Hard Tissue Regeneration under Inflammatory Microenvironments. *ACS Appl Bio Mater*. **2021**;4(9). doi:10.1021/acsabm.1c00620

166. Palacio MLB, Bhushan B. Research article: Bioadhesion: A review of concepts and applications. *PHILOS T R SOC A or Phil. Trans. R. Soc. A*. **2012**;370(1967). doi:10.1098/rsta.2011.0483

167. Saha N, Saha N, Sáha T, et al. Polymer based bioadhesive biomaterials for medical application—a perspective of redefining healthcare system management. *Polymers*. **2020**;12(12). doi:10.3390/polym12123015

168. Teng D. From chitin to chitosan. In: *Chitosan-Based Hydrogels: Functions and Applications*. **2016**. doi:10.1201/b11048-2

169. Ferguson J, Nürnberger S, Redl H. Fibrin: The Very First Biomimetic Glue — Still a Great Tool. In: *Biological Adhesive Systems*. **2010**. doi:10.1007/978-3-7091-0286-2_15

170. Pandey A, Singh MK, Singh A. Bacterial cellulose: A smart biomaterial for biomedical applications. *J Mater Res*. **2024**;39(1). doi:10.1557/s43578-023-01116-4

171. Avsar G, Agirbasli D, Agirbasli MA, Gunduz O, Oner ET. Levan based fibrous scaffolds electrospun via co-axial and single-needle techniques for tissue engineering applications. *Carbohydr Polym*. **2018**;193. doi:10.1016/j.carbpol.2018.03.075

172. Erginer M, Akcay A, Coskunkan B, et al. Sulfated levan from Halomonas smyrnensis as a bioactive, heparin-mimetic glycan for cardiac tissue engineering applications. *Carbohydr Polym*. **2016**;149. doi:10.1016/j.carbpol.2016.04.092

173. Smith AM. *Biological Adhesives, Second Edition*.**2016**. doi:10.1007/978-3-319-46082-6

174. Vrabič Brodnjak U. Influence of ultrasonic treatment on properties of bio-based coated paper. *Prog Org Coat*. **2017**;103. doi:10.1016/j.porgcoat.2016.10.023

175. Lozano-Navarro JI, Díaz-Zavala NP, Velasco-Santos C, et al. Chitosan-starch films with natural extracts: Physical, chemical, morphological and thermal properties. *Materials*. **2018**;11(1). doi:10.3390/ma11010120

176. Torres F, Commeaux S, Troncoso O. Biocompatibility of Bacterial Cellulose Based Biomaterials. *J Funct Biomater*. **2012**;3(4). doi:10.3390/jfb3040864

177. Öner ET, Hernández L, Combie J. Review of Levan polysaccharide: From a century of past experiences to future prospects. *Biotechnol Adv*. **2016**;34(5). doi:10.1016/j.biotechadv.2016.05.002

178. Sezer AD, Kazak Sarılmışer H, Rayaman E, Çevikbaş A, Öner ET, Akbuğa J. Development and characterization of vancomycin-loaded levan-based microparticular system for drug delivery. *Pharm Dev Technol*. **2017**;22(5). doi:10.3109/10837450.2015.1116564

179. Nürnberger S, Wolbank S, Peterbauer-Scherb A, et al. Properties and Potential Alternative Applications of Fibrin Glue. In: *Biological Adhesive Systems*. **2010**. doi:10.1007/978-3-7091-0286-2_16

180. von Byern J, Mebs D, Heiss E, et al. Salamanders on the bench – A biocompatibility study of salamander skin secretions in cell cultures. *Toxicon*. **2017**;135. doi:10.1016/j.toxicon.2017.05.021

181. Minervini G, Franco R, Marrapodi MM, Di Blasio M, Cicciù M, Ronsivalle V. The effectiveness of chitosan as a hemostatic in dentistry in patients with antiplatelet/anticoagulant therapy: systematic review with meta-analysis. *BMC Oral Health*. **2024**;24(1). doi:10.1186/s12903-023-03568-w

182. Cassano R, Perri P, Scarcello E, et al. Chitosan Hemostatic Dressings: Properties and Surgical Applications. *Polymers*. **2024**;16(13). doi:10.3390/polym16131770

183. Osman A, Oner ET, Eroglu MS. Novel levan and pNIPA temperature sensitive hydrogels for 5-ASA controlled release. *Carbohydr Polym*. **2017**;165. doi:10.1016/j.carbpol.2017.01.097

184. Sezer AD, Kazak H, Öner ET, Akbua J. Levan-based nanocarrier system for peptide and protein drug delivery: Optimization and influence of experimental parameters on the nanoparticle characteristics. *Carbohydr Polym*. **2011**;84(1). doi:10.1016/j.carbpol.2010.11.046

185. Ji Y, Ji T, Liang K, Zhu L. Mussel-inspired soft-tissue adhesive based on poly(diol citrate) with catechol functionality. *J Mater Sci Mater Med*. **2016**;27(2). doi:10.1007/s10856-015-5649-2

186. Hennig K, Meyer W. Synthesis and Characterization of Catechol-Containing Polyacrylamides with Adhesive Properties. *Molecules*. **2022**;27(13). doi:10.3390/molecules27134027

187. Anand PP, Vardhanan YS. Computational modelling of wet adhesive mussel foot proteins (Bivalvia): Insights into the evolutionary convolution in diverse perspectives. *Sci Rep*. **2020**;10(1). doi:10.1038/s41598-020-59169-y

188. Corral-Nájera K, Chauhan G, Serna-Saldívar SO, Martínez-Chapa SO, Aeinehvand MM. Polymeric and biological membranes for organ-on-a-chip devices. *Microsyst Nanoeng*. **2023**;9(1). doi:10.1038/s41378-023-00579-z

189. Delon LC, Guo Z, Oszmiana A, et al. A systematic investigation of the effect of the fluid shear stress on Caco-2 cells towards the optimization of epithelial organ-on-chip models. *Biomaterials*. **2019**;225. doi:10.1016/j.biomaterials.2019.119521

190. Fadilah NIM, Isa ILM, Zaman WSWK, Tabata Y, Fauzi MB. The Effect of Nanoparticle-Incorporated Natural-Based Biomaterials towards Cells on Activated Pathways: A Systematic Review. *Polymers*. **2022**;14(3). doi:10.3390/polym14030476

191. Cojocaru FD, Botezat D, Gardikiotis I, et al. Nanomaterials designed for antiviral drug delivery transport across biological barriers. *Pharmaceutics*. **2020**;12(2). doi:10.3390/pharmaceutics12020171

192. Nasir A, Kausar A, Younus A. A Review on Preparation, Properties and Applications of Polymeric Nanoparticle-Based Materials. *Polym.-Plast. Technol. Eng.*. **2015**;54(4). doi:10.1080/03602559.2014.958780

193. Yang R, Zheng Y, Wang Q, Zhao L. Curcumin-loaded chitosan–bovine serum albumin nanoparticles potentially enhanced Aβ 42 phagocytosis and modulated macrophage polarization in Alzheimer's disease. *Nanoscale Res Lett*. **2018**;13. doi:10.1186/s11671-018-2759-z

194. Mondal D, Griffith M, Venkatraman SS. Polycaprolactone-based biomaterials for tissue engineering and drug delivery: Current scenario and challenges. *Int. J. Polym. Mater. Polym. Biomater.* **2016**;65(5). doi:10.1080/00914037.2015.1103241

195. Masood F. Polymeric nanoparticles for targeted drug delivery system for cancer therapy. *Mater. Sci. Eng. C.***2016**;60. doi:10.1016/j.msec.2015.11.067

196. Feng H, Lu X, Wang W, Kang NG, Mays JW. Block copolymers: Synthesis, self-assembly, and applications. *Polymers*. **2017**;9(10). doi:10.3390/polym9100494

197. Mallamace F, Beneduci R, Gambadauro P, Lombardo D, Chen SH. Glass and percolation transitions in dense attractive micellar system. In: *Physica A: Statistical Mechanics and Its Applications*. Vol 302. **2001**. doi:10.1016/S0378-4371(01)00465-4

198. Lombardo D, Calandra P, Barreca D, Magazù S, Kiselev MA. Soft interaction in liposome nanocarriers for therapeutic drug delivery. *Nanomaterials*. **2016**;6(7). doi:10.3390/nano6070125

199. Salehi B, Calina D, Docea AO, et al. Curcumin's nanomedicine formulations for therapeutic application in neurological diseases. *J Clin Med*. **2020**;9(2). doi:10.3390/jcm9020430

200. Olguín Y, Campos C, Catalán J, et al. Effects of liposomes contained in thermosensitive hydrogels as biomaterials useful in neural tissue engineering. *Materials*. **2017**;10(10). doi:10.3390/ma10101122

201. Santos A, Veiga F, Figueiras A. Dendrimers as pharmaceutical excipients: Synthesis, properties, toxicity and biomedical applications. *Materials*. **2020**;13(1). doi:10.3390/ma13010065

202. Mishra V, Bansal KK, Verma A, et al. Solid lipid nanoparticles: Emerging colloidal nano drug delivery systems. *Pharmaceutics*. **2018**;10(4). doi:10.3390/pharmaceutics10040191

203. Nemanashi M, Noh JH, Meijboom R. Dendrimers as alternative templates and pore-directing agents for the synthesis of micro- and mesoporous materials. *J Mater Sci*. **2018**;53(18). doi:10.1007/s10853-018-2527-6

204. Delgado-Pujol EJ, Martínez G, Casado-Jurado D, et al. Hydrogels and Nanogels: Pioneering the Future of Advanced Drug Delivery Systems. *Pharmaceutics*. **2025**;17(2). doi:10.3390/pharmaceutics17020215

205. Peressotti S, Koehl GE, Goding JA, Green RA. Self-Assembling Hydrogel Structures for Neural Tissue Repair. *ACS Biomater Sci Eng*. **2021**;7(9). doi:10.1021/acsbiomaterials.1c00030

206. Karnwal A, Kumar Sachan RS, Devgon I, et al. Gold Nanoparticles in Nanobiotechnology: From Synthesis to Biosensing Applications. *ACS Omega*. *American Chemical Society*. **2024**;9(28):29966-29982. doi:10.1021/acsomega.3c10352

207. Nayak AK, Rath SK, Subudhi U. Preparation of Stable Branched DNA Nanostructures: Process of Cooperative Self-Assembly. *J. Phys. Chem. B*. 2019;123(17). doi:10.1021/acs.jpcb.9b00353

208. Sharma A, Vaghasiya K, Verma RK, Yadav AB. DNA nanostructures: Chemistry, self-assembly, and applications. In: *Emerging Applications of Nanoparticles and Architectural Nanostructures: Current Prospects and Future Trends*. **2018**. doi:10.1016/B978-0-323-51254-1.00003-8

209. Li Z, Wang J, Li Y, Liu X, Yuan Q. Self-assembled DNA nanomaterials with highly programmed structures and functions. *Mater Chem Front*. **2018**;2(3). doi:10.1039/c7qm00434f

210. Halley PD, Patton RA, Chowdhury A, Byrd JC, Castro CE. Low-cost, simple, and scalable self-assembly of DNA origami nanostructures. *Nano Res*. **2019**;12(5). doi:10.1007/s12274-019-2384-x

211. Lim S, Choi YS, Kang DG, Song YH, Cha HJ. The adhesive properties of coacervated recombinant hybrid mussel adhesive proteins. *Biomaterials*. **2010**;31(13). doi:10.1016/j.biomaterials.2010.01.063

212. Feksa LR, Troian EA, Muller CD, Viegas F, Machado AB, Rech VC. Hydrogels for biomedical applications. *Nanostruct. Eng. Cells Tissues Organs.* **2018**. doi:10.1016/B978-0-12-813665-2.00011-9

213. Cascone S, Lamberti G. Hydrogel-based commercial products for biomedical applications: A review. *Int J Pharm*. **2020**;573. doi:10.1016/j.ijpharm.2019.118803

214. Lee BP, Dalsin JL, Messersmith PB. Synthesis and gelation of DOPA-modified poly(ethylene glycol) hydrogels. *Biomacromol.* **2002**;3(5). doi:10.1021/bm025546n

215. Lee BP, Chao CY, Nelson Nunalee F, Motan E, Shull KR, Messersmith PB. Rapid gel formation and adhesion in photocurable and biodegradable block copolymers with high DOPA content. *Macromolecules*. **2006**;39(5). doi:10.1021/ma0518959

216. Mehdizadeh M, Weng H, Gyawali D, Tang L, Yang J. Injectable citrate-based mussel-inspired tissue bioadhesives with high wet strength for sutureless wound closure. *Biomaterials*. **2012**;33(32). doi:10.1016/j.biomaterials.2012.07.055

217. Kim K, Shin M, Koh MY, et al. TAPE: A medical adhesive inspired by a ubiquitous compound in plants. *Adv Funct Mater*. **2015**;25(16). doi:10.1002/adfm.201500034

218. Fan H, Wang J, Zhang Q, Jin Z. Tannic acid-based multifunctional hydrogels with facile adjustable adhesion and cohesion contributed by polyphenol supramolecular chemistry. *ACS Omega*. **2017**;2(10). doi:10.1021/acsomega.7b01067

219. Chan Choi Y, Choi JS, Jung YJ, Cho YW. Human gelatin tissue-adhesive hydrogels prepared by enzyme-mediated biosynthesis of DOPA and Fe3+ ion crosslinking. *J Mater Chem B*. **2014**;2(2). doi:10.1039/c3tb20696c

220. Wong SHD, Deen GR, Bates JS, et al. Smart Skin-Adhesive Patches: From Design to Biomedical Applications. *Adv Funct Mater*. **2023**;33(14). doi:10.1002/adfm.202213560

221. Wilke P, Börner HG. Mussel-glue derived peptide-polymer conjugates to realize enzyme-activated antifouling coatings. *ACS Macro Lett*. **2012**;1(7). doi:10.1021/mz300258m

222. Kim M, Chung H. Photo-responsive bio-inspired adhesives: Facile control of adhesion strength: Via a photocleavable crosslinker. *Polym Chem*. **2017**;8(40). doi:10.1039/c7py01535f

223. White EM, Seppala JE, Rushworth PM, Ritchie BW, Sharma S, Locklin J. Switching the adhesive state of catecholic hydrogels using phototitration. *Macromol.* **2013**;46(22). doi:10.1021/ma401594z

224. Cui M, Wang X, An B, et al. Exploiting mammalian low-complexity domains for liquid-liquid phase separation–driven underwater adhesive coatings. *Sci Adv*. **2019**;5(8). doi:10.1126/sciadv.aax3155

225. Brannigan RP, Dove AP. Synthesis, properties and biomedical applications of hydrolytically degradable materials based on aliphatic polyesters and polycarbonates. *Biomater Sci*. **2017**;5(1). doi:10.1039/c6bm00584e

226. Park SA, Lee SH, Kim WD. Fabrication of porous polycaprolactone/hydroxyapatite (PCL/HA) blend scaffolds using a 3D plotting system for bone tissue engineering. *Bioprocess Biosyst Eng*. **2011**;34(4). doi:10.1007/s00449-010-0499-2

227. Zhang H, Bré LP, Zhao T, Zheng Y, Newland B, Wang W. Mussel-inspired hyperbranched poly(amino ester) polymer as strong wet tissue adhesive. *Biomaterials*. **2014**;35(2). doi:10.1016/j.biomaterials.2013.10.017

228. Madhurakkat Perikamana SK, Lee J, Lee Y Bin, et al. Materials from Mussel-Inspired Chemistry for Cell and Tissue Engineering Applications. *Biomacromol.* **2015**;16(9). doi:10.1021/acs.biomac.5b00852

229. Tsai WB, Chen WT, Chien HW, Kuo WH, Wang MJ. Poly(dopamine) coating to biodegradable polymers for bone tissue engineering. *J Biomater Appl*. **2014**;28(6). doi:10.1177/0885328213483842

230. Li Y, Shi Y, Duan S, et al. Electrospun biodegradable polyorganophosphazene fibrous matrix with poly(dopamine) coating for bone regeneration. *J Biomed Mater Res A*. **2014**;102(11). doi:10.1002/jbm.a.35065

5.7. Annexes

5.7.1. Conceptual Explanations

5.7.1.1. Advanced Biomaterials

Advanced biomaterials are synthetic materials which have been designed to induce a specific biological activity. The biggest difference with other materials is that biomaterials have the characteristic of staying in a biological environment without damaging the surrounding tissues and without being damaged themselves in the process.[138] For example, the polifeporsan 20 polymeric network of Gliadel® wafers can be considered a biomaterial.[33]

5.7.1.1.1. Key Characteristic Advantages of Advanced Biomaterials

Biocompatibility. A biomaterial is a synthetic material used to replace a part of a living system or to function in intimate contact with living tissue. Biomaterials are designed to interact safely with biological systems, minimising adverse reactions such as toxicity, inflammation, or immune response, assuring compatibility and acceptance by the body.[34]

Biofunctionality. Biomaterials are often designed with the role, not only to be biocompatible, but also to interact with biological systems to perform specific functions actively. Such materials not only provide passive structural support but also contribute to specific biological processes, including tissue regeneration, targeted drug delivery, antimicrobial activity, and biosensing.[35,36,139]

Customisability. Biomaterial devices utilise customised material chemistry, fabrication, bioactive components, and patient-specific data to treat diseases or injuries tailored to a patient's individual needs. Such properties can target porosity, surface chemistry, mechanical strength, and degradation rate.[38]

Stimuli-Responsiveness. Stimuli-responsive materials undergo triggered changes when presented with specific environmental cues. Such behaviour can leverage biological signals found within their immediate environment, or external responsiveness, to provide specific stimuli-dependent activation.[39] Such materials encompass a wide range of external signals, including pH, oxidative species, specific enzymes and biomolecules, photostimulation, electrical stimulation, ultrasound activation, magnetic field stimulation, mechanical stimulation, ionic concentration response, specific immune environment response, and piezoelectricity response.[40,41,43,44]

5.7.1.1.2. Applications of Advanced Biomaterials

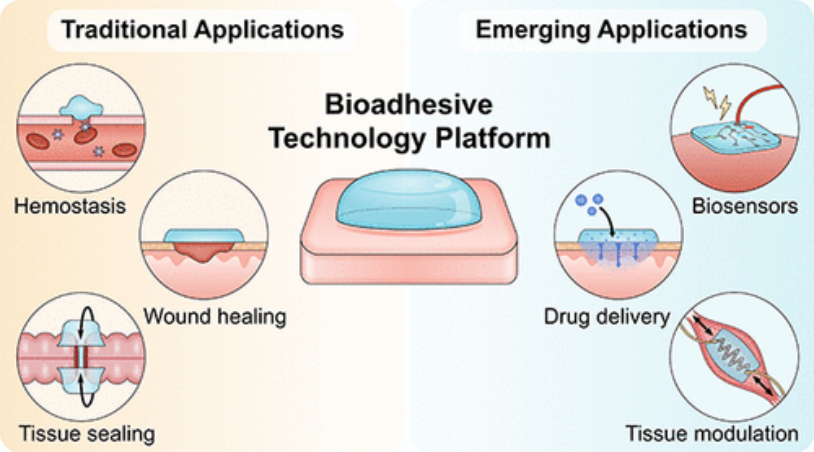
Biomaterials have a profound impact on human healthcare and have received considerable attention in the development of medical devices, diagnostic sensors, tissue engineering and, more importantly, drug delivery systems.138 Examples of such applications include;

Cardiovascular medical devices, such as bioresorbable stents, are now clinically common.[46]

Extracorporeal artificial organs, examples of which are numerous, can range from cardiopulmonary, cardiac, neuromuscular, pancreatic, orthopaedic, colorectal, to renal support.[47]

Tissue engineering devices, like the Integra dermal regeneration template, a porous bovine collagen scaffold crosslinked with chondroitin-6-sulphate, are used for treating burns and other acute wounds.[140]

Bioadhesives, which have found applications as homeostatic bioadhesives, wound dressings, tissue sealants, chemical biosensors, and, more relevant to our research, drug delivery (Annexe **5.1**).[49]



Annexe 5.1. Bioadhesive applications as a platform, as reported by Sarah et al.[49]

5.7.1.2. Types of Advanced Biomaterials

In general, biomaterials can be classified into three classical types (metallic, ceramic, polymeric) with the recent addition of three innovative ones (nanomaterials, bioadhesives, and hydrogels).

5.7.1.2.1. Metallic Biomaterials

As the name suggests, these are metal-based materials, with titanium and its alloys being the most commonly used, as well as chromium, cobalt, and stainless steel. In addition to the metals listed, the use of biodegradable metals, such as iron, zinc, and magnesium, is under evaluation for temporary implants, which naturally degrade in the body after their function has been completed.[141]

5.7.1.2.2. Ceramic Biomaterials

Ceramic biomaterials have become increasingly more important due to their biocompatibility, high resistance to corrosion and compression, and low thermal and electrical conductivity. Initially available only as a powder and used as fillers, it was later discovered that these materials promoted bone regeneration when hydroxyapatite or tricalcium phosphate was included in their composition. Less dense than metals, they are hard, brittle and with minimal plastic deformation.[142]

5.7.1.2.3. Polymeric Biomaterials

Polymeric biomaterials used in medical applications encompass a wide variety of both biodegradable and non-biodegradable materials.

Non-degradable polymers, which include polyethylene, polypropylene, polyurethane, polyamide, polytetrafluoroethylene, polymethylmethacrylate, polyethylene terephthalate,

synthetic rubbers, polystyrene, and polyetheretherketone. These materials are valued in long-term implants and devices—such as joint replacements, vascular grafts, intraocular lenses, and catheters—due to their mechanical strength, chemical resistance, and biostability.[143,144]

Biodegradable polymers, on the other hand, can be grouped into:[143]

- Natural-based materials, such as polysaccharides (i.e., chitosan, alginate, and hyaluronic acid) and proteins (i.e., collagen, gelatine, and fibrin), are known for their biocompatibility.
- Synthetic biodegradable polyesters, including PLA, polyglycolide (PGA), poly(lactic-co-glycolic acid) (PLGA), and polycaprolactone (PCL), which offer tuneable degradation rates and broad use in drug delivery, tissue engineering scaffolds, and controlled-release implants.[145,146]

Contemporary classifications recognise materials by both origin (natural, synthetic, or semi-synthetic) and degradability (degradable vs. non-degradable). Biodegradable synthetic polymers have gained importance because they naturally resorb without secondary surgery once their function, such as supporting tissue regeneration or controlled drug release, is complete.[147,148]

The following three biomaterials can be classified into the categories mentioned previously. However, they have recently gained enough traction and been specialised enough to be differentiated into their own categories.

5.7.1.2.4. Hydrogel Biomaterials

Hydrogel biomaterials are three-dimensional materials that can absorb large amounts of water while maintaining their stability.[149] Such materials are constituted by an array of crosslinking polymers that allow them to maintain their physical and chemical properties in the presence of water.[150]

Such polymers consist of hydrophilic polymeric chains that, unless crosslinked, would otherwise dissolve and lose structural integrity. Such phenomena allow polymers to swell and absorb water, water-soluble drugs, enzymes and similar substances.[151]

As such, most of the applications hydrogels have found are in:

3D cell cultures, in which cells are embedded in an extracellular matrix forming 3D scaffolds. Collagen,[152] hyaluronic acid,[153] fibrin,[154] and alginate[155] are the most usually natural sourced hydrogels[156].

Drug delivery, under this category, interest has been gained in stimuli-sensitive polymers that change mechanical properties, swelling capacity, hydrophilicity, or permeability of bioactive molecules, while achieving a sustained release over time. Examples of such include; thermoresponsive hydrogels,[157] pH-responsive hydrogels,[158] photo-responsive hydrogels,[159] and dual-response hydrogels.[160]

Wound dressing, such application comes from the ability of hydrogels to provide a moist environment to promote the process of wound healing, while providing an injectable/sprayable material that can fill irregularly shaped wounds.[156] Such hydrogels can present high-performing

biological activities such as antibacterial properties, promoting blood coagulation, or blood regeneration.[161–163]

Tissue engineering, such application focuses on the treatment of patients suffering from failure and irreparable tissue destruction.[164] The objective of tissue engineering consists of developing a scaffold that mimics *in vivo* extracellular matrix to support tissue regeneration. An example of such can be observed from reports of Bordini e*t al.* who reports on Dex-loaded nanotube-modified gelatine hydrogel that induced bone regeneration in inflammatory microenvironments.[165]

5.7.1.2.5. Bioadhesives Biomaterials

Consists of natural or synthetic polymeric materials that have been designed to optimise and potentiate adhesion to biological surfaces like tissues, mucous membranes or cells through the use of interfacial forces. Such interactions are based on nonspecific interactions like hydrogen bonding, electrostatic forces, mechanical interlocking, and specific ones like covalent bonding.[166,167] Bioadhesives have the benefit over classical adhesives used in medicinal practices of benefiting from; i) Enhanced biocompatibility, reducing immune rejection,[168,169] ii) Inherent biodegradability,[170] and iii) Chemical versatility and adaptability to work in wet and dry environments while allowing for use-specific modifications.[171–173]

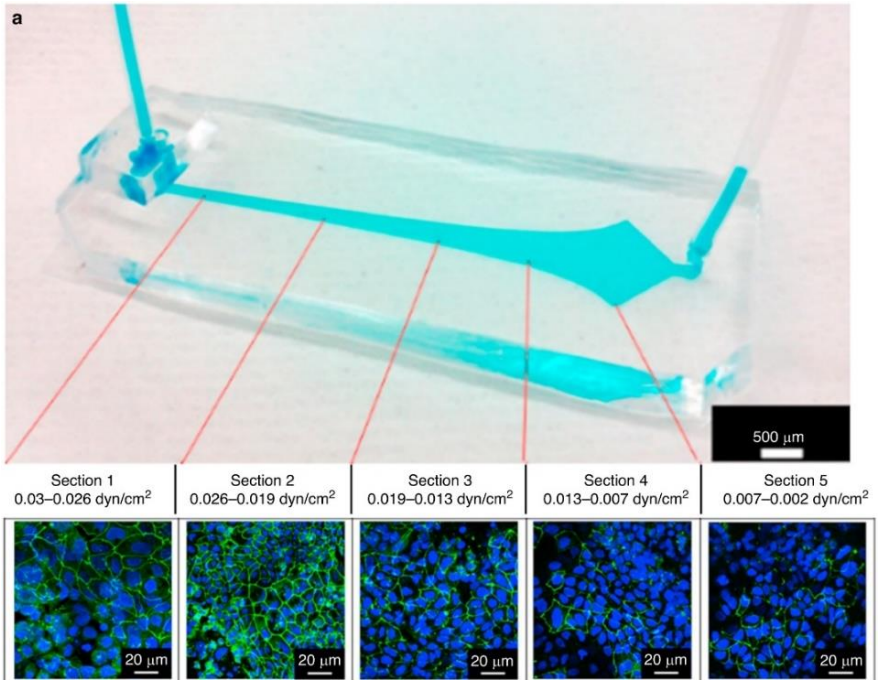
Bioadhesives are generally classified by their scaffold structure components; as such, they can either be considered; i) Polysaccharide-based, like chitosan, bacterial cellulose, or levan,[174–178] and ii) Protein-based, like fibrin, or mussel adhesive proteins.[169,173,179,180]

Bioadhesives have found their way in applications like:

Wound healing and haemostasis, with examples ranging from chitosan-based materials displaying antimicrobial activity to promote wound closure through TFs and coatings with commercial products like Axiostat® and HemCon™[181,182] to fibrin-based adhesives used as homeostatic sealants thanks to their biocompatibility and importance in blood clotting.[169,179] Bacterial cellulose has also found use in scaffolds for bone, skin and cardiovascular tissue engineering.[176]

Drug delivery systems with examples from levan-controlled temperature release of 5-aminosalicylic acid via stimuli-responsive bioadhesive and as a carrier for peptide/protein,[178,183,184] and chitosan formulations used in nasal, gastrointestinal, and ocular drug delivery.[168]

Surgical and implantable devices, like mussel adhesive proteins that exhibit strong wet adhesion and have been used in tissue sealing and implantable chip-membrane inserts using catecholic DOPA monomer units.[185–188]



Annexe 5.2. An organ-on-chip developed by Delon et al. to investigate the effect of fluid shear stress on Caco-2 intestinal epithelial cells.[189]

5.7.1.2.6. Nanomaterials Biomaterials

Nanomaterials compress components or structures that range in the nanoscale, at which point such components demonstrate dramatically new and unique properties attributable to their size scale.[190] As such, the biomaterials mentioned above can be defined as nanomaterials if their size scale accommodates such a definition. NPs are not a new topic of research, and neither are nanomaterials based on biomaterials. Uses for such a system are varied and plentiful, some examples, although not limited to, are:

Drug delivery. Nanomaterials enable the protection of cargo from degradation/interaction with biomolecules in the body, while also benefiting from the EPR effect. This effect is further enhanced by the high surface-to-volume ratio that these systems present, allowing for increased targeting through surface modifications.[191] Biosynthetic polymers and natural polymers, such as PLA, PGA, chitosan, and dextran, have been used to increase drug release, enhance bioavailability, and reduce toxicity in anticancer, anti-inflammatory, and antimicrobial settings.[192–195] Amphiphilic block copolymers made from PEG-PLA copolymers have been utilised in micelles, polymerosomes, and hydrogels for the encapsulation of drugs, aiming to achieve sustained release and targeted delivery.[196,197] Liposomes and solid lipid NPs have also been used to improve drug solubility, BBB penetration, and tumour targeting.[198–200] And finally, dendrimers made from polyamidomine have been utilised for gene therapy and drug delivery.[201–203]

Tissue regeneration. As explained before, in hydrogels, nano-sized hydrogels, or nanogels, can be used to promote wound healing and closing. Stimuli-responsive nanogels have been developed in these platforms, made from chitosan, which mimics extracellular matrices and supports cell proliferation and tissue regeneration.[204] Also, self-assembled nanofibers mimicking peptide amphiphiles have been used to create bioactive scaffolds for neural and soft tissue regeneration.[205]

Biosensing. High surface-to-volume ratio, multifunctionality of such platforms, enhanced stability and biocompatibility, and controlled surface chemistry have allowed NPs to benefit from an amplitude of attention in the biosensing field.[206] For example, DNA/RNA-functionalised nanostructures have enabled ultrasensitive biomarker detection, like microRNA and molecular lithography with DNA-based photodetectors, achieving attomole detection limits.[207–210]

5.7.1.3. Examples of DOPA-Containing Biomaterials in Biomedical Applications

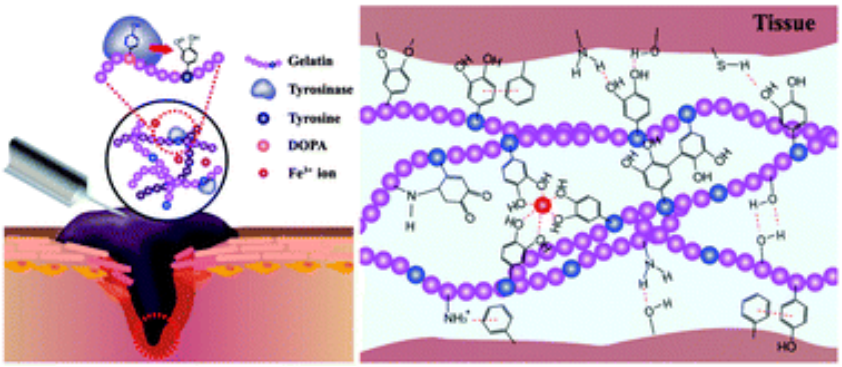
As expected, DOPA-containing adhesives, due to their excellent biocompatibility and strong adhesion properties to multiple substrates, have received considerable research and applications. To which we will briefly mention some examples in biomedical applications.

5.7.1.3.1. DOPA-Containing Adhesives

When it comes to DOPA-containing adhesives, microencapsulation of hyaluronic acid in recombinant Mfps has been reported by Cha *et al., demonstrating* the ability of such systems to be used in drug delivery.[211]

5.7.1.3.2. DOPA-Containing Hydrogels

The highly water-swollen and 3D structural network of hydrogels allows hydrogels to possess structural resemblance to biological tissues and high permeability to oxygen and nutrients. As such, DOPA-based hydrogels have been designed as platforms widely used in drug delivery, tissue engineering, and implantable devices.[212,213] For example, PEG, one of the most widely-used synthetic polymers in the development of hydrogels due to its outstanding hydrophilicity and biocompatibility, have been used for the incorporation of DOPA or catechol functional groups as terminal groups in a family of PEG polymers with different structures by Messersmith *et al.* to generate a rapid gel-forming, photocurable, and biodegradable block copolymer.[214,215] Injectable bio-adhesives based on PEG, citrate, and DA have also been reported by Yang *et al.*, exhibiting strong adhesiveness to wet tissue surfaces. With the addition of hyaluronic acid, these hydrogels significantly enhanced both their mechanical strength and biomineralisation, promoting neovascularisation and bone formation.[216] Natural polyphenol tannic acid, which contains five pyrogallol and five catechol groups, has been used in the development of wet adhesives with homeostatic properties by simply mixing it with PEG solutions.[217] For example, Jin *et al.* has developed a tannic acid-based polyphenol hydrogel with cationic poly(dimethyl diallyl ammonium chloride) that boasted of both strong cohesion and adhesion.[218]

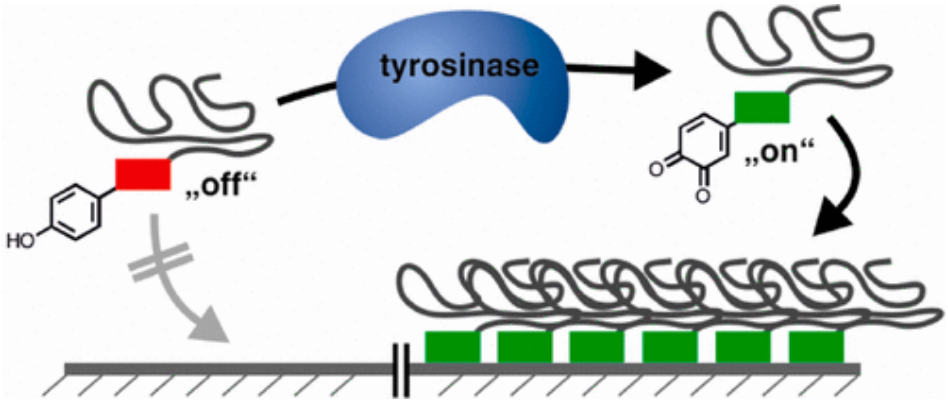


Annexe **5.3**. Schematic representation of a Dopa containing hydrogel as reported by Young *et al.*[219]

5.7.1.3.3. DOPA-Containing Smart Adhesives

Smart adhesives consist of adhesives that can undergo on-demand attachment/detachment to a surface in response to an external stimulus, such as temperature, pH, or light. Precise control over the adhesiveness formation has allowed such adhesives to benefit from a growing interest.[220]

Examples of such adhesives can be found in the work reported by Wilke *et al.*, who describe enzyme-activated adhesives based on Mfp-derived peptides containing tyrosine residues, with tyrosine dictating the on-off switching of the adhesive (Annexe **5.4**).[221] Zwitterionic hydrogels have also been developed by Kim *et al.* by combining catechol functionalised adhesives with o-nitrobenzyl.[222] Locklin *et al.* have also reported on carechol-Fe^{3+} complexation-based hydrogel adhesives doped with photo-acid generators, which, after exposure to UV light, acid production leads to a decrease in pH that weakens the adhesiveness of the material.[223] Chao *et al.* have also designed protein-based underwater adhesives inspired by recombinant DOPA-containing proteins that lead to phase separation induced by nanofiber formations.[224]



Annexe **5.4**. Turn-on effect of Mfp-derived peptides containing tyrosine residues by tyrosinase, as reported by Wilke *et al.*[221]

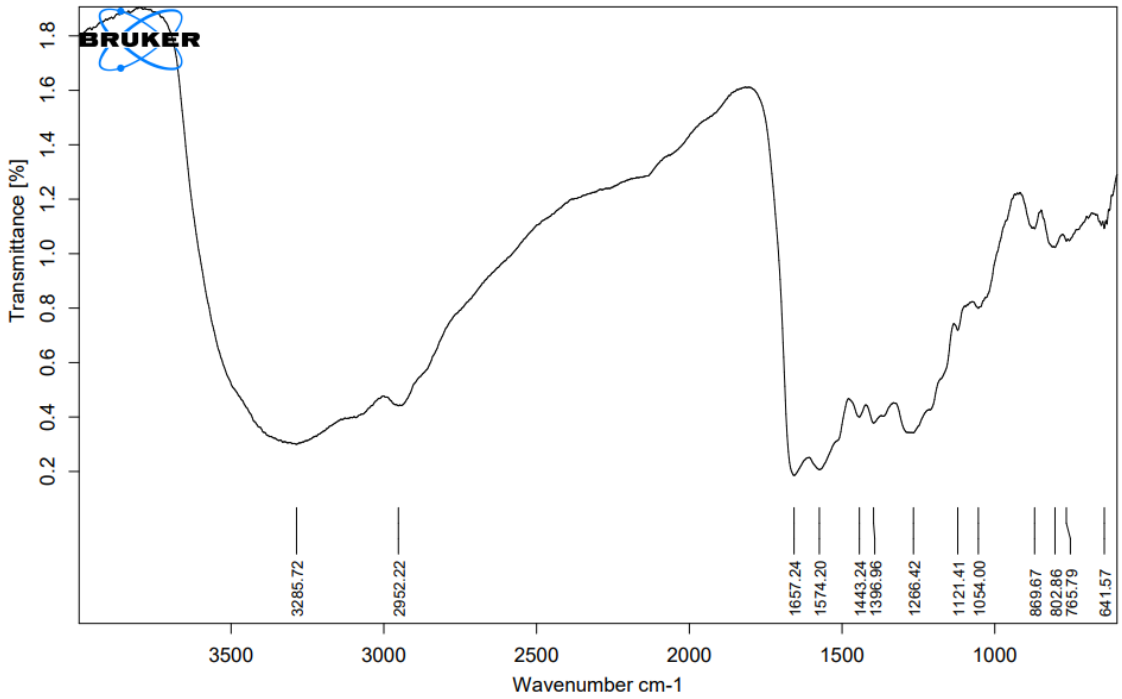
5.7.1.3.4. DOPA-Containing Adhesive Polyesters

Synthetic polyesters have received extensive applications in biomedical fields due to their good mechanical properties, ease of production, and controllable biodegradation.[225,226] The combination of biodegradable and biocompatible polyesters with DOPA derivatives have led to successful bone glues. For example, Wang *et al.* has reported on hyperbranched poly(β-amino esters) with DA monomers, obtained through Michael addition reactions, that demonstrated the nanocomposite was able to act as efficient bone adhesives for sternal closure.[227]

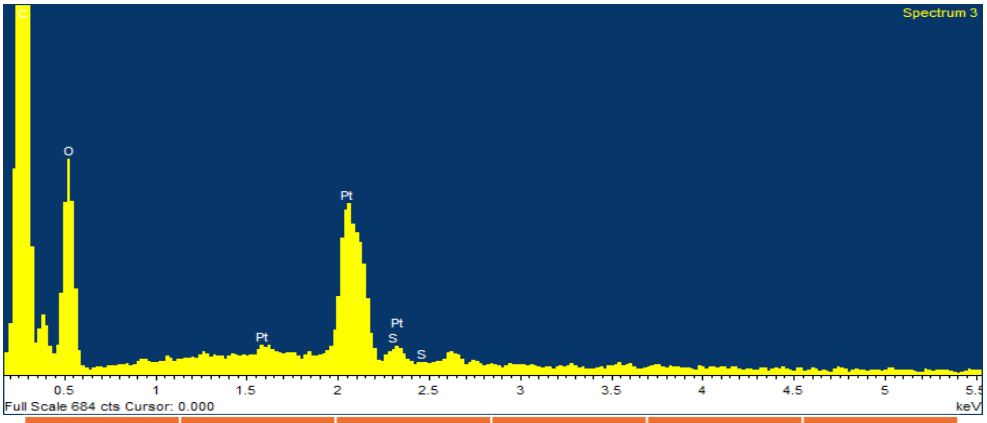
Aside from functionalisation of catechol groups into the backbone of the polyester, PDA deposition on polyester has also demonstrated a convenient way to develop adhesive scaffolds and patches.[228] For example, PDA coatings on top of biodegradable poly(Ɛ-caprolactone), poly(lactic-*co*-glycolic acid) and poly(alanine ethyl ester-co-glycine ethyl ester), or phosphazene have been shown to promote the mineralisation of bone tissue.[229,230]

5.7.2. Experimental Data

Characterisation of FSM-PtBC



Annexe **5.5**. FTIR of **FSM-PtBC**.

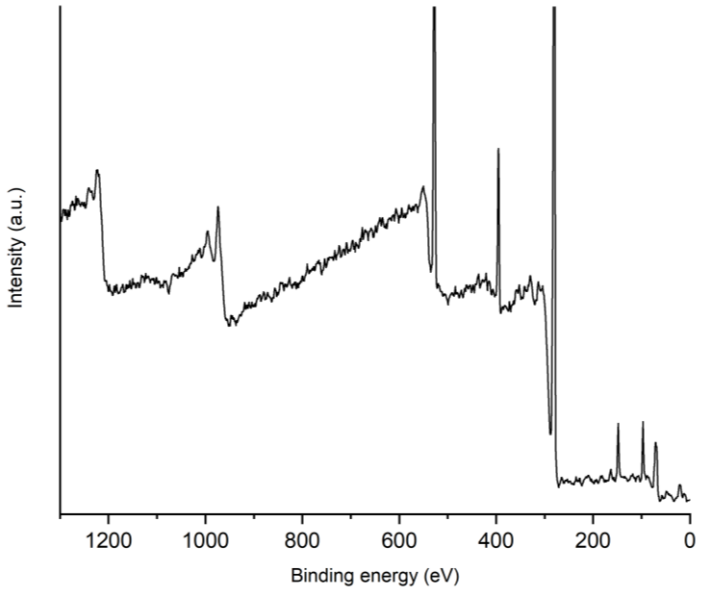


Element	C K	O K	S K	Pt M	Total
Weight (%)	59.71	17.05	0.85	22.39	100
Atomic (%)	80.46	17.25	0.43	1.86	100

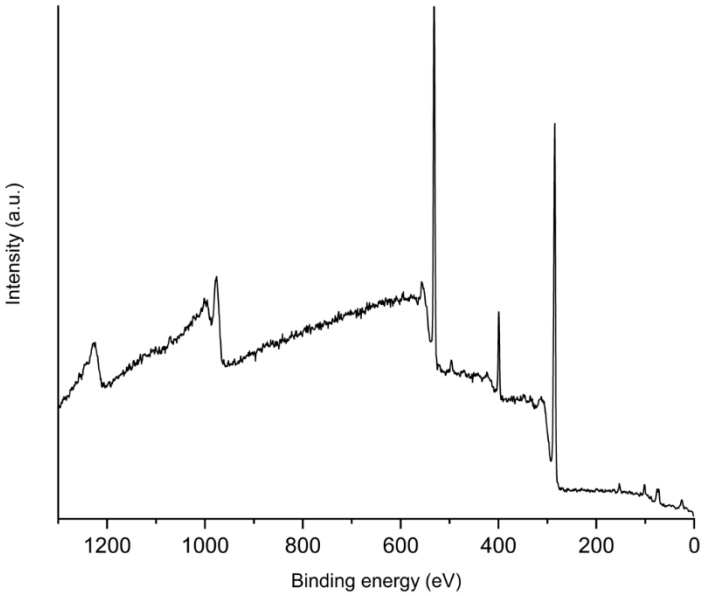
Annexe **5.6**. EDX of **FSM-PtBC**.

	Pt [He]	
Sample Name	Conc. [%]	Conc. RSD
RG4_57 dil2	9,38	0,5
RG4_57 dil1	9,90	0,6

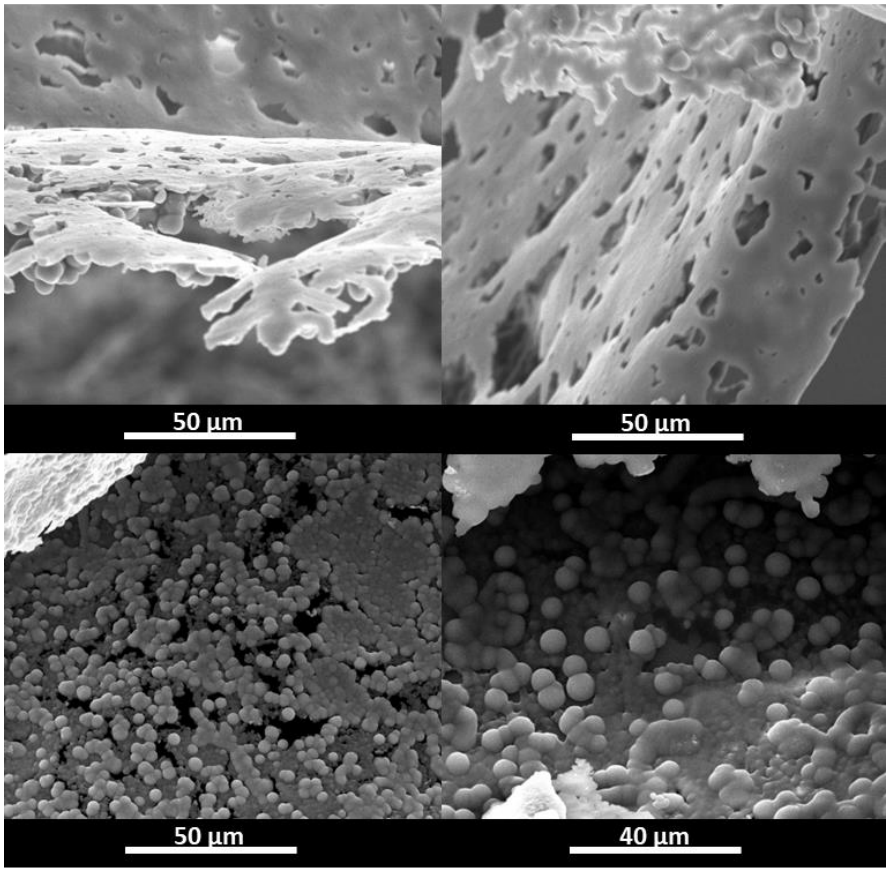
Annexe **5.7**. ICP-MS of Pt% in w/w in **FSM-PtBC** of two different batches of samples.



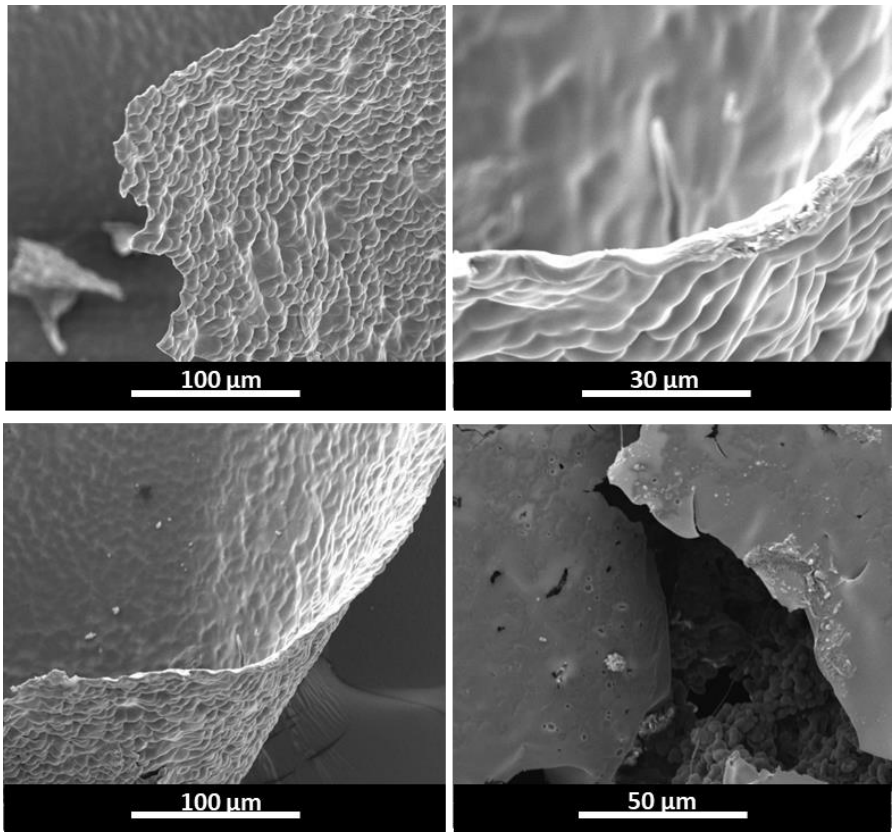
Annexe **5.8**. Full spectrum XPS measurements recorded at room temperature (298K) of **FSM-PtBC** pre-cell viability assays, the peaks corresponding to Si 2p and O 1s are due to the silicon substrates used for the deposition of the samples.



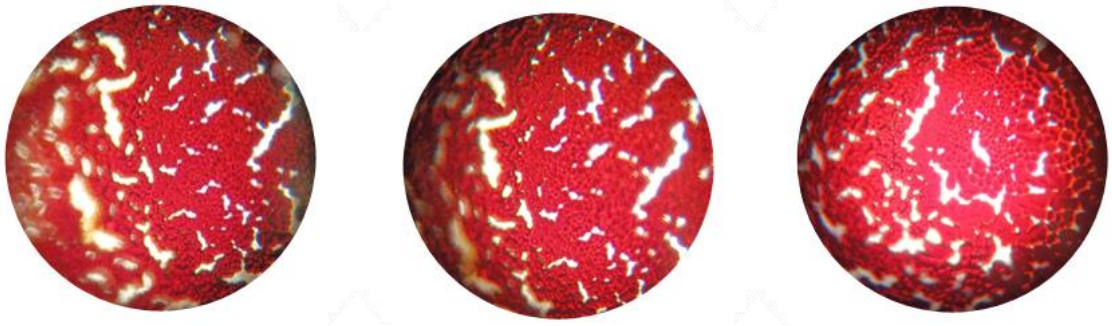
Annexe **5.9**. Full spectrum XPS measurements recorded at room temperature (298 K) of **FSM-PtBC** post-cell viability assays, the peaks corresponding to Si 2p and O 1s are due to the silicon substrates used for the deposition of the samples.



Annexe **5.10**. Representative SEM images of **FSM-PtBC** under a 5 nm Pt thin film coating for imaging.

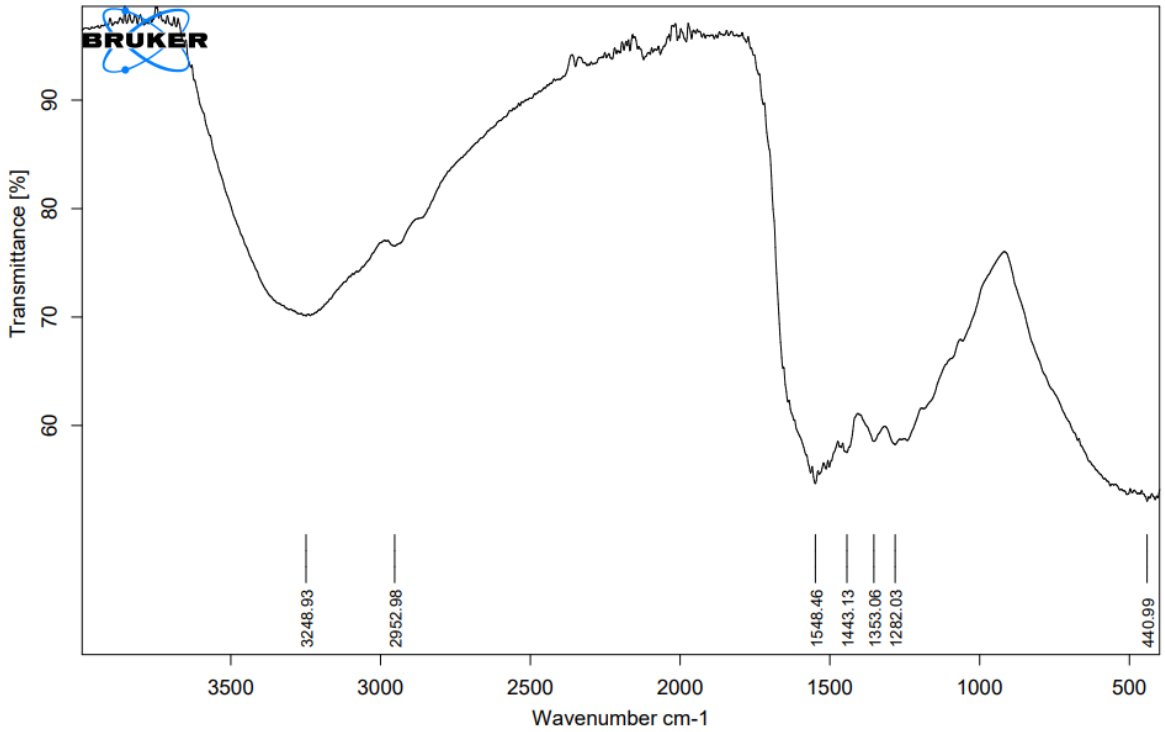


Annexe **5.11.** Representative SEM images of **FSM-PtBC** post cell viability assays under a 5 nm Pt thin film coating for imaging.

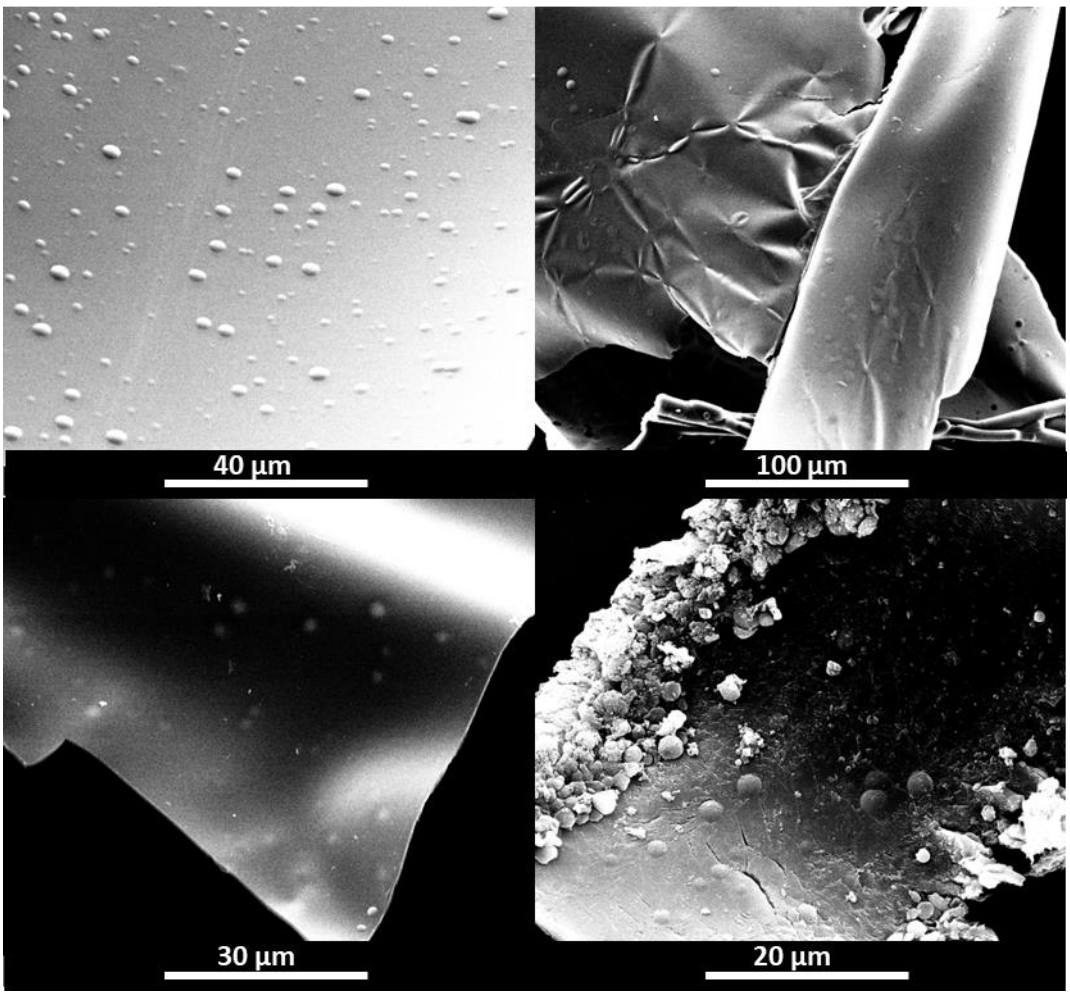


Annexe **5.12.** Representative optical microscope imaging of **FSM-PtBC** at x10 augmentations.

Characterisation of FSM-TrisCat



Annexe **5.13**. FTIR of **FSM-TrisCat.**



Annexe **5.14**. Representative SEM imaging of **FSM-TrisCat.**



Annexe **5.15.** Representative optical microscope imaging of **FSM-TrisCat** at x10 augmentations.

Chapter 6

General Conclusions

This Thesis has addressed the urgent need for novel therapeutic approaches in GBM. By combining Pt-based CT, ROS generation, MHT, and advanced bioinspired biomaterials, several platforms have been designed, synthesised, and evaluated to overcome the limitations of existing therapies.

1. **Bioinspired Neuromelanin-like Pt(IV) Polymeric Nanoparticles for Glioblastoma treatment:**
   - Pt(IV)-based NPs with neuromelanin-like chemistry (**pPtBC NPs**) were synthesised with controlled size, stability, and dual pH/redox responsiveness.
   - **pPtBC NPs** demonstrated efficient cellular uptake, sustained Pt release, and selective brain accumulation after intranasal delivery.
   - *In vitro* cytotoxicity of **PtBC** and **pPtBC NPs** displayed comparable activity against CDDP over longer periods of time.
   - *In vivo*, therapeutic efficacy in tumour-bearing mice was not significant, highlighting the challenge of translating *in vitro* performance and the IN administration route.

2. **Supramolecular Photoactivatable Squaraine Pt(II) Complex Nanoparticles:**
   - New squaraine ligand (**SQL**) and SQ Pt(II) complex (**SQC**) were successfully synthesised. Supramolecular based nanoplatforms **SQL NP** and **SQC NP** from the aforementioned molecules were also achieved.
   - **SQC NPs** displayed photoactivity and light triggered Pt release.
   - Although **SQC NPs** posed stability and synthetic challenges, **SQL NP** exhibited easy preparation and photodynamic activity.
   - **SQL NPs** displayed aggregation dependant ROS generation, confirming their value as photosensitizers for light-activated therapies, displaying a moderate PI at *in vitro* cytotoxicity and potential in PDT.

3. **Singlet Oxygen Storage and on-demand Magnetic Induced Release for a Multi-Approach therapy:**
   - Core-shell NP for a multifunctional treatment platform of GBM **pDPA-CNP@Fe NP**s, and shell-based coordination polymer for magnetically triggered anti-GBM **pDPA-CNP** were successfully prepared.
   - **pDPA-CNP@Fe NPs** displayed capable to store SO, magnetically release loaded SO via hyperthermia, and enhanced MRI T_{2w} contrast *in vitro*.
   - *In vivo* biodistribution and MRI assays displayed poor accumulation to the brain but selective targeting of **pDPA-CNP@Fe NPs** towards bladder, presenting alternative imaging applications in bladder. **pDPA-CNP@Fe NPs** also displayed excellent tolerability *in vivo*.
   - *In vitro* assays demonstrated **pDPA-CNP@Fe NPs** therapeutic activity against GBM through combined ROS and hyperthermia.
   - Combination of properties presented by **pDPA-CNP@Fe NPs** present this platform as a promising theragnostic agent for multimodal cancer treatment.
   - On the other hand, **pDPA-CNP** displayed enhanced magnetically triggered behaviour against GBM *in vitro*.

- *In vitro* assays of **pDPA-CNP** and **pDPA-CNP@Fe NPs** displayed strong cell membrane adhesion and indicated cell membrane damage as a result of such interaction. Furthermore **pDPA-CNP** displayed excellent *in vitro* biocompatibility under no magnetic stimulation.
- A combination of analytical techniques that encompassed powder, XRD, SEM, TEM, EDX, EELS, ICP, TGA and EA, paved a hypothesis towards the key role of zirconia formation and oxygen vacancies in the network as a key component in targeted cell membrane ROS generation as an explanation to cell death observed.
- The sum of the results accrued for **pDPA-CNP** hint towards excellent applications in GBM although further research in ROS generation is required.

Future Perspectives:

- Refine magnetic and coordination-polymer design to increase brain accumulation of **pDPA-CNP@Fe NPs**.
- Investigate applications of **pDPA-CNP@Fe NPs** in other tumour types where biodistribution is favourable (i.e., bladder) as potential theragnostic agent, from re-evaluating *in vitro* assays and cell culture models to *in vivo* MRI assays focussed on the target tissues.
- Evaluated magnetically triggered ROS generation of **pDPA-CNP**.
- Study *in vivo* preclinical models of **pDPA-CNP** for GBM treatment.

4. **Development of Bioinspired Catechol-Based Pt(IV) Free-Standing Membranes for Post-Surgery Glioblastoma Treatment:**
    - Flexible FSMs (**FSM-PtBC**) for local post-surgical CT were developed as a proof-of-concept approach to incorporate multitargeted cancer treatment to this platform.
    - **FSM-PtBC** displayed excellent structural integrity and drug release profiles in biological environments.
    - *In vitro* cell viability assays of **FSM-PtBC** displayed satisfactory cytotoxicity against cancer cell lines, especially murine GBM GL261 cell line, at 72-hour periods, while displaying reduced cytotoxicity against healthy 1Br3G fibroblasts.
    - The combination of Pt release profile, toxicity, and previous assays conducted for **PtBC** and **pPtBC**, indicate towards a sustained release of cytotoxic cargo and sustained therapeutic effect over long periods of time.
    - Preliminary studies were carried that indicate potential applicability of **FSM-PtBC** platform in combination therapy with PTT.

Future Perspectives:

- Evaluate *in vitro* ROS generation from ***FSM-PtBC.***
- Evaluate *in vivo* performance of **FSM-PtBC** in resection models.
- Explore integration with additional therapeutic modalities (i.e., PTT).

Summary and Closing Remarks

Overall, this Thesis demonstrates the potential of integrating Pt-based CT with bioinspired and multifunctional delivery systems. This approach enhances selectivity, minimizes systemic toxicity, and introduces multimodal therapeutic mechanisms in GBM treatment. Several approaches in this Thesis started with a targeted platform, but different challenges and opportunities prompted the development of what is reported in this work. As a result, several platforms achieved proof-of-concept validation at various stages of development.